Optimization of composite structures: A shape and topology sensitivity analysis

Gabriel Delgado

▶ To cite this version:

HAL Id: pastel-01005520

https://pastel.hal.science/pastel-01005520v2

Submitted on 24 Feb 2017
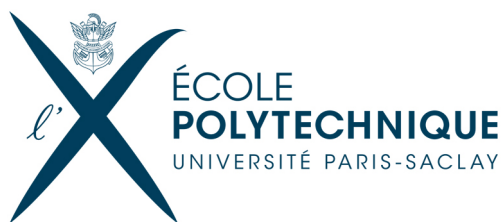
Thesis submitted to obtain the title of

Doctor of École Polytechnique

Specialty: APPLIED MATHEMATICS

Optimization of composite structures
A shape and topology sensitivity analysis

by

Gabriel DELGADO KEEFFE

under the supervision of

Grégoire ALLAIRE

defended publicly on 11 June 2014 in front of the jury composed of

Grégoire ALLAIRE	École Polytechnique	Thesis advisor
Samuel AMSTUTZ	Université d'Avignon	Reviewer
Marc BONNET	ENSTA Paritech	Examiner
Eric BONNETIER	Université Joseph Fourier	Reviewer
Marc DAMBRINE	Université de Pau et des Pays de l'Adour	Examiner
Eduard OUDET	Université Joseph Fourier	Examiner
Olivier PANTZ	École Polytechnique	Examiner
Vassili SRITHAMMAVANH	Airbus Group	Industrial advisor

Prepared at
Centre de Mathématiques Appliquées,
École Polytechnique, Palaiseau, France,
&
Airbus Group Innovations,
Suresnes, France.

Ce que nous connaissons est peu de chose, ce que nous ignorons est immense.
- Pierre Simon Laplace.

To my parents Lily and Carlos,
who have always encouraged me to go further.

In the loving memory of
my grandparents Jack and Nina,
and my great aunt Emily.

Remerciements

Le doctorat est une période de la vie riche en apprentissages, rencontres et je dirais même en aventures. Par le biais de ce bref paragraphe, je souhaiterais remercier tous ceux qui ont fait de ce "voyage" une expérience inoubliable.

Je tiens tout d'abord à remercier le directeur de cette thèse, Grégoire Allaire, pour m'avoir guidé, encouragé et conseillé durant ces années à travers son savoir encyclopédique et sa profonde intuition mathématique (qui s'avérait dans certaines circonstances presque mystique), tout en me laissant une grande liberté d'action. Au-delà de ses qualités d'encadrant et de chercheur, Grégoire a aussi été un maître exceptionnel, tant sur le plan technique qu'humain, montrant toujours beaucoup de respect et de patience envers ses collègues et étudiants. Pour moi, en tant que chilien, ce sera toujours un plaisir de discuter avec lui de deux de ses passions: les montagnes et le bon vin.

Mes remerciements vont également à Marc Bonnet, qui a été comme un deuxième directeur de thèse pour moi. Sans lui, je n'aurais jamais pu développer une partie importante de cette thèse. Accompagné de son caractère décontracté et chaleureux, Marc a toujours témoigné à mon égard un énorme intérêt pour mes problématiques de dérivée topologique, acceptant avec gentillesse et patience de partager ses extraordinaires connaissances en mécanique des solides et méthodes asymptotiques. Je me réjouis d'avoir eu l'honneur de travailler à ses côtés dans la préparation de deux articles.

Je souhaiterais aussi manifester ma gratitude à Olivier Pantz, qui a su me transmettre avec bienveillance ses connaissances arcanes sur Freefem++, ingrédient essentiel dans "la cuisine numérique" de cette thèse, ainsi que des notions de dérivée de forme discrète dans un cadre multiphasique.

En ce qui concerne l'encadrement industriel de ces travaux, je remercie Vasssili Srithammavanh qui m'a aidé à positionner le sujet de ma thèse au sein d'Airbus et qui a contribué par ses nombreuses remarques et suggestions à améliorer la qualité de cette thèse, toujours avec patience et bonne humeur. Je tiens également à exprimer ma gratitude à Stéphane Grihon, qui a proposé le sujet principal de ce travail: l'application de la mèthode de lignes de niveau à la conception des pièces composites. Ses remarques et son aperçu industriel ont été d'une grande utilité.

Je remercie Samuel Amstutz et Eric Bonnetier qui m'ont fait l'honneur d'accepter d'être les rapporteurs de cette thèse, de même que pour leur participation au Jury. Je suis également reconnaissant à Marc Dambrine et Edouard Oudet pour leur participation au Jury en tant qu'examinateurs.

Conscient d'avoir pu préparer cette thèse dans un environnement de travail exceptionnel, mes remerciements s'adressent également à Fabien Mangeant, Eric Duceau et Isabelle Terrasse, qui m'ont permis de financer et réaliser cette thèse au sein d'Airbus Innovations dans des conditions privilégiées. Je leur sais particulièrement gré de leurs encouragements lors de ma procédure de naturalisation française et pour la préparation d'une transition en douceur vers mon nouveau poste de travail à l'IRT SystemX.

Ces dernières années, mon travail de thèse s'est déroulé principalement entre deux bureaux, l'un à Suresnes et l'autre à Palaiseau.

Du coté de Suresnes, je souhaiterais exprimer mes remerciements les plus sincères à mes

anciens collègues eadsiens Vincent, Régis, Nabil, Pierre, Lionel, Gilles, Michel F., Michel B., Sofiane, Jay, Anabelle, Benoît, Charles, Etienne, Amandine, Sophie et tant d'autres, qui ont su m'intégrer à leur équipe et partager avec moi des moments mémorables, soit dans le cadre des projets Airbus (piles à combustible et ballon stratosphérique), soit autour d'un déjeuner ou d'un pot animé.

Du coté de Palaiseau, mon séjour au laboratoire CMAP a été une expérience privilégiée. Ceci est en grand partie dû à la vie insufflée par ses permanents et thésards. Je remercie Nasséra, Alex, Sandra, Wallis et Nathalie, qui en tant que personnel administratif ont rendu ma vie de thésard beaucoup plus facile, s'occupant toujours de moi avec grand soin et gentillesse. Je sais gré également à Frédéric Coquel pour son attention à mon égard à la fin de mon stage et au début de ma thèse, Jean-Claude Nédélec pour son profond intérêt pour le Chili, Aldjia Mazari pour ses recommandations en escalade, Sylvain Ferrand pour ses dépannages SSH et Marc Albertelli pour ses méthodes d'optimisation dans le cadre du projet RODIN, ainsi que Thomas, Daphné, Gwenael, Jean-Leopold, Abdul, Laetitia, Laurent, Xavier, Zheng, Camille, Franck et Aymeric, qui ont contribué de manière directe ou indirecte à ma thèse, au travers de leurs suggestions, discussions ou bonne humeur autour d'une tasse de café ou de thé.

J'adresse un remerciement particulier aux amis et collègues suivants: À Zixian et Anna pour la découverte de la cuisine chinoise et russe, à LiMa pour ce Noël inoubliable aux Alpes, à Mamadou pour ces bières dans le quartier Latin ou à Bellavista, à Christophe pour ces délicieux repas d'hiver à la Cité U, à Harsha, Matteo et Joakim pour ce mariage extraordinaire en Inde, et à Charles et Georgios, mes camarades d'armes, pour cet article écrit à 3+1 et ces voyages de rêve autour le monde, expérimentant des inondations d'été dans un quartier baroque de Copenhague, des conférences près des plus belles plages de Grèce et du Brésil, et des promenades avec les alligators aux États-Unis.

Malgré les années écoulées, les paysages défilés et les océans traversés, je souhaiterais exprimer ma gratitude et rendre hommage à deux maîtres qui m'ont fait découvrir la beauté des mathématiques dans ma jeunesse, il y a déjà plus de 15 ans dans un lycée perdu dans le désert d'Atacama. Ma plus haute estime pour Oscar Martinez et Manuel Rodriguez.

Durant ce long chemin, le soutien inconditionnel de mes parents, à qui je dédie cette thèse, a été un élément indispensable dans ma formation académique, professionnelle et humaine. Je ne serai pas là aujourd'hui sans eux.

Enfin, je n'oublie pas de remercier la plus belle femme de toutes, Elodie, dont la tendresse et les encouragements ont été précieux dans les moments les plus difficiles de la thèse où selon Camus il fallait imaginer Sisyphe heureux.

Merci à tous et à toutes.

Optimization of composite structures
A shape and topology sensitivity analysis

Abstract

This thesis is devoted to the study of two main problems, namely the optimal design of multi-layered composite laminates and the topological sensitivity analysis in anisotropic elastostatics. Concerning the composite design, we consider minimal weight structures subjected to stiffness and buckling constraints, where the design variables are the shape/topology of each ply and the stacking sequence. Indeed, the composite laminate is made up of a collection of fiber reinforced orthotropic plies whose main axes can take four different orientations: $0^o, 90^o, 45^o, -45^o$. The way these orientations are arranged within the composite defines the stacking sequence. The physical behavior of the multi-layered laminate is governed by the system of linearized von Kármán equations for plates. In order to optimize both design variables, we rely on a decomposition technique which aggregates the constraints into one unique constraint called margin function. Thanks to this approach, a rigorous equivalent bi-level optimization problem is established. The latter problem is made up of a lower level represented by the combinatorial optimization of the stacking sequence and a higher level represented by the shape/topology optimization of each ply. We propose for the stacking sequence optimization an outer approximation method which iteratively solves a set of mixed integer linear problems associated to the evaluation of the constraint margin function. For the shape/topology optimization of each ply, we lean on the level set method for the description of the interfaces and the Hadamard method for boundary variations by means of the computation of the shape gradient. An aeronautic test case is exhibited for different constraints, namely compliance, reserve factor and first buckling load. The second main problem of this thesis deals with the topological derivative of cost functionals that depend on the stress and the displacement (assuming a linearly elastic material behavior) in a general 2D and 3D anisotropic setting, where both the background and the inhomogeneity may have arbitrary anisotropic elastic properties. A small-inhomogeneity expansion of the cost function is mathematically justified for a wide class of displacement and stress-based cost functionals having smooth densities and computational procedures are then discussed. Several 2D and 3D numerical examples are presented, in particular demonstrating the proposed formulation of the topological derivative on practical cases involving anisotropic elasticity and non-quadratic cost functionals. Independently of the foregoing subjects, we treat additionally two optimal design problems. First we consider the optimal distribution of several elastic materials in a fixed working domain with either a sharp or a smooth interface. In order to optimize both the geometry and topology of the mixture, we rely on the level set method and the signed distance function for the description of the interfaces between the different phases. Secondly, in the framework of efficient power complements to aircraft engines, we seek to come up with the optimal micro-structure of micro-tubular fuel cells via an inverse homogenization technique which maximizes the contact surface subjected to a pressure drop and a permeability constraint. The optimal periodic design (fluid/solid) emerges from the application of a shape gradient algorithm coupled to a level-set method for the geometrical description of the corresponding cell problem.

Keywords

Optimisation des structures composites
Une analyse de sensibilité géométrique et topologique

Résumé

Cette thèse est consacrée principalement à l'étude de deux problèmes, à savoir la conception optimale des drapages composites et l'analyse de sensibilité topologique élastostatique anisotrope. En ce qui concerne la conception des composites, nous considérons des structures de masse minimale soumises à des contraintes de raideur et flambage, où les variables de conception sont la forme de chaque pli et la séquence d'empilement. En effet, le drapage composite est constitué d'une collection de plis orthotropes dont les axes principaux peuvent prendre quatre orientations différentes: $0^o, 90^o, 45^o, -45^o$. La manière dont ces orientations sont disposées dans le composite définit la séquence d'empilement. Le comportement physique du composite est modélisé par le système d'équations des plaques linéarisées de von Kármán. Afin d'optimiser les deux variables de conception, nous nous appuyons sur une technique de décomposition qui regroupe les contraintes dans une seule fonction qui dépend des formes de chaque pli uniquement. Grâce à cette approche, un problème équivalent d'optimisation à deux niveaux est établi de manière rigoureuse. Le premier niveau, aussi appelé inférieur, représente l'optimisation combinatoire de la séquence d'empilement tandis que le deuxième niveau, ou niveau supérieur, représente l'optimisation de la forme de chaque pli. Nous proposons ainsi pour le niveau inférieur une méthode combinatoire convexe, alors que pour le niveau supérieur une méthode des lignes de niveaux couplé à la notion de gradient de forme. Un cas test aéronautique est détaillé pour diverses contraintes, à savoir la compliance, le facteur de réserve et la première charge de flambement. Ensuite, nous étudions la dérivée topologique des fonctions coût qui dépendent de la déformation et du déplacement (en supposant un comportement du matériau élastique linéaire) dans un cadre 2D et 3D anisotrope général, c'est à dire où à la fois le milieu et l'inclusion peuvent avoir des propriétés élastiques arbitraires. Le développement asymptotique de la fonction coût par rapport à l'inclusion est mathématiquement justifié pour une large classe des critères et des procédures de calcul sont plus tard discutées à la vue de plusieurs exemples numériques 2D et 3D. Finalement, en dehors des sujets mentionnés précédemment, nous traitons en outre deux problèmes de conception optimale. Premièrement, nous considérons la meilleure répartition de plusieurs matériaux élastiques dans un domaine fixe, où l'interface peut être nette ou lisse. Afin d'optimiser à la fois la géométrie et la topologie du mélange, nous nous appuyons sur la méthode des lignes de niveau et la fonction distance signée pour la description des interfaces entre les différentes phases. Deuxièmement, dans le cadre de l'étude des dispositifs énergétiques complémentaires aux moteurs d'avions, nous cherchons à trouver la micro-structure optimale d'une pile à combustible micro-tubulaire par une technique d'homogénéisation inverse. Le motif périodique trouvé vise à maximiser la surface d'échange électrochimique soumis à une contrainte de perte de charge et une contrainte de perméabilité. L'agencement optimal liquide/solide découle de l'application de la méthode de lignes de niveau au problème de cellule correspondant.

Mots-clés

Optimisation de forme, méthode des lignes de niveau, matériaux composites, contrainte de flambage, séquence d'empilement, dérivée topologique, optimisation à plusieurs phases, pile à combustible, homogénisation.

Contents

4 The topological derivative in anisotropic elasticity   151

Introduction

Structural optimization stands as a very active area in the industry of aeronautics and aerospace. Thanks to the exponential increase of computing resources over the last 40 years, the development of numerical tools oriented to structural optimization has been outstanding, reaching nowadays a practical use widespread in industry. Even more, structural optimization has acquired a paramount importance in the quest of faster and more efficient devices; the development of lightweight structures responding to the overwhelming need of reducing fuel consumption for economical and environmental reasons; and the design of innovative components made of "new materials", such as metal alloys and composites.

Throughout these years, the composite material technology has been continuously and progressively introduced in commercial aircraft, attaining more than 50% of the total weight in today most popular models, such as the A350-XWB of Airbus Group and the 787 Dreamliner of Boeing. Composite materials have become thus, an asset of major importance in the development of the current and future aircrafts.

Despite the efforts accomplished so far to adapt classical structural optimization tools to composites, currently aeronautical industry lacks of robust methods capable to master the optimal design of detailed composite coatings, such as the fuselage or the central wing box of an airplane.

(a)   (b)
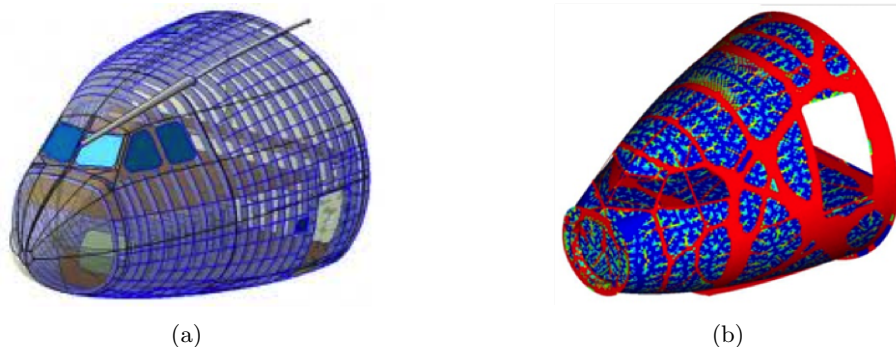
Figure 1: Classical optimization of the design of a metallic aircraft nose fuselage. (a): Traditional configuration with horizontal and vertical stiffeners. (b): Weight optimized structure with angled stiffeners (in red). Figure extracted from Sogeti Lab.

Indeed, a delicate point when dealing with composites stems from the necessity to guarantee the compatibility between a "continuous medium" vision, necessary for the overall understanding of the phenomena related to the stiffness level, and the discrete nature of laminated composites. Thereby, composite optimization techniques usually propose a two-level strategy where a continuous representation of the composite is applied at the system level (fuselage or wing), meanwhile the subsystem level (ply lay-up or stacking sequence of the panel) is treated with discrete algorithms (see Figure 2).

The aforementioned approach has proved effective, however, it does not address all the degrees of freedom and constraints within composite structures. In fact, the design of the in-
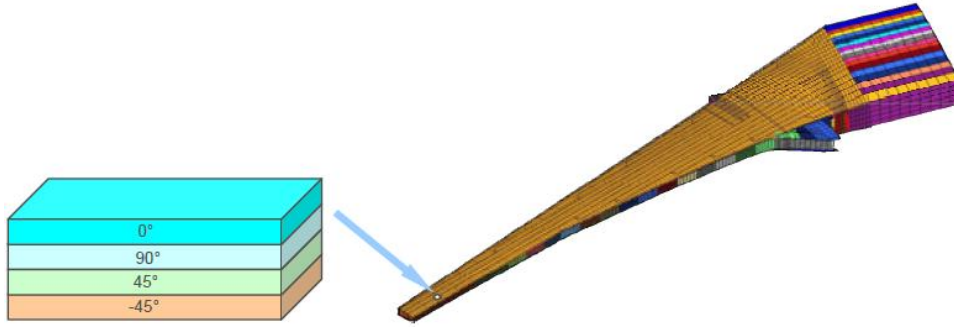
Figure 2: Two-level optimization of a composite wing. On the right side the stiffness properties of the wing (system level) meanwhile on the left side the local ply lay-up (subsystem level). Figure extracted from Altair Engineering Ltd.

plane shape of each layer has scarcely been considered so far, despite of its importance in terms of structural strength and manufacturability. The in-plane shape as a design variable can only be treated satisfactorily through a continuous approach, which leads to reconsider the former continuous/discrete framework.

In order to define the shape of each ply within a composite laminate, only a few works on topology optimization have been carried out hitherto. Furthermore, most of these works rely on the Solid Isotropic Material with Penalization (SIMP) method (see Figure 3). Within this context, the shape design problem is replaced by the quest of finding the best density distribution of material inside a reference domain. Typically the optimal distribution takes intermediate values between 0 (void) and 1 (material), spawning fictitious microscopic composites. In order to get rid of these intermediate values, which can be neither interpreted nor manufactured by means of classical procedures, a penalization scheme is performed, favoring the generation of binary $0 - 1$ shapes.

In a complex mechanical framework however, where e.g. buckling or tensile failure constraints are fundamental, the impact of such penalization schemes is not always evident and in some cases the optimal solutions remain with large areas of intermediate density values. When those situations occur, engineers extract a $0 - 1$ shape by means of their mechanical experience and intuition. Unfortunately most of the time this "interpretation" is not trivial and leads to non-optimal structures.

Over the last years, the boundary variation approach of the level set method has become an interesting alternative to the SIMP method in topology optimization of massive structures. In a nutshell, the level set method for topology optimization implicitly describes the boundary of a shape Ω enclosed in a "hold-all" computational domain D, via an auxiliary function ψ such that (see Figure 4)

$$\begin{cases} \psi(x) = 0 & \text{if } x \in \partial\Omega \cap D, \\ \psi(x) < 0 & \text{if } x \in \Omega, \\ \psi(x) > 0 & \text{if } x \in \left(D \setminus \overline{\Omega}\right). \end{cases}$$

The complement of Ω in D can either represent a weak "ersatz" material, whose elastic properties are adjusted to have a negligible mechanical contribution, or rather another arbitrary material, thus constituting a multi-phase configuration. While keeping a "clear" $0 - 1$ description of the shape, the level-set method easily manages topological changes within a fixed grid, avoiding the need of re-meshing.

Financed by Airbus Group, the ensuing thesis work is mainly devoted to introduce the level set setting to the current design process of laminated composites, enabling a natural control of the contour of each ply. In this way, both design variables, namely the shape of each ply and the lay-up sequence, are optimally determined by means of a rigorous mixed or bi-level

(a) Fiber orientation 0° (b) Fiber orientation 90°

(c) Fiber orientation $+45^o$ (d) Fiber orientation -45°
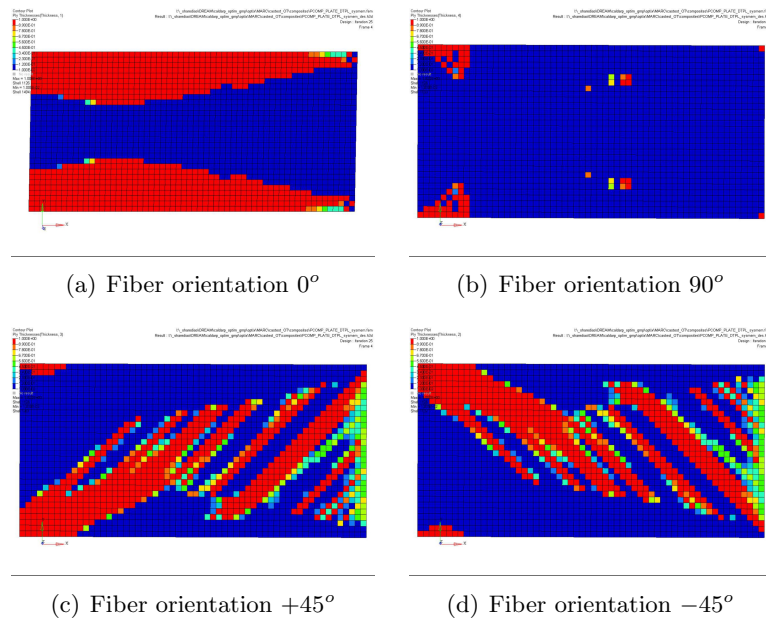
Figure 3: Topology optimization of a composite laminate made of 4 layers obtained from the industrial software Optistruct (Altair). The density color red represents a density equal to 1 (material) meanwhile the blue represents a density equal to 10^{-2} (void). Each ply depicts the shape of an unidirectionally reinforced orthotropic material with a particular fiber orientation. We remark that the plies reinforced in 45° and -45^0 display important areas with intermediate density values (green/yellow). For more details see Section 3.9 in Chapter 3.

strategy. Although the subject is rather exploratory, it is expected that the mathematical and algorithmic contributions of this work will allow the development in the near future of an aid decision tool for the design of large composite surfaces subjected to manufacturing and bending stiffness constraints. This tool should help Airbus Group to increase the performances while reducing the cost by cycle during the design of composite structures.

(a)   (b)
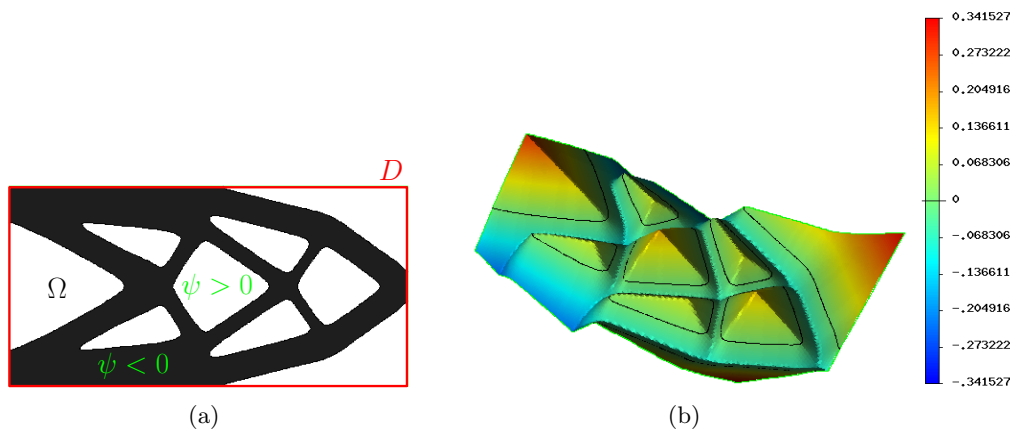
Figure 4: (a): Optimized shape Ω (in black), enclosed in a square working domain D; (b): level-set representation of the shape and color scale of the values of ψ.

Along with the foregoing subject on composite materials, three other topics are developed within this thesis, thanks to the fruitful interaction with other researchers and Airbus Group engineers.

The first one deals with the concept of topological derivative which measures the sensitivity of a given shape functional with respect to an infinitesimal singular domain perturbation, such as the insertion of holes, inclusions, source-terms or even cracks. Nowadays, the topological derivative stands as a sprightly domain of research on topology optimization, inverse problems and image processing. However, its treatment has been mostly limited so far to an isotropic setting where the cost functional does not depend upon the elastic stresses. Due to the importance of some potential applications on problems involving inherent anisotropy, such as bone tissue imaging, flaw identification in composites and topology optimization subject to the Hill-Tsai failure criterion, the developed work is intended to mend this lack of material by giving an extensive and general treatment of the subject.

The second topic regards the optimal distribution of several elastic materials (phases) in a fixed working domain. This corresponds to a generalization of the multi-layered composite case described above, without taking into account the stacking sequence of course. Considering either a sharp or a smooth interface between phases, a shape differentiable parameterization via a level-set function is presented. The proposed algorithm represents a robust and rigorous tool for the optimal design of the so-called graded materials.

In view of further applications of the level-set method for topology optimization other than elasticity, the third subject addresses the optimal design of a solide oxide fuel cell as a complement of an aircraft engine. In general fuel cells are extremely efficient energy devices that converts chemical energy into electricity. Although they are very efficient compared to conventional power machines, their large weight and volume represent a major drawback for aeronautical applications. In view of the recent development of additive manufacturing techniques capable of miniaturizing the fuel cell lay-out, the design of an optimized micro-tubular fuel cell is presented. This design is obtained via an inverse homogenization procedure coupled to a level-set method for topology optimization.

The thesis is divided in five chapters. We present a brief outline of each one separately.

Chapter 1: Background and review of the state of the art

This chapter provides the necessary background material and state of the art for the ensuing analysis. In particular we give all necessary references to the previous literature on the topics covered by this thesis (in contrast with the present introduction which does not contain any reference). We start by recalling the main features of shape optimization, explaining the basic differences between its three main categories, namely the parametric, geometric and topology optimization. Then we focus our attention on the latter type. A general topology optimization problem can be stated as follows

$$\inf_{\Omega \in \mathcal{U}_{ad}} J(\Omega), \tag{1}$$

where $\Omega \subset \mathbb{R}^d$ is the domain occupied by the structure, J is the objective function to be minimized and $\mathcal{U}_{ad}$ is a set of admissible shapes. The criterion $J(\Omega)$ is supposed to depend upon the solution of a PDE, e.g. the elastic displacement of the linearized elastic system

$$\begin{cases} -\mathrm{div}\,(A\,e(u)) &=& f & \text{in } \Omega, \\ u &=& 0 & \text{on } \Gamma_D, \\ (A\,e(u))\cdot n &=& g & \text{on } \Gamma_N, \end{cases}$$

where A is the elastic tensor of the medium, $e(u) = (\nabla u + \nabla u^T)/2$ is the symmetrized strain tensor, f is the applied body force, g is the surface load applied on $\Gamma_N \subset \partial\Omega$ and $\Gamma_D \subset \partial\Omega$ is the clamping zone.

We furnish a brief description of the main techniques in topology optimization (homogenization, SIMP, level-set, etc.) and some theoretical existence results for (1). Also, a short

description of the main tools in shape sensitivity analysis, namely the shape derivative and the topological derivative, is delivered.

Then we describe the level-set method for topology optimization. This method combines the aforementioned shape sensitivity analysis to obtain a descent direction and a level-set method to parameterize the shape. Thanks to this particular description, topology changes can naturally occur during the optimization process. We consider for that purpose all shapes Ω to be included in a hold-all computational domain D, and represented implicitly via the zero level-set of a scalar function ψ, defined as:

$$\begin{cases} \psi(x) = 0 & \text{if } x \in \partial\Omega \cap D, \\ \psi(x) < 0 & \text{if } x \in \Omega, \\ \psi(x) > 0 & \text{if } x \in \left(D \setminus \overline{\Omega}\right). \end{cases} \tag{2}$$

If the domain Ω evolves in pseudo-time t (hence we rather denote the level-set function as $\psi(t, x)$), its deformation under the action of a velocity field $\theta(t, x)$ is governed by a Hamilton-Jacobi type equation on ψ:

$$\frac{\partial\psi}{\partial t}(t, x) + V(t, x)|\nabla\psi(t, x)| = 0, \quad \forall t, \forall x \in D, \tag{3}$$

where $V(t, x) = \theta \cdot n$ corresponds to the normal component of the advection field θ,

$$n = \frac{\nabla\psi(t, x)}{|\nabla\psi(t, x)|}$$

the natural extension of the normal on $\partial\Omega$ throughout D and θ is chosen such that $\theta \cdot n = 0$ on ∂D. The level set method for topology optimization thus, consists in finding the solution of (1) by iteratively deforming an initial shape Ω_0, using each time as advection field V in (3) the descent direction furnished by the shape derivative $-J'(\Omega)$. The detailed ingredients of the optimization algorithm are explained and a couple of numerical examples are shown.

Finally we recall the definition and the main properties of composite materials, giving a particular emphasis to the laminated ones. Denoting as $2h$ the thickness of a laminated composite plate with in-plane shape Ω, the horizontal displacements u and the deflection w of the plate obey the von Kármán equations

$$\begin{cases} -\text{div}(\mathcal{A}E(u, w)) = 0 & \text{in } \Omega, \\ \nabla^2 : (\mathcal{D}\nabla^2 w) - \mathcal{A}E(u, w) : \nabla^2 w = P & \text{in } \Omega, \\ w = 0, u = 0, \nabla w \cdot n = 0 & \text{on } \Gamma_D, \\ \mathcal{A}E(u, w) \cdot n = 2hg & \text{on } \Gamma_N, \\ (\mathcal{D}\nabla^2 w)_{nn} = 0 & \text{on } \Gamma_N, \\ \nabla \cdot (\mathcal{D}\nabla^2 w) \cdot n + \frac{\partial}{\partial\tau}(\mathcal{D}\nabla^2 w)_{n\tau} = 2hg \cdot \nabla w & \text{on } \Gamma_N, \end{cases} \tag{4}$$

where the tensors $\mathcal{A}, \mathcal{D}$ represent respectively the extensional and bending stiffness of the plate, $E(u, w) = e(u) + \frac{1}{2}\nabla w^T \nabla w$, P is a pressure load, g is a surface load applied on $\Gamma_N \subset \partial\Omega$ and $\Gamma_D \subset \partial\Omega$ represents the clamped zone. The associated linearized buckling problem is also presented, in view of the later need to invoke its first positive eigenvalue as a buckling constraint. The chapter is closed with a short explanation of the main mathematical properties of the von Kármán model, notably those related to bifurcation theory.

Chapter 2: Multi-phase structural optimization

This chapter sets forth the problem of optimal distribution of two materials with elastic tensor A_0 and A_1, occupying two domains Ω^0 and $\Omega^1 = D\backslash\Omega^0$, respectively.

First, the classical "sharp-interface" model is studied. The global elastic tensor A is assumed discontinuous on the interface between the materials and given by

$$A = \chi_{\Omega^0} A_0 + (1 - \chi_{\Omega^0})A_1,$$

where χ_{Ω^0} is the characteristic function of the domain Ω^0. The shape derivative for a general criterion is computed within this framework and the inherent difficulties estimating the involved jumps are evoked. A discretized model is introduced as an alternative to the continuous setting. Thus, we propose instead to differentiate the discretized problem, providing a consistent approximation. The shape differentiability and the directional differentiability are established according to the lay-out of the contours of each phase. This study contributes to clarify and enrich the existent literature on the topic, rendering the right numerical usage of the shape derivative for multi-phase problems.

Then we consider a "smoothed-interface" model, where the material properties are interpolated between the two phases in an area of width 2ε. The "intermediate interface" is defined through a level-set function ψ. The smooth elastic interpolation arises from the use of a regular function $h_\varepsilon(d_{\Omega^0})$ which depends on the signed distance function to the domain Ω^0

$$d_{\Omega^0}(x) = \begin{cases} -d(x, \partial\Omega^0) & \text{if } x \in \Omega^0, \\ 0 & \text{if } x \in \partial\Omega^0, \\ d(x, \partial\Omega^0) & \text{if } x \in D \backslash \bar{\Omega}^0, \end{cases}$$

where $d(\cdot, \partial\Omega)$ is the usual Euclidean distance. In the case of the compliance

$$J(\Omega^0) = \int_D Ae(u) : e(u)dx,$$

where u is the unique solution of (2), the shape derivative of J reads

$$J'(\Omega^0)(\theta) = -\int_\Gamma \theta(x) \cdot n(x)\Big(f_0(x) + f_1(x)\Big)dx,$$

where Γ is the optimizable boundary, n is the outer unit normal to Ω^0 and f_0, f_1 are scalar functions defined by

$$f_0(x) = \int_{\mathrm{ray}_\Gamma(x) \cap \Omega^0} h'_\varepsilon\left(d_{\Omega^0}(z)\right)(A_1 - A_0)e(u)(z) : e(u)(z)\prod_{i=1}^{d-1}(1 + d_{\Omega^0}(z)\kappa_i(x))dz,$$

$$f_1(x) = \int_{\mathrm{ray}_\Gamma(x) \cap \Omega^1} h'_\varepsilon\left(d_{\Omega^0}(z)\right)(A_1 - A_0)e(u)(z) : e(u)(z)\prod_{i=1}^{d-1}(1 + d_{\Omega^0}(z)\kappa_i(x))dz,$$

$\kappa_i(x), 1 \le i \le d-1$, are the principal curvatures and z denotes a point in the ray emerging from $x \in \Gamma$, i.e. the line connecting $x \in \Gamma$ with its corresponding point on the skeleton of the shape.

We emphasize the differences with respect to previous publications on the topic, and we propose consistent simplified formulae. We show how the method is extended for more than two phases, exhibiting some test cases of compliance minimization (see Fig. 5). The above results settle this smooth-interface approach as a promising technique in the optimal design of the so-called "graded materials".

Chapter 3: Optimization of laminated composite plates

This chapter treats the main object of this thesis work, namely laminated composite optimization. According to Figure 6, let $\mathcal{O}$ be a symmetric laminated composite structure composed of the superposition of $2N$ anisotropic layers, each one of constant thickness $\varepsilon > 0$ and variable shape $\Omega_i \subset \Omega$, where Ω is a regular sub-domain of $\mathbb{R}^2$. By abuse of notation we denote $\mathcal{O}$ as

$$\mathcal{O} = \{\Omega_i\}_{i \in \mathbb{Z}\backslash\{0\}, i=-N..N} \,.$$

Since we suppose $\mathcal{O}$ symmetric ($\Omega_{-i} = \Omega_i$), we consider only N layers. The collection of complementary shapes of each ply within the laminate ($\Omega\backslash\Omega_i$) can be understood either: (a)

(a)   (b)
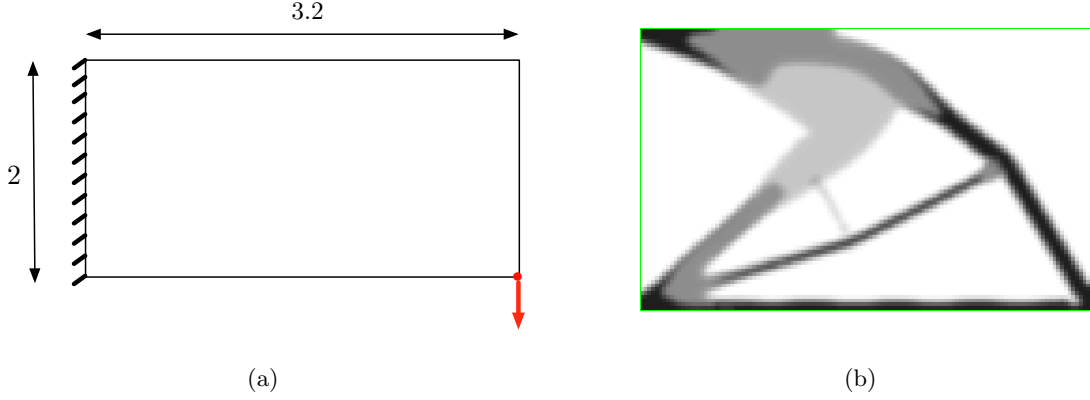
Figure 5: Medium cantilever optimization using three isotropic materials with different stiffness ratios (1:black, 0.5: dark gray and 0.25: light gray).

filled with a different material from the one occupying Ω_i, rendering each ply biphasic, (b) constituting a true "hole" so when gluing together the plies towards the plane of symmetry $\Pi = 0$, the distal layers bend and fill the holes to keep contact with the proximal layers (See Fig. 6). The elastic material inside each ply Ω_i is denoted as $\mathcal{A}_i$, and we assume it corresponds to an unidirectionally fiber-reinforced orthotropic material with 4 possible orientations w.r.t. the canonical axis: 0°, 90°, $+45^o$ and -45°.

(a)

(b)   (c)
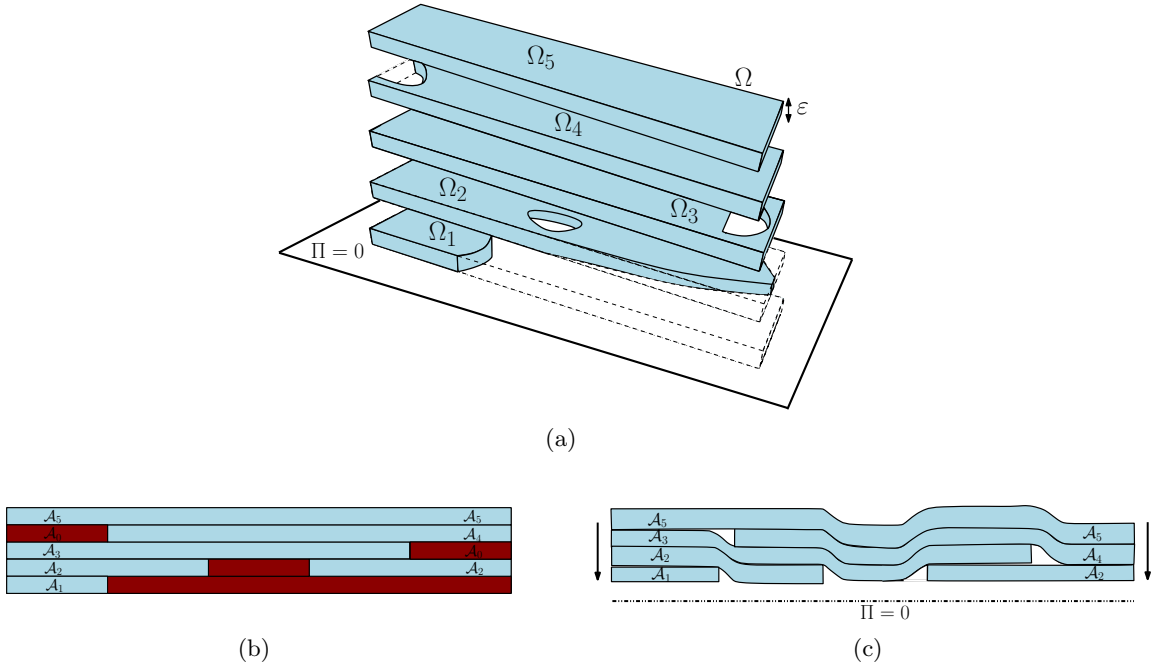
Figure 6: Multi-layered setting. (a): Half-part of a multi-shape composite design with plane of symmetry $\Pi = 0$. Each ply has its own shape $\Omega_i \subset \Omega$. (b),(c): The "holes" are either filled with another material or rather inwardly flatten within the laminate.

Likewise Chapter 1, we suppose the same partition of $\partial\Omega$ ($\partial\Omega = \Gamma_D \cup \Gamma_N$) and loading configuration (g, P). Then the in-plane displacement u and the vertical displacement w within $\mathcal{O}$ satisfy the limit two-dimensional von Kármán plate model (4). The total extensional and bending stiffness tensors, respectively denoted as $\mathcal{A}$ and $\mathcal{D}$, stem from the superposition of plies according to the classical theory of plates.

Apart from the shape of each ply, the tensors $\mathcal{A}$ and $\mathcal{D}$ depend on the sequence of fiber orientations constituting the laminate and the way they are distributed along the thickness. This variable is called stacking sequence and we define it by means of the binary matrix $\xi \in Y$ with

$$\xi_{mn} = \begin{cases} 1, & \text{if the layer in position } m \text{ has fiber orientation } n, \\ 0, & 1 \text{ if not,} \end{cases}$$

and

$$Y = \left\{ \xi = (\xi_{mn}) \in \{0,1\}^{N \times 4} \mid \sum_{n=1}^{4} \xi_{mn} = 1, \forall m; r(\xi) \le 0 \right\}.$$

The function r inside the foregoing definition represents the set of manufacturing constraints.

Henceforth, the mixed problem we contemplate to solve reads

$$\begin{cases} \min_{\mathcal{O} \in \mathcal{U}_{ad}, \xi \in Y} J(\mathcal{O}) \\ \text{s.t} \\ \quad G(\mathcal{O}, \xi) \le 0, \end{cases} \tag{5}$$

where the objective function $J(\mathcal{O})$ does not depend on the stacking sequence ξ and it represents the mass of the structure meanwhile the vectorial constraint $G = \{G_j(\Omega, \xi)\}_{j=1...m}$ represents a sequence of regular measures of the stiffness of the plate, e.g. the compliance, the Hill-Tsai failure criterion or the first eigenvalue of the linearized buckling problem associated to (4). The admissible set $\mathcal{U}_{ad}$ is defined as

$$\mathcal{U}_{ad} = \left\{ \{\Omega_i\}_{i=1...N} \mid \Omega_i \subset \Omega \text{ and } P(\Omega_i) \le \varsigma, \ \forall i = 1...N \right\},$$

where the constraint on the perimeter of each ply $P(\Omega_i) \le \varsigma$, with $\varsigma > 0$, ensures the existence of an optimal solution to (5).

In order to write the continuous optimality conditions of problem (5) in view of the later implementation of a descent gradient method, the following equivalent problem to (5) is introduced

$$\min_{\mathcal{O} \in \mathcal{U}_{ad}} \left\{ J(\mathcal{O}) \mid \mathcal{M}(\mathcal{O}) \le 0 \right\}, \tag{6}$$

where $\mathcal{M}$ stands as the constraint margin function

$$\mathcal{M}(\mathcal{O}) := \min_{\xi \in Y} \max_{1 \le j \le m} \left\{ G_j(\mathcal{O}, \xi) \right\}. \tag{7}$$

Thereby, the optimality conditions of (5) can be casted at $\mathcal{O}^* \in \mathcal{U}_{ad}$ as the existence of multipliers $\lambda, \mu \in \mathbb{R}$ (not both zero) such that

$$\begin{cases} 0 \in \lambda J'(\mathcal{O}^*) + \mu \partial \mathcal{M}(\mathcal{O}^*), \\ \mu \mathcal{M}(\mathcal{O}^*) = 0, \\ \mathcal{M}(\mathcal{O}^*) \le 0, \\ \lambda, \mu \ge 0, \end{cases}$$

where J' is the sequence of partial shape derivatives with respect to the shape of each ply and $\partial \mathcal{M}$ is the sub-gradient (or equivalently generalized gradient) of $\mathcal{M}$, which arises from the non-differentiability of the constraint margin function due to non-uniqueness of the solution $\xi \in Y$ in the definition (7).

Finally we implement a multi level set method to solve (6), meanwhile the evaluation of the constraint margin function $\mathcal{M}$ in (7) is achieved thanks to an outer approximation scheme, which stands as an exact method for convex non-linear integer programming problems. A numerical example for a fuselage section subjected to different constraints is detailed.

Chapter 4: The topological derivative in anisotropic elasticity

This chapter investigates the topological derivative $\mathrm{D}J$ of a general cost functional J depending on the stress and the displacement in a full anisotropic elastic framework. The topological derivative $DJ(z)$ quantifies the perturbation induced to a cost functional J by the virtual creation of an object $B_a(z)$ (cavity, inhomogeneity, source term, etc) of vanishingly small characteristic radius a at a prescribed location z inside a solid $\Omega \subset \mathbb{R}^3$.

Consider an inhomogeneity of elastic tensor $\mathcal{C}^\star$, which is embedded in Ω. The elastic properties within Ω without the inclusion are given by the elastic tensor $\mathcal{C}$. Then we define the topological derivative through the following asymptotic development

$$J(\mathcal{C}_a) = J(\mathcal{C}) + \delta(a)DJ(z) + o(\delta(a)),$$

where the elastic tensor $\mathcal{C}_a$ describes the whole solid elastic properties

$$\mathcal{C}_a = \chi_{B_a}\mathcal{C}^\star + (1 - \chi_{B_a})\mathcal{C},$$

$\delta(a)$ vanishes as $a \to 0$, and the inclusion B_a occupies the domain

$$B_a = z + a\mathcal{B}, \quad \mathcal{B} \subset \mathbb{R}^3 \text{ bounded and regular.}$$

We assume that the cost functional J has the form

$$J(\mathcal{C}_a) = \mathbb{J}_a(u_a, \nabla u_a) \quad \text{with} \quad \mathbb{J}_a(u, d) = \int_\Omega \psi_a\big(x, u(x), d(x)\big)dx + \int_{\partial\Omega} \psi_S(x, u(x))ds. \quad (8)$$

The densities $\psi_S : \Omega \times \mathbb{R}^3 \to \mathbb{R}$ and $\psi, \psi^\star : \Omega \times \mathbb{R}^3 \times \mathbb{R}^{3\times3} \to \mathbb{R}$, with

$$\psi_a = (1 - \chi_{B_a})\psi + \chi_{B_a}\psi^\star,$$

are supposed to be twice differentiable in all their arguments and to satisfy adequate growth conditions. The function u_a stands for the elastic displacement field in the solid containing the small inhomogeneity B_a.

We split the boundary $\partial\Omega$ as $\partial\Omega = \Gamma_\mathrm{D} \cup \Gamma_\mathrm{N}$ (where $\Gamma_\mathrm{D} \cap \Gamma_\mathrm{N} = \emptyset$ and $|\Gamma_\mathrm{D}| \neq 0$) and define the kinematically admissible spaces

$$W(\bar{u}) := \big\{v \in H^1(\Omega; \mathbb{R}^3), \ v = \bar{u} \text{ on } \Gamma_\mathrm{D}\big\}, \qquad W_0 := W(0),$$

where $\bar{u}$ corresponds to an arbitrary prescribed Dirichlet data. Then the displacement field $u_a \in W(\bar{u})$ solves the transmission problem

$$\mathrm{div}(\mathcal{C}_a e(u_a)) + f = 0 \text{ in } \Omega, \quad (\mathcal{C}e(u_a))\cdot n = g \text{ on } \Gamma_\mathrm{N}, \quad u_a = \bar{u} \text{ on } \Gamma_\mathrm{D},$$

where f and g hold as the applied volume and surface loads, respectively.

We also introduce the free-space transmission problem

$$\mathrm{div}\big(\mathcal{C}_\mathcal{B} : e(u_\mathcal{B}[E])\big) = 0 \text{ in } \mathbb{R}^3, \qquad u_\mathcal{B}(\xi) - E \cdot \xi = \mathcal{O}(|\xi|^{-2}) \ (|\xi| \to \infty),$$

with $\mathcal{C}_\mathcal{B} = \chi_\mathcal{B}\mathcal{C}^\star + (1 - \chi_\mathcal{B})\mathcal{C}$ and E an arbitrary constant second-order tensor, and the elastic moment tensor $\mathcal{A}$:

$$\mathcal{A} : E = \int_\mathcal{B} (\mathcal{C}^\star - \mathcal{C}) : \nabla u_\mathcal{B} dx \qquad \forall E \in \mathbb{R}^{3\times3}.$$

Then we prove, by virtue of an asymptotic development of u_a, that the topological derivative DJ at z of the cost functional (8) has the following structure

$$DJ(z) = |\mathcal{B}|\Delta\psi(z, u(z), \nabla u(z)) - \nabla p(z) : \mathcal{A} : \nabla u(z)$$

$$+ \partial_d(\Delta\psi)(z, u(z), \nabla u(z)) : \int_\mathcal{B} \nabla v_\mathcal{B}(x)dx$$

$$+ \int_{\mathbb{R}^3 \backslash \mathcal{B}} \mathcal{G}(z, \nabla v_\mathcal{B}(x))dx + \int_\mathcal{B} \mathcal{G}^\star(z, \nabla v_\mathcal{B}(x))dx, \quad (9)$$

where $\Delta\psi = \psi - \psi^\star$ and $v_{\mathcal{B}}(x) = u_{\mathcal{B}}[\nabla u(z)](x) - \nabla u(z)\cdot x$. The functions $\mathcal{G}$ and $\mathcal{G}^\star\colon \mathbb{R}^3 \times \mathbb{R}^{3\times 3} \to \mathbb{R}$ are defined, for a given background solution u, by

$$\mathcal{G}(z,d) := \psi(z, u(z), \nabla u(z) + d) - \psi(z, u(z), \nabla u(z)) - \partial_d \psi(z, u(z), \nabla u(z)) : d$$
$$\mathcal{G}^\star(z,d) := \psi^\star(z, u(z), \nabla u(z) + d) - \psi^\star(z, u(z), \nabla u(z)) - \partial_d \psi^\star(z, u(z), \nabla u(z)) : d,$$

meanwhile the adjoint state $p \in W_0$ solves

$$-\mathrm{div}(\mathcal{C}e(p)) = \partial_u \mathbb{J}_0(u, \nabla u) - \mathrm{div}(\partial_d \mathbb{J}_0(u, \nabla u)) \text{ in } \Omega, \quad (\mathcal{C}e(p))n = \partial_d \mathbb{J}_0(u, \nabla u) \text{ on } \Gamma_{\mathrm{N}}, \quad p = 0 \text{ on } \Gamma_{\mathrm{D}}.$$

The computation of (9) is largely discussed and a few 2D and 3D numerical examples are exhibited.

Chapter 5: Optimal design of a micro-tubular fuel cell

In this chapter we study the problem of finding the optimal configuration for a micro-tubular solide oxide fuel cell (see Fig. 7 (a)). Fuel cells are energy devices which can efficiently convert chemical energy into electrical energy. Unfortunately, due to their high weight and volume, their application to aeronautics has been limited so far. However, thanks to recent developments in additive manufacturing techniques, capable of reducing the size of complex structures by allowing the design of extremely small features from a CAD model, the aforementioned limitation is becoming obsolete.

A generic fuel cell is mainly composed of two porous electrodes (anode and cathode) and a dense electrolyte. Thus, let $\Omega_\epsilon \subset \mathbb{R}^d$ be the porous volume of the fuel cell where the air flows freely, delimited by the boundaries Γ_D, Γ_N and Γ_ϵ (see Fig. 7 (b)). The air is injected through Γ_D, meanwhile Γ_N is impermeable. A periodic arrangement of anode/electrolyte/cathode tubes constitutes the interface Γ_ϵ. The air transports several species but we concentrate on the oxygen O_2, which is consumed in the electrochemical reaction on the surface Γ_ϵ. The adimensional parameter ϵ corresponds to the ratio between the characteristic size of each tube and a macroscopic characteristic length.

(a)   (b)
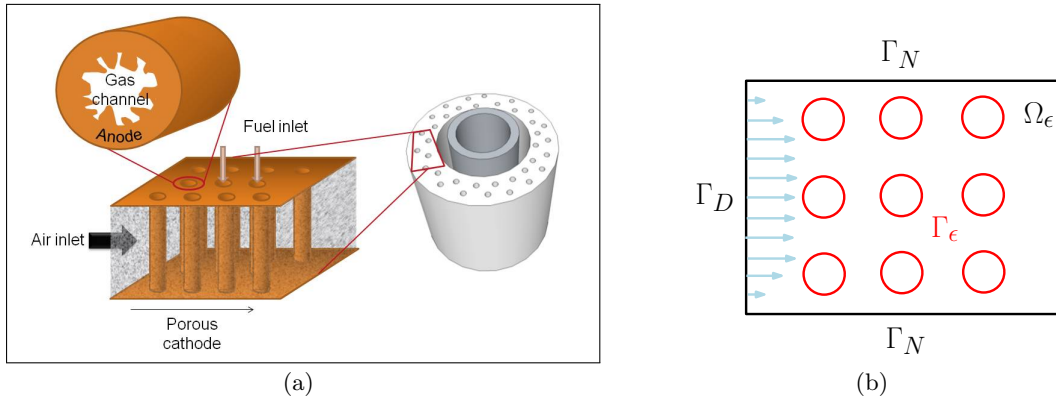
Figure 7: (a): Proposed micro-tubular design with arbitrary shaped tubes. (b): Transversal section of the porous fuel cell and boundary conditions. The air flows from the left to the right. The fuel penetrates orthogonally through the figure inside the red tubes. Γ_ϵ represents the anode/electrolyte/cathode lumped structure.

Under some classical simplifications of the internal structure and the fluid within the fuel cell (laminar and incompressible flow, isothermal state, etc.), the upscaled (homogenized) state equations read

$$\begin{cases} \text{div}(u^*) = 0 & x \in \Omega \\ u^* = -\frac{K}{\mu}\nabla p^* & x \in \Omega \\ \frac{\partial X^*}{\partial t} + u^* \cdot \nabla X^* = \lambda\text{div}(D\nabla X^*) + |\partial\omega|\mathcal{R}(X^*) & x \in \Omega \\ X^* = X_{\text{init}} & t = 0, x \in \Omega, \end{cases} \quad (11)$$

subjected to the following boundary conditions

$$\begin{cases} u^* = u_D & X^* = X_D & t > 0, x \in \Gamma_D, \\ u^* \cdot n = 0 & \nabla X^* \cdot n = 0 & t > 0, x \in \Gamma_N. \end{cases}$$

The preceding homogenized equations (11) can be identified to the classical Darcy law for the fluid flow (air) in a porous media and a convection-diffusion-reaction equation for the transport of the solute (O_2). The functions u^*, p^* correspond to the homogenized velocity and pressure of the air, X^* the homogenized O_2 concentration, μ the viscosity of the air, λ the diffusion coefficient, $|\partial\omega|$ the perimeter of the micro-fuel-tube ω scaled to the unit cell $Y = [0,1] \times [0,1]$, $\mathcal{R}(X^*)$ the Butler-Volmer reaction term and (u_D, X_D) the velocity of the air and the concentration of O_2 at the inflow boundary Γ_D. The effective porous media diffusion tensor D and the permeability tensor K are defined by means of the solutions of two cell problems.

In order to optimize the performances of a periodic micro-tubular fuel cell with variable shaped fuel tubes, we propose the shape optimization problem

$$\begin{cases} \max_{\omega \subset Y} |\partial\omega| \\ \text{s.t.} \\ |\omega| \geq C_f|\partial\omega| \\ \frac{tr(K)}{d} \geq k_{min}, \end{cases} \quad (12)$$

where ω stands for the shape of each tube inside the unit-cell Y, K is the aforementioned permeability tensor in (11), and $tr()$ is the trace operator. The idea is thus to find the shape ω with the largest perimeter (so as to maximize the electro-chemical reaction within the fuel cell) subjected to a pressure drop and a permeability constraint, parameterized through the coefficients C_f and k_{min}, respectively.

Problem (12) is efficiently solved via the level-set method for topology optimization described in Chapter 1, where each shape $\omega \subset Y$ is described by means of a level-set function ψ.

(a)   (b)
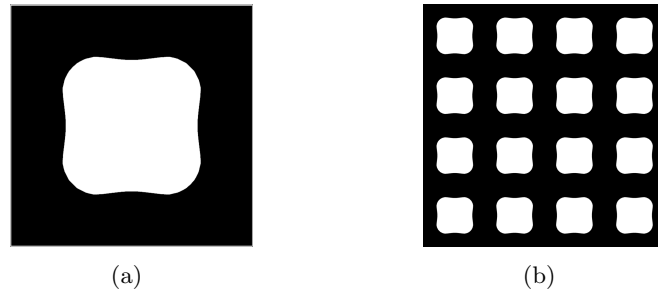
Figure 8: Example of an optimal fuel cell design. (a): stands for the base cell optimized result, meanwhile (b): corresponds to the respective periodic structure.

Communications

The work presented in Chapter 2 on multi-phase optimization was accepted for publication under the title:

- G. ALLAIRE, C. DAPOGNY, G. DELGADO, AND G. MICHAILIDIS. *Mutli-phase structural optimization via a level-set method.* ESAIM: Control, Optimisation and Calculus of Variations (2014).

Also, the study on the anisotropic topological derivative presented in Chapter 4 leaded to the publications

- M. BONNET, G. DELGADO. *The topological derivative in anisotropic elasticity.* Quarterly Journal of Mechanics and Applied Mathematics (2013).

- G. DELGADO, M. BONNET. *The topological derivative of stress-based cost functionals in anisotropic elasticity.* Submitted (2014).

Finally, an article based on the work of Chapter 3 is currently in preparation through the following preprint:

- G. ALLAIRE, G. DELGADO. *Stacking sequence and shape optimization of laminated composite plates via a level-set method.* In preparation (2014).

Chapter 1

Background and review of the state of the art

Contents

1.1 Structural optimization

Shape optimization attempts to find the optimal shape of a domain which minimizes or maximizes a given criterion subject to a set of constraints. This quest has inspired humanity since a quite long time, going back at least to the Antiquity. We can cite e.g. the so-called "Problem of Queen Dido": Tells the Roman poet Vergil in his famous epic Aeneid, that after the Phoenician princess Dido escaped from Tyre (now part of Lebanon), she disembarked in Africa, at the place that later became Carthage. The local ruler (King Jarbas of Numidia), accepted the settlement of Dido and her people under the condition that the queen would obtain only as much land as she could enclose with the skin of an ox. Cutting the skin in very thin strips and tying them together, Dido chose to draw her territory as a semi-circle enclosing the coast, solution that yields the largest possible area. The mathematical translation of the latter property reads by means of the isoperimetric inequality: If Ω is a plane domain with a finite area $|\Omega|$ and perimeter $P(\Omega)$, then

$$|\Omega| \leq \frac{1}{4\pi} P(\Omega)^2,$$

with equality only if Ω is a circle. We conclude thus that the circle maximizes the area for a fixed perimeter.

Nowadays, shape optimization is a key tool in modern industrial design. Notably the industry of aeronautics has enjoyed enormous advances e.g. on optimization of the profile of a wing

Dido Purchases Land for the Foundation of Carthage. Engraving by Matthäus Merian the Elder, in Historische Chronica, Frankfurt a.M., 1630. Dido's people cut the hide of an ox into thin strips and try to enclose a maximal domain.

Figure 1.1: Dido's people cut the hide of an ox into thin strips and try to enclose a maximal domain [148].

to improve the penetration into the air or the lift; construction of quieter aircraft, especially supersonic aircraft; and research on stealth aircraft.

In general the preceding problems are highly non-trivial, since the criterion to optimize is computed through the solution of a partial differential equation (the so-called state equation). Let us e.g. explain more in detail the optimization problem of designing the profile of an airplane wing [255]. Consider a wing whose shape is given by $A \subset \mathbb{R}^3$. We search to minimize the drag coefficient c_d defined as

$$c_d(A) = \int_{\partial A} \left[\mu(\nabla u + \nabla u^T) - \frac{2\mu}{3}\mathrm{div}u \right] \cdot n \cdot u_\infty ds - \int_{\partial A} pn \cdot u_\infty ds$$

where u is the velocity of the fluid, μ is the viscosity, p the pressure and u_∞ is the speed of the wing in the fluid. The foregoing quantities (except from u_∞) are computed by solving the compressible Navier-Stokes equations in the complement of the volume A occupied by the wing. The fact of solving the 3D Navier-Stokes equations in an unbounded domain in the presence of a high Reynolds number makes this problem very difficult, both numerically and theoretically.

During the last decades, thanks to the exponential development in computing power, the process of optimizing structures has rapidly evolved from experience and knowledge of engineers to automatic tools based on more or less classical mathematical algorithms and techniques. These advancements have enable the possibility of efficiently treat complicated problems where e.g. the mechanical intuition is very limited (dynamics, non-linear problems, etc...) and reduce the cost of long periods of design through trial and error.

Due to the increasing interest in the subject, many methods have been studied and developed in structural optimization during the last years. Among the vast literature available on the field, we refer the reader e.g. to [4, 45, 144, 285, 255] and references therein.

Depending on the choice of geometric representation of the shape, a subdivision of shape optimization problems can be established. Thus, three main categories are recognized: parametric (or size), geometric (or shape) and topology optimization. We give a short description of each one of them, emphasizing the last one though.

1) Parametric (or Size) optimization. The shape is described *a priori* using a limited number of parameters. Such control variables can be for example the thickness distribution of the structure, the size of structural members or the size of bars in a truss. Many approaches have also been presented, in which the boundary of the structure is parametrized using polynomials,

such as Bézier curves, splines or NURBS. This type of optimization is widely used in industrial applications, but offers a limited possibility of shape variations [41, 5, 86, 44].

2) *Geometric (or Shape) optimization.* The optimization variable is the boundary of the structure itself. This boundary is not *a priori* limited to a certain family of curves (splines, NURBS, etc...), but rather completely free [14, 5, 255, 224]. It can be numerically represented using e.g. a non-structured mesh which is deformed. Even though the domain has the freedom to vary according to the boundary, no topology changes can take place.

3) *Topology optimization.* We search to find the best shape without imposing any previous restriction. Unless it exists some reason to use a parametrization of the shape or to keep a specific topology, this category of shape optimization is the most interesting and allows to explore a larger set of shapes, increasing the possibility to obtain "better optimal" solutions. Currently several methods for topology optimization exist in literature. The mainly differ in the way topological changes occur. We give a rapid glance to each one of them.

The first efforts to create optimal topologies in structural optimization employed the homogenization method introduced by Murat and Tartar [232, 301, 302]. Also important contributions are due to Cherkaev, Gibianski and Lurie [85, 126, 206], together with Kohn and Strang [182]. The article of Bendsoe and Kikuchi [43] popularized this method and had an enormous impact among engineers applying shape optimization. We also refer the reader to [4]. Within this method, the shapes are described by a distribution of intermediates densities going from zero to one. In the case of linear elasticity, the relaxed physical properties of the medium belong to the space of homogenized elasticity tensors G_θ, representing the set of "composite" materials made from the mixture of one material and void in a certain proportion θ. A typical solution of an homogenized problem results in an optimal shape like the one on the left of Figure 1.2. In general the notion of "shape" with clear boundaries is lost, giving way to a "composite", in the sense of graded structure. Unfortunately for engineering applications, this is a cumbersome drawback which does not allow to construct structures by classical manufacturing procedures such as machining or molding. However, the recent outstanding development in additive manufacturing techniques such as 3D printing, enables to consider the fabrication of graded materials in a near future (see Figure 1.3).
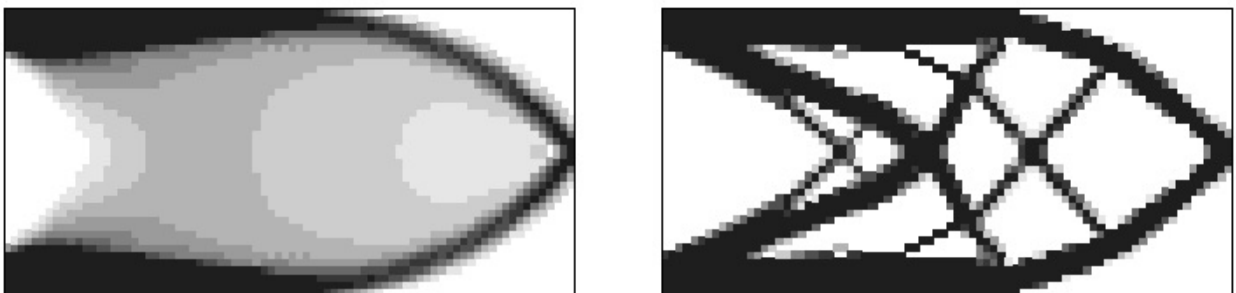
Figure 1.2: Left: density distribution of a composite optimal shape; right: penalized optimal shape (figure extracted from [4]).

In order to obtain a classical shape from the homogenized optimum, usually one penalizes intermediate densities through fictitious interpolation schemes for the material properties, which has the tendency to produce $0-1$ shapes (see Figure 1.2 on the right).

A part from problems involving the compliance and eigenfrequency optimization in elasticity, the homogenization method is not fully operative due to the lack of knowledge of the set of homogenized elasticity tensors G_θ [4]. One must thus conform with approximations of the foregoing set where the global optimality cannot be necessarily guaranteed. The most well-known approximation is the one that entails the SIMP method (Solid Isotropic Material with

Penalization) [45, 44].Indeed, G_θ is approximated by the set of elasticity tensors of the form $A_{ijkl}(\theta) = \theta^p A_{ijkl}$, where A_{ijkl} represents the elasticity tensor of the full material ($\theta = 1$) and p is the penalization power, used to enforce shapes with approximative $0-1$ designs (usually $p = 3$). We can also cite e.g. other schemes, such as RAMP [291] and combinations of penalization techniques with Heaviside projection functions [131].

Due to its robustness and simplicity, the SIMP method has been applied to several engineering problems with excellent results [44]. Furthermore, most of commercial softwares dedicated to topology optimization, such as GENESIS (Vanderplaats), NASTRAN (MSC Software), OPTISTRUCT (Altair) and TOPOL (Samtech), are based on the SIMP method. Nevertheless, despite of all these good features, in many cases where the position of the interface is a critical matter, such as those involving manufacturing [220] or pointwise constraints, the use of the SIMP method seems not to be the most suitable due to the remaining intermediate density zones. For the interested reader, we recommend [262].
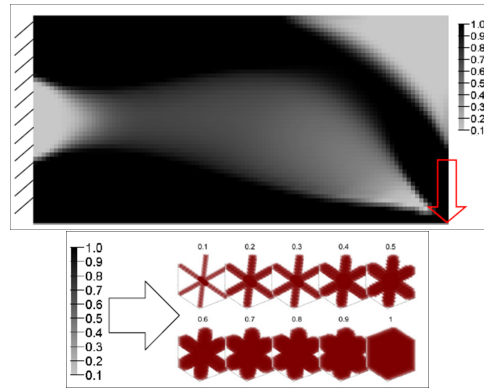
(a) Homogenized structure and mapping of density to micro-structure
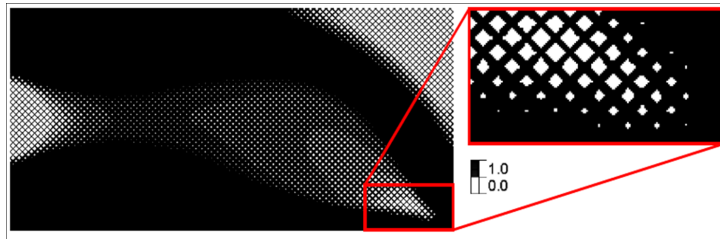
(b) Combined solid and lattice structure
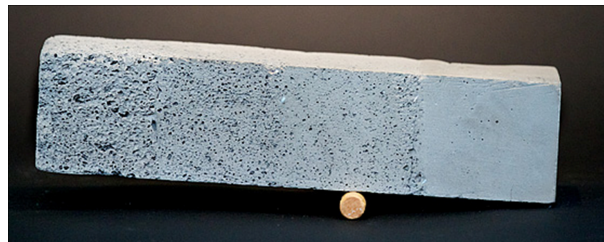
(c) Concrete samples made by hand to illustrate the concept of density gradient in concrete. MIT Media Lab

Figure 1.3: Applications of additive manufacturing to graded materials for topology optimization [58].

Another way of doing topology optimization without invoking intermediate densities is through the boundary variations methods. These methods combine classical shape sensitivity analysis tools with geometric representation methods that allow topological changes to occur in a natural way. Therefore the position of the interface is known at every iteration. We can cite

e.g. the level-set method for topology optimization [11, 319], explicit mesh representations of the domain [87, 97], the phase-field method [320, 329, 322, 300] and topological derivative-based methods [245, 283, 123, 25]. The level-set method will be presented in detail in Section 1.2.

Finally among the so-called non-gradient based methods, we can cite genetic algorithms [5, 172, 142], integer programming [297], cellular automata [179] and evolutionary algorithms [159]. One of the most well-known method in the last category is the Soft Kill Option (SKO) [211, 34]. This heuristic, inspired by nature, removes the less efficient elements of the structure in order to obtain an iso-stressed configuration.

Generally speaking, the aforementioned methods are very easy to implement since they do not require any gradient and the shape description is simpler. However, they have been largely criticized, e.g. in [276], due to their restricted application to academic test cases and their excessive numerical cost.

1.1.1 Do optimal shapes exist?

We give a brief review of some fundamental ideas on the existence of optimal shapes, which is of course not exhaustive. In general a shape optimization problem can formally be written as

$$\inf_{\Omega \in \mathcal{U}_{ad}} J(\Omega), \tag{1.1}$$

where Ω is the domain occupied by the structure, J is the objective function to be minimized and $\mathcal{U}_{ad}$ is a set of admissible shapes. Suppose additionally that J depends on the set $\mathcal{U}_{ad}$ via a second order elliptic PDE.

The main method for proving the existence of a solution to (1.1) is to endow $\mathcal{U}_{ad}$ with a certain topology $\mathcal{T}$ which ensures that $\mathcal{U}_{ad}$ is compact and J is a lower semi-continuous function. This method is called *Direct method* in the calculus of variations [94] and can be stated as follows

Proposition 1.1.1. *Suppose $\mathcal{U}_{ad}$ compact and J bounded from below and sequentially lower semi-continuous w.r.t. the topology $\mathcal{T}$. Then there exists a certain $\Omega^* \subset \mathcal{U}_{ad}$ such that the minimizing sequence $(\Omega_n)_n \subset \mathcal{U}_{ad}$ admits a sub-sequence $(\Omega_{n_k})_{n_k} \to \Omega^*$ and Ω^* is solution of (1.1).*

One of the most typical difficulties in shape optimization is the generic non-existence of well-defined solutions (i.e. domains in the admissible space). In the light of Proposition 1.1.1, this fact is generally justified by either the lack of compactness of $\mathcal{U}_{ad}$, or the absence of lower semi-continuity of J. This seems to be just a theoretical problem for mathematicians, but it has a dramatic consequence for practical and numerical applications. Indeed, most algorithms are not convergent under mesh refinement or highly sensitive to initial guesses, which implies that the result of a computation is never guaranteed to be optimal, even approximately.

Counter-examples to the existence of optimal designs have been quite detailed in literature [228, 30, 84]. In order to fix the ideas, let us cite an example from [5]

An example of non-existence

Consider a membrane occupying the domain $D = [0, 1] \times [0, 1]$, on which two horizontal uniform loads (denoted as e_1) are respectively applied on its left and right sides (see Figure 1.4). The membrane is filled with two isotropic elastic materials, respectively characterized by the coefficients α and β. The coefficient β is set to a very small value representing void (thus $\alpha >> \beta$). Assuming that the strong phase α occupies the domain $\Omega \subset D$, the elastic coefficient α_χ for the whole domain D is written as

$$\alpha_\chi = \alpha\chi + \beta(1 - \chi),$$

where characteristic function χ reads

$$\chi(x) = \begin{cases} 1 & \text{if } x \in \Omega, \\ 0 & \text{if } x \notin \Omega. \end{cases} \tag{1.2}$$

Then the displacement u_χ solves the state equation

$$\begin{cases} -\mathrm{div}(\alpha_\chi \nabla u_\chi) & = & 0 & \text{in } D, \\ \alpha_\chi \nabla u_\chi \cdot n & = & e_1 \cdot n & \text{on } \partial D. \end{cases} \tag{1.3}$$

Problem (1.1) can be written in this case as

$$\inf_{\chi \in \mathcal{U}_{ad}} J(\chi), \tag{1.4}$$

where we look for the shape of the membrane that maximizes its rigidity (or rather minimizes
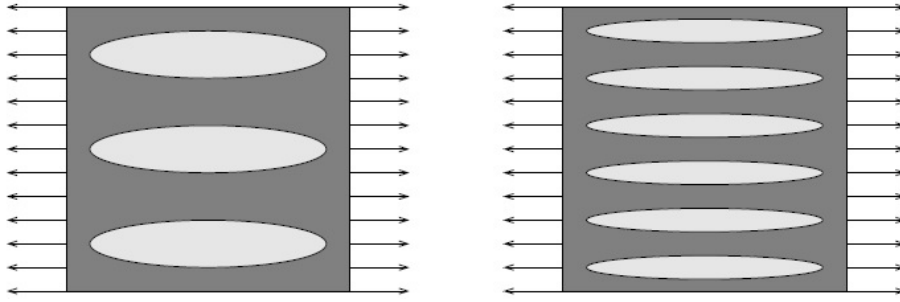
Figure 1.4: Membrane having the same volume, but different number of holes. The shape on the right is more rigid than that on the left (figure extracted from [5]).

the potential elastic energy/compliance) for a certain specific volume V_α of the rigid material. Mathematically the optimization problem reads

$$\inf_{\chi \in \mathcal{U}_{ad}} J(\chi) = \int_{\partial D} (e_1 \cdot n) u_\chi ds, \tag{1.5}$$

where the admissible set $\mathcal{U}_{ad}$ is defined as

$$\mathcal{U}_{ad} = \left\{ \chi \in L^\infty(D; \{0,1\}) \text{ such that } \frac{1}{|D|} \int_D \chi dx = V_\alpha \right\}.$$

Then one can prove

Proposition 1.1.2. *There exists no optimal solution for problem (1.5) in the set $\mathcal{U}_{ad}$.*

An intuitive explanation of the above result is that the rigidity of the structure could be always further improved by creating smaller and smaller inclusions of weak phase aligned with the direction of the force. Since the admissible set $\mathcal{U}_{ad}$ imposes no constraint on the size or smoothness of the holes, this process could be continued without any limit. In fact, the sequence of such shapes does not converge to a classical shape described by a characteristic function, but instead to a composite material, a mixture of materials α and β with densities $\theta = \frac{V_\alpha}{|D|}$ and $1 - \theta$.

In order to palliate the inconvenient of non-existence of an optimal solution, two methodologies arise to ensure the compactness of $\mathcal{U}_{ad}$ (while assuming the lower semi-continuity of J). The first one is to restrict the class of admissible designs by adding further constraints which ensure the existence of an optimum. On the contrary, the second one searches to enlarge the class of admissible designs by allowing for generalized designs for which there are optimal solutions. We proceed to give a rapid glance to each one of the above solutions for different classical PDE's (not exactly the aforementioned membrane model even though the results can usually be generalized). For the interested reader we recommend [4, 5, 144, 9, 64] and the references within.

Restriction of the admissible set

In general these constraints are intended to prevent shapes to oscillate too much or to change of topology. Some of them have a geometrical interpretation meanwhile others are a consequence of purely technical arguments introduced in the optimization model.

1) Uniform regularity constraint of the boundary.

A first natural idea to prevent oscillations of the minimizing sequences consists in working with domains which have some uniform regularity. This regularity can be expressed either in terms of uniform Lipschitz regularity of the boundary or in term of uniform cone condition. Let us choose the latter one which is more geometric.

Definition 1.1.3. *Let y be a point in $\mathbb{R}^d$, ξ a unit vector and $\epsilon > 0$. We denote by $C(y, \xi, \epsilon)$ the cone defined by:*

$$C(y, \xi, \epsilon) = \left\{ z \in \mathbb{R}^d | (z - y, \xi) \geq \cos(\epsilon)|z - y| \text{ and } 0 < |x - z| < \epsilon \right\}.$$

Furthermore we say that an open set Ω has the $\epsilon-$cone property if:

$$\forall x \in \partial\Omega, \exists \xi_x \text{ unit vector such that } \forall y \in \bar{\Omega} \cap B(x, \epsilon), C(y, \xi_x, \epsilon) \subset \Omega,$$

where $B(x, \epsilon)$ is the ball centered at x with radius ϵ.

It can be proved [83], that the previous property is equivalent to uniform Lipschitz property of the boundary of Ω.

For a fixed $\epsilon > 0$, we now introduce the following class of admissible domains:

$$\mathcal{U}_{ad} = \{\Omega \subset B \text{ open set and } \Omega \text{ has the } \epsilon - \text{cone property}\}, \tag{1.6}$$

where B is a fixed ball. Then the following statement enables us to prove the existence of an optimal shape in $\mathcal{U}_{ad}$

Theorem 1.1.4 (Chenais [83])**.** *Let $f \in L^2(B)$ and for all $\omega \subset B$, let u_ω and v_ω be the solutions of the following Dirichlet and Neumann problems:*

$$\begin{cases} -\Delta u_\omega = f & in \ \omega, \\ u_\omega = 0 & on \ \partial\omega. \end{cases} \quad and \quad \begin{cases} -\Delta v_\omega + v_\omega = f & in \ \omega, \\ \frac{\partial v_\omega}{\partial n} = 0 & on \ \partial\omega. \end{cases}$$

Define the cost functions

$$J_1 = \int_\omega j(x, u_\omega, \nabla u_\omega)dx \quad and \quad J_2 = \int_\omega j(x, v_\omega, 0)dx + \alpha \int_\omega |\nabla v_\omega|^2 dx, \tag{1.7}$$

with $\alpha \geq 0$ and $\forall x \in B, r \in \mathbb{R}, p \in \mathbb{R}^d \ |j(x, r, p)| \leq C(1 + r^2 + |p|^2)$. We assume moreover that J_1, J_2 can be estimated from below. Then for a fixed ϵ, there exists at least one solution of (1.1) with $J = J_1$ or $J = J_2$ and $\mathcal{U}_{ad}$ given by (1.6).

The proof relies on the use of the Hausdorff convergence for open sets (see Remark 1.1.10).

2) Limited number of connected components

In two dimensions, we can state a constraint of topological nature that assumes that the number of connected components of the complementary must stay bounded. Indeed, let B an arbitrary bounded set and $l \geq 1$ integer. For every open set $\omega \subset B$ we denote by $\sharp\omega^c$ the number of connected components of the complementary of ω. Then the following existence result due to Šverak follows

Theorem 1.1.5 (Šverak [298])**.** *Consider the same framework than Theorem 1.1.4 but this time with the definition of $\mathcal{U}_{ad}$ as*

$$\mathcal{U}_{ad} = \{\omega \subset B | \sharp \omega^c \leq l\}\,.$$

Then there exists at least one solution of (1.1) *with $J = J_1$.*

From a mechanical point of view, the aforementioned result can be interpreted as the existence of an optimal shape for an isotropic and homogeneous membrane, where u corresponds to the vertical displacement [5]. The generalization to linearized 2D elasticity (where the displacement u is now a vector) is due to Chambolle in [81].

3) PERIMETER CONSTRAINT.

There are several cases where imposing constraints on the perimeter of the admissible domains appear very natural. This is the case, in particular, when the perimeter appears directly in the functional we want to minimize as a surface tension term. It can also be a good measure of the cost of the design we want to construct.

For a shape $\Omega \subset D$, with D an open subset of $\mathbb{R}^d$, we recall the definition generalized perimeter P introduced by De Georgi as

$$P(\Omega) = \sup \left\{ \int_D \chi_\Omega \mathrm{div}(\phi)dx; \quad \phi \in C_c^\infty(D; \mathbb{R}^d), \|\phi\|_{L^\infty}(D) \leq 1 \right\}$$

In other words, $P(\Omega)$ represents the total variation of the gradient of the characteristic function considered as a Radon measure. We will denote by $\mathcal{M}_b(D)$ the set of Radon measures in D with finite total mass. Then the compact embedding

$$BV(D) = \{f \in L^1(D) | \nabla f \in \mathcal{M}_b(D; \mathbb{R}^d)\} \hookrightarrow L^1(D)$$

yields the following result due to Ambrosio and Buttazzo [16, 144]

Theorem 1.1.6. *Let $(\Omega_n)_n$ be a sequence of measurable sets in an open set $D \subset \mathbb{R}^d$. We assume that there exists an uniform constant C such that*

$$|\Omega_n| + P(\Omega_n) \leq C, \forall n.$$

Then there exists $\Omega^* \subset D$ measurable and a subsequence $(\Omega_{n_k})_{n_k}$ satisfying:

$$\chi_{\Omega_{n_k}} \to \chi_{\Omega^*} \text{ strongly in } L^1_{loc}(\mathbb{R}^d) \qquad and \qquad \nabla \chi_{\Omega_{n_k}} \to \nabla \chi_{\Omega^*} \text{ weakly-* in } \mathcal{M}_b(D; \mathbb{R}^d),$$

$$|\Omega^*| \leq \liminf_{k \to \infty} |\Omega_{n_k}| \qquad and \qquad P(\Omega^*) \leq \liminf_{k \to \infty} P(\Omega_{n_k}).$$

Moreover, if D has finite measure, the convergence of $\chi_{\Omega_{n_k}}$ towards χ_{Ω^*} takes place in $L^1(D)$ and $|\Omega^*| = \lim |\Omega_{n_k}|$.

Theorem 1.1.7. *Consider two materials with constant conductivities α, β, respectively (0 < $\alpha < \beta$). Let $f \in L^2(D)$ be a charge density source and u_Ω the electrostatic potential, solution of the problem*

$$\begin{cases} -\mathrm{div}((\alpha\chi_\Omega + \beta(1 - \chi_\Omega))\nabla u_\omega) = f & in \ D, \\ u_\Omega = 0 & on \ \partial D. \end{cases}$$

For $C > 0$, introduce also the set of admissible shapes

$$\mathcal{U}_{ad} = \{\Omega \subset D, \ |\Omega| + P(\Omega) \leq C\}.$$

Then there exists an unique solution to problem (1.1) *with $J = \int_D j(x, \chi_\Omega, u_\Omega, \nabla u_\Omega)dx$, where j is lower semi-continuous and satisfies adequate growth conditions.*

The aforementioned elements will play a key role in the existence results of Section 3.3 for composite optimization.

4) REGULARITY OF THE LEVEL-SET FUNCTIONS.

Consider the weak formulation of the conductivity problem

$$\int_D \Big((a_1 \chi_\Omega + a_2(1 - \chi_\Omega)) \nabla u_\Omega \cdot \nabla v + (b_1 \chi_\Omega + b_2(1 - \chi_\Omega)) u_\Omega v \Big) dx = \int_D f v dx, \forall v \in V \subset H^1(D),$$

where $a_i, b_i > 0$, $i = 1, 2$ represent two materials, $D \subset \mathbb{R}^d$ is a fixed domain and $f \in L^2(D)$. We search thus to optimize the position of the interface between both materials. The idea in [240] is to take $\chi_\Omega = H(p_\Omega)$, with H the maximal monotone extension of the heaviside function

$$H(p) = \begin{cases} 1, & p > 0 \\ [0, 1], & p = 0 \\ 0, & p < 0 \end{cases}$$

and the level set function $p_\Omega \in W(D)$ representing Ω, with

$$W(D) = \{ \quad p \in H^1(D) | \exists r_K, M_K, \nu > 0 \text{ such that } |p| + |\nabla p| \geq \nu > 0 \text{ and } \|p\|_{H^{1 + r_K}(K)} \leq M_K \\ , \forall K \subset D \text{ compact} \},$$

where the constants r_K and M_K depend of the compact K at issue. Then

Proposition 1.1.8. *Define the admissible set*

$$\mathcal{U}_{ad} = \{\Omega \subset D | \exists p_\Omega \in W(D) \text{ such that } \chi_\Omega = H(p_\Omega)\}.$$

Then any sequence $(\Omega_n)_n \subset \mathcal{U}_{ad}$ admits a subsequence $(\Omega_{n_k})_{n_k}$ such that there exists $\Omega^* \in \mathcal{U}_{ad}$ and $\chi_{\Omega_{n_k}} \to \chi_{\Omega^*}$ a.e. in D. Moreover there exists an unique solution to problem (1.1) with $J = \int_D j(x, \chi_\Omega, u_\Omega, \nabla u_\Omega) dx$, where j is lower semi-continuous and satisfies adequate growth conditions.

5) REGULAR PERTURBATIONS OF THE IDENTITY

The following condition is due mainly to Murat and Simon [231, 230], but the approach is quite similar to the one of Micheletti [221, 104] through the Courant metric. Let $\Omega_0 \subset \mathbb{R}^d$ be a smooth reference domain and the space of diffeomorphism (differentiable bijections with differentiable inverses)

$$\mathbb{D} = \{T \text{ such that } (T - Id) \in W^{1,\infty}(\mathbb{R}^d; \mathbb{R}^d), (T^{-1} - Id) \in W^{1,\infty}(\mathbb{R}^d; \mathbb{R}^d)\}. \tag{1.8}$$

We introduce the space of admissible shapes obtained by deformation of Ω_0 as

$$\mathbb{C}(\Omega_0) = \{\Omega \mid \exists T \in \mathbb{D}, \Omega = T(\Omega_0)\}. \tag{1.9}$$

We remark that since $T \in \mathbb{D}$ is a homeomorphism (continuous bijection with a continuous inverse), all $\Omega = T(\Omega_0)$ preserve the same topology than Ω. We also define the pseudo-distance

$$d^{\mathbb{D}}(\Omega_1, \Omega_2) = \inf_{T \in \mathbb{D} | T(\Omega_1) = \Omega_2} \Big(\|T - Id\|_{W^{1,\infty}} + \|T^{-1} - Id\|_{W^{1,\infty}} \Big).$$

Then the following existence result follows

Theorem 1.1.9 (Murat and Simon [230]). *Let $V_0, R > 0$ be two constants. Define the admissible set*

$$\mathcal{U}_{ad} = \{\Omega \in \mathbb{C} | d^{\mathbb{D}}(\Omega, \Omega_0) \leq R, \int_{\Omega} dx = V_0\}. \tag{1.10}$$

Then any sequence $(\Omega_n)_n \subset \mathcal{U}_{ad}$ admits a subsequence $(\Omega_{n_k})_{n_k}$ such that there exists $\Omega^* \in \mathcal{U}_{ad}$ and

$$\sup \left(d_H(\Omega_{n_k}, \Omega^*), d_H(\partial\Omega_{n_k}, \partial\Omega^*), d_H(\mathbb{R}^d \backslash \Omega_{n_k}, \mathbb{R}^d \backslash \Omega^*) \right) \to 0,$$

where d_H is the Hausdorff metric (see Remark 1.1.10).

Thanks to the definition of $\mathcal{U}_{ad}$, any admissible element Ω can be obtained by applying a regular diffeomorphism to the reference domain Ω_0, restricting in this way the possible topology changes of the shapes. This vector space representation of every admissible shape will allow us to introduce the right framework to perform some calculus of variations through the notion of the shape derivative (Subsection 1.1.2).

Several of the preceding conditions rely on the compactness induced by the Hausdorff metric to the set of subdomains of a compact.

Definition 1.1.10. *Let $K_1, K_2 \subset B$ and B a fixed compact set of $\mathbb{R}^d$. Define the Hausdorff metric d_H as*

$$d_H(K_1, K_2) = \max \left(\sup_{x \in K_1} \inf_{y \in K_2} \|x - y\|, \sup_{y \in K_2} \inf_{x \in K_1} \|x - y\| \right),$$

We say that a sequence $(\Omega_n)_n$ converges to Ω in the Hausdorff sense if

$$d_H(B \backslash \Omega_n, B \backslash \Omega) \to 0 \quad \text{when } n \to \infty.$$

Theorem 1.1.11 ([144]). *The set $\{\Omega \subset B\}$ is compact for the Hausdorff metric d_H.*

In the context of this thesis, the constraints 3) and 5) will be used to prove the existence of optimal shapes.

Relaxation or homogenization of the admissible set

As it was seen in the counter-example of Proposition 1.1.2, when the existence of a classic solution fails, frequently a relaxation process occurs. This is the situation in which a minimizing sequence of shapes leads to a "mixture" between material and void. Thus, the non-existence problem is avoided by enlarging the set of admissible shapes by including "homogenized" structures in $\mathcal{U}_{ad}$ [4, 302, 232]. In this way the characteristic function χ is replaced by a density field θ which varies continuously in the interval $[0, 1]$. The elastic properties of each phase are replaced by the homogenized properties of the composite material created by their mixture. Once the properties of the homogenized elasticity tensor A^* have been optimized, problem (1.4) is replaced by the *relaxed* or *homogenized* problem

$$\inf_{\theta \in \mathcal{U}_{ad}^*} J(\theta), \tag{1.11}$$

where

$$\mathcal{U}_{ad}^* = \left\{ \theta \in L^\infty(D; [0, 1]) \text{ such that } \int_D \theta dx = V_\alpha \right\}.$$

This problem admits a solution that can be proved to correspond to the limit of a sequence of shapes of problem (1.4).

Despite the foregoing methodologies to guarantee the existence of an optimal solution, the fact of just being aware of the existence of an optimal solution does not necessarily imply the

knowledge to construct it. Thereby, optimality conditions expressed through the shape or topological derivatives will play an important role to numerically compute "optimal" (or rather local optimal) solutions. We remark however that the family of open subsets or shapes of $\mathbb{R}^d$ has not a normed vector space structure, hence the classical optimization theory (differential calculus) does not apply [144].

In the sequel we give a short review on the shape and the topological derivatives.

1.1.2 Shape sensitivity analysis

The boundary variations of a shape Ω are studied through the notion of a "shape" gradient, which leans on a particular parameterization of the admissible set of shapes, allowing to endow the problem with a normed vectorial space structure. Shape differentiation is a classical topic that goes back at least to Hadamard in 1908 [138]. We present here the approach of Murat and Simon [279]. For more details see e.g. [285, 144].

Introduction

Consider $\Omega_0 \subset \mathbb{R}^d$ a smooth open reference domain, we will suppose that all admissible shapes Ω are obtained by applying a smooth vector (or advection) field θ such that

$$\Omega = \{x + \theta(x) \ , \ x \in \Omega_0\} .$$

In other words, every admissible shape Ω will be represented by a vector field $\theta : \mathbb{R}^d \to \mathbb{R}^d$ and
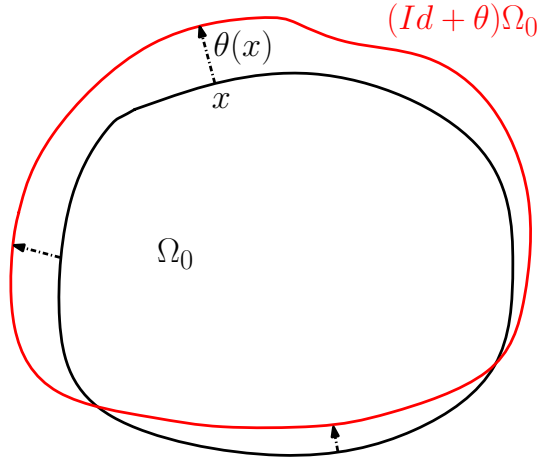
Figure 1.5: Variations of a shape using Hadamard's method.

we will write $\Omega = (\operatorname{Id} + \theta)(\Omega_0)$ (see Figure 1.5). The space of admissible shapes obtained by such a deformation coincides with $\mathbb{C}$ in (1.9) by taking $T = Id + \theta$, at least for θ small. Indeed, one can prove that if $\|\theta\|_{W^{1,\infty}(\mathbb{R}^d)} < 1$, then $T = Id + \theta$ is a bijection of $\mathbb{R}^d$ that belongs to $\mathbb{D}$ in (1.8).

Remark 1.1.12. *We could have also defined θ belonging to $C_b^1(\mathbb{R}^d; \mathbb{R}^d)$, the space of continuously differentiable functions and uniformly bounded so as their gradients. We recall that the functions belonging to $W^{1,\infty}(\mathbb{R}^d; \mathbb{R}^d)$ are continuous.*

We are now ready to define a notion of differentiability with respect to the domain.

Definition 1.1.13. *The functional $J : \Omega \to \mathbb{R}$ is said to be shape differentiable at Ω_0 if the application*

$$\theta \to J\left((\operatorname{Id} + \theta)(\Omega_0)\right)$$

is Fréchet differentiable at 0 in the Banach space $W^{1,\infty}(\mathbb{R}^d;\mathbb{R}^d)$. Then, the following asymptotic expansion holds in the vicinity of 0:

$$J\big((Id+\theta)(\Omega_0)\big) = J(\Omega_0) + J'(\Omega_0)(\theta) + o(\theta) \quad with \quad \lim_{\theta\to 0}\frac{|o(\theta)|}{\|\theta\|} = 0 , \qquad (1.12)$$

where $J'(\Omega_0)$ is a continuous linear form on $W^{1,\infty}(\mathbb{R}^d;\mathbb{R}^d)$.

It is also convenient for our purposes, to define a weaker notion of differentiability, namely a directional derivative $J'(\Omega_0)(\theta)$, which is defined as the limit in $\mathbb{R}$ (if it exists)

$$J'(\Omega_0)(\theta) = \lim_{t\to 0^+}\frac{J((Id+t\theta)(\Omega_0)) - J(\Omega_0)}{t}.$$

Definition 1.1.14. *Let $\mathcal{U}_{ad}$ a set of admissible shapes and suppose the functional $J:\mathcal{U}_{ad}\to\mathbb{R}$ directionally shape differentiable at $\Omega_0\in\mathcal{U}_{ad}$. We say that Ω_0 satisfies the necessary optimality condition w.r.t. the shape derivative if*

$$J'(\Omega_0)(\theta) \geq 0, \forall\theta\in W^{1,\infty}(\mathbb{R}^d;\mathbb{R}^d). \qquad (1.13)$$

Remark 1.1.15. *In order for the above definition to have a full meaning, $(Id+t\theta)\Omega_0\in\mathcal{U}_{ad}$ for small t. I.e. the set $\mathcal{U}_{ad}$ must be stable for vector fields deformations.*

The classical Hadamard's structure theorem states that under certain regularity hypothesis, the shape derivative depends only on the normal component of θ on the boundary $\partial\Omega$, i.e. the tangential component can be omitted.

Proposition 1.1.16. *Let Ω_0 be a smooth bounded open set of $\mathbb{R}^d$ and J a differentiable function at Ω_0. If $\theta_1,\theta_2\in W^{1,\infty}(\mathbb{R}^d;\mathbb{R}^d)$ are such that $\theta_2-\theta_1\in C^1(\mathbb{R}^N;\mathbb{R}^N)$ and $\theta_1\cdot n = \theta_2\cdot n$ on $\partial\Omega_0$, then the derivative $J'(\Omega_0)$ verifies*

$$J'(\Omega_0)(\theta_1) = J'(\Omega_0)(\theta_2).$$

In order to fix the ideas, we expose some classical examples of shape derivatives of integrals, whose integrand does not depend on the domain Ω.

Proposition 1.1.17. *Let Ω_0 be a smooth bounded open set of $\mathbb{R}^d$. If $f\in W^{1,1}(\mathbb{R}^d)$ and $J:\mathbb{C}(\Omega_0)\to\mathbb{R}$ is defined by*

$$J(\Omega) = \int_\Omega f(x)\,dx,$$

then J is shape differentiable at Ω_0 and

$$J'(\Omega_0)(\theta) = \int_{\Omega_0}\mathrm{div}\,(\theta(x)f(x))\,dx = \int_{\partial\Omega_0}\theta(x)\cdot n(x)f(x)ds,$$

for all $\theta\in W^{1,\infty}(\mathbb{R}^N;\mathbb{R}^N)$.

Proof. We apply a change of variables in order to bring back the integral defining J to the reference domain Ω_0, namely

$$J(\Omega) = J((\mathrm{Id}+\theta)(\Omega_0)) = \int_{(\mathrm{Id}+\theta)(\Omega_0)}f(x)dx = \int_{\Omega_0}f\circ(\mathrm{Id}+\theta)\,|\det(I+\nabla\theta)|\,dx,$$

where $I=\nabla\mathrm{Id}$ is the constant identity matrix. Substituting to the above expression the identities

$$\det(I+\nabla\theta) = 1+\mathrm{div}\theta+o(\theta) \quad with \quad \lim_{\theta\to 0}\frac{\|o(\theta)\|_{L^\infty(\mathbb{R}^d)}}{\|\theta\|_{W^{1,\infty}(\mathbb{R}^d;\mathbb{R}^d)}} = 0$$

and

$$f \circ (\,\mathrm{Id} + \theta\,)\,(x) = f(x) + \nabla f(x) \cdot \theta(x) + o(\theta) \quad with \quad \lim_{\theta \to 0} \frac{\|o(\theta)\|_{L^\infty(\mathbb{R}^N)}}{\|\theta\|_{W^{1,\infty}(\mathbb{R}^N;\mathbb{R}^N)}} = 0,$$

yields the desired result. The last identity stems from the regularity $W^{1,1}(\mathbb{R}^d)$ of f. $\qquad\square$

Proposition 1.1.18. *Let Ω_0 be a smooth bounded open set of $\mathbb{R}^d$. If $f \in W^{2,1}(\mathbb{R}^d)$ and $J : \mathbb{C}(\Omega_0) \to \mathbb{R}$ is defined by*

$$J(\Omega) = \int_{\partial\Omega} f(x)\,ds,$$

then J is differentiable at Ω_0 and $\forall \theta \in C^1(\mathbb{R}^d;\mathbb{R}^d)$ we have

$$J'(\Omega_0)(\theta) = \int_{\partial\Omega_0} (\nabla f \cdot \theta + f\,(\mathrm{div}\theta - \nabla\theta n \cdot n))\,ds = \int_{\partial\Omega_0} \theta \cdot n \left(\frac{\partial f}{\partial n} + \kappa f \right) ds,$$

where $\kappa = \mathrm{div}n$ is the mean curvature of $\partial\Omega_0$.

Proof. Using a change of variables as previously, we get

$$J(\Omega) = J\left((\,\mathrm{Id} + \theta\,)(\Omega_0)\right) = \int_{\partial\Omega_0} f \circ (\,\mathrm{Id} + \theta\,) \,|\det (I + \nabla\theta)| \left\| \left((I + \nabla\theta)^{-1}\right)^T n \right\|_{\mathbb{R}^d} ds.$$

Substituting the expansions around $\theta = 0$

$$\left((I + \nabla\theta)^{-1}\right)^T n = n - (\nabla\theta)^T n + o(\theta) \quad with \quad \lim_{\theta \to 0} \frac{\|o(\theta)\|_{L^\infty(\partial\Omega_0;\mathbb{R}^d)}}{\|\theta\|_{C^1(\mathbb{R}^d;\mathbb{R}^d)}} = 0$$

and

$$\left\| \left((I + \nabla\theta)^{-1}\right)^T n \right\|_{\mathbb{R}^d} = 1 - (\nabla\theta)^T n \cdot n + o(\theta) \quad with \quad \lim_{\theta \to 0} \frac{\|o(\theta)\|_{L^\infty(\partial\Omega_0;\mathbb{R}^d)}}{\|\theta\|_{C^1(\mathbb{R}^d;\mathbb{R}^d)}} = 0,$$

it follows

$$J'(\Omega_0)(\theta) = \int_{\partial\Omega_0} (\nabla f \cdot \theta + f\,(\mathrm{div}\theta - \nabla\theta \cdot n \cdot n))\,ds.$$

Finally an integration by parts at the boundary $\partial\Omega$ (see Lemma 6.25 in [5]) entails the result

$$J'(\Omega_0)(\theta) = \int_{\partial\Omega_0} \theta \cdot n \left(\frac{\partial f}{\partial n} + \kappa f \right) ds.$$

$\qquad\square$

Shape derivative of the solution of an equation depending of the domain

We are interested in the shape derivative of the general cost functional $J(\Omega, u(\Omega))$, where $u(\Omega) \in H^1(\Omega)$ is the solution of a partial differential equation that depends on Ω. A rigorous computation of the shape derivative of $J(\Omega, u(\Omega))$ hence implies estimating the derivatives of $u((Id+\theta)\Omega)$ w.r.t. θ. For that purpose, two kinds of derivatives of $u(\Omega)$ stand: the Lagrangian derivative $Y(\Omega)(\theta)$ and the Eulerian derivative $u'(\Omega)(\theta)$.

Definition 1.1.19. *The function $u : \Omega \to u(\Omega)$ admits a Lagrangian (or material) derivative $Y(\Omega_0)(\theta)$ at a given domain Ω_0, provided that the application*

$$\theta \in W^{1,\infty}(\mathbb{R}^d;\mathbb{R}^d) \to \tilde{u}_\theta(\Omega_0) := u((Id + \theta)\Omega_0) \circ (Id + \theta) \in H^1(\Omega_0).$$

is Fréchet differentiable at $\theta = 0$. Then $Y(\Omega_0)(\theta) = \tilde{u}'_\theta(\Omega_0)$.

On the other side, applying the chain rule, the derivative of $u((Id + \theta)\Omega_0)(x)$ at a fixed $x \in (Id + \theta)\Omega_0$ would formally read

$$\frac{d}{d\theta}u((Id + \theta)\Omega_0)(x + \theta(x))|_{\theta=0} = \frac{d}{d\theta}u((Id + \theta)\Omega_0)(x)|_{\theta=0} + \frac{d}{d\theta}u(\Omega_0)(x)|_{\theta=0}$$
$$Y(\Omega_0)(\theta)(x) = u'(\Omega_0)(\theta)(x) + \nabla u(\Omega_0)(x) \cdot \theta(x).$$

Definition 1.1.20. *The function* $u : \Omega \to u(\Omega)$ *admits a Eulerian derivative* $u'(\Omega_0)(\theta)$ *at a given domain* Ω_0*, if* u *admits a Lagrangian derivative* $Y(\Omega_0)(\theta)$ *at* Ω_0 *in the direction* θ *and* $\nabla u(\Omega_0) \cdot \theta \in H^1(\Omega_0)$*. In that case*

$$u'(\Omega_0)(\theta) = Y(\Omega_0)(\theta) - \nabla u(\Omega_0) \cdot \theta.$$

As it will be seen through this thesis, notably for transmission problems, the function $u(\Omega)$ is not always regular enough to ensure the existence of an Eulerian derivative. Thereby when needed, we will rather prefer to use the Lagrangian derivative of $u(\Omega)$.

Unfortunately in most of the cases, calculating either $Y(\Omega)(\theta)$ or $u'(\Omega)(\theta)$ is not an easy task and often implies long and tedious calculations [5]. Happily there exists a much simpler alternative which does not involve the explicit calculation of the derivatives of $u(\Omega)$: the Lagrangian derivation method of Céa [74]. Thanks to this method, the shape gradient of $J(\Omega, u(\Omega))$ can easily be calculated by establishing the stationarity conditions of a Lagrangian function. Within this function, the partial differential equation that solves $u(\Omega)$ is introduced by means of a Lagrange multiplier. However, this method remains formal, since the smoothness of the shape and the shape differentiability of all the concerned functions must be assumed *a priori*. Let us explain the method with the following example

Application of Céa's method to linear elasticity

Consider a regular elastic body $\Omega \subset \mathbb{R}^d$, whose boundary is decomposed into two parts as $\partial\Omega = \Gamma_D \cup \Gamma_N$. The structure is fixed on Γ_D and a surface load $g \in H^1(\Omega; \mathbb{R}^d)$ is applied on Γ_N. Additionally Ω is subjected to a volume force $f \in L^2(\Omega; \mathbb{R}^d)$ and characterized by the elastic tensor $A = \{A_{ijkl}\}$, with $i, j, k, l = 1, ..., d$. Then the displacement of the structure $u \in H^1(\Omega; \mathbb{R}^d)$ is the unique solution of the linearized elasticity system

$$\begin{cases} -\text{div}\,(A\,e(u)) & = & f & \text{in } \Omega, \\ u & = & 0 & \text{on } \Gamma_D, \\ (A\,e(u)) \cdot n & = & g & \text{on } \Gamma_N, \end{cases} \tag{1.14}$$

where $e(u) = (\nabla u^T + \nabla u)/2$ denotes the symmetrized gradient of u and

$$A\,e(u) = A : e(u) = \sum_{ijkl} A_{ijkl}e(u)_{kl} \tag{1.15}$$

denotes the twice contracted product between the tensors A and $e(u)$. Now, suppose that we want to compute the shape gradient for a functional of the type

$$J(\Omega, u(\Omega)) = \int_\Omega j(x, u(\Omega, x))dx + \int_{\Gamma_N} l(x, u(\Omega, x))ds, \tag{1.16}$$

where j, l are regular densities such that (1.16) is well defined [10]. Then

Proposition 1.1.21. *Assuming the functions u, p smooth, the shape derivative of (1.16) in the direction θ reads*

$$J'(\Omega, u(\Omega))(\theta) = \int_{\Gamma_N} \theta \cdot n \Big(j(x, u) + Ae(u) \cdot e(p) - f \cdot p \Big) ds + \int_{\Gamma_N} \theta \cdot n \left(\frac{\partial l(u)}{\partial n} + \kappa l(u) \right) ds$$
$$- \int_{\Gamma_N} \theta \cdot n \left(\frac{\partial (g \cdot p)}{\partial n} + \kappa (g \cdot p) \right)$$
$$+ \int_{\Gamma_D} \theta \cdot n \left(j(x, u) - Ae(u) : e(p) \right) ds,$$

where κ is the mean curvature, u is the solution of (1.14) and p is the adjoint state, solution of

$$\begin{cases} -\mathrm{div}\,(A\,e(p)) &=& -j'(u) & \text{in } \Omega, \\ p &=& 0 & \text{on } \Gamma_D, \\ \big(A\,e(p)\big) \cdot n &=& -l'(u) & \text{on } \Gamma_N. \end{cases} \tag{1.17}$$

Proof. Instead of deriving directly the functional $J(\Omega, u(\Omega))$ and compute either the Eulerian or Lagrangian derivative of $u(\Omega)$ (which is most of the time a long and tedious task), we introduce the Lagrangian function

$$\mathcal{L}(\Omega, v, q, \mu) = \int_{\Omega} j(x, v) dx + \int_{\Gamma_N} l(x, v) ds + \int_{\Omega} (-\mathrm{div}\,(Ae(v)) - f) \cdot q dx$$
$$+ \int_{\Gamma_N} (Ae(v) \cdot n - g) \cdot q ds + \int_{\Gamma_D} v \cdot \mu ds, \tag{1.18}$$

where the test functions $v, q, \mu \in H^1(\mathbb{R}^d; \mathbb{R}^d)$ do not depend on the domain Ω. As we will see in the sequel, the shape derivative of the objective functional J at Ω will be derived by fixing the domain Ω and taking the optimality conditions for the Lagrangian function $\mathcal{L}$.

Setting the partial derivative of $\mathcal{L}$ with respect to q in the direction of a test function $\phi \in H^1(\mathbb{R}^d; \mathbb{R}^d)$ at the optimal point (Ω, u, p, μ^*) equal to zero, we get

$$\frac{\partial \mathcal{L}}{\partial q}(\Omega, u, p, \mu^*)(\phi) = \int_{\Omega} (-\mathrm{div}\,(Ae(u)) - f) \cdot \phi dx + \int_{\Gamma_N} (Ae(u) \cdot n - g) \cdot \phi ds = 0.$$

Taking ϕ with compact support in Ω ($\phi = 0$ on $\partial\Omega$) gives

$$-\mathrm{div}\,(Ae(u)) = f \quad \text{in } \Omega. \tag{1.19}$$

Varying the trace of ϕ on Γ_N gives

$$Ae(u) \cdot n = g \quad \text{on } \Gamma_N \tag{1.20}$$

In the same way, setting the partial derivative of $\mathcal{L}$ with respect to μ in the direction ϕ equal to zero

$$\frac{\partial \mathcal{L}}{\partial \mu}(\Omega, u, p, \mu^*)(\phi) = \int_{\Gamma_D} u \cdot \phi ds = 0$$

results in

$$u = 0 \quad \text{on } \Gamma_D. \tag{1.21}$$

Equations (1.19),(1.20) and (1.21) show that the function u is in fact the unique solution of the state equation (1.14).

We write again the function $\mathcal{L}$, after an integration by parts, in the form

$$\mathcal{L}(\Omega, v, q, \mu) = \int_{\Omega} j(x, v) dx + \int_{\Gamma_N} l(x, v) ds + \int_{\Omega} (Ae(v) \cdot e(q) - f \cdot q) \, dx$$
$$- \int_{\Gamma_N} g \cdot q ds - \int_{\Gamma_D} Ae(v) \cdot n \cdot q ds + \int_{\Gamma_D} v \cdot \mu ds.$$

The partial derivative of $\mathcal{L}$ with respect to v, at the optimal point, in the direction $\phi \in H^1(\mathbb{R}^d; \mathbb{R}^d)$ gives

$$\frac{\partial \mathcal{L}}{\partial v}(\Omega, u, p, \mu^*)(\phi) = \int_\Omega j'(x, u) \cdot \phi dx + \int_{\Gamma_N} l'(x, u) \cdot \phi ds + \int_\Omega Ae(p) \cdot e(\phi) dx$$
$$- \int_{\Gamma_D} Ae(\phi) \cdot n \cdot p ds + \int_{\Gamma_D} \phi \cdot \mu^* ds,$$

where $j'(x, u)$ and $l'(x, u)$ represent the partial derivatives of j and l w.r.t. their second argument. Setting this derivative equal to zero and taking ϕ with compact support in Ω yields

$$- \operatorname{div}(Ae(p)) = -j'(x, u) \quad \text{in } \Omega. \tag{1.22}$$

Varying the trace of ϕ on Γ_N yields

$$Ae(p) \cdot n = -l'(x, u) \quad \text{on } \Gamma_N. \tag{1.23}$$

Varying the trace of ϕ on Γ_D with $Ae(\phi) \cdot n = 0$ yields

$$\mu^* = -Ae(p) \cdot n \quad \text{on } \Gamma_D. \tag{1.24}$$

Varying the normal stress $Ae(\phi) \cdot n$ on Γ_D with $\phi = 0$ on Γ_D yields

$$p = 0 \quad \text{on } \Gamma_D. \tag{1.25}$$

Therefore, p is the unique solution in Ω of the adjoint equation (1.17).
Finally, the shape derivative of the functional J at Ω will be equal to the shape derivative of the Lagrangian function $\mathcal{L}$ at the optimal point (Ω, u, p, μ^*), i.e.

$$\frac{\partial \mathcal{L}}{\partial \Omega}(\Omega, u, p, \mu^*)(\theta) = J'(\Omega)(\theta). \tag{1.26}$$

To prove this, take first any $q \in H^1(\mathbb{R}^d)$ and remark that

$$\mathcal{L}(\Omega, u(\Omega), q) = J(\Omega),$$

where u is the solution of the state equation. Then, taking the shape derivative of both members and using the chain rule yields

$$J'(\Omega)(\theta) = \frac{\partial \mathcal{L}}{\partial \Omega}(\Omega, u(\Omega), q, \mu)(\theta) + \left\langle \frac{\partial \mathcal{L}}{\partial v}(\Omega, u(\Omega), q, \mu), u'(\Omega)(\theta) \right\rangle. \tag{1.27}$$

Supposing the existence of the Eulerian derivative $u'(\Omega)(\theta)$, taking $q = p(\Omega)$ (the solution of the adjoint state), $\mu = \mu^*$ and $u'(\Omega)(\theta) \in H^1(\mathbb{R}^d)$, the last term in (1.27) disappears and relation (1.26) is revealed.

Applying the results of Propositions 1.1.17 and 1.1.18, we obtain the desired result

$$\frac{\partial \mathcal{L}}{\partial \Omega}(\Omega, u, p, \mu^*)(\theta) = \int_{\Gamma_N} \theta \cdot n \Big(j(x, u) + Ae(u) \cdot e(p) - f \cdot p \Big) ds + \int_{\Gamma_N} \theta \cdot n \left(\frac{\partial l(u)}{\partial n} + \kappa l(u) \right) ds$$
$$- \int_{\Gamma_N} \theta \cdot n \left(\frac{\partial (g \cdot p)}{\partial n} + \kappa (g \cdot p) \right)$$
$$+ \int_{\Gamma_D} \theta \cdot n \left(j(x, u) - Ae(u) : e(p) \right) ds,$$

where we have used the relation

$$Ae(u) : e(p) = \frac{\partial u}{\partial n} \cdot (Ae(p) \cdot n) = \frac{\partial p}{\partial n} \cdot (Ae(u) \cdot n), \quad \text{on } \Gamma_D.$$

$\square$

A classical application of the above result is the minimization of the compliance, where $j(u) = f \cdot u$ and $l(u) = g \cdot u$. In such a case, we can easily check that $p = -u$, so the problem is self-adjoint. Denote as $\Gamma_0 \subset \Gamma_N$ the traction-free part of the Neumann boundary condition ($g = 0$). Then if we assume $\theta = 0$ on $\Gamma_D \cup \Gamma_N \backslash \Gamma_0$, then the shape derivative of J reads

$$J'(\Omega)(\theta) = \int_{\Gamma_0} \Big(2f \cdot u - Ae(u) : e(u) \Big)(\theta \cdot n) ds.$$

1.1.3 Topology sensitivity analysis

The topological derivative measures the sensitivity of a given shape functional with respect to an infinitesimal singular domain perturbation, such as the insertion of holes, inclusions, source-terms or even cracks. The topological derivative was rigorously introduced by Sokolowski and Zochowski in [284] and Masmoudi in [208]. In particular, it can be seen as a mathematical justification for the topological optimization algorithm proposed by Céa et al. [76, 77], based on the combination of the shape gradient and a fixed point method, and the bubble method of Schumacher et al. [113, 268]. Since then, this concept has proved to be extremely useful in the treatment of a wide range of problems, namely topology optimization [75, 8, 12, 27, 28, 52, 67, 127, 245, 180, 246, 243, 244, 310], inverse analysis [26, 71, 116, 135, 39, 150, 152, 169, 170, 209, 18, 21, 78, 23] and image processing [32, 168, 149, 151, 188]. For a general presentation see e.g. the book [245].

The topological derivative is obtained by the combined asymptotic analysis of shape functionals and classical solutions to elliptic boundary value problems in singularly perturbed domains with respect to the small parameter which measures the size of the perturbation.

In the present work we will focus on the topological derivative for linear elastostatics. So as to fix the ideas, consider $\Omega \subset \mathbb{R}^d$ ($d = 2$ or 3) with characteristic elastic properties $\mathcal{C}$ and a point $z \in \Omega$. Furthermore let

$$B_a(z) = z + a\mathcal{B}, \quad \mathcal{B} \subset \mathbb{R}^d, \quad \mathcal{B} \text{ regular and bounded,}$$

be an inclusion in Ω with a vanishingly small characteristic radius a at a prescribed location z inside the solid. We denote by $\mathcal{C}^\star$ the elastic tensor inside B_a. The topological derivative $DJ(z)$ quantifies the perturbation induced to a cost functional $J(\Omega)$ by the virtual creation of the inhomogeneity or cavity B_a such that the new elastic law $\mathcal{C}_a$ in Ω reads

$$\mathcal{C}_a = \chi_{B_a}\mathcal{C}^\star + (1 - \chi_{B_a})\mathcal{C}. \tag{1.28}$$

More precisely,

Definition 1.1.22 (Topological derivative)**.** *Define $\Omega_a := \Omega \backslash B_a$ and assume that $J(\Omega_a)$ can be expanded in the form*

$$J(\Omega_a) = J(\Omega) + \delta(a)DJ(z) + o(\delta(a)) \tag{1.29}$$

where $\delta(a)$ is assumed to vanish as $a \to 0$ and characterizes the small-inhomogeneity asymptotic behavior of $J(\Omega_a)$. Then, the coefficient $DJ(z)$ is called the topological derivative *of J at $z \in \Omega$.*

Remark 1.1.23. *Terminology for the concept of topological derivative varies, with "gradient" or "sensitivity" sometimes used instead of "derivative".*

Remark 1.1.24. *Typically the notation $\Omega_a := \Omega \backslash B_a$ is used to define the topological derivative for cavities. Nevertheless, the foregoing notation also stands for inclusions, as it is illustrated in Proposition 1.1.27. Within Chapter 4, however, a notation rather oriented to inclusions (inhomogeneities) will be used.*

Remark 1.1.25. *One can show that the expression for the topological derivative induced by a cavity coincides with the one induced by an inhomogeneity with vanishing elastic tensor $\mathcal{C}^\star$. See e.g. [237, 245]*

The topological derivative in an anisotropic framework will be extensively developed in Chapter 4. We close this section with two examples to illustrate the computation of the topological derivative in an isotropic setting (see the proofs in [12]).

Lemma 1.1.26. *The topological derivative of $J(\Omega_a) = \int\limits_{\Omega_a} dx$ simply reads*

$$DJ(z) = -|\mathcal{B}|.$$

Proposition 1.1.27. *Consider the linear elastic problem (1.14) in dimension 2, and denote its solution as u_a when $A = \mathcal{C}_a$ in (1.28) and u when $A = \mathcal{C}$. Moreover take $\mathcal{B}$ to be the unit disk in $\mathbb{R}^2$ and set the constants $(\lambda, \mu), (\lambda^\star, \mu^\star)$ to be the Lamé coefficients of $\mathcal{C}$ and $\mathcal{C}^\star$, respectively. Suppose the loads f, g are regular. Then for any $z \in \Omega$ the topological derivative of the compliance*

$$J(\Omega_a) = \int_{\Omega_a} \mathcal{C}e(u_a) : e(u_a)dx + \int_{\Omega \setminus \Omega_a} \mathcal{C}^\star e(u_a) : e(u_a)dx$$

reads

$$
\begin{aligned}
DJ(z) &= 4\pi \frac{\mu \Delta \mu (\lambda + 2\mu)}{\lambda(\mu + \mu^\star) + \mu(\mu + 3\mu^*)} e(u)(z) : e(u)(z) \\
&- \pi \left(-\frac{(\lambda + 2\mu)\Delta(\lambda + \mu)}{\lambda^\star + \mu^\star + \mu} + 2\frac{\mu \Delta \mu (\lambda + 2\mu)}{\lambda(\mu^\star + \mu) + \mu(\mu + 3\mu^\star)} \right) tr(e(u))(z) tr(e(u))(z),
\end{aligned}
$$

where $\Delta \lambda = \lambda - \lambda^\star$ and $\Delta \mu = \mu - \mu^\star$.

1.2   The level set-method for topology optimization

1.2.1   The level-set method

Introduced in the seminal work of S. Osher and J. Sethian [252] in the framework of a flame propagation model, the level-set method is a technique for capturing interfaces which are implicitly defined via the zero level-set of an auxiliary function. Since its appearance, it has been applied in a great variety of fields such as two-phase flow, solid-fluid coupling, liquid-gas interactions, image processing, computer graphics, meshing, topology optimization, etc [271, 250, 251, 296, 313, 108]. Beyond the simplicity of the geometric description of an interface, the level-set method allow us to easily manage topology changes on a fixed Cartesian grid. Let us give an example to better explain this point.

Suppose we are given two circles that evolve in time and finally merge at some point. If we choose to track this movement by parameterizing their boundaries (Lagrangian approach), we need to update this parameterization at each time step, identify the exact moment at which the topological change occurs. The precedent procedure is easy to understand but both theoretically and numerically difficult.

Instead of this, we can choose to use an one-dimension higher function, a so-called level-set function, and reveal the boundaries of the shapes as its zero level-set (Eulerian approach).

At the upper part of Figure 1.6, we see a three-dimensional function, and several level-sets depicted in black color. The zero level-set corresponds to the lines separating the blue from the red region and represents two circles. At the lower part of the figure, we see that the function has changed and the zero level-set has evolved so now represents a domain with a different topology, i.e. the circles have merged. This topological change has occurred in a very natural way, by simply modifying the level-set function.

Define as working domain $D \subset \mathbb{R}^d$ bounded and as admissible shape $\Omega \subset D$ (see Figure 1.7). Then, the boundary of Ω is defined by means of a level set function ψ such that

$$
\begin{cases}
\psi(x) = 0 & \text{if } x \in \partial \Omega \cap D, \\
\psi(x) < 0 & \text{if } x \in \Omega, \\
\psi(x) > 0 & \text{if } x \in \left(D \setminus \overline{\Omega} \right).
\end{cases}
\tag{1.30}
$$
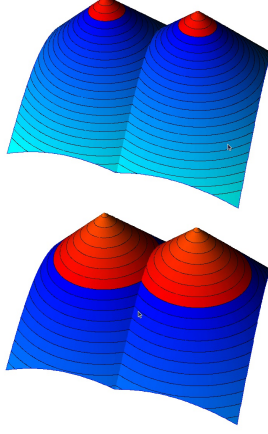
Figure 1.6: Level-set representation of two circles that finally merge.
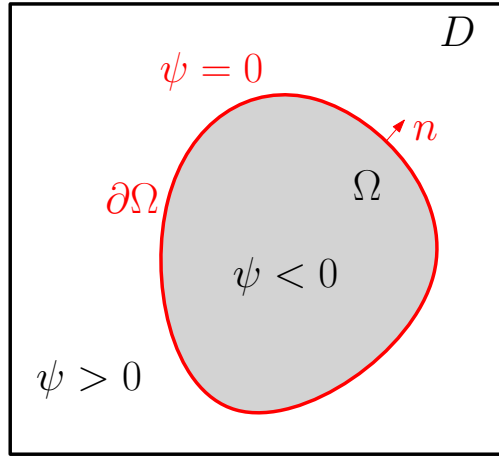
Figure 1.7: Level-set representation of a structure (in grey).

If the domain Ω is regular enough, for any point $x \in \partial\Omega$ at which $\nabla\psi(x) \neq 0$, the unit normal vector to $\partial\Omega$, pointing outward of Ω, and the mean curvature $\kappa(x)$ can be expressed as

$$n(x) = \frac{\nabla\psi(x)}{|\nabla\psi(x)|}, \quad \kappa(x) = \operatorname{div}\left(\frac{\nabla\psi(x)}{|\nabla\psi(x)|}\right). \tag{1.31}$$

Since the level-set function ψ is defined everywhere in D, (1.31) yields natural extensions of $n(x)$ and $\kappa(x)$ throughout D.

For a domain $\Omega(t)$ that evolves in the time interval $t = [0, T]$, according to an externally generated velocity field $\theta(t, x)$, we define a time-depended level-set function $\psi(t, x(t))$, such that the boundary of the domain, $\partial\Omega(t)$, is given by the set of points $x(t)$ satisfying

$$\psi(t, x(t)) = 0, \quad \forall t \in [0, T].$$

A simple derivation in time yields

$$\frac{\partial\psi}{\partial t}(t, x) + \dot{x}(t) \cdot \nabla\psi(t, x) = 0, \quad \forall t \in [0, T], \ \forall x \in \partial\Omega(t), \tag{1.32}$$

which is a PDE that describes the advection of the boundary under a velocity field $\dot{x}(t)$. Since the shape moves accordingly to the advection field $\theta(t, x)$, each point $x(t) \in \partial\Omega(t)$ satisfies a Lagrangian type ODE

$$\dot{x}(t) = \theta(t, x(t)). \tag{1.33}$$

Substituting (1.33) in (1.32), we get

$$\frac{\partial \psi}{\partial t}(t,x) + \theta(t,x(t)) \cdot \nabla \psi(t,x) = 0, \quad \forall t, \ \forall x(t) \in \partial \Omega(t). \tag{1.34}$$

The above equation can be extended to every $x(t)$ in the whole computational domain D, since the same reasoning is valid for any value c of the level-set $\psi(t,x(t)) = c$. Now, decompose the vectorial velocity field θ in orthogonal components as

$$\theta(t,x) = V(t,x)n(t,x) + \theta^c(t,x),$$

with $V(t,x) = \theta \cdot n$ a scalar field, $n(t,x)$ the extension of the unit normal as (1.31) and $\theta^c(t,x)$ defined as:

$$\theta^c = \theta - (\theta \cdot n)n.$$

Then, equation (1.34) takes the form of the Hamilton-Jacobi equation

$$\frac{\partial \psi}{\partial t}(t,x) + V(t,x)|\nabla \psi(t,x)| = 0, \quad \forall t, \ \forall x \in D, \tag{1.35}$$

since by definition the vector $\nabla \psi$ is collinear w.r.t. n (and thus orthogonal w.r.t. θ^c).

Regarding the boundary conditions, we are free the values of ψ on ∂D. For geometrical reasons, we will select one among the ensuing Neumann type boundary conditions

$$\frac{\partial \psi}{\partial n} = 0 \quad \text{or} \quad \frac{\partial^2 \psi}{\partial n^2} = 0.$$

In fact, the first condition implies that the iso-contours of the zero level-set function are orthogonal to ∂D, meanwhile the second one enforces the smoothness of the interface by letting it cut ∂D in an arbitrary angle.

As it is classically known, equation (1.35) have to be understood in a weaker sense, which involves additional information about the physics of the evolution process. Indeed, among the multiple solutions of (1.35), one has to select the "good solutions" having a physical meaning. This is done thanks to the theory of viscosity solutions initiated by P.-L. Lions and M.G. Crandall in the 80's.

From a numerical point of view, equation (1.35) can be solved in a structured mesh via adapted upwind finite differences schemes. These methods consist in choosing an approximation of the spacial derivatives according to the sign of the velocity V. In our case we employ the explicit second-order upwind scheme developed by S. Osher and J. Sethian in [252] to solve (1.35). In one space dimension, the scheme reads

$$\frac{\psi_i^{n+1} - \psi_i^n}{\Delta t} + \min(V_i^n, 0)g^-(D_x^+ \psi_i^n, D_x^- \psi_i^n) + \max(V_i^n, 0)g^+(D_x^+ \psi_i^n, D_x^- \psi_i^n) = 0$$

with $D_x^+ \psi_i^n = \frac{\psi_{i+1}^n - \psi_i^n}{\Delta x}$, $D_x^- \psi_i^n = \frac{\psi_i^n - \psi_{i-1}^n}{\Delta x}$, and

$$\begin{aligned} g^+(d^+, d^-) &= \sqrt{\min(d^+, 0)^2 + \max(d^-, 0)^2}, \\ g^-(d^+, d^-) &= \sqrt{\max(d^+, 0)^2 + \min(d^-, 0)^2}. \end{aligned}$$

Since the scheme is explicit, the stability of the scheme is enforced using a CFL (Courant-Friedrichs-Lewy) condition

$$\Delta t = \alpha \frac{\Delta x}{\max |V|}, \quad 0 < \alpha < 1 \text{ (a typical conservative choice is } \alpha = 0.5 \ [250])$$

When the underlying mesh is unstructured, the numerical implementation is much more complex and, for example, rely on the method of characteristics [292, 97]. We address the interested reader to [98] and to the references therein for more information.

Signed-distance function

For each shape Ω, there is an infinity of level-set functions that can be used to describe it. The only criterion that they must fulfill is to be enough regular so as (1.31) make sense.

It is well-known [251, 271] that, during evolution, the level-set function can become too steep or flat, even if it starts from a smooth initialization. A way to guarantee its smoothness is to reinitialize it periodically as the *signed distance function* to the domain Ω.

Definition 1.2.1. *The signed distance function to Ω is the function $d_\Omega(x) : x \in \mathbb{R}^d \to \mathbb{R}$ defined by :*

$$d_\Omega(x) = \begin{cases} -d(x, \partial\Omega) & if\, x \in \Omega, \\ 0 & if\, x \in \partial\Omega, \\ d(x, \partial\Omega) & if\, x \in D\backslash\bar{\Omega}, \end{cases}$$

where $d(\cdot, \partial\Omega)$ is the usual Euclidean distance.

Several methods have been proposed for the numerical construction of the signed distance function [251, 271, 98], such as Fast-Marching method, Fast-Sweeping method, etc. In the present work we perform the reinitialization by solving a PDE in a structured mesh, as proposed in [251]. As a matter of fact, since d_Ω satisfies the Eikonal equation

$$|\nabla d_\Omega| = 1 \quad \text{a.e.} \quad \text{in } D, \tag{1.36}$$

starting from an initial level-set function $\psi_0(x)$ parameterizing Ω, d_Ω can be obtained as the stationary solution of the following initial value problem

$$\begin{cases} \dfrac{\partial \psi}{\partial t} + sgn(\psi_0)(|\nabla \psi| - 1) = 0 & \forall t > 0, x \in \mathbb{R}^d, \\ \psi(t = 0, x) = \psi_0(x) & \forall x \in \mathbb{R}^d, \end{cases} \tag{1.37}$$

where $sgn(x)$ is the sign function. In other words $\psi \underset{t\to\infty}{\longrightarrow} d_\Omega$. The equation (1.37) is solved using the same numerical scheme as for the advection equation (1.35).

1.2.2 Coupling the level-set method and the shape derivative

In the subsection 1.1.2 we have calculated a shape derivative of a cost functional $J(\Omega)$, which in general reads

$$J'(\Omega)(\theta) = \int_{\partial\Omega} (\theta(x) \cdot n(x))\, j(x) ds, \tag{1.38}$$

for some density function $j(x) \in H^1(D)$. In the case of linear elasticity, the function j depends upon the functions u and p, solutions of the state equation (1.14) and the adjoint problem (1.17), respectively. Thereby, if one intends to minimize $J(\Omega)$, a descent direction is revealed by selecting

$$\theta^\star(x) = -j(x)n(x). \tag{1.39}$$

Indeed, substituting $\theta^\star(x)$ in the definition of the shape derivative in (1.12), we can formally write for $J(\Omega_t) = J((\text{Id} + t\theta^\star)(\Omega))$:

$$J(\Omega_t) = J(\Omega) - t\int_{\partial\Omega} j(x)^2 ds + o(t) \leq J(\Omega), \quad t > 0, \tag{1.40}$$

which guarantees a descent direction for t small enough.

The level set method for topology optimization [10, 319], links together the above descent direction furnished by the shape derivative and the level-set method for the shape description. Indeed, although formula (1.39) makes sense only on the boundary $\partial\Omega$, it can be extended to

the entire domain D by means of the level-set representation (1.31), so one can chose as scalar advection field in (1.35) the descent direction

$$V(x) = -j(x). \tag{1.41}$$

Within a shape optimization setting, the aforementioned procedure enjoys the capabilities of the level-set method to easily track the interface of Ω when topology changes take place and, at the same time, modify Ω according to the steepest descent direction provided by the shape derivative. Thereby, the shape and the topology of the structure are simultaneously optimized.

The careful reader might have identified a conflict between coupling the shape sensitivity analysis and the level-set method. In fact, Hadamard's method for shape variations supposes that the topology of the shape remains the same, while the level-set method let such changes to occur in a natural way. This apparent incompatibility does not however cause any numerical problems in numerical practice.

Numerical experience shows that if a feature of a structure tends to disappear or merge following the descent direction provided by the shape derivative, then in general this adjustment improves the final structure. Of course, this sort of temporary violation in the definition of descent direction by virtue of the shape derivative might provoke a local increase of the value of the objective function. Nevertheless, the method seems to be always capable of finding afterwards a better shape. Otherwise we could have also chosen to move at a step t so small such no topology changes happen and the objective function is always decreased. However, we are not interested to do so, since we want to find the best possible topology!

Thus, from a numerical point of view, when a topological change occurs and the method cannot further decrease the objective function, we allow a small increase of the cost function at the iteration n under the condition

$$J(\Omega_{n+1}) < (1 + \eta_{tol})J(\Omega_n),$$

where $\Omega_{n+1} = (Id + t_n \theta^\star)\Omega_n$ and η_{tol} is a small tolerance value (≈ 0.05).

Calculus toolbox and ersatz material

According to (1.30), the level-set method represents a powerful implicit representation of $\Omega \subset D$, allowing us to easily determine geometric properties as (1.31), but also perform volume and surface integrals, as it will be needed for the evaluation of the associated FE method and shapes derivatives as (1.38). We first remark that by virtue of (1.30), one can establish the characteristic function χ_Ω by means of the Heaviside function as

$$\chi_\Omega = \mathbb{H}(\psi) = \begin{cases} 0 & \text{if } \psi \leq 0, \\ 1 & \text{if } \psi > 0. \end{cases}$$

Thus, a volume integral defined on Ω can be expressed as

$$\int_\Omega f(x)dx = \int_D \mathbb{H}(\psi)f dx.$$

Similarly, a surface integral can be stated in the sense of distributions as [250]

$$\int_{\partial\Omega} f(x)ds = \int_D \delta(\psi)|\nabla\psi|f dx, \tag{1.42}$$

where δ is Dirac delta function $\delta = \mathbb{H}'$.

For numerical purposes however, since $\delta(\psi)$ is zero everywhere except on $\partial\Omega$, one must introduce an approximation of the aforementioned quantities. Thus, we define the smeared-out Heaviside function

$$\chi_\Omega \approx \mathbb{H}(\psi) = \begin{cases} 0 & \text{if} & \psi < -\epsilon_H, \\ \frac{1}{2}(1 + \frac{\psi}{\epsilon_H} + \frac{1}{\pi}\sin(\frac{\pi\psi}{\epsilon_H})) & \text{if} & -\epsilon_H \leq \psi \leq \epsilon_H, \\ 1 & \text{if} & \psi > \epsilon_H, \end{cases} \tag{1.43}$$

where ϵ_H is a tunable parameter that determines the size of the bandwidth of numerical smearing. Typically we will take $\epsilon_H = 1.5\max(\Delta x, \Delta y)$. In the meantime, the Dirac delta function is approximated by [12]

$$\delta \approx \frac{1}{2}|\nabla s_{\epsilon_\delta}(\psi)|, \tag{1.44}$$

where the function s_{ϵ_δ} corresponds to the following approximation of the sign function

$$s_{\epsilon_\delta}(\psi) = \frac{\psi}{\sqrt{\psi^2 + \epsilon_\delta^2}},$$

and $\epsilon_\delta > 0$ is a small parameter chosen in order to spread the integration over a few cells around the interface. Typically $\epsilon_\delta = \max(\Delta x, \Delta y)$.

In elasticity, in order to give a sense to the material properties in $D\backslash\overline{\Omega}$ when this is void, we use the so-called "ersatz material" approach. For this purpose, the complement of Ω in D is filled up with a weak phase that mimics the void. In this way the associated stiffness matrix remains positive definite (hence invertible).

More precisely, we define an elasticity tensor $A^*(x)$, which is a mixture of A in Ω and of the weak material mimicking holes in $D \setminus \Omega$, as

$$A^*(x) = \mathbb{H}(\psi)A + \varepsilon(1 - \mathbb{H}(\psi))A, \tag{1.45}$$

where $\varepsilon \approx 10^{-3}$ and $\mathbb{H}$ according to (1.43). Thus, consider problem (1.14) and decompose the boundary ∂D of the working domain in three parts

$$\partial D = \partial D_D \cup \partial D_N \cup \partial D_0,$$

where ∂D_D corresponds to the Dirichlet boundary condition, ∂D_N the non-homogeneous Neumann boundary condition and ∂D_0 the homogeneous Neumann boundary condition (traction free). Admissible shapes Ω are further constrained to satisfy

$$\Gamma_D \subset \partial D_D \quad \text{and} \quad \Gamma_N = \partial D_N \cup \Gamma_0,$$

where Γ_0 supports an homogeneous Neumann boundary condition (traction-free). Consequently, the only optimized part of the shape boundary with the level set method is Γ_0. Then the solution of (1.14) is fairly approximated by the solution of

$$\begin{cases} -\text{div}\,(A^*\,e(u)) & = & f & \text{in } D, \\ u & = & 0 & \text{on } \partial D_D, \\ (A^*\,e(u))n & = & g & \text{on } \partial D_N, \\ (A^*\,e(u))n & = & 0 & \text{on } \partial D_0. \end{cases} \tag{1.46}$$

For more details see [4, 95].

Optimization algorithm

The information given from the shape gradient is local, i.e. it refers to a neighborhood around the current shape Ω. Therefore, an iterative algorithm needs to be constructed so as to minimize progressively the cost functional. Using a simple steepest descent algorithm, which guarantees the decrease of the objective function at each time step, the optimization algorithm proposed in [10] has the following structure:

- Start with an initial guess shape Ω_0, described by a level-set function ψ_0.

- Iterate until convergence, for $k \geq 0$:

  1. Solve the state and adjoint equations for the domain Ω_k to obtain u_k and p_k (see (1.17)).

  2. Compute the shape gradient for the current domain Ω_k, which has the form

  $$J'(\Omega_k)(\theta_k) = \int_{\partial\Omega_k} (\theta_k \cdot n) j_k \, ds,$$

  where j_k depends upon u_k and p_k (see Proposition 1.1.21).

  3. Choose $\theta_k = -j_k n$ as an advection velocity and solve the Hamilton-Jacobi equation

  $$\frac{\partial \psi_k}{\partial t}(t, x) - j_k(x)|\nabla \psi_k(t, x)| = 0, \quad \forall t \in [0, T_k], \, \forall x \in D,$$

  in order to get a new level-set function $\psi_{k+1} = \psi(T_k, x)$, representing the domain Ω_{k+1}. The total advection time T_k is chosen so that $J(\Omega_{k+1}) < J(\Omega_k)$. In order to chose this advection time, one could apply a linear search method. However, due to the cost of evaluating the finite element model, we prefer to keep dividing the advection time by two (starting from a reference value T), until $J(\Omega_{k+1}) < J(\Omega_k)$ is fulfilled.

- From time to time, for stability reasons, reinitialize the level-set function by solving (1.37).

Several convergence criteria can be adopted. They usually test the decrease in the objective function and the total advection time, i.e. the algorithm terminates when $|J(\Omega_{k+1}) - J(\Omega_k)| < \varepsilon_k$ and $T_k < T_{lim}$, where ε_k and T_{lim} are scalar parameters defined by the user. The aforementioned criterion stands as an approximation of the optimality condition (1.13), since at each iteration the shape is deformed according to the steepest descent direction given by the shape derivative. Nevertheless, the choice of ε_k and T_{lim} is not a priori obvious, so it is a common practice to rather set the computational stop criterion in terms of the total number of iterations.

Two examples of the presented algorithm for the minimization of the compliance are detailed in Figures 1.8 and 1.9. Both applications were performed in Freefem++ [118].

Extension and regularization of the velocity field

In some cases, notably when there are jumps of the elastic properties through $\partial\Omega$, the function $j(x)$ in (1.38) is not properly defined outside of $\partial\Omega$. Hence the trivial extension (1.41) within D makes no sense. One way to settle this issue is to consider $V = 0 \, \forall x \in D \setminus \partial\Omega$. Such a choice would slow down the proposed algorithm. Indeed, for each finite element computation (which is the most costly part of the algorithm), we want to perform several transport steps for the advection equation (1.35). If the velocity is extended by 0 at a small distance away from the boundary, the shape will stop there and the total movement will be too small, probably resulting in a huge number of iterations before convergence.

So as to avoid this difficulty, we rather compute V by means of the dual identification of $J'(\Omega)$ and the scalar product in $H^1(D)$ (also called Hilbertian method [100, 66]). Indeed, supposing the density j in (1.38) regular, the evaluation of $J(\Omega)(Vn)$ (according to (1.38) and (1.39)) is well defined for any $V \in H^1(D)$. Hence the functional $J'(\Omega)$, when applied to a vector field collinear to the extension n, belongs to the dual of $H^1(\Omega)$. We can thus define the normal descent direction $V \in H^1(D)$ as the unique solution of

$$\langle V, \nu \rangle_{H^1} = -J'(\Omega)(\nu n), \forall \nu \in H^1(D). \tag{1.47}$$

From a numerical point of view, for the sake of limiting the regularization and the spreading of the velocity around the interface, we rather use as scalar product in (1.47)

$$\langle V, \nu \rangle_{H^1} = \int_D \Big(V\nu + \alpha \nabla V \cdot \nabla \nu \Big) dx, \tag{1.48}$$

where $\alpha > 0$ is proportional to squared size of the mesh.

The evaluation of $J'(\Omega)$ in (1.47) is performed following the approximation of the surface integral (1.38) as

$$J'(\Omega)(Vn) = \int_{\partial\Omega} V(x)j(x)ds = \int_D \delta(x)V(x)j(x)dx,$$

where δ is the Dirac mass function (1.44) and the term $|\nabla\psi(x)|$ in (1.42) is equal to 1 since we assume ψ to be the signed distance function (1.36).

Remark 1.2.2. *Relation* (1.47) *yields*

$$J'(\Omega)(Vn) = -\langle V, V \rangle_{H^1} \leq 0,$$

and V stands as a descent direction by virtue of the development (1.40).

Remark 1.2.3. *Even if the regularity $V \in H^1(\Omega)$ is enough from a numerical point of view, strictly speaking the vector $\theta = Vn$ does not necessarily belong to $W^{1,\infty}(D; \mathbb{R}^d)$. To achieve the required regularity, one needs to assume Ω regular enough (through its normal n) and employ the space $H^s(D)$, with $s \geq 2$, instead of $H^1(D)$ in (1.47).*

1.3 Multi-layered composite plates

1.3.1 Composite materials

The term composite material (or just composite) refers to those materials formed by combining two or more constituent materials in a macroscopic scale such that the outcome has better engineering properties than each one of the constituent materials. The idea of manufacturing this kind of materials is not new in human history. We can cite for example the traditional Japanese swords or sabers that have their blades made of stratified steel into which the soft iron is placed. The sword has in this way a good resistance for flexure and impact.

In general composite are made of two materials: a reinforcement material and a base and weaker material, also called *matrix* material. The latter one serves to distribute and transmit the loads to the reinforcement. According to this dual configuration, composite materials are commonly classified in three different types: (1) fibrous composites, which consists of fibers of one material embedded in the matrix of another; (2) particulate composites, which are composed of macro size particles of one material in the matrix of another; and (3) laminated composites, which are made of layers of different materials.

The principal fiber materials in industrial applications are Glass, Aramid or Kevlar (very light), Carbon (high modulus or high strength), Boron (high modulus or high strength) and Silicon carbide (high temperature resistant). On the other side, the matrix materials are typically
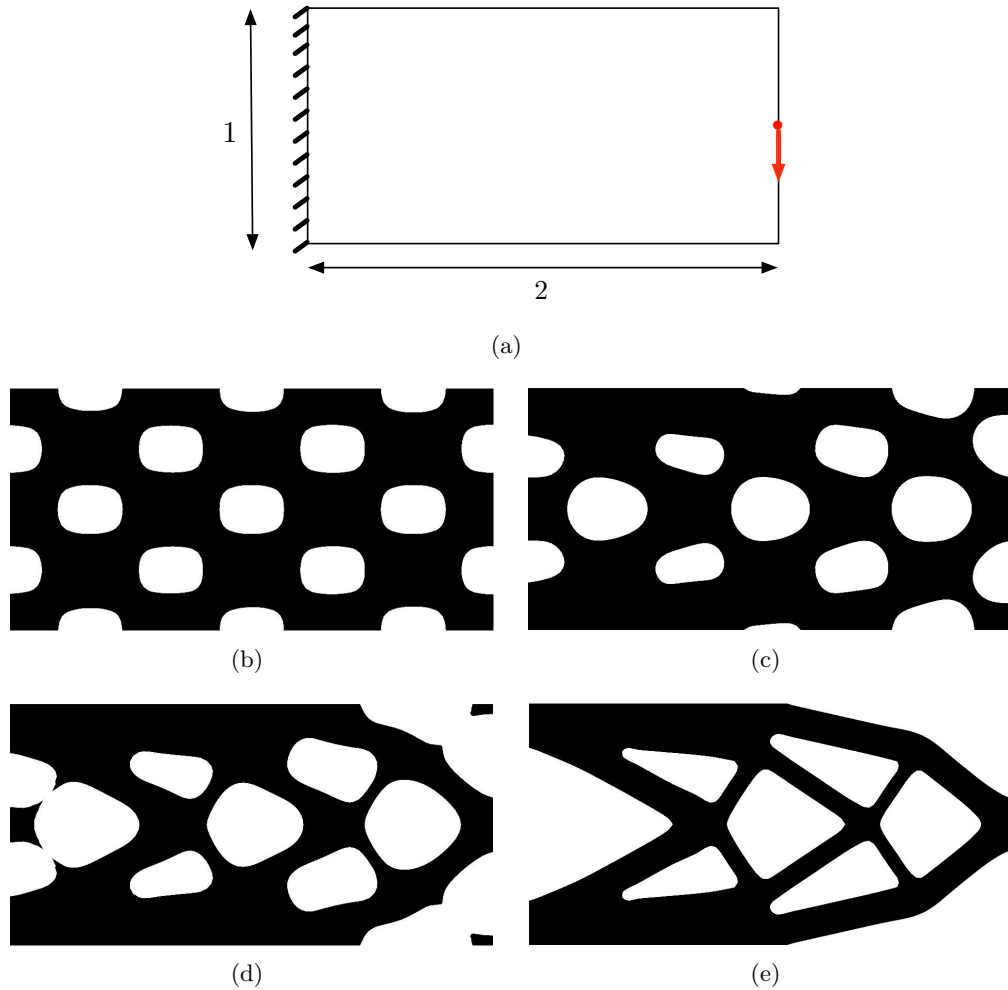
Figure 1.8: Application of the level-set method on a structured mesh. (a) Classical stiffness maximization of a long-cantilever whose left boundary is clamped and on its right boundary a vertical load is applied. The cantilever is meshed with 51×110 elements. (b) initialization of the structure, (c) iteration 5, (d) iteration 15 and (e) iteration 30.

polymers, either thermoplastic resins or thermoset resins (silicones, epoxy, etc.), but it can also be mineral (silicon carbide, carbon) or metal (aluminium or titanium alloys).

The bonding between fibers and matrix is created during the manufacturing phase of the composite material. Thus, the mixture of reinforcement/resin does not really become a composite material until the last phase of the fabrication, i.e. when the matrix is hardened. After this step, it would be impossible to modify the material, as in the way one would like to modify the structure of a metal alloy using heat treatment, for example. In the case of polymer matrix composites, the hardening process takes place by polymerization of the resin through the action of a chemical accelerator or heat. Among the main procedures to manufacture composite materials, we can cite e.g. different types of molding (autoclave, resin injection, pultrusion), filament winding, centrifugal casting, etc. In general the chosen manufacturing procedure will have a fundamental influence on the mechanical properties of the resultant composite material.

The modern range of applications of composite materials is extremely large, encompassing day-to-day electronic devices, sport items, furniture, orthopedic implants, car wheels, transmission shafts and aeronautical/aerospace components, such as wing leading edges, ailerons, helicopter blades, propellers, rocket boosters, reservoirs, nozzles, shields for atmosphere re-entry, etc.
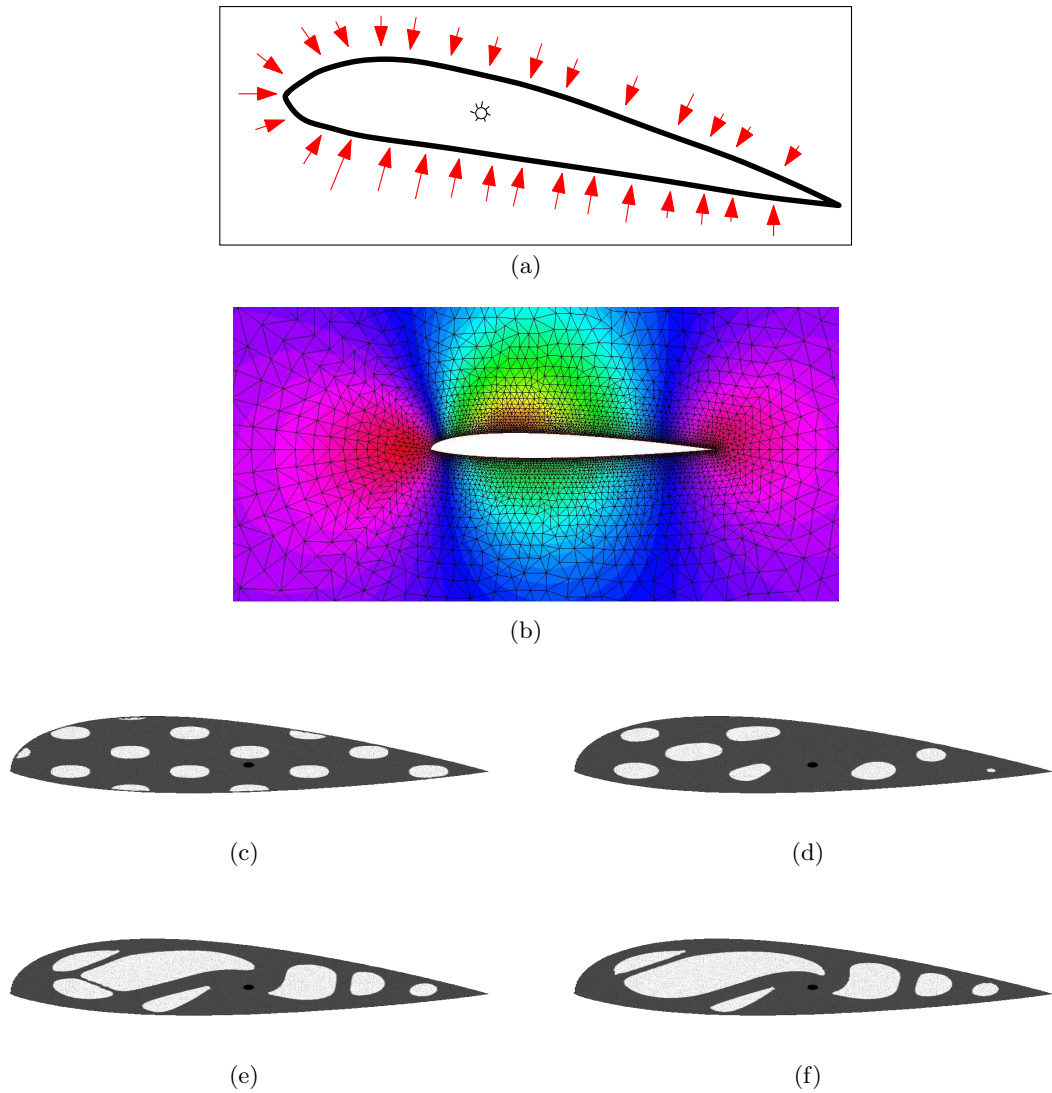
Figure 1.9: Application of the level-set method on an unstructured mesh (5000 elements). The stiffness of the airfoil is maximized subjected to a constraint on the volume occupied by the fuel (white). (a,b) Outer mesh and pressure distribution generated from a potential flow around the airfoil (low values in red/orange and higher values in blue/violet). The airfoil is clamped to circular interior point so as to remain static. (c) initialization of the structure, (d) iteration 5, (e) iteration 30 and (f) iteration 45.

The characteristics that make composite materials appealing for various industries include outstanding strength to weight ratio, lightweight, good fatigue resistance and good corrosion/fire resistance. Moreover when one compares the cost of the composite solution against the conventional one, composites remain competitive. Nevertheless, composite materials own also some drawbacks, such as medium to low level impact resistance compared to metallic materials and aging when subject to humidity and heat. Additionally from a mechanical point of view, composite materials behave as brittle materials which do not yield, i.e. their elastic limits correspond to the rupture limit. This feature eventually generates incompatibilities with metal alloys or the inability to dissipate stress concentrations.

The main failure modes leading to damage in laminated composites are fiber rupture, matrix rupture and delamination. The last phenomenon is due to weak resistance to shear stresses produced between the layers. Due to the anisotropic nature of each ply, it is important to remark that one cannot rely on classical failure criteria for isotropic materials. An adapted criterion
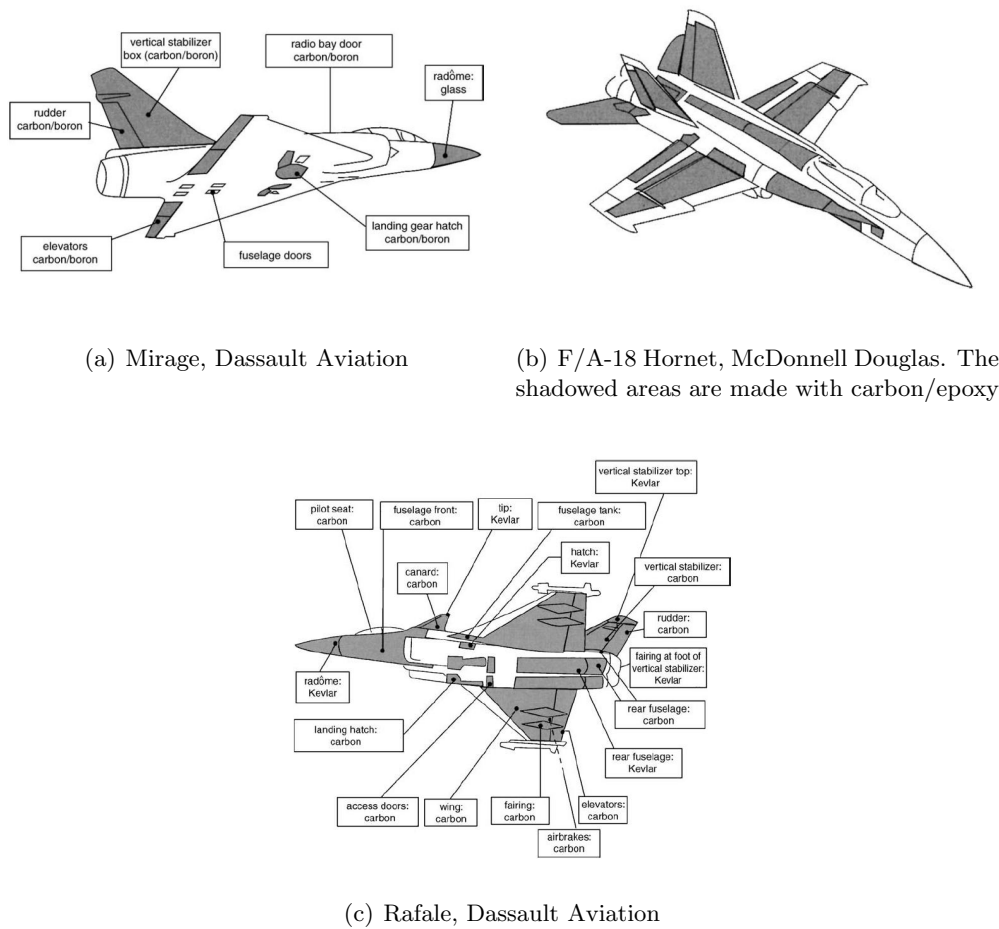
(a) Mirage, Dassault Aviation

(b) F/A-18 Hornet, McDonnell Douglas. The shadowed areas are made with carbon/epoxy

(c) Rafale, Dassault Aviation

Figure 1.10: Composite elements in current fighter aircraft. Figures extracted from [125].

must take into account the evolution of the rupture resistance w.r.t. the loading direction. A standard criterion for this purpose is the so-called Hill-Tsai failure criterion. This criterion associates to each direction a critical tensile strength. For the study for compression loads, one must rather rely on the buckling study of the structure.

For a more detailed explanation of composite materials, see e.g. [157, 171, 125].

1.3.2   Laminated composite plates

Composite laminates are formed by stacking multiple reinforced laminae or plies, in order to achieve the desired stiffness and thickness. Each of these plies consists in a sheet where many fibers are embedded in a matrix material, which can be a metal or a polymer. The layers are usually bonded together with the same matrix material as that in a lamina. We will consider unidirectional fiber-reinforced laminae, so the composite laminate corresponds to a collection of laminae which are orientated in different directions. This sequence of various orientations is termed the *lamination scheme* or *stacking sequence*. The stacking sequence and material properties of individual lamina provide an added flexibility to designers to tailor the stiffness and strength of the laminate.

In order to describe the mechanical behavior of a typical composite laminate, we lean on the classical laminated plate theory [257], which assumes the so-called *Kirchhoff hypothesis*:

1. Straight lines perpendicular to the mid-surface (i.e. transverse normals) before deformation remain straight after deformation.

2. The transverse normals do not experience elongation.

3. The transverse normals rotate such that they remain perpendicular to the mid-surface after deformation.

These hypothesis imply that the elastic displacement field U inside the laminate has the form

$$
\begin{aligned}
U_1(x_1, x_2, x_3) &= u_1(x_1, x_2) - x_3 \frac{\partial w}{\partial x_1}(x_1, x_2), \\
U_2(x_1, x_2, x_3) &= u_2(x_1, x_2) - x_3 \frac{\partial w}{\partial x_2}(x_1, x_2), \\
U_3(x_1, x_2, x_3) &= w(x_1, x_2),
\end{aligned}
\tag{1.49}
$$

where (u_1, u_2, w) are the in-plane and vertical displacements along the mid-plane, respectively. The strains associated to this displacement can be computed by means of the Green-Lagrange strain tensor

$$
\epsilon(U) = \frac{1}{2}(\nabla U + \nabla U^T + \nabla U \cdot \nabla U^T).
\tag{1.50}
$$
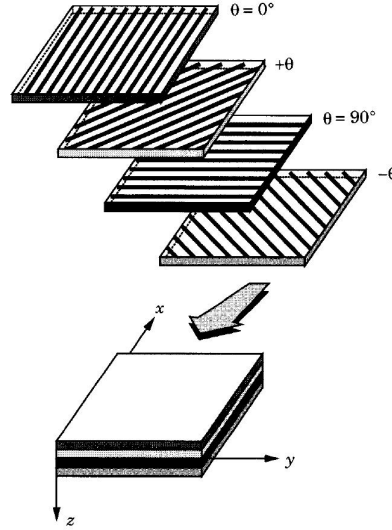
Figure 1.11: A laminate made up of plies with different fiber orientations. Figure extracted from [257].

Assuming small strains and moderate rotations [257], introducing (1.49) into (1.50), the strain-displacement relation within the laminate can be approximated as

$$
\epsilon_{11} = \frac{\partial u_1}{\partial x_1} + \frac{1}{2}\left(\frac{\partial w}{\partial x_1}\right)^2 - x_3 \frac{\partial^2 w}{\partial x_1^2}, \quad \epsilon_{22} = \frac{\partial u_2}{\partial x_2} + \frac{1}{2}\left(\frac{\partial w}{\partial x_2}\right)^2 - x_3 \frac{\partial^2 w}{\partial x_2^2},
\tag{1.51}
$$

$$
\epsilon_{12} = \frac{1}{2}\left(\frac{\partial u_1}{\partial x_2} + \frac{\partial u_2}{\partial x_1} + \frac{\partial w}{\partial x_1}\frac{\partial w}{\partial x_2}\right) - x_3 \frac{\partial^2 w}{\partial x_1 \partial x_2},
\tag{1.52}
$$

$$
\epsilon_{13} = \frac{1}{2}\left(-\frac{\partial w}{\partial x_1} + \frac{\partial w}{\partial x_1}\right) = 0, \quad \epsilon_{23} = \frac{1}{2}\left(-\frac{\partial w}{\partial x_2} + \frac{\partial w}{\partial x_2}\right) = 0, \quad \epsilon_{33} = 0.
\tag{1.53}
$$

The above strains are called the *von Kármán strains*, and the associated plate theory is termed the *von Kármán* plate theory.

The von Kármán plate model

Let $\mathcal{O}$ be a symmetric laminated composite structure composed of the superposition of $2N$ anisotropic layers, each one of constant thickness $\varepsilon > 0$ and shape Ω, where Ω a regular subdomain of $\mathbb{R}^2$. We denote as $h = N\varepsilon << 1$ half of the total thickness of the laminate. Each ply is considered as an orthotropic material, i.e. an anisotropic material where there are two mutually perpendicular planes of symmetry in material properties. So as to ease the exposition, we do not explicit the material properties in the vertical direction (which are most of the time equal to one of the in-plain main direction). In the case of an unidirectional reinforced composite, the material properties can be thus described by the angle of rotation of the fibers with respect to the canonical axis. Indeed, let $\mathcal{A}_i = (\mathcal{A}_i)_{klmn}$ with $k, l, m, n = 1, 2$, be the elastic tensor associated to the ply i and denote as $\mathcal{C} = (A_i)_i$ the underlying piecewise constant elastic tensor through the whole laminate. Furthermore introduce the elastic tensor $\mathcal{A}_0$ of a fixed orthotropic material whose principal directions coincide with the canonical axis. The 2D components of $\mathcal{A}_0$ can thus be expressed via a matrix notation as

$$\mathcal{A}_0 = \frac{1}{1 - \nu_{xy}\nu_{yx}} \begin{pmatrix} E_x & \nu_{yx}E_x & 0 \\ \nu_{xy}E_y & E_y & 0 \\ 0 & 0 & 2G_{xy} \end{pmatrix} \qquad (1.54)$$

where E_x, E_y are the Young modulus in the orthotropy directions, ν_{xy} is the Poisson's ratio, G_{xy} is the shear modulus and $\nu_{yx}E_x = \nu_{xy}E_y$. Then from now on, we will admit that for each layer i, the tensor A_i can be characterized through a rotation of the tensor $\mathcal{A}_0$ according to an angle α_i as follows

$$\mathcal{A}_i = \mathcal{Q}^T(\alpha_i)\,\mathcal{A}_0\,\mathcal{Q}(\alpha_i) \quad \text{where } \mathcal{Q}(\alpha) = \begin{pmatrix} c^2(\alpha) & s^2(\alpha) & \sqrt{2}s(\alpha)c(\alpha) \\ s^2(\alpha) & c^2(\alpha) & -\sqrt{2}s(\alpha)c(\alpha) \\ -\sqrt{2}s(\alpha)c(\alpha) & \sqrt{2}s(\alpha)c(\alpha) & c^2(\alpha) - s^2(\alpha) \end{pmatrix}$$
$$(1.55)$$

is the rotation tensor with $c = \cos(\alpha), s = \sin(\alpha)$ [261].
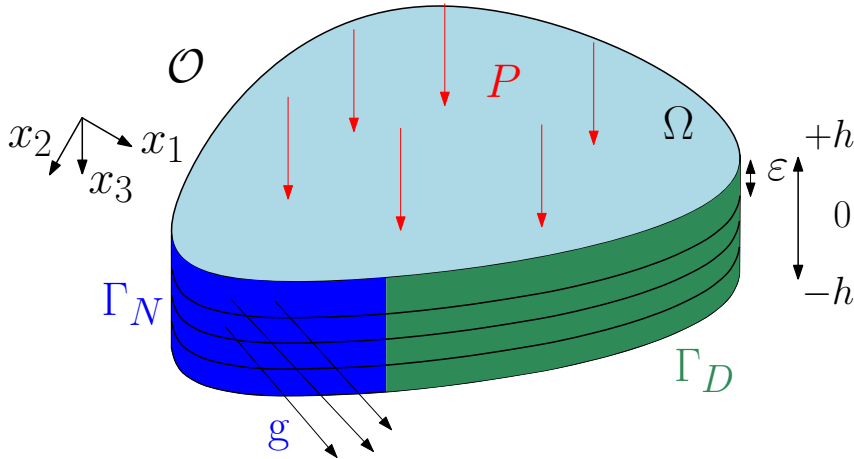
Figure 1.12: Applied forces and boundary conditions of the composite laminate $\mathcal{O}$.

Assume that the boundary of Ω can be split into two different disjoints subsets $\partial\Omega = \Gamma_N \cup \Gamma_D$, $\Gamma_N \cap \Gamma_D = \emptyset$, such that on $\Gamma_N \times [-h, h]$ a surface load $(g, 0)$, with $g \in L^2(\Gamma_N; \mathbb{R}^2)$ is applied and on $\Gamma_D \times [-h, h]$ the structure is clamped. A vertical load (pressure) $P \in L^2(\Omega)$ is applied over $\Omega \times \{h\}$. See Figure 1.12. Define the kinematically admissible spaces

$$H_D^1(\Omega; \mathbb{R}^2) = \left\{ v \in H^1(\Omega; \mathbb{R}^2) | v = 0 \text{ on } \Gamma_D \right\}, \qquad (1.56)$$
$$H_D^2(\Omega) = \left\{ \eta \in H^2(\Omega) | \eta = \nabla\eta \cdot n = 0 \text{ on } \Gamma_D \right\}. \qquad (1.57)$$

Then the averaged force and momentum equilibrium equations inside Ω according to the von Kármán strains (1.51), (1.53), (1.52) read

$$\frac{\partial N_{11}}{\partial x_1} + \frac{\partial N_{12}}{\partial x_2} = 0$$

$$\frac{\partial N_{12}}{\partial x_1} + \frac{\partial N_{22}}{\partial x_2} = 0$$

$$\frac{\partial^2 M_{11}}{\partial x_1^2} + 2\frac{\partial^2 M_{12}}{\partial x_1 x_2} + \frac{\partial^2 M_{22}}{\partial x_2^2} + \mathcal{N}(w) = P,$$

where the in-plane *force resultants* N_{mn} and the *moment resultants* M_{mn} according to Einstein's summation convention are defined as

$$N_{mn} = \int_{-h}^{h} \mathcal{C}_{mnkl}\epsilon_{kl}\, dx_3 = 2\varepsilon\Big(\sum_{i=1}^{N}(\mathcal{A}_i)_{mnkl}\Big)E(u,w)_{kl}, \quad \text{with: } E(u,w) = e(u) + \frac{1}{2}\nabla w^T\nabla w,$$

(1.58)

$$M_{mn} = \int_{-h}^{h} \mathcal{C}_{mnkl}\epsilon_{kl}\, x_3\, dx_3 = 2\frac{\varepsilon^3}{3}\Big(\sum_{i=1}^{N}(i^3 - (i-1)^3)(\mathcal{A}_i)_{mnkl}\Big)(\nabla^2 w)_{kl}, \qquad (1.59)$$

$$\mathcal{N}(w) = \frac{\partial}{\partial x_1}\Big(N_{11}\frac{\partial w}{\partial x_1} + N_{12}\frac{\partial w}{\partial x_2}\Big) + \frac{\partial}{\partial x_2}\Big(N_{12}\frac{\partial w}{\partial x_1} + N_{22}\frac{\partial w}{\partial x_2}\Big).$$

The differential operators $\nabla^2(\cdot)$ and $e(u) = \frac{\nabla u +^T \nabla u}{2}$ are the Hessian matrix and the classical linearized strain tensor, respectively.

Definition 1.3.1. *We say that in-plane and vertical displacements $u \in H_D^1(\Omega;\mathbb{R}^2)$ and $w \in H_D^2(\Omega)$ satisfy the limit two-dimensional von Kármán plate model [88, 257] if*

$$\begin{cases} -\text{div}(\mathcal{A}E(u,w)) = 0 & in\ \Omega, \\ \nabla^2 : (\mathcal{D}\nabla^2 w) - \mathcal{A}E(u,w) : \nabla^2 w = P & in\ \Omega, \\ w = 0, u = 0, \nabla w \cdot n = 0 & on\ \Gamma_D, \\ \mathcal{A}E(u,w)\cdot n = 2hg & on\ \Gamma_N, \\ (\mathcal{D}\nabla^2 w)_{nn} = 0 & on\ \Gamma_N, \\ \nabla\cdot(\mathcal{D}\nabla^2 w)\cdot n + \frac{\partial}{\partial\tau}(\mathcal{D}\nabla^2 w)_{n\tau} = 2hg\cdot\nabla w & on\ \Gamma_N, \end{cases} \qquad (1.60)$$

where $\mathcal{A}$ is the extensional stiffness tensor

$$\mathcal{A}_{klmn} = 2\varepsilon\sum_{i=1}^{N}(\mathcal{A}_i)_{klmn}, \quad k,l,m,n = 1,2 \qquad (1.61)$$

and $\mathcal{D}$ the bending stiffness tensor

$$\mathcal{D}_{klmn} = \frac{2\varepsilon^3}{3}\sum_{i=1}^{N}\Big(i^3 - (i-1)^3\Big)(\mathcal{A}_i)_{klmn}, \quad k,l,m,n = 1,2 \qquad (1.62)$$

We remark that the factor "2" in the definition of (1.61) and (1.62) is due to the symmetry of the laminate. The last boundary condition in (1.60), also called *Kirchhoff free-edge condition* [257], stands for the free vertical displacement on Γ_N and represents the equilibrium between the bending moments and the shear forces [285, 51]. The orthonormal couple (n, τ) corresponds to the local basis of normal and tangent vectors on $\partial\Omega$. We recall that the twice contracted products in (1.60) read

$$\mathcal{A}E(u,w) = \mathcal{A} : E(u,w) = \mathcal{A}_{ijkl}E(u,w)_{kl}, \qquad \nabla^2 : (\mathcal{D}\nabla^2 w) = \nabla^2 : (\mathcal{D} : \nabla^2 w) = \partial_{ij}^2\mathcal{D}_{ijkl}\partial_{kl}^2 w,$$

according to Einstein's summation convention.

Remark 1.3.2. *Typically in classical laminated plate theory, the constitutive relation between the strain and the averaged stresses within the plate presents an additional stiffness tensor apart from $\mathcal{A}$ and $\mathcal{D}$. This tensor yields the influence of the coupling curvature/in-plane tractions and extensional strain/bending moments. In real applications this effect is usually undesirable, so by making the laminate symmetric about the mid-plane (as we did), this tensor cancels. In some cases however, this extension-curvature coupling can be used as an interesting design feature. For instance, it is possible to design a composite propeller blade whose angle of attack changes automatically with its rotational speed: increased speed increases the in-plane centripetal loading, which induces a twist into the blade [261].*

The linearized buckling problem

Definition 1.3.3. *We introduce the linearized buckling problem of (1.60) as the following eigenvalue problem: Find $\lambda \in \mathbb{R}$ and $w \neq 0$ such that*

$$\begin{cases} \nabla^2 : (\mathcal{D}\nabla^2 w) = \lambda(\mathcal{A}e(u)) : \nabla^2 w & in\ \Omega, \\ w = 0, \nabla w \cdot n = 0 & on\ \Gamma_D, \\ (\mathcal{D}\nabla^2 w)_{nn} = 0 & on\ \Gamma_N, \\ \nabla \cdot (\mathcal{D}\nabla^2 w) \cdot n + \frac{\partial}{\partial \tau}(\mathcal{D}\nabla^2 w)_{n\tau} = \lambda 2hg \cdot \nabla w & on\ \Gamma_N, \end{cases} \tag{1.63}$$

where u solves

$$\begin{cases} -\mathrm{div}(\mathcal{A}e(u)) = 0 & in\ \Omega, \\ u = 0 & on\ \Gamma_D, \\ \mathcal{A}e(u) \cdot n = 2hg, & on\ \Gamma_N. \end{cases} \tag{1.64}$$

Equivalently, the variational formulation of the linearized buckling problem (1.63),(1.64) reads

$$\begin{aligned} \int_\Omega \mathcal{D}_{ijkl}\, \partial_{kl}w\, \partial_{ij}\eta\, dx &= -\lambda \int_\Omega \mathcal{A}_{ijkl}\, e(u)_{kl}\, \partial_i w\, \partial_j \eta\, dx, \forall \eta \in H_D^2(\Omega), \\ \int_\Omega \mathcal{A}_{ijkl}\, e(u)_{kl}\, e(v)_{ij}\, dx &= 2h \int_{\Gamma_N} g \cdot v ds, \forall v \in H_D^1(\Omega; \mathbb{R}^2), \end{aligned} \tag{1.65}$$

where we have used Einstein's tensorial summation convention. We denote by λ_1 the smallest positive eigenvalue of (1.63). This value is usually called "buckling load factor" or "buckling critical reserve factor" and it is an indicator of the degree of safety against buckling [139, 49]. The computed vertical displacement eigenvector $\hat{w}$ is referred here as the "buckling mode". The existence of λ_1 is guaranteed by the compactness of the buckling operator (Lemma 2.2-7 [90]). Furthermore this operator is self-adjoint so λ_1 can be express through the Rayleigh quotient

$$\frac{1}{\lambda_1} = \max_{w \in H_D^2(\Omega) \setminus \{0\}} -\frac{\int_\Omega \mathcal{A}e(u) \cdot \nabla w \cdot \nabla w dx}{\int_\Omega \mathcal{D}\nabla^2 w : \nabla^2 w dx}. \tag{1.66}$$

The foregoing properties will be rigorously recalled in the next subsection.

1.3.3   A few mathematical properties of the von Kármán plate model

Better known as the father of supersonic flight, Théodore von Kármán proposed in [315] an equivalent form of the precedent set of equations describing a two-dimensional non-linear elastic plate. This plate theory plays an almost mythical role in applied mathematics and has been extensively studied from a mathematical point of view, notably treating various questions of existence, regularity and bifurcation of their solutions. We briefly recall some of these mathematical properties, especially those concerning bifurcation theory.

A rigorous justification in a nutshell

The full physical justification of the von Kármán equations has been longtime criticized [309] (notably the pertinence of (1.51),(1.53), (1.52)), but "recently" achieved from the exact three dimensional equations of non-linear elasticity. This justification can be found e.g. in [88], by means of the leading term of a formal asymptotic expansion regarding the thickness of the plate, or in [120] through $\Gamma-$convergence. Here we present a rapid glance of the main result in [120].

Let $\varepsilon > 0$ and consider a 3D non-linear hyperelastic model [89] (for ease of exposition a St Venant-Kirchhoff material) written in the reference configuration Ω^ε

$$\begin{cases} -\text{div}(T^\varepsilon(I + \nabla U^\varepsilon)) = F^\varepsilon & \text{in } \Omega^\varepsilon, \\ U^\varepsilon = 0 & \text{on } \Gamma_D^\varepsilon, \\ T^\varepsilon(I + \nabla U^\varepsilon) \cdot n = G^\varepsilon & \text{on } \Gamma_N^\varepsilon \cup \Gamma^{+\varepsilon} \cup \Gamma^{-\varepsilon}, \end{cases} \qquad (1.67)$$

where $\Omega^\epsilon = \Omega \times [-\varepsilon/2, \varepsilon/2]$, $\Gamma_D^\varepsilon = \Gamma_D \times [-\varepsilon/2, \varepsilon/2]$, $\Gamma_N^\varepsilon = \Gamma_N \times [-\varepsilon/2, \varepsilon/2]$, $\Gamma^{\pm\varepsilon} = \Omega \times \{\pm\epsilon/2\}$, T^ε is the first Piola-Kirchhoff stress tensor and $U^\varepsilon := \Omega^\varepsilon \to \mathbb{R}^3$ is the elastic displacement. The volume forces F^ε and the surface loads G^ε are suppose to be dead loads, i.e. independent of the displacement U^ε. Since the material is supposed to be hyperelastic, the first Piola-Kirchhoff stress tensor T^ε derives from the elastic energy function

$$T_{ij}^\varepsilon = \frac{\partial W^\varepsilon(\mathcal{F}^\varepsilon)}{\partial \mathcal{F}_{ij}}, \quad i, j \in \{1, 2, 3\}$$

where $\mathcal{F}^\varepsilon = I + \nabla U^\varepsilon$ denotes the deformation gradient and the (constant) elasticity tensor $\mathcal{C}$ is defined by

$$\mathcal{C}_{ijkl} = \frac{\partial^2 \mathcal{W}^\varepsilon(\mathcal{F}^\varepsilon)}{\partial \mathcal{F}_{ij} \partial \mathcal{F}_{kl}}. \qquad (1.68)$$

The variational formulation of (1.67) is

$$\int_{\Omega^\varepsilon} T^\varepsilon(I + \nabla U^\varepsilon) \cdot \nabla V dx - \int_{\Omega^\varepsilon} F^\varepsilon \cdot V dx - \int_{\Gamma_N^\varepsilon \cup \Gamma^{+\varepsilon} \cup \Gamma^{-\varepsilon}} G^\varepsilon \cdot V ds, \quad \forall V \in H^1(\Omega^\varepsilon)^3, V = 0 \text{ on } \Gamma_D^\varepsilon. \qquad (1.69)$$

Now, it is convenient to introduce the fixed domain $\omega = \Omega \times [-1/2, 1/2]$ and the change of variables

$$\mathcal{V}(x) = V(x^\varepsilon), \quad \mathcal{U}^\varepsilon(x) = U^\varepsilon(x^\varepsilon),$$

where $x^\varepsilon = (x_1, x_2, \varepsilon x_3)$, $x = (x_1, x_2, x_3) \in \omega$. Then (1.69) is formally equivalent (under some regularity and convexity conditions on W^ε [33]) to the energy minimization problem

$$\inf_{\substack{\mathcal{V} \in H^1(\omega; \mathbb{R}^3) \\ \mathcal{V}=0 \text{ on } \Gamma_D \times [-1/2, 1/2]}} I^\varepsilon(\mathcal{V}) = \int_{\Omega^\varepsilon} W^\varepsilon(I + \nabla V) dx - \int_{\Omega^\varepsilon} F^\varepsilon \cdot V dx - \int_{\Gamma_N^\varepsilon \cup \Gamma^{+\varepsilon} \cup \Gamma^{-\varepsilon}} G^\varepsilon \cdot V ds. \qquad (1.70)$$

Assuming and setting different scalings for the applied forces $F^\varepsilon, G^\varepsilon$, the elastic energy W^ε and the displacements U^ε w.r.t. the thickness of the plate ε, one can prove that a hierarchy of plate models arises from (1.70) via Γ-convergence [120, 191]. In particular the von Kármán model, as it was also remarked in [88], stems from the choice

$$\begin{aligned} F^\varepsilon(x^\varepsilon) &= (0, 0, f_3^\varepsilon(x^\varepsilon)) = \varepsilon^3(0, 0, f_3(x)), \\ G^\varepsilon(x^\varepsilon) &= (g_1^\varepsilon(x^\varepsilon), g_2^\varepsilon(x^\varepsilon), 0) = \varepsilon^2(g_1(x), g_2(x), 0) \text{ on } \Gamma_N^\varepsilon, \\ G^\varepsilon(x^\varepsilon) &= (0, 0, g_3^{\pm\varepsilon}(x)) = \varepsilon^4(0, 0, g_3^\pm(x)) \text{ on } \Gamma^{\pm\varepsilon}, \end{aligned}$$

where the functions $f_3, g = (g_1, g_2), g_3^\pm$ are independent of ε.

Proposition 1.3.4. *Let $\mathcal{U}^\epsilon$ be a minimizing sequence for (1.70) when $\varepsilon \to 0$ in the sense*

$$\frac{1}{\varepsilon^4}\left(I^\varepsilon(\mathcal{U}^\varepsilon) - \inf_{\substack{\mathcal{V}\in H^1(\omega;\mathbb{R}^3)\\ \mathcal{V}=0 \ on \ \Gamma_D\times[-1/2,1/2]}} I^\varepsilon(\mathcal{V})\right) \to 0.$$

Then there exists constants $R^\varepsilon \in SO(3)$ (the group of 3D rotations) and $c^\varepsilon \in \mathbb{R}^3$ such that the function

$$\tilde{\mathcal{U}}^\varepsilon := R^\varepsilon \mathcal{U}^\varepsilon - c^\varepsilon$$

and the averaged in-plane and out-of-plane displacements

$$u^\varepsilon := \frac{1}{\varepsilon^2}\int_{-1/2}^{1/2}(\tilde{\mathcal{U}}_1^\varepsilon, \tilde{\mathcal{U}}_2^\varepsilon)dx_3, \qquad w^\varepsilon := \frac{1}{\varepsilon}\int_{-1/2}^{1/2}\tilde{\mathcal{U}}_3^\varepsilon dx_3,$$

satisfy (for a subsequence)

$$\nabla\tilde{\mathcal{U}}^\varepsilon \to Id \ in \ L^2(\omega;\mathbb{R}^{3\times3})$$

and $u^\varepsilon \to u$ in $H^1(\Omega;\mathbb{R}^2)$ and $w^\varepsilon \to v$ in $H^1(\Omega)$. Moreover (u,v) minimizes the limit scaled von Kármán elastic energy

$$\mathcal{J}(u,w) = \frac{1}{6}\int_\Omega \mathcal{C}_{ijkl}\partial_{kl}w\partial_{ij}wdx + \frac{1}{2}\int_\Omega \mathcal{C}_{ijkl}E(u,w)_{ij}E(u,w)_{kl}dx - \int_\Omega Pwdx - \int_{\Gamma_N} guds, \ (1.71)$$

   where

$$P = \int_{-1/2}^{1/2} f_3dx + g_3^+ + g_3^-.$$

Remark 1.3.5. *The commonly used ansatz (Kirchhoff-love displacement) (1.49)*

$$U^\epsilon = (u^\varepsilon + x_3\nabla w^\varepsilon, w^\varepsilon)$$

is consistent with the above result [120].

Remark 1.3.6. *The variational formulation of the von Kármán model (1.60) for one ply with elastic properties $\mathcal{C}$, can be deduced from the stationarity conditions (euler-lagrange equations) of the de-scaled version of $\mathcal{J}(u,w)$ (1.71). Indeed, setting $\hat{u}^\varepsilon = \varepsilon^2 u$ and $\hat{w}^\varepsilon = \varepsilon w$,*

$$0 = \left\langle \frac{\partial \mathcal{J}^\varepsilon}{\partial u}(\hat{u}^\varepsilon, \hat{w}^\varepsilon), v\right\rangle = \int_\Omega \varepsilon\mathcal{C}_{ijkl}E(\hat{u}^\varepsilon, \hat{w}^\varepsilon)_{kl}e(v)_{kl}dx - \varepsilon\int_{\Gamma_N} gvds, \forall v \in H_D^1(\Omega;\mathbb{R}^2) (1.72)$$

$$0 = \left\langle \frac{\partial \mathcal{J}^\varepsilon}{\partial w}(\hat{u}^\varepsilon, \hat{w}^\varepsilon), \eta\right\rangle = \int_\Omega \frac{\varepsilon^3}{3}\mathcal{C}_{ijkl}\partial_{kl}\hat{w}^\varepsilon \partial_{ij}\eta dx + \int_\Omega \varepsilon\mathcal{C}_{ijkl}E(\hat{u}^\varepsilon, \hat{w}^\varepsilon)_{kl}\partial_i\hat{w}^\varepsilon \partial_j\eta dx$$

$$- \int_\Omega P^\varepsilon \eta dx, \forall \eta \in H_D^2(\Omega).$$

Where

$$P^\varepsilon = \int_{-\varepsilon/2}^{\varepsilon/2} f_3^\varepsilon dx + g_3^{+\varepsilon} + g_3^{-\varepsilon}.$$

Bifurcation theory and linearized buckling load

Bifurcation theory attempts to explain various phenomena that have been discovered and described in the natural sciences over the centuries. The buckling of the Euler rod, the appearance of Taylor vortices, and the onset of oscillations in an electric circuit, for instance, all have a common cause: A specific physical parameter crosses a threshold, and that event forces the system to the organization of a new state that differs considerably from that observed before [178]. In our case we are interested in the phenomenon of buckling, which can be characterized by a sudden failure of a structural member subjected to high compressive or torsional stress. It is particularly useful in engineering to describe the ultimate load g (with $P = 0$) such that a plate is capable of withstand before bending (i.e. $w \neq 0$).

But first, in order to facilitate the ensuing analysis, we give the canonical or reduced form of the von Kármán equations [90]

Let us introduce the Airy stress function $\phi : \Omega \to \mathbb{R}$ such that

$$\partial_{xx}\phi = N_{yy}, \ \partial_{yy}\phi = N_{xx}, \ \partial_{xy}\phi = -N_{xy} = -N_{yx},$$

with the force resultant tensor N defined in (1.58). The existence of such functions stems from the equation $\mathrm{div}(N) = 0$ in (1.60). Let $\hat{P} \in H_D^2(\Omega)$ be solution of

$$\begin{cases} \nabla^2(\mathcal{D}\nabla^2\hat{P}) = P & \text{in } \Omega, \\ (\mathcal{D}\nabla^2\hat{P}) = 0 & \text{on } \Gamma_N, \\ \nabla \cdot (\mathcal{D}\nabla^2\hat{P}) \cdot n + \frac{\partial}{\partial\tau}(\mathcal{D}\nabla^2\hat{P})_{n\tau} = 2hg \cdot \nabla\hat{P} & \text{on } \Gamma_N, \end{cases}$$

with P introduced in (1.60) and define the tensor $\tilde{\mathcal{A}}$

$$\tilde{\mathcal{A}} = \begin{pmatrix} a_{22} & a_{12} & -a_{32} \\ a_{21} & a_{11} & -a_{31} \\ -a_{23} & -a_{13} & a_{33} \end{pmatrix}, \text{ where } \mathcal{A}^{-1} = (a_{ij}).$$

Let $\theta_0 \in H_D^2(\Omega)$ be the solution of

$$\begin{cases} \nabla^2(\tilde{\mathcal{A}}\nabla^2\theta_0) = 0 \text{ , in } \Omega, \\ \theta_0 = \phi, \partial_n\theta_0 = \partial_n\phi \text{ on } \Gamma_N. \end{cases}$$

Furthermore, define the following operators [88]:

(a) $\mathcal{B}, \tilde{\mathcal{B}} := (\eta_1, \eta_2) \in H_D^2(\Omega) \times H_D^2(\Omega) \to \mathcal{B}(\eta_1, \eta_2), \tilde{\mathcal{B}}(\eta_1, \eta_2) \in H_D^2(\Omega)$, solutions of

$$\begin{cases} \nabla^2(\mathcal{D}\nabla^2\mathcal{B}) = [\eta_1, \eta_2] & \text{in } \Omega, \\ (\mathcal{D}\nabla^2\mathcal{B}) = 0 & \text{on } \Gamma_N, \\ \nabla \cdot (\mathcal{D}\nabla^2\mathcal{B}) \cdot n + \frac{\partial}{\partial\tau}(\mathcal{D}\nabla^2\mathcal{B})_{n\tau} = 2hg \cdot \nabla\mathcal{B} & \text{on } \Gamma_N. \end{cases} \quad \begin{cases} \nabla^2(\tilde{\mathcal{A}}\nabla^2\tilde{\mathcal{B}}) = [\eta_1, \eta_2] & \text{in } \Omega, \\ \tilde{\mathcal{B}} = 0 & \text{on } \Gamma_N, \\ \partial_n\tilde{\mathcal{B}} = 0 & \text{on } \Gamma_N. \end{cases}$$

where $[\cdot, \cdot]$ is the Monge-Ampère form defined as

$$[\eta_1, \eta_2] = \partial_{11}\eta_1\partial_{22}\eta_2 + \partial_{22}\eta_1\partial_{11}\eta_2 - 2\partial_{12}\eta_1\partial_{12}\eta_2.$$

(b) $\mathcal{G} := \eta \in H_D^2(\Omega) \to \mathcal{G}(\eta) = \mathcal{B}(\frac{1}{2}\tilde{\mathcal{B}}(\eta, \eta), \eta) \in H_D^2(\Omega)$.

(c) $\mathcal{L} := \eta \in H_D^2(\Omega) \to \mathcal{L}(\eta) = \mathcal{B}(\theta_0, \eta) \in H_D^2(\Omega)$ (linear).

Proposition 1.3.7. *Let $\gamma : [0,1] \to \mathbb{R}^2$ be a regular parametrization of Γ_N. Then functions $(u,w) \in (H^1_D(\Omega;\mathbb{R}^2), H^2_D(\Omega))$ are solution of (1.60) if and only if $w \in H^2_D(\Omega)$ satisfies the equation*

$$(Id - \mathcal{L})w + \mathcal{G}(w) = \hat{P}, \tag{1.73}$$

where $\phi \in H^2(\Omega)$ is given by

$$\phi = \theta_0 - \frac{1}{2}\tilde{\mathcal{B}}(w,w). \tag{1.74}$$

Moreover the values of ϕ and $\partial_n\phi$ on Γ_N read

$$\phi(x(t)) = -x_1 \int_{\gamma(s), s\in[0,t]} g_2 ds + x_2 \int_{\gamma(s), s\in[0,t]} g_1 ds + \int_{\gamma(s), s\in[0,t]} (x_1 g_2 - x_2 g_1) ds$$

$$\partial_n\phi(x(t)) = -n_1 \int_{\gamma(s), s\in[0,t]} g_2 ds + n_2 \int_{\gamma(s), s\in[0,t]} g_1 ds.$$

Proof. We give a sketch of the proof based on similar arguments for the isotropic and orthotropic case [90, 51]. Typically in literature the von Kármán equations (1.60) are expressed through the simpler equivalent system

$$\begin{cases} \nabla^2(\mathcal{D}\nabla^2 w) = [\phi, w] + P \\ \nabla^2(\tilde{\mathcal{A}}\nabla^2 \phi) = -\frac{1}{2}[w,w]. \end{cases} \tag{1.75}$$

Indeed, the first equation of (1.75) follows immediately from the definition of the Airy function ϕ, meanwhile the second relation is less clear. Remarking that $E(u,w) = \mathcal{A}^{-1}N$ and invoking the definition of the Airy function plus the identity

$$\partial^2_{x_1 x_1}(\partial_{x_2} u_2) + \partial^2_{x_2 x_2}(\partial_{x_1} u_1) - \partial^2_{x_1 x_2}(\partial_{x_2} u_1 + \partial_{x_1} u_2) = 0,$$

the following cascade of equations (after some tedious computations) stem the desired equation

$$\begin{aligned}
-\frac{1}{2}[w,w] &= \frac{\partial^2}{\partial x_1^2}\big(E(u,w)\big)_{22} + \frac{\partial^2}{\partial x_2^2}\big(E(u,w)\big)_{11} - 2\frac{\partial^2}{\partial x_1 \partial x_2}\big(E(u,w)\big)_{12} \\
&= \frac{\partial^2}{\partial x_1^2}\big(\mathcal{A}^{-1}N\big)_{22} + \frac{\partial^2}{\partial x_2^2}\big(\mathcal{A}^{-1}N\big)_{11} - 2\frac{\partial^2}{\partial x_1 \partial x_2}\big(\mathcal{A}^{-1}N\big)_{12} \\
&= \nabla^2(\tilde{A}\nabla^2\phi)
\end{aligned}$$

Once established the equivalence between (1.75) and (1.60), one can easily prove that (w,ϕ) is the solution of the system (1.75) if and only if w satisfies (1.73) and ϕ is given by relation (1.74). In fact, if (w,ϕ) satisfy the latter conditions, the formal application of the operators $\nabla^2(\mathcal{D}\nabla^2)$ and $\nabla^2(\tilde{A}\nabla^2)$ to (1.73) and (1.74) respectively, entails the system (1.75) as well as the boundary conditions. On the contrary, if (w,ϕ) solves (1.75), then (1.73) and (1.74) stem from the uniqueness of the solutions of the problems defining the operators $\mathcal{B}, \tilde{\mathcal{B}}$. Finally the boundary values of ϕ and $\partial_n\phi$ on Γ_N are obtained by integration by parts from

$$(g_1, g_1) = (\partial^2_{xx}\phi, -\partial^2_{xy}\phi).$$

For more details see Lemma 1.5-1 in [90]. $\qquad\square$

Thanks to the canonical form of the von Kármán equation, taking $\hat{P} = 0$ we can comfortably formulate the buckling problem in terms of a bifurcation point of (1.73)

Definition 1.3.8. *Consider the eigenvalue problem*

$$\mathcal{S}(\lambda, w) = (Id - \lambda\mathcal{L})w + \mathcal{G}(w) = 0. \tag{1.76}$$

We say that the point $(\lambda(\epsilon_0), w(\epsilon_0))$ is a bifurcation point of equation (1.76) with respect to the solution curve $(\lambda(\epsilon), w(\epsilon))$ if for every neighborhood around this point there exist another solution of (1.76)(i.e. a solution which does not belong to $(\lambda(\epsilon), w(\epsilon)))$.

In a buckling problem we are concerned by the bifurcation points from the trivial branch $w = 0$. With the purpose of calculating the smallest λ such that the plate buckles (i.e. it deviate from the trivial branch), we recast the following result [90]

Proposition 1.3.9. *$(\lambda_0, 0)$ is a bifurcation point of the trivial branch $\{(\lambda, 0), \lambda \in \mathbb{R}\}$ for S in (1.76) only if λ_0 is a characteristic value of $\mathcal{L}$:*

$$\exists w \in H_D^2(\Omega) \backslash \{0\} : (Id - \lambda_0 \mathcal{L})w = 0. \tag{1.77}$$

Reciprocally, if the eigenvalue λ_0 has odd-numbered algebraic multiplicity, then it is effectively a bifurcation point.

Problem (1.77) corresponds to the linearized buckling problem introduced in (1.63),(1.64), where λ_1 stands for the first positive eigenvalue. Indeed, applying the operator $\nabla^2(\mathcal{D}\nabla^2)$ on both sides of (1.77), one obtains

$$\nabla^2(\mathcal{D}\nabla^2 w) = \lambda_0 \nabla^2(\mathcal{D}\nabla^2 \mathcal{L}w) = \lambda_0[\theta_0, w].$$

Furthermore, for every $\lambda \in \mathbb{R}$ which is not a characteristic value of $\mathcal{L}$, the Airy function ϕ_0 corresponding to the plane strain stress with deflection $w = 0$ (i.e. $\mathcal{A}e(u) = \mathcal{A}E(u, w)$) satisfies according to the relation (1.74)

$$\lambda \phi_0 = \lambda \theta_0,$$

hence $\phi_0 = \theta_0$ and

$$\lambda_0[\theta_0, w] = \lambda_0 \mathcal{A}e(u) : \nabla^2 w.$$

For more details see [51].

Remark 1.3.10. *It can be proven [90, 47] that if g is a purely compressive load, then the operator $\mathcal{L}$ is positive definite and all eigenvalues are positive. Furthermore if $P = 0$ then for $\lambda \leq \lambda_1$ the plate does not buckle (according to Definition 1.3.8) meanwhile for $\lambda > \lambda_1$ the plate buckles and has at least three solutions $(0, w, -w)$. Otherwise if $P \neq 0$, there exist $\lambda^*(|P|) < \lambda_1$ such that for every $\lambda < \lambda^*$ the plate does not buckle (i.e. has an unique solution).*

Once established the equivalence between the linearized eigenvalue problem (1.77) and (1.63), (1.64), we proceed to expose some spectral properties

Proposition 1.3.11. *Let the tensor $\mathcal{D}$ in (1.62) be elliptic with constant δ. Then:*

1) *The set of eigenvalues λ of Problem (1.77) is discrete, infinite, with only limit point at zero and*

$$\frac{1}{\lambda} \in \left[-\frac{\|\mathcal{A}e(u)\|_{L^2(\Omega)}}{\delta}, \frac{\|\mathcal{A}e(u)\|_{L^2(\Omega)}}{\delta} \right]$$

2) *λ_1 can be expressed through the Rayleigh quotient*

$$\lambda_1^{-1} = \max_\eta \frac{-\int_\Omega \mathcal{A}e(u)\nabla\eta\nabla\eta dx}{\int_\Omega \mathcal{D}\nabla^2\eta : \nabla^2\eta dx}. \tag{1.78}$$

Remark 1.3.12. *The definition of λ_1^{-1} makes only sense if this biggest eigenvalue is positive (thus we avoid non-physical negative eigenvalues from the definition as a $\min$). If not, the plate does not buckle and λ_1 is set to infinity.*

Proof. Define the linear operator

$$\mathbb{T}(z) := z \in H_D^2(\Omega) \to w \in H_D^2(\Omega),$$

where w is the unique solution of the variational formulation of the linearized buckling problem

$$\int_\Omega (\mathcal{D}\nabla^2 w) : \nabla^2\eta dx = \int_\Omega (\mathcal{A}e(u) : \nabla^2 z)\eta dx = -\int_\Omega \mathcal{A}e(u)\nabla z\nabla\eta dx, \quad \forall\eta \in H_D^2(\Omega). \qquad (1.79)$$

The last equality stems from the fact that $\operatorname{div}(\mathcal{A}e(u)) = 0$. We are going to prove that $\mathbb{T}$ is continuous, compact and self-adjoint.

1) First, the existence and uniqueness of w follows from the Lax-Milgram theorem. Indeed, thanks to the Sobolev embedding of $H^2(\Omega) \hookrightarrow W^{1,4}(\Omega)$, the integral on the right side of (1.79) is continuous w.r.t. η

$$\left|\int_\Omega \mathcal{A}e(u)\nabla z\nabla\eta dx\right| \leq \|\mathcal{A}e(u)\|_{L^2(\Omega)} |z|_{W^{1,4}(\Omega)} |\eta|_{W^{1,4}(\Omega)} \leq \|\mathcal{A}e(u)\|_{L^2(\Omega)} |z|_{W^{1,4}(\Omega)} \|\eta\|_{H^2(\Omega)}.$$

Additionally, the continuity and coercitivity of the left term in (1.79) arises from the ellipticity of $\mathcal{D}$ and the Poincaré's inequality (since $|\Gamma_D| \neq 0$). Thus, the Lax-Milgram theorem yields the classical estimate

$$\|\mathbb{T}(z)\|_{H^2(\Omega)} \leq \frac{1}{\delta} \|\mathcal{A}e(u)\|_{L^2(\Omega)} |z|_{W^{1,4}(\Omega)}, \qquad (1.80)$$

so $\|\mathbb{T}\|_{H^2(\Omega)} \leq \frac{\|\mathcal{A}e(u)\|_{L^2(\Omega)}}{\delta}$ and the operator $\mathbb{T}$ is continuous. Now we show that this operator is compact. Since $H^2(\Omega)$ is a reflexive space, the unit ball is weakly sequentially compact, so we just need to prove that if (z_n) is a weakly convergent sequence to z^*, then $w_n \to w^*$ strongly. Indeed, let be (z_n) a weakly convergent sequence to z^* in $H^2(\Omega)$. Since the injection $H^2(\Omega) \hookrightarrow W^{1,4}(\Omega)$ is compact, (1.80) yields:

$$z_n \to z^* \text{ strongly in } W^{1,4}(\Omega) \Rightarrow \mathbb{T}(z_n) \to \mathbb{T}(z^*) \text{ strongly in } H^2(\Omega),$$

hence $\mathbb{T}$ is compact. Thanks to this feature, the set of eigenvalues of the problem

$$\mu w = \mathbb{T}(w),$$

which is equivalent to (1.77) with $\mu = 1/\lambda$, belongs to the interval $[-\frac{\|\mathcal{A}e(u)\|_{L^2(\Omega)}}{\delta}, \frac{\|\mathcal{A}e(u)\|_{L^2(\Omega)}}{\delta}]$, is discrete, has only a limit point at zero and the algebraic multiplicity of each eigenvalue is finite [60].

The only element that remains to prove is that $\mathbb{T}$ is self-adjoint. Let $w, w' \in H_D^2(\Omega)$, where thanks to the Poincaré inequality and the ellipticity of $\mathcal{D}$ we endow $H_D^2(\Omega)$ with the inner product

$$\langle w, w' \rangle_{H_D^2(\Omega)} = \int_\Omega \mathcal{D}\nabla^2 w : \nabla^2 w' dx. \qquad (1.81)$$

Then

$$\langle \mathbb{T}(w), w' \rangle_{H_D^2(\Omega)} = \int_\Omega \mathcal{D}\nabla^2\mathbb{T}(w) : \nabla^2 w' dx = \int_\Omega (\mathcal{A}e(u) : \nabla^2 w)w' dx = -\int_\Omega (\mathcal{A}e(u)\nabla w) \cdot \nabla w' dx$$

$$= \int_\Omega (\mathcal{A}e(u) : \nabla^2 w')w dx = \int_\Omega \mathcal{D}\nabla^2\mathbb{T}(w') : \nabla^2 w dx = \langle w, \mathbb{T}(w') \rangle_{H_D^2(\Omega)}.$$

Henceforth the set of eigenvalues must be infinite since $H^2(\Omega)$ is a separable space and $\mathbb{T}$ is a compact and self-adjoint operator (so $H^2(\Omega)$ admits a Hilbert basis composed of the eigenvectors of $\mathbb{T}$).

2) Finally the fact that λ_1 can be written by means of the Rayleigh quotient stems from the min-max theorem for compact and self-adjoint operators.

$\square$

Remark 1.3.13. *When g is not a compressive force (i.e $g = -\hat{g}n, \hat{g} \geq 0$ and n the normal to $\partial\Omega$), $\mathbb{T}$ is not necessarily positive-definite since the stress tensor $\sigma = \mathcal{A}e(u)$ is not a priori positive-definite. Thus all eigenvalues may not be positive and typical eigenvalue solvers as the package ARPACK [192], which uses the Implicitly Restarted Arnoldi Method, can not be applied straightforward. Hence a prior modification must be done first by introducing the following auxiliary problem*

Corollary 1.3.14. *Let β be a positive constant and let $w \in H_D^2(\Omega)$ be the solution of the following modified version of the eigenvalue problem* (1.77)

$$\int_\Omega \mathcal{D}\nabla^2 w : \nabla^2\eta dx = \mu\Big(-\int_\Omega \mathcal{A}e(u)\nabla w\nabla\eta dx + \beta\int_\Omega \mathcal{D}\nabla^2 w : \nabla^2\eta dx\Big), \forall\eta \in H_D^2(\Omega). \quad (1.82)$$

Then for β large enough the set of eigenvalues μ is strictly positive and

$$\lambda_1 = \frac{\mu_1}{1-\mu_1\beta},$$

where μ_1 the smallest eigenvalue of (1.82).

Proof. Let $\mathbb{S}(z) := z \in H_D^2(\Omega) \to w \in H_D^2(\Omega)$, where w is the solution of

$$\int_\Omega (\mathcal{D}\nabla^2 w) : \nabla^2\eta dx = -\int_\Omega \mathcal{A}e(u)\nabla z\nabla\eta dx + \beta\int_\Omega (\mathcal{D}\nabla^2 z) : \nabla^2\eta dx, \quad \forall\eta \in H_D^2(\Omega).$$

We remark that the operator $\mathbb{S}$ is not compact since $\mathbb{S}(z) = \mathbb{T}(z) + \beta Id(z)$ (the identity operator is not compact). However $\mathbb{S}$ is positive definite. Indeed, thanks to the Poincaré inequality and the Sobolev embedding $H^2(\Omega) \hookrightarrow W^{1,4}(\Omega)$, there exist $C > 0$ such that for $\forall\beta \geq \beta^* = \frac{C}{\delta}\|\mathcal{A}e(u)\|_{L^2(\Omega)}$

$$\int_\Omega \mathcal{A}e(u)\nabla\eta\nabla\eta dx \leq \|\mathcal{A}e(u)\|_{L^2(\Omega)}\|\eta\|_{W^{1,4}(\Omega)}^2 \leq C\|\mathcal{A}e(u)\|_{L^2(\Omega)}\|\eta\|_{H^2(\Omega)}^2 \leq \beta\int_\Omega (\mathcal{D}\nabla^2\eta) : \nabla^2\eta dx,$$

and $\mathbb{S}$ is elliptic (so in particular positive definite)

$$\langle\mathbb{S}(w), w\rangle_{H_D^2(\Omega)} = \int_\Omega \mathcal{D}\nabla^2\mathbb{S}(w) : \nabla^2 w dx = -\int_\Omega \mathcal{A}e(u)\nabla w\nabla w dx + \beta\int_\Omega (\mathcal{D}\nabla^2\eta) : \nabla^2\eta dx$$
$$\geq (\beta - \beta^*)\|w\|_{H_D^2(\Omega)}^2.$$

Hence all eigenvalues μ are be positive. Now let $\hat{\lambda}$ be defined as

$$\hat{\lambda} = \frac{\mu_1}{1-\mu_1\beta}.$$

We easily remark that $1/\hat{\lambda}$ is an eigenvalue of the resolvent $\mathbb{T}$, introduced in the proof of Proposition 1.3.11. In order to prove $\hat{\lambda} = \lambda_1$, we proceed by contradiction. Supposing that the plate buckles, i.e. $\infty > \lambda_1 > 0$, let us say first that $\hat{\lambda} > \lambda_1$. Since λ_1 is positive, then $1 - \mu_1\beta > 0$ and

$$\frac{\mu_1}{1-\mu_1\beta} > \lambda_1 \quad \text{is equivalent to} \quad \mu_1 > \frac{\lambda_1}{1+\beta\lambda_1},$$

which contradicts the fact that μ_1 is the smallest positive eigenvalue of (1.82). Otherwise if $\hat{\lambda} < \lambda_1$, since λ_1 is the smallest positive eigenvalue of (1.77), then $\hat{\lambda} \leq 0$. Nevertheless, in that case

$$\frac{\mu_1}{1-\mu_1\beta} < \lambda_1 \quad \text{is equivalent to} \quad \mu_1 > \frac{\lambda_1}{1+\beta\lambda_1},$$

resulting to be the same precedent contradiction. Hence

$$\lambda_1 = \frac{\mu_1}{1-\mu_1\beta}.$$

$\square$

Chapter 2

Multi-phase structural optimization

Contents

We consider the optimal distribution of several elastic materials in a fixed working domain. In order to optimize both the geometry and topology of the mixture we rely on the level set method for the description of the interfaces between the different phases. We discuss various approaches, based on Hadamard method of boundary variations, for computing shape derivatives which are the key ingredients for a steepest descent algorithm. The shape gradient obtained for a sharp interface involves jump of discontinuous quantities at the interface which are difficult to numerically evaluate. Therefore we suggest an alternative smoothed interface approach which yields more convenient shape derivatives. We rely on the signed distance function and we enforce a fixed width of the transition layer around the interface (a crucial property in order to avoid increasing "grey" regions of fictitious materials). It turns out that the optimization of a diffuse interface has its own interest in material science, for example to optimize functionally graded materials. Several 2-d examples of compliance minimization are numerically tested which allow us to compare the shape derivatives obtained in the sharp or smoothed interface cases.

This chapter is based on a joint work with G. Allaire, C. Dapogny and G. Michailidis which has been accepted for publication as

- G. Allaire, C. Dapogny, G. Delgado and G. Michailidis, *Multi-phase structural optimization via a level-set method*, in ESAIM: Control, Optimisation and Calculus of Variations (2013)

2.1 Introduction

Many industrial applications and problems in material science are concerned with finding the optimal distribution of several materials in a fixed working domain, in order to minimize a criterion related to the overall mechanical behavior or cost of the phases mixture. Intuition is usually very limited in such problems and shape and topology optimization can provide valuable help to the designers and researchers.

A crucial issue in the modeling of this problem is the parametrization of the phases mixture. While the exact formulation requires the material properties, or the global Hooke's tensor, to be discontinuous at the interfaces between two materials, it is often convenient, for numerical purposes, to devise an appropriate interpolation scheme to smoothen the coefficients or equivalently to replace sharp interfaces by diffuse ones using some monotonic interpolation scheme. This diffuse or smeared interface approach has its own interest when one is interested in the optimization of functionally graded materials, where more general interpolation functions can be used [68], [199], [295], [306], [312].

There is already a vast literature about multiphase optimization with constant material properties and various methods have been proposed to address this problem. The Hadamard method of geometric shape optimization, as described in [104], [144], [279], [285] was used, for example, in [143] for optimal composite design. The homogenization method [4], [85], [302] was the main tool in the multiphase problem studied in [7] for the optimal reloading of nuclear reactors (sequential laminates were shown to be optimal composite materials). In the framework of the SIMP (Solid Isotropic Material with Penalization) method, several interpolation schemes have been proposed for the mathematical formulation of the Hooke's tensor of the mixture [44], [299], [324]. In general, material interpolation schemes can be quite involved [324] and one may design such a model in order to favor certain phases [299]. Applications range from the design of materials with extreme or unusual thermal expansion behavior [277] to multi-material actuators [275], through conductivity optimization for multi-phase microstructural materials [329]. In the framework of the phase-field method, a generalized Cahn-Hilliard model of multiphase transition was implemented in [328] to perform multimaterial structural optimization.

The first publications on multiphase optimization, using the level set method, are these of Mei et al. [217] and Wang et al. [317] (see also [216], [316], [318]). Following an idea of Vese and Chan [313], the authors in [217], [317] used m level set functions to represent up to $n = 2^m$ materials: we shall adhere to this setting (see section 2.5). The level set functions are advected through eikonal Hamilton-Jacobi equations in which the normal velocity is given by the shape derivative of the objective function. Unfortunately, the shape derivatives, derived in [217] and [317], are not correct in full mathematical rigor as we explain in section 2.4. Fortunately, these shape derivatives are approximations of the correct formula upon various assumptions. A first goal of the present chapter is to clarify the issue of shape differentiability of a multiphase optimization problem. In section 2.2 we give the correct shape derivative in the setting of a sharp interface between phases (see Proposition 2.2.1). It was first obtained in [12] for a problem of damage and fracture propagation but, in a scalar setting, previous contributions can be found in [147], [48], [254]. Because the phase properties are discontinuous through the interfaces, the transmission conditions imply that only the elastic displacement and the normal stress are continuous at the interfaces, leaving the tangential stress and the normal strain discontinuous. These discontinuities yield obvious difficulties which must be handled carefully. The exact or continuous shape derivative turns out to be somehow inadequate for numerical purposes since it involves jumps of strains and stresses through the interfaces, quantities which are notably hard to evaluate with continuous finite elements. Therefore, Proposition 2.2.5 gives a discrete

variant of this shape derivative which does not involve any jumps and is similar to the result of [217] and [317]. The idea is to consider a finite element approximation of the elasticity system, the solution of which has no derivative jumps through the interface, implying that the shape derivative is much easier to compute.

Another delicate issue in multiphase optimization using the level set method is that the interface is inevitably diffuse and its thickness may increase, thus deteriorating the performance of the analysis and eventually of the optimization. Note that, for most objective functions, it is always advantageous to introduce intermediate values of the material properties, so that the interface spreading is produced by the optimization process itself and not merely by the numerical diffusion. In [217] the authors introduced a penalization term to control the width of the interpolation zone between the materials. In [317] the level set functions are re-initialized to become signed distance functions, which permits a more explicit control of the interpolation width. A second goal of the present chapter is to propose a smoothed interface setting which guarantees a fixed thickness of the interface without any increase in its width (as it is already the case in the standard single material level set method for shape and topology optimization). In section 2.3 we describe a regularization of the interface which relies on the signed distance function to the interface. Note that the signed distance function has nothing to do with the level set function which is used in numerical simulations. Indeed, the solution of the advection Hamilton-Jacobi equation (with a velocity given by the shape derivative) is usually not the signed distance function (which explains why reinitialization is often used in practice). In such a smoothed interface setting our main result is Theorem 2.3.13 which gives the shape derivative of the objective function. It requires several intermediate technical results, notably finding the shape derivative of the distance function (first obtained in [103]) and using a coarea formula to reduce a volume integral to a product integral on the interface and along normal rays. Once again, we show in section 2.3.5 that, when a regularized Heaviside function is used as interpolation function for the material properties and the regularization parameter (or the thickness of the diffuse interface) is vanishingly small, the exact shape derivative can be approximated by the formula already obtained in Proposition 2.2.5 which corresponds to the result of [217] and [317] too.

Section 2.3.6 explains how the smoothed interface model converges to the sharp interface problem as the regularization parameter goes to zero. Next, Section 2.4 is devoted to a comparison with [217] and [317]. Since, for simplicity, all the previous theoretical results were stated in the case of a single interface between two phases, we explain how to generalize our smoothed interface setting to more materials in section 2.5. In section 2.6 we show several 2-d results and make comparisons between the different settings and formulae for the shape derivatives. Some optimal designs obtained by our approach are compared to those previously computed in [317] and [318]: ours are more symmetric and sometimes slightly different. We believe it is due to our use of a correct shape derivative instead of an approximate one.

2.2 Sharp-interface formulation in a fixed mesh framework

To simplify the exposition in the first sections we limit ourselves to the case of two materials. Of course, the proposed approach extends to more phases and the corresponding details are given in section 2.5.

2.2.1 Description of the problem

The general purpose in multi-phase optimization is to find the best position of the interface Γ between two linear elastic materials, hereafter labeled as 0 and 1, with respective Hooke's laws A_0, A_1. These materials fill two respective subdomains Ω^0, Ω^1 of a (bounded) working domain D of $\mathbb{R}^d$, ($d = 2$ or 3) which accounts for the resulting structure of the optimal distribution of materials, i.e. $D = \Omega^0 \cup \Gamma \cup \Omega^1$. To avoid mathematical technicalities, we assume that Γ is a

smooth surface without boundary and strictly included in D, that is, $\Gamma \cap \partial D = \emptyset$. We refer to Ω^1 as the *exterior* subdomain, so that $\partial \Omega^0 = \Gamma$ (see Figure 2.1). Thus, the shape of the interface Γ is altogether conditioned by that of Ω^0, and conversely. In the sequel, the variable of shape optimization is denoted either by Γ or Ω^0, without distinction.
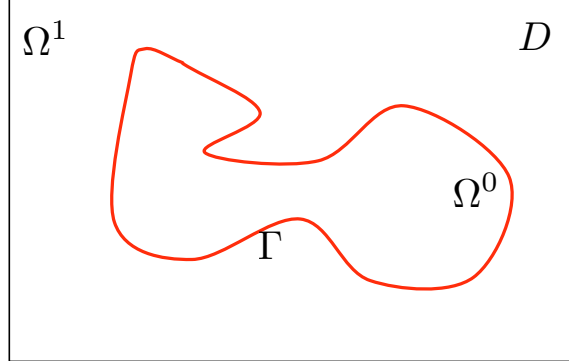
Figure 2.1: Fixed working domain D occupied by two distinct materials Ω^0 and Ω^1 separated by a smooth interface Γ.

The structure D is clamped on a part $\Gamma_D \subset \partial D$ of its boundary, and is submitted to *body forces* and *surface loads* (the latter one applied on a part $\Gamma_N \subset \partial D$), which are given as two vector-valued functions defined on D, respectively denoted as $f \in L^2(D)^d$ and $g \in H^1(D)^d$.

Perhaps the most natural and physical way to model such a distribution of two materials among a fixed working domain is the so-called *sharp-interface formulation*. More specifically, the total Hooke's law on D is defined as $A_\chi := A_0 \chi_0 + A_1 \chi_1$, where χ_i stands for the characteristic function of the phase Ω^i. In this context, the *displacement field* u is the unique solution in $H^1(D)^d$ to the linearized elasticity system

$$\begin{cases} -\mathrm{div}\,(A_\chi\, e(u)) & = & f & \text{in } D \\ u & = & 0 & \text{on } \Gamma_D \\ (A_1\, e(u)) \cdot n & = & g & \text{on } \Gamma_N, \end{cases} \tag{2.1}$$

where $e(u) = \frac{\nabla u^T + \nabla u}{2}$ is the strain tensor, and n stands for the outer unit normal vector to ∂D.

Our purpose is to minimize an objective function of the interface Γ, which is rather expressed as a function $J(\Omega^0)$ of the interior subdomain,

$$J(\Omega^0) = \int_D j(x, u)\, dx + \int_{\Gamma_N} k(x, u)\, ds, \tag{2.2}$$

where $j(x, u)$ and $k(x, u)$ are smooth functions satisfying adequate growth conditions. A typical example is the *compliance* of the structure D, which reads

$$J(\Omega^0) = \int_D f \cdot u\, dx + \int_{\Gamma_N} g \cdot u\, ds. \tag{2.3}$$

2.2.2   Shape-sensitivity analysis of the sharp-interface problem

There exists a vast literature on the Hadamard method for computing derivatives with respect to the exterior boundary (see e.g. [5], [103], [144], [279] and references therein) but relatively few works on the derivation with respect to an interface between two regions. In the conductivity context (i.e. replacing (2.1) by a scalar equation), derivatives with respect to an interface have

been obtained in [147], [48], [254]. These results were extended to the elasticity setting in [12]. Let us also mention the works [173], [248] where similar results are obtained for a stratified media (where the interfaces are flat and parametrized by a single scalar parameter).

As noticed in [12] and [254], the essential ingredients that must be considered in the calculation of the shape derivative of a problem such as (2.1) are the transmission conditions and the differentiability of the solution u with respect to the interface Γ. Furthermore, when a numerical implementation is sought, an additional element must be taken into account: the way in which the transmission conditions (continuity of the displacement and continuity of the normal stress across the interface) are interpreted by finite element methods in a fixed mesh framework. In general these methods either partially preserve the transmission conditions (e.g. classical Lagrange finite elements method) or exactly preserve the transmission conditions (e.g. extended finite elements XFEM [293], adapted interface meshing [97], etc.).

It is known [12], [254] that the solution $u \in H^1(D)$ of (2.1) is not shape differentiable with respect to the interface Γ. The reason is that some spatial derivatives of u are discontinuous across the interface because of the jump of the material elastic properties. Note however that the transported (or pull-back) function $u_\theta := u \circ (Id + \theta)$ is indeed differentiable with respect to θ (this is the difference introduced in Definitions 1.1.19 and 1.1.20 between the material derivative, in the latter case, and the shape derivative in the former case). As it was remarked in Section 1.1, it is not necessary to use the concept of material derivative for computing the shape derivative of the objective function. One can stay in a Eulerian framework and use Céa's formal Lagrangian method [74] to find the correct formula for the shape derivative $J'(\Omega^0)(\theta)$. In order to circumvent the non-differentiability of u, the idea is to introduce the restrictions of u on Ω^0 and Ω^1, denoted by $u^0 := u|_{\Omega^0}$ and $u^1 := u|_{\Omega^1}$.

We recall the result of [12] for the shape derivation of the objective function (2.2). We need to introduce some notations about jumps through the interface Γ. For any quantity s which is discontinuous across Γ, taking values s^0 (resp. s^1) on Ω^0 (resp. Ω^1), denote as $[\![s]\!] = s^1 - s^0$ the *jump* of s. We also introduce at each point of Γ the local basis obtained by gathering the unit normal vector n (pointing outward Ω^0) and a collection of unit tangential vectors, denoted by τ, such that (τ, n) is an orthonormal frame. For a symmetric $d \times d$ matrix $\mathcal{M}$, written in this basis, we introduce the notation

$$\mathcal{M} = \begin{pmatrix} \mathcal{M}_{\tau\tau} & \mathcal{M}_{\tau n} \\ \mathcal{M}_{n\tau} & \mathcal{M}_{nn} \end{pmatrix}$$

where $\mathcal{M}_{\tau\tau}$ stands for the $(d-1) \times (d-1)$ minor of $\mathcal{M}$, $\mathcal{M}_{\tau n}$ is the vector of the $(d-1)$ first components of the d-th column of $\mathcal{M}$, $\mathcal{M}_{n\tau}$ is the row vector of the $(d-1)$ first components of the d-th row of $\mathcal{M}$, and $\mathcal{M}_{nn}$ the (d,d) entry of $\mathcal{M}$. Finally, we define the adjoint problem

$$\begin{cases} -\mathrm{div}\,(A_\chi\, e(p)) & = & -j'(x,u) & \text{in } D, \\ p & = & 0 & \text{on } \Gamma_D, \\ (A_1\, e(p)) \cdot n & = & -k'(x,u) & \text{on } \Gamma_N, \end{cases} \tag{2.4}$$

where the symbol $\prime$ denotes differentiation with respect to u.

Proposition 2.2.1. *The shape derivative of the cost function J, defined in (2.2), reads*

$$J'(\Omega^0)(\theta) = -\int_\Gamma \mathcal{D}(u,p)\, \theta \cdot n\, ds,$$

$$\mathcal{D}(u,p) = -\sigma(p)_{nn} : [\![e(u)_{nn}]\!] - 2\sigma(p)_{n\tau} : [\![e(u)_{n\tau}]\!] + [\![\sigma(u)_{\tau\tau}]\!] : e(p)_{\tau\tau}. \tag{2.5}$$

where $[\![\cdot]\!] = \cdot^1 - \cdot^0$ denotes the jump through Γ, $n = n^0 = -n^1$, p is the adjoint state solution of (2.4) and $\sigma(v) = A_\chi\, e(v)$.

Remark 2.2.2. *To better appreciate the expression (2.5) where some terms have jumps and others not, we recall that the tangential strain tensors $e(u)_{\tau\tau}$ and $e(p)_{\tau\tau}$ are continuous through the interface Γ while the normal components $e(u)_{nn}$, $e(u)_{n\tau}$, $e(p)_{nn}$ and $e(p)_{n\tau}$ are discontinuous. On the contrary, the normal components of the stress tensors $\sigma(u)_{nn}$, $\sigma(u)_{n\tau}$, $\sigma(p)_{nn}$ and $\sigma(p)_{n\tau}$ are continuous through Γ while their tangential parts $\sigma(u)_{\tau\tau}$ and $\sigma(p)_{\tau\tau}$ are discontinuous.*

Proof. We merely sketch the proof that can be found in [12]. In order to apply Céa's Lagrangian method [74], we first introduce the restrictions of u on Ω^0 and Ω^1, denoted by $u^0 := u|_{\Omega^0}$ and $u^1 := u|_{\Omega^1}$, which satisfy the transmission problem:

$$
\begin{cases}
-\mathrm{div}\left(A_1\, e(u^1)\right) = f & \text{in } \Omega^1 \\
u^1 = 0 & \text{on } \Gamma_D \cap \partial\Omega^1 \\
\left(A_1\, e(u^1)\right)\cdot n = g & \text{on } \Gamma_N \cap \partial\Omega^1 \\
u^1 = u^0 & \text{on } \Gamma \\
(A_0 e(u^0))\cdot n^0 + (A_1 e(u^1))\cdot n^1 = 0 & \text{on } \Gamma,
\end{cases}
\tag{2.6}
$$

and

$$
\begin{cases}
-\mathrm{div}\left(A_0\, e(u^0)\right) = f & \text{in } \Omega^0 \\
u^1 = u^0 & \text{on } \Gamma \\
(A_0 e(u^0))\cdot n^0 + (A_1 e(u^1))\cdot n^1 = 0 & \text{on } \Gamma.
\end{cases}
\tag{2.7}
$$

Of course, (2.1) and (2.6)-(2.7) are equivalent. Note that, by standard regularity theory [213], u is smooth on each subdomain, namely $u^0 \in H^2(\Omega^0)$ and $u^1 \in H^2(\Omega^1)$. Then, we define the Lagrangian

$$
\begin{aligned}
\mathcal{L}(\theta, v^1, v^0, q^1, q^0) &= \sum_{i=0,1}\left(\int_{(Id+\theta)\Omega^i} j(x,v^i)dx + \int_{\Gamma_N} k(x,v^i)ds\right) \\
&+ \sum_{i=0,1}\left(\int_{(Id+\theta)\Omega^i} A_i e(v^i):e(q^i)dx - \int_{(Id+\theta)\Omega^i} f\cdot q^i dx - \int_{\Gamma_N} g\cdot q^i ds\right) \\
&+ \frac{1}{2}\int_{(Id+\theta)\Gamma}(\sigma^1(v^1)+\sigma^0(v^0))n\cdot(q^1-q^0)ds \\
&+ \frac{1}{2}\int_{(Id+\theta)\Gamma}(\sigma^1(q^1)+\sigma^0(q^0))n\cdot(v^1-v^0)ds,
\end{aligned}
\tag{2.8}
$$

where the last two surface integrals account for the transmission conditions. Differentiating $\mathcal{L}$ with respect to q^1, q^0 yields the state equations (2.6)-(2.7), while differentiating with respect to v^1, v^0 leads to the adjoint equation (2.4). Then a standard, albeit nasty, computation (see [12] for full details) shows that

$$
J'(\Omega^0)(\theta) = \frac{\partial\mathcal{L}}{\partial\theta}(0, u^1, u^0, p^1, p^0)(\theta),
$$

which yields the result. $\qquad\square$

Remark 2.2.3. *Proposition 2.2.1 can be extended in several ways. For example, if the integrand j depends on χ, namely if the objective function is*

$$
J(\Omega^0) = \int_D j_\chi(x,u)dx + \int_{\Gamma_N} k(x,u)ds := \sum_{i=0,1}\int_{\Omega^i} j_i(x,u)dx + \int_{\Gamma_N} k(x,u)dx,
$$

we obtain a shape derivative which is

$$
J'(\Omega^0)(\theta) = -\int_\Gamma\left(\llbracket j_\chi(x,u)\rrbracket + \mathcal{D}(u,p)\right)\theta\cdot n\, ds,
$$

with the same expression (2.5) for $\mathcal{D}(u,p)$.

Although formula (2.5) for the shape derivative makes perfect sense in a continuous setting, its numerical discretization is not obvious. Indeed, (2.5) involves jumps through the interface which are difficult to evaluate from a numerical point of view if the interface is not exactly meshed. Let us explain the difficulty by making some specific discretization choices, keeping in mind that any other numerical method will feature similar drawbacks. Suppose D is equipped with a conformal simplicial mesh $D_h = \bigcup_{i=1}^N K_i$ with N elements K_i of maximal size h. Let $\Pi_1(D_h)$ and $\Pi_0(D_h)$ be the finite-dimensional spaces of Lagrange $\mathbb{P}^1$, respectively $\mathbb{P}^0$, finite element functions. Define $u_h, p_h \in \Pi_1(D_h)$ the internal approximations of u and p (we recall weak solutions of (2.1) and (2.4) respectively), i.e.,

$$\int_D A_\chi e(u_h) : e(v_h)\, dx = \int_D f \cdot v_h\, dx + \int_{\Gamma_N} g \cdot v_h\, ds, \quad \forall v_h \in \Pi_1(D_h), \qquad (2.9)$$

and

$$\int_D A_\chi e(p_h) : e(v_h)\, dx = -\int_D j'(x, u_h) \cdot v_h\, dx - \int_{\Gamma_N} k'(x, u_h) \cdot v_h\, ds, \quad \forall v_h \in \Pi_1(D_h). \quad (2.10)$$

Since the discrete strain tensors $e(v_h)$ are constant in each cell K_i, we can replace A_χ in the above internal approximate variational formulation by its $\mathbb{P}^0$ interpolate A^* defined by

$$A^*|_K = \rho A^0 + (1 - \rho)A^1, \quad \text{with } \rho = \int_K \chi dx.$$

Within this discretized framework the naive evaluation of the jumps in (2.5) has no meaning. Indeed, consider the generic case of an element K cut in its interior by the interface Γ (see Figure 2.2). For $\mathbb{P}^1$ Lagrange finite elements the strain tensors $e(v_h)$, for $v_h = u_h, p_h$, are constant in K, thus yielding a zero jump. Similarly, if the stress tensors are evaluated as $\sigma_h = A^* e(v_h)$, they are constant in K and their jump is again zero, leading to a vanishing shape derivative ! There is an alternative formula for the stress tensor which is $\sigma_h = A_\chi e(v_h)$: it yields a non-vanishing jump $[\![A]\!]e(v_h)$ and the discretization of (2.5) would be

$$(\mathcal{D}(u, p))_h = ([\![A]\!]e(u))_{\tau\tau} : e(p)_{\tau\tau}, \qquad (2.11)$$

which is different from the discrete formula (3.23) by lack of any normal components. On the same token, note that the "exact" continuity of the normal stress through Γ does not hold for $\sigma_h = A_\chi e(v_h)$ with $v_h = u_h, p_h$ since

$$[\![\sigma_h \cdot n]\!] = ([\![A]\!]e(v_h)) \cdot n \neq 0.$$

Therefore some special care is required for the numerical approximation of (2.5). A complicated process was proposed in [12] for computing the jump of a discontinuous quantity s_h, based on the diffuse interface approximation

$$[\![s_h]\!] \approx \left((1 - \chi)s_h - \chi s_h\right). \qquad (2.12)$$

Although this approximation seems to work well when the contrast between the two elastic phases is very large (as is the case in damage or fracture models, see [12]), more general numerical experiences for comparable elastic moduli indicate a much worse behavior of this approximation, up to the point that (2.5) does not any longer provide a proper descent direction to minimize (2.2) (see section 2.6.2).

One way to overcome the difficulty of computing the jumps involved in the shape derivative, consists in expressing $J'(\Omega^0)$ not as a surface integral but rather as a volume integral. Indeed, applying a sort of "divergence theorem", one can formulate (2.5) as a volume integral on Ω, where no jumps are actually needed.
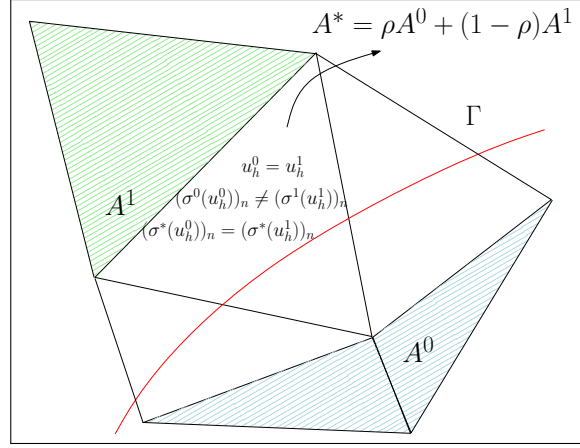
Figure 2.2: Transmission condition in a fixed mesh framework.

Proposition 2.2.4. *Suppose $f = 0$ and $\theta = 0$ on Γ_N. Then the shape derivative of the cost function J defined in (2.2) reads*

$$J'(\Omega^0)(\theta) = -\int_D \Big(A_\chi e(p) : \mathcal{E}(\theta, u) + A_\chi e(u) : \mathcal{E}(\theta, p) \Big) dx + \int_D A_\chi e(u) : e(p) \, div(\theta) dx, \quad (2.13)$$

where p is the same adjoint state of (2.4) and the tensor $\mathcal{E}$ is given by

$$\mathcal{E}_{ij}(\theta, q) = \frac{1}{2} \sum_k \Big(\partial_k q_j \partial_i \theta_k + \partial_k q_i \partial_j \theta_k \Big). \quad (2.14)$$

Equations (2.5) and (2.13) are thus equivalent.

Proof. Denote as $u(Id + \theta)$ the solution of (2.1) for the deformed configuration $\chi_\theta = \chi \circ (Id + \theta)^{-1}$ (we recall that the domain D does not change since $\theta \cdot n = 0$ on ∂D). As it was quoted in [254], even though the function $u(Id + \theta)$ is not shape differentiable (i.e. we can not take an Eulerian derivative), we can introduce however the notion of Lagrangian derivative through the transported of $u(Id + \theta)$ [5]

$$u_\theta = u(Id + \theta) \circ (Id + \theta). \quad (2.15)$$

Setting as test function $\overline{v} = v \circ (Id + \theta)^{-1}$, then $\forall v \in H^1(D)^d$ such that $v_{\Gamma_D} = 0$ the variational formulation of (2.1) in the deformed configuration yields

$$\int_D A_{\chi_\theta} e\big(u(Id + \theta)\big) : e(\overline{v}) dx = \int_D f \cdot \overline{v} dx + \int_{\Gamma_N} g \cdot \overline{v} ds.$$

So applying the change of coordinates $x = (Id + \theta)\overline{x}$

$$\int_D \Big(A_\chi e(u(Id + \theta)) \circ (Id + \theta) : e(\overline{v}) \circ (Id + \theta) \Big) |\det(\nabla(Id + \theta))| d\overline{x}$$
$$= \int_D f \circ (Id + \theta) \cdot v |\det(\nabla(Id + \theta))| d\overline{x}$$
$$+ \int_{\Gamma_N} g \circ (Id + \theta) \cdot v |\det(\nabla(Id + \theta))| \Big| \big((\nabla(Id + \theta))^{-1} \big)^T n \Big| d\overline{s}. \quad (2.16)$$

Furthermore by the very definition of the strain of $u(Id + \theta)$

$$e(u(Id + \theta))_{ij} = \frac{1}{2}(\partial_i u^j(Id + \theta) + \partial_j u^i(Id + \theta)),$$

so invoking (2.15) entails

$$\partial_j \big(u^i (Id + \theta) \big) = \sum_k \partial_k u^i_\theta \partial_j (Id + \theta)^{-1}_k.$$

Hence

$$e(u(Id + \theta)) \circ (Id + \theta) = \frac{1}{2} \sum_k \Big(\partial_k u^i_\theta \partial_j (Id + \theta)^{-1}_k + \partial_k u^j_\theta \partial_i (Id + \theta)^{-1}_k \Big) \circ (Id + \theta).$$

Deriving thus with respect to θ around 0

$$\frac{\partial}{\partial \theta} e(u(Id+\theta)) \circ (Id+\theta) = \frac{1}{2} \Big(\partial_j (u'_\theta)^i + \partial_i (u'_\theta)^j \Big) - \frac{1}{2} \sum_k \Big(\partial_k u^i_\theta \partial_j \theta_k + \partial_k u^j_\theta \partial_i \theta_k \Big) = e(u'_\theta) - \mathcal{E}(\theta, u_\theta),$$

where $u'_\theta \in H^1(D)$, with $u'_\theta = 0$ on Γ_D, denotes the Lagrangian derivative of u. Moreover introducing

$$|\det(\nabla(Id + \theta))| = 1 + \mathrm{div}\theta + o(\theta),$$
$$\Big| \big((\nabla(Id + \theta))^{-1} \big)^T n \Big| = 1 - (\nabla\theta)^T n \cdot n + o(\theta),$$

in (2.16), one finds the variational problem that satisfies the Lagrangian derivative of u_θ at 0 following the direction θ (Theorem 3.10 [285]),

$$
\begin{aligned}
\int_D \Big(A_\chi e(u'_\theta) : e(v) \Big) dx \;=&\; \int_D \Big(A_\chi e(u) : \mathcal{E}(\theta, v) + A_\chi e(v) : \mathcal{E}(\theta, u) \Big) dx - \int_D A_\chi e(u) : e(v) \mathrm{div}(\theta) dx \\
&+ \int_D \Big(\nabla f \cdot \theta + \mathrm{div}(\theta) f \Big) \cdot v dx \\
&+ \int_{\Gamma_N} \Big(((\mathrm{div}\theta - (\nabla\theta)^T n \cdot n) g \cdot v + \nabla g \cdot \theta \cdot v \Big) ds
\end{aligned}
$$

Similarly, if we apply the same development to the cost function $J((Id + \theta)\Omega^0)$ using the hypothesis $f = 0$ and $\theta = 0$ on Γ_N

$$
\begin{aligned}
&\int_D j(x, u_\theta \circ (Id + \theta)^{-1}) dx + \int_{\Gamma_N} k(x, u_\theta \circ (Id + \theta)^{-1}) ds \\
=&\; \int_D j((Id + \theta)x, u_\theta) |\det(\nabla(Id + \theta))| dx + \int_{\Gamma_N} k(x, u_\theta) |\det(\nabla(Id + \theta))| \Big| \big((\nabla(Id + \theta))^{-1} \big)^T n \Big| ds \\
=&\; J(\Omega^0) + \int_{\partial D} j\theta \cdot n ds + \int_D j' \cdot u'_\theta dx + \int_{\Gamma_N} k' \cdot u'_\theta ds + o(\theta) \\
=&\; J(\Omega^0) - \int_D \Big(A_\chi e(p) : e(u'_\theta) \Big) dx + o(\theta), \qquad\qquad (2.17)
\end{aligned}
$$

where the functions $j(,\cdot), k(,\cdot)$ are $C^1(D)$. Finally inserting the weak formulation of u'_θ into (2.17) the desired result follows. $\qquad\square$

From a pragmatic point of view, the volume form of the shape derivative of J (2.13) allows us to easily find a descent direction $\theta^\star$ without the need of estimating the jumps involving the stresses and strains of u and p. The vector $\theta^\star$ can be e.g. estimated by a dual identification method with a Hilbert subspace $W \subset W^{1,\infty}(\Omega)^d$ by solving

$$\langle \theta^\star, \theta \rangle_W = -J'(\Omega^0)(\theta), \forall \theta \in W.$$

Unfortunately, (2.13) is not quite suited for numerical purposes. Indeed, in a typical discrete framework, the values of $\theta^\star$ for both formulae (2.5) and (2.13) are not exactly equal.

This fact is illustrated in Figure 2.3 for the compliance (2.3) of a cantilever composed of two anisotropic materials (in black and red), where the values of $\theta^\star$ are plotted for both formulae taking $W = \Pi_1(D_h)^2$ and the scalar product of $L^2(D_h)$. This choice of FE (classically used in linear elasticity) is not a subspace of $W^{1,\infty}(D)^2$ and moreover does not fulfill the normal stress continuity conditions, hence not allowing an "integration by parts" between (2.13) and (2.5) to reach the equivalence. This feature restricts the use of (2.13) to some particular families of FE, see e.g. [281].
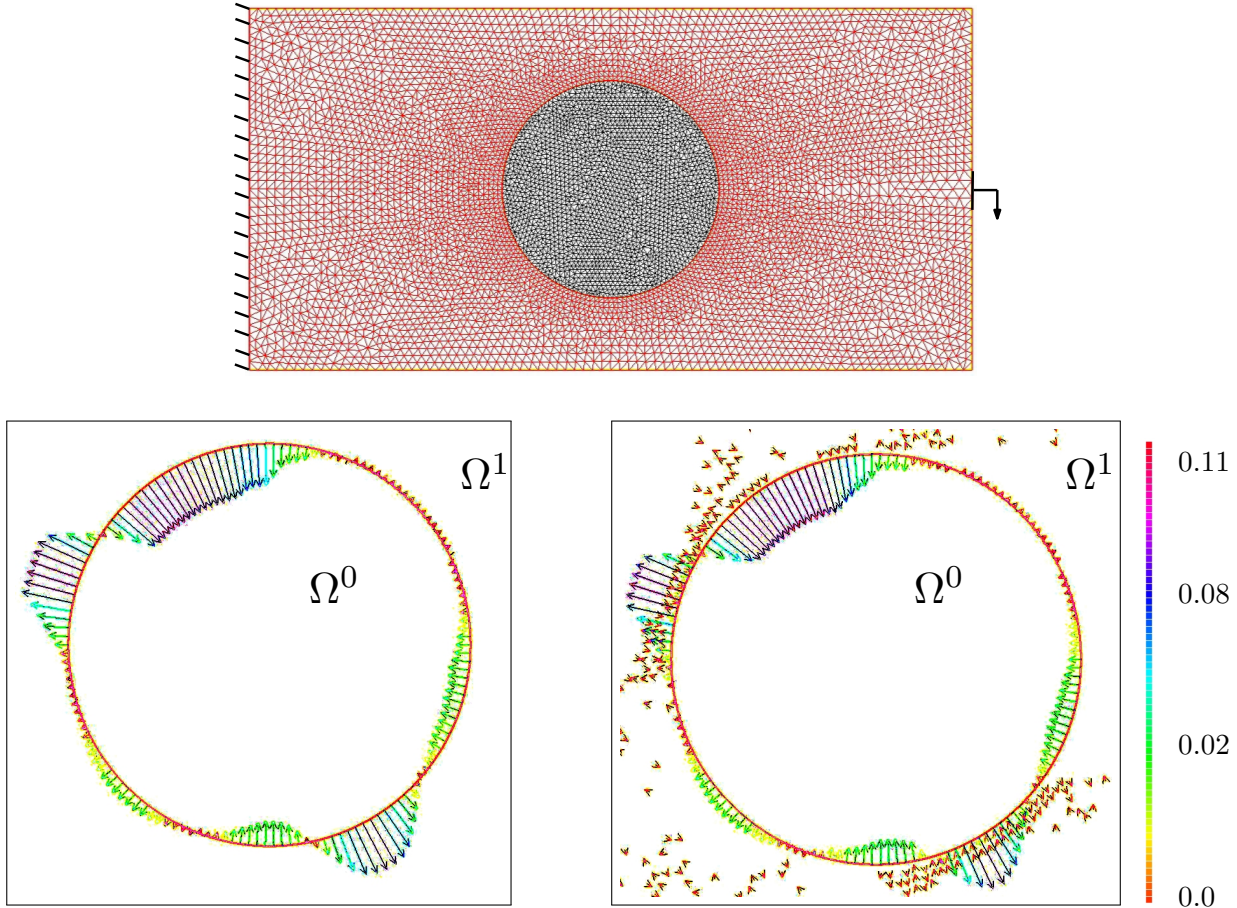
Figure 2.3: Zoom around the circular domain Ω^0 (in black) surrounded by Ω^1 (in red). The interface Γ is perfectly meshed. The descent direction fields $\theta^\star$ for the "surface" (2.5) and "volume" (2.13) formulae of $J'(\Omega^0)(\theta)$ are plotted at the left and the right sides, respectively. We remark that the values of both formulae do not match perfectly due to the choice of finite elements.

All these difficulties in the numerical evaluation of the shape derivatives (2.5) and (2.13) are summarized just as another example of the well-known paradigm "should we differentiate first and then discretize or *vice versa*?" as already studied in [249]. In order to get around this issue it is tempting, and we do so now, to investigate the case when we first discretize and then differentiate. In other words we consider the objective function

$$J_h(\Omega^0) = \int_D j(x, u_h)\, dx + \int_{\Gamma_N} k(x, u_h)\, ds,$$

where $u_h \in \Pi_1(D_h)$ is the discrete solution of (3.21).

Proposition 2.2.5. *Assume that the interface Γ generically cuts the mesh D_h, namely that it is never aligned with part of a face of any cell K_i. Then, the solution u_h of (3.21) is shape*

differentiable and the shape derivative of the cost function J_h is given by

$$J_h'(\Omega^0)(\theta) = -\int_\Gamma [\![A_\chi]\!] e(u_h) : e(p_h)\, \theta \cdot n\, ds, \tag{2.18}$$

where $[\![\cdot]\!]$ denotes the jump through Γ and p_h is the solution of (3.22).

Remark 2.2.6. *Note that Proposition 2.2.5 holds true for most finite elements discretization and not merely $\mathbb{P}^1$ Lagrange finite elements. The assumption on the interface Γ is necessary in the sense that, if a face of an element K of the mesh is embedded in Γ, then neither u_h nor J_h are shape differentiable. However, if instead of Lagrange finite elements, we use Hermite finite elements which ensure that $e(u_h)$ is continuous on D, then the results of Proposition 2.2.5 hold true without any assumption on Γ.*

Proof. Let us denote by $\phi_i(x)$ the basis functions of the finite element space $\Pi_1(D_h)$. The solution $u_h \in \Pi_1(D_h)$ is decomposed as

$$u_h(x) = \sum_i U_i^h \phi_i(x),$$

and the vector U^h of components U_i^h is the solution of the linear system

$$K^h U^h = F^h,$$

where the stiffness matrix K^h and the right hand side F^h are defined as

$$K_{i,j}^h = \int_{D_h} A_\chi e(\phi_i) : e(\phi_j)\, dx, \text{ and } F_i^h = \int_{D_h} f \cdot \phi_i\, dx + \int_{\Gamma_N} g \cdot \phi_i\, ds.$$

The basis functions ϕ_i are independent of Γ so the shape differentiability of the function u_h reduces to that of the vector U^h and thus of the rigidity matrix K^h. Fix an arbitrary element $K \in D_h$. We first prove the shape differentiability of

$$L_{i,j}^K := \int_K A_\chi e(\phi_i) : e(\phi_j) dx. \tag{2.19}$$

An important difference when calculating the shape derivative of (2.19) w.r.t. classical boundary variations of domain integrals, is that the interface Γ intersects the boundary of ∂K, which is fixed, constraining the possible movements of Γ on its extremal points to those given by θ such that $\theta \cdot n = 0$ on ∂K (see Fig. 2.4). Thus, in order to get rid of this constraint on the boundary variations of Γ, we take any $\theta \in W^{1,\infty}(D)^d$ and we rely on a product rule formula which reads

$$\frac{d}{d\theta}\left(\int_K A_{\chi_\theta} e(\phi_i) : e(\phi_j) dx\right) = -\frac{d}{d\theta}\left(\int_{K_\theta} A_\chi e(\phi_i) : e(\phi_j) dx\right) + \frac{d}{d\theta}\left(\int_{K_\theta} A_{\chi_\theta} e(\phi_i) : e(\phi_j) dx\right), \tag{2.20}$$

where the expression at the left represents the derivative we are looking for ($\chi_\theta = \chi \circ (Id + \theta)^{-1}$), the first term at the right the boundary variation of the domain K when A_χ is fixed ($K_\theta = (Id + \theta)K$) and the second expression and the right the derivative when the interface Γ and the boundary ∂K move simultaneously. Thus assuming that $e(\phi_i)$ is regular inside K (in our case it is actually constant) and that Γ does not overlap any face of K,

$$\frac{d}{d\theta}\left(\int_{K_\theta} A_\chi e(\phi_i) : e(\phi_j) dx\right) = \int_{\partial K} A_\chi e(\phi_i) : e(\phi_j)(\theta \cdot n) ds$$

and
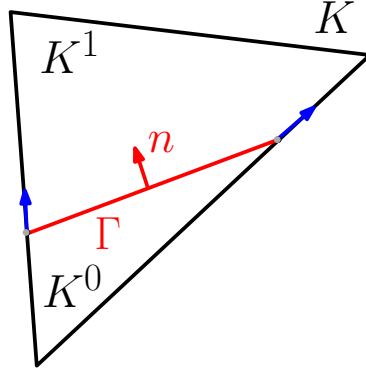
$$\frac{d}{d\theta}\left(\int_{K_\theta} A_{\chi_\theta} e(\phi_i) : e(\phi_j) dx\right) = \frac{d}{d\theta}\left(\int_{K_\theta^0} A_0 e(\phi_i) : e(\phi_j) dx\right) + \frac{d}{d\theta}\left(\int_{K_\theta^1} A_1 e(\phi_i) : e(\phi_j) dx\right)$$

$$= \int_{\partial K^0} A_0 e(\phi_i) : e(\phi_j)(\theta \cdot n) ds + \int_{\partial K^1} A_1 e(\phi_i) : e(\phi_j)(\theta \cdot n) ds$$

Figure 2.4: Boundary variation of the interface Γ in the fixed element K. The extremal points of Γ are constrained to move following the tangential directions (in blue) of ∂K.

where $K_\theta^0 = K_\theta \cap \Omega^0$, $K_\theta^1 = K_\theta \backslash K^0$ (see Fig. 2.4). Adding the foregoing equations, the desired term in (2.20) reads (as expected)

$$\int_{\Gamma \cap K} [\![A_\chi]\!] e(\phi_i) : e(\phi_j)\, \theta \cdot n\, ds. \tag{2.21}$$

The shape derivative of $(K^h)_{i,j} = \sum_{K \in D_h} L_{i,j}^K$, steams from (2.21) by linearity

$$\left(K_{ij}^h\right)'(\Omega^0)(\theta) = \int_\Gamma [\![A_\chi]\!] e(\phi_i) : e(\phi_j)\, \theta \cdot n\, ds,$$

since $e(\phi_i) : e(\phi_j)$ is integrable on Γ. Hence

$$u_h'(\Omega^0)(\theta) = \sum_i \left(U_i^h\right)'(\Omega^0)(\theta)\phi_i, \text{ where } \left(U^h\right)'(\Omega^0)(\theta) = -(K^h)^{-1}\left(K^h\right)'(\Omega^0)(\theta)U^h.$$

Once u_h is shape differentiable, it is not necessary anymore to consider a complicated Lagrangian like (2.8), taking into account the transmission conditions through Γ (which, by the way, do not hold true for u_h). Therefore we define a discrete Lagrangian as

$$\begin{aligned}\mathcal{L}_h(\theta, v_h, q_h) &= \int_D j(x, v_h)\, dx + \int_{\Gamma_N} k(x, v_h)\, ds + \int_D A_{\chi \circ (Id+\theta)^{-1}} e(v_h) : e(q_h)\, dx \\ &- \int_D f \cdot q_h\, dx - \int_{\Gamma_N} g \cdot q_h\, ds,\end{aligned}$$

to which it is easy to apply Céa's method. Note that the adjoint problem obtained by differentiating $\mathcal{L}_h$ with respect to v_h is exactly (3.22) which was a discretization of the continuous adjoint. Therefore we deduce

$$J_h'(\Omega^0)(\theta) = \frac{\partial \mathcal{L}_h}{\partial \theta}(0, u_h, p_h)(\theta),$$

which yields the desired result. $\qquad\square$

There is a clear difference between the discrete derivative (3.23) and the continuous one (2.5). Even if the continuous derivative is further discretized as suggested in (2.11), there is still a difference between (3.23) and (2.11) which is that the latter one is restricted to the tangential components of the stress and strain tensors.

There is however one case where both formulae coincide which is when one of the phases is void. Indeed, assume that $A_0 = 0$ (and similarly that $f = 0$ and $j = 0$ in Ω^0 so that no loads are applied to the void region). Then, in the domain Ω^0 we have

$$\sigma(p)_{nn} = 0, \ \sigma(p)_{n\tau} = 0, \ \sigma(u)_{nn} = 0 \text{ and } \sigma(u)_{n\tau} = 0.$$

Thus, we deduce that the continuous derivative (2.5) becomes

$$J'(\Omega^0)(\theta) = -\int_\Gamma \sigma(u^1)_{\tau\tau} : e(p^1)_{\tau\tau} \, \theta \cdot n \, ds,$$

which, upon discretization, coincides with the discrete derivative (3.23)

$$J'_h(\Omega^0)(\theta) = -\int_\Gamma A^1 e(u_h) : e(p_h) \, \theta \cdot n \, ds,$$

since $\sigma(u^1)_{nn} = \sigma(u^1)_{n\tau} = 0$ on Γ.

The above study shows that the numerical discretization of the sharp-interface problem should be handled carefully when a standard finite element method is used for solving the state and adjoint systems (2.1) and (2.4) in a fixed mesh setting. The main reason of this difficulty lies in the difference of regularity of the exact and approximated solutions through the interface.

We finish this section with a complement of Proposition 2.2.5 when a face of an element K is aligned with the interface Γ. In this case J_h is directionally shape differentiable.

Proposition 2.2.7. *Let $\mathcal{O} \subset D$ be a regular open subset. Define the piece-wise functions*

$$h = \chi h^0 + (1 - \chi)h^1 \quad \text{and} \quad c = \xi\alpha + (1 - \xi)\beta$$

where $h^0, h^1, \alpha, \beta \in C^1(D)^d$ and ξ, χ are the characteristic functions of Ω^0 and $\mathcal{O}$, respectively. Suppose that Γ and $\partial\mathcal{O}$ are piece-wise aligned.

Then the shape functional

$$J(\Omega^0) = \int_D hc \, dx$$

is directionally shape differentiable and $J'(\Omega^0)(\theta)$ reads

$$J'(\Omega^0)(\theta) = \int_\Gamma [\![h]\!]\Big(c^0(\theta \cdot n)^+ + c^1(\theta \cdot n)^-\Big)ds, \tag{2.22}$$

where $c^0 = c(x)|_{\Omega^0}$ and $c^1 = c(x)|_{\Omega^1}$ and $(\cdot)^+, (\cdot)^-$ are the positive and negative part operators.

Remark 2.2.8. *Since an integral on Γ has no sense if the integrated quantities are discontinuous (otherwise from which side would we take the trace), formula (2.22) must be conceived in the following way: If $c(x)$ is discontinuous through Γ, (2.22) takes the value of one side (α) or the other (β) according to the sign of $(\theta \cdot n)$. On the contrary, if $c(x)$ is continuous, then there is no issue and (2.22) simply reads*

$$J'(\Omega^0)(\theta) = \int_\Gamma [\![h]\!]\Big(c(\theta \cdot n)\Big)ds, \tag{2.23}$$

given that $(\theta \cdot n)^+ + (\theta \cdot n)^- = (\theta \cdot n)$.

Proof. Notice that in the context of Proposition 2.2.5 (formally speaking $h = A_\chi$ and $c = e(\phi_i)e(\phi_j)$), if $c(x)$ is continuous across the interface Γ (or the set of points where it is discontinuous is negligible), then we recover (3.23).

Now we concentrate in the case where the surfaces Γ and $\partial\mathcal{O}$ are piece-wise aligned. The Gateaux derivative (directional derivative) of $J(\Omega^0)$ is defined as

$$J'(\Omega^0)(\theta) = \lim_{t \to 0} \frac{J((Id + t\theta)(\Omega^0)) - J(\Omega^0)}{t}. \tag{2.24}$$

Denote for $t > 0$ small, $\Omega_{t\theta}^0 = (Id + t\theta)\Omega^0$. Then

$$J(\Omega_{t\theta}^0) - J(\Omega^0) = \Delta J,$$

where

$$\Delta J = \int_{\Delta\Omega_+} (h^0 - h^1)c^0 + dx - \int_{\Delta\Omega_-} (h^0 - h^1)c^1 dx,$$

and $\Delta\Omega_+ = \Omega_{t\theta}^0 \backslash \Omega^0$ and $\Delta\Omega_- = \Omega^0 \backslash \Omega_{t\theta}^0$.
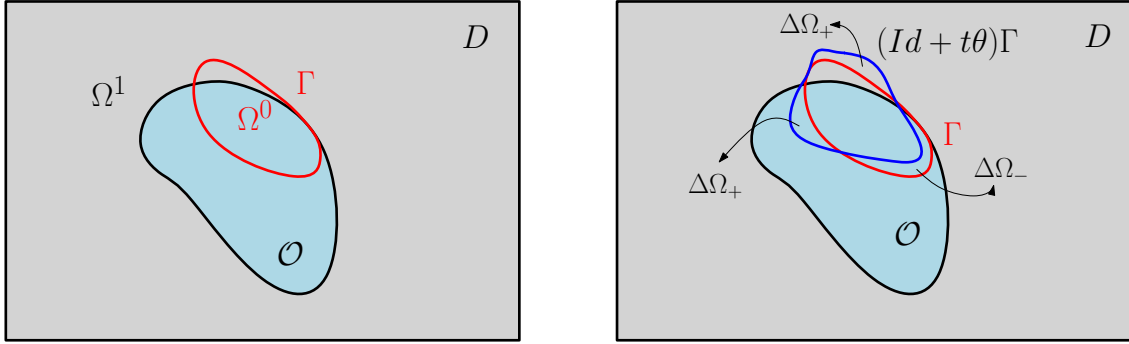
Figure 2.5: Variation of Γ in a discontinuous framework.

Now introduce the change of coordinates

$$x(\mu, \nu) = (Id + \mu\theta) \circ \gamma(\nu), \mu \in [0, t], \nu \in [0, 1]^{d-1},$$

where $\gamma(\nu)$ is a regular parametrization of Γ. We remark that the jacobian of this transformation reads

$$\left|\det\left(\frac{\partial x(\mu, \nu)}{\partial(\mu, \nu)}\right)\right| = |n(\nu) \cdot \theta|\left|\det\left(\frac{\partial\gamma(\nu)}{\partial\nu}\right)\right| + \mathcal{O}(\mu),$$

where n is the unit normal vector on Γ. Thus

$$\begin{aligned}
\Delta J &= \int_{\gamma^{-1}(v)\in\Gamma, \theta(\gamma)\cdot n(\gamma)>0} \int_0^t (h^0 - h^1)(x(\mu, \nu))c^0(x(\mu, \nu))\left|\det\left(\frac{\partial x(\mu, \nu)}{\partial(\mu, \nu)}\right)\right| d\mu d\nu \\
&\quad - \int_{\gamma^{-1}(\nu)\in\Gamma, \theta(\gamma)\cdot n(\gamma)<0} \int_0^t (h^0 - h^1)(x(\mu, \nu))c^1(x(u, v))\left|\det\left(\frac{\partial x(\mu, \nu)}{\partial(\mu, \nu)}\right)\right| d\mu d\nu. \quad (2.25)
\end{aligned}$$

Since $t << 1$, the functions h^0, h^1, c^0, c^1 are C^1 in (2.25), so the Taylor expansion of each function around $\mu = 0$ reads

$$\begin{aligned}
h^i(x)(\mu, \nu) &= h^i(x)(0, \nu) + \mu\nabla h^i(x)(0, \nu) \cdot \theta(x)(0, v) + o(\mu), i = 0, 1 \\
c^0(x)(\mu, \nu) &= c^0(x)(0, \nu) + \mu\nabla c^0(x)(0, \nu) \cdot \theta(x)(0, v) + o(\mu) \\
c^1(x)(\mu, \nu) &= c^1(x)(0, \nu) + \mu\nabla c^1(x)(0, \nu) \cdot \theta(x)(0, v) + o(\mu).
\end{aligned}$$

So integrating between 0 and t in (2.25)

$$
\begin{aligned}
\Delta J &= \int_{\gamma^{-1}(\nu)\in\Gamma,\theta(\gamma)\cdot n(\gamma)>0} t(h^0-h^1)(x)(0,\nu)c^0(x)(0,\nu)|n(\nu)\cdot\theta|\left|\det\left(\frac{\partial\gamma(\nu)}{\partial\nu}\right)\right|d\nu \\
&\quad - \int_{\gamma^{-1}(\nu)\in\Gamma,\theta(\gamma)\cdot n(\gamma)<0} t(h^0-h^1)(x)(0,\nu)c^1(x)(0,\nu)|n(\nu)\cdot\theta|\left|\det\left(\frac{\partial\gamma(\nu)}{\partial\nu}\right)\right|d\nu + o(t).
\end{aligned}
$$

The application of the following identities

$$
|(\theta\cdot n)| = (\theta\cdot n)^+ - (\theta\cdot n)^-, \quad \int_\Gamma F(x)ds = \int_{\gamma^{-1}(\nu)\in\Gamma} F(\gamma(\nu))\left|\det\left(\frac{\partial\gamma(\nu)}{\partial\nu}\right)\right|d\nu,
$$

yields

$$
\Delta J = t\int_\Gamma [\![h]\!]\left(c^0(\theta\cdot n)^+ + c^1(\theta\cdot n)^-\right)ds + o(t).
$$

Finally the desired result stems from definition (2.24).

$\square$

2.3 Shape derivative in the smoothed-interface context

2.3.1 Description of the problem

We now present an alternative approach to that of section 2.2 which can be coined as smoothed or diffuse interface approach. It can be seen as a mathematically convenient approximation of the sharp-interface problem but, as explained in the introduction, it has its own merits for some problems in material science which feature physically thick transition zones [68], [295], [306], [312]. More precisely, either for a mathematical approximation or for physical reasons, it may be desirable to model the interface Γ between Ω^0 and Ω^1 as a thin layer of (small) width $2\varepsilon > 0$ rather than as a sharp interface. In this context, we rely on the notion of the *signed distance function* (see Definition 1.2.1)

The material properties in D are defined as a smooth interpolation between A_0 and A_1 in the layer of width 2ε around Γ, so that the resulting Hooke's tensor $A_{\Omega^0,\varepsilon}$ reads

$$
A_{\Omega^0,\varepsilon}(x) = A_0 + h_\varepsilon(d_{\Omega^0}(x))(A_1 - A_0), \quad \forall x \in D, \tag{2.26}
$$

where $h_\varepsilon : \mathbb{R} \to \mathbb{R}$ is a smooth approximation of the Heaviside function, that is, a smooth monotone function enjoying the properties : $h_\varepsilon(t) = 0$ for $t < -\varepsilon$, $h_\varepsilon(t) = 1$ for $t > \varepsilon$. In the sequel, we chose the $\mathcal{C}^2$ function

$$
\forall t \in \mathbb{R}, \ h_\varepsilon(t) = \begin{cases} 0 & \text{if} \quad t < -\varepsilon \\ \frac{1}{2}\left(1 + \frac{t}{\varepsilon} + \frac{1}{\pi}\sin(\frac{\pi t}{\varepsilon})\right) & \text{if} \quad -\varepsilon \le t \le \varepsilon \\ 1 & \text{if} \quad t > \varepsilon. \end{cases} \tag{2.27}
$$

Remark 2.3.1. *Formula (2.27) expresses a simple choice for the interpolation of the material properties between the two materials, and of course, one could think of different interpolation rules. Moreover, the interpolation function could also contain parameters that are themselves subject to optimization (e.g. the layer width ε) and both a geometric and parametric optimization could be combined using a method of alternating directions. Therefore, this method could be generalized to the shape and topology optimization of functionally graded materials in a straightforward way (see [312] for the use of non-monotone interpolation functions).*

We modify (2.1) so that the elastic displacement now solves

$$
\begin{cases} -\mathrm{div}\left(A_{\Omega^0,\varepsilon}\,e(u)\right) &= f & \text{in } D \\ u &= 0 & \text{on } \Gamma_D \\ (A_1\,e(u))\cdot n &= g & \text{on } \Gamma_N. \end{cases} \tag{2.28}
$$

The objective function does not change and we still minimize (2.2) which depends on d_{Ω^0} through (2.26).

2.3.2   Shape differentiability of the signed distance function

The purpose of this section is to recall some results on the signed distance function and to explore its shape differentiability which holds in a non-classical and subtle sense (see below for details). For simplicity we drop the index 0 of Ω^0 in the sequel.

Let us start by collecting some definitions (see Figure 2.6 for a geometric illustration).

Definition 2.3.2. *Let $\Omega \subset \mathbb{R}^d$ be a Lipschitz bounded open set.*

- *For any $x \in \mathbb{R}^d$, $\Pi_{\partial\Omega}(x) := \{y_0 \in \partial\Omega \text{ such that } |x - y_0| = \inf_{y \in \partial\Omega} |x - y|\}$ is the set of projections of x on $\partial\Omega$. It is a closed subset of $\partial\Omega$. When $\Pi_{\partial\Omega}(x)$ reduces to a single point, it is called the projection $p_{\partial\Omega}(x)$ of x onto $\partial\Omega$.*

- *$\Sigma := \left\{ x \in \mathbb{R}^d \text{ such that } (d_\Omega)^2 \text{ is not differentiable at } x \right\}$ is the skeleton of $\partial\Omega$ (or Ω by a small abuse in terminology).*

- *For any $x \in \partial\Omega$, $\mathrm{ray}_{\partial\Omega}(x) := \{y \in \mathbb{R}^d \text{ such that } d_\Omega \text{ is differentiable at } y \text{ and } p_{\partial\Omega}(y) = x\}$ is the ray emerging from x. Equivalently, $\mathrm{ray}_{\partial\Omega}(x) = p_{\partial\Omega}^{-1}(x)$.*

We now recall some classical results (see [104], chapter 7, theorems 3.1, 3.3 and [15]).

Lemma 2.3.3. *Let $\Omega \subset \mathbb{R}^d$ be a Lipschitz bounded open set.*

- *A point $x \notin \partial\Omega$ has a unique projection $p_{\partial\Omega}(x)$ on $\partial\Omega$ if and only if $x \notin \Sigma$. In such a case, it satisfies $d(x, \partial\Omega) = |x - p_{\partial\Omega}(x)|$ and the gradient of d_Ω at x reads*

$$\nabla d_\Omega(x) = \frac{x - p_{\partial\Omega}(x)}{d_\Omega(x)}.$$

- *As a consequence of Rademacher's theorem ([115], section 3.1.2), Σ has zero Lebesgue measure in $\mathbb{R}^d$. Furthermore, when Ω is $\mathcal{C}^2$, $\overline{\Sigma}$ has zero Lebesgue measure too [207].*

- *For any $x \in \mathbb{R}^d$, $p \in \Pi_{\partial\Omega}(x)$, $\alpha \in [0, 1]$, denoting $x_\alpha := p + \alpha(x - p)$ the points of the ray of x lying between p and x, we have $d_\Omega(x_\alpha) = \alpha d_\Omega(x)$ and $\Pi_{\partial\Omega}(x_\alpha) \subset \Pi_{\partial\Omega}(x)$.*

- *If Ω is of class $\mathcal{C}^k$, for $k \geq 2$, then d_Ω is $\mathcal{C}^k$ too in a tubular neighborhood of $\partial\Omega$. In that case, d_Ω is differentiable at every point $x \in \partial\Omega$, and $\nabla d_\Omega(x) = n(x)$, the unit normal vector to Ω.*

Unfortunately, the signed distance function is not, strictly speaking, shape differentiable in the sense of Definition 1.1.13. One reason is the lack of smoothness of the gradient of d_Ω at the skeleton Σ. However, its pointwise values $d_\Omega(x)$ are shape differentiable for $x \in D \setminus \Sigma$. This is the purpose of the next result which can be found in [103] (without much details however ; see [97] for a detailed and pedagogical proof).

Proposition 2.3.4. *Assume $\Omega \subset D$ is an open set of class $\mathcal{C}^1$, and fix a point $x \notin \Sigma$. Then $\theta \mapsto d_{(Id+\theta)\Omega}(x)$ is Gâteaux-differentiable at $\theta = 0$, as an application from $W^{1,\infty}(D, \mathbb{R}^d)$ into $\mathbb{R}$, and its derivative is*

$$d_\Omega'(\theta)(x) = -\theta(p_{\partial\Omega}(x)) \cdot n(p_{\partial\Omega}(x)).$$

Remark 2.3.5. *Actually, a more general result than that of Proposition 2.3.4 holds. Indeed, retaining the hypothesis that Ω is of class $\mathcal{C}^1$, for any point $x \in \mathbb{R}^d$, and denoting, for a real parameter $t > 0$,*

$$\Omega_{t\theta} = (I + t\theta)\Omega,$$

the application $t \mapsto d_{\Omega_{t\theta}}(x)$ is right-differentiable at $t = 0^+$, and

- if $x \in \Omega$, $\frac{d}{dt}\left(d_{\Omega_{t\theta}}(x)\right)|_{t=0^+} = -\inf_{y \in \Pi_{\partial\Omega}(x)} \theta(y) \cdot n(y)$.

- if $x \in {}^c\overline{\Omega}$, $\frac{d}{dt}\left(d_{\Omega_{t\theta}}(x)\right)|_{t=0^+} = -\sup_{y \in \Pi_{\partial\Omega}(x)} \theta(y) \cdot n(y)$.

Of course, these formulae agree with the previous result since $\Pi_{\partial\Omega}(x) = \{p_{\partial\Omega}(x)\}$ if $x \notin \Sigma$.

Note also that a similar analysis could be performed when Ω is only assumed to be Lipschitz. However, the results are then more tedious to write, since the normal vector field n is not defined everywhere on $\partial\Omega$ (which is an indicator of specific geometric phenomena, see [97]).

Remark 2.3.6. *The signed distance function can also be seen as a solution of the following Hamilton-Jacobi equation*

$$\begin{cases} |\nabla d_\Omega(x)| = 1 & in\ D, \\ d_\Omega(x) = 0 & on\ \partial\Omega. \end{cases}$$

The behavior of the variations of d_Ω with respect to the domain can be retrieved by a formal computation. Indeed, assuming that d_Ω is shape differentiable, a formal computation yields that the directional shape derivative $d'_\Omega(\theta)$ satisfies

$$\begin{cases} \nabla d_\Omega(x) \cdot \nabla d'_\Omega(\theta)(x) = 0 & in\ D, \\ d'_\Omega(\theta)(x) = -\theta(x) \cdot n(x) & on\ \partial\Omega. \end{cases}$$
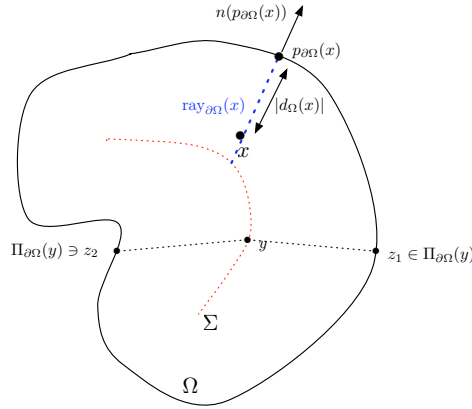
Figure 2.6: For a point x lying outside the skeleton Σ of Ω, unique projection point $p_{\partial\Omega}(x)$ and line segment $\text{ray}_{\partial\Omega}(x)$. For a point $y \in \Sigma$, at least two points z_1, z_2 belong to the set of projections $\Pi_{\partial\Omega}(y)$.

Corollary 2.3.7. *Let Ω be a bounded domain of class $\mathcal{C}^1$ and $m(x,s) : \mathbb{R}^d_x \times \mathbb{R}_s \to \mathbb{R}$ a function of class $\mathcal{C}^1$. Define the functional $J(\Omega)$ as*

$$J(\Omega) = \int_D m(x, d_\Omega(x))\, dx. \tag{2.29}$$

The application $\theta \mapsto J((Id + \theta)\Omega)$, from $W^{1,\infty}(D, \mathbb{R}^d)$ into $\mathbb{R}$, is Gâteaux-differentiable at $\theta = 0$ and its derivative reads

$$J'(\Omega)(\theta) = -\int_D \frac{\partial m}{\partial s}(x, d_\Omega(x))\, \theta(p_{\partial\Omega}(x)) \cdot n(p_{\partial\Omega}(x))\, dx. \tag{2.30}$$

The shape derivative (2.30) satisfies the Hadamard structure theorem since it depends only on the values of $\theta \cdot n$ on the boundary of $\partial\Omega$. However (2.30) is not a surface integral on $\partial\Omega$ as usual. Therefore the task of the next subsection is to transform (2.30) into a surface integral by using the notion of *rays* (see Definition 2.3.2), along which d_Ω and $p_{\partial\Omega}$ take very simple forms, altogether with the coarea formula.

2.3.3 An application of the coarea formula to integral functions of the signed distance function

The purpose of this section is to derive a Fubini-like formula for integrals of the form (2.30) and transform them in surface integrals. To this end, we use the following coarea formula [82].

Proposition 2.3.8. *Let X, Y be two smooth Riemannian manifolds of respective dimension $m \geq n$, and $f : X \to Y$ a surjective map of class $\mathcal{C}^1$, whose differential $\nabla f(x) : T_x X \to T_{f(x)} Y$ is surjective for almost every $x \in X$. Let φ an integrable function over X. Then:*

$$\int_X \varphi(x) dx = \int_Y \left(\int_{z \in f^{-1}(y)} \varphi(z) \frac{1}{\mathrm{Jac}(f)(z)} dz \right) dy$$

where $\mathrm{Jac}(f)(z)$ is the Jacobian of the function f.

Remark 2.3.9. *If $m \geq n$, and $f : \mathbb{R}^m \to \mathbb{R}^n$ is a differentiable function at a point $x \in \mathbb{R}^m$, the Jacobian $\mathrm{Jac}(f)(x)$ of f at x is defined as*

$$\mathrm{Jac}(f)(x) := \sqrt{\det(\nabla f(x) \, \nabla f(x)^T)}.$$

The definition of the Jacobian is similar when f is a map between two Riemannian manifolds X and Y, once the tangent planes $T_x X, T_{f(x)} Y$ have been identified to $\mathbb{R}^m$ and $\mathbb{R}^n$ respectively (see [82], exercise III.11). In any case, the Jacobian is positive $\mathrm{Jac}(f)(x) > 0$ if and only if $\nabla f(x)$ is of maximum rank, or equivalently $\nabla f(x)$ is surjective from $\mathbb{R}^m$ to $\mathbb{R}^n$.

We apply this formula in our context to $X = \Omega$, $Y = \partial \Omega$ and $f = p_{\partial \Omega}$. To apply Proposition 2.3.8 we need the differentiability of $p_{\partial \Omega}$ which will be deduced from the following classical result on the second-order differentiability of the signed distance function [72].

Lemma 2.3.10. *Assume Ω is of class $\mathcal{C}^2$. For $i = 1, ..., d - 1$, denote by κ_i the principal curvatures of $\partial \Omega$ and e_i its associated directions (see Figure 2.7). For every $x \in D$, and every $y \in \Pi_{\partial \Omega}(x)$, we have*

$$- \kappa_i(y) d_\Omega(x) \leq 1, \quad 1 \leq i \leq d - 1. \tag{2.31}$$

Define Γ the singular set of Ω, namely the set of points $x \notin \Sigma$ such that, for some i, one of the inequality (2.31) is actually an equality. Then, $\overline{\Sigma} = \Sigma \cup \Gamma$ and $\overline{\Sigma}$ has zero Lebesgue measure. If $x \notin \overline{\Sigma}$, then all inequalities (2.31) are strict and d_Ω is twice differentiable at x. Its Hessian reads

$$\mathcal{H} d_\Omega(x) = \sum_{i=1}^{d-1} \frac{\kappa_i(p_{\partial \Omega}(x))}{1 + \kappa_i(p_{\partial \Omega}(x)) d_\Omega(x)} e_i(p_{\partial \Omega}(x)) \otimes e_i(p_{\partial \Omega}(x)).$$

Lemma 2.3.11. *Let $x \in D \setminus \overline{\Sigma}$. The projection map $p_{\partial \Omega}$ is differentiable at x and, in the orthonormal basis $\{e_1, ..., e_{d-1}, n\} (p_{\partial \Omega}(x))$ of $\mathbb{R}^d$ (see Figure 2.7), its gradient is a $d \times d$ diagonal matrix*

$$\nabla p_{\partial \Omega}(x) = \begin{pmatrix} 1 - \frac{d_\Omega(x) \kappa_1}{1 + d_\Omega(x) \kappa_1} & 0 & \cdots & 0 \\ 0 & \ddots & \ddots & \vdots \\ \vdots & \ddots & 1 - \frac{d_\Omega(x) \kappa_{d-1}}{1 + d_\Omega(x) \kappa_{d-1}} & 0 \\ 0 & \cdots & 0 & 0 \end{pmatrix}, \tag{2.32}$$

where the principal curvatures κ_i are evaluated at $p_{\partial \Omega}(x)$.

Proof. The proof starts from the characterization of the projection map when $x \in D \setminus \Sigma$ (see Lemma 2.3.3)

$$p_{\partial \Omega}(x) = x - d_\Omega(x) \nabla d_\Omega(x).$$

This last equality can then be differentiated once more for $x \in D \setminus \overline{\Sigma}$

$$\nabla p_{\partial\Omega}(x) = Id - \nabla d_\Omega(x) \, \nabla d_\Omega(x)^T - d_\Omega(x)\mathcal{H}d_\Omega(x). \tag{2.33}$$

Since $\nabla d_\Omega(x) = n(p_{\partial\Omega}(x))$, a simple calculation ends the proof. $\qquad\square$
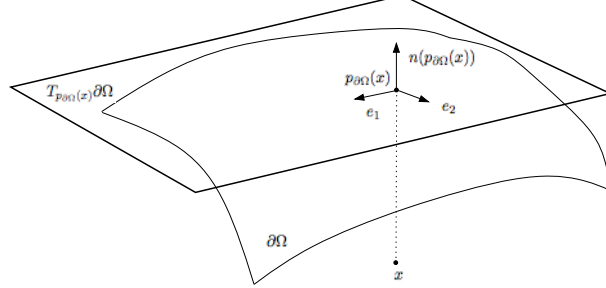
Figure 2.7: Principal directions, normal vector at the projection point of $x \in \mathbb{R}^d$.

Corollary 2.3.12. *Let $\Omega \subset D$ be a $\mathcal{C}^2$ bounded domain, and let φ an integrable function over D. Then,*

$$\int_D \varphi(x)dx = \int_{\partial\Omega} \left(\int_{\mathrm{ray}_{\partial\Omega}(y)\cap D} \varphi(z) \prod_{i=1}^{d-1} (1 + d_\Omega(z)\kappa_i(y))dz \right) dy, \tag{2.34}$$

where z denotes a point in the ray emerging from $y \in \partial\Omega$ and dz is the line integration along that ray.

Proof. Since $\overline{\Sigma}$ is of zero Lebesgue measure, we have

$$\int_D \varphi(x)dx = \int_{D\setminus\overline{\Sigma}} \varphi(x)dx.$$

Applying Lemmas 2.3.10 and 2.3.11, $p_{\partial\Omega}$ is a surjective and differentiable map from $D \setminus \overline{\Sigma}$ into $\partial\Omega$, with a positive finite Jacobian for any $x \in D \setminus \overline{\Sigma}$

$$\mathrm{Jac}\,(p_{\partial\Omega})\,(x) = \frac{1}{\displaystyle\prod_{i=1}^{d-1} \left(1 + d_\Omega(x)\kappa_i(p_{\partial\Omega}(x)) \right)}.$$

Proposition 2.3.8 then yields the desired result. $\qquad\square$

2.3.4 Shape derivative in the multi-materials setting

We now differentiate the cost function (2.2) with respect to the domain. We keep the geometrical assumptions of section 2.2, namely for a given bounded open set $D \subset \mathbb{R}^d$ which is partitioned in two subdomains $\Omega^0, \Omega^1 \subset D$, Ω^0 is a strict subset of D in the sense that its boundary Γ, as well as its thick approximation, does not touch ∂D (see Figure 2.1) and Γ is smooth.

We define the adjoint problem

$$\begin{cases} -\mathrm{div}\left(A_{\Omega^0,\varepsilon}\,e(p)\right) & = & -j'(x,u) & \text{in } D, \\ p & = & 0 & \text{on } \Gamma_D, \\ (A_1\,e(p))\cdot n & = & -k'(x,u) & \text{on } \Gamma_N, \end{cases} \tag{2.35}$$

where the symbol $\prime$ denotes differentiation with respect to u.

We now come to the main result of this section.

Theorem 2.3.13. *The objective function (2.2) is shape differentiable in the sense of Gâteaux, namely $\theta \mapsto J((Id + \theta)\Omega^0)$ admits a Gâteaux derivative at $\theta = 0$, which is*

$$J'(\Omega^0)(\theta) = -\int_\Gamma \theta(x) \cdot n(x) \Big(f_0(x) + f_1(x)\Big) dx, \quad \forall \theta \in W^{1,\infty}(D, \mathbb{R}^d), \qquad (2.36)$$

where n is the outer unit normal to Ω^0 and f_0, f_1 are scalar functions defined by

$$f_0(x) = \int_{\mathrm{ray}_\Gamma(x) \cap \Omega^0} h'_\varepsilon\left(d_{\Omega^0}(z)\right)(A_1 - A_0)e(u)(z) : e(p)(z) \prod_{i=1}^{d-1} (1 + d_{\Omega^0}(z)\kappa_i(x)) dz,$$

$$f_1(x) = \int_{\mathrm{ray}_\Gamma(x) \cap \Omega^1} h'_\varepsilon\left(d_{\Omega^0}(z)\right)(A_1 - A_0)e(u)(z) : e(p)(z) \prod_{i=1}^{d-1} (1 + d_{\Omega^0}(z)\kappa_i(x)) dz,$$

where z denotes a point in the ray emerging from $x \in \Gamma$.

Proof. The rigorous proof of existence of the shape derivative stems from classical arguments (typically the implicit function theorem) similar to those invoked in [279] or chapter 5 in [144]. We rather focus on the actual computation of the shape derivative and use once again the formal Lagrangian method of Céa [74]. As the computation unfolds very similarly to that in the proof of Theorem 3.6 in [12], we limit ourselves to the main arguments.

Define first the functional space $V := \{v \in H^1(D)^d \text{ such that } v = 0 \text{ on } \Gamma_D\}$, in which are sought the solution of the state equation (2.28) and of the adjoint equation (2.35). We introduce the Lagrangian $\mathcal{L} : W^{1,\infty}(D, \mathbb{R}^d) \times V \times V \to \mathbb{R}$, defined by

$$\mathcal{L}(\theta, v, q) = \int_D j(x, v)\, dx + \int_{\Gamma_N} k(x, v)\, ds + \int_D A_{(Id+\theta)\Omega^0, \varepsilon} e(v) : e(q)\, dx - \int_D f \cdot q\, dx - \int_{\Gamma_N} g \cdot q\, ds.$$
$$(2.37)$$

Here, q is intended as the Lagrange multiplier associated to the enforcement of the state equation. As usual, stationarity of the Lagrangian provides the optimality conditions for the minimization problem. At $\theta = 0$, canceling the partial derivative of $\mathcal{L}$ with respect to q yields the variational formulation of the state u. In the same way, the nullity of the partial derivative of $\mathcal{L}$ with respect to v leads to the variational formulation of the adjoint p.

Eventually, the shape derivative of the objective function is the partial derivative of $\mathcal{L}$ with respect to θ, evaluated at u and p

$$J'(\Omega^0)(\theta) = \frac{\partial \mathcal{L}}{\partial \theta}(0, u, p)(\theta).$$

Some elementary algebra, using the shape differentiability of $d_{\Omega^0}(x)$ for almost every $x \in D$, yields

$$\begin{aligned} J'(\Omega^0)(\theta) &= \int_D \left(A_{(Id+\theta)\Omega^0, \varepsilon}\right)'(\theta) e(u) : e(p)\, dx \\ &= -\int_D h'_\varepsilon(d_{\Omega^0}(x)) (\theta(p_\Gamma(x)) \cdot n(p_\Gamma(x))) (A_1 - A_0)e(u) : e(p)\, dx, \end{aligned} \qquad (2.38)$$

where $\left(A_{(Id+\theta)\Omega^0, \varepsilon}\right)'(\theta)$ is the directional shape derivative of $A_{(Id+\theta)\Omega^0, \varepsilon}$ while h'_ε is the standard derivative of the real function h_ε. It remains to transform this expression by the coarea formula in order to deduce a boundary integral. Using formula (2.34) for (2.38), we get

$$J'(\Omega^0)(\theta)$$
$$= -\int_\Gamma \theta(x) \cdot n(x) \left(\int_{\mathrm{ray}_\Gamma(x) \cap D} h'_\varepsilon(d_{\Omega^0}(z))(A_1 - A_0)e(u)(z) : e(p)(z) \prod_{i=1}^{d-1} (1 + d_{\Omega^0}(z)\kappa_i(x)) dz \right) dx.$$

Now decomposing the above integral over Ω^0 and Ω^1 readily yields the desired result. $\qquad \square$

Remark 2.3.14. *Theorem 2.3.13 provides a simple way of choosing a descent direction for a shape gradient based algorithm. Indeed it is enough to perturb the interface Γ by choosing the vector field*

$$\theta(x) = \Big(f_0(x) + f_1(x)\Big)n(x),$$

which ensures that the directional derivative (2.36) is negative and thus yields a decrease of the objective function (2.3). This is in sharp contrast with Corollary 2.3.7 which provided formula (2.30) for the shape derivative. However it was impossible to extract directly from (2.30) an explicit value of θ which was a guaranteed descent direction.

Remark 2.3.15. *In the case of compliance minimization, namely for the objective function (2.3), we have $j' = f$, $k' = g$ and thus $p = -u$. If we assume that material 1 is stronger than material 0, in the sense that $A^1 \geq A^0$ as positive definite tensors, we deduce from the formulae of Theorem 2.3.13 that both f_0 and f_1 are non-positive because $1 + \kappa_i(x)d_{\Omega^0}(z) \geq 0$ by virtue of Lemma 2.3.10. Thus, a descent direction is obtained by choosing θ such that $\theta(x) \cdot n(x) < 0$ on Γ, namely we expand Ω^1. This is in accordance with the mechanical intuition that a more robust mixture of the two materials is achieved when A^1 prevails over A^0. Of course, for the problem to be reasonable, a volume constraint is imposed on the phases.*

2.3.5   Approximate formulae for the shape derivative

Although formula (2.36) is satisfying from a mathematical point of view, its numerical evaluation is not completely straightforward. There are two delicate issues. First, one has to compute the principal curvatures $\kappa_i(x)$ for any point $x \in \Gamma$ on the interface. Second, one has to perform a 1-d integration along the rays of the energy-like quantity $[\![A]\!]e(u) : e(p)$. This is a classical task in the level-set framework [271] but, still, it is of interest to devise a simpler approximate formula for the shape derivative.

A first approximate formula is to assume that the interface is roughly plane, namely to assume that the principal curvatures κ_i vanish. In such a case we obtain a "Jacobian-free" approximate shape derivative

$$\begin{aligned}
J'(\Omega^0)(\theta) &= -\int_\Gamma \theta(x) \cdot n(x)\Big(f_0(x) + f_1(x)\Big)dx \\
f_i(x) &= \int_{\mathrm{ray}_\Gamma(x) \cap \Omega^i} h'_\varepsilon\left(d_{\Omega^0}(z)\right)(A_1 - A_0)e(u)(z) : e(p)(z)dz.
\end{aligned} \tag{2.39}$$

A second approximate formula is obtained when the smoothing parameter ε is small. Note that, since the support of the function h'_ε is of size 2ε, the integral in formula (2.36) is confined to a tubular neighborhood of Γ of width 2ε. Therefore, if ε is small, one may assume that the functions depending on z are constant along each ray, equal to their value at $x \in \Gamma$. In other words, for small ε we assume

$$e(u)(z) \approx e(u)(x), \quad e(p)(z) \approx e(p)(x) \ \text{ and } d_{\Omega^0}(z) \approx d_{\Omega^0}(x) = 0,$$

which yields the approximate formulae, for $x \in \Gamma$,

$$f_0(x) \approx (A_1 - A_0)e(u)(x) : e(p)(x) \int_{ray_\Gamma(x) \cap \Omega^0} h'_\varepsilon\left(d_{\Omega^0}(z)\right) dz,$$

$$f_1(x) \approx (A_1 - A_0)e(u)(x) : e(p)(x) \int_{ray_\Gamma(x) \cap \Omega^1} h'_\varepsilon\left(d_{\Omega^0}(z)\right) dz.$$

Furthermore, most rays have a length larger than 2ε so that

$$\int_{ray_\Gamma(x) \cap \Omega^0} h'_\varepsilon\left(d_{\Omega^0}(z)\right) dz + \int_{ray_\Gamma(x) \cap \Omega^1} h'_\varepsilon\left(d_{\Omega^0}(z)\right) dz = h_\varepsilon(\varepsilon) - h_\varepsilon(-\varepsilon) = 1.$$

In turn we obtain the following approximate formula for (2.36)

$$J'(\Omega^0)(\theta) \approx - \int_\Gamma (A_1 - A_0)e(u) : e(p)\, \theta \cdot n\, dx, \tag{2.40}$$

which is nothing but the discrete shape derivative (3.23) that we obtained in the sharp-interface case. This computation seems a bit miraculous but makes sense as a kind of commutation property between interface regularization and optimization.

Our numerical results show that the latter simplification (2.40), which we shall refer to as the *approximate shape derivative*, works very well in practice for problems of compliance minimization. Formula (2.40) is also used by other authors in their numerical simulations [317].

2.3.6   Convergence of the smoothed-interface to the sharp-interface

When the smoothed-interface setting is used as an approximation of the sharp-interface case, it is a natural task to prove that this approximation is mathematically consistent. In this section, we present a result in this direction. More specifically, for a given regular interface Γ, we prove that the shape gradient obtained in Theorem 2.3.13 for a smoothed transition layer of width 2ε converges, as ε goes to 0, to the corresponding shape gradient in the sharp-interface context, recalled in Proposition 2.2.1.

To set ideas, let us limit ourselves to the case of compliance minimization, the case of a general objective function such as (2.2) being no different in principle. In order to make explicit the dependence on the half-thickness ε of the smoothed transmission area, the solution of the state system (2.28) is denoted u_ε in this section. Similarly the stress tensor is $\sigma(u_\varepsilon) = A_{\Omega^0,\varepsilon}\, e(u_\varepsilon)$ and the compliance is

$$J_\varepsilon(\Omega^0) = \int_D \sigma(u_\varepsilon) : e(u_\varepsilon)\, dx.$$

The solution of the state system (2.1) in the sharp-interface case is still denoted as u, and the associated compliance as $J(\Omega^0)$.

To find the limit of $J_\varepsilon'(\Omega_0)$, as $\varepsilon \to 0$, requires some knowledge of the asymptotic behavior of $e(u_\varepsilon)$ and $\sigma(u_\varepsilon)$ in the vicinity of the interface Γ. Unfortunately, one cannot expect all the components of $e(u_\varepsilon)$ and $\sigma(u_\varepsilon)$ to converge toward their counterpart in $e(u)$ and $\sigma(u)$ in any space of smooth enough functions. Indeed, for fixed ε, $e(u_\varepsilon)$ is smooth over D (because so is the associated Hooke's tensor), whereas we recalled in Remark 2.2.2 that $e(u)_{\tau n}$ and $e(u)_{nn}$ are discontinuous across Γ, as imposed by the transmission conditions. However, some of the components of $e(u_\varepsilon)$ and $\sigma(u_\varepsilon)$ do behave well as $\varepsilon \to 0$. This is the purpose of the following lemma, which is a consequence of rather classical results in elliptic regularity theory (see [97] for a proof).

Lemma 2.3.16. *Assuming Γ is a $\mathcal{C}^2$ interface, there exists a tubular neighborhood $V \subset\subset D$ of Γ such that one can define a smooth extension in V of the normal n and of a set of tangentials and orthonormal vectors τ. Then, the following strong convergences hold true*

$$\begin{aligned}
e(u_\varepsilon)_{\tau\tau} &\overset{\varepsilon \to 0}{\longrightarrow} e(u)_{\tau\tau} && \text{in } H^1(V)^{(d-1)^2} \text{ strong,} \\
\sigma(u_\varepsilon)_{\tau n} &\overset{\varepsilon \to 0}{\longrightarrow} \sigma(u)_{\tau n} && \text{in } H^1(V)^{d-1} \text{ strong,} \\
\sigma(u_\varepsilon)_{nn} &\overset{\varepsilon \to 0}{\longrightarrow} \sigma(u)_{nn} && \text{in } H^1(V) \text{ strong.}
\end{aligned}$$

Remark 2.3.17. *The components of the strain and stress tensors which converge in Lemma 2.3.16 correspond exactly to those which are continuous through the interface Γ as explained in Remark 2.2.2.*

We are now in a position to state the main result of the present section which implies that the shape derivative of the smoothed-interface objective function is a consistent approximation of the corresponding shape derivative in the sharp-interface case.

Theorem 2.3.18. *Under the above assumptions, we have*

$$\lim_{\varepsilon \to 0} J'_\varepsilon(\Omega^0)(\theta) = J'(\Omega^0)(\theta) \quad \forall \theta \in W^{1,\infty}(D, \mathbb{R}^d).$$

Sketch of the proof. As the proof involves rather classical arguments, but tedious computations, we limit ourselves with an outline of the main steps, referring to [97] for details. The goal is to pass to the limit $\varepsilon \to 0$ in formula (2.36), for a fixed $\theta \in W^{1,\infty}(D, \mathbb{R}^d)$. To achieve this, the rays $\text{ray}_\Gamma(x) \cap \Omega^0$ and $\text{ray}_\Gamma(x) \cap \Omega^1$ are expressed as integrals over the segment $(0, 1)$. Therefore, (2.36) becomes

$$J'_\varepsilon(\Omega^0)(\theta) = -\int_\Gamma \theta(x) \cdot n(x) \Big(f^\varepsilon_0(x) + f^\varepsilon_1(x) \Big) dx,$$

where $f^\varepsilon_0, f^\varepsilon_1 \in L^1(\Gamma)$ are defined as

$$f^\varepsilon_0(x) = \int_{-1}^0 h'_\varepsilon(s\varepsilon)(A_1 - A_0)e(u_\varepsilon)(x + s\varepsilon n(x)) : e(u_\varepsilon)(x + s\varepsilon n(x)) \, k_\varepsilon(x, s) \, ds, \qquad (2.41)$$

$$f^\varepsilon_1(x) = \int_0^1 h'_\varepsilon(s\varepsilon)(A_1 - A_0)e(u_\varepsilon)(x + s\varepsilon n(x)) : e(u_\varepsilon)(x + s\varepsilon n(x)) \, k_\varepsilon(x, s) \, ds, \qquad (2.42)$$

with

$$k_\varepsilon(x, s) = \prod_{i=1}^{d-1} \left(1 + s\varepsilon\kappa_i(x)\right).$$

Since $h'_\varepsilon(s\varepsilon)$ does not depend on ε, to pass to the limit in (2.41) and (2.42) requires merely the following simple technical convergence result (see [97] for a proof)

$$\int_0^1 v(s) \, f_\varepsilon(x + s\varepsilon n(x)) g_\varepsilon(x + s\varepsilon n(x)) \, ds \xrightarrow{\varepsilon \to 0} \left(\int_0^1 v(s) \, ds\right) f(x)g(x) \quad \text{in } L^1(\Gamma) \qquad (2.43)$$

for a smooth function $v(s)$ and any sequences $f_\varepsilon, g_\varepsilon \in H^1(D)$, which converge strongly in $H^1(D)$ to f, g respectively. In order to apply (2.43) we rewrite expressions (2.41) and (2.42) in terms of the components $e(u_\varepsilon)_{\tau\tau}$ and $\sigma(u_\varepsilon)_{\tau n}$, $\sigma(u_\varepsilon)_{nn}$ of the strain and stress tensors, which have a fine behavior at the limit $\varepsilon \to 0$ as guaranteed by Lemma 2.3.16. After some algebra, we obtain the following rearrangement for the integrand in f^ε_0 and f^ε_1:

$$h'_\varepsilon(s\varepsilon)(A_1 - A_0)e(u_\varepsilon) : e(u_\varepsilon)(x + s\varepsilon n(x))$$

$$= \mu'(s) \left(e(u_\varepsilon)_{\tau\tau} : e(u_\varepsilon)_{\tau\tau}\right)(x + s\varepsilon n(x)) + \frac{\mu'(s)}{\mu(s)^2} \left(\sigma^\varepsilon(u_\varepsilon)_{\tau n} \cdot \sigma^\varepsilon(u_\varepsilon)_{\tau n}\right)(x + s\varepsilon n(x))$$

$$+ \frac{4\mu^2(s)\lambda'(s) + 2\mu'(s)\lambda^2(s)}{(2\mu(s) + \lambda(s))^2} \, \text{tr}(e(u_\varepsilon)_{\tau\tau})^2(x + s\varepsilon n(x))$$

$$+ \frac{2\mu'(s) + \lambda'(s)}{(2\mu(s) + \lambda(s))^2} \, \sigma^\varepsilon(u_\varepsilon)^2_{nn}(x + s\varepsilon n(x))$$

$$+ \frac{4\mu(s)\lambda'(s) - 4\mu'(s)\lambda(s)}{(2\mu(s) + \lambda(s))^2} \left(\sigma^\varepsilon(u_\varepsilon)_{nn} \, \text{tr}(e(u_\varepsilon)_{\tau\tau})\right)(x + s\varepsilon n(x))$$

with

$$\lambda(s) = \lambda_0 + h_\varepsilon(s\varepsilon)(\lambda_1 - \lambda_0), \quad \mu(s) = \mu_0 + h_\varepsilon(s\varepsilon)(\mu_1 - \mu_0),$$

where λ_0, μ_0 and λ_1, μ_1 are the Lamé coefficients of materials 0, 1 respectively. Note that all the functions of s involving $\lambda(s)$ and $\mu(s)$ appearing in the above expression arise as exact derivatives of functions of $\lambda(s)$ and $\mu(s)$. Passing to the limit in the above expression using (2.43) leads to

$$(f^\varepsilon_0 + f^\varepsilon_1) \to \mathcal{D}(u, u) \quad \text{in } L^1(\Gamma),$$

where $\mathcal{D}(u, u)$ is defined as

$$
\begin{aligned}
\mathcal{D}(u, u)(x) \quad = \quad & 2[\![\mu]\!]e(u)_{\tau\tau}(x) : e(u)_{\tau\tau}(x) - [\![\tfrac{1}{\mu}]\!]\sigma(u)_{\tau n}(x) \cdot \sigma(u)_{\tau n}(x) \\
& + [\![\tfrac{2\lambda\mu}{(2\mu+\lambda)}]\!]\mathrm{tr}(e(u)_{\tau\tau}(x))^2 - [\![\tfrac{1}{2\mu+\lambda}]\!]\sigma(u)(x)_{nn}^2 \\
& + [\![\tfrac{2\lambda}{2\mu+\lambda}]\!]\sigma(u)_{nn}(x)\,\mathrm{tr}(e(u)_{\tau\tau}(x))
\end{aligned}
\qquad ,
$$

which after some algebra rewrites as (2.5). This completes the proof. $\square$

2.4   Some comments about previous results in literature

To our knowledge, the first works on multi-phase optimization using a level-set method are [217] and [317]. Further references include [216], [316], [318]. In all these works the computation of the shape derivative is not mathematically rigorous and the obtained formulae are not strictly correct. Indeed, either the shape differentiation is performed in the sharp-interface case and then the non-differentiable character of the solution of (2.1) is ignored (as explained in section 2.2.2), or the shape derivative is evaluated in the smoothed-interface case and then the derivative of the signed distance function is not taken into account. Fortunately, the shape derivative formulae in [217] and [317] coincide with what we called our approximate shape derivatives obtained in Proposition 2.2.5 for a discretization of the sharp-interface case and in (2.40) for a very thin smoothed interface. A third possibility for interpreting these works is to consider that the regularization of the interface is made with the help of the level set function ψ (used in numerical practice for representing and advecting the shape, see section 2.6 below) rather than with the signed distance function d_Ω. Then the differentiation is performed with respect to ψ rather than with respect to the shape Ω. It alleviates all the technical details of section 2.3 but it has one major flaw that we now describe.
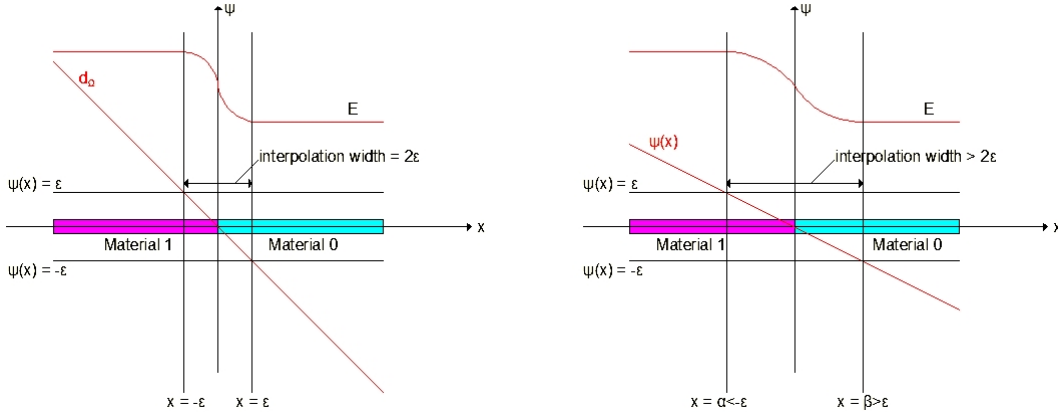
Figure 2.8: Intermediate zone for regularization with the signed distance function (left) or with a level set function (right).

Indeed, in the context of section 2.3 on the smoothed interface approach, one may replace the regularization formula (2.26) by a similar one

$$
A_{\Omega^0, \varepsilon}(x) = A_0 + h_\varepsilon(\psi(x))(A_1 - A_0), \quad \forall x \in D, \tag{2.44}
$$

where the signed distance function d_Ω has simply been replaced by the level set function ψ. Then, as is done in [217] and [216], one may differentiate the objective function with respect to ψ. A serious problem that rises directly from this choice, is that the interpolation zone, where $A_{\Omega^0, \varepsilon}$ takes intermediate values between A_0 and A_1, can thicken during the optimization process, especially if the level set function ψ is not frequently reinitialized towards the signed distance function to the boundary (see Figure 2.8). The reason is that the interpolation zone corresponds to some kind of homogenized material made of A_0 and A_1, which is known to be

more advantageous than pure phases in most problems [5]. The optimization process therefore does not only move the interface location but also flatten the level set function ψ so that the interpolation zone gets thicker. Even when the level set function is reinitialized, there remains a difficulty in the sense that the value of the objective function may change before and after reinitialization. A partial remedy to this inconvenient, as suggested in [217], is to add to the objective function a penalization term to control the enlargement.

The computation of the shape derivative is slightly different in [317]: the authors carry out the derivation with the level set function ψ but in the resulting formula they assume that ψ coincides with the signed distance function to the interface d_Ω. More precisely, following the notations of Corollary 2.3.7, they consider a functional

$$J(\Omega) = \int_D m(x, \psi(x)) \, dx, \tag{2.45}$$

where ψ is a solution of the Hamilton-Jacobi equation

$$\frac{\partial \psi}{\partial t} + \theta \cdot n \, |\nabla \psi| = 0.$$

Then, the authors claim that the shape derivative is

$$J'(\Omega)(\theta) = -\int_D \frac{\partial m}{\partial \psi}(x, \psi(x)) \, \theta(x) \cdot n(x) \, dx. \tag{2.46}$$

Note the difference with our formula (2.30), which involves the projection $p_\Gamma(x)$ of x on the boundary $\Gamma = \partial \Omega$, and that we recall as

$$J'(\Omega)(\theta) = -\int_D \frac{\partial m}{\partial \psi}(x, d_\Omega(x)) \, \theta(p_\Gamma(x)) \cdot n(p_\Gamma(x)) \, dx.$$

Unfortunately, there is no a priori guarantee that the transported signed distance function to the boundary $\partial \Omega$ remains the signed distance function to the transported boundary $(Id + \theta)\partial \Omega$. Therefore, the shape derivative $d'_\Omega(\theta)(x)$ cannot be replaced by the expression $\frac{\partial \psi}{\partial t} = -\theta \cdot n \, |\nabla \psi|$ coming from the Hamilton-Jacobi equation, as it is done in [217] and [317], without making any further assumptions. For example, in [128] it is shown that the transported level set function remains the signed distance function (at least for a small time) if the advection velocity remains constant along the normal, namely $(\theta \cdot n)(x) = (\theta \cdot n)(p_\Gamma(x))$.

A difficulty with (2.46) is that it does not satisfy the Hadamard structure theorem (see e.g. [5], [104], [144], [279] and references therein) since it does not depend solely on the normal trace $\theta \cdot n$ on the interface $\Gamma = \partial \Omega$. In fact, assuming that the support of $\frac{\partial m}{\partial \psi}$ is concentrated around Γ, formula (2.46) would be similar to what we called earlier approximate shape derivative, obtained in Proposition 2.2.5 for a discretization of the sharp-interface case and in (2.40) for the smoothed-interface case when the regularization parameter ε is small. In any case, (2.46) does not guarantee a descent direction in general, unless $\frac{\partial m}{\partial \psi}$ keeps a constant sign along the normal, at least for the width of the intermediate zone.

2.5 Extension to more than 2 materials

The methods presented in sections 2.2 and 2.3 for two phases can be extended to the case of several materials to be optimally placed in the domain D, following a classical idea in the level-set framework [313], [317].

Hitherto, we considered a single subdomain $\Omega^0 \subset D$, which allows to account for two separate phases within D, occupying respectively the domains Ω^0 and $\Omega^1 := {}^c\overline{\Omega^0}$ (where ^{c} denotes the complementary part in D). To consider more phases, we introduce m subdomains $\mathcal{O}^0, ..., \mathcal{O}^{m-1} \subset D$ which are not subject to any geometrical constraints (they can intersect, or
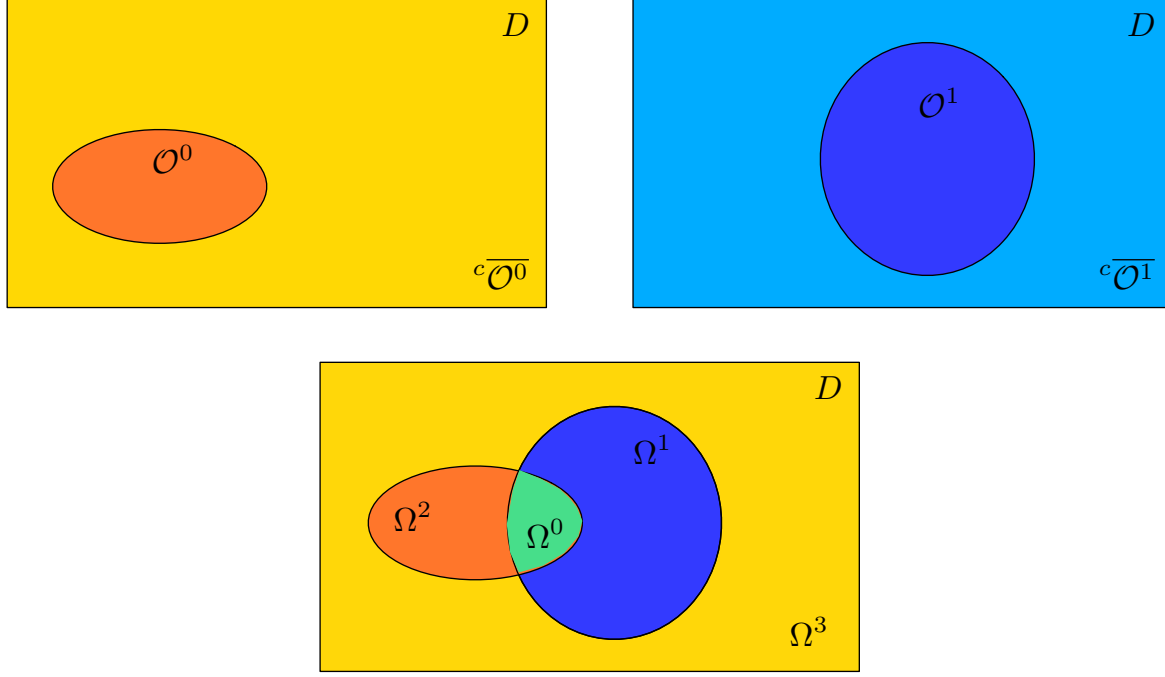
Figure 2.9: Two subdomains of D (top) and the four phase domains derived by combining them together (down).

not, and they don't need to cover D). These m subdomains allows us to treat up to 2^m distinct phases, filling respectively the phase domains $\Omega^0, ..., \Omega^{2^m-1} \subset D$, defined as (see Figure 2.9)

$$\begin{cases} \Omega^0 &= \quad \mathcal{O}^0 \cap \mathcal{O}^1 \cap ... \cap \mathcal{O}^{m-1}, \\ \Omega^1 &= \quad {}^c\overline{\mathcal{O}^0} \cap \mathcal{O}^1 \cap ... \cap \mathcal{O}^{m-1}, \\ &\vdots \\ \Omega^{2^m-1} &= \quad {}^c\overline{\mathcal{O}^0} \cap {}^c\overline{\mathcal{O}^1} \cap ... \cap {}^c\overline{\mathcal{O}^{m-1}}. \end{cases} \tag{2.47}$$

Note that $\Omega^0, ..., \Omega^{2^m-1}$ is a partition of D. To simplify the exposition, from now on we take $m = 2$, meaning that we consider four different materials, with respective Hooke's law A_0, A_1, A_2, A_3. Two subdomains $\mathcal{O}^0, \mathcal{O}^1$ of D are then introduced, and each material A_i fills an area $\Omega^i \subset D$, defined through formula (2.47).

For the sharp-interface problem, the definition of the mixture Hooke's tensor A_χ is standard. Introducing χ_0 and χ_1 the characteristic functions of $\mathcal{O}^0$ and $\mathcal{O}^1$, respectively, we define

$$A_\chi(x) := \chi_0(x)\chi_1(x)A_0 + (1 - \chi_0(x))\,\chi_1(x)A_1 + \chi_0(x)\,(1 - \chi_1(x))\,A_2 + (1 - \chi_0(x))\,(1 - \chi_1(x))\,A_3. \tag{2.48}$$

For the smoothed-interface problem, we propose a formula inspired from (2.48)

$$\begin{aligned} A_{\mathcal{O}^0,\mathcal{O}^1,\varepsilon}(x) &= \quad (1 - h_\varepsilon(d_{\mathcal{O}^0}(x)))(1 - h_\varepsilon(d_{\mathcal{O}^1}(x)))A_0 + h_\varepsilon(d_{\mathcal{O}^0}(x))(1 - h_\varepsilon(d_{\mathcal{O}^1}(x)))A_1 \\ &\quad + \quad (1 - h_\varepsilon(d_{\mathcal{O}^0}(x)))h_\varepsilon(d_{\mathcal{O}^1}(x))A_2 + h_\varepsilon(d_{\mathcal{O}^0}(x))h_\varepsilon(d_{\mathcal{O}^1}(x))A_3, \end{aligned} \tag{2.49}$$

where h_ε is the smooth approximation (2.27) of the Heaviside function and $d_{\mathcal{O}^0}, d_{\mathcal{O}^1}$ are the signed distance functions to $\mathcal{O}^0$ and $\mathcal{O}^1$ respectively. Of course, there are other interpolation

formulae and any alternative choice which, as (2.49), satisfies the following consistency

$$A_{\mathcal{O}^0,\mathcal{O}^1,\varepsilon}(x) = \begin{cases} A_0 & \text{if} \quad d_{\mathcal{O}^0}(x) < -\varepsilon \quad \text{and} \quad d_{\mathcal{O}^1}(x) < -\varepsilon, \\ A_1 & \text{if} \quad d_{\mathcal{O}^0}(x) > +\varepsilon \quad \text{and} \quad d_{\mathcal{O}^1}(x) < -\varepsilon, \\ A_2 & \text{if} \quad d_{\mathcal{O}^0}(x) < -\varepsilon \quad \text{and} \quad d_{\mathcal{O}^1}(x) > +\varepsilon, \\ A_3 & \text{if} \quad d_{\mathcal{O}^0}(x) > +\varepsilon \quad \text{and} \quad d_{\mathcal{O}^1}(x) > +\varepsilon, \\ \text{a smooth interpolation between } A_0, A_1, A_2, A_3 \text{ otherwise,} \end{cases} \tag{2.50}$$

will do. In particular, for applications in material science where the thick interface has a clear physical interpretation, one could choose a physically relevant choice of the interpolant Hooke's law for the mixture of A_0, A_1, A_2, A_3 in the intermediate areas, like a sequential laminate or another microstructure achieving Hashin and Shtrikman bounds [223]. On the other hand, if the smoothed-interface problem is merely a mathematical approximation of the sharp-interface case, then it is a consistent approximation since, as the regularizing parameter ε goes to 0, the smooth tensor $A_{\mathcal{O}^0,\mathcal{O}^1,\varepsilon}$ converges to the discontinuous one A_χ.

In the multiphase case, the definition of the objective function (2.2) does not change

$$J(\mathcal{O}^0, \mathcal{O}^1) = \int_D j(x, u)\, dx + \int_{\Gamma_N} k(x, u)\, ds, \tag{2.51}$$

and the state or adjoint equations are the same, up to changing the previous Hooke's tensor by $A_{\mathcal{O}^0,\mathcal{O}^1,\varepsilon}$. There are now two variable subdomains, $\mathcal{O}^0, \mathcal{O}^1$, as design variables for the optimization problem. Accordingly, we introduce two separate vector fields $\theta_0, \theta_1 \in W^{1,\infty}\left(D, \mathbb{R}^d\right)$ in order to vary the subdomains $\mathcal{O}^0, \mathcal{O}^1$.

According to Corollary 2.3.7, the partial shape derivative of the objective function (2.51) with respect to $\mathcal{O}^0$ and $\mathcal{O}^1$, which we shall denote as $\frac{\partial J}{\partial \mathcal{O}^0}$ and $\frac{\partial J}{\partial \mathcal{O}^1}$ respectively, in the direction of θ^0 and θ^1, respectively, are

$$\frac{\partial J}{\partial \mathcal{O}^0}(\mathcal{O}^0, \mathcal{O}^1)(\theta_0) = \int_D \theta_0(p_{\partial \mathcal{O}^0}(x)) \cdot n_0(p_{\partial \mathcal{O}^0}(x)) \frac{\partial A}{\partial d_{\mathcal{O}^0}}(d_{\mathcal{O}^0}, d_{\mathcal{O}^1}) e(u) : e(p)\, dx, \tag{2.52}$$

$$\frac{\partial J}{\partial \mathcal{O}^1}(\mathcal{O}^0, \mathcal{O}^1)(\theta_1) = \int_D \theta_1(p_{\partial \mathcal{O}^1}(x)) \cdot n_1(p_{\partial \mathcal{O}^1}(x)) \frac{\partial A}{\partial d_{\mathcal{O}^1}}(d_{\mathcal{O}^0}, d_{\mathcal{O}^1}) e(u) : e(p)\, dx, \tag{2.53}$$

where $A(d_{\mathcal{O}^0}, d_{\mathcal{O}^1}) = A_{\mathcal{O}^0,\mathcal{O}^1,\varepsilon}$, defined in (2.50). Of course, one can apply Theorem 2.3.13 to simplify (2.52) and (2.53) and transform them in surface integrals on $\partial \mathcal{O}^0$ and $\partial \mathcal{O}^1$.

Remark 2.5.1. *In the sharp interface context one could compute shape derivatives of the objective function J with respect to $\mathcal{O}^0$ and $\mathcal{O}^1$ too, thus recovering formulae similar to (2.52) and (2.53). However, it is possible only if we assume that the boundary of $\mathcal{O}^0$ and $\mathcal{O}^1$ do not superpose. Indeed if, for example, $\partial \mathcal{O}^0 = \partial \mathcal{O}^1$, then moving $\mathcal{O}^0$ inside $\mathcal{O}^1$, or vice versa, implies that one phase or another one appears. This means that a topology change is occurring which cannot be handled by Hadamard's method. At most, one can expect to compute two different directional derivatives (inward and outward) which clearly shows that there is no differentiability in this case. Note that there is no such difficulty in the smoothed interface setting: formulae (2.52) and (2.53) hold true for any geometrical situation of $\mathcal{O}^0$ and $\mathcal{O}^1$ since $A_{\mathcal{O}^0,\mathcal{O}^1,\varepsilon}$ is a smooth function of x in D.*

2.6 Numerical results

2.6.1 Level-set representation

Following the lead of [11], [12], we represent the moving and optimizable interfaces by level set functions [252] defined on a fixed mesh in an Eulerian framework. According to Section 2.5, using m level-set functions we can represent up to 2^m separate phases.

When there are only two phases to optimize, it suffices to use one level-set function to represent the interface Γ between two complementary sub-domains Ω^0 and Ω^1 of the working domain D. The level set function ψ (see Figure 2.10) is defined by

$$\begin{cases} \psi(x) = 0 & \text{for } x \in \Gamma = \partial\Omega_0, \\ \psi(x) < 0 & \text{for } x \in \Omega^0, \\ \psi(x) > 0 & \text{for } x \in \Omega^1. \end{cases}$$
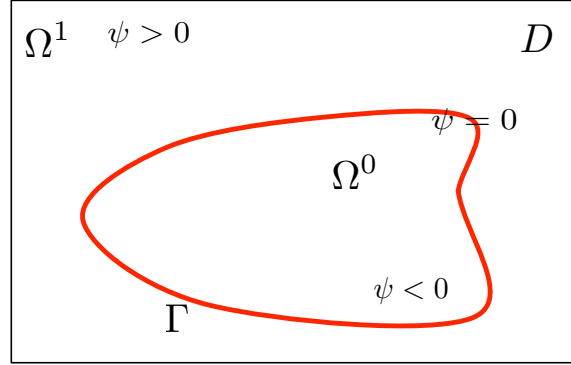

Figure 2.10: Level-set representation of the domains Ω^0 and Ω^1.

In order to describe up to four distinct phases, two level-set functions ψ_0 and ψ_1 are defined such that

$$\begin{cases} \psi_0(x) = 0 & \text{for } x \in \partial\mathcal{O}^0, \\ \psi_0(x) < 0 & \text{for } x \in \mathcal{O}^0, \\ \psi_0(x) > 0 & \text{for } x \in {}^c\overline{\mathcal{O}^0}, \end{cases} \quad and \quad \begin{cases} \psi_1(x) = 0 & \text{for } x \in \partial\mathcal{O}^1, \\ \psi_1(x) < 0 & \text{for } x \in \mathcal{O}^1, \\ \psi_1(x) > 0 & \text{for } x \in {}^c\overline{\mathcal{O}^1}, \end{cases}$$

following the notations of Figure 2.9. Then, each level-set function ψ_i, $i = 0, 1$, is transported independently solving (1.35), where V_i, $i = 0, 1$ results from the formulae (2.52) and (2.53).

2.6.2   Two materials in the sharp interface context

We work in the context of Section 2.2, namely in a sharp interface framework. We compare the two shape derivatives: the continuous formula furnished by Proposition 2.2.1 and the discrete formula given in Proposition 2.2.5. The numerical implementation of the continuous formula of the shape derivative in Proposition 2.2.1 is achieved according to the scheme proposed in [12] for computing the jump approximation (2.12). We consider a long cantilever of dimensions 2×1, discretized by 100×50 $\mathbb{P}_1$ elements, clamped at its left side and submitted to a unit vertical load at the middle of its right side (see Figure 2.13). The domain is filled by two isotropic materials 0 and 1, with different Young's moduli, respectively $E^0 = 0.5$ and $E^1 = 1$ (material 1 is stiffer than material 0) but with the same Poisson ratio $\nu = 0.3$. We minimize the compliance (2.3) with a constraint of fixed volume for the two phases. The computations are done with the software FreeFem++ [118].

For all the numerical examples in this paper, an augmented Lagrangian method is applied to handle the constraints. Following the approach in [242], supposing that our problem contains m equality constraints of the type $c_i(\Omega^0) = 0$ $(i = 1, ..., m)$, an augmented Lagrangian function is constructed as

$$L(\Omega^0, \ell, \mu) = J(\Omega^0) - \sum_{i=1}^{m} \ell_i c_i(\Omega^0) + \sum_{i=1}^{m} \frac{\mu_i}{2} c_i^2(\Omega^0),$$

where $\ell = (\ell_i)_{i=1,...,m}$ and $\mu = (\mu_i)_{i=1,...,m}$ are Lagrange multipliers and penalty parameters for the constraints. The Lagrange multipliers are updated at each iteration n according to the

optimality condition $\ell_i^{n+1} = \ell_i^N - \mu_i c_i(\Omega_n^0)$. The penalty parameters are augmented every 5 iterations. With such an algorithm the constraints are enforced only at convergence (see for example Figure 2.12). Of course, other (and possibly more efficient) optimization algorithms could be used instead.

The results are displayed on Figure 2.11. As usual the strong phase 1 is black and the weak phase 0 is white. The design obtained with the discrete formula is quite similar to the one exposed in Figure 2.14 (c). However the continuous formula gives a different optimal shape which is worse in terms of the objective function than the one obtained with the discrete formula (see Figure 2.12). This is completely natural, since the discrete shape gradient is exactly the gradient of the (discrete) indeed computed objective function.
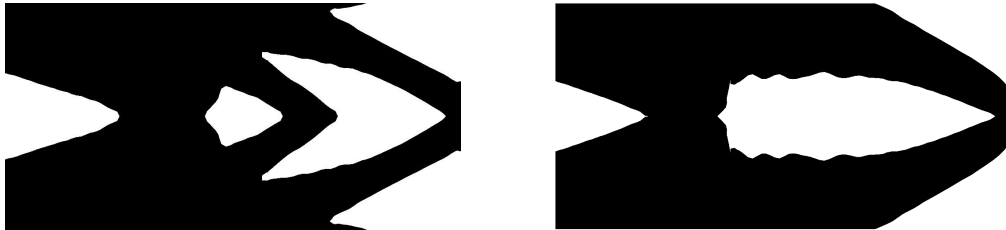
Figure 2.11: Optimal shapes for the using the discrete shape gradient (left) and the continuous formula (right).

2.6.3 Two materials in the smoothed-interface context

We now switch to the smoothed-interface setting as described in Section 2.3. All examples using a smoothed-interface are coded in Scilab [269]. We perform the same test case, with the same parameter values, as in Section 2.6.2. A mesh composed of 160×80 elements is used. A first goal is to compare the smoothed-interface approach to the sharp-interface one. A second goal is to compare the various formulae for the shape derivative obtained in Section 2.3.

We minimize again the compliance (2.3) with a constraint of fixed volume for the two phases which is written

$$\int_D h_\varepsilon(d_{\Omega^0}(x))dx = V_T,$$

where V_T is the target volume of the strong phase occupying Ω^1.

We test three different formulae for the shape gradient. The first one is the "true" formula given by (2.36) (see also (2.52) and (2.53) in the case of more than two phases). The second one, called "Jacobian-free", is (2.39) which is obtained from (2.36) by neglecting the part of the integrand corresponding to the Jacobian of the projection application $p_{\partial\Omega}$ (see Remark 2.3.9). The reason for this choice is that the curvature is not precisely calculated using a fixed mesh and therefore we may introduce a significant approximation error. In any case, it amounts to neglecting a positive factor (because of Lemma 2.3.10). The third one is the "approximate" formula (2.40) obtained for a very thin smoothing zone around the interface.

First, we consider the case of a "thin" interface. The interpolation width is chosen as $\varepsilon = 2\Delta x$, where Δx is the uniform mesh size. The results for $V_T = 0.7|D|$ in Figure 2.14. We plot the Young modulus distribution (black being the strong material A_1 and white the weak material A_0). The convergence histories are almost identical for the "true" and "Jacobian-free" formulae of the shape derivative. It is slightly more oscillating for the "approximate" formula although it converges to almost the same value of the objective function. The resulting optimal designs are very similar.

For a larger interpolation width $\varepsilon = 8\Delta x$ ("thick" interface), the results are shown in Figure 2.15. We clearly see a difference for the optimal shape obtained using the "true" formula of the
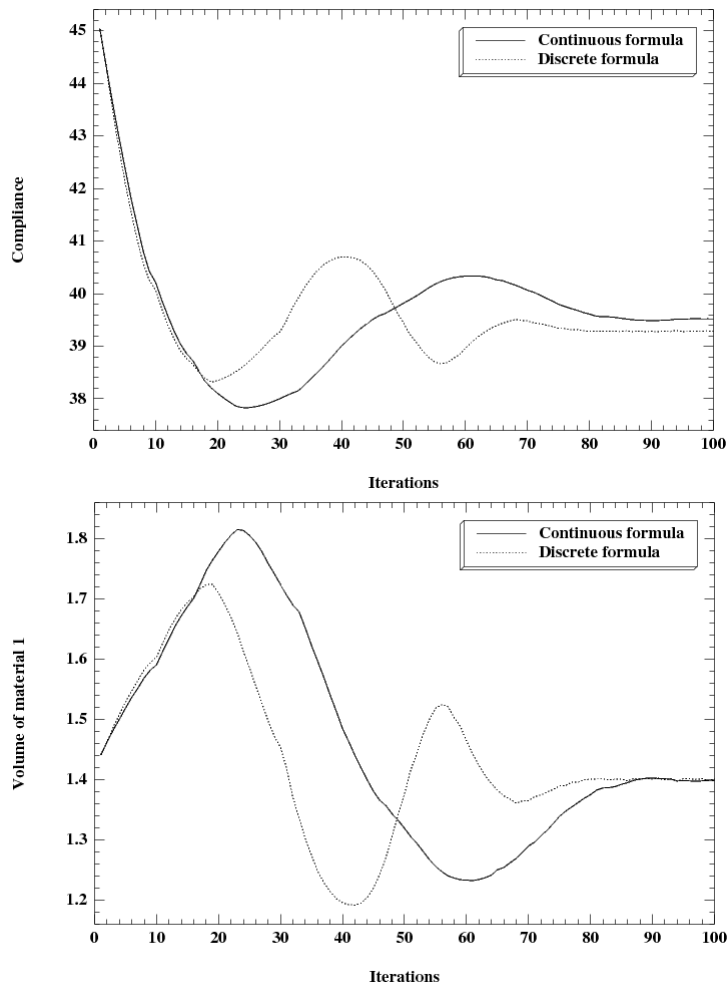
Figure 2.12: Convergence history of the compliance (left) and the volume (right) for the sharp interface
results displayed on Figure 2.11.

shape derivative: in this case, the algorithm produces a very long and oscillating interface in
such a way that the overall structure is almost like a composite structure. This is due to the fact
that the intermediate zone inside the interface is very favorable compared to the pure phases.
Nevertheless, despite the differences in the final shapes, the values of the compliance are almost
the same for the "true" and "Jacobian-free" formulae, slightly worse for the "approximate"
formula of the shape gradient.

Figure 2.13: Boundary conditions for the 2×1 cantilever.
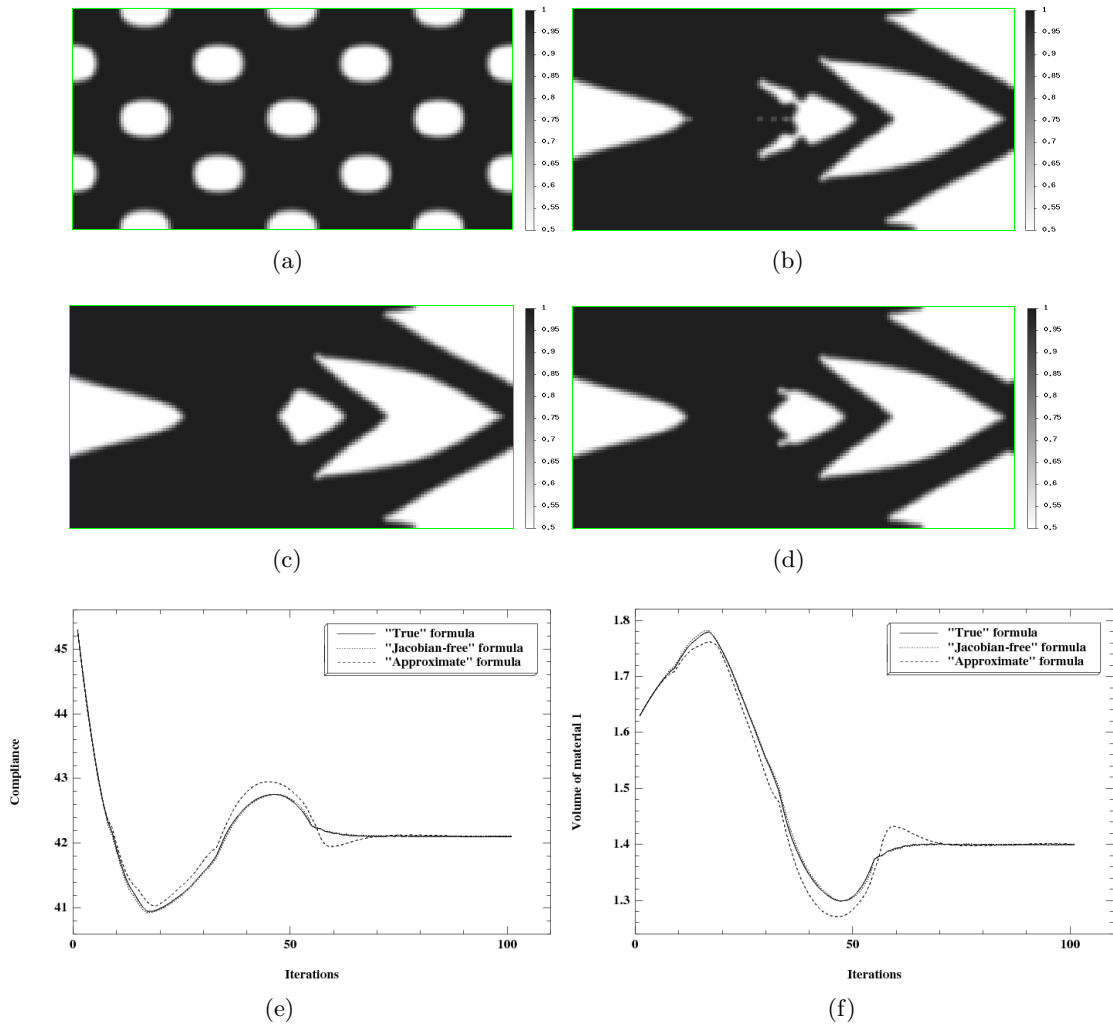
Figure 2.14: *"Long cantilever" using two phases with $V_T = 0.7|D|$ and a small smoothing parameter $\varepsilon = 2\Delta x$; (a): initialization; (b): optimized shape using the "true" formula; (c): optimized shape using the "Jacobian-free" formula; (d): optimized shape using the "approximate" formula; (e): convergence of the compliance; (f): convergence of the volume.*

Mesh-dependency study

In order to examine the mesh-dependency of the smoothed-interface method, the same example as in Section 2.6.3 is considered and two different tests are performed. First, the grid size "Δx" varies and the interface half-width "ε" is chosen as $\varepsilon = 2\Delta x$. In the second case, ε has the constant value 0.025 (the same as in Figure 2.14) independently of the grid size variation. For all tests, the "Jacobian-free" formula and the initialization of Figure 2.14 (a) has been used. The results are shown in Figure 2.16 and 2.17. Comparing qualitatively the results, we can say that they look quite similar, as soon as the grid resolution allows for a satisfying enough description of the geometry and an accurate enough approximation of the geometric quantities in play.

2.6.4 Four materials in the smoothed interface context

We consider now the case of using up to four phases and consequently two level-set functions. A smoothed approximation of the characteristic function of each phase can be constructed using

Figure 2.15: *"Long cantilever" using two phases with $V_T = 0.7|D|$ and a large smoothing parameter $\varepsilon = 8\Delta x$; (a): initialization; (b): optimized shape using the "true" formula; (c): optimized shape using the "Jacobian-free" formula; (d): optimized shape using the "approximate" formula; (e): convergence of the compliance; (f): convergence of the volume.*
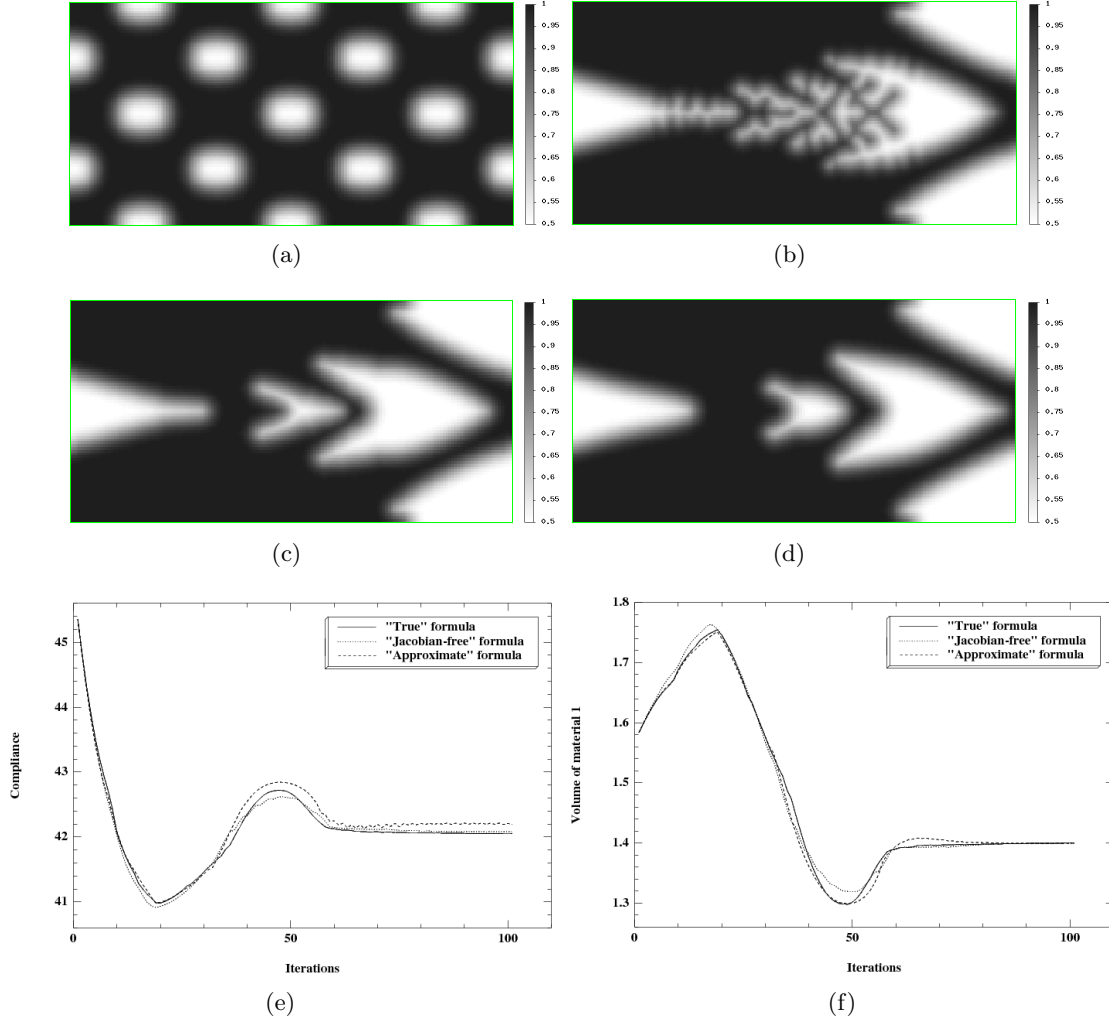
combinations of the functions h_ε, defined in equation (2.27), as follows

$$
\begin{cases}
\chi_0 = (1 - h_\varepsilon(d_{\mathcal{O}^0}))(1 - h_\varepsilon(d_{\mathcal{O}^1})), \\
\chi_1 = h_\varepsilon(d_{\mathcal{O}^0})(1 - h_\varepsilon(d_{\mathcal{O}^1})), \\
\chi_2 = (1 - h_\varepsilon(d_{\mathcal{O}^0}))h_\varepsilon(d_{\mathcal{O}^1}), \\
\chi_3 = h_\varepsilon(d_{\mathcal{O}^0})h_\varepsilon(d_{\mathcal{O}^1}),
\end{cases}
\tag{2.54}
$$

and the global Hooke's tensor in given by (2.49). The optimization problem now reads

$$
\min_{\mathcal{O}^0, \mathcal{O}^1 \in \mathcal{U}_{ad}} J(\mathcal{O}^0, \mathcal{O}^1) = \int_D A_{\mathcal{O}^0, \mathcal{O}^1, \varepsilon}(x)e(u) : e(u)\, dx
$$
$$
\text{s.t.} \quad \int_D \chi_i dx = V_T^i,\ i = 0, ..., 3\,,
\tag{2.55}
$$

where V_T^i is the target volume for the phase i (they sum up to the volume of D). As previously, an augmented Lagrangian algorithm is applied to enforce the constraints. In this section we work with a "thin" interface, namely $\varepsilon = 2\Delta x$.

We test our method with several benchmark examples presented in [317] and [318]. Since the initial designs are different, as well as the numerical methods, it is hard to make a quantitative comparison and we satisfy ourselves with a qualitative comparison.
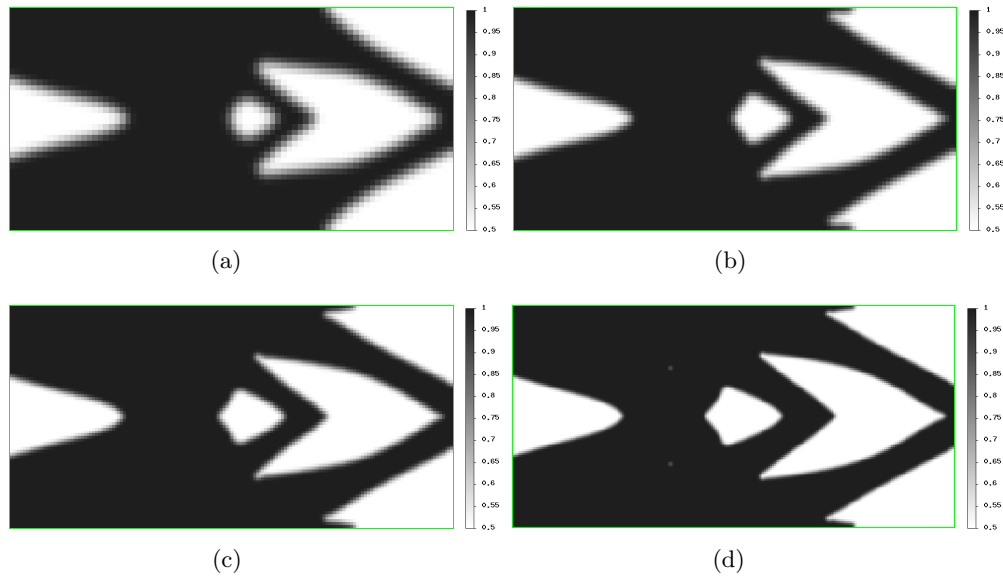
Figure 2.16: *Long cantilever using two phases with $V_T = 0.7|D|$, $\varepsilon = 2\Delta x$ and a grid of; (a): 80×40; (b): 120×60; (c): 160×80; (d): 240×120 elements.*
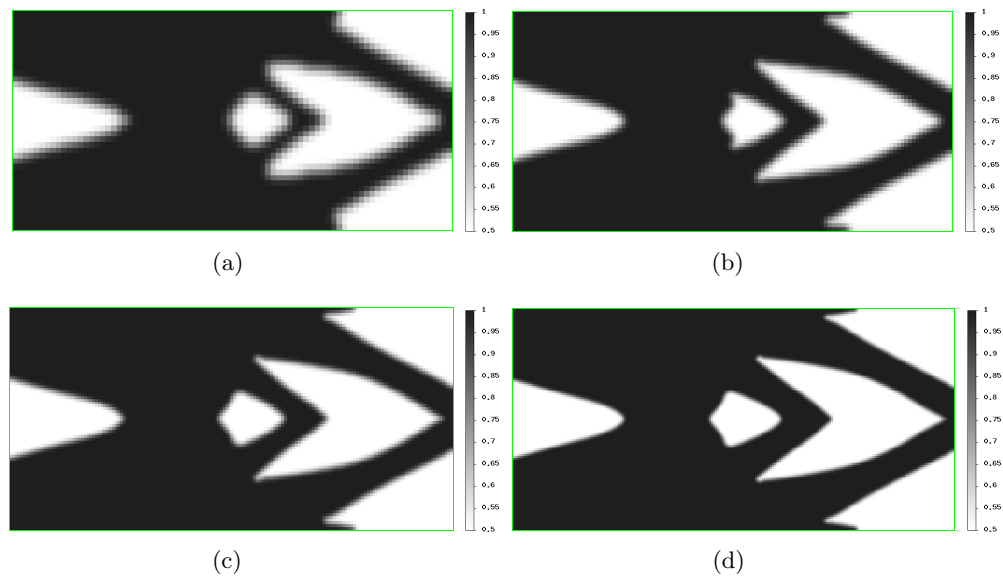
Figure 2.17: *Long cantilever using two phases with $V_T = 0.7|D|$, $\varepsilon = 0.025$ and a grid of; (a): 80×40; (b): 120×60; (c): 160×80; (d): 240×120 elements.*

Short-cantilever using two materials and void

In this paragraph we consider only three phases, made of two materials and void. The first structure to be optimized is a two-dimensional short cantilever, of dimensions 1×2, discretized using 80×160 $\mathbb{Q}_1$ elements. The left part of the structure is clamped and a unitary vertical force is applied at the mid point of its right part (see Figure 2.18). The Young moduli of the four phases are defined as $E^0 = 0.5, E^1 = 10^{-3}, E^2 = 1$ and $E^3 = 10^{-3}$, where both phases 1 and 3 represent void. The target volumes for phases 0 and 2 are set to $V_T^0 = 0.2|D|$ and $V_T^2 = 0.1|D|$. Remark that phases 1 and 3 are the same, corresponding to void. The fact that the void zone is represented by two different characteristic functions has no influence on the numerical results (at least in all our numerical experiments). The initial and the optimal shape (obtained after 200 iterations) are shown in Figure 2.19 (a) and (b). We plot the Young modulus with a grey

scale: dark stands for the stronger phase, white for void and grey for the intermediate phase.

This test case was previously studied in [317] (see figures 7 and 8 therein for two different initializations). Our results are roughly similar to those in [317] and even slightly better since the designs of Figure 2.19 are symmetric (as expected), contrary to the results in [317].
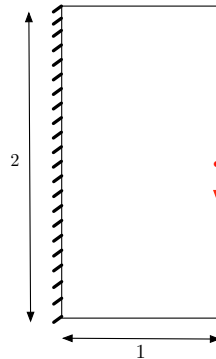
Figure 2.18: Boundary conditions and initialization for the 2d short-cantilever.
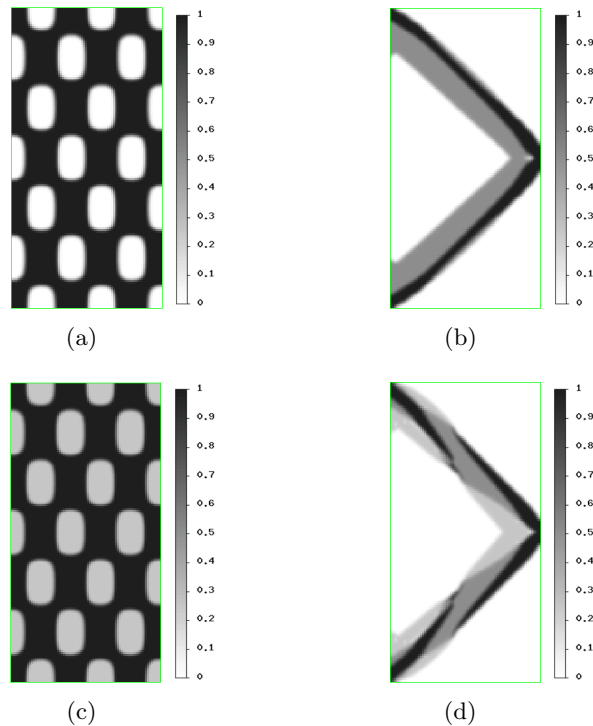
Figure 2.19: Short cantilever using two or three phases and void; (a) initialization for two phases and void, (b) optimal shape for two phases and void, (c) initialization for three phases and void, (d) optimal shape for three phases and void.

Short-cantilever using three materials and void

The same example as in the previous paragraph is considered here with an additional phase: half of the volume of material 0 is replaced by a weaker material 1. More precisely, the Young moduli of the four phases are defined as $E^0 = 0.5, E^1 = 0.25, E^2 = 1$ and $E^3 = 10^{-3}$, while the target volumes for the three materials 0, 1 and 2 are set to $V_T^0 = V_T^1 = V_T^2 = 0.1|D|$. The initial and optimal shapes (after 200 iterations) are displayed on Figure 2.19 (c) and (d).

This test case was also studied in [317] (see figures 11 and 12 therein for two different initializations). Our result differs notably from these previous ones. Indeed, in [317] the strong material 2 always forms a two-bar truss which is further reinforced by the other materials. On the contrary, in our Figure 2.19 (d) the strong phase is disconnected and the intermediate material 0 plays a more active role in the transfer of the load to the fixed wall.

3-force bridge using two materials and void

A bridge-type structure of dimensions 2×1 is discretized by 160×80 $\mathbb{Q}_1$ elements. Both the horizontal and vertical displacement are fixed at the lower left part as well as the vertical displacement of the lower right part. Three equally spaced forces are applied at the lower part (see Figure 2.20). The value of F is set to 1. The Young moduli of the four phases are set to $E^0 = 0.5, E^1 = 10^{-3}, E^2 = 1$ and $E^3 = 10^{-3}$ and the target volumes for phases 0 and 2 are set to $V_T^0 = 0.2|D|$ and $V_T^2 = 0.1|D|$. The initial and optimal designs (after 250 iterations) are shown in Figure 2.21 (a) and (b).

Once again this test case was performed in [317] (see figure 13 therein). Our result is quite different. First, our design in Figure 2.21 (b) is symmetric, as it should be. Second, a major difference occurs in the use of the strong phase. In our design, the strong material is used in the lower part of the "radial" bars whereas it was absent in figure 13 of [317] (and rather used in the upper "arch").

Figure 2.20: Boundary conditions and initialization for the 3-force bridge.
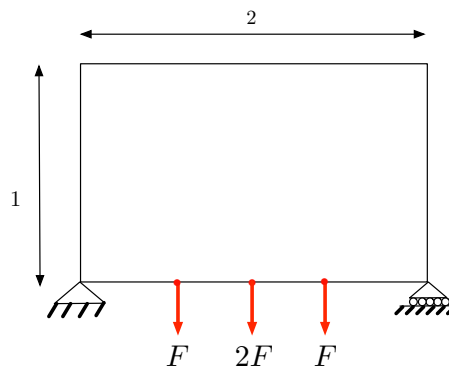
3-force bridge using three materials and void

The same example as in the previous paragraph is considered here with an additional phase: half of the volume of material 0 is replaced by a weaker material 1. The Young moduli of the four phases are defined as $E^0 = 0.5, E^1 = 0.25, E^2 = 1$ and $E^3 = 10^{-3}$, while the target volumes for phases 0, 1 and 2 are set to $V_T^0 = V_T^1 = V_T^2 = 0.1|D|$. The initial and optimal designs (after 250 iterations) are displayed on Figure 2.19 (c) and (d).

This test case can be found in [317] (figure 14) too, and again our result is quite different.

Medium cantilever using three materials and void

The next structure is a medium cantilever, of dimensions 3.2×2, discretized using 120×75 $\mathbb{Q}_1$ elements. The left part of the structure is clamped and a unitary vertical force is applied at the bottom of its right part (see Figure 2.22). The Young moduli of the four phases are defined again as $E^0 = 0.5, E^1 = 0.25, E^2 = 1$ and $E^3 = 10^{-3}$ and the target volumes for phases 0, 1 and 2 are set to $V_T^0 = V_T^1 = V_T^2 = 0.1|D|$. The results are shown in Figure 2.23.

This test case was also performed in [318] (see Figure 7 therein). Our optimal designs have a more complex topology and a different layout of the three materials. However, the final volumes
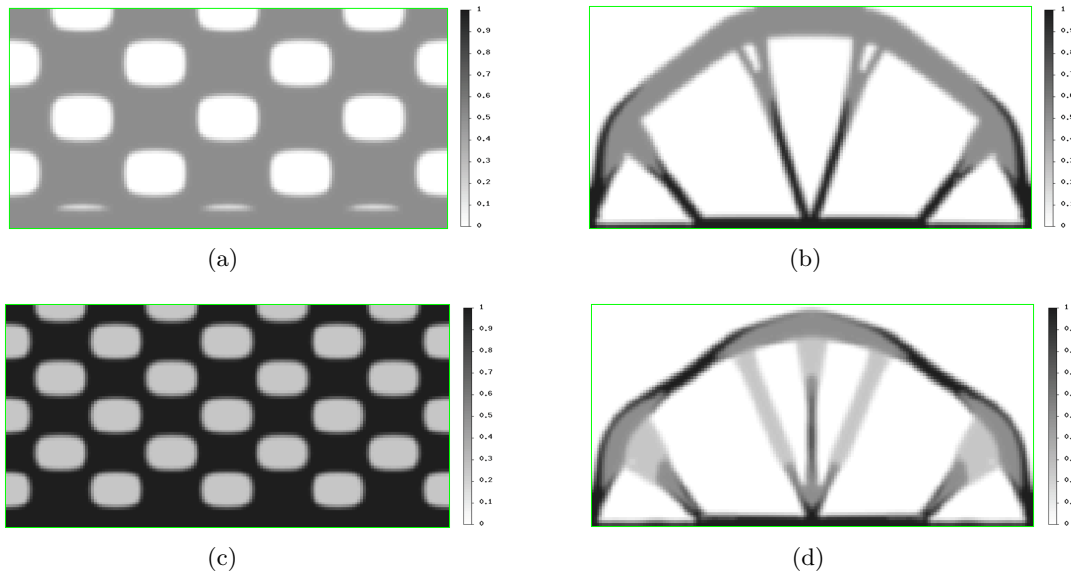
Figure 2.21: 3-force bridge using two or three phases and void; (a) initialization for two phases and void, (b) optimal shape for two phases and void, (c) initialization for three phases and void, (d) optimal shape for three phases and void.

of the three materials in [318] are not the same as ours and thus a comparison is not easy to establish.
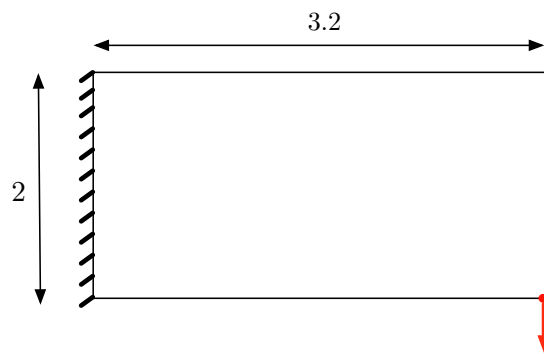
Figure 2.22: Boundary conditions and initialization for the 2D medium-cantilever.
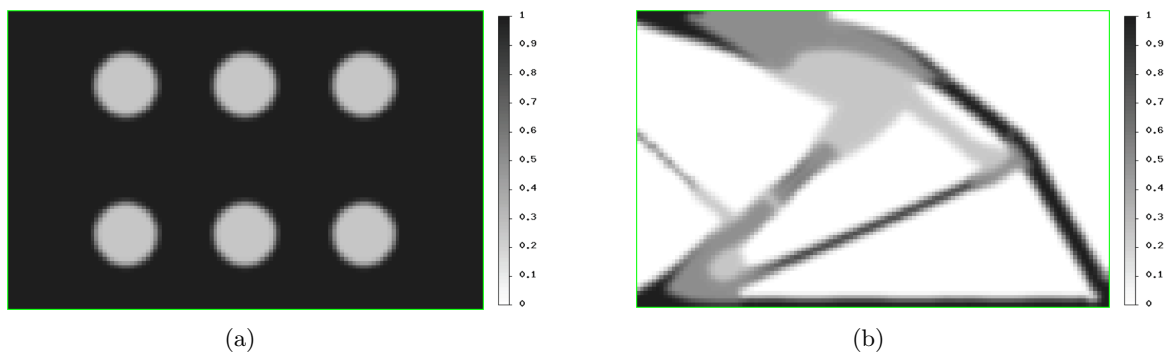
Figure 2.23: Medium cantilever using three materials and void; (a) initialization, (b) optimal shape.

L-shaped structure

The example of an L-shaped structure of dimensions 1×1 is borrowed from Chapter 2.9 in [44]. The domain is discretized using 120×120 $\mathbb{Q}_1$ elements and a non-optimizable area of dimensions 0.6×0.6 is imposed on its upper-right part. The structure is clamped on its upper side and a unitary vertical force is applied on the middle of its right side (see Figure 2.24).

Figures 2.25 (a), (b), (c) present the results of using two phases with ratio of Young moduli equal to 0.2, 0.5 and 0.8. The two materials are represented by phases 0 and 2. The Young modulus of phase 0 is set to $E^0 = 1.0$. Phases 1 and 3 represent void and their Young moduli are set to $E^1 = E^3 = 10^{-4}$. The target volumes for phases 0 and 2 are $V_T^0 = V_T^2 = 0.25|D|$. The results are slightly different than those in [44], but they follow the same logic in the placement of materials.
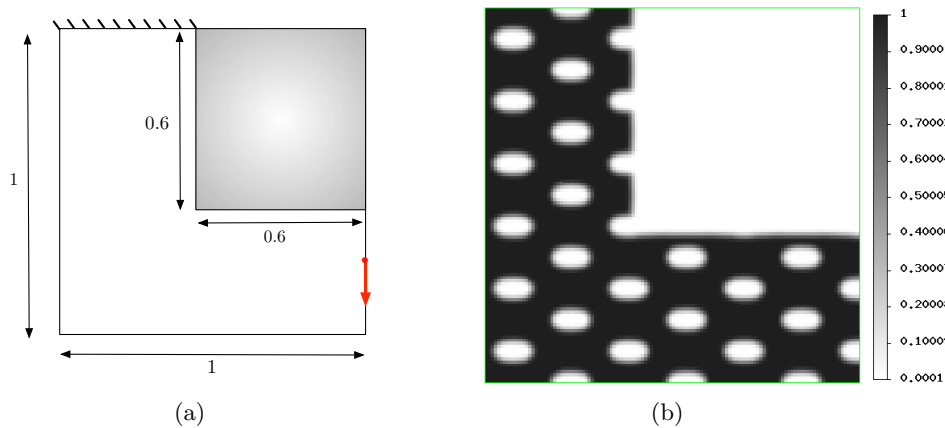
Figure 2.24: (a): Boundary conditions and (b): initialization for the L-shaped structure.
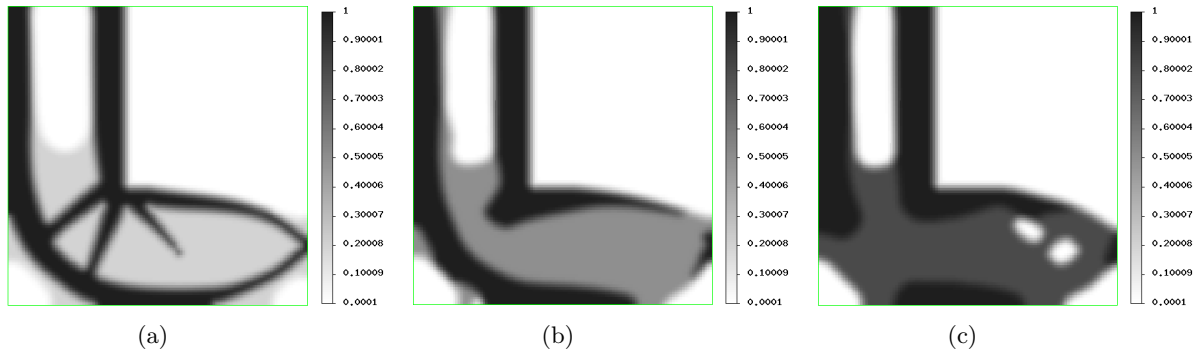
Figure 2.25: *Results for the L-shaped structure.*

Long cantilever using two materials and void

The goal of this last paragraph is twofold. First, we consider again the 2×1 long cantilever, as in Figure 2.13, but with four phases, defined by their Young moduli $E^0 = 0.5, E^1 = 10^{-3}, E^2 = 1$ and $E^3 = 10^{-3}$. Second, we switch to an unconstrained optimization algorithm. We do not impose equality constraints for the volume of each phase. Rather, we fix Lagrange multipliers and we minimize an objective function $J(\mathcal{O}^0, \mathcal{O}^1)$, which reads

$$J(\mathcal{O}^0, \mathcal{O}^1) = \int_D A(d_{\mathcal{O}^0}, d_{\mathcal{O}^1})e(u) : e(u)dx + \sum_{i=0}^{3} \ell^i \int_D \chi_i(x)dx. \tag{2.56}$$

We then carry out a standard constraint-free steepest descent algorithm in order to minimize J.
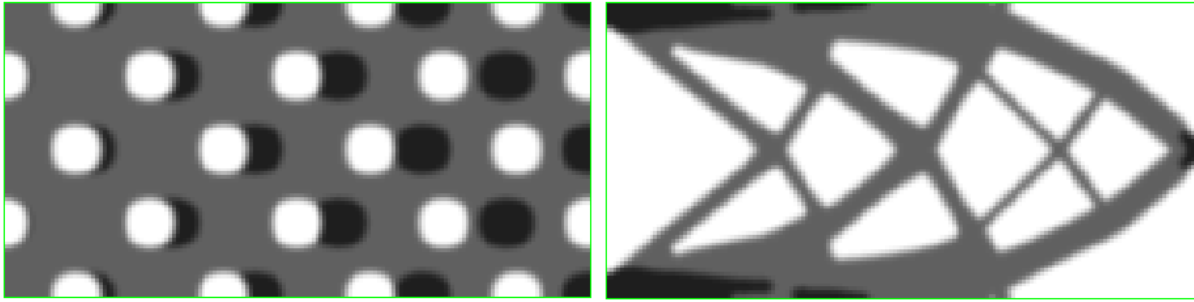
Figure 2.26: Initialization with two materials (top left), optimial shape (top right) and convergence history of the objective function (bottom).

A small tolerance parameter $tol > 0$ (in the example below, we used $tol = 0.02$) over acceptance of the produced shapes is introduced so as to ease the occurrence of topological changes and is then turned off after some iterations. More accurately, in the course of the optimization process, a step $\mathcal{O}_n^0 \to \mathcal{O}_{n+1}^0$ and $\mathcal{O}_n^1 \to \mathcal{O}_{n+1}^1$ is accepted provided:

$$J(\mathcal{O}_{n+1}^0, \mathcal{O}_{n+1}^1) < (1 + tol)J(\mathcal{O}_n^0, \mathcal{O}_n^1).$$

For the results shown in Figure 2.26, the Lagrange multipliers in (2.56) are set to $\ell^0 = 100, \ell^1 = 0, \ell^2 = 200, \ell^3 = 0$. As can be expected the strong material is distributed at the areas of high stress, while the weak material completes the shape of the optimal cantilever.

It is interesting to see the optimal subdomains $\mathcal{O}^0$ and $\mathcal{O}^1$ (defined in Section 2.5) in Figure 2.27. Recall that it is the intersections of these two subdomains and their complementaries which give rise to the phase domains in the optimal design of Figure 2.26.

Figure 2.27: Final subdomains $\mathcal{O}^0$ (left) and $\mathcal{O}^1$ (right).

Chapter 3

Optimization of laminated composite plates

Contents

We consider the optimal design of composite laminates by allowing a variable stacking sequence and in-plane shape of each ply. The plate is modeled according to the linearized von Kármán equations for plates. In order to optimize both variables we rely on a decomposition technique which aggregates the constraints into one unique constraint margin function. Thanks to this approach, a rigorous equivalent bi-level optimization problem is established. This problem is made up of a lower level represented by the combinatorial optimization of the stacking

sequence and a higher level represented by the topology and geometry optimization of each ply. We propose for the stacking sequence optimization an outer approximation method which iteratively solves a set of mixed integer linear problems associated to the evaluation of the constraint margin function. For the topology optimization of each ply, we lean on the level set method for the description of the interfaces and the Hadamard method for boundary variations by means of the computation of the shape gradient. An aeronautic test case is exhibited subject to different constraints, namely compliance, reserve factor and first buckling load.

3.1   Introduction

Structural optimization in aeronautics usually looks for the lightest structure which sustains the forces and environmental conditions that an aircraft will typically find during operation. Within this framework, frequently the objective function (total mass) is easy to evaluate if a good parametrization of the structure is available, meanwhile the constraints are in general much more complicated. Evaluate them requires a general physical model which can be more or less prompt to evaluate depending on the choice of variables. Classically, this optimization process has been done by the engineer expertise. However, the increment of the size of the design space does not allow to find the best design without automatizing the process. As a response to this challenge, several techniques for size, shape and topology optimization have successfully been developed and applied to aircraft design [44, 5, 224, 133, 258, 282, 183].

During the last years, a special type of material has become quite popular in automotive and aerospace industries: multi-layered composites. These materials benefit from very attractive features such as low weight, high fatigue resistance and good endurance against corrosion and other harsh environmental conditions. The properties of multi-layered composite structures strongly depend on the shape, the orientation of the reinforcement and the stacking sequence of the laminate. Indeed the directional nature of the fibers in a fiber-reinforced laminate introduces directional dependence of the strength, thermal and electrical conductivity, environmental resistance, etc.; meanwhile the stacking sequence has an important incidence on the bending behavior of the laminate.

In view of the increasing use of composite materials within industry, their optimal design has drawn great attention of the scientific community. We refer e.g. to Gürdal, Haftka and co-workers [139, 133, 282, 189, 286, 2, 287] and [167, 219, 222, 196]. In fact, composite materials possess a large number of design possibilities which enforces the complexity of the design problem. Even more, the development of new multi-materials or manufacturing techniques, as for example, the automated fiber placement or tow-placed steered fibers [303, 235, 59], still enlarges the size of the design space of the problem. A typical composite laminate may be characterized by design variables which are continuous (geometric size of the structure, wing profile), discrete (orientation of the fibers and lay-up), or even distribution of the material in each ply for topology optimization. Additionally, when designing composite aircraft structural components, one must take into account constraints on the structural performance (accelerations, buckling factors, displacement, material failure criteria, etc.) and equally constraints on the global and local manufacturing rules imposed during the composite manufacturing process. This constraints are specific to the type of technology used and industrial policies (symmetric and balanced laminates, ply drops and overlaps, etc.). A particularly difficult constraint to deal with is structural integrity or blending, i.e. the continuity of the stacking sequence across multiple panels making up the structure [311, 270, 1].

The large number of design variables, and the complex relationship between these variables and the output performance in an aircraft, make composite structure design extremely challenging. Decomposition procedures have risen as particularly appealing approaches to treat the aforementioned complexity of composite optimization. A typical decomposition/bi-level scheme aims to break up the large problem into many problems that matches the different levels of analysis taking into account its interactions during the design process. In the case

of composite design, this technique looks to guarantee the compatibility between a "continuous medium" vision, necessary for the overall understanding of the phenomena related to the stiffness level, and the discrete nature of laminated composites. For example a continuous representation of the composite is applied at the system level (fuselage or wing), meanwhile the subsystem level (lay-up of the panel) is treated with discrete algorithms. We refer the reader to [288, 204, 29, 202, 203, 49, 200, 73].

Once the problem is decomposed, the optimal design of the composite lay-up or stacking sequence emerges naturally as a mixed integer non linear programming problem. For this kind of problems, many methods exist in the literature. Among the so-called deterministic methods, we can cite e.g. the application of branch and bound method to linear formulations of minimal mass problems with a buckling constraint [233, 133, 140] and the benders decomposition method to the optimization of tailored fiber orientation composites [226]. These methods guarantee in general to find a global solution provided that the problem satisfies certain conditions such as convexity. When no such conditions are satisfied, an efficient complement and/or alternative to deterministic methods are heuristics. We can mention e.g. the penalty function approach [63, 290] and a rounding procedure using lamination parameters [307, 146, 145]. The latter optimization approach has the strong advantage with respect to the others, of dwelling on lamination parameters [222]. This provides a very efficient parametrization of a continuous variable fiber orientation plate, allowing to split the optimization problem into two steps: continuous optimization with respect the lamination parameters and a round off procedure of the founded solution to the closest discrete neighbor. Finally among the so-called stochastic methods (whose convergence properties rely on probability theory) most of the existent literature refers to Gürdal and his co-workers on genetic algorithms [189, 201, 286, 287, 234, 2], with only a few exceptions (see e.g. [112] for simulated annealing). Broadly speaking, these methods avoid the enumeration of many of the integer assignments, effectuating a global research. Nevertheless, the high number of evaluations of the objective function and constraints through the optimization process can eventually become too expensive.

The aforementioned approach has proved effective, however, it does not address all the degrees of freedom and constraints within composite structures. In fact, the design of the in-plane shape of each layer has much less been considered so far, despite of its importance in terms of structural strength and manufacturability. The in-plane shape as a design variable can only be treated satisfactorily through a continuous approach, which leads to reconsider the former continuous/discrete framework. We can cite however the works on topology optimization applied to fiber orientation tailoring of laminated composites, carried out by Lund and his co-workers [290, 205, 241, 197, 162] and [62, 102]. Most of these works rely on a density-based method (DMO, SIMP).

The following chapter addresses the structural optimization of a composite laminate by adding a new design variable to the fiber orientation and lay-up sequence: the in-plane shape and topology of each ply. Indeed we suppose that each ply is made up of two phases (where one of them might be void) and the position of the interface is the design variable. When the second phase is not void, the composite laminate constitutes a multi-material. To the knowledge of the author, this approach is relatively novel and very few industrial design tools show similar features. Moreover the problem we contemplate to solve is different to the fiber orientation tailoring problem mentioned above, since the fiber orientation within each phase remains constant. As a similar approach, we can cite the composite optimization routine of the software Optistruct of Altair [121, 327]. In fact, the software generates a sequence of ply shapes that are afterwards post-processed from the optimized thickness of each fiber orientation within the laminate (see Figure 3.1). In our case we intend to perform the composite optimization without making use of any thickness analysis. This should confer us a higher optimality and design liberty.

(a) Generation of ply shapes from the thickness distribution (color scale)

(b) Post-processing of each ply shape into several manufacturable shapes
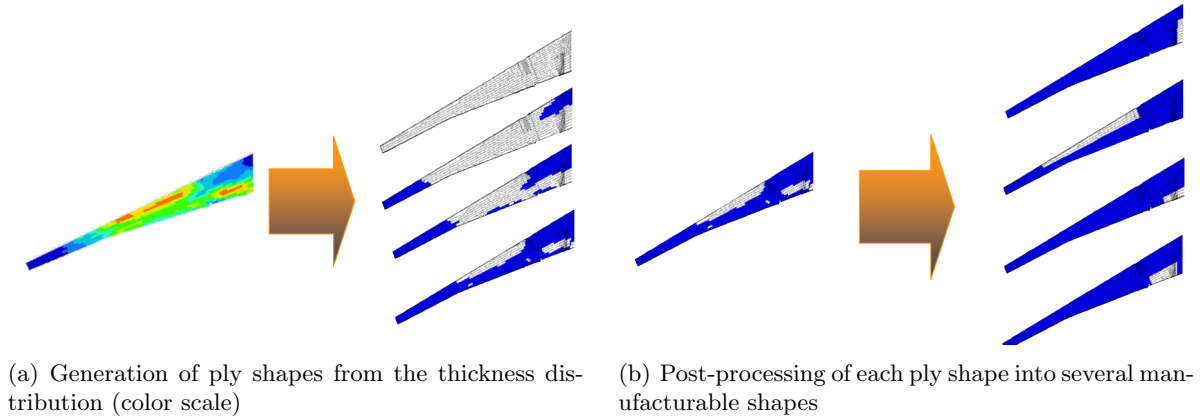
Figure 3.1: Optimization of a laminated composite wing with Optistruct. Images from [121].

For the topology design of each ply, we lean on the level-set method for multi-phase optimization introduced in Chapter 2. This enables us to achieve a better description and control of the geometrical properties of the interface without need of any intermediate density. Thanks to this approach, the typical drawbacks of the homogenization and SIMP methods are avoided, such as intermediate density penalization and possible spurious physical behavior during the optimization process.

Finally due to the mixed character of the composite optimization problem (continuous shape and discrete stacking sequence), a decomposition technique is presented. This technique splits the problem into different levels according to the "difficulty" of each variable. Thus, the optimization is carried in each ply by a level-set method to find the optimal shape coupled to an outer approximation method to find the best fiber orientation and stacking sequence. The outer approximation method [110] is a deterministic method which is exact for convex functions and consists in iteratively approximating the objective and constraints of the problem by linear under-estimators. The choice of this classical method searches to highlight the pertinence of linear integer programming-based solvers to handle stacking sequence problems with a moderate number of variables (e.g. thin composite structures), and avoid the inherent limitations of the most popular heuristics and stochastic methods when treating a multiple-shape lay-up design (e.g. intensive evaluation of objective function and constraints, not clear ply shape, etc.).

This chapter is organized as follows. In Section 3.2 the composite multi-layered optimization problem is enunciated by means of a mixed optimization approach. Then in Section 3.3, we discuss the existence of optimal solutions of the latter problem in light of Section 1.1. The shapes derivatives in a continuous and discrete framework of the functions concerned in the composite problem are derived in Section 3.4, meanwhile the stacking sequence problem is detailed through the constraint margin function in Section 3.5. The foregoing elements are linked altogether in a general decomposition framework in Section 3.6. Finally the proposed optimization algorithm and a numerical example for three different types of constraints are respectively developed in Section 3.8 and Section 3.9.

3.2   Setting of the problem

3.2.1   Multi-shape composite design

Similarly to Section 1.3, let $\mathcal{O}$ be a symmetric laminated composite structure composed of the superposition of $2N$ anisotropic layers, each one of constant thickness $\varepsilon > 0$, but this time each one with a variable shape $\Omega_i \subset \Omega$, where Ω a regular sub-domain of $\mathbb{R}^2$. By abuse of notation

we denote $\mathcal{O}$ as

$$\mathcal{O} = \{\Omega_i\}_{i \in \mathbb{Z} \setminus \{0\}, i = -N..N} \, .$$

Since we suppose $\mathcal{O}$ symmetric, i.e. $\Omega_{-i} = \Omega_i$, we consider only N layers, so we rather write $\mathcal{O} = \{\Omega_i\}_{i=1...N}$. The index i grows from the inside to the outside of the laminated composite structure.

As it was explained in Section 1.3, we consider each laminate to be an orthotropic material and unidirectionally reinforced.
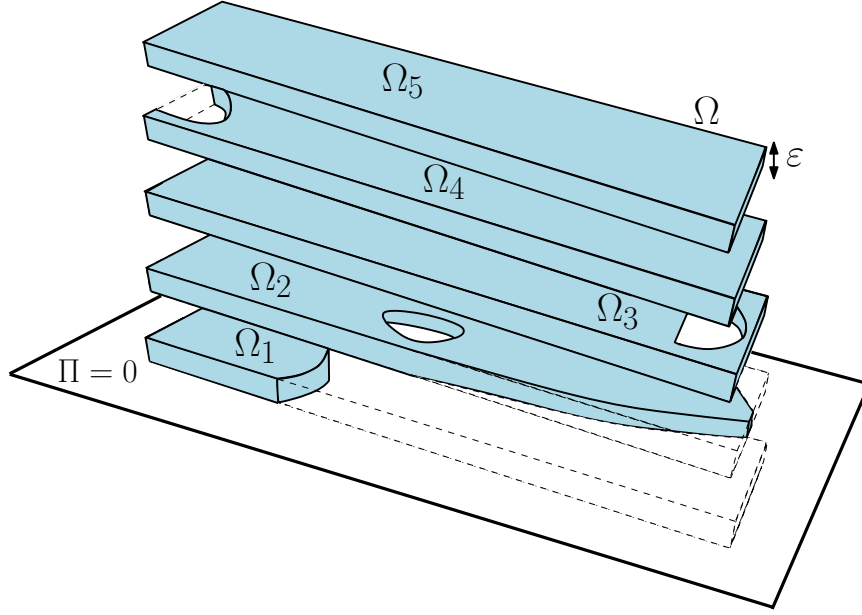
Figure 3.2: Half-part of a multi-shape composite design with plane of symmetry $\Pi = 0$. Each ply has its own shape $\Omega_i \subset \Omega$. Compare with Figure 1.12

For the purpose of this study, the shape of each plate Ω_i and their superposition within the multi-layered structure can be understood in two different ways (see Figure 3.3):

- Configuration I: Each layer is a non-homogeneous two-phase material, where each "hole" is filled with another "weak" material with different physical properties (weight, electric or heat conductivity, etc.). We will denote this weak material as $\mathcal{A}_0$. We will mainly focus on this configuration.

- Configuration II: The holes in each ply are really "void" (in this case $\mathcal{A}_0 = 0$) and, when gluing together the plies towards the plane of symmetry $\Pi = 0$ (inwardly blended), the distal layer bends and fills the holes to keep contact with the proximal layers. The mostly outer layers will be always full in order to avoid the existence of holes throughout the laminate.

Let χ_i be the characteristic function of the i-layer. According to the classical theory of plates, the composite structure $\mathcal{O}$ is characterized by the superposition of the elastic properties of each layer. Adapting formulae (1.61) and (1.62) to the multi-shape design at issue, the new extensional stiffness tensor $\mathcal{A}$ reads

$$\mathcal{A}(x) = 2\varepsilon \sum_{i=1}^{N} \left(\chi_i(x)\mathcal{A}_i + (1 - \chi_i(x))\mathcal{A}_0 \right), \tag{3.1}$$

(a) Configuration I. Multi-material.

$$\Pi = 0$$

(b) Configuration II. Inwardly blended.
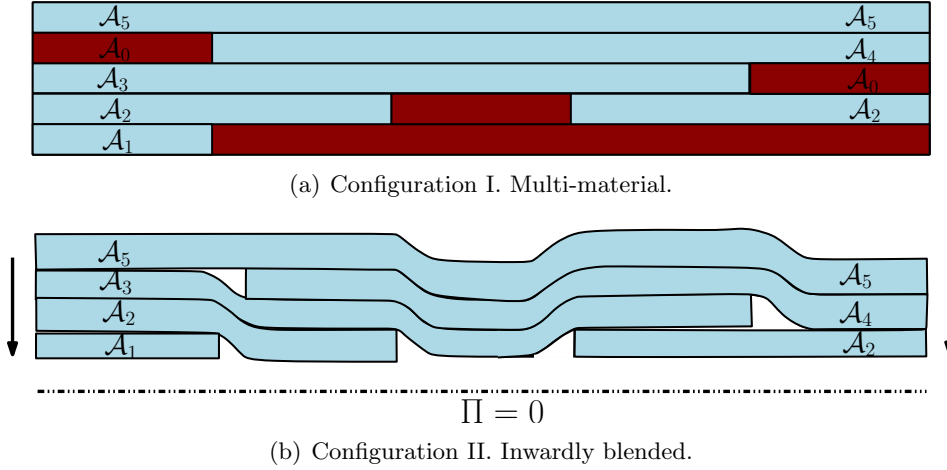
Figure 3.3: Example of transversal cut of a multi-shape composite. For simplification the cut was divided into 5 panels. Different stacking sequence are defined according to each configuration.

where $\mathcal{A}_i$ is the extensional stiffness of the i-layer, meanwhile the bending stiffness tensor $\mathcal{D}$ reads

$$\mathcal{D}(x) = \frac{2\varepsilon^3}{3} \sum_{i=1}^{N} \left\{ \left(i^3 - (i-1)^3 \right) \left(\chi_i \mathcal{A}_i + (1 - \chi_i)\mathcal{A}_0 \right) \right\}, \qquad (3.2)$$

for configuration I and

$$\mathcal{D}(x) = \frac{2\varepsilon^3}{3} \sum_{i=1}^{N} \left\{ \left(\left(\sum_{j=1}^{i} \chi_j(x) \right)^3 - \left(\sum_{j=1}^{i-1} \chi_j(x) \right)^3 \right) \mathcal{A}_i \right\}. \qquad (3.3)$$

for configuration II.

Likewise Section 1.3, we assume the same partition of $\partial\Omega$ ($\partial\Omega = \Gamma_D \cup \Gamma_N$) and loading configuration $(g, P) \in (L^2(\Gamma_N; \mathbb{R}^2), L^2(\Omega))$. Then the in-plane displacement $u \in H_D^1(\Omega; \mathbb{R}^2)$ and vertical displacement $w \in H_D^2(\Omega)$ within the composite plate $\mathcal{O}$, satisfy the limit two-dimensional von Kármán plate model (1.60). The kinematically admissible spaces $H_D^1(\Omega; \mathbb{R}^2)$ and $H_D^2(\Omega)$ are respectively defined in (1.56) and (1.57). In the same way, we also introduce the linearized buckling problem (1.63), (1.64), denoting always by λ_1 the smallest positive eigenvalue of (1.63) and $\hat{w}$ the associated eigenvector.

3.2.2 Stacking sequence

Even though the fiber orientation might take any possible rotation angle, in real applications due to manufacturing constraints, it only takes discrete values [133]. We will consider four values, namely: $0^o, 45^o, -45^o, 90^o$. We denote by $\mathcal{C}_{0^o}, \mathcal{C}_{45^o}, \mathcal{C}_{-45^o}, \mathcal{C}_{-90^o}$ their respective extensional stiffness tensors. We assume that the fiber orientation is constant in each ply.
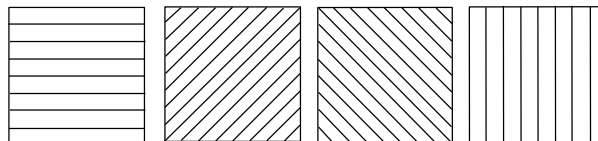
Figure 3.4: Fiber orientation of $0^o, 45^o, -45^o, 90^o$.

Definition 3.2.1. *We define the stacking sequence as the set of ply orientations and the way they are arranged within the composite laminate. We represent it through a binary matrix* $\xi = (\xi_{mn}) \in \{0,1\}$, *where* $m = 1, ..., N$, $n = 1, ..., 4$, *and*

$$\xi_{mn} = \left\{ \begin{array}{ll} 1, & \text{if the layer in position } m \text{ has fiber orientation } n, \\ 0, & 1 \text{ if not.} \end{array} \right.$$

We identify fiber orientations $1, 2, 3, 4$ *to the angles* $0^0, 90^0, 45^0, -45^0$, *respectively. A compatibility constraint must be imposed to obtain one and only one orientation in each ply, namely*

$$\sum_{n=1}^{4} \xi_{mn} = 1, \forall m.$$

Remark 3.2.2. *We recall than since the laminate* $\mathcal{O}$ *is symmetric, only half of the stacking sequence is studied and thus encoded in the matrix* ξ.

Thanks to the above definition, the extensional stiffness tensor of the laminate can be parametrized as
$$\mathcal{A}_i(\xi) = \xi_{i1}\mathcal{C}_{0^o} + \xi_{i2}\mathcal{C}_{90^o} + \xi_{i3}\mathcal{C}_{45^o} + \xi_{i4}\mathcal{C}_{-45^o}, \tag{3.4}$$

and thus the stiffness tensors $\mathcal{A}(\mathcal{O}, \xi)$, $\mathcal{D}(\mathcal{O}, \xi)$ are functions of the shapes of the laminate $\mathcal{O}$ and the stacking sequence ξ. In particular $\mathcal{A}$ and $\mathcal{D}$ are are linear functions of ξ.

Lemma 3.2.3. *If the proportion of plies of each fiber orientation is fixed within the laminate, then for every compatible choice of* ξ *respecting these proportions, the tensor* $\mathcal{A}$ *remains constant.*

Proof. Let p_j with $j = 0^o, 90^o, 45^o, -45^o$, be the proportion of plies of each fiber orientation within the composite laminate. Then thanks to the linear structure of the extensional stiffness tensor $\mathcal{A}$ in equations (3.1),(3.4)

$$\mathcal{A} = \frac{N}{N} \sum_{i=1}^{N} \sum_{j} \xi_{ij}\mathcal{C}_j = N \sum_{j} \mathcal{C}_j \frac{1}{N} \sum_{i=1}^{N} \xi_{ij} = N \sum_{j} \mathcal{C}_j p_j.$$

Hence if p_j remains constant, then it also does the tensor $\mathcal{A}$.

$\square$

Lemma 3.2.4. *Under the above hypothesis, the in-plane displacement u remains constant according to (1.64).*

3.2.3   Goal of the present study

We look for a multi-layered composite plate with optimal stacking sequence and ply shapes. Typically the optimization problem will be set as a mass minimization problem subject to a set of manufacturing constraints, local failure criteria, in-plane stiffness and avoidance of buckling.

General problem

From a mathematical point of view, the above problem can be cast as a mixed optimization problem, namely
$$\left\{ \begin{array}{l} \min_{\mathcal{O} \in \mathcal{U}_{ad}, \xi \in Y} J(\mathcal{O}) \\ \text{s.t} \\ \quad G(\mathcal{O}, \xi) \leq 0. \end{array} \right. \tag{3.5}$$

The objective function $J(\mathcal{O})$ does not depend on the stacking sequence ξ and it represents the mass of the structure

$$J(\mathcal{O}) = \rho \sum_{i=1}^{N} \int_{\Omega} \chi_i dV, \text{supposing constant density } \rho.$$

The scalar constraint G represents a regular measure of the stiffness of the plate. Notably, we focus our attention on three kinds of measures, namely

$$(a)\left(\lambda_1^{-1}(\mathcal{O}, \xi) - 1\right) \quad (b) \int_{\Omega} s(x, \mathcal{O}, \xi, u(\mathcal{O}, \xi), \nabla u(\mathcal{O}, \xi)) dV \quad (c) \|r(x, \mathcal{O}, \xi, u(\mathcal{O}, \xi), \nabla u(\mathcal{O}, \xi))\|_{L^{\infty}(\Omega)}. \tag{3.6}$$

The first criterion express the buckling avoidance through the load factor or first positive eigenvalue of (1.63), meanwhile the last two criteria represent a global failure and a local stiffness criterion respectively, with r, s regular functions. These functionals could represent e.g. the Compliance, the von Mises or the Tsai-Hill local failure criteria.

Remark 3.2.5. *When the proportions of plies with a certain fiber orientation are fixed, then according to Lemma 3.2.4, the constraint configurations (b),(c) in (3.6) become independent w.r.t the stacking sequence matrix ξ.*

The sets Y and $\mathcal{U}_{ad}$ represent the stacking sequence and the set of admissible shapes, respectively. An explicit definition of the set Y will be given in Section 3.5. We define the set of admissible shapes $\mathcal{U}_{ad}$ as the $N-$collection of open subsets of the working domain Ω with bounded perimeter

$$\mathcal{U}_{ad} = \left\{ \{\Omega_i\}_{i=1...N} \,|\, \Omega_i \subset \Omega \text{ and } P(\Omega_i) \leq \varsigma, \;\; \forall i = 1...N \right\}, \tag{3.7}$$

where $P(A)$ is the perimeter of the open set $A \subset \mathbb{R}^2$ and $\varsigma > 0$ constant. The existence of an optimal solution to problem (3.5) relies essentially on the definition of $\mathcal{U}_{ad}$. A rigorous proof of the existence of an optimal shape of (3.5) is developed in Section 3.3, and it is based on classical ideas of [16].

Remark 3.2.6. *For some applications (as it was noticed in Section 1.1), controlling the perimeter of each phase is important, even though we don't posses any reference value ς. In that case the functional $J(\mathcal{O})$ can be re-defined as a linear combination of the weight and the total perimeter, which is also independent of the stacking sequence ξ*

$$J(\mathcal{O}) = \sum_{i=1}^{N} \left\{ \rho \int_{\Omega} \chi_i dV + \gamma \int_{\partial \Omega_i} dS \right\}, \gamma > 0.$$

Simplification of the buckling problem

In order to reduce the numerical cost of calculating λ_1 at each iteration, a common point-wise approximation of the criterion (a) in (3.6) is

$$\lambda_{RF}^{-1}(\mathcal{O}, \xi) - 1 \leq 0, \text{ with } \lambda_{RF}(\mathcal{O}, \xi) := \min_{x \in \Omega} \left(\frac{\frac{2\pi}{b}\sqrt{\mathcal{D}_{11}\mathcal{D}_{22}} + \mathcal{D}_{12} + 2\mathcal{D}_{33}}{|(\mathcal{A}e(u))_{xx}^-|} \right). \tag{3.8}$$

The factor

$$\frac{2\pi}{b}\left(\sqrt{\mathcal{D}_{11}\mathcal{D}_{22}} + \mathcal{D}_{12} + 2\mathcal{D}_{33}\right), \tag{3.9}$$

stands for the value of the buckling load of an homogeneous simply supported composite plate under a compression through the $x-$axis [257], b is the length of the plate, meanwhile $(\mathcal{A}e(u))_{xx}^-$

corresponds to the projection of the negative (compressed) values of the stress tensor in the $x-$axis. When we switch (3.8) to (a)(3.6) in (3.5), the simplified optimization problem has the advantage of requiring only the evaluation of problem (1.64), alleviating the numerical cost of solving (1.63). Nevertheless, λ_{RF} remains a coarse approximation of λ_1 in a more general setting, notably when there exists coupled compression/shear loads and the plates are non-homogeneous. Thus, the objective of this study is to also compare numerically the optimal solution of (3.5) for both choices of G.

3.3 On the existence of an optimal shape

In the following section the existence of a solution to problem (3.5) is analyzed by means of the induced topology of the convergence of characteristic functions quoted in Theorem 1.1.6. The notation however changes slightly w.r.t. Chapter 1.1, labeling rather as Ω the fixed domain D and denoting as ω an arbitrary open subset of Ω. Thereby, we can establish that the set $\{\omega \subset \Omega\}$ with bounded perimeter is compact. Moreover Theorem 1.1.6 stipulates that the volume and the perimeter are lower semi-continuous w.r.t. to the aforementioned topology. Hence in order to prove the existence of a solution through Proposition 1.1.1, it only remains to prove that the constraints in (3.5) are lower semi-continuous.

The principle of the ensuing demonstrations is rather classic, however the study of some constraints within (4.27), notably the point-wise constraint and λ_1 for the von Kármán model, seems untreated in literature so far.

So as to ease the notation, only a one layered composite structure is considered to describe $\mathcal{U}_{ad}$. The case with (finite) multiple plies follows straightaway, since the stacking sequence remains constant so the same principle can be repeated to every admissible stacking sequence until reaching the global optimality. Denote as u_ω the plane stress solution of (1.64) with extensional and bending stiffness tensors $\mathcal{A}_\omega = \chi_\omega \mathcal{A}_1 + (1 - \chi_\omega)\mathcal{A}_0$ and $\mathcal{D}_\omega = \chi_\omega \mathcal{D}_1 + (1 - \chi_\omega)\mathcal{D}_0$, respectively. The tensors $(\mathcal{A}_0, \mathcal{D}_0)$ and $(\mathcal{A}_1, \mathcal{D}_1)$ correspond to two different elastic materials.

First we recall some classical results, in particular Meyer's theorem for strongly elliptic systems [70]

Theorem 3.3.1. *Let $\Omega \subset \mathbb{R}^2$ a bounded open domain of class C^2 and $\Gamma_N \cup \Gamma_D = \partial\Omega$, with $\Gamma_D \cap \Gamma_N = \emptyset$ and $|\Gamma_D| \neq 0$. Let $0 < \alpha < \beta$ two real numbers and the fourth order tensor function $\mathcal{C} = \{\mathcal{C}_{ijkl}\}$, $\mathcal{C}_{ijkl} \in L^\infty(\Omega)$ $i, j, k, l = 1, 2$, such that*

$$\forall x \in \Omega, \xi \in \mathbb{R}^2, \ \alpha\|\xi\|^2 \leq \mathcal{C}(x) \leq \beta\|\xi\|^2.$$

For $f \in H^{-1}(\Omega; \mathbb{R}^2), g \in H^{-1/2}(\Omega; \mathbb{R}^2)$, let u be the unique solution in $H_D^1(\Omega; \mathbb{R}^2)$ of:

$$- div(\mathcal{C}e(u)) = f \ in \ \Omega, \quad (\mathcal{C}e(u)) \cdot n = g \ on \ \Gamma_N \tag{3.10}$$

Denote as $W_D^{1,q}(\Omega; \mathbb{R}^2)$ the subspace of $W^{1,q}(\Omega; \mathbb{R}^2)$ such that the trace of the functions is zero on Γ_D. Then there exists $p > 2$ and a constant $C > 0$ which both depend only on α, β and Ω, such that, if $f \in W^{-1,p}(\Omega; \mathbb{R}^2), g \in W^{-1/2,p}(\Omega; \mathbb{R}^2)$, u belongs to $W_D^{1,p}(\Omega; \mathbb{R}^2)$ and satisfies:

$$\|u\|_{W^{1,p}(\Omega)} \leq C(\|f\|_{W^{-1,p}(\Omega)} + \|g\|_{W^{-1/2,p}(\Omega)}).$$

Lemma 3.3.2. *Let p the constant provided by the Meyer's theorem and u solution of (3.10), $\mathcal{B} = \{\mathcal{B}_{ijkl}\}$, $\mathcal{B}_{ijkl} \in L^\infty(\Omega)$, $i, j, k, l = 1, 2$ and $u_B \in H_D^1(\Omega; \mathbb{R}^2)$ the unique solution of*

$$-div(\mathcal{B}e(u_B)) = f \ in \ \Omega, \quad (\mathcal{B}e(u_B)) \cdot n = g \ on \ \Gamma_N.$$

Then for some $r > 0$ and $\tilde{C} > 0$

$$\|u - u_B\|_{C^{0,\gamma}(\Omega)}^{m_1} \leq \tilde{C} \|\mathcal{C} - \mathcal{B}\|_{L^r(\Omega)} (\|f\|_{W^{-1,p}(\Omega)} + \|g\|_{W^{-1/2,p}(\Omega)})^{m_2}, \ for \ every \ 0 < \gamma < 1 - 2/p,$$

with $m_1(p, \gamma), m_2(p, \gamma) > 0$ constants.

Proof. For any $v \in H_D^1(\Omega; \mathbb{R}^2)$, one has

$$\int_\Omega \mathcal{C}e(u) : e(v)dV = \int_\Omega f{\cdot}vdV + \int_{\Gamma_N} g{\cdot}vdS \quad ; \quad \int_\Omega \mathcal{B}e(u_B) : e(v)dV = \int_\Omega f{\cdot}vdV + \int_{\Gamma_N} g{\cdot}vdS.$$

Consequently

$$\int_\Omega \mathcal{B}e(u_B - u) : e(v)dV = \int_\Omega (\mathcal{C} - \mathcal{B})e(u) : e(v)dV. \tag{3.11}$$

Let C and $p > 1$ the constants provided by Meyer's theorem 3.3.1 associated to Ω, $\bar{\alpha} = \min(\mathcal{C}, \mathcal{B})$, $\bar{\beta} = \max(\mathcal{C}, \mathcal{B})$. Putting $v = u - u_B$ in (3.11) and using Hölder and Korn inequality yields

$$\bar{\alpha} \|u - u_B\|_{H_0^1(\Omega)}^2 \leq \|\mathcal{C} - \mathcal{B}\|_{L^r(\Omega)} \|u\|_{L^p(\Omega)} \|u - u_B\|_{H_0^1(\Omega)},$$

for some $r > 0$ such that $1/r + 1/p + 1/2 = 1$ (which is possible since $p > 2$). Hence applying Poincare's inequality and Theorem 3.3.1,

$$\bar{\alpha} \|u - u_B\|_{H^1(\Omega)} \leq C \|\mathcal{C} - \mathcal{B}\|_{L^r(\Omega)} (\|f\|_{W^{-1,p}(\Omega)} + \|g\|_{W^{-1/2,p}(\Omega)}). \tag{3.12}$$

Let $2 < q < p$ and $t \in (0, 1)$ such that $q = 2t + (1 - t)p$. Then one has applying again Hölder inequality

$$\int_\Omega |\nabla u - \nabla u_B|^q dV \leq \left(\int_\Omega |\nabla u - \nabla u_B|^2 dV \right)^{1/t} \left(\int_\Omega |\nabla u - \nabla u_B|^p dV \right)^{1/(1-t)},$$

thus Poincare's inequality entails

$$\|u - u_B\|_{W^{1,q}(\Omega)} \leq C \|u - u_B\|_{H^1(\Omega)}^{2/(tq)} \|u - u_B\|_{W^{1,p}(\Omega)}^{p/(q(1-t))} \tag{3.13}$$

According to Meyer's theorem

$$\|u - u_B\|_{W^{1,p}(\Omega)} \leq \|u\|_{W^{1,p}(\Omega)} + \|u_B\|_{W^{1,p}(\Omega)} \leq C \Big(\|f\|_{W^{-1,p}(\Omega)} + \|g\|_{W^{-1/2,p}(\Omega)} \Big)$$

is bounded so inserting (3.13) into (3.12) yields

$$\bar{\alpha} \|u - u_B\|_{W^{1,q}(\Omega)}^{tq/2} \leq C \|\mathcal{C} - \mathcal{B}\|_{L^r(\Omega)} (\|f\|_{W^{-1,p}(\Omega)} + \|g\|_{W^{-1/2,p}(\Omega)})^{\frac{1+t(p/2-1)}{1-t}}. \tag{3.14}$$

Finally the desired result stems from the Sobolev embedding in dimension 2 of $W^{1,q}$ into $C^{0,\gamma}$ for $0 < \gamma = 1 - 2/q$, taking $m_1 = tq$, $m_2 = 1 + pt/(2(1-t))$ and $\tilde{C} = C/\bar{a}$. $\qquad \square$

Proposition 3.3.3 (Global and local stiffness). *Let the function $s := \Omega \times \mathbb{R}^2 \times \mathbb{R}^{2,2} \to \mathbb{R}$ be a non-negative, measurable and lower semi-continuous function with respect each argument such there exist $C > 0$ and*

$$\forall x \in \Omega, d_1 \in \mathbb{R}^2, d_2 \in \mathbb{R}^{2,2}, |s(x, d_1, d_2)| \leq C(1 + \|d_1\|_{\mathbb{R}^2}^2 + \|d_2\|_{\mathbb{R}^{2,2}}^2). \tag{3.15}$$

Introduce also $r_1 := \Omega \times \mathbb{R} \times \mathbb{R}^2 \to \mathbb{R}$ and $r_2 := \Omega \times \mathbb{R} \times \mathbb{R}^{2,2} \to \mathbb{R}$ lower semi-continuous with respect to each argument. Define a fixed "non-optimizable" domain $\Omega_{No} \subset \Omega$ and the functionals G_1, G_2, in the same spirit that (4.27), as

$$G_1(\omega) = \int_\Omega s(x, u_\omega, \nabla u_\omega)dV \quad G_2(\omega) = \|r_1(x, \chi_\omega, u_\omega)\|_{L^\infty(\Omega)} + \|r_2(x, \chi_\omega, \nabla u_\omega)\|_{L^\infty(\Omega_{No})} \tag{3.16}$$

Let $(\omega_n)_n \subset \Omega$ be a sequence of measurable shapes and $\omega \subset \Omega$ measurable, such that for all $n \geq 1$, $\Omega_{No} \subset \omega_n$ and $\chi_{\omega_n} \to \chi_\omega$ strongly in $L^1(\Omega)$. As we have seen, this is the case (in virtue of Theorem 1.1.6) when we suppose Ω and the perimeter of Ω_n uniformly bounded. Then there exists a subsequence ω_{n_k} such that $u_{\Omega_{n_k}}$ converges strongly in $H^1(\Omega; \mathbb{R}^2)$ to u_ω and moreover the functionals G_1, G_2 are sequentially lower semi-continuous w.r.t. that subsequence, i.e.

$$G_1(\omega) \leq \liminf_{k \to \infty} G_1(\omega_{n_k}),$$
$$G_2(\omega) \leq \liminf_{k \to \infty} G_2(\omega_{n_k}).$$

Remark 3.3.4. *The need of defining a "non-optimizable" domain Ω_{No} stems from the lack of regularity of ∇u_{ω_n}. Indeed, the jumps or discontinuities of the elastic laws $\mathcal{A}_{\omega_n}$ inside Ω imply that $\|\nabla u_{\omega_n}\|_{L^\infty(O)}$ is only bounded in the regions $O \subset \Omega$ where $\mathcal{A}_{\omega_n}$ is regular [195]. Thereby, by defining Ω_{No} as a non-optimizable zone, i.e. a subregion of Ω where there are no shape changes (or rather modifications in the elastic properties), we assure that the second term in $G_2(\omega_n)$ is well defined for every n.*

Proof. Let $\bar{\alpha} = \min(\mathcal{A}_0, \mathcal{A}_1)$. Then for every n we have

$$\bar{\alpha} \int_\Omega e(u_{\omega_n}) : e(u_{\omega_n})dx \leq \int_\Omega \mathcal{A}_{\omega_n} e(u_{\omega_n}) : e(u_{\omega_n})dx = \int_\Omega f \cdot u_{\omega_n}dx + \int_{\Gamma_N} g \cdot u_{\omega_n}ds \leq M \|u_{\omega_n}\|_{H^1(\Omega)},$$

where $M = \max(\|f\|_{H^{-1}(\Omega)}, \|g\|_{H^{-1/2}(\Omega)})$. Applying Korn's inequality

$$\|u_{\omega_n}\|_{H^1(\Omega)} \leq C \|e(u_{\omega_n})\|_{L^2(\Omega)},$$

it follows that the sequence u_{ω_n} is bounded in $H^1(\Omega; \mathbb{R}^2)$ and a subsequence (by abuse of notation denoted with the same index n) converges weakly in $H^1(\Omega; \mathbb{R}^2)$ to some $u^* \in H^1(\Omega; \mathbb{R}^2)$, due to the compactness of bounded reflexive Banach spaces with respect the weak topology [60]. Furthermore using Rellich-Kondrachov compact embedding theorem

$$u_{\omega_n} \longrightarrow u^*, \text{ strongly in } L^2(\Omega; \mathbb{R}^2).$$

In fact we can still improve the foregoing convergence result. Let the fourth order square root tensor $\mathcal{A}^{1/2}$ of $\mathcal{A}$ be such that

$$\mathcal{A}_{ijkl} = \mathcal{A}^{1/2}_{ijmn}\mathcal{A}^{1/2}_{mnkl},$$

and denote by $\mathcal{A}^{1/2}_{\omega_n}$ and $\mathcal{A}^{1/2}_\omega$ those corresponding to $\mathcal{A}_{\omega_n}$ and $\mathcal{A}_\omega$. The existence of these tensors stems from the positive semi-definite character of $\mathcal{A}_{\omega_n}$ and $\mathcal{A}_\omega$ [65]. Due to the definition of $\mathcal{A}_{\omega_n} = \chi_{\omega_n}\mathcal{A}_0 + (1 - \chi_{\omega_n})\mathcal{A}_1$, we easily remark that $\left(\mathcal{A}_{\omega_n}\right)_{ijkl} \to \left(\mathcal{A}_\omega\right)_{ijkl}$ and $\left(\mathcal{A}^{1/2}_{\omega_n}\right)_{ijkl} \to \left(\mathcal{A}^{1/2}_\omega\right)_{ijkl}$ strongly in $L^q(\Omega)$, for every $i, j, k, l = 1, 2$ and $q \geq 1$. Furthermore we know that

$$\nabla u_{\omega_n} \longrightarrow \nabla u^* \text{ weakly in } L^2(\Omega; \mathbb{R}^{2,2}),$$

so in particular

$$e(u_{\omega_n}) \longrightarrow e(u^*) \text{ weakly in } L^2(\Omega; \mathbb{R}^{2,2}), \quad \text{and} \quad \mathcal{A}^{1/2}_{\omega_n}e(u_n) \longrightarrow \mathcal{A}^{1/2}_\omega e(u^*), \text{ weakly in } L^2(\Omega; \mathbb{R}^{2,2}).$$

Multiplying (1.64) by u_n and integrating by parts it follows

$$\int_\Omega (\mathcal{A}^{1/2}_\omega e(u^*)) : (\mathcal{A}^{1/2}_\omega e(u^*))dV = \int_\Omega f \cdot u^* dV + \int_{\Gamma_N} g \cdot u^* dS$$

$$= \lim_{n \to \infty} \int_\Omega f \cdot u_{\omega_n}dV + \int_{\Gamma_N} g \cdot u_{\omega_n}dS = \lim_{n \to \infty} \int_\Omega (\mathcal{A}^{1/2}_{\omega_n}e(u_{\omega_n})) : (\mathcal{A}^{1/2}_{\omega_n}e(u_{\omega_n}))dV,$$

so by the Radon-Riesz property of Hilbert spaces,

$$\mathcal{A}^{1/2}_{\omega_n}e(u_{\omega_n}) \longrightarrow \mathcal{A}^{1/2}_\omega e(u^*), \text{ strongly in } L^2(\Omega; \mathbb{R}^{2,2}).$$

Hence applying Korn's inequality and multiplying now by $\mathcal{A}^{-1/2}_{\omega_n}$ the above expression

$$\nabla u_{\omega_n} \longrightarrow \nabla u^*, \text{ strongly in } L^2(\Omega; \mathbb{R}^{2,2})$$

and we obtain the strong convergence of ∇u_{ω_n} to ∇u^* in $L^2(\Omega; \mathbb{R}^{2,2})$.

Now we prove that $u^* = u_\omega$ or equivalently

$$\int_\Omega \mathcal{A}_\omega e(u^*) : e(v) dV = \int_\Omega f \cdot v dV + \int_{\Gamma_N} g \cdot v dS,$$

for every test function $v \in H^1_D(\Omega; \mathbb{R}^2)$. Due to the uniqueness of the solution, it is enough to show that for every fixed v the following equality stands

$$\lim_{n\to\infty} \int_\Omega \mathcal{A}_{\omega_n} e(u_{\omega_n}) : e(v) dV = \int_\Omega \mathcal{A}_\omega e(u^*) : e(v) dV.$$

This is an immediate consequence of the properties of the weak convergence [60] for the linear application

$$\langle \mathcal{A}_{\omega_n}, u_{\omega_n} \rangle = \int_\Omega \mathcal{A}_{\omega_n} e(u_{\omega_n}) : e(v) dV,$$

since $\mathcal{A}_{\omega_n}$ converges strongly and $e(u_n)$ converges weakly (we know that rather strongly).

The only thing that remains to prove is the lower semi-continuity of G_1 and G_2 in (3.16). Since every element of the sequence (u_{ω_n}) and u_ω belong to $H^1(\Omega; \mathbb{R}^2)$, the growth condition (4.29) entails the finitude of G_1. Next, applying lower semi-continuity of s, Fatou's lemma yields

$$G_1(\omega) = \int_\Omega s(x, u_\omega, \nabla u_\omega) dV \leq \liminf_{n\to\infty} \int_\Omega s(x, u_{\omega_n}, \nabla u_{\omega_n}) dV = \lim_{n\to\infty} \inf G_1(\omega_n),$$

and G_1 is lower semi-continuous. On the other side, taking e.g. $\mathcal{A} = \mathcal{A}_{\omega_n}$ (respectively $\mathcal{A} = \mathcal{A}_\omega$) and $\mathcal{B} = \frac{1}{2}\mathcal{A}_{\omega_n}$ (respectively $\mathcal{B} = \frac{1}{2}\mathcal{A}_\omega$) in Lemma (3.3.2), one has that u_{ω_n} (respectively u_ω) belongs to $L^\infty(\Omega; \mathbb{R}^2)$ and the term involving r_1 in G_2 is finite. The lower semi-continuity of the first term of G_2 stems one more time from Lemma (3.3.2) by taking $\mathcal{B} = \mathcal{A}_\omega$ and $\mathcal{A} = \mathcal{A}_{\omega_n}$, since the convergence in $C^{0,\alpha}(\Omega)$ implies convergence in $L^\infty(\Omega)$ and every component of $\mathcal{A}_{\omega_n}$ converges strongly to $\mathcal{A}_\omega$ in $L^r(\Omega), \forall r \geq 1$.

The analysis of the term involving k_2 in G_2 (3.16) is slightly more delicate, as it was noticed in Remark 3.3.4, since the functions ∇u_{ω_n} and ∇u_ω do not belong to $L^\infty(\Omega; \mathbb{R}^{2,2})$. First we remark that the convergence $\chi_{\omega_n} \to \chi_\omega$ in $L^1(\Omega)$ implies in particular the one in $L^1(\Omega_{No})$. Hence $\|\chi_\omega - 1\|_{L^1(\Omega_{No})} = 0$ and $\chi_\omega(x) = 1$ a.e. for $x \in \Omega_{No}$, since $\Omega_{No} \subset \omega_n$ for all n by hypothesis. Moreover, the strong formulation of (1.64) for u_{ω_n}, u_ω yields

$$-\text{div}\big(\mathcal{A}_{\omega_n} e(u_{\omega_n} - u_\omega)\big) = \text{div}\big((\mathcal{A}_{\omega_n} - \mathcal{A}_\omega) e(u_\omega)\big).$$

So thanks to the precedent remark and according to the definition of $\mathcal{A}_{\omega_n}$ and $\mathcal{A}_\omega$, the difference $\mathcal{A}_{\omega_n} - \mathcal{A}_\omega = 0$ a.e. on Ω_{No} and

$$-\text{div}\big(\mathcal{A}_{\omega_n} e(u_{\omega_n} - u_\omega)\big) = 0, \text{a.e. in } \Omega_{No}.$$

Finally the desired result is achieved by a classical interior regularity result for second order elliptic systems [213]

$$\|u_{\omega_n} - u_\omega\|_{C^{1,\alpha}(\varpi)} \leq C \|u_{\omega_n} - u_\omega\|_{H^1(\Omega)}, \forall \varpi \Subset \Omega_{No} \tag{3.17}$$

and the continuity of r_2. We remark in (3.17) that the constant C does not depend on n due to the uniform boundedness of $(\mathcal{A}_{\omega_n})_n$.

$\square$

Proposition 3.3.5 (Buckling constraint)**.** *Let $(\omega_n)_n \subset \Omega$ be a sequence of measurable shapes such that $\chi_{\omega_n} \to \chi_\omega$ strongly in $L^1(\Omega)$. Then there is a subsequence n_k such*

$$\lim_{k\to\infty} \lambda_1(\omega_{n_k}) = \lambda_1(\omega),$$

where λ_1 (4.27) is the smallest positive eigenvalue of (1.63)*.*

Proof. Let $\mathbb{T}_{\omega_n}$ be the sequence of resolvent operators defined as

$$\mathbb{T}_{\omega_n}(z) := z \in H^2_D(\Omega) \to w_{\omega_n}(z) \in H^2_D(\Omega),$$

where w_{ω_n} is the unique solution of the variational formulation of the linearized buckling problem

$$\int_\Omega (\mathcal{D}_{\omega_n} \nabla^2 w_{\omega_n}) : \nabla^2 \eta \, dx = -\int_\Omega \mathcal{A}_{\omega_n} e(u) \nabla z \nabla \eta \, dx, \quad \forall \eta \in H^2_D(\Omega). \tag{3.18}$$

As it was shown in Proposition 1.3.11, for every n, the operator $\mathbb{T}_{\omega_n}$ is compact. Furthermore, according to Proposition 3.3.3, there exists a subsequence of (ω_n) (by abuse of notation we denote it with the same index) such that $u_{\omega_n} \to u_\omega$ strongly in $H^1(\Omega; \mathbb{R}^2)$, where u_{ω_n}, u_ω are the solution of the flexural problem (1.64) for the elastic tensors $\mathcal{A}_{\omega_n}, \mathcal{A}_\omega$. Now we would like to prove that the same result holds for w_{ω_n} in $H^2(\Omega)$. For that purpose, we first stand that the sequence w_{ω_n} is bounded in $H^2(\Omega)$. Indeed, developing each side of the bending equation (3.18)

$$
\begin{aligned}
\delta \int_\Omega |\nabla^2 w_{\omega_n}|^2 dV &\leq \int_\Omega (\mathcal{D}_{\omega_n} \nabla^2 w_{\omega_n}) : \nabla^2 w_{\omega_n} dV \\
&= -\int_\Omega \mathcal{A}_{\omega_n} e(u_{\omega_n}) \cdot \nabla z \cdot \nabla w_{\omega_n} dV \\
&\leq \alpha \|e(u_{\omega_n})\|_{L^2(\Omega)} \|\nabla z\|_{L^4(\Omega)} \|\nabla w_{\omega_n}\|_{L^4(\Omega)} \\
&\leq C^* \Big(\|f\|_{H^{-1}(\Omega)} + \|g\|_{H^{-1/2}(\Omega)} \Big) \|z\|_{H^2(\Omega)} \|w_{\omega_n}\|_{H^2(\Omega)},
\end{aligned}
$$

where $\delta = \min(\mathcal{D}^0, \mathcal{D}^1)$, $\alpha = \max(\mathcal{A}^0, \mathcal{A}^1)$ and we have used the compact injection of $H^2(\Omega)$ into $W^{1,4}(\Omega)$ and the boundedness in $H^1(\Omega; \mathbb{R}^2)$ of u_{ω_n} according to Proposition 3.3.3. Applying the Poincaré inequality to the above cascade of equations yields

$$\|w_{\omega_n}\|_{H^2(\Omega)} \leq C^* \Big(\|f\|_{H^{-1}(\Omega)} + \|g\|_{H^{-1/2}(\Omega)} \Big) \|z\|_{H^2(\Omega)},$$

and we conclude that w_{ω_n} is bounded. Similarly to Proposition 3.3.3, the Sobolev embedding theorem implies that the canonical injection of $H^2(\Omega)$ into $H^1(\Omega)$ is compact so there exist $w^* \in H^2(\Omega)$ such that $w_n \to w^*$ weakly in $H^2(\Omega)$ and strongly in $H^1(\Omega)$. Moreover, carrying out the same argument with the square root tensors (but this time with $\mathcal{D}$ and the quadratic form $\int_\Omega \mathcal{D}\nabla^2 w_{\omega_n} : \nabla^2 w_{\omega_n} dV$), $w_{\omega_n} \to w^*$ strongly in $H^2(\Omega)$. Now it only remains to prove that $w^* = w_\omega$ or equivalently

$$\int_\Omega \mathcal{D}_\omega \nabla^2 w^* : \nabla^2 \eta \, dV = \int_\Omega \mathcal{A}_\omega e(u_\omega) \cdot \nabla z \cdot \nabla \eta \, dV, \forall \eta \in H^2_D(\Omega).$$

Then it is enough to show

$$\lim_{n\to\infty} \int_\Omega \mathcal{D}_{\omega_n} \nabla^2 w \nabla^2 w_{\omega_n} : \nabla^2 \eta \, dV = \int_\Omega \mathcal{D}_\omega \nabla^2 w^* : \nabla^2 \eta \, dV, \forall \eta \in H^2_D(\Omega)$$

$$\lim_{n\to\infty} \int_\Omega \mathcal{A}_{\omega_n} e(u_{\omega_n}) \cdot \nabla z \cdot \nabla \eta \, dV = \int_\Omega \mathcal{A}_\omega e(u_\omega) \cdot \nabla z \cdot \nabla \eta \, dV, \forall \eta \in H^2_D(\Omega).$$

Both equalities are immediate consequence of the properties of the weak convergence as in Proposition 3.3.3.

Hence until now we have demonstrated that w_{ω_n} converges strongly to w_ω in $H^2(\Omega)$. In other words, $\mathbb{T}_{\omega_n}(z) \to \mathbb{T}_\omega(z)$, for every $z \in H_D^2(\Omega)$ It can be proved [144] (lemma 4.7.3) that the above type of convergence (also called $\gamma-$convergence) is equivalent to the convergence in the uniform operator topology $\mathcal{L}(H^2(\Omega))$, i.e.

$$\lim_{n \to \infty} \sup_{\|z\|_{H_D^2(\Omega)} \leq 1} \|\mathbb{T}_{\omega_n}(z) - \mathbb{T}_\omega(z)\| = 0,$$

and desired result yields from a classical result of spectral theory for compact operators [109] (Lemma 5, page 1091) which says that if $\mathbb{T}_{\omega_n} \to \mathbb{T}_\omega$ in the uniform operator topology, then

$$\lim_{n \to \infty} \mu_k(\omega_n) = \mu_k(\omega),$$

where $\mu_k(\omega_n)$ is the k-th eigenvalue of the operator $\mathbb{T}_{\omega_n}$. Thus equivalently

$$\lim_{n \to \infty} \lambda_1(\omega_n) = \lambda_1(\omega),$$

since $\lambda_1 = 1/\max_k \mu_k$. □

3.4   Shape sensitivity analysis

In this section we briefly recall the main results of the shape derivative in the context of composite optimization for dimension $d = 2$, using as a basis the Section 1.1, notably Definition 1.1.13.

Suppose the stacking sequence ξ fixed and consider the linearized buckling problem (1.63),(1.64). For simplicity we deem here only two phases on one ply. Let $\Omega_1 \Subset \Omega$ be and denote as n as the outer normal to Ω_1. We define the complement of Ω_1 as $\Omega_0 = \Omega \backslash \Omega_1$. Then the extensional stiffness tensor $\mathcal{A}$ reads

$$\mathcal{A} = \chi_1 \mathcal{A}_1 + (1 - \chi_1)\mathcal{A}_0 = \mathcal{A}_0 + \chi_1(\mathcal{A}_1 - \mathcal{A}_0),$$

where $\mathcal{A}_0$ and $\mathcal{A}_1$ are two different anisotropic elastic laws and χ_1 the characteristic function of Ω_1. This situation corresponds to a one-layered composite structure as described in Section 3.2, i.e. $\mathcal{O} = \{\Omega_1\}$. The extension to the multi-layer case follows directly by analogy changing the index "1" by any $i = 1, ..., N$, since each ply is considered independent from the others.

Remark 3.4.1. *When dealing with the multi-layered case, we must assume that the measure of the common interior interface between two plies with shapes Ω_i, Ω_j is negligible, i.e. $|\partial\Omega_i \cap \partial\Omega_j| = 0, \forall i, j = 1, ..., N$, in order to avoid non-differentiability. To make this feature clear, compare the variation of a cost functional J w.r.t. to the application of an advection fields θ and $-\theta$ to one interface, always keeping the other fixed. Due to the discontinuity in the elastic properties entailed by the fixed interface, one can easily check that in general $J'(\Omega)(-\theta) \neq -J'(\Omega)(\theta)$.*

We divide the ensuing analysis in a continuous and a discrete framework where slightly different formulae of the shape derivative of (4.27) arise in multi-phase problems as it was quoted in Chapter 2. We remark that the point-wise functional (c) in (3.6) is not shape differentiable but different techniques are capable of approximating it by (b),(3.6) type-functionals.

3.4.1   Continuous framework

Apart from λ_1, the shape derivative formulae of the functions involved in (3.6) are quite classic in a continuous framework (see Chapter 2). In general they involve adding the elastic transmission conditions to the Lagrangian in Céa's derivation method [74]. The following proposition for the shape derivative of λ_1 illustrates this procedure

Proposition 3.4.2. *Let λ_1 be the smallest positive eigenvalue in* (1.63). *Suppose $\Omega_1 \Subset D$, λ_1 is simple and normalize the respective eigenvector $\hat{w}$ in order to satisfy*

$$\int_\Omega (\sigma(u) \cdot \nabla \hat{w}) \cdot \nabla \hat{w} dV = -1. \tag{3.19}$$

Then λ_1 is shape differentiable and the shape derivative in the direction θ at 0 reads

$$
\begin{aligned}
\lambda_1'(\Omega_1)(\theta) &= \lambda_1 \int_{\partial\Omega_1} [\![\sigma(u)_{tt}]\!]\partial_t\hat{w}\partial_t\hat{w}\,(\theta \cdot n)dS \\
&+ \int_{\partial\Omega_1}\Big(\sigma(p)_{nn}[\![e(u)_{nn}]\!] + 2\sigma(p)_{nt}[\![e(u)_{nt}]\!] - [\![\sigma(u)_{tt}]\!]e(p)_{tt}\Big)\,(\theta\cdot n)dS \\
&+ \int_{\partial\Omega_1}\Big((\mathcal{D}\nabla^2\hat{w})_{nn}[\![(\nabla^2\hat{w})_{nn}]\!] + 2[\![(\mathcal{D}\nabla^2\hat{w})_{nt}]\!](\nabla^2\hat{w})_{nt} - [\![(\mathcal{D}\nabla^2\hat{w})_{tt}]\!](\nabla^2\hat{w})_{tt}\Big)\,(\theta\cdot n)dS,
\end{aligned}
$$

where $[\![\cdot]\!] = \cdot_1 - \cdot_0$ denotes the jump of a discontinuous quantity through $\partial\Omega_1$, $\sigma = \mathcal{A}e(u)$ and the index n, t indicate the normal and tangential components.

Proof. When supposing λ_1 simple, its shape differentiability follows from classical arguments [260]. Now, so as to apply Céa's fast derivation method, the first step is to define the Lagrangian $\mathcal{L}$ on each sub-domain Ω_0, Ω_1

$$
\begin{aligned}
&\mathcal{L}(\Sigma, \eta_0, \eta_1, v_0, v_1, q_0, q_1, \Lambda, z_1, z_2, \gamma_1, \gamma_2) \\
&= \Lambda - \sum_{i=0,1}\left\{\Lambda\int_{\Omega_i}(\mathcal{A}_i e(v_i)\cdot\nabla\eta_i)\cdot\nabla\eta_i dV + \int_{\Omega_i}(\mathcal{D}_i\nabla^2\eta_i) : \nabla^2\eta_i dV + \int_{\Omega_i}\sigma_i(v_i) : e(q_i)dV\right\} \\
&+ \int_{\Gamma_N} g\cdot q_0 dS \\
&+ \int_\Sigma z_1(v_0 - v_1)dS + \int_\Sigma z_2(q_0 - q_1)dS + \int_\Sigma \gamma_1(\eta_0 - \eta_1)dS + \int_\Sigma \gamma_2(\nabla\eta_0\cdot n - \nabla\eta_1\cdot n)dS,
\end{aligned}
$$

where the four natural interface transmission conditions where added by means of the multipliers $z_1, z_2, \gamma_1, \gamma_2$. The stationarity conditions of $\mathcal{L}$ w.r.t. each argument yield the state equation, adjoint equation and boundary conditions. Then the shape derivative of λ_1 results from $\partial\mathcal{L}/\partial\Sigma$. We proceed thus to take the partial derivatives w.r.t. each variable and verify each condition:

State equation and stress transmission condition:

$$\frac{\partial}{\partial q_i}\mathcal{L}(\partial\Omega_1, w_0, w_1, u_0, u_1, p_0, p_1, \lambda_1, Z_1, Z_2, G_1, G_2, G_3, G_4) = 0,\ i = 0, 1.$$

Let the test function $\phi \in H_D^1(\Omega; \mathbb{R}^2)$

$$
\begin{aligned}
0 &= \left\langle\frac{\partial}{\partial q_i}\mathcal{L}(\Sigma_1, w_0, w_1, u_0, u_1, p_0, p_1, \lambda_1, Z_1, Z_2, G_1, G_2), \phi\right\rangle \\
&= -\int_{\Omega_i}\sigma_i(u_i) : e(\phi)dV + \int_{\Gamma_N} g\cdot\phi dS + \int_{\partial\Omega_1}(-1)^i Z_2\phi dS \\
&= \int_{\Omega_i}\text{div}(\sigma_i(u_i))\cdot\phi dV + \int_{\Gamma_N}(g - \sigma_0(u_0)\cdot n_0)\cdot\phi dS + \int_{\partial\Omega_1}((-1)^i Z_2 - \sigma_i(u_i)\cdot n_i)\phi.
\end{aligned}
$$

The above set of equations entails the state equation and the Neumann boundary condition for the in-plane displacements $u_0, u_1 \in H_D^1(\Omega; \mathbb{R}^2)$. Also the stress transmission condition on $\partial\Omega_1$

$$Z_2 = \sigma_0(u_0)\cdot n = \sigma_1(u_1)\cdot n,\ \text{with } n = n_0.$$

Transmission conditions of the in-plane displacements and adjoint state:

$$\frac{\partial}{\partial z_j}\mathcal{L}(\partial\Omega_1, w_0, w_1, u_0, u_1, p_0, p_1, \lambda_1, Z_1, Z_2, G_1, G_2) = 0, \ j = 1, 2.$$

Namely $u_0 = u_1$; $\ p_0 = p_1$, on $\partial\Omega_1$.

First two transmission conditions of the vertical displacement

$$\frac{\partial}{\partial\gamma_j}\mathcal{L}(\partial\Omega_1, w_0, w_1, u_0, u_1, p_0, p_1, \lambda_1, Z_1, Z_2, G_1, G_2) = 0, \ j = 1, 2$$

Namely $w_0 = w_1$; $\ \nabla w_0 \cdot n = \nabla w_1 \cdot n$, with $n = n_0$, on $\partial\Omega_1$.

Adjoint state equation and second transmission condition.

$$\frac{\partial}{\partial v_i}\mathcal{L}(\partial\Omega_1, w_0, w_1, u_0, u_1, p_0, p_1, \lambda_1, Z_1, Z_2, G_1, G_2) = 0, \ i = 0, 1.$$

Let the test function $\phi \in H_D^1(\Omega; \mathbb{R}^2)$

$$\begin{aligned}
0 &= \left\langle \frac{\partial}{\partial v_i}\mathcal{L}(\partial\Omega_1, w_0, w_1, u_0, u_1, p_0, p_1, \lambda_1, Z_1, Z_2, G_1, G_2), \phi \right\rangle \\
&= -\lambda_1 \int_{\Omega_i} (\mathcal{A}_i e(\phi) \cdot \nabla w_i) \cdot \nabla w_i dV - \int_{\Omega_i} \sigma_i(\phi) : e(p_i) dV \\
&\quad + \int_{\Sigma_1} Z_1(-1)^i \phi.
\end{aligned}$$

So integrating by parts,

$$\begin{aligned}
0 &= \lambda_1 \int_{\Omega_i} \operatorname{div}(b_i(w_i, w_i))\phi dV + \int_{\Omega_i} \operatorname{div}(\sigma_i(p_i)) \cdot \phi dV \\
&\quad - \int_{\Gamma_N} \sigma_i(p_i) \cdot n_i \phi dS - \lambda_1 \int_{\Gamma_N} b_i(w_i, w_i) \cdot n_i \phi dS \\
&\quad + \int_{\partial\Omega_1} \left(Z_1(-1)^i - \sigma_i(p_i) \cdot n_i - \lambda_1 b_i(w_i, w_i) \cdot n_i\right)\phi dS,
\end{aligned}$$

where the bilinear form $b_i(\eta_1, \eta_2)$ for $\eta_1, \eta_2 \in H^2$ reads

$$b_i(\eta_1, \eta_2) = \mathcal{A}_i : (\nabla\eta_1^T \nabla\eta_2), \quad \text{so} \quad (\sigma_i(u_i) \cdot \nabla w_i) \cdot \nabla w_i = b_i(w_i, w_i) : e(u_i).$$

By varying the values of ϕ inside Ω_i the adjoint equation reads

$$-\operatorname{div}(\sigma_i(p_i)) = \lambda_1 \operatorname{div}(b_i(w_i, w_i)) \quad \text{in } \Omega_i,$$

with $p_i = 0$ on Γ_D. Furthermore

$$\sigma(p) \cdot n = -\lambda_1 b(w, w) \cdot n \quad \text{on } \Gamma_N,$$

and the multiplier Z_1 fulfills on $\partial\Omega_1$

$$Z_1 = \sigma_0(p_0) \cdot n + \lambda_1 b_0(w_0, w_0) \cdot n = \sigma_1(p_1) \cdot n + \lambda_1 b_1(w_1, w_1) \cdot n, \ n = n_0$$

gives the second transmission condition of the adjoint state p.

State equation vertical displacements:

$$\frac{\partial}{\partial \eta_i} \mathcal{L}(\partial \Omega_1, w_0, w_1, u_0, u_1, p_0, p_1, \lambda_1, Z_1, Z_2, G_1, G_2) = 0, \ i = 0, 1$$

Let the test function $\Phi \in H_D^2(\Omega)$

$$
\begin{aligned}
0 &= \left\langle \frac{\partial}{\partial \eta_i} \mathcal{L}(\partial \Omega_1, w_0, w_1, u_0, u_1, p_0, p_1, \lambda_1, Z_1, Z_2, G_1, G_2), \Phi \right\rangle \\
&= -2\lambda_1 \int_{\Omega_i} (\mathcal{A}_i e(u_i) \cdot \nabla \Phi) \cdot \nabla w_i dV - 2 \int_{\Omega_i} (\mathcal{D}_i \nabla^2 \Phi) : \nabla^2 w_i dV \\
&\quad + \int_{\partial \Omega_1} G_1 (-1)^i \Phi dS + \int_{\partial \Omega_1} G_2 (-1)^i \nabla \Phi \cdot n dS
\end{aligned}
$$

Integrating by parts, we find

$$
\begin{aligned}
0 &= 2\lambda_1 \left\{ \int_{\Omega_i} (\sigma_i(u_i) \nabla^2 w_i) \Phi dV - \int_{\partial \Omega_i} (\sigma_i(u_i) \cdot \nabla w_i) \cdot n_i \Phi dS \right\} \\
&\quad + 2 \int_{\partial \Omega_i} \mathrm{div}(\mathcal{D}_i \nabla^2 w_i) \cdot n_i \Phi dS - 2 \int_{\partial \Omega_i} (\mathcal{D}_i \nabla^2 w_i) \cdot n_i \cdot \nabla \Phi dS - 2 \int_{\Omega_i} \nabla^2 (\mathcal{D}_i \nabla^2 w_i) \Phi dV \\
&\quad + \int_{\partial \Omega_1} G_1 (-1)^i \Phi dS + \int_{\partial \Omega_1} G_2 (-1)^i \nabla \Phi \cdot n dS \qquad\qquad (3.20)
\end{aligned}
$$

Varying the values of the test function Φ in each Ω_i, we deduce the state equation for the vertical displacement

$$\nabla^2 (\mathcal{D}_i \nabla^2 w_i) = \lambda_1 \sigma_i(u_i) : \nabla^2 w_i, \text{ in } \Omega_i.$$

Furthermore $w_i = 0, \partial_n w_i = 0$ on Γ_D. Equally using the independence of $(\Phi, \partial_t \Phi)$ w.r.t. the normal derivative $\partial_n \Phi$ on $\partial \Omega_i$, we obtain the free boundary conditions on Γ_N

$$-\lambda_1 (\sigma_i(u_i) \cdot \nabla w_i) \cdot n_i + \left(\mathrm{div}(\mathcal{D}_i \nabla^2 w_i) \cdot n_i + \frac{\partial}{\partial \tau} (\mathcal{D}_i \nabla^2 w_i)_{n\tau} \right) = 0,$$

$$(\mathcal{D}_i \nabla^2 w_i)_{nn} = 0,$$

where the second term of the second row of (3.20) was developed as

$$
\begin{aligned}
\int_{\partial \Omega_i} (\mathcal{D}_i \nabla^2 w_i) \cdot n_i \cdot \nabla \Phi dS &= \int_{\partial \Omega_i} (\mathcal{D}_i \nabla^2 w_i)_{nn} \partial_n \Phi dS + \int_{\partial \Omega_i} (\mathcal{D}_i \nabla^2 w_i)_{nt} \partial_t \Phi dS \\
&= \int_{\partial \Omega_i} (\mathcal{D}_i \nabla^2 w_i)_{nn} \partial_n \Phi dS - \int_{\partial \Omega_i} \partial_t (\mathcal{D}_i \nabla^2 w_i)_{nt} \Phi dS.
\end{aligned}
$$

The optimal values for the multipliers G_1, G_2 on $\partial \Omega_1$ reads

$$G_1 = -2 \left\{ -\lambda_1 (\sigma_i(u_i) : \nabla w_i) \cdot n_i + \left(\mathrm{div}(\mathcal{D}_i \nabla^2 w_i) \cdot n_i + \frac{\partial}{\partial \tau} (\mathcal{D}_i \nabla^2 w_i)_{n\tau} \right) \right\}, i = 0, 1,$$

$$G_2 = 2(\mathcal{D}_i \nabla^2 w_i)_{nn}, i = 0, 1,$$

giving rise to the third and fourth transmission conditions of the vertical displacement w_0, w_1.

Normalization of the vertical displacement

$$\frac{\partial}{\partial \Lambda} \mathcal{L}(\partial \Omega_1, w_0, w_1, u_0, u_1, p_0, p_1, \lambda_1, Z_1, Z_2, G_1, G_2) = 0$$

We perform a classical derivation with respect to the scalar Λ to obtain (3.19), namely

$$0 = 1 - \sum_{i=0,1} \int_{\Omega_i} (\sigma_i(u_i) \cdot \nabla w_i) \cdot w_i dV, \quad \text{so:} \quad -1 = \int_{\Omega} (\sigma(u) \cdot \nabla w) \cdot \nabla w dV.$$

Shape derivative Let $\theta \in W^{1,\infty}(\Omega; \mathbb{R}^2)$ such that $\theta \cdot n = 0$ on $\partial\Omega$. Then

$$\frac{\partial}{\partial\Sigma}\mathcal{L}(\partial\Omega_1, w_0, w_1, u_0, u_1, p_0, p_1, \lambda_1, Z_1, Z_2, G_1, G_2, G_3, G_4)(\theta) = \lambda_1'(\Omega_1)(\theta).$$

Thus,

$$
\begin{aligned}
\lambda_1'(\Omega_1)(\theta) \; = \; & -\int_{\partial\Omega_1}\left\{\lambda_1[\![(\sigma(u)\cdot\nabla w)\cdot\nabla w]\!] + [\![(\mathcal{D}_i\nabla^2 w):\nabla^2 w]\!] + [\![\sigma(u):e(p)]\!]\right\}(\theta\cdot n)dS \\
& + \int_{\partial\Omega_1} Z_1\partial_n(u_0 - u_1)(\theta\cdot n)dS + \int_{\partial\Omega_1} Z_2\partial_n(p_0 - p_1)(\theta\cdot n)dS \\
& + \int_{\partial\Omega_1} G_2\partial_n(\nabla w_0\cdot n - \nabla w_1\cdot n)(\theta\cdot n)dS \\
= \; & -\int_{\partial\Omega_1}\left\{\lambda_1[\![(\sigma(u)\cdot\nabla w)\cdot\nabla w]\!] + [\![(\mathcal{D}_i\nabla^2 w):\nabla^2 w]\!] + [\![\sigma(u):e(p)]\!]\right\}(\theta\cdot n)dS \\
& + \int_{\partial\Omega_1}(\sigma(p)\cdot n + \lambda_1 b(w,w)\cdot n)\partial_n(u_0 - u_1)(\theta\cdot n)dS + \int_{\partial\Omega_1}(\sigma(u)\cdot n)\partial_n(p_0 - p_1)(\theta\cdot n)dS \\
& + 2\int_{\partial\Omega_1}(\mathcal{D}\nabla^2 w)_{nn}\partial_n(\nabla w_0\cdot n - \nabla w_1\cdot n)(\theta\cdot n)dS,
\end{aligned}
$$

where various terms where canceled according to the transmission conditions (notably those involving the curvature in the second and third row) and the optimal values of Z_1, Z_2, G_2 employed. Moreover since $u_0 - u_1 = 0, \nabla(w_0 - w_1)\cdot n = 0$ on $\partial\Omega_1$, the following relations stand on $\partial\Omega_1$

$$
\begin{aligned}
(b_i(w_i, w_i)\cdot n)\cdot\partial_n(u_0 - u_1) &= 2(b_i(w_i, w_i)\cdot n)\cdot(e(u_0 - u_1)\cdot n) - b_i(w_i, w_i)_{nn}e(u_0 - u_1)_{nn}, \\
\sigma_i(p_i)\cdot n\cdot\partial_n(u_1 - u_0) &= 2(\sigma_i(p_i)\cdot n)\cdot(e(u_1 - u_0)\cdot n) - \sigma_i(p_i)_{nn}e(u_1 - u_0)_{nn},
\end{aligned}
$$

and also

$$
\begin{aligned}
\sigma(u)\cdot n\cdot\partial_n(p_0 - p_1) &= 2(\sigma(u)\cdot n)\cdot(e(p_1 - p_0)\cdot n) - \sigma(u)_{nn}e(p_1 - p_0)_{nn}, \\
(\mathcal{D}\nabla^2 w)_{nn}\partial_n(\nabla(w_0 - w_1)\cdot n) &= 2((\mathcal{D}\nabla^2 w)\cdot n)\cdot(\nabla^2(w_0 - w_1)\cdot n) - (\mathcal{D}\nabla^2 w)_{nn}(\nabla^2(w_0 - w_1))_{nn}.
\end{aligned}
$$

Inserting these relations in the cascade of equations for λ_1' yields

$$
\begin{aligned}
\lambda_1'(\Sigma_1) \; = \; & \lambda_1\int_{\partial\Omega_1}[\![b(w,w)_{tt}\cdot e(u)_{tt}]\!](\theta\cdot n)dS \\
& + \int_{\partial\Omega_1}[\![\sigma(p)_{nn}e(u)_{nn} + 2\sigma(p)_{nt}e(u)_{nt} - \sigma(u)_{tt}e(p)_{tt}]\!](\theta\cdot n)dS \\
& + \int_{\partial\Omega_1}[\![(\mathcal{D}\nabla^2 w)_{nn}(\nabla^2 w)_{nn} + 2(\mathcal{D}\nabla^2 w)_{nt}(\nabla^2 w)_{nt} - (\mathcal{D}\nabla^2 w)_{tt}(\nabla^2 w)_{tt}]\!](\theta\cdot n)dS.
\end{aligned}
$$

The desired result stems from the continuity relations

$$
\begin{aligned}
[\![(\mathcal{D}\nabla^2 w)_{nn}]\!] &= 0, \quad [\![(\nabla^2 w)_{nt}]\!] = 0, \quad [\![(\nabla^2 w)_{tt}]\!] = 0, \\
[\![(\sigma(p))_{nn}]\!] &= 0, \quad [\![(\sigma(p))_{nt}]\!] = 0, \quad [\![(e(p))_{tt}]\!] = 0, \\
[\![(\sigma(u))_{nn}]\!] &= 0, \quad [\![(\sigma(u))_{nt}]\!] = 0, \quad [\![(e(u))_{tt}]\!] = 0.
\end{aligned}
$$

$\square$

3.4.2 Discrete framework

Similarly to the sharp shape derivative presented in Chapter 2 for a cost functional depending only on u, the rigorous computation of the shape derivative of λ_1 involves jumps of the stress and the strain functions through the interface $\partial\Omega_1$. Nevertheless, these quantities are difficult to estimate numerically. From now on, we avoid any of these technical issues by calculating the shape derivative of the discretized problem which seems to be more useful from a numerical point of view, as it was pointed in Chapter 2.

Thus suppose Ω equipped with a conformal simplicial mesh $\Omega_h = \bigcup_{i=1}^{M} T_i$ with M triangles T_i of maximal size h. Let $\Pi_D^1(\Omega_h; \mathbb{R}^2)$ be a finite-dimensional approximation of $H_D^1(\Omega; \mathbb{R}^2)$, for instance the space of $\mathbb{P}^1$ Lagrange finite elements. Define $u_h \in \Pi_D^1(\Omega_h; \mathbb{R}^2)$ as the internal approximations of u, solution of

$$\int_{\Omega_h} \mathcal{A}e(u_h) : e(v_h)\, dV = \int_{\Gamma_N} g \cdot v_h\, dS, \quad \forall v_h \in \Pi_D^1(\Omega_h; \mathbb{R}^2), \tag{3.21}$$

and $\sigma_h = \mathcal{A}e(u_h)$. Let ξ be a fixed stacking sequence. In order to facilitate the analysis, the discretization of functional (b) (3.6) is split into two cases $G_{h,1}, G_{h,2}$ given by the smooth densities s_1, s_2

$$G_{h,1}(\Omega_1, \xi) = \int_{\Omega_h} s_1(x, u_h(\Omega_1, \xi))dV \quad and \quad G_{h,2}(\Omega_1, \xi) = \int_{\Omega_h} s_2(x, \sigma_h(\Omega_1, \xi))dV.$$

The first density function s_1 depends only on the displacement meanwhile the second one s_2 depends on the stress $\sigma_h = \mathcal{A}e(u_h)$. Both satisfy adequate growth conditions. Then the discrete shape derivatives of the foregoing discretized criteria are given respectively by the following propositions

Proposition 3.4.3. *Assume that the interface $\partial\Omega_1$ generically cut the mesh Ω_h, namely that it is never aligned with part of an edge of any triangle T_i. Define the discrete adjoint state $p_h \in \Pi_D^1(\Omega_h; \mathbb{R}^2)$ as the solution of*

$$\int_{\Omega_h} \mathcal{A}e(p_h) : e(v_h)\, dV = -\int_{\Omega_h} s_1'(x, u_h) \cdot v_h\, dV, \quad \forall v_h \in \Pi_D^1(\Omega_h; \mathbb{R}^2). \tag{3.22}$$

where the symbol $'$ denotes the differentiation w.r.t. u. Then, the solution u_h of (3.21) is shape differentiable and the shape derivative of $G_{h,1}$ for a fixed ξ is given by

$$G_{h,1}'(\Omega_1, \xi)(\theta) = \int_{\partial\Omega_1} [\![\mathcal{A}]\!] e(u_h) : e(p_h)\, \theta \cdot n\, dS, \tag{3.23}$$

where $[\![\cdot]\!] = \cdot_1 - \cdot_0$ denotes the jump of a discontinuous quantity through $\partial\Omega_1$.

Proof. See Chapter 2. □

Proposition 3.4.4. *Assume the same hypothesis than the above proposition but this time define the discrete adjoint state $p_h \in \Pi_D^1(\Omega_h; \mathbb{R}^2)$ as the solution of*

$$\int_{\Omega_h} \mathcal{A}e(p_h) : e(v_h)\, dV = -\int_{\Omega_h} s_2'(x, \sigma_h) \cdot \mathcal{A}e(v_h)\, dV, \quad \forall v_h \in \Pi_D^1(\Omega_h; \mathbb{R}^2). \tag{3.24}$$

where the symbol $'$ denotes the differentiation w.r.t. σ and $\sigma_h = \mathcal{A}e(u_h)$. Then the shape derivative of $G_{h,2}$ for a fixed ξ is given by

$$G_{h,2}'(\Omega_1, \xi)(\theta) = \int_{\partial\Omega_1} \left([\![s_2(x, \sigma_h)]\!] + [\![\mathcal{A}]\!] e(u_h) : e(p_h) \right) \theta \cdot n\, dS, \tag{3.25}$$

where $[\![\cdot]\!] = \cdot_1 - \cdot_0$ denotes the jump of a discontinuous quantity through $\partial\Omega_1$.

Proof. The demonstration is quite similar to the one of Proposition 3.4.3. The only difference lies in the definition of the Lagrangian, which is

$$\mathcal{L}_h(\theta, v_h, q_h) = \int_\Omega s_2(x, \mathcal{A} \circ (Id + \theta)^{-1} e(v_h)) dV + \int_\Omega \mathcal{A} \circ (Id + \theta)^{-1} e(v_h) : e(q_h) dV - \int_{\Gamma_N} g \cdot q_h dS.$$

$\square$

Now let $\Pi_D^2(\Omega_h)$ be a conformal finite-dimensional subspace of the space $H_D^2(\Omega)$ (so the basis elements are $C^1(\Omega_h)$), e.g. Hermite cubic finite element [160]. Let $w_h \in \Pi_D^2(\Omega_h)$ be the internal approximation of w, solution of the discrete eigenvalue problem

$$\int_{\Omega_h} E(w_h, \eta_h) dV = -\lambda \int_{\Omega_h} B(u_h; w_h, \eta_h) dV, \forall \eta_h \in \Pi_D^2(\Omega_h), \tag{3.26}$$

where u_h solves (3.21). We denote as λ_h the first positive eigenvalue. The bilinear and trilinear forms $E(\eta_1, \eta_2)$ and $B(v, \eta_1, \eta_2)$ are respectively defined $\forall \eta_1, \eta_2 \in \Pi_D^2(\Omega_h), v \in \Pi_D^1(\Omega_h; \mathbb{R}^2)$ as

$$\begin{aligned} E(\eta_1, \eta_2) &:= \mathcal{D}\nabla^2\eta_1 : \nabla^2\eta_2 = \mathcal{D}_{ijkl}\partial_{kl}\eta_1\partial_{ij}\eta_2, \\ B(v; \eta_1, \eta_2) &:= (\mathcal{A}e(v) \cdot \nabla\eta_1) \cdot \nabla\eta_2 = \mathcal{A}_{ijkl}e(v)_{kl}\partial_i\eta_1\partial_j\eta_2. \end{aligned} \tag{3.27}$$

The first positive eigenvalue λ_h of the discretized problem (3.26) can be also defined through the Rayleigh quotient

$$\lambda_h^{-1} = \max_{\eta \in \Pi_D^2(\Omega_h)} \frac{-\int_{\Omega_h} B(u_h; \eta, \eta) dV}{\int_{\Omega_h} E(\eta, \eta) dV}. \tag{3.28}$$

Proposition 3.4.5. *Assume the same hypothesis than Proposition 3.4.3, let $u_h \in \Pi_1(\Omega_h; \mathbb{R}^2)$ be solution of (3.21) and define the discrete adjoint state $\hat{p}_h \in \Pi_D^2(\Omega_h)$ as the solution of*

$$\int_{\Omega_h} \mathcal{A}e(\hat{p}_h) : e(v_h) dV = \lambda_h \int_{\Omega_h} B(v_h; w_h, w_h) dV \quad \forall v_h \in \Pi_D^1(\Omega_h; \mathbb{R}^2).$$

Moreover suppose λ_h is a simple eigenvalue of problem (3.26) and let the buckling mode $w_h \in \Pi_D^2(\Omega_h)$ be normalized as $\int_\Omega B(u_h; w_h, w_h) dV = -1$. Then λ_h is shape differentiable and its shape derivative for a fixed ξ reads

$$\lambda_h'(\Omega_1, \xi)(\theta) = \int_{\partial\Omega_1} \left([\![\mathcal{D}]\!]\nabla^2 w_h : \nabla^2 w_h + \lambda_h([\![\mathcal{A}]\!]e(u_h) \cdot \nabla w_h) \cdot \nabla w_h - [\![\mathcal{A}]\!]e(u_h) : e(\hat{p}_h) \right) \theta \cdot n dS$$

$$\tag{3.29}$$

where $[\![\cdot]\!] = \cdot_1 - \cdot_0$ denotes the jump through $\partial\Omega_1$.

Proof. Let us denote $\omega_i^h(x)$ and $\phi_i^h(x)$ the basis functions of the finite element spaces $\Pi_D^2(\Omega_h)$ and $\Pi_D^1(\Omega_h, \mathbb{R}^2)$, respectively. The solutions $w_h \in \Pi_D^2(\Omega_h)$ and $u_h \in \Pi_D^1(\Omega_h, \mathbb{R}^2)$ are decomposed as

$$w_h = \sum_i W_i^h \omega_i^h(x), \ u_h = \sum_i U_i^h \phi_i^h(x),$$

and the vectors W^h, U^h (with respective components W_i^h, U_i^h) are solutions of

$$E^h W^h = -\lambda_h B^h W^h \text{ and } K^h U^h = G^h, \text{ respectively.} \tag{3.30}$$

The matrices E^h, B^h, K^h and the vector G^h are respectively defined as

$$E^h_{i,j} = \int_{\Omega_h} E(\omega^h_i, \omega^h_j)dV, \ B^h_{ij} = \int_{\Omega_h} B(u_h; \omega^h_i, \omega^h_j)dV,$$

$$K^h_{i,j} = \int_{\Omega_h} \mathcal{A}e(\phi^h_i) : e(\phi^h_j)dV, \ G^h_i = \int_{\Gamma_N} g \cdot \phi^h_i dS. \tag{3.31}$$

We remark that the basis functions ω^h_i and ϕ^h_i are independent of $\partial\Omega_1$. Thus, under the assumption that $\partial\Omega_1$ does not overlap any edge of $T_i \in \Omega_h$, the shape derivatives of K^h, E^h and B^h according to (3.31) and (3.27) read (for more details see Chapter 2)

$$(K^h_{i,j})'(\Omega_1)(\theta) = \int_{\partial\Omega_1} [\![\mathcal{A}]\!]e(\phi^h_i) : e(\phi^h_j)(\theta \cdot n)dS,$$

$$(E^h_{i,j})'(\Omega_1)(\theta) = \int_{\partial\Omega_1} [\![\mathcal{D}]\!]\nabla^2\omega^h_i : \nabla^2\omega^h_j(\theta \cdot n)dS,$$

$$(B^h_{i,j})'(\Omega_1)(\theta) = \int_{\partial\Omega_1} ([\![\mathcal{A}]\!]e(u_h) \cdot \nabla\omega^h_i) \cdot \nabla\omega^h_j(\theta \cdot n)dS + \int_{\Omega_h} (\mathcal{A}e(u'_h(\Omega_1)(\theta)) \cdot \nabla\omega^h_i) \cdot \nabla\omega^h_j dV.$$

The last equality stands from the shape differentiability of u_h (Proposition 3.4.3), which satisfies the equation

$$K^h(U^h)' = -(K^h)'U^h. \tag{3.32}$$

Applying the chain rule lemma, classical spectral theory for matrices tell us that if the matrices E^h and B^h are Fréchet differentiable (shape differentiable) and the eigenvalue λ_h is simple, then the eigenfunction (suitable normalized) w_h and the eigenvalue λ_h are differentiable [260]. Thus, taking the shape derivative of each side of the Rayleigh quotient (3.28) and using equation (3.30), the derivative of λ_h reads

$$\lambda'_h(\Omega_1, \xi)(\theta) = -\frac{^TW^h \left[(E^h)'(\Omega_1)(\theta) + \lambda_h(B^h)'(\Omega_1)(\theta) \right] W^h}{^TW^h B^h W^h}.$$

Choosing w_h such that $\int_\Omega B(u_h; w_h, w_h)dV = {}^TW^h B^h W^h = -1$, it follows

$$\begin{aligned} \lambda'_h(\Omega_1)(\theta) &= \int_{\partial\Omega_1} [\![\mathcal{D}]\!]\nabla^2 w_h : \nabla^2 w_h(\theta \cdot n)dS + \lambda_h \int_{\partial\Omega_1} ([\![\mathcal{A}]\!]e(u_h) \cdot \nabla w_h) \cdot \nabla w_h(\theta \cdot n)dS \\ &+ \lambda_h \int_{\Omega_h} (\mathcal{A}e(u'_h(\Omega_1)(\theta)) \cdot \nabla w_h) \cdot \nabla w_h dV. \end{aligned}$$

Finally the desired result arises from the definition of the adjoint state $\hat{p}_h$ and equation (3.32)

$$\begin{aligned} \lambda_h \int_{\Omega_h} (\mathcal{A}e(u'_h(\Omega_1)(\theta)) \cdot \nabla w_h) \cdot \nabla w_h dV &= \int_{\Omega_h} \mathcal{A}e(\hat{p}_h) : e(u'_h(\Omega_1)(\theta))dV \\ &= -\int_{\partial\Omega_1} [\![\mathcal{A}]\!]e(\hat{p}_h) : e(u_h)(\theta \cdot n)dS. \end{aligned}$$

$\square$

Remark 3.4.6. *When λ_h is not simple, only directional differentiability can be established [260, 99].*

3.5 Stacking sequence optimization

3.5.1 Manufacturing constraints

From an engineering point of view, when a composite laminate is designed, some additional composite design rules must be respected. Following the typical industrial approach (see e.g. Airbus in [63, 49]) we consider the following rules

- (R1) Continuity rule, no more than 4 successive plies with the same angle.

- (R2) Disorientation rule, maximum gap between two adjacent (superposed) plies is 45°.

- (R3) Balanced laminate w.r.t. the principal direction (0°), i.e. same number of plies at 45° and -45°.

- (R4) Minimum proportion of each fiber orientation (typically between 5% and 10 % [125]). We note this proportion as p_n.

- (R5) Symmetric laminate. This ensures to avoid the coupling between in-plane traction and bending of the laminate, eliminating thermal residual stresses from the cooling process after being placed within an autoclave for curing.

Thanks to the stacking sequence matrix ξ, all the above manufacturing constraints can be easily formulated as linear inequalities or equalities

Proposition 3.5.1. *Let $\{0,1\}^{N\times 4}$ be the set of binary matrices of N rows and 4 columns. Define the applications $r_1 : \{0,1\}^{N\times 4} \to \mathbb{R}^{4(N-8)}$, $r_2 : \{0,1\}^{N\times 4} \to \mathbb{R}^{2(N-1)}$, $r_3 : \{0,1\}^{N\times 4} \to \mathbb{R}$, $r_4 : \{0,1\}^{N\times 4} \to \mathbb{R}^4$. Then if $N \geq 5$ the design rules (R1), (R2), (R3), (R4) can be expressed as linear constraints w.r.t the stacking sequence matrix ξ as follows*

$$(R1) \iff r_1(\xi) = \begin{cases} \sum_{m=k}^{k+5} \xi_{mn} - 4 \leq 0 & \forall n = 1,...,4, \forall k = 0,...,N-5, \\ \sum_{m=1}^{3} \xi_{mn} - 2 \leq 0 & \forall n = 1,...,4. \textit{(plane of symmetry)} \end{cases}$$

$$(R2) \iff r_2(\xi) = \begin{cases} \xi_{m1} + \xi_{\ell 2} - 1 \leq 0 & \ell = m+1, \forall m = 1,...,N-1. \\ \xi_{m3} + \xi_{\ell 4} - 1 \leq 0 & \ell = m+1, \forall m = 1,...,N-1. \end{cases}$$

$$(R3) \iff \qquad r_3(\xi) = \sum_{m=1}^{N} \xi_{m3} - \xi_{m4} = 0.$$

$$(R4) \iff \qquad r_4(\xi) = p_n N - \sum_{m=1}^{N} \xi_{mn} \leq 0, \forall n = 1,...,4.$$

The rule $(R5)$ is satisfied by just studying half of the stacking sequence.

Remark 3.5.2. *The above constraint functions $r_1(\xi), r_2(\xi), r_3(\xi), r_4(\xi)$ are affine hence convex.*

Once the design rules have been established, the definition of the feasible stacking sequence set Y follows

Definition 3.5.3. *We define the feasible stacking sequence set Y as*

$$Y = \left\{ \xi = (\xi_{mn}) \in \{0,1\}^{N\times 4} | \sum_{n=1}^{4} \xi_{mn} = 1, \forall m; r_1(\xi) \leq 0; \ r_2(\xi) \leq 0; \ r_3(\xi) = 0; \ r_4(\xi) \leq 0 \right\}.$$

Remark 3.5.4. *The definition of Y is independent of $\mathcal{O}$. This simplification implies that the manufacturing rules are not point-wise (hence not depending on the shape of each ply) but rather global between the plies.*

3.5.2 The constraint margin function

In order to treat problem (3.5) with a decomposition technique (separating continuous and discrete variables), as it will be explained in the next section, an element of paramount importance is the constraint margin function $\mathcal{M}(\mathcal{O})$. The scalar version of this function is defined as

Definition 3.5.5. *Let $G(\mathcal{O}, \xi) \leq 0$ be a general scalar constraint of problem (3.5) which represents a regular measure of the stiffness of the plate, e.g. $G = \lambda_1^{-1} - 1$ or $G = \lambda_{RF}^{-1} - 1$. Then the constraint margin function $\mathcal{M}(\mathcal{O})$ is defined as*

$$\mathcal{M}(\mathcal{O}) = \min_{\xi \in Y} G(\mathcal{O}, \xi). \tag{3.33}$$

In simple words, the constraint margin function represents the value of maximum slackness of the constraint $G \leq 0$. The evaluation of $\mathcal{M}(\mathcal{O})$ implies solving a non-linear integer problem. In general, this kind of problems are quite hard to solve due to the discrete nature of the variables. However, when the problem is linear, quadratic or convex, there exists a collection of algorithms which can be quite efficient [194]. In particular we now check the following property

Proposition 3.5.6. *If the proportions of plies of each fiber orientation is fixed in the laminate, then for every $\xi \in Y$ respecting these proportions, the functions $\lambda_1^{-1}(\mathcal{O}, \xi)$ and $\lambda_{RF}^{-1}(\mathcal{O}, \xi)$ are convex w.r.t. ξ.*

Proof. Define the function

$$l(\xi, w) = -\frac{\int_{\Omega_h} \mathcal{A}(\xi) e(u(\xi)) \cdot \nabla w \cdot \nabla w dV}{\int_{\Omega_h} \mathcal{D}(\xi) \nabla^2 w : \nabla^2 w dV}, \ \xi \in Y, w \in H_D^2(\Omega), \tag{3.34}$$

and denote as $\bar{Y}$ the subset of $\xi \in Y$ respecting the fiber orientation proportions. If we fix a vertical displacement w, then for every $\xi \in \bar{Y}$ the numerator of (3.34) is constant (in particular it does not change sign) thanks to Lemmas 3.2.3 and 3.2.4, meanwhile the denominator is a positive linear function of ξ. Furthermore let $\Lambda \subset H_D^2(\Omega)$ be the set of functions w such that $l(\xi, w) > 0 \ \forall \xi \in \bar{Y}$. Since we suppose the existence of $\lambda_1 > 0$, then $\Lambda \neq \emptyset$. Hence, applying Lemma 3.5.8, for every fixed $w \in \Lambda$ the function $l(\xi, w)$ is convex w.r.t. ξ. Finally noticing that

$$\lambda_1^{-1}(\xi) = \max_{w \in \Lambda} l(\xi, w),$$

the convexity of $\lambda_1^{-1}(\xi)$ stems from the fact that the maximum or supremum of a set of convex functions is convex. On the other hand, by virtue of Lemma 3.5.7, the function (3.35) is concave and positive w.r.t ξ so from definition (3.8),

$$\lambda_{RF}^{-1}(\xi) = \max_{x \in \Omega} \left(\frac{|(\mathcal{A}e(u))_{xx}^-|(\xi)}{\frac{2\pi}{b}\left(\sqrt{\mathcal{D}_{11}(\xi)\mathcal{D}_{22}(\xi)} + \mathcal{D}_{12}(\xi) + 2\mathcal{D}_{33}(\xi)\right)} \right)$$

is equally convex for $\xi \in \bar{Y}$ in view of Lemma 3.5.8. $\square$

Lemma 3.5.7. *For a fixed $\mathcal{O}$, let D_{RF} be the function*

$$D_{RF}(\xi) := \sqrt{\mathcal{D}_{11}(\mathcal{O}, \xi)\mathcal{D}_{22}(\mathcal{O}, \xi)} + \mathcal{D}_{12}(\mathcal{O}, \xi) + 2\mathcal{D}_{33}(\mathcal{O}, \xi), \tag{3.35}$$

numerator of λ_{RF} in (3.8). Then $D_{RF}(\xi)$ is a concave function of ξ.

Proof. Let us fix $\mathcal{O}$. In order to alleviate the notation, we make only explicit the dependency of a function w.r.t. ξ. Now, since the tensor $\mathcal{D}(\xi)$ is a linear function of ξ, the concavity of $D_{RF}(\xi)$ reduces to prove the concavity of the term $\hat{D}(\xi) := \sqrt{\mathcal{D}_{11}(\xi)\mathcal{D}_{22}(\xi)}$. Define the two variable

function $\hat{d}(x_1, x_2) = \sqrt{x_1 x_2}$, with $(x_1, x_2) \in (\mathbb{R}^+)^2 \backslash \{(0,0)\}$. We will prove that $\hat{d}$ is concave on $(\mathbb{R}^+)^2 \backslash \{(0,0)\}$. Indeed, the Hessian matrix of $\hat{d}$ reads

$$\nabla^2 \hat{d}(x_1, x_2) = \begin{pmatrix} -\frac{1}{4(x_1 x_2)^{3/2}} x_2^2 & \frac{1}{4(x_1 x_2)^{1/2}} \\ \frac{1}{4(x_1 x_2)^{1/2}} & -\frac{1}{4(x_1 x_2)^{3/2}} x_1^2 \end{pmatrix}.$$

The first principal minor of $\nabla^2 \hat{d}$ satisfy

$$-\frac{1}{4(x_1 x_2)^{3/2}} x_2^2 < 0, \forall (x_1, x_2) \in (\mathbb{R}^+)^2 \backslash \{(0,0)\},$$

meanwhile the second one satisfy

$$\frac{1}{16(x_1 x_2)^3} x_1^2 x_2^2 - \left(\frac{1}{4(x_1 x_2)^{1/2}}\right)^2 = 0, \forall (x_1, x_2) \in (\mathbb{R}^+)^2 \backslash \{(0,0)\}.$$

Hence $\nabla^2 \hat{d}$ is negative semidefinite and $\hat{d}$ is concave. Finally the desired property follows from the linearity and positiveness of the functions $\mathcal{D}_{11}(\xi), \mathcal{D}_{22}(\xi)$ plus the above properties of $\hat{d}$ by composition. $\qquad \square$

Lemma 3.5.8. *Let $f(\xi) := Y \to \mathbb{R}_*^+$ be a twice differentiable function and define the function $g(\xi) = 1/f(\xi)$. Then if $f(\xi)$ is positive and concave then $g(\xi)$ is convex. In particular if $f(\xi)$ is an affine application, then $g(\xi)$ is convex if and only if $f(\xi)$ is positive.*

Proof. For every $\xi_0 \in Y$, the quadratic form involving the Hessian matrix reads

$$(\nabla^2 g(\xi) \cdot \xi_0) \cdot \xi_0 = \frac{2}{f^3(\xi)} (\nabla f(\xi) \cdot \xi_0)^2 - \frac{1}{f(\xi)^2} (\nabla^2 f(\xi) \cdot \xi_0) \cdot \xi_0.$$

Analyzing each term the result follows. $\qquad \square$

The above result gives us a clue of the importance of exploring adapted method for convex integer programming to evaluate (3.33).

3.5.3 Evaluation of the constraint margin function

Convex case

Among the algorithms for discrete convex optimization, the outer approximation method (OA) distinguishes as one of the most relevant [247, 194]. First introduced by [110] and then extended in [326, 117] for convex problems, the algorithm solves mixed integer programming problems through a finite sequence of alternately non linear programming subproblems (in which the integer variables are fixed) and mixed integer linear problems (MILP). The optimal solution of each subproblem provides a point at which supporting hyperplanes of the functions are generated. These linearizations are collected in an MILP master program who determines the new integer assignment for the next iteration. Even though the OA method is capable of tackle mixed integer problems, in our case we use it in the full discrete case (integer nonlinear programming).

Now we proceed to explain the method. Let be $\mathcal{Y} = \{0, 1\}^{N \times 4}$ and consider the following generalization of problem (3.33)

$$\min_{\xi \in \mathcal{Y}} \left\{ f(\xi) | g(\xi) \leq 0 \right\}, \tag{3.36}$$

where f and g are convex and one-continuously differentiable. Indeed, according to Definition 3.5.3, the constraints defining $Y \subset \mathcal{Y}$ (represented by "$g \leq 0$" in (3.36)) are linear (thus convex) and moreover, as it was proven in Proposition 3.5.6, when the proportions of fiber orientations
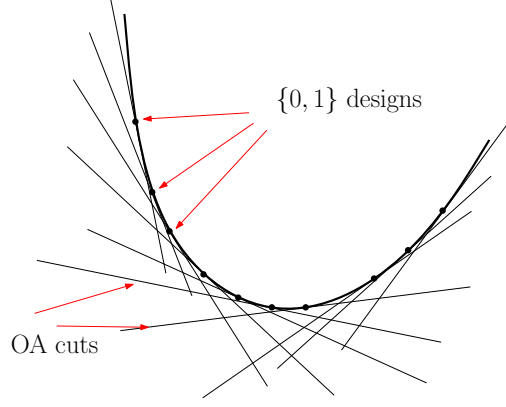
Figure 3.5: Scheme of the Outer approximation method.

are fixed, $G = \lambda_1^{-1}$ and $G = \lambda_{RF}^{-1}$ (represented by "f" in (3.36)) are convex too.

Due to the convexity of the functions f and g, for each $\hat{\xi} \in \mathcal{Y}$ there are linear under-estimators such that

$$
\begin{aligned}
f(\hat{\xi}) + \nabla f(\hat{\xi}) \cdot (\xi - \xi_i) &\leq f(\xi), \ \forall \xi \in \mathcal{Y}, \\
g(\hat{\xi}) + \nabla g(\hat{\xi}) \cdot (\xi - \xi_i) &\leq g(\xi), \ \forall \xi \in \mathcal{Y}.
\end{aligned}
$$

Let $\epsilon > 0$ be a decreasing parameter. Then the OA method reads

Algorithm 3.5.9. *Let ξ^0 be an initial feasible solution of (3.36), $T \subset \mathcal{Y}$ the set of generated admissible solutions so far and ξ^* the current best computed solution. Initialize $T = \{\xi^0\}$ and set the upper bound constant $UBD = +\infty$.*

$\left\{\begin{array}{l}
\textit{For} \quad k \geq 0, \\[1em]
\quad \textit{1) If $(f(\xi^k) \leq UBD - \epsilon)$, then update $\xi^* = \xi^k$ and $UBD = f(\xi^k)$.} \\
\quad \ \textit{Otherwise, do nothing.} \\[1em]
\quad \textit{2) Solve the current master problem:} \\
\quad \textit{(M)} \min\limits_{\xi \in \mathcal{Y}, \eta \in \mathbb{R}} \left\{\eta \ \big| \eta \leq UBD - \epsilon; f(\hat{\xi}) + \nabla f(\hat{\xi}) \cdot (\xi - \hat{\xi}) \leq \eta; g(\hat{\xi}) + \nabla g(\hat{\xi}) \cdot (\xi - \hat{\xi}) \leq 0 \ \forall \hat{\xi} \in T\right\}. \\[1em]
\quad \textit{3) If the problem is infeasible: STOP. The optimal solution is ξ^*.} \\[1em]
\quad \textit{4) Otherwise let ξ^{k+1} be the optimal solution of (M). Update T as $T = T \cup \{\xi^{k+1}\}$} \\
\quad \ \textit{and return to 1).}
\end{array}\right.$

It was proved in [117], that for ϵ small enough, the sequence of points $(\xi^k)_k \in \mathcal{Y}$ generated by the OA algorithm terminates in a finite number of steps at an optimal solution of (3.36).

Remark 3.5.10. *The algorithm can tackle also problems where $\mathcal{Y}$ is a general finite set and in the worst of cases, the algorithm takes $|\mathcal{Y}|$ steps before convergence.*

Remark 3.5.11. *Since all the constraints defining the set $Y \subset \mathcal{Y}$ in (3.33) are linear, there is no need of any under-estimator.*

Extension to the non-convex case

In the situation where the proportions of plies with a fiber orientation is not fixed, problem (3.33) is not necessarily convex, hence an extension of the OA method must be introduced. Attempts to generalize OA to solve non-convex problems are proposed e.g. in [177].

In our case we focus our attention on the convexification of (3.36) by means of convex under-estimators [194]. Even though a large family of under-estimators for MILP is available in literature (see e.g. [247]), an important class when treating with binary or boolean variables are the so-called $\alpha-$under-estimators. In fact, taking advantage of the identity

$$\alpha(y^2 - y) \leq 0, \forall y \in [0,1], \forall \alpha \in \mathbb{R}^+,$$

the following classical results stands

Lemma 3.5.12. *Suppose f and g twice-differentiable, and introduce respectively the under-estimators (also called $\alpha-$under-estimator) of f and g on $[0,1]^{N \times 4}$*

$$\hat{f}^\alpha(\xi) = f(\xi) + \alpha \sum_{m,n}(\xi_{mn}^2 - \xi_{mn}), \ \hat{g}^\alpha(\xi) = g(\xi) + \alpha \sum_{m,n}(\xi_{mn}^2 - \xi_{mn}).$$

Then $\forall \xi \in \mathcal{Y}, f(\xi) = \hat{f}^\alpha(\xi), g(\xi) = \hat{g}^\alpha(\xi)$ and for α large enough, $\hat{f}^\alpha, \hat{g}^\alpha$ are convex.

Proof. Since $\mathcal{Y} = \{0,1\}^{N \times 4}$, the first statement follows trivially. Now denote as $\nabla^2 f, \nabla^2 g \in \mathbb{R}^{4N \times 4N}$ the Hessian matrices of f and g, respectively. In such a case, the Hessian matrices of $\hat{f}^\alpha, \hat{g}^\alpha$ read

$$\nabla^2 \hat{f}^\alpha = \nabla^2 f + 2\alpha Id \text{ and } \nabla^2 \hat{g}^\alpha = \nabla^2 g + 2\alpha Id,$$

where $Id \in \mathbb{R}^{4N \times 4N}$ is the identity matrix. Then for large enough α the functions $\hat{f}^\alpha, \hat{g}^\alpha$ are convex. $\square$

Lemma 3.5.12 thus implies, that by choosing a large enough α, we can solve exactly (3.36) through the application of Algorithm 3.5.9 to the convex problem

$$\min_{\xi \in \mathcal{Y}} \left\{ \hat{f}^\alpha(\xi) | \hat{g}^\alpha(\xi) \leq 0 \right\}.$$

An optimal convex $\alpha-$under-estimator can be computed as the smallest coefficient α for which $\nabla^2 \hat{f}^\alpha(\xi)$ and $\nabla^2 \hat{g}^\alpha(\xi)$ are positive semidefinite for every ξ. In the case of quadratic binary problems, the optimal value of α is the absolute value of the smallest eigenvalue of the matrices $\nabla^2 f$ and $\nabla^2 g$. In general cases finding α is quite difficult, so several heuristics have been proposed, e.g. in [247].

3.6 General decomposition framework

The optimization problem of finding the best shape and stacking sequence of a composite plate corresponds to a mixed problem, i.e. a problem where there are two different types of optimization variables. On one side, the shape optimization problem corresponds to a continuous infinite dimensional problem, meanwhile on the other side, the stacking sequence optimization belongs to the class of combinatorial programming problems due to finiteness of the set Y.

In the present section we address the interaction and articulation of continuous and discrete techniques to solve the composite problem (3.5) in the framework of decomposition methods [139]. Decomposition techniques are used to solve large-scale (or complex) problems, replacing them by a sequence of reduced or easier local problems called followers linked by a leader or

master program. This gives rise to a bi-level optimization scheme [105]. These methods prove efficient when the structure of the problem is naturally separable. This separability comes for instance from the structure of the objective function and constraints (e.g. data is block-separable) or when the variables can be split into "complicated" and "simple" ones, for example. We present notably an infinite dimensional adaptation of the scheme *Maxmargin* (from maximum margin or constraint margin) [141, 49].

3.6.1 Maxmargin technique

We start studying problem (3.5) through the general formulation

$$\min_{\mathcal{O} \in \mathcal{U}_{ad}, \xi \in Y} \left\{ J(\mathcal{O}) | G(\mathcal{O}, \xi) \leq 0 \right\}, \tag{3.37}$$

where $G : (\mathcal{U}_{ad} \times Y) \to \mathbb{R}^m$, is a regular general constraint function vector of m components.

Problem (3.37) turns out to be a quasi separable subsystem [141], so thanks to this particular structure, we can write this mixed problem as a bi-level optimization problem whose higher level only relies on the variable $\mathcal{O}$ through a *Maxmargin* scheme

Proposition 3.6.1. *Let $\mathcal{O}^*$ be in $\mathcal{U}_{ad}$. Then $\mathcal{O}^*$ is a global solution of (3.37) if and only if it is a global solution of*

$$\min_{\mathcal{O} \in \mathcal{U}_{ad}} \left\{ J(\mathcal{O}) | \mathcal{M}(\mathcal{O}) \leq 0 \right\}, \tag{3.38}$$

where the vectorial constraint margin function $\mathcal{M}$ reads

$$\mathcal{M}(\mathcal{O}) := \min_{\xi \in Y} \max_{1 \leq i \leq m} \left\{ G_i(\mathcal{O}, \xi) \right\}. \tag{3.39}$$

Proof. Define the set

$$V = \left\{ \mathcal{O} \in \mathcal{U}_{ad} | \exists \xi \in Y \text{ such that } G(\mathcal{O}, \xi) \leq 0 \right\}.$$

It is straightforward that $\mathcal{O}^*$ solves (3.37) if and only if it solves $\min \left\{ J(\mathcal{O}) | \mathcal{O} \in V \right\}$. Then, $\bar{\mathcal{O}} \in V$ if and only if

$$\mathcal{M}(\bar{\mathcal{O}}) = \min_{\xi \in Y} \max_{1 \leq i \leq m} \left\{ G_i(\bar{\mathcal{O}}, \xi) \right\} \leq 0.$$

$\square$

Problem (3.38) has the advantage with respect (3.37) to optimize only over $\mathcal{U}_{ad}$ and not over $\mathcal{U}_{ad} \times Y$. Unfortunately, from a numerical point of view, global optimality (as formulated in Proposition 3.6.1) is difficult to reach when e.g. no convexity properties are present. We must thus conform ourselves with a local optimum. If we define a *local solution* of (3.37) as an element $\mathcal{O} \in \mathcal{U}_{ad}$ satisfying the local optimality conditions of (3.37) for a fixed assignment of integer variables $\xi \in Y$, then one can demonstrate (see [141]) that the *Maxmargin* scheme does not introduce any artificial local minimum. In other words, any local minimum of the decomposition formulation (3.38) is indeed a local minimum of the original problem (3.37).

Remark 3.6.2. *In the present work, local optimality in $\mathcal{U}_{ad}$ will be understood in the sense of Definition 1.1.14, i.e. $\hat{\mathcal{O}}$ is a local minimizer of J if and only if there exist $\delta > 0$ such that for every collection of vector fields $\Theta = \{\theta_i\}_{i=1,..,N}$ (where each $\theta_i \in W^{1,\infty}(\Omega; \mathbb{R}^2)$ corresponds to the advection field of the ply i),*

$$J(\hat{\mathcal{O}}) \leq J((Id + t\Theta)\hat{\mathcal{O}}), \forall t \leq \delta.$$

For other kinds of local optimality conditions, see [64].

3.6.2   First order optimality conditions

As it was quoted in [141], generally the constraint margin function $\mathcal{M}$ is non-smooth and is not known analytically. The reason of this is that the optimization problem posed by $\mathcal{M}$ may have many solutions. As a consequence the bi-level problem (3.38) is usually non-differentiable. There exits various strategies to tackle this kind of bi-level optimization problem [218, 105]. We can cite e.g. the construction of piece-wise continuous approximation or response surface of $\mathcal{M}$; non-smooth adaptations of classical algorithms (penalty, trust region, descent or feasible direction methods); and non-smooth algorithms as bundle methods.

In order to write the first order optimality conditions (stationarity conditions) of problem (3.38), we need to differentiate a non-differentiable shape function $\mathcal{M}$. This problem has been treated e.g. in [285]. The idea in our case is to invoke the notion of generalized gradient introduced in [91] for Lipschitz functions (see for instance [99]).

Lemma 3.6.3. *For a fixed $\xi \in Y$ and $\mathcal{O} \in \mathcal{U}_{ad}$, let the constraint function $G((Id + \Theta)\mathcal{O}, \xi)$ be continuously shape differentiable on $U \subset W^{1,\infty}(\Omega; \mathbb{R}^2)^N$, a neighborhood (thus bounded) of $\Theta = 0$. Then the function $\mathcal{M}((Id + \Theta)\mathcal{O})$ is locally Lipschitz on U, i.e. there exists $K > 0$ such that*

$$|\mathcal{M}((Id + \Theta_1)\mathcal{O}) - \mathcal{M}((Id + \Theta_2)\mathcal{O})| \le K \, \|\Theta_1 - \Theta_2\|_{W^{1,\infty}(\Omega;\mathbb{R}^2)^N} \, , \forall \Theta_1, \Theta_2 \in U.$$

Proposition 3.6.4. *Denote $\mathcal{M}(\mathcal{O}, \xi) := \max_{1 \le i \le m} G_i(\mathcal{O}, \xi)$, for a fixed choice of $\mathcal{O} \in \mathcal{U}_{ad}, \xi \in Y$. Then there exists a sub-gradient (generalized gradient) $\partial \mathcal{M} \subset (W^{1,\infty}(\Omega; \mathbb{R}^2)^N)'$ of $\mathcal{M}((Id + \Theta)\mathcal{O})$ at $\Theta = 0$ and it reads*

$$\partial \mathcal{M}(\mathcal{O}) = co\Big\{\partial \mathcal{M}(\mathcal{O}, \xi), \xi \in I_Y(\mathcal{O})\Big\} = co\Big\{G_j'(\mathcal{O}, \xi), \xi \in I_Y(\mathcal{O}), j \in I_\lambda(\mathcal{O}, \xi)\Big\},$$

where $co\,\{\}$ is the convex hull and the sets $I_Y(\mathcal{O})$ and $I_\lambda(\mathcal{O}, \xi)$ are respectively defined as

$$
\begin{aligned}
I_Y(\mathcal{O}) &= \Big\{\xi \in Y | \mathcal{M}(\mathcal{O}) = \mathcal{M}(\mathcal{O}, \xi)\Big\} \\
I_\lambda(\mathcal{O}, \xi) &= \Big\{1 \le j \le m | \mathcal{M}(\mathcal{O}, \xi) = G_j(\mathcal{O}, \xi)\Big\}.
\end{aligned}
\tag{3.40}
$$

Proof. Apply Proposition 2.3.12 of [91] twice, using the fact that

$$\min_{\xi \in Y} \max_{1 \le j \le m} \{G_j\} = -\max_{\xi \in Y} -\{\max_{1 \le j \le m} \{G_j\}\} \text{ and } \partial(sG) = s\partial G, \forall s \in \mathbb{R}.$$

$\square$

Proposition 3.6.5. *The directional derivative of $\mathcal{M}((Id + \Theta)\mathcal{O})$ at the point $\Theta = 0$ in the direction Θ_0 exists and its reads*

$$\mathcal{M}'(\mathcal{O})(\Theta_0) = \max_{\xi \in I_Y(\mathcal{O}), j \in I_\lambda(\mathcal{O}, \xi)} G_j'(\mathcal{O}, \xi)(\Theta_0),$$

where the sets $I_Y(\mathcal{O})$ and $I_\lambda(\mathcal{O}, \xi)$ are given in (3.40).

Proof. Use Proposition 3.6.4 and the definition of directional derivative [91]

$$\mathcal{M}'(\mathcal{O})(\Theta_0) = \max_{\zeta \in \partial \mathcal{M}(\mathcal{O})} \langle \zeta, \Theta_0 \rangle = \max_{\xi \in I_Y(\mathcal{O}), j \in I_\lambda(\mathcal{O}, \xi)} G_j'(\mathcal{O}, \xi)(\Theta_0).$$

$\square$

Thus, the necessary optimality condition for a Lipschitz optimization problem can be expressed by means of generalized gradients. In the case of problem (3.38), they may be cast at $\mathcal{O}^* \in \mathcal{U}_{ad}$ as the existence of multipliers $\lambda, \mu \in \mathbb{R}$, not both zero, such that (Th. 6.1.8 [56])

$$\begin{cases} 0 \in \lambda J'(\mathcal{O}^*) + \mu \partial \mathcal{M}(\mathcal{O}^*), \\ \mu \mathcal{M}(\mathcal{O}^*) = 0, \\ \mathcal{M}(\mathcal{O}^*) \leq 0, \\ \lambda, \mu \geq 0. \end{cases} \tag{3.41}$$

Remark 3.6.6. *If there exists $\Theta \in W^{1,\infty}(\Omega; \mathbb{R}^2)^N$ such that $\mathcal{M}'(\mathcal{O})(\Theta) < 0$, then we can take $\lambda = 1$. This is the so-called Mangasarian-Fromovitz constraint qualification (MFCQ) .*

3.6.3 Application of a descent direction method

In this subsection we propose the application of a theoretical descent direction method to (3.38). Generally speaking, a descent direction method searches at each iteration a descent direction able to move from the current point to an approximation of a local solution of (3.38), by using the local information of the gradient of the objective function and constraints. The proximity to the local solution is measured through the fulfillment of the stationarity conditions. From now on we suppose J and G continuously shape differentiable. Let $\epsilon > 0$ be the stop criterion tolerance. Then the descent direction algorithm reads

Algorithm 3.6.7. *Let $\mathcal{O}^0 \in \mathcal{U}_{ad}$ be an initial feasible point of problem (3.38). Define the sequence of designs $\{\mathcal{O}^k\}_k$ generated by the following algorithm*

$$\begin{cases} \text{For } k \geq 0, \\ \qquad 1) \text{ Fix } \mathcal{O}^k \text{ and solve } \mathcal{M}(\mathcal{O}^k) = \min_{\xi \in Y} \max_{1 \leq j \leq m} G_j(\mathcal{O}^k, \xi). \text{ Define } \xi^k \in I_Y(\mathcal{O}^k) \\ \\ \qquad 2) \text{ Via a descent direction method } \mathbb{D}(\mathcal{O}^k, \xi^k) \text{ solve:} \\ \qquad\qquad \text{Find } \mathcal{O}^{k+1} \text{ such that } J(\mathcal{O}^{k+1}) < J(\mathcal{O}^k) \text{ and } G(\mathcal{O}^{k+1}, \xi^k) \leq 0. \\ \\ \qquad 3) \text{ If } |J(\mathcal{O}^{k+1}) - J(\mathcal{O}^k)| \leq \epsilon, \text{ then STOP. Otherwise return to 1)} \end{cases}$$

$$\tag{3.42}$$

Proposition 3.6.8. *Let $\mathbb{D}$ be the descent direction method applied in step 2) for Algorithm 3.6.7, such that for each iteration k*

$$\mathcal{O}^{k+1} = \left(Id + \Delta t^k \Theta^k\right) \mathcal{O}^k,$$

where $\Theta^k \in W^{1,\infty}(\Omega; \mathbb{R}^2)^N$, $\left\|\Theta^k\right\|_{W^{1,\infty}(\Omega;\mathbb{R}^2)^N} < 1$ and $\Delta t^k \in (0, 1)$ is an adequate descent step fulfilling $J(\mathcal{O}^{k+1}) < J(\mathcal{O}^k)$ and $G(\mathcal{O}^{k+1}, \xi^k) \leq 0$. Suppose that for a fixed $\xi \in Y$ the method $\mathbb{D}(\mathcal{O}^k, \xi)$ generates a sequence whose limit point $\mathcal{O}^*_\xi$ is a KKT point.
Now consider additionally that there exists a positive constant $C \leq 1$ such that for every k

$$-C \left\|\Theta^k\right\|^2_{W^{1,\infty}(\Omega;\mathbb{R}^2)^N} \geq J'(\mathcal{O}^k)(\Theta^k). \tag{3.43}$$

Then if we set $\epsilon = 0$ in Algorithm 3.6.7, the generated sequence $\{\mathcal{O}^k\}_k$ is convergent in the sense of the L^p norm for characteristic functions. Moreover, the limit point $\mathcal{O}^*$ of this sequence satisfies the stationary conditions (3.41).

Remark 3.6.9. *Let $\{\omega^k\}_k$ be a sequence of measurable subsets of Ω. According to Theorem 1.1.6, we say that $\omega_k \to \omega^* \subset \Omega$ in the sense of the L^p norm for characteristic functions if and only if $\lim_{k\to\infty} \|\chi_{\omega_k} - \chi_{\omega^*}\|_{L^p(\Omega)} = 0$.*

Proof. First of all, the existence of a limit point $\mathcal{O}^*$ of the sequence $\{\mathcal{O}^k\}_k$ follows from the compactness of $\mathcal{U}_{ad}$. Then since $\{J(\mathcal{O}^k)\}_k$ monotonically decreasing, the continuity of J implies that the sequence $\{J(\mathcal{O}^k)\}_k$ is convergent. Define $\rho \in (0,1)$. One can easily show using (3.43) that there exists $t^k > 0$ such that

$$J((Id + t\Theta^k)\mathcal{O}^k) - J(\mathcal{O}^k) \leq \rho t J'(\mathcal{O}^k)(\Theta^k), \quad \forall t \in (0, t^k). \tag{3.44}$$

Choosing $t = \Delta t^k \leq t^k$ in (3.44) and passing to the limit

$$J((Id + \Delta t^k \Theta^k)\mathcal{O}^k) - J(\mathcal{O}^k) \leq -C\rho \Delta t^k \left\|\Theta^k\right\|_{W^{1,\infty}}^2,$$

it follows that $\lim_{k\to\infty} \Delta t^k \left\|\Theta^k\right\|_{W^{1,\infty}}^2 = 0$, since $\{J(\mathcal{O}^k)\}_k$ is convergent. Trivially $\lim_{k\to\infty} \Delta t^k \left\|\Theta^k\right\|_{W^{1,\infty}} = 0$ and then the convergence of the sequence $\{\mathcal{O}^k\}_k$ in the desired sense stems from the fact that (Th. 2.4 ii)[279])

$$d_H\left((Id + \Delta t^k\Theta^k)\mathcal{O}^k, \mathcal{O}^k\right) \leq 2\Delta t^k \left\|\Theta^k\right\|_{W^{1,\infty}} \text{ and } d_H^C\left((Id + \Delta t^k\Theta^k)\mathcal{O}^k, \mathcal{O}^k\right) \leq 2\Delta t^k \left\|\Theta^k\right\|_{W^{1,\infty}},$$

where d_h, d_H^C are respectively the Hausdorff and complementary Hausdorff metrics (see Remark 1.1.10 and [104]), plus the property that the convergence in the sense of d_H and d_H^C implies the convergence in L^p in the sense of characteristic functions (Proposition 2.2.21 [144]).

Finally let be $\mathcal{O}^*$ the limit point of the sequence $\{\mathcal{O}^k\}_k$. Since G is continuous w.r.t. the induced topology of Theorem 1.1.6, for k large enough, the solution ξ^k of the step 1) in Algorithm 3.6.7 can be chosen constant and equal to a certain $\xi^* \in I_Y(\mathcal{O}^*)$. Hence by hypothesis, the method $\mathbb{D}(\mathcal{O}^k, \xi^*)$ generates a sequence whose limit point $\mathcal{O}^*$ satisifes

$$0 = J'(\mathcal{O}^*) + \sum_{i=1}^m \mu_i G'(\mathcal{O}^*, \xi^*), \quad G(\mathcal{O}^*, \xi^*) \leq 0 \quad \text{and} \quad \mu_i G_i(\mathcal{O}^*, \xi^*) = 0, \mu_i \geq 0 \quad \forall i = 1, ..., m.$$

By its very definition $\mathcal{M}(\mathcal{O}^*) = \mathcal{M}(\mathcal{O}, \xi^*) \leq 0$, so in order $\mathcal{O}^*$ to fulfill the stationary conditions (3.41), it only remains to prove that

$$\sum_{i=1}^m \mu_i G'(\mathcal{O}^*, \xi^*) \in \mu \partial \mathcal{M}(\mathcal{O}^*), \mu \geq 0. \tag{3.45}$$

If $\mathcal{M}(\mathcal{O}^*) < 0$, $\mu = 0$ and (3.45) is trivial. Otherwise, $\mathcal{M}(\mathcal{O}^*) = 0$ and the result is enforced by taking $\mu = \sum_{i=1}^m \mu_i$. $\qquad\square$

3.7 Shape representation by the level set method

Consider $\Omega \subset \mathbb{R}^2$ a bounded domain in which all admissible shapes are included. In numerical practice, the domain Ω will be uniformly meshed once and for all. We apply the level set method described in Section 1.2 to implicitly represent the collection of shapes $\Omega_i \subset \Omega$ of the composite laminate. We define thus the collection of level set functions $\{\psi_i\}_i$ such that

$$\begin{cases} \psi_i(x) = 0 & \text{if } x \in \partial\Omega_i \\ \psi_i(x) > 0 & \text{if } x \in \Omega_i \\ \psi_i(x) < 0 & \text{if } x \in \Omega \backslash \overline{\Omega}_i \end{cases}$$

The normal n_i and the mean curvature κ_i of each ply are recovered thanks to equations (1.31). In order to compute the extensional and the bending stiffness tensors in (3.1) and (3.2) or (3.3), we rely on (1.43) to approximate χ_i.

During the optimization process, the set of shapes $\{\Omega_i(t)\}_i$ is going to evolve according to a fictitious time $t \in \mathbb{R}^+$, which corresponds to the descent stepping. The evolution of each level set function ψ_i is governed by a Hamilton-Jacobi equation (1.35). The velocity advection field is provided by the "partial" shape derivative of the cost functional, as it was explained in the second part of Section 1.2.

When computing the shape derivative w.r.t. each ply, notably at the initialization of the algorithm where the shapes of all plies coincide, we avoid the non-differentiability problem evoked in Remark 3.4.1 by considering a smoothed version of the discontinuous elastic properties (see Remark 2.5.1). Similarly to the smoothed framework introduced in Chapter 2, although adapted to the composite problem at issue, the global extensional stiffness for two plies will read accordingly to (2.49), where

$$
\begin{aligned}
A_0 &= \mathcal{A}_0 + \mathcal{A}_1 + \mathcal{A}_2 \\
A_1 &= \mathcal{A}_0 + \mathcal{A}_1 \\
A_2 &= \mathcal{A}_0 + \mathcal{A}_2 \\
A_3 &= \mathcal{A}_0.
\end{aligned}
$$

Thus, the shapes derivatives w.r.t. each ply stem from equations (2.52) and (2.53) and

$$
\frac{\partial A}{\partial d_{\Omega_1}} = \mathcal{A}_1 \delta_{\epsilon_\delta}(x) \quad \text{and} \quad \frac{\partial A}{\partial d_{\Omega_2}} = \mathcal{A}_2 \delta_{\epsilon_\delta}(x),
$$

where the notations were adapted to δ_{ϵ_δ} and d_{Ω_i}, respectively defined in (1.44) and (1.2.1). Finally, casting the equivalence quoted in Section 2.4 between the sharp and smooth frameworks when the bandwidth of regularization (measured by ϵ_δ) around the interface is small, we approximate the jumps within formulae (3.23), (3.25) and (3.29) w.r.t. the ply i as

$$
[\![\mathcal{A}]\!] = \mathcal{A}_i.
$$

The extension to more than two plies and to the bending stiffness tensor $\mathcal{D}$ follows the same strategy.

3.8   Optimization algorithm

At each iteration of Algorithm 3.6.7, the current stacking sequence and collection of shapes of each ply within the composite are updated. The optimization algorithm can be thus summarized as two nested loops

$\rightarrow$ A higher level loop that solves (3.37) for a fixed stacking sequence via a descent direction method, which is based in a shape sensitivity analysis coupled to a level set method described in Section 1.2.

$\quad \rightarrow$ A lower level loop where the constraint margin function $\mathcal{M}$ is evaluated by solving the integer programming problem (3.33) via Algorithm 3.5.9.

Let N_{stack} be the frequency at which the lower level is solved and $\epsilon > 0$ the stop criterion tolerance. We propose the following iterative optimization algorithm for the composite design problem

Algorithm 3.8.1. *Initialize $\mathcal{O}^0 \in \mathcal{U}_{ad}$ through a collection of level set functions $\{\psi_i^0\}_i$ representing each layer, defined as the signed distance function of a chosen initial topology. Evaluate the constraint margin function $\mathcal{M}(\mathcal{O}^0)$ in (3.39) and define the initial optimal stacking sequence ξ^0.*

$$
\left\{
\begin{array}{l}
\textit{For } k \geq 0, \\[6pt]
\quad \textit{1) Computation of } u^k, \lambda_1^k \textit{ and } w_1^k \textit{ by solving problems (1.63), (1.64).} \\
\quad \textit{If the stiffness criterion is } \lambda_{RF}, \textit{ then only compute of } u^k. \\[8pt]
\quad \textit{2) Calculate in accordance to Section 3.7 the discrete shape derivatives } J_h' \textit{ and } G_h' \\
\quad \textit{in (3.5) w.r.t. each layer.} \\[8pt]
\quad \textit{3) Definition of a set of descent velocities } \Theta^k = \{\mathcal{V}_i^k n_i^k\}_i \textit{ and transport of } \psi_i^k, \\
\quad \textit{pursuant to Section 1.2. The pseudo-time step } \Delta t_i^k \textit{ is chosen so as} \\
\quad \mathcal{O}^{k+1} = (Id + \Delta t_i^k \Theta^k)\mathcal{O}^k, \ J(\mathcal{O}^{k+1}, \xi^k) \leq J(\mathcal{O}^k, \xi^k) \textit{ and } \mathcal{M}(\mathcal{O}^{k+1}, \xi^k) \leq 0. \\[8pt]
\quad \textit{4) Depending if } k \textit{ is a multiple of } N_{stack} \textit{ either} \\[6pt]
\quad\quad \textit{(a) Compute } \xi^{k+1} \textit{ through } \mathcal{M}(\mathcal{O}^{k+1}) \textit{ via the OA method.} \\
\quad\quad \textit{(b) Set } \xi_i^{k+1} = \xi^k. \\[8pt]
\quad \textit{5) If } |J(\mathcal{O}^{k+1}) - J(\mathcal{O}^k)| \leq \epsilon, \textit{ then STOP. Otherwise return to 1)}
\end{array}
\right.
$$

$$(3.46)$$

Remark 3.8.2. *Due to the structure of the optimization algorithm, steps 2) and 3) can be parallelized e.g. via MPI.*

3.9   Numerical results

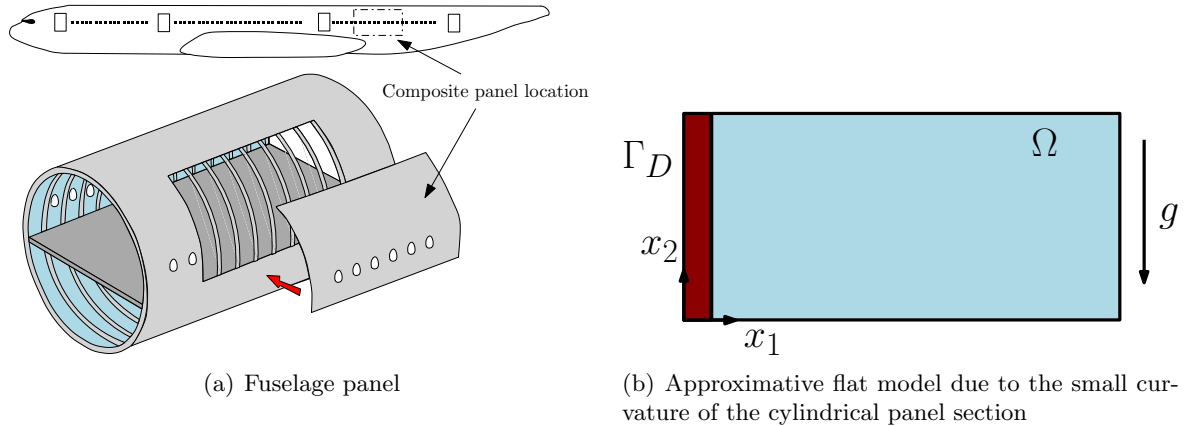### 3.9.1   Test case description

The chosen problem consist in designing a composite fuselage skin panel, subjected to a shear load, as illustrates Figure 3.6. More specifically we try to determine the influence of the orthotropic plies oriented in 45^0 and -45^0 in the prevention of buckling. Due to the small curvature of the cylindrical panel section, an approximative plate model is used. The *hold-all* domain $\Omega = \{x \in [0,2] \times [0,1]\}$ is modeled as a multi-layered plate, in accordance to Configuration I detailed in Section 3.2: Each ply is composed of two phases where the "holes" are filled up with a weaker material $\mathcal{A}_0$. For numerical purposes the tensor $\mathcal{A}_0$ is equal to the main material of each ply multiplied by a factor $1e-3$.

The panel boundary conditions are described in Fig. 3.6, namely Ω is clamped on Γ_D, the upper and lower boundaries are free and a vertical in-plane load g is applied on the right side.

The elastic properties of the main phase of each layer are described through one of the following tensors: $\mathcal{C}_{0^o}, \mathcal{C}_{90^o}, \mathcal{C}_{45^o}, \mathcal{C}_{-45^o}$. Each of them corresponds to the rotation of an orthotropic material $\mathcal{C}$, in accordance to relations (1.54) and (1.55). The elastic parameters of the tensor $\mathcal{C}$ are normalized to Young moduli $E_{x_1} = 1., E_{x_2} = 0.05$, shear modulus $G_{x_1 x_2} = 0.03$ and Poisson ratio $\nu_{x_1 x_2} = 0.3$. These values approximatively match the elastic parameter proportions of carbon fiber/epoxy. The thickness of each ply is fixed to $\varepsilon = 0.125$.

The in-plane elastic and adjoint problems were solved via $\mathbb{P}^1$ Lagrange finite elements, meanwhile the bending problem was solved through Morley finite elements (Piecewise $\mathbb{P}^2$ nonconform). Even though the aforementioned FE is non-conform as assumed in Section 3.4, it is enough for numerical purposes.

(a) Fuselage panel

(b) Approximative flat model due to the small curvature of the cylindrical panel section

Figure 3.6: Composite test case.

As it was evoked in Section 3.8, the composite optimization algorithm 3.46 is made of two loops, namely a lower level loop, which consists in solving the non-linear integer problem (3.33) so as to determine the best stacking sequence, and a higher level loop (see (3.46)) that defines the best in-plane shape for each ply. The lower level loop is solved by means of the *MILP* routine of the commercial software CPLEX (IBM-ILOG) [164] for MATLAB [210], meanwhile the higher level loop is settled via a method of feasible direction for level-set [3] and the software Freefem++ [118]. Freefem++ stands as a versatile non-commercial programming language and software oriented to the resolution of PDE's by means of the finite element method.

Remark 3.9.1. *For the interested reader, we can cite as efficient alternatives to CPLEX the solvers Gurobi [134] and SCIP [330], being the latter one non-commercial. Generally speaking, the aforementioned solvers (also CPLEX) perform a combination of the branch-and-cut method, cutting planes, heuristics, etc., to solve very efficiently mixed integer linear and semi-definite positive quadratic programming problems.*

3.9.2 Previous comments about the algorithm

Before describing the numerical results for the preceding test-case, three issues regarding the proposed algorithm are discussed:

1) Perimeter penalization. Even though the level-set method leans on a sharp interface description for each phase, according to the smeared-out version of the Heaviside function (1.43), there always exists a bandwidth of intermediate elastic material between one phase and another. It is well known in structural optimization (see e.g. [4]), that optimal structures favor intermediate or mixed materials. Hence when dealing with a multi-phase framework, during the optimization process, we observe that each phase attempts to increase the interface length in order to foster intermediate zones along other interfaces. However, from an engineering point of view, one looks for shapes as much smooth and convex as possible, in order to limit the manufacturing cost. Therefore, owing to the foregoing issue plus the existence condition established in (3.7), a small perimeter penalization is added to the objective function (weight). Denoting $P(\mathcal{O})$ the total perimeter of the laminate (i.e. the addition of the perimeters of each ply), the penalization term reads $\gamma P(\mathcal{O})$, where $\gamma = 0.1 \max(\Delta x, \Delta y)$. See also Remark 3.2.6.

2) Uniform distribution of fiber orientations within the laminate. During the optimization process, one also remarks that the proposed algorithm tends to empty (or rather to fill up with the weaker material $\mathcal{A}_0$) the closest laminae to the composite core. Taking as

analogy an Euler-Bernoulli beam, the outer layers contribute more to the inertia moment of the structure than the inner ones. Hence they are preferable to avoid buckling. Additionally, due to the vertical direction of the surface load g for this particular test-case, the principal stress lines promote the use of reinforced fibers in 0° and 45°, which tends to eliminate the rest of reinforcement orientations (especially in 90°).

The foregoing features might be undesirable when e.g. we expect the total mass of the structure to be distributed "uniformly" through the laminate, or minimum proportions of each fiber orientation are required within the composite. In order to limit the above bias, a constraint on the minimum volume of each fiber orientation is applied.

3) Stacking sequence optimization. So as to reduce the numerical cost, the constraint margin function is exactly evaluated only during the first 10 iterations of the algorithm, with a frequency of 5 iterations.

Now we present the optimization problem at issue subjected to different constraints. Since we deal with symmetric laminates, we only present half of the stacking.

3.9.3   Mass minimization with a compliance constraint

We solve the problem

$$
\begin{cases}
\min_{\mathcal{O} \in \mathcal{U}_{ad}} V(\mathcal{O}) \\
\quad \text{s.t.} \\
\qquad \int_{\Omega} \mathcal{A}e(u) : e(u)dV \leq C_0,
\end{cases}
$$

where $\mathcal{O}$ is a 4-layered composite with fiber orientations $0^o, 90^o, -45^0, 45^0$. We remark that according to Lemma 3.2.3 and Lemma 3.2.4 the stacking sequence does not play any role. The constant C_0 is chosen as twice the initial compliance of the structure and the load $g = (0, -1)$ is defined according to Fig 3.6 (b) throughout the right boundary of Ω. The "hold-all" domain Ω is meshed with 30×60 elements. The optimal results between the level-set method and the SIMP method are presented in Fig. 3.7.

3.9.4   Mass minimization with a bending constraint: λ_1

We solve the problem

$$
\begin{cases}
\min_{\mathcal{O} \in \mathcal{U}_{ad}, \xi \in Y} V(\mathcal{O}) + \gamma P(\mathcal{O}) \\
\quad \text{s.t.} \\
\qquad \lambda_1^{-1}(\mathcal{O}, \xi) \leq 1,
\end{cases}
$$

where $\mathcal{O}$ is a 8-layered composite laminate whose optimal stacking sequence and in-plane shape of each ply must be determined. The load $g = (0, -1)$ is defined according to Fig 3.6 (b), but this time on the segment $x = 2, y = [0.75, 1.25]$. Ω is meshed with 51×102 elements. Due to the tendency of the algorithm to eliminate the plies with certain fiber orientations, even if we increase the modulus of the applied load, a volume constraint is applied to the orientations -45° and 90° . The optimal results and the convergence curve are respectively exposed in Fig. 3.8 and Fig 3.9.
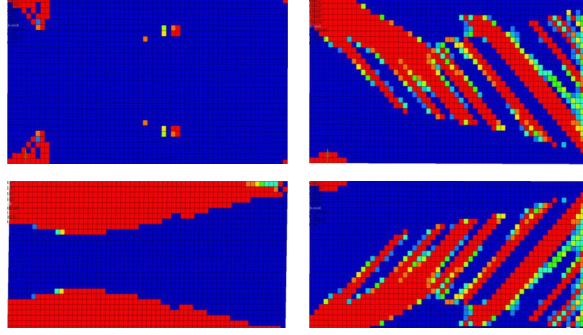
(a) Topology optimization via a SIMP method with the software Optistruct. The red and blue colors represent the highest and lowest densities of material, respectively.
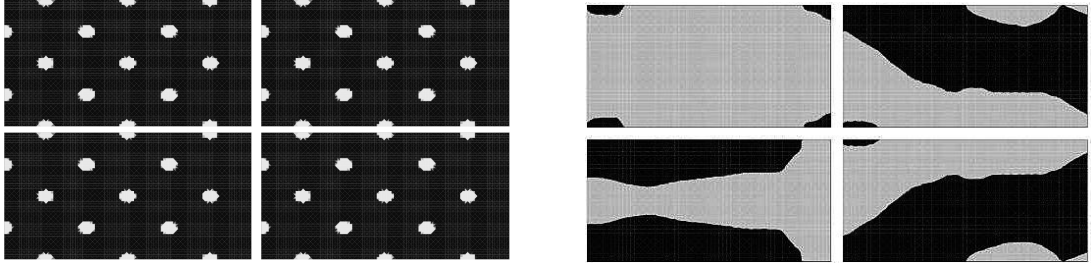
(b) Initial configuration and optimal structure. The black color stands for the material meanwhile white is "void".

Figure 3.7: Comparison between the SIMP method and the level set method for the optimal design of a 4-layered composite according to Problem 3.9.3. The fiber orientations for each set of four figures reads: 90° upper-left, 0^0 lower-left, -45° upper-right and 45° lower-right.

3.9.5   Mass minimization with a bending constraint: λ_{RF}

The last problem we intend to solve is

$$
\begin{cases}
\min_{\mathcal{O} \in \mathcal{U}_{ad}, \xi \in Y} V(\mathcal{O}) + \gamma P(\mathcal{O}) \\
\quad \text{s.t.} \\
\qquad \mathcal{X}(\mathcal{O}, \xi) \leq 1, \\
\qquad \int_{\Omega} \mathcal{A}e(u) : e(u) dV \leq C_0,
\end{cases}
\tag{3.47}
$$

where

$$
\mathcal{X} = \left(\int_{\Omega} \frac{|(\mathcal{A}e(u))_{xx}^-|^p}{(\frac{2\pi}{b} \sqrt{\mathcal{D}_{11}\mathcal{D}_{22}} + \mathcal{D}_{12} + 2\mathcal{D}_{33})^p} dV \right)^{1/p}
$$

is a L^p-approximation of λ_{RF}^{-1}, which according to (3.8) satisfies

$$
\lambda_{RF}^{-1} = \left\| \frac{|(\mathcal{A}e(u))_{xx}^-|}{(\frac{2\pi}{b} \sqrt{\mathcal{D}_{11}\mathcal{D}_{22}} + \mathcal{D}_{12} + 2\mathcal{D}_{33})} \right\|_{L^\infty(\Omega)} \leq 1.
$$

We will take $p = 2$, assuring in this way the differentiability of $|\mathcal{A}e(u))_{xx}^-|$ at 0 (in fact we could have taken any even exponent p). The need of adding a compliance constraint to the problem, is due to the nature of λ_{RF}, which penalizes only the compressed zones inside the solid, allowing the generation of zones under critical positive tensile strains (which indicate that the structure is close to break). Ω is meshed with 51×102 elements. We consider two load cases, namely

First load case

The surface load $g = (0, -1)$ is applied on the segment $x = 2, y = [0.75, 1.25]$ and C_0 equal to three times the initial compliance. The numerical results and the convergence curves are exhibited in Fig. 3.10 and Fig. 3.11, respectively.
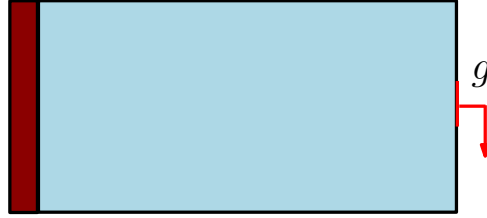
Second load case

The surface load $g = (0, -0.5)$ applied all over the right boundary of Ω and C_0 defined as twice the initial compliance. The numerical results and the convergence curves are exhibited in Fig. 3.12 and Fig. 3.13, respectively.

We remark that in both configurations, the constraints within (3.47) are active at the optimum. Moreover, the optimal design favors the fiber orientations in 45° and -45^0.
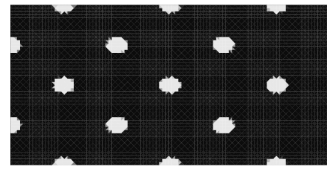
(a) Total density, iteration 0
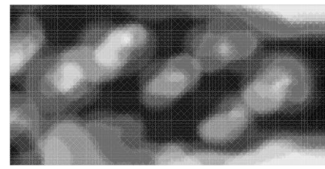
(b) Total density, iteration 5
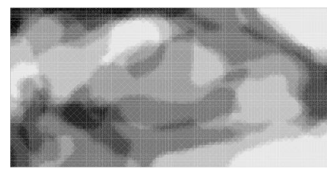
(c) Total density, iteration 10

(d) Final total density (iteration 45)
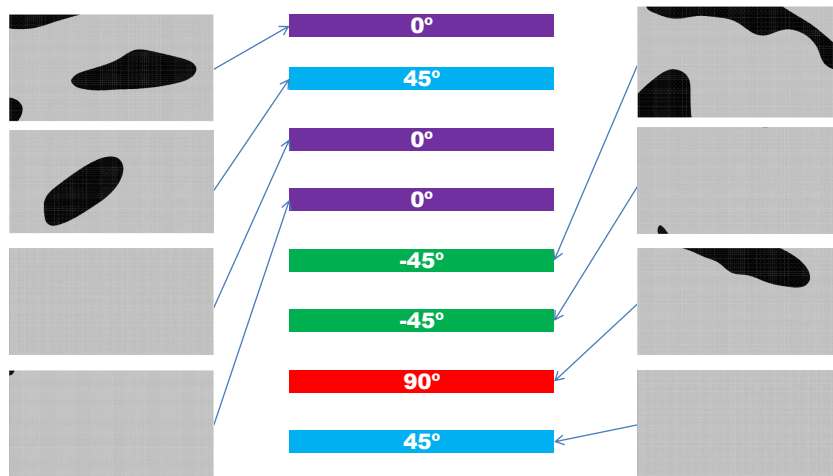
(e) Optimal stacking sequence and shape of each ply. The outer layers are upper in the figure.

Figure 3.8: Results of Problem 3.9.4. (a),(b),(c),(d): Evolution of the total addition of densities of each ply (darker gray means more plies superposed). (e): Optimal stacking sequence and in-plane shape of each ply (black represents material). We remark the presence of the four fiber orientations within the laminate thanks to the imposed constraint on their minimal volumes. Sub-figure (d) looks thicker than the superposition of plies in (e) due to the regularization between the densities and the level-sets.
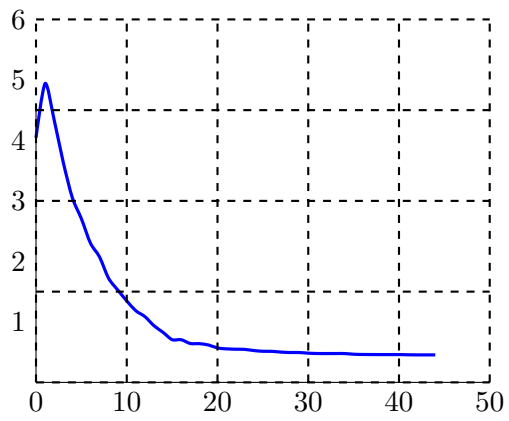
(a) Evolution of the objective function
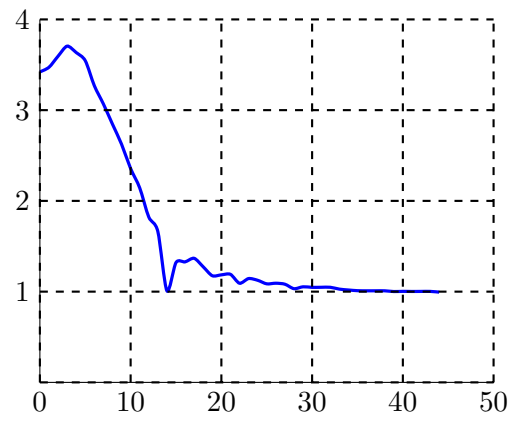
(b) Evolution of the value of λ_1

Figure 3.9: Convergence curves for Problem 3.9.4.
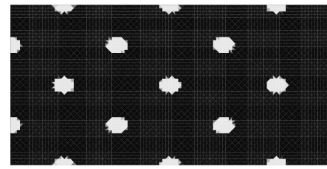
(a) Total density, iteration 0
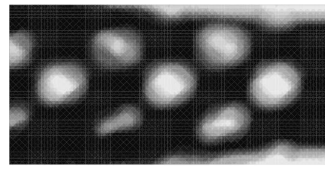
(b) Total density, iteration 5
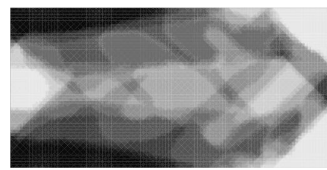
(c) Total density, iteration 30
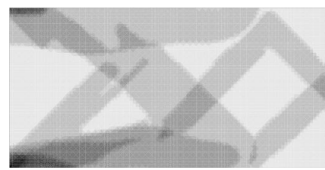
(d) Final total density (iteration 167)
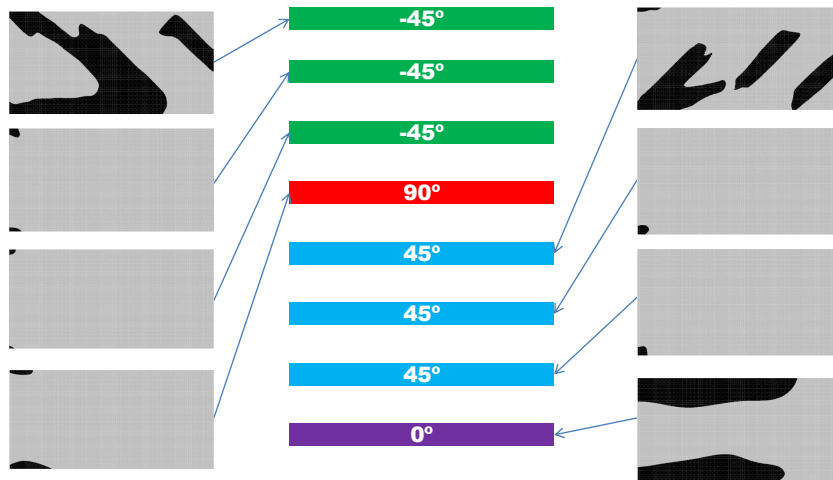
(e) Optimal stacking sequence and shape of each ply. The outer layers are upper in the figure.

Figure 3.10: Results of Problem 3.9.5 under the **first load case** (concentrated vertical force). (a),(b),(c),(d): Evolution of the total addition of densities of each ply (darker gray means more plies superposed). (e): Optimal stacking sequence and in-plane shape of each ply (black represents material). We remark that the optimal "long cantilever-type shape" in (d) is due to the compliance constraint. Sub-figure (d) looks thicker than the superposition of plies in (e) due to the regularization between the densities and the level-sets.

(a) Evolution of the objective function

(b) Evolution of the value of $\mathcal{X}$
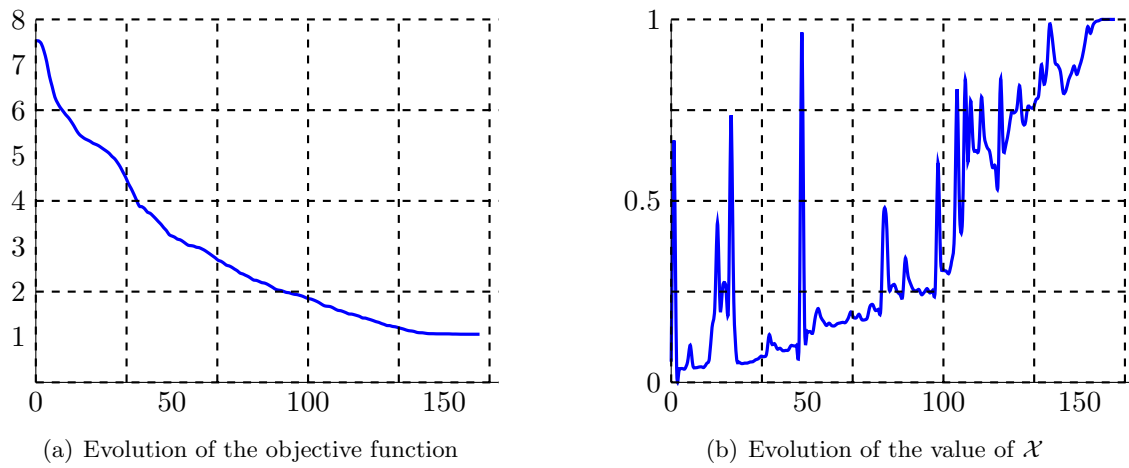
Figure 3.11: Convergence curves for Problem 3.9.5 under the first load case.
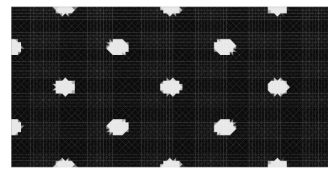
(a) Total density, iteration 0
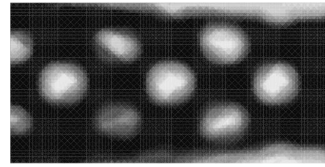
(b) Total density, iteration 5
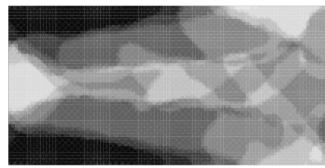
(c) Total density, iteration 30
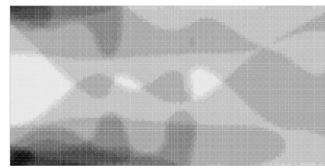
(d) Final total density (iteration 167)
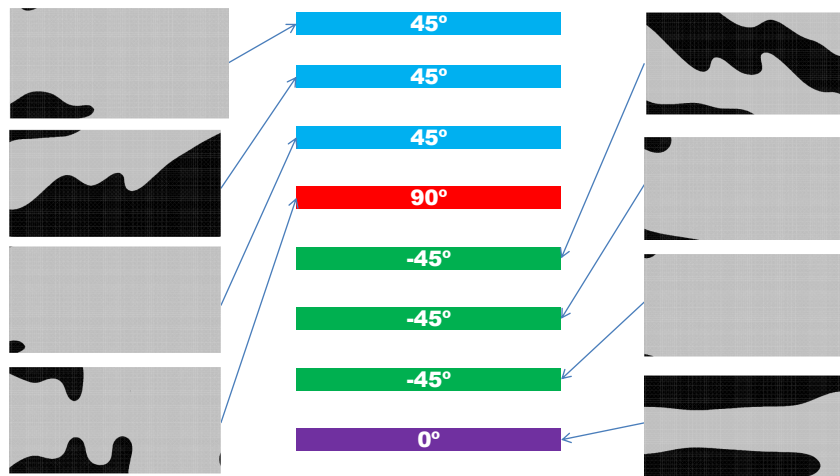
(e) Stacking sequence and shape of each ply. The outer layers are upper in the figure.

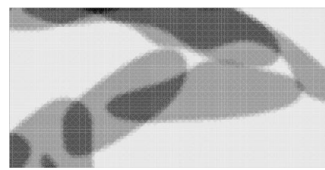**Figure 3.12:** Results of Problem 3.9.5 under the **second load case** (uniform vertical force). (a),(b),(c),(d): Evolution of the total addition of densities of each ply (darker gray means more plies superposed). (e): Optimal stacking sequence and in-plane shape of each ply (black represents material). Sub-figure (d) looks thicker than the superposition of plies in (e) due to the regularization between the densities and the level-sets.

(a) Evolution of the objective function

(b) Evolution of the value of $\mathcal{X}$
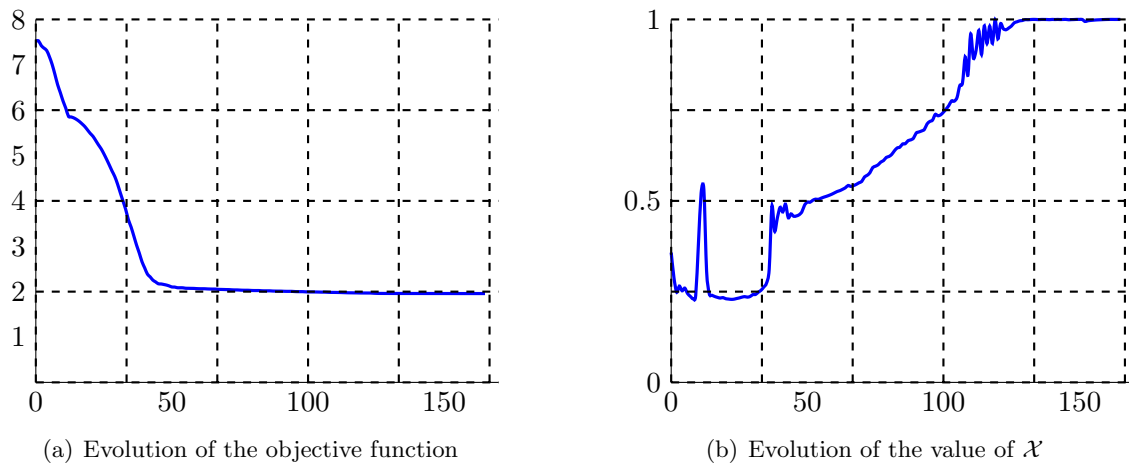
Figure 3.13: Convergence curves for Problem 3.9.5 under the second load case.

Chapter 4

The topological derivative in anisotropic elasticity

Contents

The topological derivative $\mathrm{D}J$ of cost functionals J that depend on the stress and the displacement (assuming a linearly elastic material behavior) is considered in a quite general 3D setting where both the background and the inhomogeneity may have arbitrary anisotropic elastic properties. A small-inhomogeneity expansion of J is mathematically justified for a wide class of displacement and stress-based cost functionals having smooth densities and computational procedures are then discussed. Several 2D and 3D numerical examples are presented, in particular

demonstrating the proposed formulation of DJ on practical cases involving anisotropic elasticity and non-quadratic cost functionals.

This chapter is a joint work with Marc Bonnet and was published and submitted for publication through the following articles

- M. Bonnet, G. Delgado, *The topological derivative in anisotropic elasticity*, The Quarterly Journal of Mechanics and Applied Mathematics (2013)

- M. Bonnet, G. Delgado, *The topological derivative of stress-based cost functionals in anisotropic elasticity*, submitted (2014)

4.1 Introduction

The concept of topological derivative was rigorously introduced by Sokolowski and Zochowski in [284] and Masmoudi in [208]. In particular, it can be seen as a mathematical justification for the topological optimization algorithm proposed by Céa et al. [76, 77], based on the combination of the shape gradient and a fixed point method, and the bubble method of Schumacher et al. [113, 268]. The topological derivative $DJ(z)$ quantifies the perturbation induced to a cost functional J by the virtual creation of an object $B_a(z)$ (e.g. a cavity or an inhomogeneity) of vanishingly small characteristic radius a at a prescribed location z inside the solid. In structural optimization, computing the field $DJ(z)$ directs the algorithm towards optimal topologies by indicating where creating new holes is most profitable from the featured cost functional viewpoint, an approach used by e.g. [263, 25], and also [8] in conjunction with the shape derivative. Moreover, computational evidence [116, 209, 37] as well as more recent theoretical and experimental studies [17, 38, 308] show that the topological derivative is also effective for flaw identification problems. Such optimization or inverse problems usually feature cost functionals that involve volume or surface integrals of densities that depend on the displacement solving (in the present context) an elastostatic equilibrium problem on the reference solid. Moreover, constitutive or flaw identification problems are sometimes formulated in terms of energy cost functionals (e.g. of the Kohn-Vogelius type [181] or error in constitutive equation functionals [187, 106]), whose densities depend on displacement gradients.

To establish the expression of the topological sensitivity for a given cost functional and a chosen set of underlying geometrical and physical assumptions, one needs information about the asymptotic behavior as $a \to 0$ of the perturbation induced to the physical field variable (e.g. displacement) by the virtual creation of $B_a(z)$. An abundant literature is available on such asymptotic analyses, see e.g. [79, 314, 212, 165, 19]. A key component for computationally efficient topological derivative formulations is the adjoint solution method which, like with other types of sensitivity analysis, provides a valuable computational shortcut by replacing the computation of many sensitivity fields (in the present context, one sensitivity field for each virtual nucleation site z used in the computation) by that of just one adjoint solution. Adjoint solutions for topological sensitivity appeared in [123, 75] and thence found more widespread use, see e.g. [54, 40, 116, 37]. Another important component of topological derivative formulae is the elastic moment tensor (EMT), whose definition and properties are extensively studied in e.g. [22] for the isotropic case and [239, 46] for the anisotropic case.

Within the present framework of linear elasticity, results available for small-inhomogeneity asymptotic expansions, as well as their application to the concept of topological derivative, often assume isotropic elasticity, see e.g. [284, 127, 123, 278, 54]. Comparatively scarce material is available for the topological derivative in the more-general case of anisotropic elasticity. It includes the formulation of the elastodynamic topological derivative for arbitrary surface-integral

cost functionals [136, 137] and that of small-inhomogeneity solution asymptotics for anisotropic materials [238, 193, 239, 46].

Furthermore, most of the studies so far devoted to the topological derivative and its applications consider cost functionals that depend on the primary variable, namely the displacement field in the solid mechanics context of this work. However, some optimization problems involve stress-based cost functionals, which is equivalent (for the present context of linearly elastic solids) to considering functionals that depend on strains or displacement gradients. Examples include topology optimization of composite structures with materials constrained by yield criteria, energy-based cost functionals (e.g. [40] for Stokes flows) and flaw identification using full-field kinematical measurements. All these types of problems may be cast as minimization problems involving stress-based cost functionals. The asymptotic behavior of such cost functionals is quite different from those depending exclusively of the displacement, due to the fact that the strain perturbation inside an elastic inhomogeneity has a finite, nonzero limit as $a \to 0$, while the asymptotics of displacement-based functionals rests upon the fact that the magnitude of the displacement perturbation vanishes as $a \to 0$.

So far, only few works have investigated the small-inhomogeneity asymptotics of stress-based functionals. The 2D isotropic case is addressed for specific stress-based functionals (elastic energy, von Mises and Drucker-Prager yield criteria) in [284, 27, 28]. Moreover, results for general quadratic stress-dependent functionals are given in [267] within a 2D and 3D anisotropic framework. The main purpose of this chapter is to formulate and justify the topological derivative for stress-dependent functionals, in a quite general three-dimensional framework where the functionals are defined in terms of domain integrals of arbitrary sufficiently smooth densities while both the background material and the small trial inhomogeneity are allowed to have anisotropic elastic properties. The results given herein for topological derivatives thus contain expressions given in [284, 27, 28] as special cases. They are illustrated by computational experiments on 2D and 3D examples involving anisotropic elasticity and stress-based quadratic or non-quadratic cost functionals, and inspired by topology optimization or flaw identification.

The chapter is organized as follows. Section 4.2, introduces notation, collects the main facts on the elastic transmission problem and elastic moment tensor and defines the cost functional. The asymptotic behavior of the perturbation of the elastic transmission problem, the concept of topological derivative and the main result are stated and established in Sections 4.3 and 4.4, respectively. The numerical evaluation of DJ is addressed in Section 4.5, and Section 4.6 is then devoted to the presentation and discussion of computational experiments.

4.2 Elastic transmission problem and cost functional

In order to make the contents presentation straightforward, only the 3D framework will be thoroughly described. Remarks on the 2D case will be furnished only when a clarification is required.

4.2.1 Notation, elastic transmission problem

Consider an elastic body occupying a smooth bounded domain $\Omega \subset \mathbb{R}^3$. The anisotropic elastic properties of the background material (against which the effect of small inhomogeneities will be considered), assumed to be homogeneous, are characterized by the fourth-order elasticity tensor $\mathcal{C}$. The boundary $\partial\Omega$ is split according to $\partial\Omega = \Gamma_{\mathrm{D}} \cup \Gamma_{\mathrm{N}}$ (where $\Gamma_{\mathrm{D}} \cap \Gamma_{\mathrm{N}} = \emptyset$ and $|\Gamma_{\mathrm{D}}| \neq 0$), so that a given force density $g \in L^2(\Gamma_{\mathrm{N}}; \mathbb{R}^3)$ is applied on Γ_{N} while a given displacement $\bar{u} \in H^{1/2}(\Gamma_{\mathrm{D}}; \mathbb{R}^3)$ is prescribed on Γ_{D}. Additionally, a body force density f assumed (for reasons given later) to have $C^{0,\beta}(\Omega)$ Hölder continuity for some $\beta > 0$ is applied to Ω.

The background solution, i.e. the displacement field arising in the reference solid due to the prescribed excitations $(f, g, \bar{u})$, is defined as the solution to

$$\mathrm{div}(\mathcal{C}\!:\!e(u)) + f = 0 \text{ in } \Omega, \quad t(u) = g \text{ on } \Gamma_{\mathrm{N}}, \quad u = \bar{u} \text{ on } \Gamma_{\mathrm{D}} \qquad (4.1)$$

where $e(w)$ and $t(w)$ denote the linearized strain tensor and the traction vector associated with a given displacement w, respectively defined by

$$\text{(a)}\quad e(w) = \frac{1}{2}(\nabla w + \nabla w^{\mathrm{T}}), \qquad \text{(b)}\quad t(w) = (\mathcal{C}\!:\!e(w))\!\cdot\!n \tag{4.2}$$

(with n the unit outward normal to Ω). In (4.2b) and hereinafter, symbols '$\cdot$' and '$:$' denote single and double inner products, e.g. $(E\!\cdot\!x)_i = E_{ij}x_j$ and $(\mathcal{C}\!:\!E)_{ij} = \mathcal{C}_{ijk\ell}E_{k\ell}$, with Einstein's convention of summation over repeated indices implicitly used throughout.

Alternatively, the background displacement is governed by the weak formulation

$$\text{Find } u \in W(\bar{u}), \qquad \langle u, w \rangle_\Omega^{\mathcal{C}} = F(w), \quad \forall w \in W_0, \tag{4.3}$$

where $\langle u, w \rangle_D^{\mathcal{C}}$ denotes the bilinear elastic energy form associated to given domain $D \subset \mathbb{R}^3$ and elasticity tensor $\mathcal{C}$, i.e.:

$$\langle u, w \rangle_D^{\mathcal{C}} := \int_D e(u)\!:\!\mathcal{C}\!:\!e(w)\,\mathrm{d}V = \int_D \nabla u\!:\!\mathcal{C}\!:\!\nabla w\,\mathrm{d}V \tag{4.4}$$

(with the second equality holding by virtue of the well-known major symmetry of $\mathcal{C}$), the linear form F associated to the loading is defined by

$$F(w) = \int_\Omega f\!\cdot\!w\,\mathrm{d}V + \int_{\Gamma_{\mathrm{N}}} g\!\cdot\!w\,\mathrm{d}S, \tag{4.5}$$

and having introduced, for given $\bar{u} \in H^{1/2}(\Gamma_{\mathrm{D}}; \mathbb{R}^3)$, the spaces $W(\bar{u})$ and W_0 of displacement fields that are kinematically admissible with respect to arbitrary and homogeneous prescribed Dirichlet data, respectively, i.e.:

$$W(\bar{u}) := \big\{ v \in H^1(\Omega; \mathbb{R}^3),\ v = \bar{u} \text{ on } \Gamma_{\mathrm{D}} \big\}, \qquad W_0 := W(0). \tag{4.6}$$

The $C^{0,\beta}(\Omega; \mathbb{R}^3)$ regularity assumption on f, which is stronger than the more-usual assumption $f \in L^2(\Omega; \mathbb{R}^3)$, ensures (e.g. from the properties of elastic volume potentials, see [186], Thm. 10.4) that u is in $C^{2,\beta}(D; \mathbb{R}^3)$ for any subset $D \Subset \Omega$. It is made in order to later permit Taylor expansions of displacements or strains about selected internal points.

Well-known properties of elasticity tensors are now recalled for convenience. For general anisotropic materials, the elasticity tensor $\mathcal{C}$ is positive definite (in the sense that $E\!:\!\mathcal{C}\!:\!E > 0$ for any symmetric second-order tensor $E \in \mathbb{R}^{3\times3}_{\mathrm{sym}}$, $E \neq 0$) and has the major and minor symmetries (i.e. $\mathcal{C}_{ijk\ell} = \mathcal{C}_{k\ell ij} = \mathcal{C}_{jik\ell} = \mathcal{C}_{ij\ell k}$); it may thus involve up to 21 independent elastic constants. For isotropic materials characterized by their bulk modulus κ and shear modulus μ, $\mathcal{C}$ is given by

$$\mathcal{C} = 3\kappa\mathcal{J} + 2\mu\mathcal{K}, \tag{4.7}$$

where $\mathcal{J}, \mathcal{K}$ are fourth-order tensors respectively defined by $\mathcal{J} = (1/3)I \otimes I$ and $\mathcal{K} = \mathcal{I} - \mathcal{J}$ (with I and $\mathcal{I}$ denoting the second-order identity and the fourth-order identity for symmetric tensors, respectively), so that $E = \mathcal{J}\!:\!E + \mathcal{K}\!:\!E$ is the decomposition of a symmetric second-order tensor $E \in \mathbb{R}^{3\times3}_{\mathrm{sym}}$ into its spherical and deviatoric parts.

4.2.2   Transmission problem for a small trial inhomogeneity

Now, consider a single small elastic inhomogeneity located at $z \in \Omega$, of characteristic linear size a, occupying the domain

$$B_a = z + a\mathcal{B}, \tag{4.8}$$

where $\mathcal{B} \subset \mathbb{R}^3$ is a bounded smooth domain and a is small enough to have $\bar{B}_a \Subset \Omega$. The inhomogeneity has anisotropic properties characterized by the elasticity tensor $\mathcal{C}^\star$, so that the elastic properties of the whole solid are defined by the tensor-valued field $\mathcal{C}_a$ given by

$$\mathcal{C}_a = (1 - \chi(B_a))\mathcal{C} + \chi(B_a)\mathcal{C}^\star = \mathcal{C} + \chi(B_a)\Delta\mathcal{C}, \tag{4.9}$$

$\chi(D)$ being the characteristic function of the domain D and $\Delta\mathcal{C} := \mathcal{C}^\star - \mathcal{C}$ denoting the elastic tensor perturbation.

The displacement field $u_a \in W(\bar{u})$ arising in the solid containing the small inhomogeneity due to the prescribed excitations $(f, g, \bar{u})$ solves the transmission problem

$$\text{div}(\mathcal{C}_a : e(u_a)) + f = 0 \text{ in } \Omega, \quad (\mathcal{C} : e(u_a)) \cdot n = g \text{ on } \Gamma_\text{N}, \quad u_a = \bar{u} \text{ on } \Gamma_\text{D}. \tag{4.10}$$

or, equivalently, the weak formulation

$$\text{Find } u_a \in W(\bar{u}), \qquad \langle u_a, w \rangle_\Omega^{\mathcal{C}_a} = F(w), \quad \forall w \in W_0. \tag{4.11}$$

Either formulation (4.10) or (4.11) implicitly enforces, by virtue of its distributional interpretation, the perfect-bonding relations $u_a|_+ = u_a|_-$ and $(\mathcal{C} : e(u_a)) \cdot n|_+ = (\mathcal{C}^\star : e(u_a)) \cdot n|_-$ on ∂B_a, where the $\pm$ subscripts indicate limiting values from outside and inside B_a, respectively, and n is the unit outward normal vector to ∂B_a. The solution u_a of (4.11) *a priori* belongs to $H^2_\text{loc}\big((\Omega \setminus \bar{B}_a) \cup B_a ; \mathbb{R}^3\big)$ for $f \in L^2(\Omega; \mathbb{R})$, however, since we suppose $f \in C^{0,\beta}(\Omega; \mathbb{R}^3)$, $u_a \in C^{2,\beta}(D; \mathbb{R}^3)$ for any subset $D \Subset \big((\Omega \setminus \bar{B}_a) \cup B_a\big)$.

The transmission problem (4.10) can alternatively be formulated in terms of the displacement perturbation $v_a := u_a - u$ rather than the total displacement u_a. Subtracting (4.3) from the corresponding weak formulation of (4.10) yields the following weak formulation for v_a:

$$\text{Find } v_a \in W_0, \quad \langle v_a, w \rangle_\Omega^{\mathcal{C}_a} = -\langle u, w \rangle_{B_a}^{\Delta\mathcal{C}}, \quad \forall w \in W_0. \tag{4.12}$$
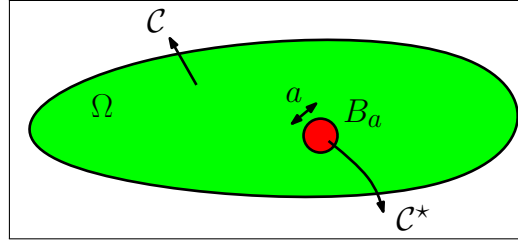
Figure 4.1: Transmission problem for a small inclusion.

Free-space transmission problem (FSTP). The auxiliary problem of a perfectly-bonded inhomogeneity $(\mathcal{B}, \mathcal{C}^\star)$ embedded in an infinite elastic medium $\Omega = \mathbb{R}^3$ subjected to a uniform remote stress will play an important role in the sequel and is thus given now for later reference together with some additional useful notation. For an arbitrary constant second-order tensor $E \in \mathbb{R}^{3 \times 3}$, let $\varphi[E]$ denote the linear vector-valued function defined by

$$\varphi[E](\xi) := E \cdot \xi. \tag{4.13}$$

Let the background solution u be chosen as $u = \varphi[E]$, noting that $\text{div}(\mathcal{C} : \nabla\varphi[E]) = 0$. The FSTP consists in finding the displacement field $u_\mathcal{B}[E]$ such that

$$\text{div}\big(\mathcal{C}_\mathcal{B} : e(u_\mathcal{B}[E])\big) = 0 \text{ in } \mathbb{R}^3, \qquad u_\mathcal{B}[E](\xi) - \varphi[E](\xi) = \mathcal{O}(|\xi|^{-2}) \ (|\xi| \to \infty) \tag{4.14}$$

where

$$\mathcal{C}_\mathcal{B} = (1 - \chi(\mathcal{B}))\mathcal{C} + \chi(\mathcal{B})\mathcal{C}^\star = \mathcal{C} + \chi(\mathcal{B})\Delta\mathcal{C}$$

It can be recast into the following weak formulation for the displacement perturbation $v_\mathcal{B}[E] := u_\mathcal{B}[E] - \varphi[E]$:

$$\text{Find } v_\mathcal{B}[E] \in W_\infty, \langle v_\mathcal{B}[E], w \rangle_{\mathbb{R}^3}^{\mathcal{C}_\mathcal{B}} = -\langle \varphi[E], w \rangle_\mathcal{B}^{\Delta\mathcal{C}}, \quad \forall w \in W_\infty, \tag{4.15}$$

with the function space W_∞ defined by $W_\infty = \big\{ w \in L^2_\text{loc}(\mathbb{R}^3; \mathbb{R}^3), \nabla w \in L^2(\mathbb{R}^3; \mathbb{R}^{3 \times 3}) \big\}$. Note that $\langle \varphi[E], w \rangle_\mathcal{B}^{\Delta\mathcal{C}} = \langle \varphi[E^\text{T}], w \rangle_\mathcal{B}^{\Delta\mathcal{C}}$, implying that $v_\mathcal{B}[E]$ solving (4.15) depends only on the symmetric part $E_\text{sym} := \frac{1}{2}(E + E^\text{T}) \in \mathbb{R}^{3 \times 3}_\text{sym}$ of E. The FSTP (4.14) is analytically solved for an ellipsoidal inhomogeneity in Eshelby's landmark paper [114].

4.2.3 Elastic moment tensor

The elastic moment tensor (EMT) [22, 239], which will be seen to play an important role in the small-inhomogeneity asymptotics of cost functionals, is now defined.

Definition 4.2.1 (elastic moment tensor). *Let $v_{\mathcal{B}}[E]$ denote the solution to the FSTP (4.15) for given $E \in \mathbb{R}^{3 \times 3}$. The (fourth-order)* elastic moment tensor *(EMT) $\mathcal{A}$ is defined by*

$$\mathcal{A} : E = \int_{\mathcal{B}} \Delta \mathcal{C} : \nabla u_{\mathcal{B}}[E] \, dV = \int_{\mathcal{B}} \Delta \mathcal{C} : (E + \nabla v_{\mathcal{B}}[E]) \, dV \qquad \forall E \in \mathbb{R}^{3 \times 3}. \tag{4.16}$$

Remark 4.2.2. *In [22, 19], the EMT is defined, for isotropic materials, in terms of the densities of two elastic layer potentials that are used there to formulate the FSTP (4.14). That definition in fact coincides with the present definition (4.16). To see this, integrating (4.16) by parts, one finds*

$$E' : \mathcal{A} : E = \int_{\partial \mathcal{B}} \left(E' : (\mathcal{C}^{\star} - \mathcal{C}) \cdot n \right) \cdot u_{\mathcal{B}}[E] \, dS = \int_{\partial \mathcal{B}} \left(t^{\star}\big(\varphi[E']\big) - t\big(\varphi[E']\big) \right) \cdot u_{\mathcal{B}}[E] \, dS.$$

This identity coincides (upon adaptation to the present notations) with the left and right contraction of eq. (10.12) in Lemma 10.3 of [19] by two tensors $E, E' \in \mathbb{R}^{3 \times 3}$.

Properties of the elastic moment tensor. The main known properties of the EMT are now collected.

Proposition 4.2.3 (symmetry). *The elastic moment tensor $\mathcal{A}$ has major and minor symmetries: for any pair of second-order tensors $E, E' \in \mathbb{R}^{3 \times 3}$, one has the major symmetry*

$$E' : \mathcal{A} : E = E : \mathcal{A} : E' \tag{4.17}$$

and the minor symmetries

$$(i) \ E' : \mathcal{A} : E = E' : \mathcal{A} : E^{T}, \quad (ii) \ E' : \mathcal{A} : E = E'^{T} : \mathcal{A} : E. \tag{4.18}$$

Proof. First, taking the left inner product of Eq. (4.16) by E', one obtains

$$E' : \mathcal{A} : E = E' : \left\{ \int_{\mathcal{B}} \Delta \mathcal{C} : \nabla v_{\mathcal{B}}[E] \, dV \right\} + E' : \left\{ \int_{\mathcal{B}} \Delta \mathcal{C} \, dV \right\} : E \tag{4.19}$$

The second term of the above right-hand side is clearly symmetric in E, E' due to the major symmetry of $\Delta \mathcal{C} = \mathcal{C}^{\star} - \mathcal{C}$, so the symmetry of the first term remains to be proved. To this aim, one starts by noting that, by virtue of definition (4.4) of $\langle \cdot, \cdot \rangle_{\mathcal{B}}^{\Delta \mathcal{C}}$, one has

$$E' : \left\{ \int_{\mathcal{B}} \Delta \mathcal{C} : \nabla v_{\mathcal{B}}[E] \, dV \right\} = \langle \varphi[E'], v_{\mathcal{B}}[E] \rangle_{\mathcal{B}}^{\Delta \mathcal{C}}. \tag{4.20}$$

Then, using variational formulation (4.15) for $v_{\mathcal{B}}[E]$ with $w = v_{\mathcal{B}}[E']$, one has

$$-\langle \varphi[E'], v_{\mathcal{B}}[E] \rangle_{\mathcal{B}}^{\Delta \mathcal{C}} = \langle v_{\mathcal{B}}[E'], v_{\mathcal{B}}[E] \rangle_{\mathbb{R}^3}^{\mathcal{C}_{\mathcal{B}}}$$
$$= \langle v_{\mathcal{B}}[E], v_{\mathcal{B}}[E'] \rangle_{\mathbb{R}^3}^{\mathcal{C}_{\mathcal{B}}} = -\langle \varphi[E], v_{\mathcal{B}}[E'] \rangle_{\mathcal{B}}^{\Delta \mathcal{C}}$$

(using the symmetry of $\langle \cdot, \cdot \rangle_{\mathbb{R}^3}^{\mathcal{C}_{\mathcal{B}}}$) which, combined with (4.20) written for E, E' and E', E, yields the desired remaining symmetry

$$E' : \left\{ \int_{\mathcal{B}} \Delta \mathcal{C} : \nabla v_{\mathcal{B}}[E] \, dV \right\} = E : \left\{ \int_{\mathcal{B}} \Delta \mathcal{C} : \nabla v_{\mathcal{B}}[E'] \, dV \right\} \tag{4.21}$$

The major symmetry (4.17) follows from (4.19), (4.21) and the known major symmetry of $\Delta \mathcal{C}$.

Moreover, the minor symmetry (4.18i) follows immediately from the corresponding minor symmetry of $\Delta \mathcal{C}$. Finally, (4.17) and (4.18i) imply (4.18ii). □

Proposition 4.2.4 (scaling)**.** *Let $\mathcal{B}_0$ have the same shape as $\mathcal{B}$ and unit volume (i.e. $\mathcal{B}_0 = |\mathcal{B}|^{-1/3}\mathcal{B}$), and assume that the contrast $\Delta\mathcal{C}$ is uniform. Then, one has*

$$\mathcal{A}(\mathcal{B},\mathcal{C},\mathcal{C}^\star) = |\mathcal{B}|\mathcal{A}(\mathcal{B}_0,\mathcal{C},\mathcal{C}^\star) \tag{4.22}$$

Proof. Denote by $v_{\mathcal{B}_0}$ the solution to problem (4.14) for the inhomogeneity $\mathcal{B}_0$, and let $\lambda = |\mathcal{B}|^{1/3}$ be the linear scaling parameter such that $\mathcal{B} = \lambda\mathcal{B}_0$. Then, on setting $(\bar{\xi},\bar{x}) = \lambda(\bar{\xi}_0,\bar{x}_0)$ in (4.42), invoking the homogeneity of ∇G_∞ and essentially repeating arguments already used in the asymptotic analysis of Sec. 4.3.3, one easily finds that $v_{\mathcal{B}}(\bar{\xi}) = \lambda v_{\mathcal{B}_0}(\bar{\xi}_0)$, and hence $\nabla v_{\mathcal{B}}(\bar{\xi}) = \nabla v_{\mathcal{B}_0}(\bar{\xi}_0)$. Exploiting this remark, and setting $\bar{\xi} = \lambda\bar{\xi}_0$, in (4.16) then yields the desired result (4.22). $\qquad\square$

The next important property of $\mathcal{A}$ to consider is its sign-definiteness. It can conveniently be formulated in terms of the generalized eigenvalue problem

$$(\mathcal{C}^\star - \Lambda\mathcal{C}):E = 0 \qquad (E \in \mathbb{R}^{3\times3}_{\mathrm{sym}}), \tag{4.23}$$

which admits six real and strictly positive eigenvalues $\Lambda_1,\ldots,\Lambda_6$ and associated eigentensors $E_1,\ldots E_6 \in \mathbb{R}^{3\times3}_{\mathrm{sym}}$, by virtue of $\mathcal{C}^\star$ and $\mathcal{C}$ defining positive-definite quadratic forms over the six-dimensional vector space $\mathbb{R}^{3\times3}_{\mathrm{sym}}$ (i.e. (4.23) could be recast as a generalized eigenvalue problem for two symmetric positive definite 6×6 matrices, see [215]).

Proposition 4.2.5 (sign-definiteness)**.** *The elastic moment tensor $\mathcal{A}$ is positive definite if $\Lambda_i > 1$ ($1 \leq i \leq 6$), and negative definite if $\Lambda_i < 1$ ($1 \leq i \leq 6$). Moreover, if $\Lambda_i = 1$ for some i, then $\mathcal{A}:E_i = 0$, i.e. E_i is in the null space of $\mathcal{A}$.*

Proof. From definition (4.16), for any $E \in \mathbb{R}^{3\times3}$, one has $E : \mathcal{A} : E = |\mathcal{B}|E : \Delta\mathcal{C} : E + \langle\varphi[E], v_{\mathcal{B}}[E]\rangle_{\mathcal{B}}^{\Delta\mathcal{C}}$. This proof now exploits two different reformulations of $E : \mathcal{A} : E$. For a first reformulation, setting $w = v_{\mathcal{B}}$ in (4.15), one has $\langle\varphi[E], v_{\mathcal{B}}[E]\rangle_{\mathcal{B}}^{\Delta\mathcal{C}} = -\langle v_{\mathcal{B}}[E], v_{\mathcal{B}}[E]\rangle_{\mathcal{B}}^{\mathcal{C}_{\mathcal{B}}}$, and hence

$$E:\mathcal{A}:E = |\mathcal{B}|E:\Delta\mathcal{C}:E - \langle v_{\mathcal{B}}[E], v_{\mathcal{B}}[E]\rangle_{\mathcal{B}}^{\mathcal{C}_{\mathcal{B}}}. \tag{4.24}$$

For a second reformulation of $E : \mathcal{A} : E$, let $Z := \mathcal{C}^{\star-1} : \Delta\mathcal{C} : E \in \mathbb{R}^{3\times3}_{\mathrm{sym}}$, so that $\langle\varphi[Z], w\rangle_{\mathcal{B}}^{\mathcal{C}_{\mathcal{B}}} = \langle\varphi[E], w\rangle_{\mathcal{B}}^{\Delta\mathcal{C}}$ holds for any $w \in H^1(\mathcal{B};\mathbb{R}^3)$, and define $\hat{v}_{\mathcal{B}}[E] := v_{\mathcal{B}}[E] + \varphi[Z]$ in $\mathcal{B}$. Then:

$$\begin{aligned}
\langle\varphi[E], v_{\mathcal{B}}[E]\rangle_{\mathcal{B}}^{\Delta\mathcal{C}} &= \langle\varphi[Z], v_{\mathcal{B}}[E]\rangle_{\mathcal{B}}^{\mathcal{C}_{\mathcal{B}}} \\
&= \langle\hat{v}_{\mathcal{B}}[E] - v_{\mathcal{B}}[E], v_{\mathcal{B}}[E]\rangle_{\mathcal{B}}^{\mathcal{C}_{\mathcal{B}}} \\
&= \langle\hat{v}_{\mathcal{B}}[E], \hat{v}_{\mathcal{B}}[E]\rangle_{\mathcal{B}}^{\mathcal{C}_{\mathcal{B}}} - \langle\hat{v}_{\mathcal{B}}[E], \varphi[Z]\rangle_{\mathcal{B}}^{\mathcal{C}_{\mathcal{B}}} - \langle v_{\mathcal{B}}[E], v_{\mathcal{B}}[E]\rangle_{\mathcal{B}}^{\mathcal{C}_{\mathcal{B}}}
\end{aligned} \tag{4.25}$$

Now, setting again $w = v_{\mathcal{B}}$ in (4.15), one obtains

$$\langle v_{\mathcal{B}}[E], v_{\mathcal{B}}[E]\rangle_{\mathcal{B}}^{\mathcal{C}_{\mathcal{B}}} = -\langle v_{\mathcal{B}}[E], v_{\mathcal{B}}[E]\rangle_{\mathbb{R}^3\setminus\mathcal{B}}^{\mathcal{C}_{\mathcal{B}}} - \langle\varphi[E], v_{\mathcal{B}}[E]\rangle_{\mathcal{B}}^{\Delta\mathcal{C}}.$$

Inserting this identity in the last equality of (4.25), using $\langle\hat{v}_{\mathcal{B}}[E], \varphi[Z]\rangle_{\mathcal{B}}^{\mathcal{C}_{\mathcal{B}}} = \langle\hat{v}_{\mathcal{B}}[E], \varphi[E]\rangle_{\mathcal{B}}^{\Delta\mathcal{C}}$ and noting that $|\mathcal{B}|E:\Delta\mathcal{C}:E = \langle\varphi[E], \varphi[E]\rangle_{\mathcal{B}}^{\Delta\mathcal{C}}$, the sought reformulation is finally:

$$E:\mathcal{A}:E = \langle\hat{v}_{\mathcal{B}}[E], \hat{v}_{\mathcal{B}}[E]\rangle_{\mathcal{B}}^{\mathcal{C}_{\mathcal{B}}} + \langle v_{\mathcal{B}}[E], v_{\mathcal{B}}[E]\rangle_{\mathbb{R}^3\setminus\mathcal{B}}^{\mathcal{C}_{\mathcal{B}}} + \langle\varphi[E], \varphi[E-Z]\rangle_{\mathcal{B}}^{\mathcal{C}_{\mathcal{B}}} \tag{4.26}$$

Let now E be an eigentensor associated with eigenvalue Λ for problem (4.23). First, (4.23) then implies $E:\Delta\mathcal{C}:E = (\Lambda-1)E:\mathcal{C}:E$; moreover, the last term in the right-hand side of (4.24) is non-positive. Therefore, $E:\mathcal{A}:E < 0$ for any eigenvalue $\Lambda < 1$.

Then, to exploit the second reformulation (4.26), a simple derivation yields

$$\langle\varphi[E], \varphi[E-Z]\rangle_{\mathcal{B}}^{\mathcal{C}_{\mathcal{B}}} = |\mathcal{B}|E:\Delta\mathcal{C}:\mathcal{C}^{\star-1}:\mathcal{C}:E = |\mathcal{B}|(\Lambda-1)E:\mathcal{C}:\mathcal{C}^{\star-1}:\mathcal{C}:E.$$

The above quantity is positive for $\Lambda > 1$ while the other terms in the right-hand side of (4.26) are non-negative. Therefore, $E:\mathcal{A}:E > 0$ for any eigenvalue $\Lambda > 1$.

Finally, the proof of Proposition 4.2.5 is completed by noting that if $\Lambda = 1$, an eigenvector E verifies $\Delta\mathcal{C}:E = 0$. This implies that $E:\mathcal{A}:E = |\mathcal{B}|E:\Delta\mathcal{C}:E + \langle\varphi[E], v_{\mathcal{B}}[E]\rangle_{\mathcal{B}}^{\Delta\mathcal{C}} = 0$. $\qquad\square$

Remark 4.2.6 (isotropic materials)**.** *If both matrix and inhomogeneity materials are isotropic,* $\mathcal{C}$ *and* $\mathcal{C}^{\star}$ *are of the form (4.7) with respective moduli pairs* κ, μ *and* $\kappa^{\star}, \mu^{\star}$*. The generalized eigenvalue problem (4.23) then reads*

$$\left[3(\kappa^{\star} - \Lambda\kappa)\mathcal{J} + 2(\mu^{\star} - \Lambda\mu)\mathcal{K} \right] : E = 0$$

or, using the relations $\mathcal{J} : \mathcal{J} = \mathcal{J}$, $\mathcal{K} : \mathcal{K} = \mathcal{K}$ *and* $\mathcal{J} : \mathcal{K} = 0$ *verified by* $\mathcal{J}$ *and* $\mathcal{K}$,

$$(\kappa^{\star} - \Lambda\kappa)\mathcal{J} : E = 0 \quad or \quad (\mu^{\star} - \Lambda\mu)\mathcal{K} : E = 0.$$

Hence there are two distinct eigenvalues: (i) $\Lambda_1 = \kappa^{\star}/\kappa$ *(multiplicity 1) with eigentensor* $E_1 = I$ *since* $\mathcal{J} : E = (1/3)tr(E)I$ *for any* $E \in \mathbb{R}^{3\times3}_{sym}$, *and (ii)* $\Lambda_2 = \mu^{\star}/\mu$ *(multiplicity 5). Proposition 4.2.5 for this case essentially correspond to Theorem 5.4 of [22].*

Remark 4.2.7. *Proposition 4.2.3, together with the inequalities*

$$E : \mathcal{C} : \mathcal{C}^{\star-1} : \Delta\mathcal{C} : E \le E : \mathcal{A} : E \le E : \Delta\mathcal{C} : E \qquad \forall E \in \mathbb{R}^{3\times3}_{sym}$$

which imply Proposition 4.2.5, constitute Proposition 1 of [46]. Moreover, it is shown in [239] that (i) positive definiteness of $\mathcal{C} - \mathcal{C}^{\star}$ *implies that of* $-\mathcal{A}$ *(Theorem 2.7) and (ii) positive definiteness of* $\mathcal{C}^{-1} - \mathcal{C}^{\star-1}$ *implies that of* $\mathcal{A}$ *(Theorem 2.8). One easily check that cases (i) and (ii) are respectively equivalent to the condition* $\Lambda_i > 1$ *(*$1 \le i \le 6$*) or* $\Lambda_i < 1$ *(*$1 \le i \le 6$*) of proposition 4.2.5.*

4.2.4   Cost functional

Cost functionals of the form

$$J(\mathcal{C}_a) = \mathbb{J}_a(u_a, \nabla u_a) \qquad \text{with} \quad \mathbb{J}_a(u, d) = \int_{\Omega} \psi_a\big(x, u(x), d(x) \big) \, \mathrm{d}V(x) + \int_{\partial\Omega} \psi_S(x, u(x)) \, \mathrm{d}S(x)$$

$$(4.27)$$

are considered, where $\psi_S : \Omega \times \mathbb{R}^3 \to \mathbb{R}$ and the density $\psi_a : \Omega \times \mathbb{R}^3 \times \mathbb{R}^{3\times3} \to \mathbb{R}$ is defined by

$$\psi_a = (1 - \chi(B_a))\psi + \chi(B_a)\psi^{\star} = \psi + \chi(B_a)\Delta\psi, \tag{4.28}$$

with functions ψ, $\psi^{\star}$ (hence also $\Delta\psi := \psi^{\star} - \psi$) and ψ_S assumed to be twice differentiable in all their arguments. Moreover, all second-order derivatives of ψ_S are assumed bounded meanwhile those of ψ and $\psi^{\star}$ are assumed to have $C^{0,\gamma}(\Omega \times \mathbb{R}^3 \times \mathbb{R}^{3\times3})$ Hölder regularity for some $\gamma > 0$. We will denote by $x \in \Omega$, $u \in \mathbb{R}^3$, $d \in \mathbb{R}^{3\times3}$ the generic arguments of a density $\psi(x, u, d)$. Then, $\partial_x\psi, \partial_u\psi, \partial_d\psi$ will denote the partial derivatives with respect of the corresponding arguments, with higher-order partial derivatives denoted similarly, e.g. $\partial^2_{ud}\psi$ (with similar notations for $\psi^{\star}$ and ψ_S). The assumed Hölder regularity of ψ can thus be expressed as the existence of a finite constant K such that, for every combination of indices $i, j = x, u, d$,

$$\sup_{\substack{x_0 \in \Omega \\ u_0 \in \mathbb{R}^3 \\ d_0 \in \mathbb{R}^{3\times3}}} \big| \partial^2_{ij}\psi(x_0, u_0, d_0) \big| + \sup_{\substack{(x_0, x_1) \in \Omega \\ (u_0, u_1) \in \mathbb{R}^3 \\ (d_0, d_1) \in \mathbb{R}^{3\times3}}} \frac{\big| \partial^2_{ij}\psi(x_0, u_0, d_0) - \partial^2_{ij}\psi(x_1, u_1, d_1) \big|}{\big(|x_0 - x_1|^{\gamma} + |u_0 - u_1|^{\gamma} + |d_0 - d_1|^{\gamma} \big)} \le K,$$

with a similar inequality holding for $\psi^{\star}$. We note that as well as $\partial^2_{ij}\psi_S$, the above assumption implies that $\partial^2_{ij}\psi$ and $\partial^2_{ij}\psi^{\star}$ are bounded over $\Omega \times \mathbb{R}^3 \times \mathbb{R}^{3\times3}$. Moreover, applying repeatedly Taylor theorem to ψ_S (w.r.t. u) on both sides of the inequality $|\partial^2_{uu}\psi_S| \le C$, ψ_S obeys the following growth conditions

$$|\psi_S(x, u)| \le C(1 + |u|^2), \quad |\partial_u\psi_S(x, u)| \le C(1 + |u|) \quad |\partial_{uu}\psi_S(x, u)| \le C. \tag{4.29}$$

Owing to the above hypothesis, we state that the criterion $\mathbb{J}_a(u_a, \nabla u_a)$ is well defined. Indeed, u_a is continuous in Ω (thus bounded), so the volume integral in (4.27) is finite in virtue of the continuity of ψ_a. Besides, $u_a \in H^2(\Omega \backslash \overline{B}_a)$, so since $\partial B_a \cap \partial \Omega = \emptyset$, the trace of u_a on $\partial \Omega$ is square integrable. The finiteness of the surface integral in (4.27) thus stems from estimates (4.29).

The partial directional derivatives $\partial_u \mathbb{J}_a$ and $\partial_d \mathbb{J}_a$ of $\mathbb{J}_a$ with respect to its first and second arguments for all $w \in W_0$ and $h \in L^2(\Omega; \mathbb{R}^{3\times 3})$ are defined, for later use, by

$$\left\langle \partial_u \mathbb{J}_a(u,d), w \right\rangle = \int_{\Omega \backslash B_a} \partial_u \psi(x,u,d) \cdot w \, dV + \int_{B_a} \partial_u \psi^\star(x,u,d) \cdot w \, dV + \int_{\partial \Omega} \partial_u \psi_S(x,u) \cdot w \, dS,$$

$$\left\langle \partial_d \mathbb{J}_a(u,d), h \right\rangle = \int_{\Omega \backslash B_a} \partial_d \psi(x,u,d) : h \, dV + \int_{B_a} \partial_d \psi^\star(x,u,d) : h \, dV.$$

$$(4.30)$$

These two directional derivatives will play an important role in the definition of the adjoint state.

Remark 4.2.8. *The choice of the variable ∇u instead of the classical strain $e(u)$ in (4.27) is completely arbitrary. One could have perfectly chosen $e(u)$ instead. The only mayor difference stands for rigid body motion (translation and rotation) for which $e(u) = 0$.*

Remark 4.2.9. *The reason of why the density ψ_S does not depend on d is due to the fact that the hypothetic term of the partial directional derivative $\partial_d \mathbb{J}_a(u,d)$ involving ψ_S would read*

$$\int_{\partial \Omega} \partial_d \psi_S(x,u,d) : h \, dS(x),$$

$$(4.31)$$

which is not properly defined for $h \in L^2(\Omega; \mathbb{R}^{3\times 3})$ (in fact one can not define the trace of h on $\partial \Omega$!). As a consequence, the regularity of the adjoint state, as it will be defined in Section 4.4, would be lesser than required. We avoid this unnecessary complication by removing the dependence of ψ_S w.r.t. the variable d. However, cases when the adjoint state is not regular have been treated in classical control theory [198], notably when the observations depend on the normal gradient of the state variable on the boundary.

Remark 4.2.10. *The assumed Hölder and boundedness conditions on the cost functional densities might seem restrictive, but are satisfied by a number of cost functions often used in applications (compliance, energy based functionals, least squares misfit functionals, yield functions). Examples include (i) all quadratic functions of d, and (ii) the useful penalization function*

$$\psi(d) = \Psi_n(q(d)), \quad \Psi_n(t) := \left(1 + t^n\right)^{1/n} - 1 \qquad (4.32)$$

(where q is any quadratic function of d), introduced in [24] to approximate pointwise yield functions with thresholds, whose derivatives Ψ_n'' and Ψ_n''' are bounded over $\mathbb{R}^+$ (one finds e.g. that $0 < |\Psi_n''| \le 2^{1/n}(n-1)$ for any $t > 0$, $n > 1$). Case (ii) is typically used with $q(\nabla u)$ chosen as the appropriate squared (von Mises, Hill-Tsai, Drucker-Prager...) yield function, normalized so that the criterion reads $q(\nabla u) \le 1$.

4.3 Asymptotic behavior of the displacement

In the present section, some results on the small-inhomogeneity asymptotic behavior of u_a [12, 46] are exposed. To facilitate this task, the transmission problem (4.12) is first reformulated as a domain integral equation involving a domain integral operator whose support is the small inhomogeneity B_a.

4.3.1   Elastostatic Green's tensor

Let the elastostatic Green's tensor $G(\xi, x)$ be defined by

$$\mathrm{div}\Big(\mathcal{C}\!:\!e\big(G(\cdot, x)\big)\Big) + \delta(\cdot - x)I = 0 \ \ \text{in } \Omega,$$

$$G(\cdot, x) = 0 \ \text{ on } \Gamma_{\mathrm{D}}, \quad t\big(G(\cdot, x)\big) = 0 \ \text{ on } \Gamma_{\mathrm{N}} \qquad (x \in \Omega), \quad (4.33)$$

i.e. $G(\cdot, x) = e_k \otimes G^k(\cdot, x)$ gathers the three linearly independent elastostatic displacement fields $G^k(\cdot, x)$ resulting from unit point forces $\delta(\cdot - x)e_k$ applied at $x \in \Omega$ along each coordinate direction k and fulfilling the homogeneous boundary conditions on $\partial\Omega$ implied by the definition of W_0.

   Moreover, the ensuing analysis will be facilitated by splitting the elastostatic Green's tensor according to

$$G(\xi, x) = G_\infty(\xi - x) + G_{\mathrm{C}}(\xi, x) \tag{4.34}$$

where $G_\infty(r)$ is the (singular) elastostatic full-space Green's tensor, such that

$$\mathrm{div}\big(\mathcal{C}\!:\!e(G_\infty)\big) + \delta I = 0 \quad (\text{in } \mathbb{R}^3), \qquad |G_\infty(r)| \to 0 \quad (|r| \to \infty), \tag{4.35}$$

and the complementary Green's tensor G_{C} is bounded at $\xi = x$ (and in fact is C^∞ for $\xi, x \in \Omega$ by virtue of being the solution of an elastostatic boundary-value problem with regular boundary data and zero body force density). The full-space Green's tensor is given by the inverse Fourier integral [227]

$$G_\infty(r) = \frac{1}{(2\pi)^3} \int_{\mathbb{R}^3} \exp(i\eta \cdot r) N(\eta) \, dV(\eta) \quad (r \in \mathbb{R}^3 \setminus \{0\}), \tag{4.36}$$

where, for given $\eta \in \mathbb{R}^3$, the second-order tensor $N(\eta)$ is given by $N(\eta) = K^{-1}(\eta)$ in terms of the *Christoffel acoustic tensor* $K(\eta)$, defined by

$$K_{ik}(\eta) = \mathcal{C}_{ijk\ell}\eta_j\eta_\ell. \tag{4.37}$$

$K(\eta)$ is invertible for any $\eta \neq 0$ and positive definite elasticity tensor $\mathcal{C}$. Moreover, G_∞ has the following homogeneity property, which plays an important role in the sequel:

Lemma 4.3.1. G_∞ *is a positively homogeneous tensor-valued function of degree -1. Hence, for any $r \in \mathbb{R}^3 \setminus \{0\}$ and $\lambda \in \mathbb{R} \setminus \{0\}$, G_∞ and ∇G_∞ verify*

$$G_\infty(\lambda r) = |\lambda|^{-1} G_\infty(r), \qquad \nabla G_\infty(\lambda r) = |\lambda|^{-3}\lambda \nabla G_\infty(r) \tag{4.38}$$

Proof. Replacing r with λr and performing the change of variable $\eta = \lambda^{-1}\eta'$ in (4.36), the homogeneity property of G_∞ follows from using (i) $N(\eta) = \lambda^2 N(\eta')$ by virtue of K being homogeneous of degree 2 in η (and hence N being homogeneous of degree -2), and (ii) $dV(\eta) = |\lambda|^{-3} \, dV(\eta')$. $\qquad\square$

4.3.2   Domain integral equation formulation

Lemma 4.3.1 implies that both $G(\cdot, x)$ and $\nabla G(\cdot, x)$ have an integrable singularity at x. By virtue of decomposition (4.34) and the known C^∞ regularity of G_∞ away from the origin, $G(\cdot, x)$ hence belongs to $W^{1,1}(\Omega; \mathbb{R}^{3\times 3})$. On applying equations (4.33) in the sense of distributions for a trial displacement $w \in W_0 \cap C^1(\omega)$ (where ω is a neighbourhood of x) and integrating by parts the resulting first term over Ω, the Green's tensor is found to verify the identity

$$\langle G(\cdot, x), w \rangle_\Omega^{\mathcal{C}} = w(x) \qquad x \in \Omega, \ \forall w \in C_c^1(\Omega), \tag{4.39}$$

whose left-hand side is well-defined. Now, take $x \in B_a \cup (\Omega \setminus \bar{B}_a)$. Setting $w = G(\cdot, x)$ in (4.12) (noting that the bilinear strain energy integral remains well-defined by virtue of u and v_a having

C^1 regularity close enough to x) and using identity (4.39) with $w = v_a$ (by the same latter argument), the displacement perturbation v_a is found to satisfy

$$\text{Find } v_a \in W_0, \quad \mathcal{L}_a[v_a](x) = -\langle u, G(\cdot, x)\rangle^{\Delta\mathcal{C}}_{B_a}, \quad \forall x \in B_a \cup (\Omega \setminus \bar{B}_a) \tag{4.40}$$

where the linear integral operator $\mathcal{L}_a$ is defined by

$$\mathcal{L}_a[v](x) = v(x) + \langle v, G(\cdot, x)\rangle^{\Delta\mathcal{C}}_{B_a} \tag{4.41}$$

Equation (4.40) is readily recognized as a compactly-written form of the Lippmann-Schwinger domain integral equation governing the elastostatic inhomogeneity problem. If $x \in B_a$, (4.40) can be solved for v_a inside B_a. Then, if $x \in \Omega \setminus \bar{B}_a$, (4.40) becomes a representation formula, expressing v_a outside of B_a explicitly knowing v_a inside B_a.

Domain integral equation formulation for the FSTP. In a similar fashion, the free-space transmission problem (4.14) can be recast as a domain integral equation by setting $w = G_\infty(\cdot - x)$ in (4.15), to obtain

$$\text{Find } v_\mathcal{B} \in W_\infty, \quad \mathcal{L}_\mathcal{B}\big[v_\mathcal{B}[E]\big](x) = -\langle \varphi[E], G_\infty(\cdot - x)\rangle^{\Delta\mathcal{C}}_{\mathcal{B}}, \quad \forall x \in \mathcal{B} \cup (\mathbb{R}^3 \setminus \bar{\mathcal{B}}) \tag{4.42}$$

with the linear integral operator $\mathcal{L}_\mathcal{B}$ defined by

$$\mathcal{L}_\mathcal{B}[v](x) = v(x) + \langle v, G_\infty(\cdot - x)\rangle^{\Delta\mathcal{C}}_{\mathcal{B}}. \tag{4.43}$$

The EMT (Sec. 4.2.3) then manifests itself naturally when considering the far-field behavior of $v_\mathcal{B}[E]$. Indeed, from (4.42), $v_\mathcal{B}[E](\bar{x})$ is given, for $\bar{x} \notin \bar{\mathcal{B}}$, by the representation formula

$$v_\mathcal{B}[E](\bar{x}) = -\int_\mathcal{B} \nabla G_\infty(\cdot - \bar{x}) : \Delta\mathcal{C} : (E + \nabla v_\mathcal{B}[E]) \, \mathrm{d}V \tag{4.44}$$

(having used $\nabla\varphi[E] = E$). Applying a Taylor expansion to $\nabla G_\infty(\bar{\xi} - \bar{x})$ about $\bar{\xi} = 0$ and invoking the homogeneity property (4.38) yields $\nabla G_\infty(\bar{\xi} - \bar{x}) = -\nabla G_\infty(\bar{x}) + \mathcal{O}(|x|^{-3})$ ($|x| \to +\infty$). Consequently, the far-field behavior of $v_\mathcal{B}[E](x)$ as given by (4.44) is obtained as

$$v_\mathcal{B}[E](x) = -\nabla G_\infty(x) : \mathcal{A} : E + \mathcal{O}(|x|^{-3}) \qquad (|x| \to +\infty) \tag{4.45}$$

4.3.3 Asymptotic behavior of v_a

The leading asymptotic behavior of v_a is now investigated, which naturally leads to seek the limiting form for $a \to 0$ of integral equation (4.40). Moreover, since equation (4.40) involves integrals over the vanishing inhomogeneity B_a, it is convenient to rescale points $\xi, x \in B_a$, and consequently the differential volume element, according to:

$$\text{(a) } (\xi, x) = z + a(\bar{\xi}, \bar{x}), \qquad \text{(b) } \mathrm{d}V(\xi) = a^3 \, \mathrm{d}V(\bar{\xi}) \qquad (\xi \in B_a, \, \bar{\xi} \in \mathcal{B}). \tag{4.46}$$

This scaling is then introduced into (4.40). Invoking the decomposition (4.34) of $G(\xi, x)$, the homogeneity property (4.38) and the boundedness of G_C in B_a, one has

$$\nabla_1 G(\xi, x) = a^{-2}\nabla G_\infty(\bar{\xi} - \bar{x}) + \nabla_1 G_\mathrm{C}(z, z) + o(1) \tag{4.47}$$

Moreover, introducing the rescaled coordinates (4.46a) into v_a and u and setting $\bar{v}_a(\bar{\xi}) := v_a(z + a\bar{\xi})$, one obtains $\nabla v_a(\xi) = a^{-1}\nabla\bar{v}_a(\bar{\xi})$ and $\nabla u(\xi) = \nabla u(z) + \mathcal{O}(a)$. Using these expansions, together with (4.47) and (4.46b), in both sides of equation (4.40) then yields the expansions

$$\mathcal{L}_a[v_a](x) = \bar{v}_a(\bar{x}) + \langle \bar{v}_a, G_\infty(\cdot, \bar{x})\rangle^{\Delta\mathcal{C}}_{\mathcal{B}} + O\big(a^2\|\nabla\bar{v}_a\|_{L^2(\mathcal{B})}\big) + o(\|\nabla\bar{v}_a\|_{L^2(\mathcal{B})})$$
$$= \mathcal{L}_\mathcal{B}[\bar{v}_a](\bar{x}) + o(\|\nabla\bar{v}_a\|_{L^2(\mathcal{B})}) \text{ and}$$
$$\langle u, G(\cdot, x)\rangle^{\Delta\mathcal{C}}_{B_a} = a\langle \varphi[\nabla u(z)], G_\infty(\cdot, \bar{x})\rangle^{\Delta\mathcal{C}}_{\mathcal{B}} + o(a).$$

By virtue of the above expansions, the integral equation resulting from retaining only the contributions of lowest order in a in (4.40) is thus found to coincide with the integral equation (4.42) governing the free-space transmission problem with $E = a\nabla u(z)$. This suggests setting v_a in the form

$$v_a(x) = av_{\mathcal{B}}[\nabla u(z)]\left(\frac{x-z}{a}\right) + \delta_a(x) \qquad x \in B_a$$

The function $av_{\mathcal{B}}[\nabla u(z)]\big((x-z)/a\big)$ indeed defines the leading contribution to the so-called inner expansion of v_a, with the remainder δ_a only contributing higher order terms in the limit $a \to 0$, as stated in Lemma 4.3 in [12] (we retrace the proof of the 3D case for the sake of clarity)

Lemma 4.3.2 (asymptotic behavior of v_a). *Let the inner approximation $\tilde{v}_a$ to v_a be defined by*

$$\tilde{v}_a(x) = av_{\mathcal{B}}[\nabla u(z)]\left(\frac{x-z}{a}\right), \tag{4.48}$$

where $v_{\mathcal{B}}[\nabla u(z)]$ solves the FSTP (4.15) with $E = \nabla u(z)$. Moreover, for any cut-off function $\theta \in C_c^\infty(\Omega)$ such that $\theta \equiv 1$ in a neighborhood D of z, let $\delta_a \in H^1(\Omega; \mathbb{R}^3)$ be defined by

$$v_a = \theta \tilde{v}_a + \delta_a \tag{4.49}$$

Assume also that f has $C^{0,\beta}$ regularity for some $\beta > 0$ in a neighbourhood of z. Then there exists a constant $C > 0$ independent of a such that

(a) $\|\nabla \tilde{v}_a\|_{L^2(\Omega;\mathbb{R}^{3\times3})} \leq Ca^{3/2}$,   (b) $\|\tilde{v}_a\|_{L^2(\Omega;\mathbb{R}^3)} \leq Ca^{5/2}$,   (c) $\|\delta_a\|_{H^1(\Omega;\mathbb{R}^3)} \leq Ca^{5/2}$ (4.50)

and

$$\text{(a)} \quad \|\nabla v_a\|_{L^2(\Omega;\mathbb{R}^{3\times3})} \leq Ca^{3/2}, \quad \text{(b)} \quad \|v_a\|_{L^2(\Omega;\mathbb{R}^3)} \leq Ca^{5/2}. \tag{4.51}$$

Moreover

$$\text{(a)} \quad \|\nabla \tilde{v}_a\|_{L^\infty(\Omega\setminus D;\mathbb{R}^{3\times3})} \leq Ca^3, \quad \text{(b)} \quad \|v_a\|_{L^2(\partial\Omega;\mathbb{R}^{3\times3})} \leq Ca^3. \tag{4.52}$$

Proof. Estimates (4.50) of $\tilde{v}_a$ are found first by rescaling (for a small enough)

$$\|\tilde{v}_a\|_{L^2(\Omega)}^2 = a^2 \int_\Omega \left| v_{\mathcal{B}}[\nabla u(z)]\left(\frac{\xi-z}{a}\right)\right|^2 \mathrm{d}V(\xi) = a^5 \int_{(\Omega-z)/a} |v_{\mathcal{B}}[\nabla u(z)](\bar{\xi})|^2 \, \mathrm{d}V(\bar{\xi})$$

$$\leq a^5 \int_{\mathbb{R}^3} |v_{\mathcal{B}}[\nabla u(z)](\bar{\xi})|^2 \, \mathrm{d}V(\bar{\xi}) = Ca^5$$

(since the far-field behavior (4.14) implies that $v_{\mathcal{B}}$ is square-integrable). Similarly,

$$\|\nabla \tilde{v}_a\|_{L^2(\Omega)}^2 = a^2 \int_\Omega \left| \nabla_\xi v_{\mathcal{B}}[\nabla u(z)]\left(\frac{\xi-z}{a}\right)\right|^2 \mathrm{d}V(\xi) \leq a^3 \int_{\mathbb{R}^3} |\nabla v_{\mathcal{B}}[\nabla u(z)](\bar{\xi})|^2 \, \mathrm{d}V(\bar{\xi}) = Ca^3$$

The estimate on the boundary $\|v_a\|_{L^2(\partial\Omega)} \leq a^3$ follows from (4.40), thanks to the C^∞ regularity of G on $\partial\Omega$ when $x \notin B_a$. Furthermore, since $v_{\mathcal{B}} = \mathcal{O}(|x|^{-2})$ and $\nabla v_{\mathcal{B}} = \mathcal{O}(|x|^{-3})$ at infinity by virtue of (4.45), one also deduces by rescaling that

$$\|\tilde{v}_a\|_{L^\infty(\Omega\setminus D)} \leq Ca^3 \qquad \text{and} \quad \|\nabla \tilde{v}_a\|_{L^\infty(\Omega\setminus D)} \leq Ca^3. \tag{4.53}$$

Attention is now directed towards the estimate (4.50) on δ_a. Combining (4.12) and a rescaled version of (4.15), the weak formulation satisfied by δ_a is found as

$$\text{Find} \quad \delta_a \in W_0, \quad \langle \delta_a, w \rangle_\Omega^{\mathcal{C}_a} = - \langle u - \varphi[\nabla u(z)], w \rangle_{B_a}^{\Delta C} - G(w), \quad \forall w \in W_0$$

where $G(w)$ is defined as

$$G(w) = \langle \theta \tilde{v}_a, w \rangle_\Omega^{\mathcal{C}_a} + \langle \varphi[\nabla u(z)], \theta w \rangle_{B_a}^{\Delta C}$$

(having used that $\theta = 0$ in $\mathbb{R}^3 \setminus \Omega$ and $\theta = 1$ in B_a). Taking $w = \delta_a$, one then has the following estimate using the coercive bilinear form (4.4) and the triangular inequality

$$C\|\nabla\delta_a\|^2_{L^2(\Omega)} \leq |\langle\delta_a, \delta_a\rangle^{\mathcal{C}_a}_\Omega| \leq |\langle u - \varphi[\nabla u(z)], \delta_a\rangle^{\Delta C}_{B_a}| + |G(\delta_a)|. \tag{4.54}$$

The local smoothness assumption on f implies that u is C^2 at z. Applying the mean value theorem, one then has

$$|\nabla u(x) - \nabla u(z)| \leq Ca \text{ in } B_a,$$

so the first term in the right-hand side of (4.54) can be bounded as

$$|\langle u - \varphi[\nabla u(z)], \delta_a\rangle^{\Delta C}_{B_a}| \leq Ca^{5/2}\|\nabla\delta_a\|_{L^2(\Omega)}.$$

Moreover, one has

$$G(\delta_a) = \langle\theta\tilde{v}_a, \delta_a\rangle^{\mathcal{C}_a}_\Omega - \langle\tilde{v}_a, \theta\delta_a\rangle^{\mathcal{C}_a}_\Omega = \int_\Omega\left\{\nabla\delta_a : \mathcal{C}_a : (\tilde{v}_a \otimes \nabla\theta) - \nabla\tilde{v}_a : \mathcal{C}_a : (\delta_a \otimes \nabla\theta))\right\}\,\mathrm{d}V.$$

Hence, since $\nabla\theta$ vanishes in a neighborhood D of B_a, by estimates (4.53), it follows that

$$|G(\delta_a)| \leq C\left\{\|\tilde{v}_a\|_{L^\infty(\Omega\setminus D)} + \|\nabla\tilde{v}_a\|_{L^\infty(\Omega\setminus D)}\right\}\|\nabla\theta\|_{L^2(\Omega\setminus D)}\|\nabla\delta_a\|_{L^2(\Omega)}$$
$$\leq Ca^3\|\nabla\delta_a\|_{L^2(\Omega)}.$$

Finally, from (4.54), the following global estimate holds:

$$\|\nabla\delta_a\|_{L^2(\Omega)} \leq C(a^3 + a^{5/2}) \leq Ca^{5/2},$$

completing the proof by the Poincaré inequality. $\qquad\square$

We finish this section with the following lemma that relates u_a and the elastic moment tensor $\mathcal{A}$

Lemma 4.3.3. *For any vector field $w \in C^2(D; \mathbb{R}^3)$, where $D \subset \Omega$ is a neighbourhood of B_a, one has*

$$\langle w, u_a\rangle^{\Delta\mathcal{C}}_{B_a} = a^3\nabla w(z) : \mathcal{A} : \nabla u(z) + o(a^3) \tag{4.55}$$

where $\mathcal{A}$ is the elastic moment tensor defined by (4.16).

Proof. one notes that the following expansion is available for ∇w:

$$\nabla w(\xi) = \nabla w(z) + \mathcal{O}(|\xi - z|) = \nabla w(z) + \mathcal{O}(a|\bar{\xi}|) \quad (\xi \in B_a).$$

Moreover, a similar expansion is available for u, while (4.49) yields

$$\nabla v_a(\xi) = \nabla v_{\mathcal{B}}[\nabla u(z)](\bar{\xi}) + \nabla\delta_a(\xi) \quad (\xi \in B_a, \bar{\xi} \in \mathcal{B}).$$

Using the above expansions and rescaling (4.46), one obtains

$$\langle w, u_a\rangle^{\Delta\mathcal{C}}_{B_a} = a^3\nabla w(z) : \left\{\int_{\mathcal{B}}\Delta\mathcal{C} : (\nabla u(z) + \nabla v_{\mathcal{B}}[\nabla u(z)](\bar{\xi}))\,\mathrm{d}V(\bar{\xi})\right\} + \langle w, \delta_a\rangle^{\Delta\mathcal{C}}_{B_a} + \mathcal{O}(a^4)$$
$$= a^3\nabla w(z) : \mathcal{A} : \nabla u(z) + \langle w, \delta_a\rangle^{\Delta\mathcal{C}}_{B_a} + \mathcal{O}(a^4)$$

using definition (4.16) of the EMT. Finally, the estimate

$$\langle w, \delta_a\rangle^{\Delta\mathcal{C}}_{B_a} \leq C\|\nabla w\|_{L^2(B_a)}\|\nabla\delta_a\|_{L^2(B_a)} \leq Ca^{3/2}\|\delta_a\|_{H^1(\Omega)} \leq Ca^{3/2}a^{5/2} = Ca^4 = o(a^3)$$

holds for some constant C by virtue of (4.50). This completes the proof. $\qquad\square$

Remark 4.3.4. *As also remarked in [12], $\tilde{v}_a$ provides the leading contribution to the inner expansion of v_a in the sense that (i) $\theta = 1$ in B_a and can be made to vanish outside of an arbitrarily small neighbourhood of B_a and (ii) $\|\nabla \delta_a\|_{L^2(\Omega)} = \mathcal{O}(a^{5/2})$ while $\|\nabla \tilde{v}_a\|_{L^2(\Omega)} = \mathcal{O}(a^{3/2})$.*

Remark 4.3.5. *Lemma 4.3.2, established assuming $\mathcal{C}$ to be constant (homogeneous background material), is expected to also hold for heterogeneous elastic properties that are smooth in a fixed neighbourhood of z (with the EMT then defined in terms of $\mathcal{C}(z)$). Both [79] for the electrostatic case and [46] for the elastic case assume smooth heterogeneous background properties in Ω, the former emphasizing that the assumption may be significantly weakened. A numerical experiment involving a piecewise constant $\mathcal{C}$ for non-destructive testing is shown in Section 4.6.*

Remark 4.3.6. *Expansion (4.49) is the specialization to diametrically-small inhomogeneities of expansions obtained by [46] for more general classes of anisotropic inhomogeneities with vanishing measure $|B_a|$ (e.g. thin or elongated inhomogeneities).*

4.4 Topological derivative

In this section, we state our main result (Theorem 4.4.2) and give its proof in Section 4.4.1. The generalization to piecewise-regular densities ψ and the regularity of the adjoint state are then addressed in Sections 4.4.2 and 4.4.3, respectively. Finally, particular instances of Theorem 4.4.2 are discussed in Section 4.4.4. In order to ease the exposition, we recall Definition 1.1.22, but this time, making explicit the dependence w.r.t. the elastic tensor $\mathcal{C}_a$.

Definition 4.4.1 (Topological derivative). *Assume that $J(\mathcal{C}_a)$ in (4.27) can be expanded with respect the inclusion B_a (4.8) in the form*

$$J(\mathcal{C}_a) = J(\mathcal{C}) + \delta(a)DJ(z) + o(\delta(a)), \tag{4.56}$$

where z is the center of the inclusion B_a, the elastic tensors $\mathcal{C}_a, \mathcal{C}$ (4.9) correspond to the perturbed and non-perturbed transmission problems (4.10) and (4.1), and $\delta(a)$ is assumed to vanish as $a \to 0$ and characterizes the small-inhomogeneity asymptotic behavior of $J(\mathcal{C}_a)$. Then, the coefficient $DJ(z)$, which also depends a priori on the shape $\mathcal{B}$ and the moduli $\mathcal{C}, \mathcal{C}^\star$, is called the topological derivative of J at $z \in \Omega$.

Theorem 4.4.2. *Assume a three-dimensional setting as laid out in Section 4.2 and so as to ease the notation, denote $v_\mathcal{B} := v_\mathcal{B}[\nabla u(z)]$. Any cost functional J of the form (4.27) and fulfilling the assumptions made in Section 4.2.4 admits an expansion of the form (4.56), with $\delta(a) = a^3$ and the topological derivative $DJ(z)$ of J at $z \in \Omega$ given by*

$$DJ(z) = |\mathcal{B}|\Delta\psi(z, u(z), \nabla u(z)) - \nabla p(z) : \mathcal{A} : \nabla u(z)$$

$$+ \partial_d(\Delta\psi)(z, u(z), \nabla u(z)) : \int_\mathcal{B} \nabla v_\mathcal{B}(\bar{x}) \, dV(\bar{x})$$

$$+ \int_{\mathbb{R}^3 \setminus \mathcal{B}} \mathcal{G}(z, \nabla v_\mathcal{B}(\bar{x})) \, dV(\bar{x}) + \int_\mathcal{B} \mathcal{G}^\star(z, \nabla v_\mathcal{B}(\bar{x})) \, dV(\bar{x}). \tag{4.57}$$

The functions $\mathcal{G}$ and $\mathcal{G}^\star$: $\mathbb{R}^3 \times \mathbb{R}^{3 \times 3} \to \mathbb{R}$ are defined, for a given background solution u, by

$$\mathcal{G}(z, d) := \psi(z, u(z), \nabla u(z) + d) - \psi(z, u(z), \nabla u(z)) - \partial_d\psi(z, u(z), \nabla u(z)) : d \tag{4.58a}$$

$$\mathcal{G}^\star(z, d) := \psi^\star(z, u(z), \nabla u(z) + d) - \psi^\star(z, u(z), \nabla u(z)) - \partial_d\psi^\star(z, u(z), \nabla u(z)) : d, \tag{4.58b}$$

and $p \in W_0$ is the adjoint state, defined as the solution of the weak formulation

$$\langle p, w \rangle^\mathcal{C}_\Omega = \langle \partial_u \mathbb{J}_0(u, \nabla u), w \rangle + \langle \partial_d \mathbb{J}_0(u, \nabla u), \nabla w \rangle \qquad \forall w \in W_0, \tag{4.59}$$

with $\partial_u \mathbb{J}_0$ and $\partial_u \mathbb{J}_0$ as defined by (4.30).

When the densities $\psi, \psi^\star$ are linear or quadratic in their third argument (i.e. when $\partial_{dd}^2 \psi$ and $\partial_{dd}^2 \psi^\star$ are independent on d), letting $\mathcal{D}(z) := \partial_{dd}^2 \psi(z, u(z))$ and $\mathcal{D}^\star(z) := \partial_{dd}^2 \psi^\star(z, u(z))$, the last two terms in (4.57) are given by the more explicit expression

$$\frac{1}{2} \int_{\mathbb{R}^3 \setminus \mathcal{B}} \nabla v_{\mathcal{B}}(\bar{x}) \colon \mathcal{D}(z) \colon \nabla v_{\mathcal{B}}(\bar{x}) \; dV(\bar{x}) + \frac{1}{2} \int_{\mathcal{B}} \nabla v_{\mathcal{B}}(\bar{x}) \colon \mathcal{D}^\star(z) \colon \nabla v_{\mathcal{B}}(\bar{x}) \; dV(\bar{x})$$

Moreover, under two-dimensional plane-strain conditions (where only in-plane displacements are nonzero), the result (4.57) still holds (with $\Omega \subset \mathbb{R}^2$, $\mathcal{B} \subset \mathbb{R}^2$ and the next-to-last integral now taken over $\mathbb{R}^2 \setminus \mathcal{B}$), while $\delta(a) = a^2$ in expansion (4.56).

4.4.1 Proof of the main result

The detailed proof to follow concentrates on the 3D case, its adaptation to the 2D case being then outlined in a comment. The proof consists in finding the leading contribution to the difference $J(\mathcal{C}_a) - J(\mathcal{C}) = \mathbb{J}_a(u_a, \nabla u_a) - \mathbb{J}_0(u, \nabla u)$ as $a \to 0$. To this end, we write

$$
\begin{aligned}
\mathbb{J}_a(u_a, \nabla u_a) - \mathbb{J}_0(u, \nabla u) = & \Big(\mathbb{J}_a(u, \nabla u) - \mathbb{J}_0(u, \nabla u) \Big) \\
& + \Big(\mathbb{J}_a(u_a, \nabla u_a) - \mathbb{J}_a(u, \nabla u_a) - \langle \partial_u \mathbb{J}_a(u, \nabla u), v_a \rangle \Big) \\
& + \Big(\mathbb{J}_a(u, \nabla u_a) - \mathbb{J}_a(u, \nabla u) - \langle \partial_d \mathbb{J}_a(u, \nabla u), \nabla v_a \rangle \Big) \\
& + \Big(\langle \partial_u \mathbb{J}_a(u, \nabla u), v_a \rangle + \langle \partial_d \mathbb{J}_a(u, \nabla u), \nabla v_a \rangle \Big),
\end{aligned}
\tag{4.60}
$$

with $\partial_u \mathbb{J}_a$ and $\partial_u \mathbb{J}_a$ as defined by (4.30), and separately evaluate the leading contribution of each bracketed term in the right-hand side of (4.60); this is done in the following Lemmas 4.4.3 to 4.4.6. Using the results of the lemmas in the above decomposition then directly establishes both the expansion (4.56) and the expression (4.57) of $\mathrm{D}J(z)$ stated in Theorem 4.4.2.

Lemma 4.4.3. *Let $\Delta\psi$ be defined as in (4.28). One has*

$$\mathbb{J}_a(u, \nabla u) - \mathbb{J}_0(u, \nabla u) = a^3 |\mathcal{B}| \Delta\psi(z, u(z), \nabla u(z)) + o(a^3).$$

Proof. By interior regularity for u and the assumed smoothness of $\psi, \psi^\star$, $\Delta\psi(x, u(x), \nabla u(x))$ is continuous at $x = z$. Therefore, the Lemma follows easily from:

$$
\begin{aligned}
\mathbb{J}_a(u, \nabla u) - \mathbb{J}_0(u, \nabla u) &= \int_\Omega \big(\psi_a(x, u, \nabla u) - \psi(x, u, \nabla u) \big) \; \mathrm{d}V(x) \\
&= \int_{B_a} \Delta\psi(x, u, \nabla u) \; \mathrm{d}V(x) = a^3 |\mathcal{B}| \Delta\psi(z, u(z), \nabla u(z)) + o(a^3),
\end{aligned}
$$

where the last step exploits the fact that the volume of B_a is $|B_a| = a^3 |\mathcal{B}|$. $\qquad\square$

Lemma 4.4.4. *Let the displacement perturbation v_a solve problem (4.12). One has*

$$\mathbb{J}_a(u_a, \nabla u_a) - \mathbb{J}_a(u, \nabla u_a) - \langle \partial_u \mathbb{J}_a(u, \nabla u), v_a \rangle = o(a^3),$$

with $\partial_u \mathbb{J}_a$ as defined by (4.30)

Proof. The proof is based on Taylor expansions. A first-order expansion of ψ with respect to its first argument first yields

$$\psi(x, u_a, \nabla u_a) - \psi(x, u, \nabla u_a) = \partial_u \psi(x, u, \nabla u_a) \cdot v_a + \tfrac{1}{2} v_a \cdot \partial_{uu}^2 \psi(x, u + \delta_u v_a, \nabla u_a) \cdot v_a$$

for some $\delta_u(x) \in [0,1]$. Moreover, a zeroth-order Taylor expansion of $\partial_u \psi$ with respect to its second argument gives

$$\partial_u \psi(x, u, \nabla u_a) \cdot v_a - \partial_u \psi(x, u, \nabla u) \cdot v_a = \nabla v_a : \partial^2_{du} \psi(x, u, \nabla u + \delta_d \nabla v_a) \cdot v_a$$

for some $\delta_d(x) \in [0,1]$. Both expansions are valid due to the assumed regularity of ψ. Similar expansions also hold for the densities $\psi^\star, \psi_S$, for some $\delta_u^\star(x), \delta_d^\star(x), \delta_S^u(x) \in [0,1]$. Combining all of these expansions, one finds

$$\mathbb{J}_a(u_a, \nabla u_a) - \mathbb{J}_a(u, \nabla u_a) = \langle \partial_u \mathbb{J}_a(u, \nabla u), v_a \rangle + R_a \tag{4.61}$$

with the remainder R_a given by

$$R_a = \int_{\Omega \backslash B_a} \left[\tfrac{1}{2} v_a \cdot \partial^2_{uu} \psi(x, u + \delta_u v_a, \nabla u_a) \cdot v_a + \nabla v_a : \partial^2_{du} \psi(x, u, \nabla u + \delta_d \nabla v_a) \cdot v_a \right] \mathrm{d}V$$

$$+ \int_{B_a} \left[\tfrac{1}{2} v_a \cdot \partial^2_{uu} \psi^\star(x, u + \delta_u^\star v_a, \nabla u_a) \cdot v_a + \nabla v_a : \partial^2_{du} \psi^\star(x, u, \nabla u + \delta_d^\star \nabla v_a) \cdot v_a \right] \mathrm{d}V$$

$$+ \int_{\partial \Omega} \tfrac{1}{2} v_a \cdot \partial^2_{uu} \psi_S(x, u + \delta_S^u v_a) \cdot v_a \, \mathrm{d}S$$

Next, thanks to the boundedness of the second-order partial derivatives of ψ, $\psi^\star$ and ψ_S, there exists a constant $C > 0$ such that

$$R_a \leq C \left(\|v_a\|^2_{L^2(\Omega)} + \|\nabla v_a\|_{L^2(\Omega)} \|v_a\|_{L^2(\Omega)} + \|v_a\|^2_{L^2(\partial\Omega)} \right)$$

Finally, estimates (4.51) and 4.52 imply that there exists a constant $C > 0$ such that

$$R_a \leq C a^4 = o(a^3).$$

Using the above estimate in (4.61) completes the proof. $\qquad \square$

Lemma 4.4.5. *One has*

$$\mathbb{J}_a(u, \nabla u_a) - \mathbb{J}_a(u, \nabla u) - \langle \partial_d \mathbb{J}_a(u, \nabla u), \nabla v_a \rangle$$

$$= a^3 \left\{ \int_{\mathbb{R}^3 \backslash \mathcal{B}} \mathcal{G}(z, \nabla v_{\mathcal{B}}(\bar{x})) \, dV(\bar{x}) + \int_{\mathcal{B}} \mathcal{G}^\star(z, \nabla v_{\mathcal{B}}(\bar{x})) \, dV(\bar{x}) \right\} + o(a^3) \tag{4.62}$$

where $\partial_d \mathbb{J}_a$ is defined by (4.30) and the functions $\mathcal{G}$ and $\mathcal{G}^\star$: $\mathbb{R}^3 \times \mathbb{R}^{3\times 3} \to \mathbb{R}$ are defined by (4.58a,b).

Proof. We remark that since ψ_S has no third argument, we omit the terms involving ψ_S in $\mathbb{J}_a$ for the following analysis. The combination to be estimated is first recast in the form

$$\mathbb{J}_a(u, \nabla u_a) - \mathbb{J}_a(u, \nabla u) - \langle \partial_d \mathbb{J}_a(u, \nabla u), \nabla v_a \rangle$$

$$= \int_{\Omega \backslash B_a} \mathcal{G}(x, \nabla v_a) \, \mathrm{d}V(x) + \int_{B_a} \mathcal{G}^\star(x, \nabla v_a) \, \mathrm{d}V(x)$$

$$= \Big(\mathbb{J}_a(u, \nabla u_a) - \mathbb{J}_a(u, \nabla u + \nabla \tilde{v}_a) - \langle \partial_d \mathbb{J}_a(u, \nabla u + \nabla \tilde{v}_a), \nabla \hat{v}_a \rangle \Big)$$

$$+ \Big(\partial_d \mathbb{J}_a(u, \nabla u + \nabla \tilde{v}_a), \nabla \hat{v}_a \rangle - \langle \partial_d \mathbb{J}_a(u, \nabla u), \nabla \hat{v}_a \rangle \Big)$$

$$+ \Big(\mathbb{J}_a(u, \nabla u + \nabla \tilde{v}_a) - \mathbb{J}_a(u, \nabla u) - \langle \partial_d \mathbb{J}_a(u, \nabla u), \nabla \tilde{v}_a \rangle \Big) \tag{4.63a}$$

having used functions $\mathcal{G}$, $\mathcal{G}^\star$ defined by (4.58a,b) for the last equality, and with $\hat{v}_a$ defined (using (4.49) in the second equality below) by

$$\hat{v}_a = v_a - \tilde{v}_a = \delta_a + (\theta - 1)\tilde{v}_a. \tag{4.63b}$$

Since $\nabla \hat{v}_a = \nabla \delta_a + (\theta - 1)\nabla \tilde{v}_a + \nabla \theta \otimes \tilde{v}_a$, we note for later use that estimates (4.50) and (4.52) (together with the fact that the support of $(\theta - 1)\nabla \tilde{v}_a$ is $\Omega \setminus D$) imply

$$\|\nabla \hat{v}_a\|_{L^2(\Omega)} = \mathcal{O}(a^{5/2}). \tag{4.63c}$$

We first focus on contributions of integrals over $\Omega \setminus B_a$, i.e. of the density $\mathcal{G}$, to (4.63a). To begin, each bracketed combination in (4.63a) is reformulated by exploiting Taylor expansions (of first-order with respect to its third argument, with integral remainder) of ψ, to obtain

$$\int_{\Omega \setminus B_a} \mathcal{G}(x, \nabla v_a) \, \mathrm{d}V(x) = \int_{\Omega \setminus B_a} \nabla \hat{v}_a(x) : D_2\big(x, u + \tilde{v}_a, \nabla \hat{v}_a(x)\big) : \nabla \hat{v}_a(x) \, \mathrm{d}V(x)$$

$$+ \int_{\Omega \setminus B_a} \nabla \hat{v}_a(x) : D_1\big(x, \nabla \hat{v}_a(x)\big) : \nabla \tilde{v}_a(x) \, \mathrm{d}V(x)$$

$$+ \int_{\Omega \setminus B_a} \nabla \tilde{v}_a(x) : D_3\big(x, \nabla \tilde{v}_a(x)\big) : \nabla \tilde{v}_a(x) \, \mathrm{d}V(x), \tag{4.63d}$$

with

$$D_1(y, d) = \int_0^1 \partial_{dd}\psi\big(y, u(y), \nabla u(y) + td)\big) \, \mathrm{d}t,$$

$$D_2(y, w, d) = \int_0^1 \partial_{dd}\psi\big(y, u(y), \nabla w(y) + td\big)(1 - t) \, \mathrm{d}t, \tag{4.63e}$$

$$D_3(y, d) = D_2(y, u, d).$$

Both $D_1\big(x, \nabla \hat{v}_a(x)\big)$ and $D_2\big(x, u(x) + \tilde{v}_a(x), \nabla \hat{v}_a(x)\big)$ are bounded over Ω, due to the boundedness of the second-order partial derivatives of ψ. This remark is exploited by applying the Cauchy-Schwarz inequality to the first two integrals I_1 and I_2 of the right-hand side of (4.63d) and invoking estimates (4.50a) and (4.63c), to obtain $I_1 = \mathcal{O}(a^5) = o(a^3)$ and $I_2 = \mathcal{O}(a^4) = o(a^3)$. Using these estimates, applying the change of variables $\bar{x} = (x - z)/a$ to the third integral of the right-hand side of (4.63d) (whereby $\mathrm{d}V(x) = a^3 \, \mathrm{d}V(\bar{x})$), and recalling definition (4.49) of $\tilde{v}_a$, we obtain

$$\int_{\Omega \setminus B_a} \mathcal{G}(x, \nabla \tilde{v}_a) \, \mathrm{d}V(x) = a^3 \int_{((\Omega - z)/a) \setminus \mathcal{B}} \nabla v_{\mathcal{B}}(\bar{x}) : D_3(z + a\bar{x}, \nabla v_{\mathcal{B}}(\bar{x})) : \nabla v_{\mathcal{B}}(\bar{x}) \, \mathrm{d}V(\bar{x}) + o(a^3)$$

$$= a^3 \int_{((\Omega - z)/a) \setminus \mathcal{B}} \nabla v_{\mathcal{B}}(\bar{x}) : D_3(z, \nabla v_{\mathcal{B}}(\bar{x})) : \nabla v_{\mathcal{B}}(\bar{x}) \, \mathrm{d}V(\bar{x}) + R + o(a^3)$$

$$= a^3 \int_{((\Omega - z)/a) \setminus \mathcal{B}} \mathcal{G}(z, \nabla v_{\mathcal{B}}(\bar{x})) \, \mathrm{d}V(\bar{x}) + R + o(a^3) \tag{4.63f}$$

(having noted that $\nabla v_{\mathcal{B}}(\bar{x}) : D_3(z, \nabla v_{\mathcal{B}}(\bar{x})) : \nabla v_{\mathcal{B}}(\bar{x}) = \mathcal{G}(z, \nabla v_{\mathcal{B}}(\bar{x}))$), where the remainder R is such that

$$R := a^3 \int_{((\Omega - z)/a) \setminus \mathcal{B}} \nabla v_{\mathcal{B}}(\bar{x}) : \big[D_3(z + a\bar{x}, \nabla v_{\mathcal{B}}(\bar{x})) - D_3(z, \nabla v_{\mathcal{B}}(\bar{x}))\big] : \nabla v_{\mathcal{B}}(\bar{x}) \, \mathrm{d}V(\bar{x})$$

$$\leq Ca^{3+\gamma} \int_{((\Omega - z)/a) \setminus \mathcal{B}} |\nabla v_{\mathcal{B}}(\bar{x})|^2 |\bar{x}|^\gamma \, \mathrm{d}V(\bar{x}) \leq Ca^{3+\gamma} \int_{\mathbb{R}^3 \setminus \mathcal{B}} |\nabla v_{\mathcal{B}}(\bar{x})|^2 |\bar{x}|^\gamma \, \mathrm{d}V(\bar{x}), \tag{4.63g}$$

by virtue of the inequality

$$|D_3(z + a\bar{x}, d) - D_3(z, d)| \leq Ca^\gamma |\bar{x}|^\gamma \tag{4.63h}$$

stemming from the assumed $C^{0,\gamma}$ Hölder regularity of $\partial_{dd}\psi$ and the known C^2 interior regularity of u in Ω, which implies that there exists $\tau', \tau'' \in [0, 1]$ such that

$$u(x) - u(z) = a\nabla u(z + \tau' a\bar{x}) \cdot \bar{x}, \qquad \nabla u(x) - \nabla u(z) = a\nabla^2 u(z + \tau'' a\bar{x}) \cdot \bar{x}. \tag{4.63i}$$

The known $\mathcal{O}(|\bar{x}|^{-3})$ far-field behavior of $\nabla v_{\mathcal{B}}(\bar{x})$ [227] implies that the last integral in (4.63g) over the unbounded domain $\mathbb{R}^3 \setminus \mathcal{B}$ is finite for any $\gamma < 3$, and hence that $R = \mathcal{O}(a^{3+\gamma}) = o(a^3)$. Finally, taking the limit $((\Omega - z)/a) \setminus \mathcal{B} \to \mathbb{R}^3 \setminus \mathcal{B}$ in (4.63f) (which is legitimate as the integral over the limiting unbounded domain $\mathbb{R}^3 \setminus \mathcal{B}$ is finite), the desired asymptotic form of (4.63d) is obtained:

$$\int_{\Omega \setminus B_a} \mathcal{G}(x, \nabla v_a)\, dV(x) = a^3 \int_{\mathbb{R}^3 \setminus \mathcal{B}} \mathcal{G}(z, \nabla v_{\mathcal{B}}(\bar{x}))\, dV(\bar{x}) + o(a^3). \tag{4.63j}$$

The second integral in the right-hand side of (4.63a) can be estimated following similar arguments. A representation similar to (4.63d) holds, with integrals taken over B_a and ψ replaced by $\psi^\star$ in (4.63e). Noting in addition that now $\hat{v}_a = \delta_a$ since $\theta = 1$ in B_a, the first two integrals in the right-hand side of the counterpart of (4.63d) are easily established to be of order $o(a^3)$ using estimates (4.50). Using again the change of variables $\bar{x} = (x - z)/a$ in the remaining integral, one then finds

$$\int_{B_a} \mathcal{G}^\star(x, \nabla v_a)\, dV(x) = a^3 \int_{\mathcal{B}} \mathcal{G}^\star(z, \nabla v_{\mathcal{B}}(\bar{x}))\, dV(\bar{x}) + R^\star + o(a^3), \tag{4.63k}$$

where, exploiting through (4.63h) the assumed Hölder regularity of $\psi^\star$, the remainder $R^\star$ is such that

$$R^\star := a^3 \int_{\mathcal{B}} \nabla v_{\mathcal{B}}(\bar{x}) : \big[D(z + a\bar{x}, \nabla v_{\mathcal{B}}(\bar{x})) - D(z, \nabla v_{\mathcal{B}}(\bar{x})) \big] : \nabla v_{\mathcal{B}}(\bar{x})\, dV(\bar{x})$$
$$\leq C a^{3+\gamma} \int_{\mathcal{B}} |\nabla v_{\mathcal{B}}(\bar{x})|^2 |\bar{x}|^\gamma\, dV(\bar{x}) = \mathcal{O}(a^{3+\gamma}).$$

The desired asymptotic form of (4.63k) is therefore obtained:

$$\int_{B_a} \mathcal{G}^\star(x, \nabla v_a)\, dV(x) = a^3 \int_{\mathcal{B}} \mathcal{G}^\star(z, \nabla v_{\mathcal{B}}(\bar{x}))\, dV(\bar{x}) + o(a^3) \tag{4.63l}$$

The lemma finally follows from using expansions (4.63j) and (4.63l) in (4.63a). $\square$

Finally, the leading contribution to the last bracketed combination of (4.60) is given in the following lemma in terms of an adjoint solution.

Lemma 4.4.6. *Let the adjoint solution $p \in W_0$ be defined by the weak formulation*

$$\langle p, w \rangle_\Omega^{\mathcal{C}} = \langle \partial_u \mathbb{J}_0(u, \nabla u), w \rangle + \langle \partial_d \mathbb{J}_0(u, \nabla u), \nabla w \rangle \qquad \forall w \in W_0, \tag{4.64}$$

with $\partial_u \mathbb{J}_0$ and $\partial_d \mathbb{J}_0$ as defined by (4.30). One has

$$\langle \partial_u \mathbb{J}_a(u, \nabla u), v_a \rangle + \langle \partial_d \mathbb{J}_a(u, \nabla u), \nabla v_a \rangle$$
$$= a^3 |\mathcal{B}| \Big\{ -\nabla p(z) : \mathcal{A} : \nabla u(z) + \partial_d(\Delta \psi)(z, u(z), \nabla u(z)) : \int_{\mathcal{B}} \nabla v_{\mathcal{B}}\, dV(\bar{x}) \Big\} + o(a^3) \tag{4.65}$$

Proof. One has

$$\langle \partial_u \mathbb{J}_a(u, \nabla u), v_a \rangle + \langle \partial_d \mathbb{J}_a(u, \nabla u), \nabla v_a \rangle = \langle \partial_u \mathbb{J}_0(u, \nabla u), v_a \rangle + \langle \partial_d \mathbb{J}_0(u, \nabla u), \nabla v_a \rangle$$
$$+ \langle \partial_u \Delta \mathbb{J}(u, \nabla u), v_a \rangle + \langle \partial_d \Delta \mathbb{J}(u, \nabla u), \nabla v_a \rangle \tag{4.66a}$$

Invoking the definition (4.64) of the adjoint solution, the identity

$$\langle v_a, w \rangle_\Omega^{\mathcal{C}} = -\langle u_a, w \rangle_{B_a}^{\Delta \mathcal{C}}, \quad \forall w \in W_0$$

verified by the transmission problem, one finds

$$
\langle \partial_u \mathbb{J}_0(u, \nabla u), v_a \rangle + \langle \partial_d \mathbb{J}_0(u, \nabla u), \nabla v_a \rangle = \langle p, v_a \rangle_\Omega^{\mathcal{C}} = -\langle u_a, p \rangle_{B_a}^{\Delta \mathcal{C}}
$$
$$
= -a^3 |\mathcal{B}| \nabla p(z) : \mathcal{A} : \nabla u(z) + o(a^3), \quad (4.66b)
$$

where the last equality holds by virtue of Lemma 4.3.3 and p having C^2 interior regularity (see Section 4.4.3). Next, using decomposition (4.49) of v_a and the fact that $\Delta \mathbb{J}$ has B_a as its geometrical support (implying in particular that no surface contribution of ψ_S is present and $\theta = 1$ in B_a), one has

$$
\langle \partial_u \Delta \mathbb{J}(u, \nabla u), v_a \rangle + \langle \partial_d \Delta \mathbb{J}(u, \nabla u), \nabla v_a \rangle
$$
$$
= \langle \partial_u \Delta \mathbb{J}(u, \nabla u), (\tilde{v}_a + \delta_a) \rangle + \langle \partial_d \Delta \mathbb{J}(u, \nabla u), \nabla(\tilde{v}_a + \delta_a) \rangle \quad (4.66c)
$$

The partial derivatives of $\Delta \psi(x, u(x), \nabla u(x))$ being bounded by virtue of the assumptions made on ψ, $\psi^\star$ and the C^2 interior regularity of u, there exists a constant $C > 0$ such that

$$
\langle \partial_u \Delta \mathbb{J}(u, \nabla u), (\tilde{v}_a + \delta_a) \rangle + \langle \partial_d \Delta \mathbb{J}(u, \nabla u), \nabla \delta_a \rangle \leq a^{3/2} (\|\tilde{v}_a\|_{L^2(\Omega;\mathbb{R}^3)} + \|\delta_a\|_{H^1(\Omega;\mathbb{R}^3)}))
$$
$$
\leq C a^4, \quad (4.66d)
$$

the last inequality stemming from estimates (4.50).

The term $\langle \partial_d \Delta \mathbb{J}(u, \nabla u), \nabla \tilde{v}_a \rangle$ remains to be estimated. By the mean value theorem applied to $\partial_d(\Delta \psi)(x, u(x), \nabla u(x))$, there exists $t(x) \in [0, 1]$ such that

$$
\partial_d(\Delta \psi)(x, u(x), \nabla u(x)) = \partial_d(\Delta \psi)(z, u(z), \nabla u(z)) + \partial_{xd}^2 \Delta \psi(x_t, u_t, \nabla u_t) \cdot (x - z)
$$
$$
+ \partial_{ud}^2 \Delta \psi(x_t, u_t, \nabla u_t) \cdot [u(x) - u(z)] + \partial_{dd}^2 \Delta \psi(x_t, u_t, \nabla u_t) : [\nabla u(x) - \nabla u(z)]
$$

where x_t, u_t, ∇u_t are defined by

$$
\begin{aligned}
x_t &:= z + t(x - z), \\
u_t &:= u(z) + t[u(x) - u(z)], \\
\nabla u_t &:= \nabla u(z) + t[\nabla u(x) - \nabla u(z)].
\end{aligned} \quad (4.66e)
$$

Introducing $x - z = a\bar{x}$ and expansions (4.63i), stemming from the C^2 interior regularity of u, in the above definitions, one obtains for $x \in B_a$

$$
\partial_d(\Delta \psi)(x, u(x), \nabla u(x)) = \partial_d(\Delta \psi)(z, u(z), \nabla u(z)) + \mathcal{O}(a)
$$

which in turn implies

$$
\langle \partial_d \Delta \mathbb{J}(u, \nabla u), \nabla \tilde{v}_a \rangle = a^3 \partial_d(\Delta \psi)(z, u(z), \nabla u(z)) : \int_{\mathcal{B}} \nabla v_{\mathcal{B}} \, dV + o(a^3) \quad (4.66f)
$$

The lemma finally follows by substituting (4.66d) and (4.66f) into the right-hand side of (4.66c) and then using the resulting estimate together with (4.66b) in (4.66a). □

Remark 4.4.7. *The foregoing analysis still holds if the cost functional format (4.27) is extended to also allow integrals of the form*

$$
\int_\Gamma \psi_S(x, u) \, dS(x)
$$

where $\Gamma \subset \bar{\Omega}$ is an arbitrary surface, provided $DJ(z)$ is evaluated at points $z \notin \Gamma$.

The two-dimensional case. The proof for the two-dimensional plane-strain case is identical, except for the fact that estimates (4.50) to (4.52) must be replaced by their following two-dimensional counterparts:

(a) $\|\nabla\tilde{v}_a\|_{L^2(\Omega;\mathbb{R}^2)} \leq Ca,$ (b) $\|\tilde{v}_a\|_{L^2(\Omega;\mathbb{R}^2)} \leq Ca^2\sqrt{|\log a|},$ (c) $\|\delta_a\|_{H^1(\Omega;\mathbb{R}^2)} \leq Ca^2,$

$$\tag{4.67a}$$

(a) $\|\nabla v_a\|_{L^2(\Omega;\mathbb{R}^2)} \leq Ca,$ (b) $\|v_a\|_{L^2(\Omega;\mathbb{R}^2)} \leq Ca^2.$ (4.67b)

(a) $\|\nabla\tilde{v}_a\|_{L^\infty(\Omega\setminus D)} \leq Ca^2,$ (b) $\|v_a\|_{L^2(\partial\Omega;\mathbb{R}^2)} \leq Ca^2,$ (4.67c)

which can be established e.g. by adapting to the two-dimensional case Lemma 4.3.2 (see [12]).

4.4.2 Case of piecewise-regular cost functional densities

Now we extend the previous results to the topological derivative of functionals J_ω defined by an integral over a portion $\omega \subset \Omega$ of the elastic body Ω, of the form

$$J_\omega(\mathcal{C}_a) = \mathbb{J}_a(u_a, \nabla u_a; \omega), \qquad \text{with} \ \ \mathbb{J}_a(u, d; \omega) = \int_\omega \psi_a(x, u, \nabla u) \, dV(x),$$

where the trial inhomogeneity B_a is assumed to satisfy either $B_a \Subset \omega$ or $B_a \Subset (\Omega\setminus\bar{\omega})$ (the case where $\overline{B_a}\cap\partial\omega \neq \emptyset$ not being considered). If $B_a \Subset \omega$, the previous analysis remains valid, with DJ still given by (4.57) and the only change concerning the adjoint solution, which now satisfies the weak formulation

$$\int_\Omega e(p) : \mathcal{C} : e(q) \, dV = \int_\Omega \chi_\omega\{\partial_d\psi : \nabla q + \partial_u\psi \cdot q\} \, dV, \qquad \forall q \in W_0(\Omega). \tag{4.68}$$

On the other hand, if $B_a \Subset (\Omega\setminus\bar{\omega})$, $\psi_a - \psi = 0$ in ω and the cut-off function θ in decomposition (4.49) can be chosen, for any sufficiently small a, such that $\theta = 0$ in ω. This choice implies that $v_a = \delta_a$ in ω for any $z \in \Omega\setminus\bar{\omega}$, and hence, by estimate (4.50c), that

$$\|v_a\|_{H^1(\omega;\mathbb{R}^3)} \leq Ca^{5/2}.$$

Consequently, retracing the proof of Theorem 4.4.2, contributions to DJ arising from $\partial_{dd}\psi$ and $\partial_{dd}\psi^\star$ in Lemma 4.4.5 are $o(a^3)$, and DJ is simply given, in terms of the solutions u of (4.3) and p of (4.68), by

$$DJ(z) = -\nabla p(z) : \mathcal{A} : \nabla u(z). \tag{4.69}$$

4.4.3 Regularity of the adjoint solution

As it was previously seen, the point-wise evaluation of DJ at some $z \in \Omega$ requires the background displacement u and the adjoint solution p to have some local regularity at z, namely $u, p \in C^{2,\alpha}(D;\mathbb{R}^3)$ for some neighborhood $D \Subset \Omega$ of z and $\alpha \in (0,1)$. The needed regularity for u follows directly from the regularity of the body force density $f \in C^{0,\alpha}(\Omega;\mathbb{R}^3)$. When the cost function J depends only on u, the adjoint state p solves

$$\text{Find} \ \ p \in W_0, \qquad \langle p, w \rangle^{\mathcal{C}}_\Omega = \langle \partial_u\mathbb{J}_0(u), w \rangle, \quad \forall w \in W_0.$$

Then, if $\partial_u\psi(x, u(x)) \in C^{0,\alpha}(\Omega;\mathbb{R}^3)$, p fulfills automatically the required interior regularity in Ω. On the contrary, the case when the cost functional depends on ∇u is slightly more delicate. In such a case p solves

$$\text{Find} \ \ p \in W_0, \qquad \langle p, w \rangle^{\mathcal{C}}_\Omega = \langle \partial_d\mathbb{J}_0(\nabla u), \nabla w \rangle, \quad \forall w \in W_0$$

Thus if $\partial_d\psi(x,\nabla u(x)) \in C^{1,\alpha}(\Omega;\mathbb{R}^{3\times3})$, p fulfills the required regularity. We remark that the components of the tensor $(\nabla u)_{ij} \in C^{1,\alpha}(\Omega)$ so we can take any function $\psi(\cdot,d) \in C^1(\mathbb{R}^{3\times3})$ for this purpose. Finally when the cost function $\mathbb{J}$ is defined in a sub-domain ω of Ω,

$$\langle\partial_d\mathbb{J}_0(\nabla u),\nabla w\rangle = \int_\omega \partial_d\psi(x,\nabla u):\nabla w \,\mathrm{d}V = \int_\Omega \chi_\omega\partial_d\psi(x,\nabla u(x)):\nabla w \,\mathrm{d}V,$$

the adjoint state p solves

$$\begin{cases} -\mathrm{div}(\mathcal{C}e(p)) = -\mathrm{div}(\chi_\omega\partial_d\psi(x,\nabla u)) & \text{in } \Omega, \\ \qquad\qquad\quad p = 0 & \text{on } \Gamma_D, \\ \qquad\;\; \mathcal{C}:e(p)\cdot n = 0 & \text{on } \Gamma_N, \end{cases}$$

where $\Gamma_N \cap \omega = \emptyset$ is assumed. We can easily check that $\mathrm{div}(\chi_\omega\partial_d\psi(x,\nabla u(x))) \in H^{-1}(\Omega;\mathbb{R}^3)$ if $\partial_d\psi(x,\nabla u(x)) \in C^{1,\alpha}(\Omega;\mathbb{R}^{3\times3})$. Then by the Lax-Milgram theorem $p \in W_0(\Omega)$. To achieve the required $C^{2,\alpha}$ local regularity of p at $z \in \Omega$, we only need to select $z \notin \partial\omega$.

Indeed, if $z \in (\Omega\setminus\bar\omega)$, there is a smooth neighborhood $D \subset \Omega\setminus\bar\omega$ of z such that $\mathrm{div}(\mathcal{C}:e(p)) = 0$ in D. Therefore (e.g. [213, Theorem 4.16]), there exists a neighborhood $D' \Subset D$ of z where $p \in C^{2,\alpha}(D';\mathbb{R}^3)$.

Otherwise if $z \in \omega$, there exists a smooth neighborhood $D \Subset \omega$ of z where p solves the problem

$$\begin{cases} -\mathrm{div}(\mathcal{C}e(q)) = -\mathrm{div}(\partial_d\psi(x,\nabla u)) & \text{in } D, \\ \qquad\qquad\quad q = p & \text{on } \partial D. \end{cases}$$

The adjoint state p can be decomposed as $p = p_1 + p_2$, where p_1 solves the problem

$$\begin{cases} -\mathrm{div}(\mathcal{C}e(q)) = 0 & \text{in } D, \\ \qquad\qquad q = p & \text{on } \partial D \end{cases}$$

and p_2 solves

$$\begin{cases} -\mathrm{div}(\mathcal{C}e(q)) = -\mathrm{div}(\partial_d\psi(x,\nabla u)) & \text{in } D, \\ \qquad\qquad\quad q = 0 & \text{on } \partial D. \end{cases}$$

Therefore, there exists a neighborhood $D' \Subset D$ of z where $p_1 \in C^{2,\alpha}(D';\mathbb{R}^3)$. Moreover $p_2 \in C^{2,\alpha}(D;\mathbb{R}^3)$ if $\partial_d\psi(x,\nabla u(x)) \in C^{1,\alpha}(D;\mathbb{R}^{3\times3})$, thanks to the interior regularity of p_2. Hence $p \in C^{2,\alpha}(D';\mathbb{R}^3)$.

4.4.4 Particular cases

A few particular instances of the general result given by Theorem 4.4.2, and their connections to previously-available results, are now discussed.

Displacement-based functional. In this case, $\partial_d\psi = \partial_d\psi^\star = 0$, and hence $\mathcal{G} = \mathcal{G}^\star = 0$. Only the first two terms in the expression (4.57) of $\mathrm{D}J$ then remain; moreover the second term in the right-hand side of the adjoint problem (4.64) vanishes. As a result, formula (4.57) reduces to known results for displacement-based functionals.

Quadratic stress-based functional. This case is such that $\partial^2_{dd}\psi = \mathcal{D}(z)$, $\partial^2_{dd}\psi^\star = \mathcal{D}^\star(z)$, where $\mathcal{D}$ and $\mathcal{D}^\star$ are symmetric fourth-order tensor fields. It is studied in [267], where $\mathcal{D}$ and $\mathcal{D}^\star$ are constant, and otherwise arbitrary, tensors. Expression (4.57) of $\mathrm{D}J$ for this case is indeed found, after adjusting for notational differences, to coincide with [267, Theorem 3.1]. Reference [267] also gives a number of useful explicit formulae on Eshelby's solution and its use in evaluating $\mathrm{D}J$ for quadratic stress-based functional, including one for the evaluation of the last two integrals in (4.57) when $\mathcal{B}$ is the unit sphere and the tensor $\mathcal{D}$ is isotropic.

Drucker-Prager penalty functional. The penalty functional considered in [28] is based on the following assumptions: (a) two-dimensional isotropic elasticity, plane-strain conditions, identical Poisson ratio in background and inhomogeneity materials, (b) circular trial inhomogeneities (i.e. $\mathcal{B}$ taken as the unit disk), (c) $\psi(d) = \Psi_n(\alpha_{\mathrm{DP}}^2(\mathcal{C} : d))$, with α_{DP}^2 denoting the yield function associated with the Drucker-Prager criterion, and a similar definition for $\psi^\star$ in terms of the inhomogeneity material. Using these assumptions in equation (4.57), we recover equation (44) of [28] as a special case.

Quadratic energy-like functional. Due to their importance in practical applications and the possibility to greatly simplify the general expression (4.57), two examples of energy-based functionals are now presented.

The first kind of energy functional measures the error in strain energy between u_a and a given vector field $u_0 \in H^1(\Omega; \mathbb{R}^3)$, and is defined by

$$E_1(\mathcal{C}_a) = \mathbb{E}_1(u_a, \mathcal{C}_a) = \frac{1}{2}\langle u_a - u_0, u_a - u_0 \rangle_\Omega^{\mathcal{C}_a} \tag{4.70}$$

The particular case of the strain energy of u_a corresponds to setting $u_0 = 0$ in (4.70).

The second kind of energy functional is the elastic counterpart of the functional used in [181] for electric impedance tomography. It is used for e.g. material or flaw identification from overdetermined boundary data. Let $\Gamma_\mathrm{N} = \Gamma_\mathrm{o} \cup \Gamma_\mathrm{no}$, assuming that a measurement u_obs of the displacement induced in the solid by the excitation $(f, g, \bar{u})$ defined in Sec. 4.1 is available on Γ_o. One can then define 'Neumann' and 'Dirichlet' displacement fields that differ only by their boundary data on Γ_o, on which either forces or displacements may be prescribed (the remaining data being as in Sec 4.1). The 'Neumann' and 'Dirichlet' fields coincide for perfect measurement u_obs and a flawless solid with correctly known material characteristics, whereas a discrepancy between them reveals that the model for the reference solid is incorrect, e.g. due to the presence of a hidden defect. The 'Neumann' and 'Dirichlet' background fields u^N and u^D are defined by the following weak formulations:

$$\text{Find } u^\mathrm{N} \in W^\mathrm{N}(\bar{u}), \qquad \langle u^\mathrm{N}, w \rangle_\Omega^\mathcal{C} = F(w), \qquad \forall w \in W_0^\mathrm{N}. \tag{4.71a}$$

$$\text{Find } u^\mathrm{D} \in W^\mathrm{D}(\bar{u}), \qquad \langle u^\mathrm{D}, w \rangle_\Omega^\mathcal{C} = F(w), \qquad \forall w \in W_0^\mathrm{D}. \tag{4.71b}$$

having set $W^\mathrm{D}(\bar{u}) = \{v \in H^1(\Omega; \mathbb{R}^3),\ v = \bar{u} \text{ on } \Gamma_\mathrm{D},\ v = u_\mathrm{obs} \text{ on } \Gamma_\mathrm{o}\}$, $W_0^\mathrm{D} := W^\mathrm{D}(0)$ and $W^\mathrm{N}(\bar{u}) = W(\bar{u})$, $W_0^\mathrm{N} = W_0$ in terms of definition (4.6). Moreover, the 'Neumann' and 'Dirichlet' fields u_a^N and u_a^D for a small trial inhomogeneity B_a located at z are defined by the following weak formulations for the perturbations $v_a^\mathrm{N} := u_a^\mathrm{N} - u^\mathrm{N}$ and $v_a^\mathrm{D} := u_a^\mathrm{D} - u^\mathrm{D}$:

$$\text{Find } v_a^\mathrm{N} \in W_0^\mathrm{N}, \qquad \langle v_a^\mathrm{N}, w \rangle_\Omega^\mathcal{C} + \langle v_a^\mathrm{N}, w \rangle_{B_a}^{\Delta\mathcal{C}} = -\langle u^\mathrm{N}, w \rangle_{B_a}^{\Delta\mathcal{C}}, \qquad \forall w \in W_0^\mathrm{N}. \tag{4.72a}$$

$$\text{Find } v_a^\mathrm{D} \in W_0^\mathrm{D}, \qquad \langle v_a^\mathrm{D}, w \rangle_\Omega^\mathcal{C} + \langle v_a^\mathrm{D}, w \rangle_{B_a}^{\Delta\mathcal{C}} = -\langle u^\mathrm{D}, w \rangle_{B_a}^{\Delta\mathcal{C}}, \qquad \forall w \in W_0^\mathrm{D}. \tag{4.72b}$$

The energy functional $E_2(\mathcal{C}_a)$ is then defined so as to evaluate the 'Neumann'–'Dirichlet' discrepancy through the strain energy of the difference $u_a^\mathrm{N} - u_a^\mathrm{D}$ defined in terms of the perturbed material $\mathcal{C}_a$, i.e.:

$$E_2(\mathcal{C}_a) = \mathbb{E}_2(u_a^\mathrm{N}, u_a^\mathrm{D}, \mathcal{C}_a) = \frac{1}{2}\langle u_a^\mathrm{N} - u_a^\mathrm{D}, u_a^\mathrm{N} - u_a^\mathrm{D} \rangle_\Omega^{\mathcal{C}_a} \tag{4.73}$$

Now we express the topological derivative of E_1, E_2 through the following Proposition via an alternative argument to Theorem 4.4.2

Proposition 4.4.8. *The topological derivative of the energy functional $E_1(\mathcal{C}_a)$ is given by*

$$DE_1(z) = \frac{|\mathcal{B}|}{2} e(u_0)(z) : \Delta\mathcal{C} : e(u_0)(z) - \frac{1}{2} e(u)(z) : \mathcal{A} : e(u+2q)(z) \tag{4.74}$$

where the adjoint solution q is defined by the weak formulation

$$\text{Find } q \in W(\gamma_D(u_0 - u)), \qquad \langle q, w \rangle_\Omega^\mathcal{C} = 0, \quad \forall w \in W_0, \tag{4.75}$$

(with $\gamma_D(w)$ denoting the trace on Γ_D of $w \in H^1(\Omega; \mathbb{R}^3)$).

The topological derivative of the energy functional $E_2(\mathcal{C}_a)$ is given by

$$DE_2(z) = \frac{1}{2} e(u^D)(z) : \mathcal{A} : e(u^D)(z) - \frac{1}{2} e(u^N)(z) : \mathcal{A} : e(u^N)(z) \tag{4.76}$$

In both (4.74) and (4.76), $\mathcal{A}$ denotes again the elastic moment tensor (4.16).

Proof. The functional $E_1(\mathcal{C}_a)$ depends quadratically on v_a. Expanding $E_1(\mathcal{C}_a)$ into terms of order 0, 1 and 2 in v_a, one obtains the following, exact, expression:

$$2E_1(\mathcal{C}_a) - 2E_1(\mathcal{C}) = \langle u - u_0, u - u_0 \rangle_{B_a}^{\Delta\mathcal{C}} + 2\langle u - u_0, v_a \rangle_\Omega^{\mathcal{C}_a} + \langle v_a, v_a \rangle_\Omega^{\mathcal{C}_a} \tag{4.77}$$

The definition (4.75) of the adjoint field q implies that $q + u - u_0 \in W_0$. Hence, one may set $w = q + u - u_0$ in (4.12), to obtain after some manipulation:

$$\langle u - u_0, v_a \rangle_\Omega^\mathcal{C} = \langle q + u - u_0, v_a \rangle_\Omega^\mathcal{C} = -\langle q + u - u_0, u_a \rangle_{B_a}^{\Delta\mathcal{C}}$$

(where the first equality exploits (4.75) with $w = v_a \in W_0$)), and thus

$$\langle u - u_0, v_a \rangle_\Omega^{\mathcal{C}_a} = \langle u - u_0, v_a \rangle_{B_a}^{\Delta\mathcal{C}} - \langle q + u - u_0, u_a \rangle_{B_a}^{\Delta\mathcal{C}} = -\langle u - u_0, u \rangle_{B_a}^{\Delta\mathcal{C}} - \langle q, u_a \rangle_{B_a}^{\Delta\mathcal{C}}$$

Next, weak formulation (4.12) with $w = v_a$ yields

$$\langle v_a, v_a \rangle_\Omega^{\mathcal{C}_a} = -\langle u, v_a \rangle_{B_a}^{\Delta\mathcal{C}}$$

Finally, inserting the last two equalities into (4.77) and rearranging terms, one finds

$$2E_1(\mathcal{C}_a) - 2E_1(\mathcal{C}) = -\langle u - u_0, u + u_0 \rangle_{B_a}^{\Delta\mathcal{C}} - 2\langle q, u_a \rangle_{B_a}^{\Delta\mathcal{C}} - \langle u, v_a \rangle_{B_a}^{\Delta\mathcal{C}}$$
$$= \langle u_0, u_0 \rangle_{B_a}^{\Delta\mathcal{C}} - \langle u + 2q, u_a \rangle_{B_a}^{\Delta\mathcal{C}},$$

with the desired result (4.74) following by applying (4.55) for the last term of the right-hand side.

The functional $E_2(\mathcal{C}_a)$ depending quadratically on v_a^D, v_a^N, one obtains the alternative expression:

$$2E_2(\mathcal{C}_a) - 2E_2(\mathcal{C}) = \langle u^N - u^D, u^N - u^D \rangle_{B_a}^{\Delta\mathcal{C}}$$
$$+ 2\langle u^N - u^D, v_a^N - v_a^D \rangle_\Omega^{\mathcal{C}_a} + \langle v_a^N - v_a^D, v_a^N - v_a^D \rangle_\Omega^{\mathcal{C}_a} \tag{4.78}$$

Now, using weak formulation (4.12) with (v_a, w) replaced in succession by $(v_a^N, v_a^N) \in W_0^N \times W_0^N$, $(v_a^D, v_a^D) \in W_0^D \times W_0^D$ and $(v_a^N, v_a^D) \in W_0^N \times W_0^N$ (noting for the last case that $v_a^D \in W_0^D \subset W_0^N$), one obtains the identities

$$\langle v_a^N, v_a^N \rangle_\Omega^{\mathcal{C}_a} = -\langle u^N, v_a^N \rangle_{B_a}^{\Delta\mathcal{C}}, \qquad \langle v_a^D, v_a^D \rangle_\Omega^{\mathcal{C}_a} = -\langle u^D, v_a^D \rangle_{B_a}^{\Delta\mathcal{C}}, \qquad \langle v_a^N, v_a^D \rangle_\Omega^{\mathcal{C}_a} = -\langle u^N, v_a^D \rangle_{B_a}^{\Delta\mathcal{C}},$$

and hence

$$\langle v_a^N - v_a^D, v_a^N - v_a^D \rangle_\Omega^{\mathcal{C}_a} = -\langle u^N, v_a^N \rangle_{B_a}^{\Delta\mathcal{C}} - \langle u^D - 2u^N, v_a^D \rangle_{B_a}^{\Delta\mathcal{C}} \tag{4.79}$$

Next, using again weak formulation (4.12), this time with (v_a, w) replaced by $(v_a^N, u^N - u^D) \in W_0^N \times W_0^N$, one has

$$\langle u^N - u^D, v_a^N \rangle_\Omega^{\mathcal{C}_a} = -\langle u^N, u^N - u^D \rangle_{B_a}^{\Delta\mathcal{C}}$$

while invoking weak formulations (4.71a) and (4.71b) with $w = v_a^{\mathrm{D}} \in W_0^{\mathrm{D}} \subset W_0^{\mathrm{N}}$ yields

$$\langle u^{\mathrm{N}} - u^{\mathrm{D}}, v_a^{\mathrm{D}} \rangle_\Omega^{\mathcal{C}} = 0$$

Combining the last two identities, one obtains

$$\langle u^{\mathrm{N}} - u^{\mathrm{D}}, v_a^{\mathrm{N}} - v_a^{\mathrm{D}} \rangle_\Omega^{\mathcal{C}_a} = -\langle u^{\mathrm{N}} - u^{\mathrm{D}}, v_a^{\mathrm{D}} \rangle_{B_a}^{\Delta\mathcal{C}} - \langle u^{\mathrm{N}}, u^{\mathrm{N}} - u^{\mathrm{D}} \rangle_{B_a}^{\Delta\mathcal{C}} \qquad (4.80)$$

Substituting (4.79) and (4.80) into (4.78) and rearranging terms yields

$$2E_2(\mathcal{C}_a) - 2E_2(\mathcal{C}) = \langle u^{\mathrm{D}}, u^{\mathrm{D}} \rangle_{B_a}^{\Delta\mathcal{C}} - \langle u^{\mathrm{N}}, u^{\mathrm{N}} \rangle_{B_a}^{\Delta\mathcal{C}} + \langle u^{\mathrm{D}}, v_a^{\mathrm{D}} \rangle_{B_a}^{\Delta\mathcal{C}} - \langle u^{\mathrm{N}}, v_a^{\mathrm{N}} \rangle_{B_a}^{\Delta\mathcal{C}}$$
$$= \langle u^{\mathrm{D}}, u_a^{\mathrm{D}} \rangle_{B_a}^{\Delta\mathcal{C}} - \langle u^{\mathrm{N}}, u_a^{\mathrm{N}} \rangle_{B_a}^{\Delta\mathcal{C}}.$$

The sought result (4.76) finally stems from applying (4.55) to each term of the right-hand side in the above equality. □

We can easily check that the above expressions of the topological derivative are particular instances of (4.57). Indeed, consider

$$\mathbb{J}_a(\nabla u) = E_1(\mathcal{C}_a) = \langle u - u_0, u - u_0 \rangle_\Omega^{\mathcal{C}_a}.$$

Then taking $\mathcal{D} = \mathcal{C}$ and $\mathcal{D}^\star = \mathcal{C}^\star$, the application of (4.57) yields

$$\mathrm{D}J(z) = |\mathcal{B}| e(u - u_0)(z) : \Delta\mathcal{C} : e(u - u_0)(z) - e(p)(z) : \mathcal{A} : e(u)(z)$$
$$+ |\mathcal{B}| e(u - 2u_0)(z) : \Delta\mathcal{C} : \int_{\mathcal{B}} e(v_{\mathcal{B}}) \, \mathrm{d}V$$
$$= |\mathcal{B}| e(u_0)(z) : \Delta\mathcal{C} : e(u_0)(z) + e(u - 2u_0 - p)(z) : \mathcal{A} : e(u)(z). \qquad (4.81)$$

We have used identities

$$\int_{\mathbb{R}^3} e(v_{\mathcal{B}}) : \mathcal{C}_a : e(v_{\mathcal{B}}) \, \mathrm{d}V = -|\mathcal{B}| e(u)(z) : \Delta\mathcal{C} : \int_{\mathcal{B}} e(v_{\mathcal{B}}) \, \mathrm{d}V$$

(obtained from (4.15) with $w = v_{\mathcal{B}}$) in the first equality of (4.81), and

$$|\mathcal{B}| e(u - 2u_0) : \Delta\mathcal{C} : \int_{\mathcal{B}} e(v_{\mathcal{B}}) \, \mathrm{d}V = e(u - 2u_0) : \left(\mathcal{A} - |\mathcal{B}| \Delta\mathcal{C} \right) : e(u)(z)$$

(resulting from left multiplication of (4.16) by $e(u - 2u_0)$) in the second equality of (4.81).

4.5   Numerical evaluation of the topological derivative

The evaluation of the topological derivative (4.57) in a 2D or 3D framework requires numerical procedures, even in the simplest cases (isotropic elasticity, spherical shape for $\mathcal{B}$). In particular an integral over the unbounded region $\mathbb{R}^3 \backslash \mathcal{B}$ must be estimated, besides to the perturbation solution of the FSDT $v_{\mathcal{B}}$ (4.15) and the elastic moment tensor $\mathcal{A}$, which are not analytically available when the medium and the inhomogeneity are fully anisotropic. The details of such procedures will depend upon whether $\mathcal{B}$ is an ellipsoid, or has some other shape, as $\nabla v_{\mathcal{B}}$ is constant inside $\mathcal{B}$ in the former case but not necessarily in the latter [114]. In the sequel, we concentrate on the ellipsoidal (respectively elliptical in 2D) case, which is sufficient for most applications.

4.5.1   3D case, ellipsoidal trial inclusion.

Define $\mathcal{B}$ as

$$\mathcal{B} = \left\{ x \in \mathbb{R}^3, \ (x_1/a_1)^2 + (x_2/a_2)^2 + (x_3/a_3)^2 \leq 1 \right\}, \quad a_1, a_2, a_3 > 0.$$

where the axes of the Cartesian frame (O, x_1, x_2, x_3) are assumed, without loss of generality, to be aligned with the ellipsoid principal axes.

Formula for interior values of $v_{\mathcal{B}}$:   Consider a constant eigenstrain $E^\star \in \mathbb{R}^{3\times3}_{\text{sym}}$ applied over $\mathcal{B}$ endowed with homogeneous elastic properties $\mathcal{C}$ [227]. The displacement field $u_\infty[E^\star]$ thus created is given explicitly by the representation formula

$$u_\infty[E^\star](x) = \langle \varphi[E^\star], G_\infty(\cdot - x)\rangle^{\mathcal{C}}_{\mathcal{B}}, \qquad x \in \mathbb{R}^3 \tag{4.82}$$

When $\mathcal{B}$ is an ellipsoid and $E^\star \in \mathbb{R}^{3\times3}_{\text{sym}}$ is uniform, the above representation can be analytically evaluated, revealing that $u_\infty[E^\star]$ depends linearly on x inside $\mathcal{B}$. The interior (fourth-order) Eshelby tensor $\mathcal{S}^{\text{int}}$ associated to $\mathcal{B}$ and $\mathcal{C}$ is then defined by setting

$$\mathcal{S}^{\text{int}}_{ijk\ell} = \frac{1}{2}\left(\tilde{\mathcal{S}}^{\text{int}}_{ijk\ell} + \tilde{\mathcal{S}}^{\text{int}}_{jik\ell}\right), \quad \nabla u_\infty(x) = \tilde{\mathcal{S}}^{\text{int}} : E^\star \qquad (x \in \mathcal{B}). \tag{4.83}$$

The Cartesian components of $\mathcal{S}^{\text{int}}$ in the orthonormal frame (e_1, e_2, e_3) are given in the general anisotropic case by ([227], eq. (17.19))

$$\mathcal{S}^{\text{int}}_{ijk\ell} = \frac{1}{8\pi}\mathcal{C}_{mnk\ell}\int_{S^2}\left(\xi_j N_{im}(\xi) + \xi_i N_{jm}(\xi)\right)\xi_n\, dS(\hat{\xi}), \tag{4.84}$$

where $S^2 := \{\hat{\xi} \in \mathbb{R}^3,\ |\hat{\xi}| = 1\}$ is the unit sphere, $\xi := a_1^{-1}\hat{\xi}_1 e_1 + a_2^{-1}\hat{\xi}_2 e_2 + a_3^{-1}\hat{\xi}_3 e_3$ and $N(\xi)$ is defined as in (4.36) and (4.37). Note that (4.84) has been expressed as an integral over the unit sphere by effecting on eq. (17.19) of [227] the transformation $u = \cos\phi$ with $\phi \in [0, \pi]$.

As it was proven in Eshelby's celebrated paper [114], the solution $v_{\mathcal{B}}[E]$ of the FSTP (4.15) can be solved analytically for an ellipsoidal inhomogeneity and has a constant strain and gradient inside $\mathcal{B}$. This gradient can be established by means of the equivalent inclusion method [227] and the interior Eshelby tensor $\mathcal{S}^{\text{int}}$ introduced in (4.84). As a matter of fact, the equivalent inclusion method consists in finding an eigenstrain $E^{\star\star}$ such that the solution $v_{\mathcal{B}}[E]$ of integral equation (4.42) has the form

$$v_{\mathcal{B}}[E] = u_\infty[E^{\star\star}] = \varphi[\mathcal{S}^{\text{int}} : E^{\star\star}] \qquad \text{in } \mathcal{B} \tag{4.85}$$

Inserting the above ansatz in (4.42) and comparing with (4.82), the equivalent-inclusion analogy is found to be achieved by setting

$$E^{\star\star} = -(\mathcal{C} + \Delta\mathcal{C} : \mathcal{S}^{\text{int}})^{-1} : \Delta\mathcal{C} : E \tag{4.86}$$

Hence $e(v_{\mathcal{B}}[E])$ can be cast explicitly inside $\mathcal{B}$ as

$$e(v_{\mathcal{B}}[E]) = -\mathcal{S}^{\text{int}} : (\mathcal{C} + \Delta\mathcal{C} : \mathcal{S}^{\text{int}})^{-1} : \Delta\mathcal{C} : E. \tag{4.87}$$

For an arbitrary anisotropic background, the evaluation of (4.84) requires a numerical quadrature (see Sec. 4.6, and also the more complete treatment of [124]), while analytical formulae involving elliptic integrals are available for isotropic background materials [227]. The latter reduce to the following elementary closed-form expression when $\mathcal{B}$ is a ball:

$$\mathcal{S}^{\text{int}} = s_1\mathcal{J} + s_2\mathcal{K}, \qquad \text{with} \quad s_1 := \frac{1+\nu}{3(1-\nu)}, \quad s_2 := \frac{8-10\nu}{15(1-\nu)}, \tag{4.88}$$

where $\mathcal{J}$ and $\mathcal{K}$ are defined as in (4.7) and $\nu := (3\kappa - 2\mu)/(6\kappa + 2\mu)$ is Poisson's ratio. The Eshelby tensor $\mathcal{S}^{\text{int}}$ has the minor symmetries $\mathcal{S}^{\text{int}}_{ijk\ell} = \mathcal{S}^{\text{int}}_{jik\ell} = \mathcal{S}^{\text{int}}_{ij\ell k}$, as is evident from (4.83). The major symmetry $\mathcal{S}^{\text{int}}_{ijk\ell} = \mathcal{S}^{\text{int}}_{k\ell ij}$ holds for the special case (4.88) but is not true in general.

Formula for exterior points of $v_{\mathcal{B}}$:   In order to evaluate the integral over $\mathbb{R}^3 \setminus \mathcal{B}$ in (4.57), more elaborate actions are needed since the integration domain is unbounded and $\nabla v_{\mathcal{B}}[E](x)$ is not anymore constant as it was for the inner case $x \in \mathcal{B}$ (in fact decays at infinity).

First we deal with the integration on $\mathbb{R}^3 \setminus \mathcal{B}$. Transform x into y according to

$$y = (x_1/a_1, x_2/a_2, x_3/a_3) \qquad (|y| \geq 1). \qquad (4.89)$$

Then it is natural to set $y = |y|\hat{y}$, with $\hat{y} \in S^2$ (let us recall the unit sphere) and $1 \leq |y| \leq +\infty$. Apply the transformation $t = |y|^{-1}$ (with $0 \leq t \leq 1$) to the radial variable, so that (4.89) represents any $x \in \mathbb{R}^3 \setminus \mathcal{B}$ in the form $x(\hat{y}, t)$. Introducing the above change of coordinates to the first integral term of (4.57), the result reads

$$\int_{\mathbb{R}^3 \setminus \mathcal{B}} \mathcal{G}(z, \nabla v_{\mathcal{B}}(x)) \, \mathrm{d}V(x) = \frac{1}{a_1 a_2 a_3} \int_0^1 \frac{1}{t^4} \Big\{ \int_{S^2} \mathcal{G}(z, \nabla v_{\mathcal{B}}(x(\hat{y}, t))) \, \mathrm{d}S(\hat{y}) \Big\} \, \mathrm{d}t, \qquad (4.90)$$

which is to be evaluated using numerical quadrature (using e.g. a Gaussian rule for t and a Lebedev rule on S^2 [190]). This in turn requires the ability to evaluate $\nabla v_{\mathcal{B}}[E](x(\hat{y}, t))$ for any given quadrature point $(\hat{y}, t)$. Applying again (4.82) for $x \in \mathbb{R}^3 \setminus \mathcal{B}$ and the equivalent inclusion method, $\nabla v_{\mathcal{B}}$ is in this case given by (Eq. (18.6) of [227])

$$\mathcal{S}_{ijk\ell}^{\mathrm{ext}} = \frac{1}{2} \Big(\tilde{\mathcal{S}}_{ijk\ell}^{\mathrm{ext}} + \tilde{\mathcal{S}}_{jik\ell}^{\mathrm{ext}} \Big), \quad \nabla v_{\mathcal{B}}[E](x) = \tilde{\mathcal{S}}^{\mathrm{ext}}(x) : E^{\star\star} \quad (x \in \mathbb{R}^3 \setminus \mathcal{B}). \qquad (4.91)$$

The tensor $E^{\star\star}$ is again defined by (4.86) and $\mathcal{S}^{\mathrm{ext}}(x)$ is the exterior (spatially varying) Eshelby tensor, given through $\tilde{\mathcal{S}}^{\mathrm{ext}}(x)$ as

$$\tilde{\mathcal{S}}_{ijmn}^{\mathrm{ext}}(x(\hat{y}, t)) = \frac{1}{4\pi} \mathcal{C}_{k\ell mn} \Big\{ \int_{S^\star(\hat{y}, t)} N_{ik}(\xi) \xi_\ell \xi_j \, \mathrm{d}S(\hat{s}) - 2 \oint_{L^+(\hat{y}, t)} t N_{ik}(\xi) \xi_\ell \xi_j \, \mathrm{d}\phi(\hat{s}) \Big\}, \qquad (4.92)$$

where $\xi = \xi(\hat{s})$ is defined for $\hat{s} \in S^2$ by

$$\xi = (\hat{s}_1/a_1, \hat{s}_2/a_2, \hat{s}_3/a_3), \qquad (4.93)$$

$S^\star(\hat{y}, t)$ is the portion of S^2 defined by $S^\star(\hat{y}, t) := \big\{ \hat{s} \in S^2 : 0 \leq \hat{s} \cdot \hat{y} \leq t \big\}$, $L^+(\hat{y}, t)$ the circular contour on S^2 defined by $L^+(\hat{y}, t) := \big\{ \hat{s} \in S^2 : \hat{s} \cdot \hat{y} = t \big\}$ (Fig. 4.2), $\mathrm{d}S(\hat{s})$ and $\mathrm{d}\phi(\hat{s})$ respectively denote the solid angle differential on S^2 and the polar angle differential on the circle $L^+(\hat{y}, t)$, and the tensor $N(\xi)$ is given by $N(\xi) = K^{-1}(\xi)$, with K given by (4.37).
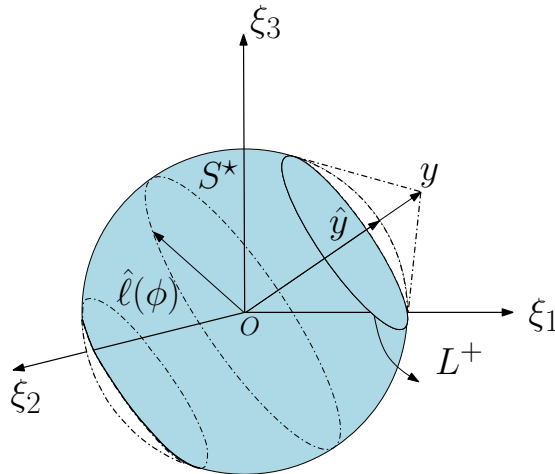

Figure 4.2: Parametrization of the set $S^\star \subset S^2$.

Remark 4.5.1. *If the point x is inside $\mathcal{B}$, the line integral in (4.92) can be dropped, and $S^\star$ in the surface integral is replaced by S^2. The symmetric part of the resulting equation is identical to (4.84).*

It is useful to recast (4.92) in a form more suitable for numerical quadrature. To this end, let $S^\star(\hat{y}, t)$ be represented in terms of coordinates (z, ϕ) spanning the fixed domain $Q := \{(z, \phi) \in [0, 1] \times [0, 2\pi[\}$ by

$$S^\star(\hat{y}, t) = \{ \hat{s} \in S^2 \mid \hat{s} = (1 - t^2 z^2)^{1/2} \hat{\ell}(\phi) + tz\hat{y} \}$$

with $\hat{\ell}(\phi)$ spanning the unit circle $S^1 := \{\hat{s}\hat{y} = 0\}$ (this representation stems from parameterizing $\hat{s}$ using angular spherical coordinates (θ, ϕ) and setting $z := t^{-1}\cos\theta$). $L^+(\hat{y}, t)$ is then the subset of $S^\star(\hat{y}, t)$ such that $z = 1$. The (z, ϕ) parametrization implies that $\mathrm{d}S(\hat{s}) = t\,\mathrm{d}z\,\mathrm{d}\phi$, and also induces a corresponding representation $\xi(tz, \phi)$ of ξ as defined by (4.93). Inserting it in (4.92) and rearranging the resulting expression, the tensor $\tilde{\mathcal{S}}^{\mathrm{ext}}$ is given, for a given evaluation point $\bar{x}(\hat{y}, t)$, by an integral over the fixed domain Q:

$$\tilde{\mathcal{S}}^{\mathrm{ext}}_{ijmn}(x(\hat{y}, t)) = \frac{t}{4\pi} \mathcal{C}_{k\ell mn} \int_0^1 \mathrm{d}z \int_0^{2\pi} \left[\Sigma_{k\ell ij}(tz, \phi) - 2\Sigma_{k\ell ij}(t, \phi) \right] \mathrm{d}\phi \qquad (4.94)$$

with

$$\Sigma_{k\ell ij}(tz, \phi) = N_{ik}(\xi(tz, \phi))\xi_\ell(tz, \phi)\xi_j(tz, \phi).$$

For a given $\bar{x}(\hat{y}, t)$, $\tilde{\mathcal{S}}^{\mathrm{ext}}(\bar{x}(\hat{y}, t))$ can then be evaluated by means of standard numerical quadrature in Q (using e.g. product rules that are Gaussian in z and uniform in ϕ). In addition, a Taylor expansion in t about $t = 0$ yields $\Sigma_{k\ell ij}(tz, \phi) - \Sigma_{k\ell ij}(t, \phi) = (z - 1)\partial_1 \Sigma_{k\ell ij}(0, \phi) + \mathcal{O}(t^2)$, where ∂_1 denotes the partial derivative w.r.t. the first argument. It is moreover straightforward to show that $\partial_1 \Sigma_{k\ell ij}(0, \phi)$ is for any $(k\ell ij)$ a polynomial in $(\cos\phi, \sin\phi)$ involving only odd-degree terms, and hence that its integral over $\phi \in [0, 2\pi]$ vanishes. Consequently, the Taylor expansion of (4.94) about $t = 0$ is $\tilde{\mathcal{S}}^{\mathrm{ext}}_{ijmn}(\bar{x}(\hat{y}, t)) = \mathcal{O}(t^3)$, implying that the integral in t of (4.90) is well defined. This remark is consistent with the otherwise known $\mathcal{O}(|x|^{-3})$ behavior of $\nabla v_\mathcal{B}(x)$ as $|x| \to +\infty$.

When the background material is isotropic, and characterized using e.g. its shear modulus μ and Poisson's ratio ν, the Christoffel tensor N has a simple closed-form expression

$$N(\xi) = \frac{1}{\mu|\xi|^2} \left[I - \frac{1}{2(1 - \nu)} \hat{\xi} \otimes \hat{\xi} \right] \qquad (4.95)$$

with $\hat{\xi} := \xi/|\xi|$ and $I_{ij} = \delta_{ij}$. The exterior Eshelby tensor for a unit ball is then found (by analytical evaluation of (4.94) using (4.95), or by completing derivations presented in [227, Sec. 11]) to have the following closed-form expression (wherein $\bar{x} := |\bar{x}|$):

$$2(1 - \nu)\mathcal{S}^{\mathrm{ext}}_{ijk\ell}(\bar{x}) = \left[\frac{7}{\bar{x}^9} - \frac{5}{\bar{x}^7} \right] x_i x_j x_k x_\ell + \left[\frac{1}{\bar{x}^5} - \frac{1}{\bar{x}^7} \right] \delta_{ij} x_k x_\ell + \left[\frac{1 - 2\nu}{\bar{x}^5} - \frac{1}{\bar{x}^7} \right] \delta_{k\ell} x_i x_j$$

$$+ \left[\frac{\nu}{\bar{x}^5} - \frac{1}{\bar{x}^7} \right] (\delta_{ik} x_j x_\ell + \delta_{jk} x_i x_\ell + \delta_{i\ell} x_j x_k + \delta_{j\ell} x_i x_k)$$

$$+ \left[\frac{1}{5\bar{x}^5} - \frac{1 - 2\nu}{3\bar{x}^3} \right] \delta_{ij} \delta_{k\ell} + \left[\frac{1}{5\bar{x}^5} + \frac{1 - 2\nu}{3\bar{x}^3} \right] (\delta_{ik} \delta_{j\ell} + \delta_{jk} \delta_{i\ell}). \qquad (4.96)$$

Moreover, $\mathcal{S}^{\mathrm{ext}}(\bar{x}) : E$ evaluated for an arbitrary tensor $E \in \mathbb{R}^{3\times3}_{\mathrm{sym}}$ using the above formula coincides with equation (23) of [267].

Computation of the elastic moment tensor $\mathcal{A}$:   With the help of (4.87), the value of $\mathcal{A}$ is then found as follows:

Lemma 4.5.2 (elastic moment tensor for an ellipsoidal inhomogeneity)**.** *The elastic moment tensor $\mathcal{A}$ associated with an ellipsoidal inhomogeneity $(\mathcal{B}, \mathcal{C} + \Delta\mathcal{C})$ embedded in a medium with elasticity tensor $\mathcal{C}$ is given by*

$$\mathcal{A} = |\mathcal{B}|\mathcal{C} : (\mathcal{C} + \Delta\mathcal{C} : \mathcal{S}^{int})^{-1} : \Delta\mathcal{C} \tag{4.97}$$

Proof. Using expression (4.87) of $e(v_{\mathcal{B}})$ in (4.16) and using the fact that the integrand in the resulting formula is constant, one obtains

$$E' : \mathcal{A} : E = |\mathcal{B}| \big(E' : \Delta\mathcal{C} : E - E' : \Delta\mathcal{C} : \mathcal{S}^{int} : (\mathcal{C} + \Delta\mathcal{C} : \mathcal{S}^{int})^{-1} : \Delta\mathcal{C} : E \big)$$

Then, since the above equality holds for any constant tensors E', E, the sought expression (4.97) is readily obtained by invoking the identity $\Delta\mathcal{C} : \mathcal{S}^{int} : (\mathcal{C} + \Delta\mathcal{C} : \mathcal{S}^{int})^{-1} = \mathcal{I} - \mathcal{C} : (\mathcal{C} + \Delta\mathcal{C} : \mathcal{S}^{int})^{-1}$. $\square$

When the background is isotropic and the inhomogeneity spherical and also isotropic, $\mathcal{A}$ admits a quite simple explicit expression. Using that $\mathcal{C}$ and $\mathcal{C}^{\star}$ are of the form (4.7) with respective moduli pairs κ, μ and $\kappa^{\star}, \mu^{\star}$ and $\mathcal{S}^{int}$ is given by (4.88), invoking the relations $\mathcal{J} : \mathcal{J} = \mathcal{J}$, $\mathcal{K} : \mathcal{K} = \mathcal{K}$ and $\mathcal{J} : \mathcal{K} = 0$ verified by $\mathcal{J}$ and $\mathcal{K}$ and noting in particular that $(A\mathcal{J} + B\mathcal{K})^{-1} = A^{-1}\mathcal{J} + B^{-1}\mathcal{K}$ for any $(A, B) \neq (0, 0)$, one easily evaluates (4.97) to obtain

$$\mathcal{A} = \frac{4\pi}{3} \left[3\kappa \frac{\Lambda_1 - 1}{1 + S_1(\Lambda_1 - 1)} \mathcal{J} + 2\mu \frac{\Lambda_2 - 1}{1 + S_2(\Lambda_2 - 1)} \mathcal{K} \right] \tag{4.98}$$

(with $\Lambda_1 := \kappa^{\star}/\kappa$, $\Lambda_2 := \mu^{\star}/\mu$). For $0 \leq \nu \leq 0.5$ one has $1/3 \leq S_1 \leq 1$ and $8/15 \geq S_2 \geq 2/5$; combined with $\Lambda_{1,2} \geq 0$. This implies that both denominators in (4.98) are strictly positive, ensuring in particular the invertibility of $\mathcal{C} + \Delta\mathcal{C} : \mathcal{S}^{int}$ upon which (4.98) depends, except for the special case $\nu = 0.5$, $\kappa^{\star} = 0$.

4.5.2   2D plane-strain case, elliptical trial inclusion.

Now define $\mathcal{B}$ as

$$\mathcal{B} = \left\{ x \in \mathbb{R}^2, \ (x_1/a_1)^2 + (x_2/a_2)^2 \leq 1 \right\}, \quad a_1, a_2 > 0,$$

where the axes of the Cartesian frame (O, x_1, x_2) are assumed, without loss of generality, to be aligned with the ellipse principal axes. Inclusion and inhomogeneity problems in plane-strain have been addressed in many references, with solution methods usually based on complex potentials, see e.g. [321, 50, 305, 163]. Here, the tensors $\mathcal{S}^{int}$ and $\mathcal{S}^{ext}$ are derived for the plane-strain case without recourse to complex potentials, from a direct evaluation of (4.82), meanwhile all tensors and inner products are defined with reference to the vector space $\mathbb{R}^2$ instead of $\mathbb{R}^3$ (in particular, $E^{\star} \in \mathbb{R}^{2,2}_{sym}$ now). Moreover, $G_{\infty}(\cdot - x)$ is now the elastostatic fundamental solution for plane-strain, with ∇G_{∞} given in Fourier integral form

$$\nabla G_{\infty}(r) = \frac{i}{(2\pi)^2} \int_{\mathbb{R}^2} \exp(i\eta \cdot r) N(\eta) \otimes \eta \, dV(\eta) \quad (r \in \mathbb{R}^2 \setminus \{0\}), \tag{4.99}$$

with $N(\eta)$ now defined in terms of the two-dimensional version of the acoustic tensor $K(\eta)$ (i.e. $K_{ik} = \mathcal{C}_{ijk\ell}\eta_j\eta_\ell$ with $1 \leq i, j, k, \ell \leq 2$).

Similarly to the 3D framework, the 2D solution $v_{\mathcal{B}}[E](x)$ of the FSTP (4.15) fulfills

$$e(v_{\mathcal{B}})(x) = \mathcal{S}^{int} : E^{\star\star}, \quad (x \in \mathcal{B}) \tag{4.100}$$

$$e(v_{\mathcal{B}})(x) = \mathcal{S}^{ext}(x) : E^{\star\star}, \quad (x \in \mathbb{R}^2 \backslash \mathcal{B}) \tag{4.101}$$

where $E^{\star\star}$ is given by the 2D adaptation of (4.86).

Proposition 4.5.3. *Set* $x = y\big(a_1 \cos\gamma, a_2 \sin\gamma \big)$, $y \in [1,\infty)$. *The plane-strain interior and exterior Eshelby tensors* $\mathcal{S}^{int}$ *and* $\mathcal{S}^{ext}(x)$, *respectively read*

$$\mathcal{S}^{int}_{ijk\ell} = \frac{1}{2}\big(\tilde{\mathcal{S}}^{int}_{ijk\ell} + \tilde{\mathcal{S}}^{int}_{jik\ell}\big), \quad \mathcal{S}^{ext}_{ijk\ell} = \frac{1}{2}\big(\tilde{\mathcal{S}}^{ext}_{ijk\ell} + \tilde{\mathcal{S}}^{ext}_{jik\ell}\big), \; where \tag{4.102}$$

$$\tilde{\mathcal{S}}^{int}_{ijk\ell} = \frac{1}{\pi}\bigg\{\int_{-\pi/2}^{\pi/2} \Big(\hat{\alpha}_i(\theta) \otimes N_{jm}\big(\hat{\alpha}(\theta)\big) \otimes \hat{\alpha}_n(\theta) \Big) \, d\theta\bigg\} : \mathcal{C}_{mnk\ell},$$

$$\tilde{\mathcal{S}}^{ext}_{ijk\ell}(x) = \tilde{\mathcal{S}}^{int}_{ijk\ell} \; - \; \frac{2}{\pi}\bigg\{\int_{-\pi/2}^{\pi/2} \Big(\alpha_i(\theta(w)) \otimes N_{jm}\big(\alpha(\theta(w))\big) \otimes \alpha_n(\theta(w)) \Big) \, dw\bigg\} : \mathcal{C}_{mnk\ell}.$$

The above parameterizations are specified through

$$\begin{aligned} \hat{\alpha}(\theta) &= \big(a_1^{-1}\cos(\theta), a_2^{-1}\sin(\theta) \big), \\ \alpha(\theta) &= \big(a_1^{-1}\cos(\theta+\gamma), a_2^{-1}\sin(\theta+\gamma) \big), \end{aligned} \tag{4.103}$$

and the function $\theta(w)$ *in the second integral is defined implicitly by* $\sin\theta = \sqrt{1-y^{-2}}\sin w$.

Proof. The derivation is done by means of a direct evaluation of the 2D version of the integral representation formula (4.82). Thus, for $E^\star \in \mathbb{R}^{2\times2}_{\text{sym}}$,

$$e\big(u_\infty[E^\star]\big)(x) = \mathcal{S}^{\text{int}} : E^\star, \quad (x \in \mathcal{B}) \tag{4.104}$$

$$e\big(u_\infty[E^\star]\big)(x) = \mathcal{S}^{\text{ext}}(x) : E^\star \quad (x \in \mathbb{R}^2\backslash\mathcal{B}). \tag{4.105}$$

Under the present conditions (anisotropic, plane-strain), (4.99) and (4.82) yield

$$u_\infty[E^\star](x) = \frac{\mathrm{i}}{(2\pi)^2}\bigg\{\int_{\mathbb{R}^2} \int_{\mathcal{B}} \exp(\mathrm{i}\eta\cdot(\xi-x))N(\eta)\otimes\eta \, dV(\xi) \, dV(\eta)\bigg\} : \mathcal{C} : E^\star \tag{4.106}$$

The above fourth-dimensional integral over $(\xi,\eta) \in \mathcal{B}\times\mathbb{R}^2$ is now evaluated with the help of coordinate transformations. The evaluation point $x \in \mathbb{R}^2$ is parameterized as

$$x(y,\gamma) = y\left(a_1\cos(\gamma), a_2\sin(\gamma)\right), \quad \gamma \in [0,2\pi], y \in (0,\infty), \tag{4.107}$$

and two mappings are introduced. First, $f : (t,\theta) \in \mathbb{R}^+\backslash\{0\}\times[0,2\pi[\longmapsto (\eta_1,\eta_2) \in \mathbb{R}^2\backslash\{(0,0)\}$ is defined by

$$\begin{cases} \eta_1(t,\theta) = t\alpha_1(\theta) \\ \eta_2(t,\theta) = t\alpha_2(\theta) \end{cases} \quad \text{with} \quad \alpha(\theta) = (\alpha_1,\alpha_2)(\theta) := \big(a_1^{-1}\cos(\theta+\gamma), a_2^{-1}\sin(\theta+\gamma)\big), \tag{4.108}$$

which implies

$$dV(\eta) = (a_1 a_2)^{-1}t \, dt \, d\theta,$$

Then, for given $\eta \in \mathbb{R}^2\backslash\{0\}$ (i.e. for given $(t,\theta) \in \mathbb{R}^+\backslash\{0\}$), $g : (z_1, z_2) \in \mathcal{D} \longmapsto (\xi_1,\xi_2) \in \mathcal{B}$ (where $\mathcal{D}\subset\mathbb{R}^2$ is the closed unit disk) is defined by

$$\begin{cases} \xi_1 = a_1(z_1\sin\theta + z_2\cos\theta) \\ \xi_2 = a_2(-z_1\cos\theta + z_2\sin\theta) \end{cases} \quad \text{with} \quad \begin{aligned} -\sqrt{1-z_2^2} \leq z_1 \leq \sqrt{1-z_2^2}, \\ -1 \leq z_2 \leq 1 \end{aligned} \tag{4.109}$$

which implies

$$dV(\xi) = a_1 a_2 \, dz_1 \, dz_2$$

Now, mappings (4.108) and (4.109) are substituted into the integral representation formula (4.106). Noting that definitions (4.107), (4.108) and (4.109) imply

$$\alpha(\theta)\cdot x = y\cos\theta, \qquad \eta\cdot(\xi-x) = t[z_2 - \alpha(\theta)\cdot x],$$

one first finds, using mapping (4.109) and the fact that the integrand of the resulting integral over (z_1, z_2) does not depend on z_1, that

$$\int_{\mathcal{B}} e^{i\eta\cdot(\xi-x)}\,\mathrm{d}V(\xi) = a_1 a_2 e^{-it\alpha(\theta)\cdot x}\int_{-1}^{1} 2\sqrt{1-z_2^2}\,e^{itz_2}\,\mathrm{d}z_2 = a_1 a_2 \frac{2\pi}{t}e^{-it\alpha(\theta)\cdot x}J_1(t),$$

where J_1 is the Bessel function of first kind and order 1, the last equality stemming from formula 3.752 of [130] together with the function $z_2 \longmapsto \sqrt{1-z_2^2}\sin kz_2$ being odd.

Then, using the above result into (4.106) and applying mapping (4.108), one obtains

$$\frac{i}{(2\pi)^2}\int_{\mathbb{R}^2}\int_{\mathcal{B}} \exp(i\eta\cdot(\xi-x))N(\eta)\otimes\eta\,\mathrm{d}V(\xi)\,\mathrm{d}V(\eta)$$

$$= \frac{i}{2\pi}\int_0^{2\pi}\left\{N\big(\alpha(\theta)\big)\otimes\alpha(\theta)\int_0^{\infty} e^{-it\alpha(\theta)\cdot x}J_1(t)\frac{\mathrm{d}t}{t}\right\}\mathrm{d}\theta$$

$$= \frac{1}{\pi}\int_{-\pi/2}^{\pi/2}\left\{N\big(\alpha(\theta)\big)\otimes\alpha(\theta)\int_0^{\infty} \sin\big(t\,\alpha(\theta)\cdot x\big)J_1(t)\frac{\mathrm{d}t}{t}\right\}\mathrm{d}\theta \qquad (4.110)$$

Remark 4.5.4. *The last equality above is established by using that (i) $\alpha(\theta)$ is 2π-periodic, (ii) $\alpha(\theta+\pi)=-\alpha(\theta)$ and (iii) $N(-\eta)=N(\eta)$ (N being homogeneous of degree -2).*

The inner integral in (4.110) in fact admits a known closed-form expression (formula 6.693(1) of [130]), which depends on the value of $\alpha(\theta)\cdot x = y\cos\theta$:

$$\int_0^{\infty} \sin\big(t\,\alpha(\theta)\cdot x\big)J_1(t)\frac{\mathrm{d}t}{t} = \alpha(\theta)\cdot x \qquad\qquad 0\le\alpha(\theta)\cdot x\le 1 \qquad (4.111\mathrm{a})$$

$$= \alpha(\theta)\cdot x - \sqrt{(\alpha(\theta)\cdot x)^2-1} \qquad \alpha(\theta)\cdot x\ge 1 \qquad (4.111\mathrm{b})$$

If $x\in\mathcal{B}$, (4.107) implies that $y\le 1$, and hence that $\alpha(\theta)\cdot x\le 1$ for any θ. From (4.106), (4.110) and (4.111a,b), $u_\infty(x)$ is then such that

$$u_\infty[E^\star](x) = \left(\tilde{\mathcal{S}}^{\mathrm{int}}{:}E^\star\right)\cdot x, \qquad \nabla u_\infty[E^\star](\bar{x}) = \tilde{\mathcal{S}}^{\mathrm{int}}{:}E^\star.$$

Thus, the constant tensor $\tilde{\mathcal{S}}^{\mathrm{int}}$ is given by

$$\mathcal{S}^{\mathrm{int}} = \left\{\frac{1}{\pi}\int_{-\pi/2}^{\pi/2}\alpha(\theta)\otimes N\big(\alpha(\theta)\big)\otimes\alpha(\theta)\,\mathrm{d}\theta\right\}{:}\mathcal{C} = \left\{\frac{1}{\pi}\int_{-\pi/2}^{\pi/2}\hat{\alpha}(\theta)\otimes N\big(\hat{\alpha}(\theta)\big)\otimes\hat{\alpha}(\theta)\,\mathrm{d}\theta\right\}{:}\mathcal{C}, \quad (4.112)$$

where $\hat{\alpha}$ was defined in (4.103) and the result stems from properties (*ii*) and (*iii*) listed in Remark 4.5.4.

If $x\in\mathbb{R}^2\setminus\bar{\mathcal{B}}$, (4.107) implies that $y>1$. Let $\bar{\theta}=\arccos(1/y)$, so that the subset of $\theta\in[-\pi/2,\pi/2]$ where $\alpha(\theta)\cdot x\ge 1$ is $\theta\in[-\bar{\theta},\bar{\theta}]$. In that case, using (4.106), (4.110) and (4.111a,b) and differentiating the resulting expression of $u_\infty(x)$ with respect to x, one finds

$$\nabla u_\infty[E^\star](x) = \tilde{\mathcal{S}}^{\mathrm{ext}}(x){:}E^\star$$

with

$$\tilde{\mathcal{S}}^{\mathrm{ext}}(x) = \tilde{\mathcal{S}}^{\mathrm{int}} - \frac{2}{\pi}\left\{\int_{-\bar{\theta}}^{\bar{\theta}}\left[\frac{(\alpha(\theta)\cdot x)}{\sqrt{(\alpha(\theta)\cdot x)^2-1}}\alpha(\theta)\otimes N\big(\alpha(\theta)\big)\otimes\alpha(\theta)\right]\mathrm{d}\theta\right\}{:}\mathcal{C}$$

Even though this representation of the 2D general Eshelby tensor is valid, it is not suited for numerical evaluation due to the term $1/\sqrt{(\alpha \cdot x)^2 - 1}$, which is (weakly) singular at the endpoints $\theta = \pm\bar{\theta}$. We recast it into a form suitable for numerical quadrature by setting

$$\sin\theta = \sqrt{1 - y^{-2}}\sin w, \qquad \theta \in [-\bar{\theta}, \bar{\theta}], \ w \in [-1, 1]$$

Then, since $\alpha(\theta)\cdot x = y\cos\theta$, one easily finds that

$$(\alpha(\theta)\cdot x)\,\mathrm{d}\theta = \sqrt{y^2 - 1}\cos w\,\mathrm{d}w, \quad \sqrt{(\alpha(\theta)\cdot x)^2 - 1} = \sqrt{y^2 - 1}\cos w$$

Consequently, $\tilde{\mathcal{S}}^{\mathrm{ext}}(x)$ is now expressed as

$$\tilde{\mathcal{S}}^{\mathrm{ext}}(x) = \tilde{\mathcal{S}}^{\mathrm{int}} - \frac{2}{\pi}\left\{\int_{-\pi/2}^{\pi/2}\Big[\alpha(\theta(w)) \otimes N\big(\alpha(\theta(w))\big) \otimes \alpha(\theta(w))\Big]\,\mathrm{d}w\right\}:\mathcal{C}$$

where the integral can now be evaluated by usual quadrature rules. $\square$

The exterior Eshelby tensor for a circular inclusion of unit radius is then found, for example by analytical evaluation of (4.102) using (4.95), to have the following closed-form expression (with all indices ranging in $\{1, 2\}$):

$$2(1-\nu)\mathcal{S}_{ijk\ell}^{\mathrm{ext}}(\bar{x}) = \left[\frac{6}{\bar{x}^8} - \frac{4}{\bar{x}^6}\right]x_i x_j x_k x_\ell + \left[\frac{1}{\bar{x}^4} - \frac{1}{\bar{x}^6}\right]\delta_{ij}x_k x_\ell + \left[\frac{1-2\nu}{\bar{x}^4} - \frac{1}{\bar{x}^6}\right]\delta_{k\ell}x_i x_j$$
$$+ \left[\frac{\nu}{\bar{x}^4} - \frac{1}{\bar{x}^6}\right]\big(\delta_{ik}x_j x_\ell + \delta_{jk}x_i x_\ell + \delta_{i\ell}x_j x_k + \delta_{j\ell}x_i x_k\big)$$
$$+ \left[\frac{1}{4\bar{x}^4} - \frac{1-2\nu}{2\bar{x}^2}\right]\delta_{ij}\delta_{k\ell} + \left[\frac{1}{4\bar{x}^4} + \frac{1-2\nu}{2\bar{x}^2}\right]\big(\delta_{ik}\delta_{j\ell} + \delta_{jk}\delta_{i\ell}\big). \qquad (4.113)$$

Meanwhile the analytical evaluation of (4.112) for a general ellipse inclusion yields the following explicit expression of $\mathcal{S}^{\mathrm{int}}$, which coincides with formulae (11.22) of [227] given for the ellipsoid infinitely elongated along the x_3 direction:

$$\begin{aligned}
\mathcal{S}_{1111}^{\mathrm{int}} &= A(1-m)(3+\gamma+m) & \mathcal{S}_{1122}^{\mathrm{int}} &= A(1-m)(1-\gamma-m) \\
\mathcal{S}_{2222}^{\mathrm{int}} &= A(1+m)(3+\gamma-m) & \mathcal{S}_{2211}^{\mathrm{int}} &= A(1+m)(1-\gamma+m) \\
\mathcal{S}_{1212}^{\mathrm{int}} &= A(1+m^2+\gamma) & \mathcal{S}_{1112}^{\mathrm{int}} &= \mathcal{S}_{2212}^{\mathrm{int}} = \mathcal{S}_{1211}^{\mathrm{int}} = \mathcal{S}_{1222}^{\mathrm{int}} = 0
\end{aligned} \qquad (4.114)$$

with $A = [8(1-\nu)]^{-1}$, $\gamma = 2(1-2\nu)$ and $m = (a_1 - a_2)/(a_1 + a_2)$.

Finally one can easily prove that Lemma 4.5.2 remains also valid for the plane-strain framework. Thus, substituting the above result into (4.97), rewriting it in matrix form using the Voigt convention and using therein the plane-strain versions $\mathcal{C} = \bar{\kappa}\overline{\mathcal{J}} + \mu\overline{\mathcal{K}}$ and $\Delta\mathcal{C} = \Delta\bar{\kappa}\overline{\mathcal{J}} + \Delta\mu\overline{\mathcal{K}}$ of the isotropic elastic constitutive relation (where $\bar{\kappa} := \kappa + \mu/3 = \lambda + \mu$ is the plane-strain bulk modulus with λ the first Lamé parameter, $\overline{\mathcal{J}} := (I \otimes I)/2$ and $\overline{\mathcal{K}} := \mathcal{I} - \overline{\mathcal{J}}$), an algebraic calculation yields

$$\mathcal{A}_{1111} = |\mathcal{B}|(\lambda + 2\mu)\frac{-\Delta\mu(\Delta\lambda + \Delta\mu)(m^2 - 2(\tau-1)m) + c}{\Delta\mu(-\Delta\mu + \lambda^\star - (1-\tau)(\lambda^\star + \mu^\star))m^2 + (\mu + \lambda^\star + \mu^\star)(\mu + \tau\mu^\star)},$$

$$\mathcal{A}_{2222} = |\mathcal{B}|(\lambda + 2\mu)\frac{-\Delta\mu(\Delta\lambda + \Delta\mu)(m^2 + 2(\tau-1)m) + c}{\Delta\mu(-\Delta\mu + \lambda^\star - (1-\tau)(\lambda^\star + \mu^\star))m^2 + (\mu + \lambda^\star + \mu^\star)(\mu + \tau\mu^\star)},$$

$$\mathcal{A}_{1122} = |\mathcal{B}|(\lambda + 2\mu)\frac{-\Delta\mu(\Delta\lambda + \Delta\mu)m^2 - \Delta\lambda(\mu^\star + \tau\mu) + \Delta\mu^2}{\Delta\mu(-\Delta\mu + \lambda^\star - (1-\tau)(\lambda^\star + \mu^\star))m^2 + (\mu + \lambda^\star + \mu^\star)(\mu + \tau\mu^\star)},$$

$$\mathcal{A}_{1212} = |\mathcal{B}|\frac{\mu\Delta\mu(1 + \tau)}{\Delta\mu m^2 - \mu - \tau\mu^\star}, \qquad (4.115)$$

with

$$c = -(\Delta\lambda + \Delta\mu)(\mu + \tau\mu^\star) + (1 - \tau)(\Delta\mu)(\mu + \lambda^\star + \mu^\star),$$

$\tau = (\lambda + 3\mu)/(\lambda + \mu)$, $\Delta\mu = \mu - \mu^\star$, $\Delta\lambda = \lambda - \lambda^\star$ and $|\mathcal{B}| = \pi a_1 a_2$. The above expression of $\mathcal{A}$ has been checked to coincide (after notational adjustment) with the corresponding result of [20] (Theorem 3.2), established using a different method.

4.6 Numerical examples

This section presents several applications and numerical results related to the topological derivative. In view of the essential role of the EMT $\mathcal{A}$ in the evaluation of DJ, its computation is examined in Sec. 4.6.1 for ellipsoidal (or spherical) inhomogeneities, corresponding to the most often used form of topological derivative. In this case, (4.97) shows that an accurate evaluation of $\mathcal{A}$ mainly hinges on that of $\mathcal{S}$, which is thus the main focus of Sec. 4.6.1. Then, a numerical validation of expression (4.57) for DJ, performed in 2D conditions by comparing $J(\mathcal{C}_a)$ evaluated either numerically or using expansion (4.56), is presented in Sec. 4.6.2. A sensibility analysis in a 2D anisotropic ply and an isotropic 3D beam is performed in Sections 4.6.3 and 4.6.4, respectively. Finally, 2D and 3D applications in flaw identification are illustrated in Sections 4.6.5 and 4.6.6 for energy misfit functionals.

The finite element analysis for each of the foregoing 2D and 3D test cases was carried out with the software Freefem++ [118]. The finite elements for the displacement and adjoint state where chosen as Lagrange $\mathbb{P}^1$ elements on a triangular and tetrahedral mesh, respectively. The mesh of the surface of a human femur was obtained from the mesh database of the GAMMA project [166], while its inner tetrahedral mesh and the surface mesh adaptation were generated thanks to TetGen [304] and FreeYams [119], respectively. The plot of the 2D, 3D functions and meshes was done with Medit [214].

The term in the topological derivative (4.57) involving an integral on $\mathbb{R}^3 \setminus \mathcal{B}$ was evaluated using (4.90) and two quadrature rule, namely a Gauss-Legendre quadrature on $t \in [0, 1]$ and a Lebedev quadrature [190] on $\hat{y} \in S^2$. In the 2D case, two Gauss-Legendre quadratures where used. The known analytical expression (4.96) of the 3D isotropic exterior Eshelby tensor $\mathcal{S}^{\mathrm{ext}}$ for the unit sphere was directly applied to avoid its high numerical cost.

Since the topological derivative depends on the derivatives of u and p, the finite element representation of $\mathrm{D}J(z)$ is $\mathbb{P}^0$ (piecewise constant). To facilitate graphical post-processing, a regularized version $\mathrm{D}J_r$ of $\mathrm{D}J$ was computed, by applying a standard regularization procedure consisting in solving the variational problem

$$\int_\Omega \left(\mathrm{D}J_r\, w + \varepsilon \nabla \mathrm{D}J_r \cdot \nabla w \right) \mathrm{d}V = \int_\Omega \mathrm{D}J\, w\, \mathrm{d}V, \qquad \forall w \in H^1(\Omega).$$

The parameter ε controls the diffusion and regularization of $\mathrm{D}J$, at a slight expense of accuracy. For this study ε was set to $\varepsilon = 10^{-6}$.

4.6.1 Numerical evaluation of the EMT for ellipsoidal inhomogeneities

Considering an ellipsoidal inhomogeneity shape $\mathcal{B}$, the computation of $\mathcal{A}$ using (4.97) is straightforward once $\mathcal{S}^{\mathrm{int}}$ is known. Evaluating the latter usually requires a numerical quadrature of integral (4.84). A set of high-accuracy quadrature rules specially designed for integrals over S^2, proposed in [190], are used here for this purpose. Each such rule is based on a set of N_L points $\hat{\eta}_q \in S^2$ and weights w_q, determined so as to integrate exactly spherical harmonics of order up to L (they are freely available, as a Matlab file `getLebedevSphere.m`, from e.g. `www.mathworks.com`). Formula (4.84) then becomes

$$\mathcal{S}^{\mathrm{int}}_{ijk\ell} = \frac{1}{8\pi} \mathcal{C}_{mnk\ell} \sum_{q=1}^{N_L} w_q \left[\eta_{q,j} N_{im}(\eta_q) + \eta_{q,i} N_{jm}(\eta_q) \right] \eta_{q,n}(\theta) + \epsilon(N_L) \qquad (4.116)$$
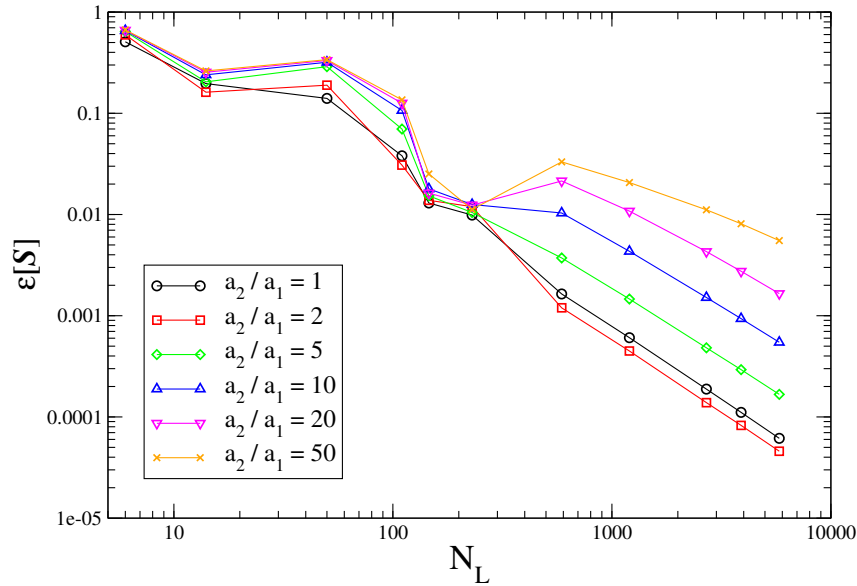
Figure 4.3: Cylindrical inclusion with elliptical cross-section: relative error $\epsilon_\infty(\mathcal{S}^{\text{int}})$ as a function of quadrature order N_L for various values of aspect ratio a_2/a_1.

(where $\epsilon(N_L)$ denotes the quadrature error). In this section, the accuracy of the numerical computation of $\mathcal{S}^{\text{int}}$ is quantified in terms of the relative L^∞ discrepancy between $\mathcal{S}^{\text{int}}$ and a reference value $\mathcal{S}^{\text{ref}}$, denoted $\epsilon_\infty(\mathcal{S}^{\text{int}})$ and defined by

$$\epsilon_\infty(\mathcal{S}^{\text{int}}) := \frac{|\mathcal{S}^{\text{int}} - \mathcal{S}^{\text{ref}}|_\infty}{|\mathcal{S}^{\text{ref}}|_\infty} = \frac{\max\limits_{i,j,k,\ell} |\mathcal{S}^{\text{int}}_{ijk\ell} - \mathcal{S}^{\text{ref}}_{ijk\ell}|}{\max\limits_{i,j,k,\ell} |\mathcal{S}^{\text{ref}}_{ijk\ell}|}, \tag{4.117}$$

First, three cases with available analytical exact solutions $\mathcal{S}^{\text{ref}}$ are considered, namely (a) a spherical inclusion ($a_1 = a_2 = a_3$), (b) a penny-shaped thin inclusion ($a_1 = a_2, a_3 \to 0$) and (c) a cylindrical inclusion with elliptical cross-section ($a_3 \to \infty$). An isotropic background material with a Poisson ratio $\nu = 0.3$ is assumed for all three cases. Numerical quadrature for cases (b) and (c) used $a_3 = 10^{-40}$ and $a_3 = 10^{40}$, respectively. In cases (a) and (b), (4.116) achieves an exact evaluation (within double-precision accuracy) with $N_5 = 14$ and $N_3 = 6$ quadrature points, respectively. Case (c) corresponds to an elliptical inclusion under two-dimensional plane-strain conditions, with the exact solution $\mathcal{S}^{\text{ref}}$ given by (4.114), but the numerical quadrature was still done using the three-dimensional formula (4.116), treating the inclusion as an extremely elongated ellipsoid ($a_3 = 10^{40}$) so as to test the numerical quadrature under more severe conditions. Relative errors $\epsilon_\infty(\mathcal{S}^{\text{int}})$ achieved for various values of N_L and the aspect ratio a_2/a_1 of the cross-section are shown in Fig. 4.3. Clearly, due to the very high aspect ratio a_3/a_1 used, sufficient accuracy (say $\epsilon(\mathcal{S}^{\text{int}}) \leq 10^{-2}$) requires hundreds to thousands of quadrature points depending on the aspect ratio a_2/a_1.

Next, the influence of either geometrical or material distortion on the quadrature order N_L required to achieve a fixed target accuracy $\epsilon(\mathcal{S}^{\text{int}}) = 10^{-5}$ in (4.116) is investigated. In Fig. 4.4a, an ellipsoidal inclusion with semiaxes (a_1, a_2, a_1) in an isotropic background material is considered, with the aspect ratio a_2/a_1 varying over the range $[1, 30]$, while Fig. 4.4b corresponds to the case of a spherical inclusion in various anisotropic materials, with the anisotropy index A_U varying between 0 (isotropic) to about 150 (highly anisotropic). The universal elastic anisotropy index, introduced in [256], is defined as

$$A_U = 5\frac{\mu_V}{\mu_R} + \frac{\kappa_V}{\kappa_R} - 6 \geq 0, \tag{4.118}$$
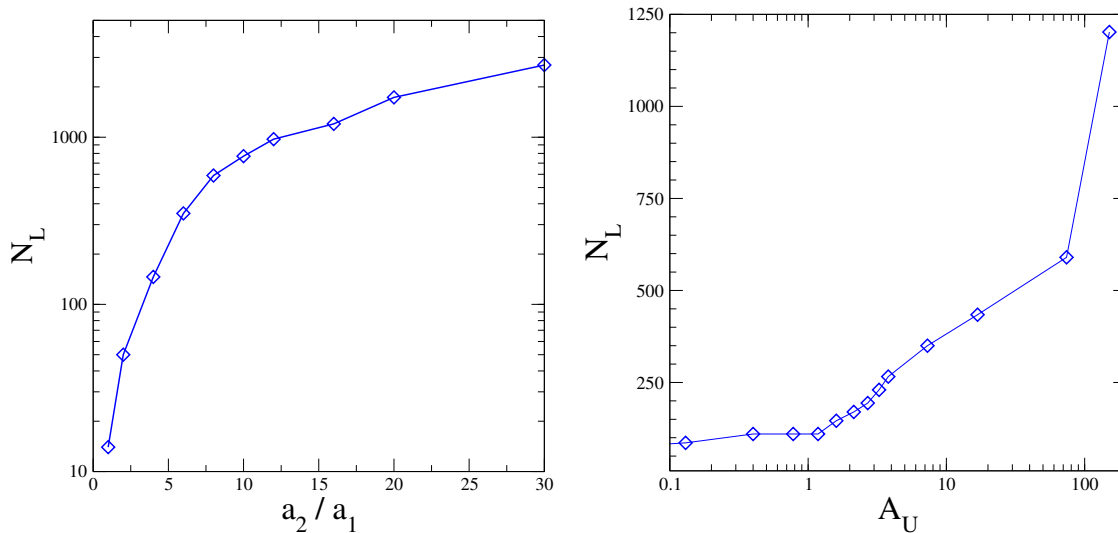
Figure 4.4: Quadrature order N_L needed to achieve target accuracy $\epsilon(\mathcal{S}^{\text{int}}) = 10^{-5}$ for (a) isotropic background material and varying values of aspect ratio a_2/a_1 or (b) varying values of anisotropy index A_{U} of background material.

where $\mathcal{C}_{\text{V}} = 3\kappa_{\text{V}}\mathcal{J} + 2\mu_{\text{V}}\mathcal{K}$ and $\mathcal{C}_{\text{R}} = 1/(3\kappa_{\text{R}})\mathcal{J} + 1/(2\mu_{\text{R}})\mathcal{K}$ are the Voigt estimate of $\mathcal{C}$ and the Reuss estimate of $\mathcal{C}^{-1}$, respectively. Both estimates are defined from averaging over all possible spatial orientations, and are hence isotropic. They are given by $\mathcal{C}_{\text{V}} = \mathcal{H}(\mathcal{C})$ and $\mathcal{C}_{\text{R}} = \mathcal{H}(\mathcal{C}^{-1})$, where $\mathcal{H}$ is the Haar measure over the set of rotations of $\mathbb{R}^3$, defined by

$$\mathcal{H}(\mathcal{E}) = \frac{1}{8\pi^2} \int_0^{2\pi} \int_0^{2\pi} \int_0^{\pi} \mathcal{Q}(\theta, \phi, \psi) : \mathcal{E} : \mathcal{Q}^{\text{T}}(\theta, \phi, \psi) \sin\theta \, d\theta \, d\phi \, d\psi \qquad (4.119)$$

$(\theta, \phi, \psi$ denoting the Euler angles). In (4.119), the fourth-order rotation tensor $\mathcal{Q}$ is defined (see [93, 215]) by $\mathcal{Q} := 1/2(Q_{ik}Q_{j\ell} + Q_{i\ell}Q_{jk})e_i \otimes e_j \otimes e_k \otimes e_\ell$ in terms of the rotation matrix $Q := Q_z(\psi)Q_x(\theta)Q_z(\phi) \in \mathbb{R}^{3\times3}$, where

$$Q_z(\alpha) = \begin{pmatrix} \cos\alpha & -\sin\alpha & 0 \\ \sin\alpha & \cos\alpha & 0 \\ 0 & 0 & 1 \end{pmatrix}, \qquad Q_x(\alpha) = \begin{pmatrix} 1 & 0 & 0 \\ 0 & \cos\alpha & -\sin\alpha \\ 0 & \sin\alpha & \cos\alpha \end{pmatrix}.$$

Clearly, suitable values of the quadrature order N_L are strongly influenced by both geometrical and material distortion. The latter effect is relevant in e.g. combined topology/material structural optimization, where the ability to accurately compute $DJ(z)$ for arbitrary trial materials spanning wide ranges of anisotropy is important.

4.6.2   Numerical assessment of the topological derivative

In this section, a simple cantilever structure featuring an anisotropic elliptic inhomogeneity B_a is considered, under plane-strain two-dimensional conditions (Fig. 4.5). The structure is clamped along its left side and loaded on its right side by $g = (0, -1)$. No body forces are applied ($f = 0$), and the remaining part of the boundary is traction-free. Two cases are considered for the constitutive properties (using the Voigt matrix notation, which reduces to 3×3 matrices for the plane-strain case): (a) a fully isotropic case with

$$\mathcal{C} = \begin{pmatrix} 1.34 & 0.57 & 0. \\ 0.57 & 1.34 & 0. \\ 0. & 0. & 0.38 \end{pmatrix}, \qquad \mathcal{C}^\star = 10^{-9}\mathcal{C}$$
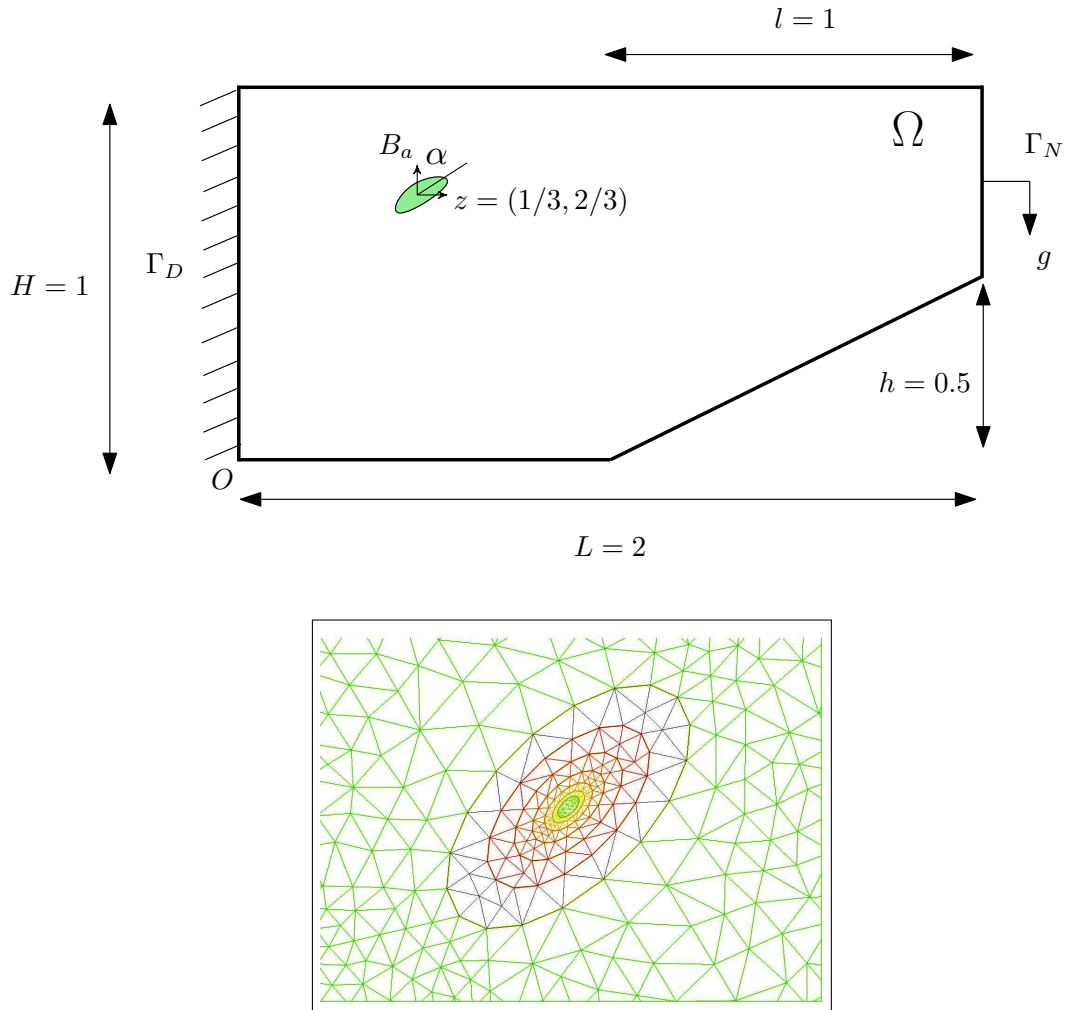
Figure 4.5: 2D Test case and the nested mesh structure of the inhomogeneities B_a.

i.e. with a very soft inhomogeneity close to a void, and (b) a fully anisotropic case with

$$
\mathcal{C} = \begin{pmatrix} 1. & 0.5 & 0. \\ 0.5 & 2. & 0. \\ 0. & 0. & 0.04 \end{pmatrix}, \qquad \mathcal{C}^{\star} = \begin{pmatrix} 3. & 0.4 & 0. \\ 0.4 & 1.5 & 0. \\ 0. & 0. & 0.03 \end{pmatrix}
$$

A specific objective function was considered, namely the potential energy (compliance)

$$
J(\mathcal{C}_a) = \mathbb{E}_{\text{pot}}(u_a) := -\frac{1}{2} \int_{\Gamma_{\text{N}}} u_a \cdot g \, \mathrm{d}s,
$$

A finite element analysis for cases (a) and (b) with various (small) values of a was performed, meanwhile the computation of $DJ(z)$ relied on a Gauss-Legendre quadrature formula for the numerical evaluation of $\mathcal{S}^{\text{int}}$ (4.102).

The discrepancy $\epsilon(a)$ between the variation of $J(\mathcal{C}_a)$ and DJ is defined by

$$
\epsilon(a) := \frac{|\Delta J - a^2 DJ(z)|}{|a^2 DJ(z)|}, \qquad \text{with } \Delta J := J(\mathcal{C}_a) - J(\mathcal{C}).
$$

$\epsilon(a)$ is plotted against a in Fig. 4.6, for an elliptic inhomogeneity with aspect ratio $a_1/a_2 = 1$ (disk) or 2m and (in the latter case) main axis rotation angles $\alpha = 0$ or $\pi/4$. A numerical test of correctness of the evaluation of $DJ(z)$ then consists in checking that $\epsilon(a) = o(1)$ for small
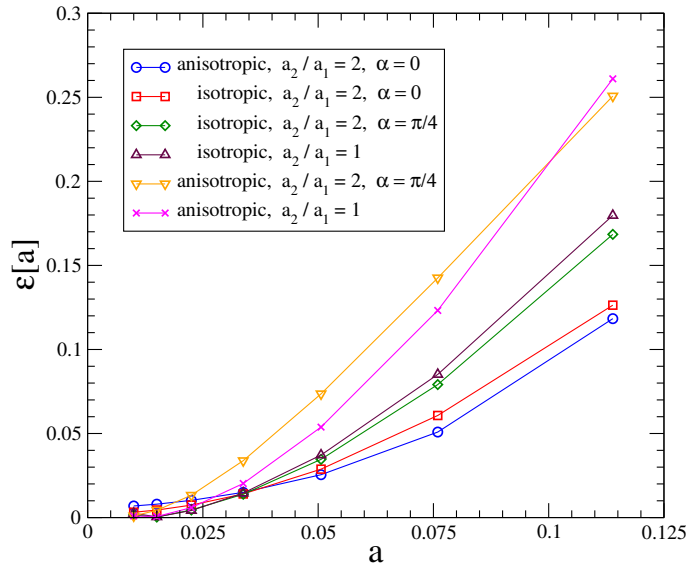
Figure 4.6: 2D Test case with nested inhomogeneities

a. This desired trend is clearly visible for all considered cases in Fig. 4.6. The results there moreover suggest that $\epsilon(a) = \mathcal{O}(a^2)$, even though one would *a priori* have expected a linear behavior. This empirical remark is consistent with higher-order topological expansions obtained in other situations [53] where for 2D problems the $\mathcal{O}(a^3)$ contribution to the objective function expansion is found to vanish whenever the shape $\mathcal{B}$ has central symmetry, which is the case of an elliptic inhomogeneity.

Remark 4.6.1. *This asymptotic validation is here limited to the 2D case because accurate numerical results require a very fine mesh of the inhomogeneity and its vicinity.*

4.6.3   Sensitivity analysis of the Hill-Tsai failure criterion

As it was evoked in Section 1.3, composite materials are quite popular in industry thanks their low weight, high fatigue resistance and good endurance against corrosion. The elastic constitutive relation for such materials, restricted for two-dimensional problems to the in-plane components of the stress tensor, may be conveniently written in the principal orthotropy directions, and using the Voigt notation, in the form

$$\left\{ \begin{matrix} \sigma_\ell \\ \sigma_t \\ \tau_{\ell t} \end{matrix} \right\} = \frac{1}{1 - \nu_{\ell t}\nu_{t\ell}} \begin{bmatrix} E_\ell & \nu_{t\ell}E_\ell & 0 \\ \nu_{\ell t}E_t & E_t & 0 \\ 0 & 0 & 2G_{\ell t} \end{bmatrix} \left\{ \begin{matrix} e_\ell \\ e_t \\ e_{\ell t} \end{matrix} \right\}$$

where the stresses are denoted as σ_ℓ in the fiber direction, σ_t in the direction transverse to the fibers, and $\tau_{\ell t}$ for the shear stresses. This model involves four independent elastic constants, since one must have $\nu_{t\ell}E_\ell = \nu_{\ell t}E_t$.

The Hill-Tsai failure criterion, suitable for orthotropic materials, is an adaptation of the von Mises yield criterion whereby the material strength depends on the direction, according to the orientation of the fiber reinforcement. This criterion can be written as [125]

$$\alpha^2(\sigma) := \frac{\sigma_\ell^2}{\hat{\sigma}_\ell^2} + \frac{\sigma_t^2}{\hat{\sigma}_t^2} - \frac{\sigma_\ell\sigma_t}{\hat{\sigma}_\ell^2} + \frac{\tau_{\ell t}^2}{\hat{\tau}_{\ell t}^2} < 1, \tag{4.120}$$

where $\hat{\sigma}_\ell$, $\hat{\sigma}_t$ and $\hat{\tau}_{\ell t}$ denote known rupture strengths.

Unlike their metal counterparts, composite structures are incapable to conduct away the extreme electrical currents and electromagnetic fields generated by lighting strikes. Hence the
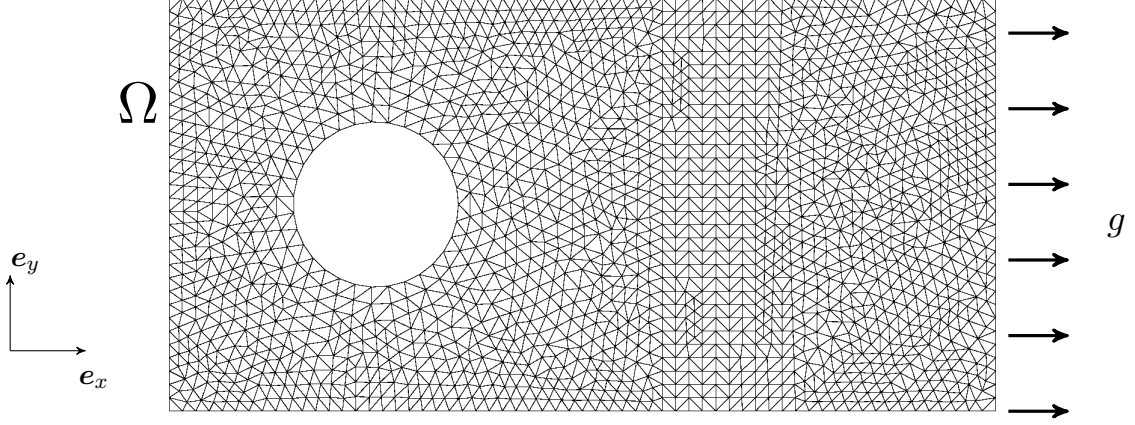
Figure 4.7: Orthotropic ply Ω clamped to a circular support: configuration and mesh ($\sim 3,700$ elements). A horizontal uniform load g is applied on its right side.

need for protection of composite structures has prompted the development of specialized lighting strike protection materials [122]. An example of such material features metallic pieces of conductive material added into the laminate. This numerical example examines, by means of the topological derivative, the sensitivity of the Hill-Tsai criterion (4.120) to the addition of small metallic inhomogeneities to the orthotropic material, so as to determine (and avoid) those locations for which this material addition make the laminate most vulnerable to failure.

Let $\Omega = \{(x,y) \in (0,1) \times (0,2)\} \subset \mathbb{R}^2$ be a rectangular 45° carbon/epoxy fiber ply (i.e. a composite membrane, with fiber direction $e_\ell = (e_x + e_y)/\sqrt{2}$ and 60% fiber volume fraction), clamped to a circular support. An uniform horizontal tensile traction $g = 10^{-5} E_\ell e_x$ is applied on its right side (Fig. 4.7).

The elastic parameters of the composite ply are $E_\ell = 135\,\text{GPa}$, $E_t = 10\,\text{GPa}$, $G_{\ell t} = 5\,\text{GPa}$, $\nu_{\ell t} = 0.3$, while the ultimate tensile failure strengths involved in the criterion (4.120) are $\hat{\sigma}_\ell = 1500\,\text{MPa}$, $\hat{\sigma}_t = 50\,\text{MPa}$, $\hat{\tau}_{\ell t} = 70\,\text{MPa}$. The metallic inclusions are considered circular and made of aluminum, whose isotropic elastic characteristics are $E = 72\,\text{GPa}$, $\nu = 0.34$, while the von Mises yield strength is $\hat{\sigma} = 20\text{MPa}$.

Let the densities $\psi, \psi^\star$ entering the definition (4.27) of the cost functional $J(\mathcal{C}_a)$ be given, in terms of the penalization function Ψ_n introduced in (4.32), by

$$\psi(d) = \Psi_n\big(\alpha^2(\mathcal{C}:d)\big), \qquad \psi^\star(d) = \Psi_n\big(\alpha_\star^2(\mathcal{C}^\star:d)\big) \tag{4.121}$$

(with $n \geq 1$). The function α for the composite membrane is given by (4.120). The corresponding function $\alpha_\star$ for the aluminum is also taken of the form (4.120) with $\hat{\sigma}_\ell = \hat{\sigma}_t = \hat{\sigma}$ and $\hat{\tau}_{\ell t} = \hat{\sigma}/\sqrt{3}$, as this choice reduces the Hill-Tsai criterion to the plane-stress von Mises criterion for isotropic materials. With this choice, $J(\mathcal{C}_a)$ is always nonnegative; moreover, in the limit $n \to \infty$, $J(\mathcal{C}_a) = 0$ unless the threshold (4.120) is violated at some location. The value $n = 5$ is used in the numerical experiments to follow. The topological derivative $\mathrm{D}J$ is given by (4.57), with

$$\mathcal{G}(z,d) = \psi(\nabla u(z) + d) - \psi(\nabla u(z)) - \partial_d \psi(\nabla u(z)):d, \tag{4.122}$$

and with $\mathcal{G}^\star$ similarly defined in terms of $\psi^\star$. The derivative $\partial_d \psi$ is found to be given by

$$\partial_d \psi(\nabla u):d = \big[\, \big(1 + \alpha^{2n}(\mathcal{C}:\nabla u)\big)^{(1-n)/n}\, \alpha^{2(n-1)}(\mathcal{C}:\nabla u)\big]\,\partial_d \alpha^2(\mathcal{C}:\nabla u):d \tag{4.123}$$

where, since $\alpha^2(\sigma)$ is a symmetric quadratic form in σ,

$$\partial_d \alpha^2(\mathcal{C}:\nabla u):d = \tfrac{1}{2}\alpha^2\big(\mathcal{C}:(\nabla u(z)+d)\big) - \tfrac{1}{2}\alpha^2\big(\mathcal{C}:(\nabla u(z)-d)\big).$$

Figure 4.10 shows the distributions of values of the Hill-Tsai criterion (4.120) and its topological derivative. The metallic inclusion should not be placed in zones where $\mathrm{D}J$ takes higher values.
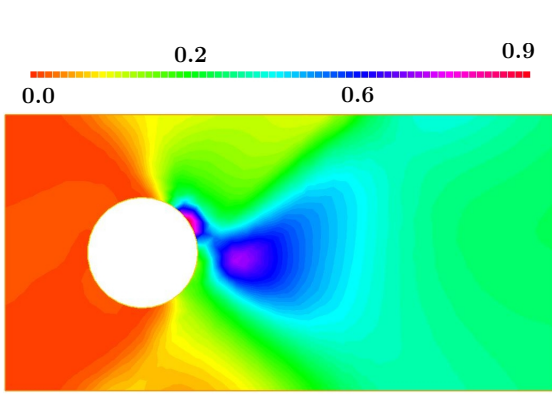
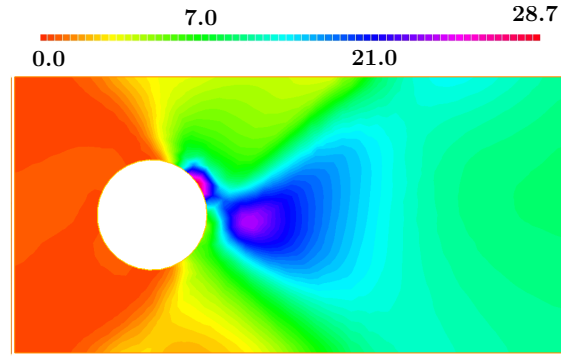**Figure 4.8:** Values of the Hill-Tsai criterion

Figure 4.9: Values of the topological derivative

Figure 4.10: Orthotropic ply: sensitivity analysis of the Hill-Tsai failure criterion.

4.6.4   Sensitivity of the von Mises criterion for an isotropic 3D beam

Consider a beam occupying the domain $\Omega = \{\,(x, y, z) \in (-0.1, 0.1) \times (-0.5, 0.5) \times (-0.1, 0.1)\,\}$, clamped on its rear face $y = -0.5$, made of an isotropic elastic material (Fig. 4.11). A traction $g = xe_z$ is applied on the front face, so as to produce torsion around the main axis $x = z = 0$. The remaining faces are traction-free.

The beam is meshed with $\sim 75,500$ tetrahedral elements and the isotropic elastic properties of the material are normalized and given as Young's modulus $E = 1$ and Poisson's ratio $\nu = 0.3$. We study the variation of the von Mises criterion when a small spherical cavity is introduced in the beam. This is a typical example of sensitivity analysis for topology optimization. The von Mises yield criterion sets a threshold on the *equivalent stress* σ_{eq}:

$$\alpha(\sigma) \leq 1, \qquad \text{with}\ \ \alpha(\sigma) := \sigma_{\mathrm{eq}}/\hat{\sigma}, \quad \sigma_{\mathrm{eq}} := \left(\tfrac{3}{2}\mathrm{dev}(\sigma)\!:\!\mathrm{dev}(\sigma)\right)^{1/2}, \qquad (4.124)$$

where $\mathrm{dev}(\sigma) := \sigma - \tfrac{1}{3}\mathrm{tr}(\sigma)I$ is the deviatoric stress tensor and $\hat{\sigma}$ is a critical stress threshold for the material, here chosen as $\hat{\sigma} = 0.1$. Under the given torsional loading, the stress state then satisfies (4.124) in the entire beam (see Figure 4.12).

Considering σ_{eq} as a function of the displacement gradient through the elastic constitutive equation $\sigma = \mathcal{C}\!:\!\nabla u$, and given that the trial cavity B_a contains no material (i.e. $\mathcal{C}^\star = 0$), ψ and
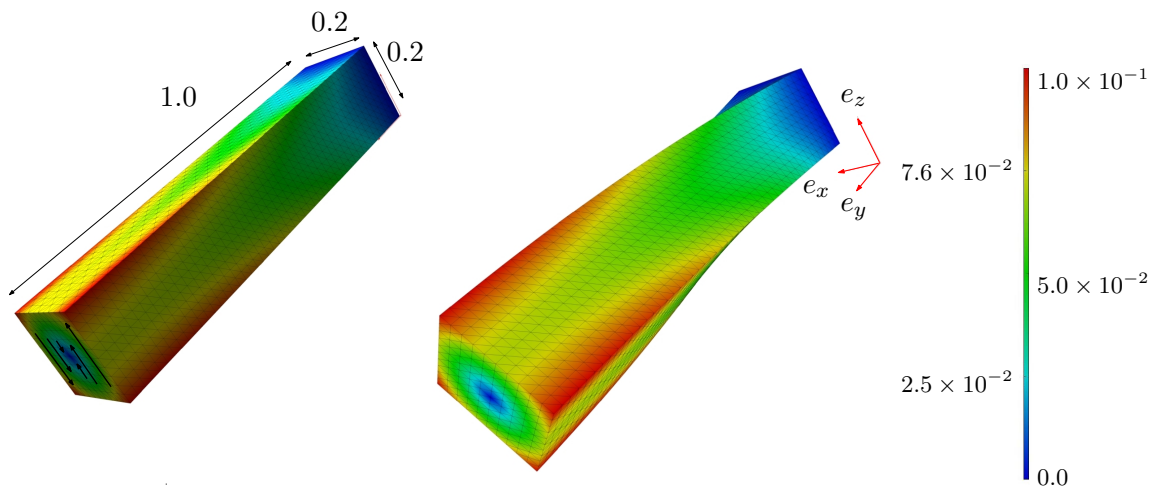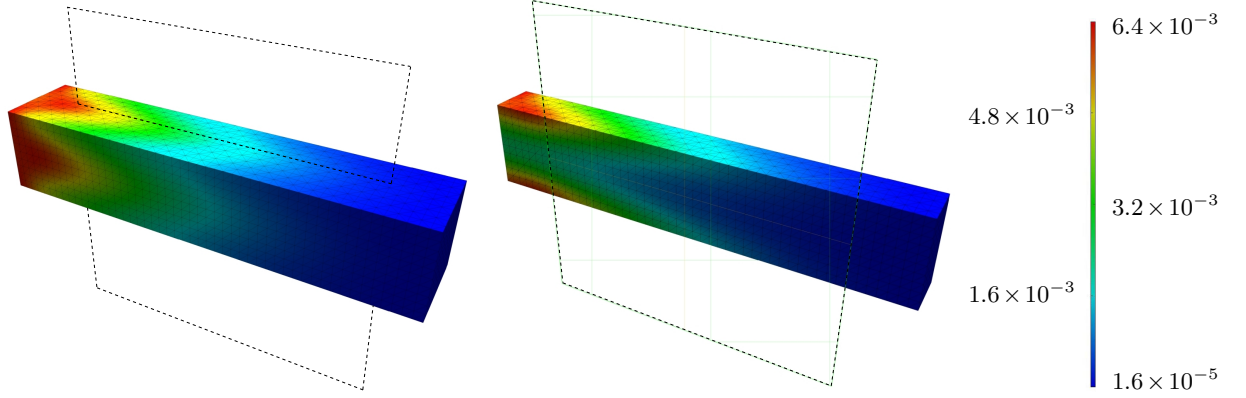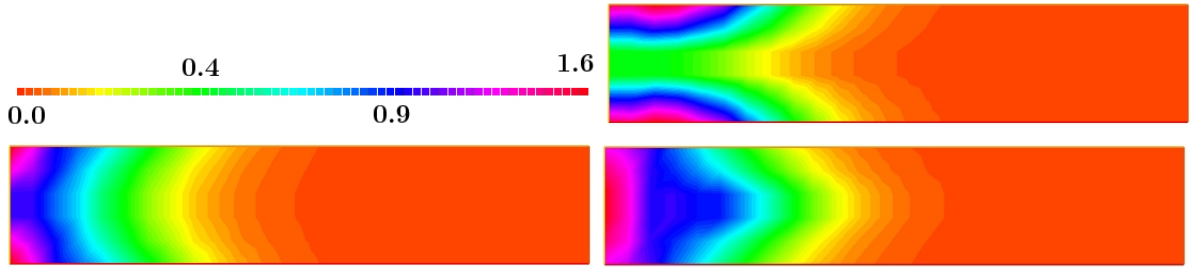

Figure 4.11: Beam under torsion: geometrical configuration, with color scale of displacement modulus (undeformed and deformed views)

Figure 4.12: Beam under torsion: contour plot of $2\sigma_{eq}^2/3 = |\mathrm{dev}(\sigma)|^2$ on the boundary (left) and inside the beam along a transversal cut (right).

Figure 4.13: Beam under torsion: color maps of $|\mathrm{D}J|$ in planes $x = 0$ (top left), $x = 0.05$ (top right) and $x = 0.1$ (bottom). The left boundary corresponds to the clamped face of the beam.

$\psi^\star$ are chosen as

$$\psi(\nabla u) = \Psi_n\big(\alpha^2(\mathcal{C}\!:\!d)\big), \quad \psi^\star(d) = 0 \tag{4.125}$$

where Ψ_n is again the penalty function (4.32), with $n \geq 1$ and α is defined by (4.124). Then if $n \to \infty$, the value of the integral of (4.125) on Ω is nonzero only if (4.124) is violated in some part of the domain. Let us take e.g. $n = 5$. Thus, noting that $\Delta\psi = -\psi$, the topological derivative of the functional

$$J_a(\mathcal{C}_a) = \mathbb{J}_a(\nabla u_a) = \int_{\Omega\setminus B_a} \psi(\nabla u_a)\,\mathrm{d}V$$

is given by

$$\mathrm{D}J(z) = -|\mathcal{B}|\psi(\nabla u(z)) - \nabla p(z)\!:\!\mathcal{A}\!:\!\nabla u(z) + \partial_d\psi(\nabla u(z)) : |\mathcal{B}|\nabla v_{\mathcal{B}}[\nabla u(z)]$$
$$+ \int_{\mathbb{R}^3\setminus\mathcal{B}} \mathcal{G}(z, \nabla v_{\mathcal{B}}[\nabla u(x)])(\bar{x})\,\mathrm{d}V,$$

where $\mathcal{G}(z, d)$ again has the form (4.122), this time with ψ defined by (4.125) and (4.124). The derivative ∂_d still has the form (4.123), now with

$$\partial_d\alpha^2(\mathcal{C}\!:\!\nabla u)\!:\!d = \frac{3}{\hat{\sigma}^2}\mathrm{dev}(\mathcal{C}\!:\!\nabla u)\!:\!\mathrm{dev}(\mathcal{C}\!:\!d)$$

The distribution of the values of $\mathrm{D}J$ for three different cut planes is plotted in Figure 4.13.

Remark 4.6.2. *The similarities between the distribution of $|\sigma_{dev}|$ in Figure 4.12 and the topological derivative in Figure 4.13 are noticeable. This observation supports the idea of using $|\sigma|$ as a sensitivity measure for topology optimization. In fact this property is exploited by evolutionary algorithms [153] and soft kill option algorithms [34] for lightweight design subjected to a yield criterion. In general, these algorithms search the optimal topology through a fully stressed design, by gradually removing the low stressed material w.r.t. a certain reference value.*

4.6.5   2D anisotropic flaw identification using an energy cost functional

To illustrate the usefulness of the topological derivative of energy-based cost functionals, the detection of three circular anisotropic inhomogeneities $B_k = B_a(z_k)$ $(k = 1, 2, 3)$ having the same radius a and embedded in an anisotropic reference material is considered,

$$\mathcal{C} = \begin{pmatrix} 1. & 3. & 0. \\ 3. & 10. & 0. \\ 0. & 0. & 0.03 \end{pmatrix} \tag{4.126}$$

again under two-dimensional plane-strain conditions (with geometry as shown in Fig. 4.14). B_1 and B_3 are softer than the background ($\mathcal{C}^\star = 0.5\mathcal{C}$), while B_2 is harder ($\mathcal{C}^\star = 2\mathcal{C}$). The solid is clamped on its bottom and lateral sides, while a uniform normal pressure $g = 1$ is applied on its top side. The displacement response u_0 of the flawed solid is computed using finite elements. The identification problem then consists of identifying the inclusions knowing the kinematic response u_0, which may in practice be available from full-field measurement techniques such as digital image correlation. In any case this remains as an academic example, due to the cost in practice of acquiring all these measures. Here, the identification problem may be formulated as minimizing the functional E_1 defined by (4.70). Figure 4.15 shows the topological derivative $DE_1(z)$ (more precisely, the normalized and thresholded quantity $z \mapsto \mathrm{Min}\big(DE_1(z), 0\big) / \big[- \mathrm{Min}\big(DE_1(z)\big)\big]$), where the EMT is defined using either $\mathcal{C}^\star = 0.5\mathcal{C}$ or $\mathcal{C}^\star = 2\mathcal{C}$. According to the choice of EMT, the topological derivative field $DE_1(z)$ is seen to reveal correctly, through locations at which $DE_1(z)$ is most negative, the locations of the softer and stiffer flaws. This is consistent with similar findings made in [136] for the elastodynamic case and using least-squares output cost functionals. Alike results have been obtained on this example for cases where $\mathcal{C}^\star$ is not proportional to $\mathcal{C}$.

4.6.6   3D anisotropic non-destructive testing

Two applications of non-destructive control in anisotropic materials are now presented, one pertaining to medical imaging and the other to composite structures. Indeed, several groups have recently investigated the topological derivative as a means for imaging hidden flaws, see for instance [325, 17], and also [308] for an application on experimental data. Existing investigations in this direction are based on usual displacement-based cost functionals (typically of the output
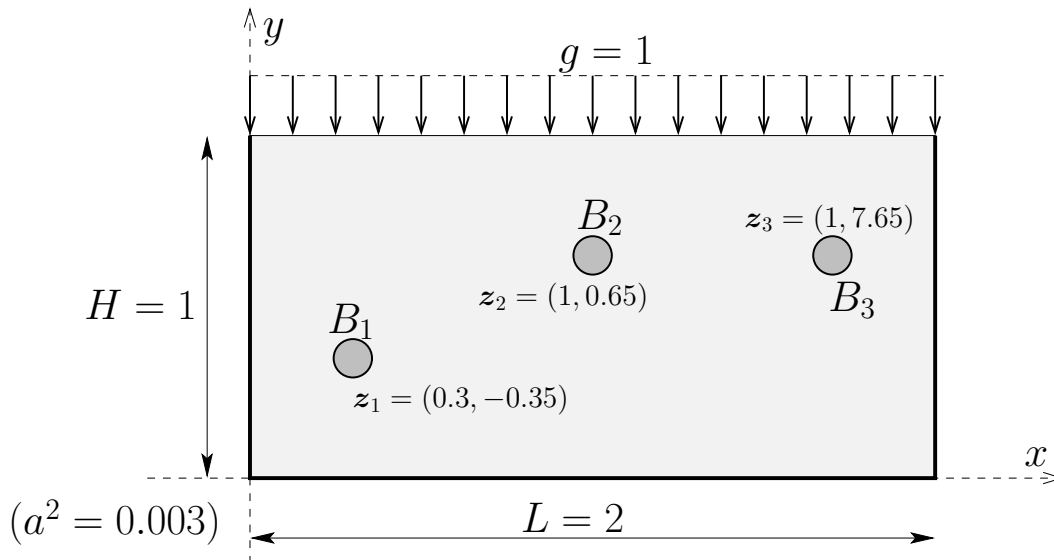

Figure 4.14: Flaw identification using an energy cost functional: setting and notations.

least-squares type). In contrast, we examine in this example an alternative approach where the misfit to experimental data is formulated in terms of an energy (and hence strain- or stress-based) cost functional. Assuming the availability of a displacement measurement u_0 over a part ω of the elastic solid Ω, using e.g. full-field kinematical data [35], the strain energy of the measurement misfit is given by

$$J_\omega(\mathcal{C}_a) = \mathbb{J}_a(\nabla u_a; \omega) = \int_\omega \nabla(u_a - u_0) : \mathcal{C}_a : \nabla(u_a - u_0) \, \mathrm{d}V. \tag{4.127}$$

Depending on whether the trial inhomogeneity B_a is located inside or outside of ω, we distinguish two cases:

1. $B_a \subset \omega$. This case is relevant when complete displacement measurements are available over a particular region ω inside Ω. Adapting (4.81), the topological derivative reads

$$\mathrm{D}J(z) = |\mathcal{B}| \nabla u_0(z) : \Delta \mathcal{C} : \nabla u_0(z) - \nabla(p + 2u_0 - u) : \mathcal{A} : \nabla u \qquad (z \in \omega),$$

where the adjoint solution p satisfies the variational formulation

$$\langle p, w \rangle_\Omega^\mathcal{C} = 2 \langle u - u_0, w \rangle_\omega^\mathcal{C}, \qquad \forall w \in W_0(\Omega).$$

2. $B_a \subset \Omega \setminus \bar{\omega}$. The interest of this situation is justified when we have a set of small control volumes inside a body and we want to identify the position of the anomaly outside the measured volumes. As it was previously seen in Section 4.4.2, there is no second order contribution in the topological derivative and $\mathrm{D}J$ simply reads

$$\mathrm{D}J(z) = -\nabla p(z) : \mathcal{A} : \nabla u(z) \qquad (z \in \Omega \setminus \bar{\omega}).$$

First application. It is concerned with the detection of anomalous femoral bone tissue. The local change of elastic properties in femoral bone may be provoked e.g. by cancer metastasis, traumatic or pathological fractures. Moreover, bone cell elasticity and morphology changes during the cell cycle [175], and elasticity differences between cancerous and healthy tissues of various kinds have been experimentally established [184, 294].

Additionally, bone is a complex material, with a multiphasic, heterogeneous and anisotropic microstructure [107]. In particular, femoral bone can be accurately modelled as transversely isotropic material whose principal orientations are defined based either on the trabecular structures or the harvesian system, according to whether the bone is cancellous or cortical [323].

Consider the proximal part Ω of a femoral bone (Fig. 4.16), contained in the box $\{ (x, y, z) \in (0.03, 0.09) \times (0.04, 0.08) \times (0.01, 0.11) \}$ and meshed with $\sim 213,600$ tetrahedral elements (mesh size $h = 0.001$). The elastic properties of the healthy bone are by simplification assumed to be homogeneous and transversely isotropic, with normalized elastic constants given by

$$E_x = E_y = 0.5, \;\; E_z = 1, \;\; \nu_{xy} = \nu_{xz} = \nu_{yz} = 0.35, \;\; G_{xz} = G_{yz} = 0.03.$$
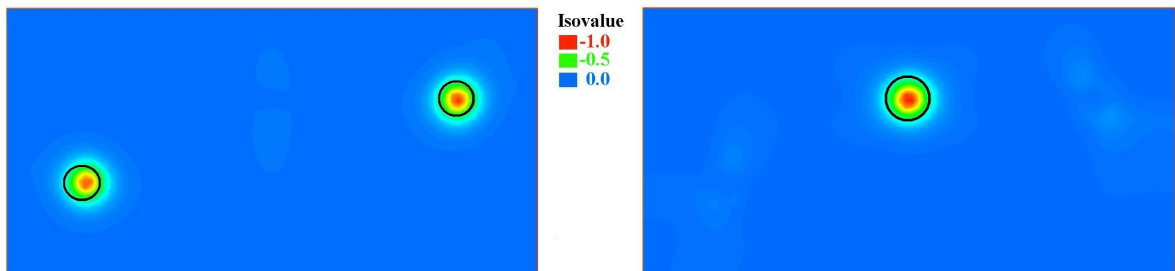
Figure 4.15: Flaw identification using an energy cost functional: topological derivative $DE_1(z)$ for $\mathcal{C}^\star = 0.5\mathcal{C}$ at the left and $\mathcal{C}^\star = 2\mathcal{C}$ at the right.
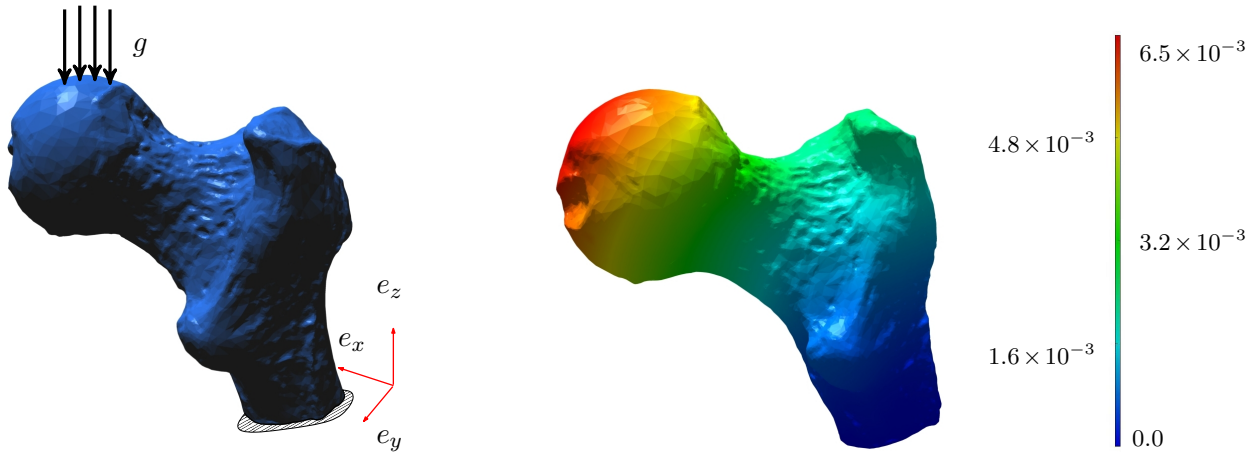
Figure 4.16: Femoral bone: a uniform vertical load $g = -10^{-3}e_z$ is applied on the head of the femur (simulating the body weight) while the distal horizontal section $z = 0.01$ is clamped (left). The right panel shows a color scale of the displacement modulus.

The anomalous tissue is assumed to be a small and stiffer spherical inhomogeneity (Fig. 4.17) with radius 0.005 and center at $(0.05, 0.06, 0.06)$. Its Young and shear moduli are twice those of the healthy bone, while both materials have the same Poisson ratios. The bone is clamped at $z = 0.01$ and loaded with a vertical force density $g = -1 \times 10^{-3}e_z$ applied on the top surface of the femur ($z \in [0.10, 0.11]$).

Figure 4.20 shows three iso-surfaces of $\mathrm{D}J$ with decreasing levels $\eta \approx -0.19$ (yellow), $\eta \approx -0.45$ (green) and $\eta \approx -0.71$ (blue), where an iso-surface S_η with level η relative to the (negative) absolute minimum $\mathrm{D}J_{\min} := \min_{z \in \Omega} \mathrm{D}J(z)$ is defined by

$$S_\eta = \big\{ z \in \Omega, \mathrm{D}J(z) = \eta |\mathrm{D}J_{\min}| \big\} \tag{4.128}$$

Those iso-surfaces show the location of the anomalous tissue to be correctly identified.

Second application. It consists in detecting a failure point leading to damage inside a composite structure. Multi-laminate composite structures, as it was detailed in Section 1.3, are made of multiple orthotropic plies, each of them composed of a weak matrix (most often polymeric) and reinforcement fibers (carbon, glass, kevlar, etc). We consider here a composite cube $\Omega = \{(x, y, z) \in (0, 0.2)^3\}$, filled up with $\sim 23,000$ tetrahedral elements (mesh size $h = 0.011$), made of three stacked layers of equal thickness (Fig. 4.23) whose constitutive elastic properties are transversely isotropic. The normalized elastic constants for the bottom layer are

$$E_x = 1 \ , E_y = E_z = 0.05, \ \ \nu_{xy} = \nu_{xz} = \nu_{yz} = 0.35, \ \ G_{xz} = G_{yz} = G_{xy} = 0.03,$$

The middle and top layers have the same elastic constants than the lowest one, but with the horizontal principal orthotropy directions resulting from a 45° and 90° rotation of the x, y axes, respectively. The failure point is modeled as a spherical inhomogeneity, of centre $(0.1, 0.15, 0.1)$ and radius 0.01, and with very low elastic moduli properties $\mathcal{C}^\star = 10^{-5}\mathcal{C}$. The considered misfit criterion is again of the form (4.127), this time with the measurement region ω consisting of a set of M small disconnected control volumes: $\omega = \cup \omega_j$ ($1 \leq j \leq M$), with $\omega_j \subset \Omega$ and $\overline{\omega}_i \cap \overline{\omega}_j = \emptyset$. Two of such configurations (but with control volumes of different size) are shown on Fig. 4.26
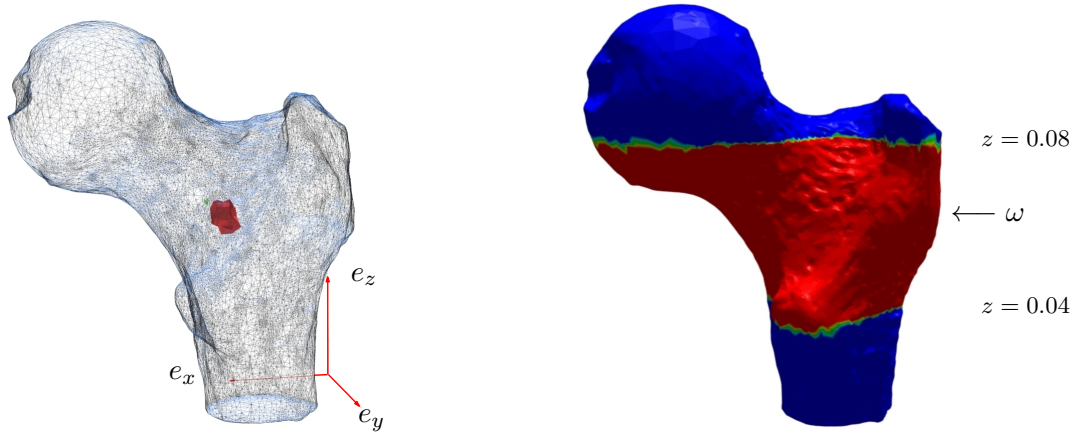
Figure 4.17: Femoral bone: anomalous tissue (left, in red) and measurement region ω (right, in red).
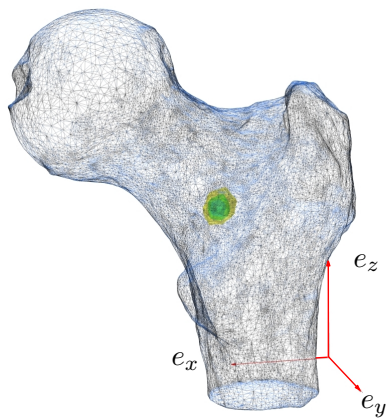
Figure 4.18: Three-dimensional view.
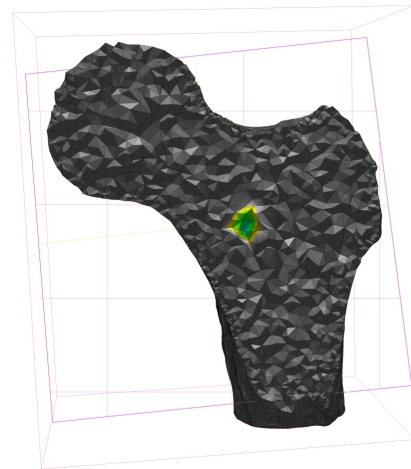

Figure 4.19: Transversal cut view.

Figure 4.20: Femural bone: iso-surfaces $\eta \approx -0.19$ (yellow), $\eta \approx -0.45$ (green) and $\eta \approx -0.71$ (blue) of $\mathrm{D}J$.

for $M = 44$ and $M = 729$. They respectively occupy 0.4% and 0.8% of the total volume. The adjoint solution p in this case solves

$$\int_\Omega \nabla p : \mathcal{C} : \nabla q \, \mathrm{d}V = 2 \sum_{i=1}^{M} \int_{\omega_i} \nabla(u - u_0) : \mathcal{C} : \nabla q \, \mathrm{d}V, \qquad \forall q \in W_0(\Omega).$$

Fig. 4.29 shows one iso-surface (in green) of $\mathrm{D}J$ with negative level surrounding the minimum of $DJ(z)$ for each control volume configuration of Figure 4.26 (with $\eta \approx -0.65$ and $\eta \approx -0.3$, respectively). As expected, the identification quality improves with the number of measurement zones. Moreover, the absolute minima of $\mathrm{D}J$ are found to be $\mathrm{D}J_{\min} \approx -1.3 \times 10^{-3}$ and $\mathrm{D}J_{\min} \approx -6.9 \times 10^{-2}$, respectively, which is another indication of configuration 2 being more sensitive to a small defect.
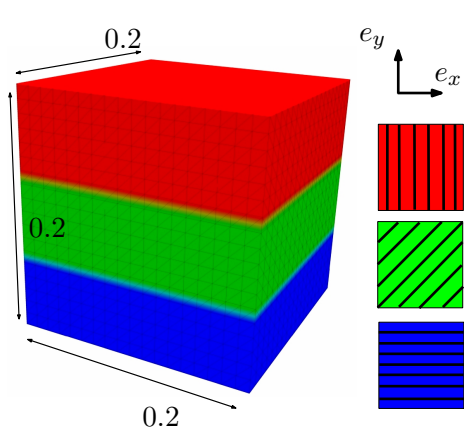
Figure 4.21: Layered cube, and fiber orientation.
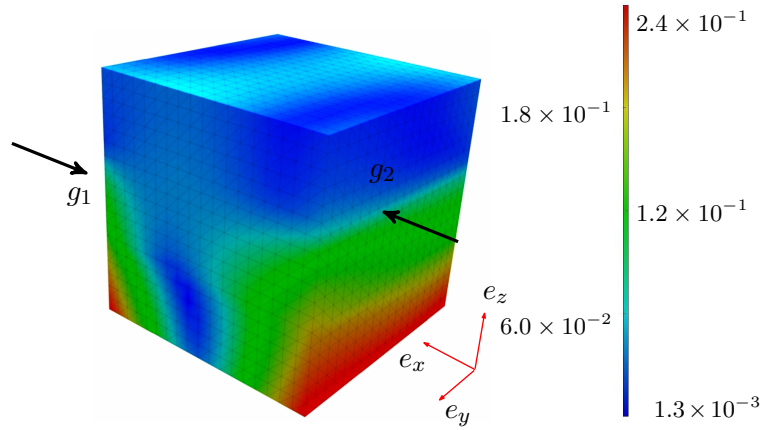
Figure 4.22: A color scale of the displacement modulus.

Figure 4.23: Layered cube: two uniform compression loads $g_1 = -0.1e_x$ and $g_2 = 0.1e_x$ are respectively applied on the faces of the cube $x = 0.2$ and $x = 0$. Displacements are not affine in the spatial coordinates due to the anisotropy.
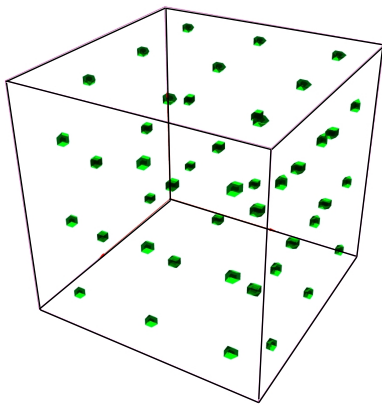
Figure 4.24: Configuration 1 ($M = 44$).
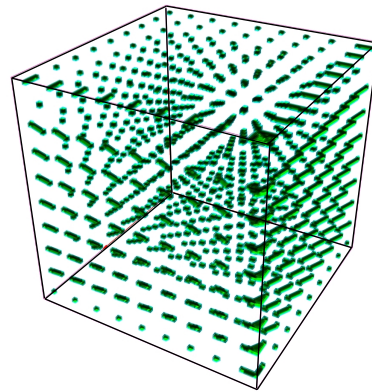
Figure 4.25: Configuration 2 ($M = 729$).

Figure 4.26: Layered cube: control volumes ω_j ($1 \leq j \leq M$).
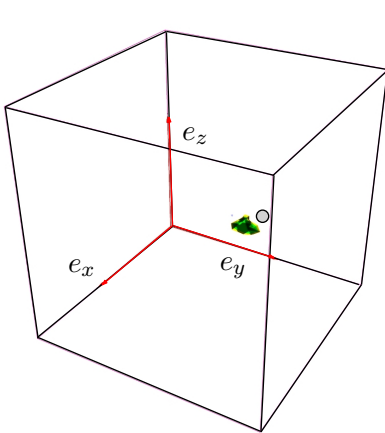
Figure 4.27: Configuration 1 ($M = 44$).
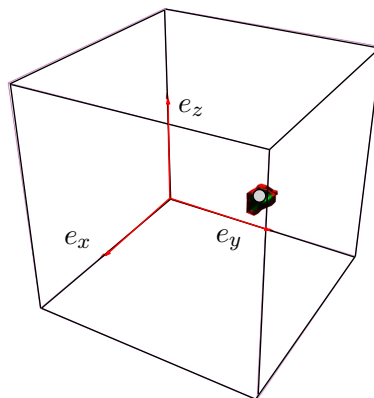
Figure 4.28: Configuration 2 ($M = 729$).

Figure 4.29: Layered cube: iso-surface S_η with $\eta \approx -0.65$ (left) and $\eta \approx -0.3$ (right) of DJ. The grey sphere shows the correct location of the failure point.

Chapter 5

Optimal design of a micro-tubular fuel cell

Contents

We discuss the problem of the optimal design of a micro-tubular fuel cell applying an inverse homogenization technique. Fuel cells are extremely clean and efficient electrochemical power generation devices, made up of a cathode/electrolyte/anode structure, whose energetic potential has not being fully exploited in propulsion systems in aeronautics due to their low power densities. Nevertheless, thanks to the recent development of additive layer manufacturing techniques (3D printing), complex structures usually impossible to design with conventional manufacturing techniques can be constructed with a low cost, allowing notably to build porous or foam-type structures for fuel cells. We seek thus to come up with the micro-structure of an arrangement of micro-tubular cathodes which maximizes the contact surface subjected to a pressure drop and a permeability constraint. The optimal periodic design (fluid/solid) emerges from the application of a shape gradient algorithm coupled to a level-set method for the geometrical description of the corresponding cell problem.

This chapter is based on a joint work with E. Moullet and Ch. Nespoulous in the framework of the internship in Airbus Group of the former one.

5.1 Introduction

Fuel cells are energy conversion devices which can continuously convert chemical energy into electrical energy and heat, without involving direct combustion. This feature offers many advantages over traditional power sources such as improved efficiency, greater fuel diversity, high scalability, no moving parts (hence less noise and vibration) and lower impact on the environment [129].

A fuel cell is a fairly simple device, mainly composed of three elements: an anode, a cathode, and an electrolyte between the two electrodes. The two electrodes are connected together by an electrical circuit. On the surface of these electrodes, electrochemical reactants react through half-redox reactions, producing (or consuming) ions, electrons, and in most cases, heat. Ions

pass through the electrolyte meanwhile electrons are "channeled" in the electric circuit and then routed to the second electrode to be consumed.

The efficiency of current fuel cells, which ranges from 40% to 60%, is higher than thermal systems such as gas turbines since their operation is not constrained by any theoretical thermodynamic limitation as the maximum Carnot efficiency. Furthermore, coupled to a gas turbine at a high temperature $(800-1000^oC)$, the spawned hybrid system can achieve really high efficiencies (near 85%), producing electricity from the waste of heat. This feature makes high temperature operating fuel cells an interesting complement to aircraft engines [253, 280, 264, 259, 289].
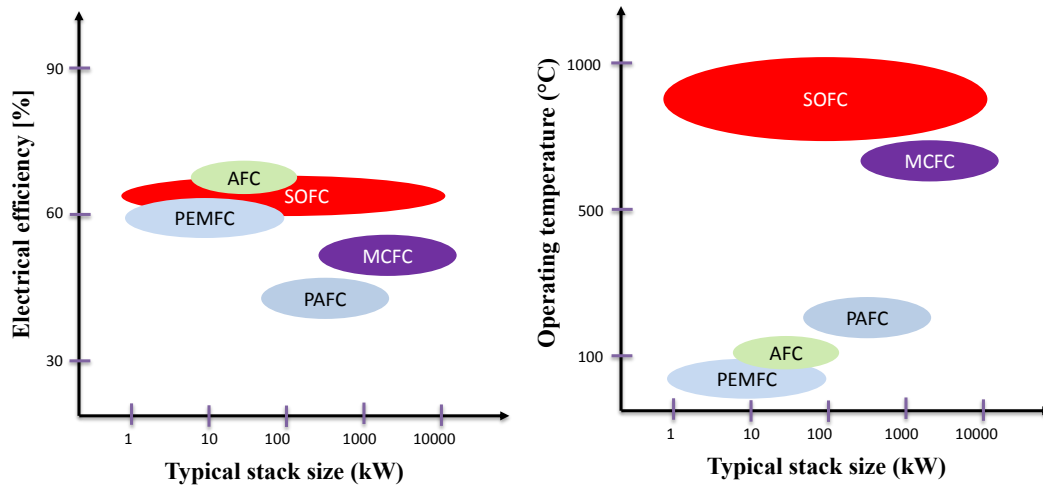
Figure 5.1: Different types of fuel cells: Polymeric Electrolyte Membrane (PEMFC), Alkaline (AFC), Phosphoric Acid (PAFC), Molten Carbonate (MCFC) and Solid Oxide (SOFC).

Among the different types of fuel cells (see Fig. 5.1), one can recognize the Solid Oxide Fuel Cells (SOFC) as a particularly appealing model for high temperature applications in hybrid systems. SOFC possesses various advantages w.r.t other fuel cells such as a solid electrolyte allowing different geometries and shapes, good performance and durability, and high operating temperature $(800-1000^oC)$ for reforming. This last attribute has the potential of hybridization with a gas turbine, as it is show in Fig. 5.3.

The cathode of a SOFC is usually an alloy of lanthanum, strontium, and manganese oxide. On its surface takes place the half reduction reaction of oxygen, producing an oxygen ion. The electrolyte is e.g. made of YSZ (yttrium stabilized zirconia). This allows the ion transport to the anode (nickel mixed with YSZ), in contact with which it reacts with hydrogen to produce water and electrons. Finally, these electrons are conducted and used by an electric device (Figure 5.2). Both the anode and the cathode must be very porous so as to allow the transport of the fuel and the oxygen, respectively.

SOFC can be designed following many geometric configurations. However, the most common designs are the planar and the tubular ones. Each design offers advantages and drawbacks depending of the application requirement. Planar design configuration has a low physical component volume profile and short current path between single cells, allowing higher power densities, meanwhile tubular designs have e.g. high thermo-mechanical properties, simple sealing requirements and good thermal shock resistance [101].

Despite of the impressive energy efficiencies achieved by the SOFC, the foregoing geometries lack of an essential property required by any aircraft system: high gravimetric and volumetric energy densities. Indeed, fuel cells are still too heavy to propel any large aircraft since they have a lower power density when compared with conventional turbines [154]. For instance, the gravimetric power density (kW/kg) of a SOFC compared to the turbojet CFM-56 (one of the most popular turbojets in the world and often used as a reference for studies of this type) is at
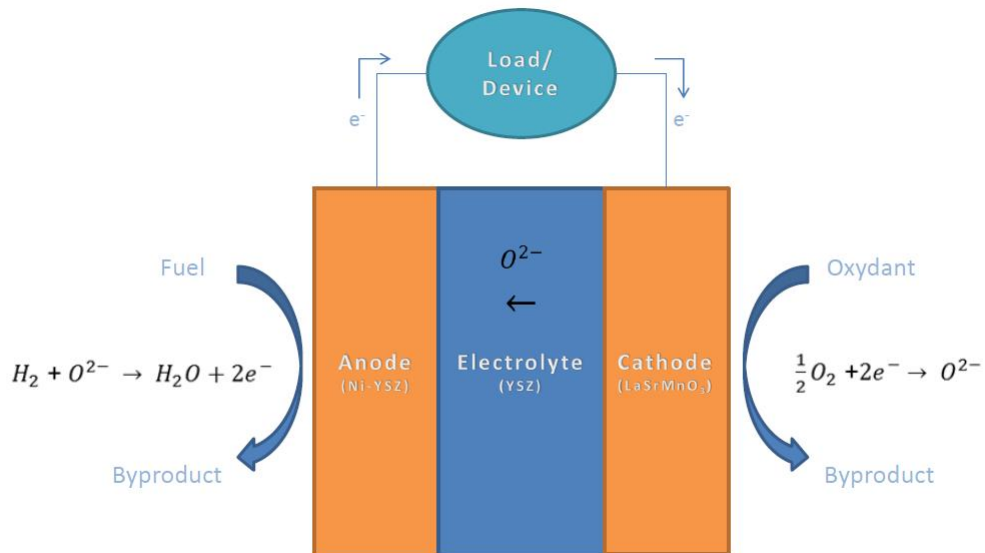
Figure 5.2: Triple structure of a solid oxide fuel cell. The O_2 from the air is consumed in the cathode, meanwhile the O^{2-} ions liberated from the reduction reaction travel through the electrolyte to the anode, where the oxidation reaction of the fuel (H_2) takes place, liberating heat, water and electricity.
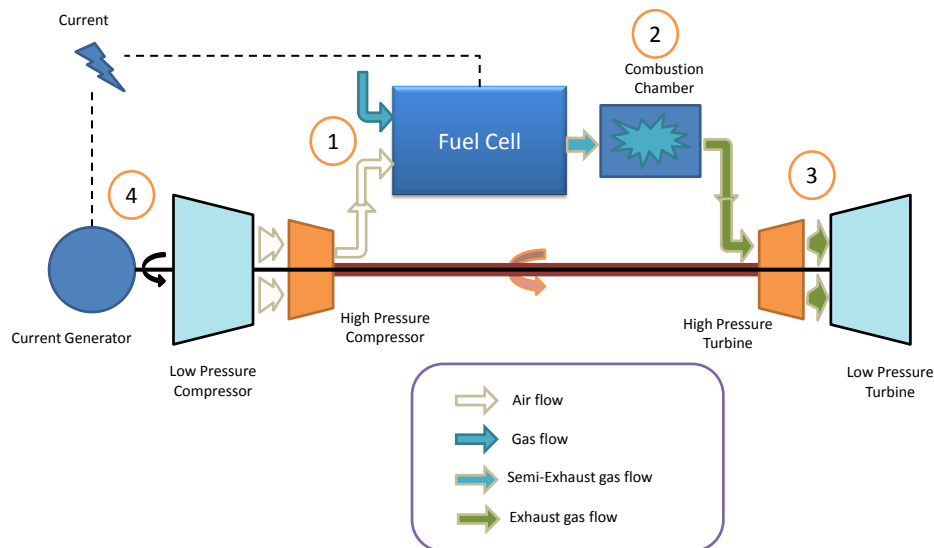
Figure 5.3: Example of an hybrid system.

least five times smaller.

In order to improve the fuel cell efficiency, various alternatives have emerged, such as miniaturization of the structure through a micro-tubular configuration [101] and the use of porous materials (foam) in the design of some components (e.g. bipolar/end plates) [185]. In general these techniques take advantage of recent developments in additive layer manufacturing or 3D printing procedures, which allow the construction of extremely complicated 3D structures from a CAD model.

Thus, the design of fuel cells with very small features, leading notably to periodic patterns, becomes a foremost challenge in the construction of future technologies (see Figure 5.4). An adapted tool for this purpose is inverse homogenization. The homogenization method for topology optimization, which has been successfully implemented in structural optimal design (see e.g. [4, 42, 85, 13, 43]), consists in admitting composites regions where the void appears at a
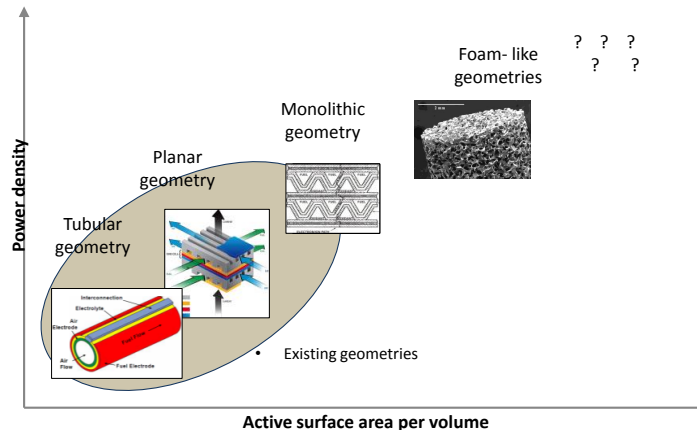
Figure 5.4: Evolution of power density vs active surface of SOFC

micro-scale (see Section 1.1). The theoretical foundations are given in [182, 302]. Meanwhile in homogenization the effective properties of a material are found from the micro-structure, in inverse homogenization the micro-structure does not exist initially but we seek to come up with a micro-structure with prescribed or extreme homogenized properties. The design of materials with extreme or prescribed properties using inverse homogenization in elasticity, fluid mechanics, wave propagation, etc., is well known in the literature [69, 274, 273, 143, 277, 328, 132, 44].

In the process of finding the optimal micro-structure, a topology optimization problem must be solved within the so-called cell problem. The cell problem defines the link between the physical macroscopic (effective) properties and the micro-structure characterized by a certain geometry. Among the most popular methods in topology optimization for fluid flow problems, the level-set method for shape optimization [11, 66, 272, 319] arises as a viable, robust and efficient alternative to more standard density-based approaches [4, 6, 42]. First introduced by [252, 271], the level-set method is capable of tracking fronts and free boundaries, allowing thus to naturally manage topology changes. Moreover, in the context of fluid flows, it enables to directly implement the no-slip boundary condition, avoiding any kind of interpolation scheme [80].

In the present chapter we propose an optimal configuration of a micro-tubular fuel cell, whose cathode constitutes a tubular periodic structure designed by inverse homogenization. This particular structure leads to a maximal surface micro-structure subjected to a permeability constraint for the air phase and a pressure drop constraint for the fuel phase. In Section 5.2, the main features of the problem are described, namely the physical modeling of a porous fuel cell, the homogenization of the equations governing the system and the optimization problem we contemplate to solve. Then the shape gradients of the functionals involved in the optimization problem, according to Definition 1.1.13, are recalled in Section 5.3. Finally an example of an optimal periodical micro-structure (fluid/solid) is detailed in Section 5.4, emerging from the application of the level-set method for topology optimization (see Section 1.2) to the corresponding cell problem.

5.2　Problem setting

5.2.1　Physical modeling of a porous fuel cell

A generic SOFC, regardless of the geometrical configuration (planar, tubular, monolithic, etc), is always composed of two porous electrodes (anode and cathode), a dense electrolyte, an anodic and cathodic gas channel and two current collectors. However, for the sake of simplicity, we propose to study a reduced model of a micro-tubular SOFC [101], as described in Figure (b) 5.5, focusing on the three former components. Thus, we consider a periodically perforated

domain, where the air flows freely around a periodic collection of cathode/electrolyte/anode tubes. The air cannot penetrate inside the tubes and the fuel flows orthogonally through them. The air transports several species but we concentrate on the O_2, which is consumed in the electrochemical reaction on the surface of the cathode.
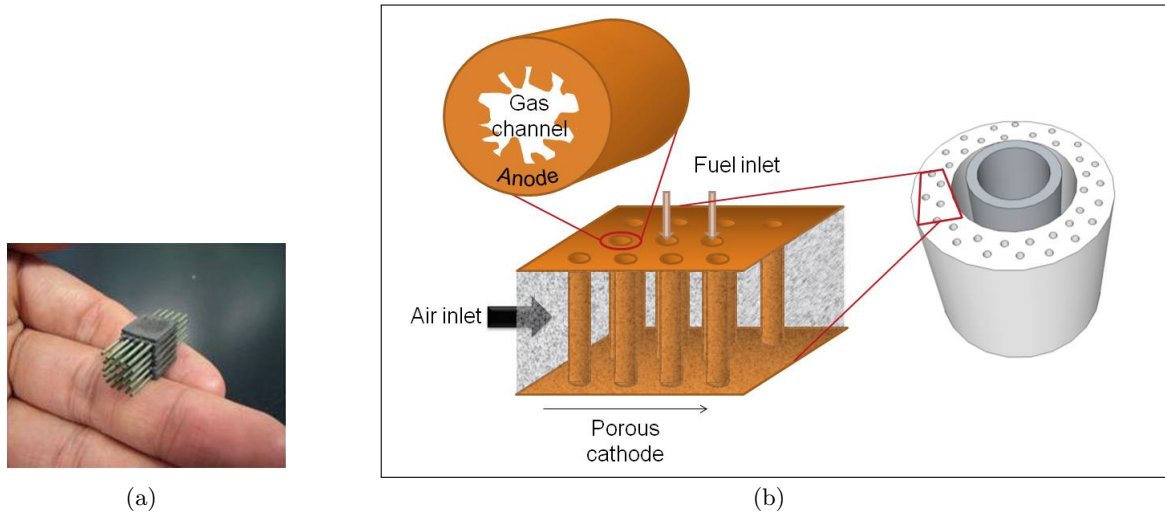
Figure 5.5: Micro-tubular fuel cell: (a) Micro-tubular SOFC of 3W, AIST [236]. (b) Micro-tubular design with arbitrary shaped tubes proposed in [225].

Assumptions. Now we list the main physical assumptions of our model, similarly to [57]

(1) *Steady state velocity of the air (also called slow steady state).*

(2) *Laminar and incompressible flow.* This assumption derives from the low gas speed in the SOFC gas channels, where the density variation of each specie is not related to compressions/expansions, but rather caused either internally by heat release of chemical reactions or externally by wall heating and by mass variation. Furthermore, considering that the gas speed in SOFC gas channels is always very low (low Mach number < 0.3), it is a common practice to assume a laminar flow in the gas channels, meaning that the non-linear term in the momentum conservation equation (inertia term) is negligible with respect to the viscous term.

(3) *Isothermal state.* Since the temperature of the SOFC is quite high ($800^o - 1000^o$C), the local variations can be underestimated. This allows in particular to avoid the dependence of the diffusion tensor and the reaction ratio of O_2 with respect to the temperature.

(4) *The electrochemical reactions are confined to the electrode-electrolyte interface.* The place where the electrochemical reaction takes place, the so-called triple-phase-boundary, is the site where ions, electrons and gas coexist, thus enabling the redox reactions. Since this place represents a small portion of the entire electrode domain and the high electronic conductivity of the electrodes compared to the ionic conductivity, the redox reactions are likely to take place very close to the electrode-electrolyte interface.

(5) *The cathode/electrolyte/anode is a lumped structure so it can be treated as one interface.*

Generally speaking, the physic of the SOFC is modeled as a complex system where chemical reactions, electrical conduction, ionic conduction, gas phase mass transport, and heat transfer take place simultaneously and are tightly coupled [158, 161, 96]. Nevertheless, we simplify the

physical description by focusing only on the gas mass transport and the chemical reaction on the cathode.
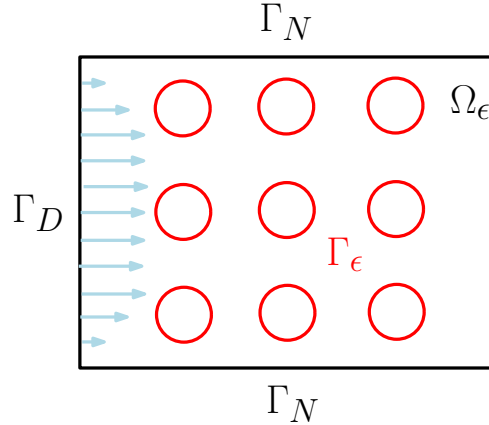
Figure 5.6: Transversal section of the porous SOFC and boundary conditions. The air flows from the left to the right. The fuel penetrates orthogonally through the figure inside the red tubes. Γ_ϵ represents the anode/electrolyte/cathode lumped structure.

Let $\Omega_\epsilon \subset \mathbb{R}^d$ be the porous volume of the fuel cell where the air flows freely, delimited by the boundaries Γ_D, Γ_N and Γ_ϵ. The air is injected through Γ_D, meanwhile Γ_N is impermeable. A periodic arrangement of anode/electrolyte/cathode tubes constitutes the interface Γ_ϵ. The redox reaction takes place on Γ_ϵ and the adimensional parameter ϵ corresponds to the ratio between the characteristic size of each tube and a macroscopic characteristic length. See Fig. 5.6.

Conservation and constitutive laws.   The fluid adimensionalized equations (mass conservation and momentum conservation) plus the specie (O_2) diffusion-convection-(surface)reaction adimensionalized equation respectively read [31]

$$\begin{cases} \text{div}(u_\epsilon) = 0 & x \in \Omega_\epsilon, \\ -\epsilon^2 \mu \Delta u_\epsilon = \nabla p_\epsilon & x \in \Omega_\epsilon, \\ \frac{\partial X_\epsilon}{\partial t} + u_\epsilon \cdot \nabla X_\epsilon = \lambda \Delta X_\epsilon & t > 0, x \in \Omega_\epsilon, \\ X_\epsilon = X_{\text{init}} & t = 0, x \in \Omega_\epsilon, \end{cases} \tag{5.1}$$

where X_ϵ, X_{init} represent the current and the initial concentrations of O_2 in the air, u_ϵ is the local velocity of the air, p_ϵ the local pressure, μ the viscosity of the air and λ the diffusion coefficient. The parameter ϵ as it was explained above, corresponds to the ratio between the characteristic size of each tube and a macroscopic characteristic length. We remark that in this model, the diffusion and the convection of the O_2 in the transport equation are equilibrated at the macro-scale.

Boundary conditions

$$\begin{cases} u_\epsilon = u_D & X_\epsilon = X_D & t > 0, x \in \Gamma_D, \\ u_\epsilon \cdot n = 0 & D_\epsilon \nabla X_\epsilon \cdot n = 0 & t > 0, x \in \Gamma_N, \\ u_\epsilon = 0 & \nabla X_\epsilon \cdot n = -\epsilon \frac{1}{4e} \mathcal{R}(X_\epsilon) & t > 0, x \in \Gamma_\epsilon, \end{cases} \tag{5.2}$$

where (u_D, X_D) are the velocity of the air and the concentration of O_2 at the inflow boundary Γ_D, e is the electron charge and $\mathcal{R}(X_\epsilon)$ is the Butler-Volmer reaction term [174], which can be simplified [266, 57] to

$$\mathcal{R}(X_\epsilon) = j_0(X_\epsilon^m, T) \exp\left(-\alpha_c \frac{zF}{RT} \eta \right).$$

j_0 corresponds to the exchange current density and depends linearly upon X_ϵ^m, m is the order of reaction, η is the over-potential with respect the Nerst equilibrium potential, α_c is the cathodic transfer coefficient, T the temperature, z the number of electrons involved in the electrode reaction, R the universal gas constant and F the Faraday constant. All the above parameters are assumed constants.

We remark that the coefficient m is positive and in order to prove the existence of a weak solution of (5.1), (5.2), m should be smaller than a certain critical value $\bar{m}$, which depends on the dimension d of the space. By taking e.g. $m \leq 1$, $\mathcal{R}(X_\epsilon) \in L^2(\Gamma_\epsilon)$ and the variational formulation of (5.1), (5.2) will be well posed. Typical values for m are e.g. 0.4 in [176], for a composite cathode made of 60% volume of LSM (lanthanum-strontium-manganite) and 40% YSZ, and 0.25 in [92, 57]. Thus, depending on the physical characteristics of the cathode, the reaction term $\mathcal{R}$ is in general non-linear.

5.2.2 Homogenized system

Before stating the homogenization of the system (5.1),(5.2), let us describe more precisely the assumptions on the porous domain Ω_ϵ [4]. As usual in periodic homogenization, a periodic structure is defined by a domain Ω and an associated micro-structure, or periodic cell $Y = (0,1)^d$, which is made of two complementary parts : the solid part ω and the fluid part $Y \backslash \omega$ (see Figure 5.7). We assume that $Y \backslash \omega$ is a smooth and connected open subset of Y, identified with the unit torus (i.e. $Y \backslash \omega$, repeated by $Y-$periodicity in $\mathbb{R}^d$, is a smooth and connected open set of $\mathbb{R}^d$). The domain Ω is covered by a regular mesh of size ϵ: each cell Y_i^ϵ is of the type $(0, \epsilon)^d$, and is divided in solid part ω_i^ϵ and fluid part $Y_i^\epsilon \backslash \omega_i^\epsilon$, i.e. is similar to the unit cell Y rescaled to size ϵ. The fluid part Ω_ϵ of a porous medium is defined by

$$\Omega_\epsilon = \Omega \backslash \bigcup_{i=1}^{N(\epsilon)} \omega_i^\epsilon,$$

where the number of cells is $N(\epsilon) = |\Omega| \epsilon^{-d}(1 + o(1))$.
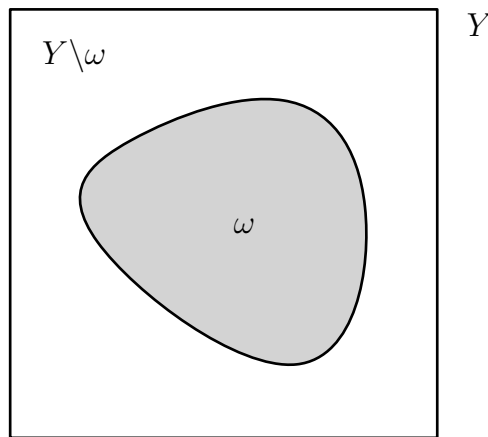
Figure 5.7: Unit cell of a porous medium.

Now according to [155, 156] for general heterogeneous catalysis and [266] for PEM fuel cells, the homogenization of the initial boundary value problem (5.1),(5.2) corresponds to the following system

$$\begin{cases} \text{div}(u^*) = 0 & x \in \Omega \\ u^* = -\frac{K}{\mu} \nabla p^* & x \in \Omega \\ \frac{\partial X^*}{\partial t} + u^* \cdot \nabla X^* = \lambda \text{div}(D \nabla X^*) + |\partial \omega| \mathcal{R}(X^*) & x \in \Omega \\ X^* = X_{\text{init}} & t = 0, x \in \Omega, \end{cases} \tag{5.3}$$

and the boundary conditions

$$\begin{cases} u^* = u_D & X^* = X_D & t > 0, x \in \Gamma_D, \\ u^* \cdot n = 0 & \nabla X^* \cdot n = 0 & t > 0, x \in \Gamma_N. \end{cases} \tag{5.4}$$

The functions u^*, p^*, X^* correspond to the homogenized velocity, pressure and O_2 concentration, respectively. D is the effective porous media diffusion tensor, $|\partial\omega|$ is the perimeter of the micro-fuel-tube ω scaled to the unit cell and K is the permeability tensor.

The definition of the tensors K and D stems from the so-called cell problems [155], namely

$$K_{ij} = \int_{Y\backslash\omega} \nabla u_i(y) : \nabla u_j(y) dy, \quad D_{ik} = \int_{Y\backslash\omega} \Big(e_i + \nabla\pi_i\Big)\cdot\Big(e_k + \nabla\pi_k\Big) dy \tag{5.5}$$

where the tensorial product " :" represents the twice-contracted tensorial product, i.e. for $A, B \in \mathbb{R}^{d\times d}$

$$A : B = \sum_{k,\ell} A_{k\ell}B_{k\ell},$$

and the respective cell problems read

$$\begin{cases} \nabla p_i - \Delta u_i = e_i, \ x \in Y\backslash\omega, \\ \mathrm{div}(u_i) = 0, \ x \in Y\backslash\omega, \\ u_i = 0, \ x \in \partial\omega, \\ y \to p_i(y), u_i(y) \ \text{Y-periodic,} \end{cases} \qquad \begin{cases} -\mathrm{div}(\nabla\pi_j + e_j) = 0, \ x \in Y\backslash\omega, \\ \nabla\pi_j \cdot n = -e_j \cdot n, \ x \in \partial\omega, \\ y \to \pi_j(y) \ \text{Y-periodic,} \end{cases} \tag{5.6}$$

with $(e_i)_{1\leq i\leq d}$ being the canonical basis of $\mathbb{R}^d$.

5.2.3 Optimization problem

The topology optimization problem consist in finding the optimal lay-out $\omega^* \subset Y$, representing the scaled shape of the fuel tubes inside the unit-cell, which solves

$$\begin{cases} \max_{\omega\subset Y} |\partial\omega| \\ \text{s.t.} \\ |\omega| \geq C_f|\partial\omega| \\ \frac{tr(K)}{d} \geq k_{min}, \end{cases} \tag{5.7}$$

where the tensor K is defined according to (5.5) and $tr()$ is the trace operator. The first constraint represents a lower bound $C_f \geq 0$ of the fuel tube hydraulic diameter, which prevents a drastic pressure drop and a "too oscillating" boundary. The constant C_f must satisfy $C_f \leq \sqrt{1/4\pi}$, according to the isoperimetric inequality. The second constraint involves a lower bound k_{min} of the trace of K (which is intended to give a mesure of the permeability [132]) avoiding a high pressure drop in the cathode. In other words, we try to find the shape ω with the largest perimeter (so it maximizes the factor on the electro-chemical reaction term $\mathcal{R}$ of the homogenized transport equation in (5.3)) such that two constraints of pressure drop inside and outside the tubes are fulfilled.

Let $\omega_0 \subset Y$ be a regular fixed open set. Then the following result (inspired in Theorem 1.1.9) yields the existence of an optimal solution of (5.7)

Proposition 5.2.1. *Denote as $\mathcal{U}_{ad}$ the collection of open subsets of Y close to ω_0 (likewise in (1.10)) in the sense of the pseudo-distance*

$$d^{\mathbb{D}}(\omega_0, \omega) = \inf_{T\in\mathbb{D}|T(\omega_0)=\omega} \Big(\|T - Id\|_{W^{2,\infty}} + \|T^{-1} - Id\|_{W^{2,\infty}} \Big),$$

where $\mathbb{D}$ (similarly to (1.8)) is the set of diffeomorphism

$$\mathbb{D} = \left\{ T \ such \ that \ (T - Id) \in W^{2,\infty}(\mathbb{R}^d; \mathbb{R}^d), (T^{-1} - Id) \in W^{2,\infty}(\mathbb{R}^d; \mathbb{R}^d) \right\}.$$

Furthermore, chose in particular the family of applications $T = Id + \theta$, where $\theta \in W^{2,\infty}(\mathbb{R}^d; \mathbb{R}^d)$ and $\|\theta\|_{W^{2,\infty}} < 1$. Then problem (5.7) admits at least one optimal solution in $\mathcal{U}_{ad}$.

Proof. It is a classical result that the set $\mathcal{U}_{ad}$ is compact w.r.t. the above topology, introduced by F.Murat and J.Simon [229]. Furthermore since $\|\theta\|_{W^{2,\infty}} < 1$, any minimizing sequence of (5.7) has a convergent subsequence in $W^{1,\infty}(\mathbb{R}^d; \mathbb{R}^d)$, due to the Sobolev embedding theorem. Finally the existence of a solution of (5.7) stems from the continuity of the perimeter, the area and the permeability tensor K w.r.t. $\|\theta\|_{W^{1,\infty}}$, thanks to their respective shape differentiability. The concept of the shape derivative will be recalled in the next section.

$\square$

Remark 5.2.2. *Another logical choice of topology to prove the existence of a solution for (5.7), could be the one induced by the $L^1(Y)$ convergence of characteristics functions (Theorem 1.1.6), allowing a richer topology variety than the above one. However, in this topology the perimeter $|\partial\omega|$ is only lower semi-continuous, preventing the application to any maximization problem.*

5.3 Shape sensitivity analysis

In this section we recall the shape gradients, according to Definition 1.1.13, of the shape functionals involved in (5.7). The respective proofs can be found in [265].

Lemma 5.3.1. *Let ω be a smooth subset of Y. Define*

$$J_{surf}(\omega) = |\partial\omega| = \int_{\partial\omega} ds \quad and \quad J_{vol}(\omega) = |\omega| = \int_{\omega} dx.$$

Then the respective shape gradients at 0 in the direction θ read

$$J'_{surf}(\omega)(\theta) = \int_{\partial\omega} \theta \cdot nH \, ds, \quad J'_{vol}(\omega)(\theta) = \int_{\partial\omega} \theta \cdot n \, ds,$$

where H is the mean curvature of $\partial\omega$ defined by $H = div(n)$.

Proposition 5.3.2. *Define the spaces*

$$H^1_{0,\#}(Y\backslash\omega)^d = \left\{ v \in H^1(Y\backslash\omega)^d : v|_{\partial\omega} = 0, y \to v(y) \ is \ Y-periodic \right\},$$

$$L^2_{0,\#}(Y\backslash\omega) = \left\{ q \in L^2(Y\backslash\omega) : \int_{Y\backslash\omega} qdx = 0, \ y \to q(y) \ is \ Y-periodic \right\}.$$

Let $u_i \in H^1_{0,\#}(Y\backslash\omega)^d$ and $p_i \in L^2_{0,\#}(Y\backslash\omega)$, $i = 1, ..., d$ be the collection of solutions of the variational formulation of the first cell problem in (5.6)

$$\int_{Y\backslash\omega} \left(\nabla u_i : \nabla v_i - div(v_i)p_i - div(u_i)q_i \right) dx = \int_{Y\backslash\omega} e_i \cdot v_i dx, \ \ \forall (v_i, q_i) \in (H^1_{0,\#}(Y\backslash\omega)^d, L^2_{0,\#}(Y\backslash\omega)).$$

(5.8)

Define the cost function (which does not depend on the pressure)

$$J(\omega) = \int_{Y\backslash\omega} j(x, u, \nabla u) dx, \ where \ u = (u_i)_{i=1...d},$$

and the collection of adjoint states $(U_i, P_i) \in (H^1_{0,\#}(Y\backslash\omega)^d, L^2_{0,\#}(Y\backslash\omega))$, such that $\forall (v_i, q_i) \in (H^1_{0,\#}(Y\backslash\omega)^2, L^2_{0,\#}(Y\backslash\omega))$

$$\int_{Y\backslash\omega} \left(\nabla U_i : \nabla v_i - div(v_i)P_i - div(U_i)q_i \right) dx = -\int_{Y\backslash\omega} \left(\frac{\partial j}{\partial u_i}(x, u_i, \nabla u_i)\cdot v_i + \frac{\partial j}{\partial \nabla u_i}(x, u_i, \nabla u_i) : \nabla v_i \right) dx.$$

$$(5.9)$$

Then $J(\omega)$ is shape differentiable at 0 in the direction θ and the shape derivative reads

$$J'(\omega)(\theta) = \int_{\partial\omega} \left\{ j(x, u, \nabla u) - \sum_{i=1}^{d} \left(\frac{\partial U_i}{\partial n} \cdot \frac{\partial u_i}{\partial n} + \frac{\partial j}{\partial \nabla u_i} \cdot n \cdot \frac{\partial u_i}{\partial n} \right) \right\} \theta \cdot n ds.$$

Corollary 5.3.3. *According to (5.5)*

$$\frac{tr(K)}{d} = \frac{1}{d}\sum_{i=1}^{d} K_{ii} = \frac{1}{d}\int_{Y\backslash\omega} \sum_{i=1}^{d} |\nabla u_i|^2 dx,$$

so the shape derivative reads

$$\frac{1}{d}tr(K)'(\omega)(\theta) = -\frac{1}{d}\sum_{i=1}^{d} \int_{\partial\omega} \left(\left(\frac{\partial u_i}{\partial n}\right)^2 + \frac{\partial u_i}{\partial n} \cdot \frac{\partial U_i}{\partial n} \right) \theta \cdot n ds,$$

with U_i solution of the adjoint problem

$$\int_{Y\backslash\omega} \left(\nabla U_i : \nabla v_i - div(v_i)P_i - div(U_i)q_i \right) dx = -2\int_{Y\backslash\omega} \nabla u_i : \nabla v_i, \forall (v_i, q_i) \in (H^1_{0,\#}(Y\backslash\omega)^2, L^2_{0,\#}(Y\backslash\omega))$$

5.4   Numerical results

Now we detail the numerical solution of problem (5.7) via a the level-set method for topology optimization described in Section 1.2.

At each iteration of the algorithm, the shape of the tube in the unit cell Y is parametrized via a level-set function

$$\begin{cases} \psi(x) = 0 & \text{for } x \in \partial\omega, \\ \psi(x) < 0 & \text{for } x \in \omega, \\ \psi(x) > 0 & \text{for } x \in Y\backslash\omega, \end{cases}$$

defined on a fixed mesh in an Eulerian framework. Since the interface $\partial\omega$ does not necessarily match with the mesh, in order to simulate an impenetrable interface in (5.6), an artificial permeability (or porosity) term is added on the left side of equations (5.8) and (5.9), respectively

$$\int_Y \frac{5}{2\rho^2}(u_i \cdot v_i)dx, \quad \int_Y \frac{5}{2\rho^2}(U_i \cdot v_i)dx, \tag{5.10}$$

where $2\rho^2/5$ represents the permeability of the medium [61, 111]. For topology optimization purposes, ρ is a regular approximation of $\mathcal{H}(\psi)$, where $\mathcal{H}$ is the Heaviside function and $\min_{x\in Y} \rho(x) = \delta > 0$ [42, 55]. Typically this value is set up to $\delta = 0.001$. We remark that thanks to the introduction of (5.10), all integrals are thus calculated in Y.

For the optimization algorithm we use an augmented Lagrangian method

$$\mathcal{L}(\omega, \ell, \mu) = |\partial\omega| - \ell_1(C_f|\partial\omega| - |\omega|) - \ell_2(k_{min} - \frac{tr(K)}{d}) + \frac{\mu_1}{2}(C_f|\partial\omega| - |\omega|)^2 + \frac{\mu_2}{2}(k_{min} - \frac{tr(K)}{d})^2,$$
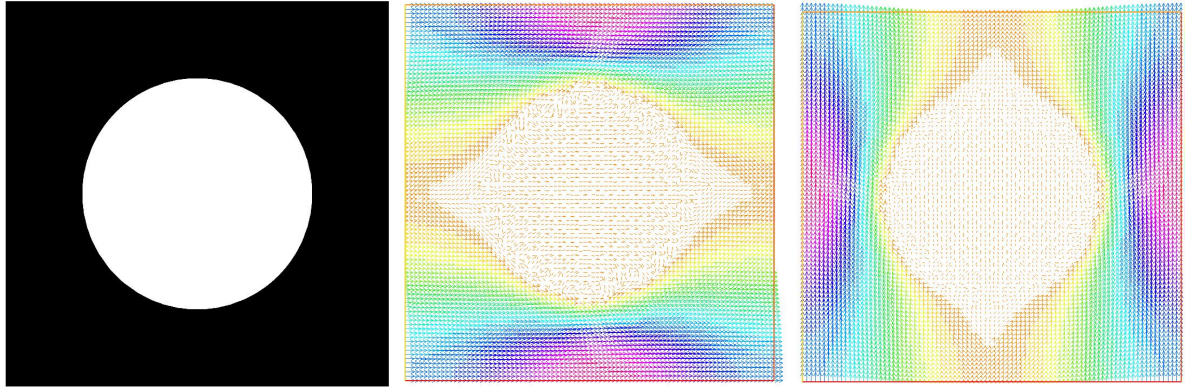
Figure 5.8: Example of the 2D stokes solutions u_1, u_2 (left and right respectively) of the cell problem for a circular domain in (5.8). The black zone represents the air phase (transporting the oxygen) meanwhile the white one the fuel phase. A solid interface lays between them. We remark that inside the fuel phase the velocity of the air is almost zero, due to (5.10).

where $\ell = (\ell_i)_{i=1,2}$ and $\mu = (\mu_i)_{i=1,2}$ are lagrange multipliers and penalty parameters for the constraints. The Lagrange multipliers are updated at each iteration n according to the optimality condition

$$\ell_1^{n+1} = \ell_1^n - \mu_1(C_f|\partial\omega_n| - |\omega_n|) \quad \text{and} \quad \ell_2^{n+1} = \ell_2^n - \mu_2(k_{min} - \frac{\text{tr}(K)}{d}).$$

The penalty parameters are augmented every 5 iterations. With such an algorithm the constraints are enforced only at convergence.

Fig. 5.9 shows different optimal periodic layouts starting from an intuitive circular arrangement. The radius of the circle in Y was set up to $r = 0.3$, meanwhile the coefficients $C_f = 0.15$ and $k_{min} = 0.011$ were calculated so as both constraints in (5.7) were active within this layout. The first optimal design (second row Fig. 5.9) corresponds to the optimal solution of the algorithm for the foregoing parameters. Then the second design (third row Fig. 5.9) was established by reducing C_f and k_{min} to the half. The perimeter gain w.r.t. the circular layout is 7% for the former design and 60% for the latter one.

The above results demonstrate the capabilities of topology optimization via a level-set method to enhance the design of micro-tubular fuel cells for the aeronautic industry. Thanks the application of an inverse homogenization technique and the level-set method, periodic optimal micro-tubular fuel cells with a sharp contour can easily be designed and then manufactured by 3D printing. The foregoing study thus suggests a promising use of these technologies in the future computer aided design of fuel cells.
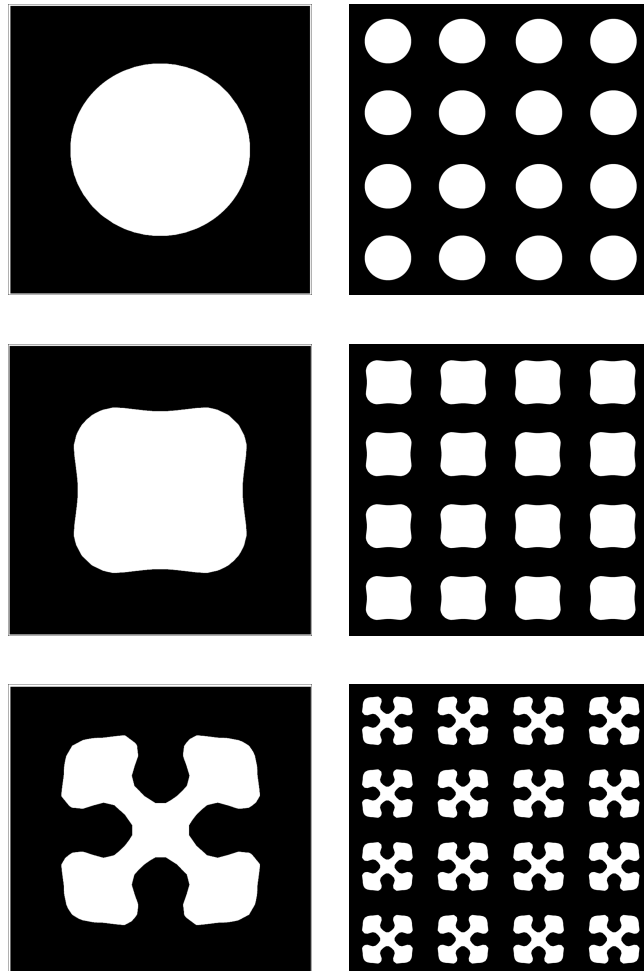
Figure 5.9: Two micro-tubular optimal designs for different values of k_{min} and C_f starting from a circular layout. The base cell results are on the left and the corresponding periodic structures on the right.

Conclusions and perspectives

Throughout this work, we have presented several topics related to optimal design and sensitivity analysis in an elastic anisotropic and a fluid/solid framework. The main contributions of this thesis thus rely on **(1)** the treatment of anisotropic topology optimization problems, notably on **(1.a)** elastic multi-phase materials and **(1.b)** laminated composite plates; **(2)** the development of the topological derivative for stress-dependent criteria within a full anisotropic framework; and **(3)** the presentation of an innovative approach for optimal design of micro fuel cells.

We proceed now to give a more detailed description in each case:

(1) The shape derivative for various mechanical criteria was established in a sharp multi-phase framework in Chapter 2 for the 2D/3D linear elasticity and in Chapter 3 for the linearized von Kármán plate equations. The main ingredients of the preceding analysis were the transmission conditions, showing that depending whether the chosen framework is discrete or continuous different formulae for the shape derivative arise. Moreover in Chapter 2 we evoked the impact of the position of the contours of each phase with respect to the others in the shape differentiability of the problem, altogether with the difficulty of calculating the jumps involved in the shape derivative. The aforementioned study contributes to enrich and enlighten some misunderstandings in the existing literature on the subject.

(1.a) We proposed in Chapter 2 a level-set method for topology optimization where the smeared interface between multiple materials is parameterized via the signed distance function. This particular parameterization is shape differentiable and it naturally avoids the non-differentiability difficulty existing in the sharp setting when multiple interfaces superpose. Furthermore, relying on the signed distance function for describing a smoothed interface enables the control of the regularization width around the interface during the optimization process, preventing the excessive generation of intermediate-density material. Also, this smooth interface approach yields a consistent formula for the shape derivative which converges to the sharp one when the regularization width tends to zero. All the above elements contribute to settle the proposed topology optimization algorithm as a robust and efficient alternative in the optimal design of the so-called graded materials.

(1.b) The main subject of this thesis was set forth in Chapter 3, introducing the in-plane shape as a new optimization variable in the design process of laminated composites. For that purpose, a full anisotropic version of the von Kármán equations was introduced, alongside with the respective linearized buckling problem. The problem of finding the optimal shape of each ply (continuous variable) and the stacking sequence (discrete variable) was presented, taking the form of a mixed optimization problem whose objective function is the total weight subjected to various stiffness constraints. By virtue of this particular structure, which commonly features lightweight design, we rigorously proved that this composite problem is equivalent to a bi-level problem, where the higher level depends upon the shape of each ply meanwhile the lower level determines the best stacking sequence for a fixed in-plane shape through the so-called constraint margin function. The stationarity conditions for the latter formulation were

established in an infinite dimensional framework, relying on the concept of generalized gradient for the shape derivative. A convergent feasible descent direction algorithm was proposed to solve the aforementioned problem and the theoretical existence of an optimal solution was discussed, contributing novel elements to the standard literature regarding pointwise and buckling constraints.

Referring to the evaluation of the constraint margin function, the typical manufacturing constraints concerned in the set up of laminated composites were discussed, formulating them as linear inequalities with respect to the stacking sequence. Moreover, fixing the proportion of plies following a certain fiber orientation within the laminate, we established the concavity with respect to the stacking sequence of the first eigenvalue of the linearized von Kármán equations and the reserve factor (simplified measure of the first buckling load). The foregoing elements, i.e. the linearity of the manufacturing constraints plus the concavity of the buckling measures, lay down a convex optimization framework for the evaluation of the constraint margin function. For this reason, a classical convex integer programming algorithm was proposed (OA method), setting up an effective alternative to the popular genetic algorithms. Besides of being capable of tackling non-convex problems by means of α-under estimators, the OA method does not bear the need of evaluating so many times the objective function and constraints like the genetic algorithms. This is a feature of paramount importance when each evaluation of the model implies to run a costly finite element computation, as it is the case when solving the von Kármán system for non-homogeneous anisotropic plates. Thus, when the laminate features a relatively "small" number of plies, the proposed algorithm to evaluate the constraint margin function remains competitive.

Despite the rigorous character of treating the composite design problem as a truly mixed programming problem by means of a suitable bi-level formalism, the proposed method undergoes the following limitations:

- **Blended panels**. An important feature of a composite laminate is the structural integrity across the multiple panels making up the structure. This can be characterized by means of the following definition of relaxed generalized blending [311]: *Two adjacent panels are completely blended if there are no dropped edges in physical contact.*
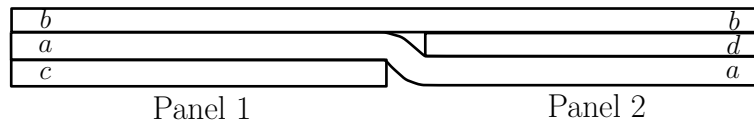
(a) Fully blendend.
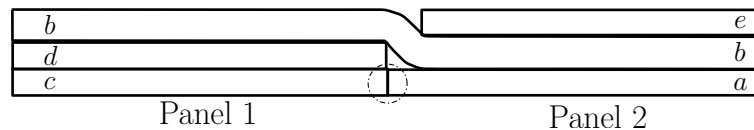
(b) Not fully blended.

Even though the concept of "panel" itself is not trivial to define within a multi-shaped laminate, one can always consider the "holes" of each ply filled with another material (Configuration I, Section 3.2), so that the blending feature does not intervene. Conversely, if the "holes" within each ply must be necessarily void and inwardly flatten (Configuration II), we must at least suppose that the measure of the common interior interface between two plies with shapes Ω_i, Ω_j is negligible, i.e. $|\partial\Omega_i \cap \partial\Omega_j| = 0, \forall i, j = 1, ..., N$. Nevertheless, since during the optimization process the shapes evolve freely, this constraint is rather difficult to verify at each iteration.

- **Fulfilling the manufacturing constraints pointwise.** At each iteration, when the

constraint margin function is evaluated, the optimal stacking sequence fulfills "globally" the manufacturing constraints, notably the minimal proportion of plies with a certain fiber orientation. Nevertheless, since the shape of each ply is different from the others, the manufacturing constraints should rather be satisfied pointwise. Unfortunately this is not possible from a numerical point of view, due to the large number of nodes involved in the mesh of Ω. This drawback is "artificially" avoided by considering the "holes" of each ply filled with a neutral material which for manufacturing purposes behaves in the same way the main material occupying the ply.

- **Worst case of the OA method.** Albeit the OA method always provides a deterministic optimal solution, the worst-case involves testing all the admissible solutions, as for any deterministic method.

(2) Chapter 4 was devoted to determine the topological derivative DJ of an ellipsoidal inclusion in an anisotropic elastostatic framework of a criterion J that depends upon the elastic displacements and stresses. These developments were motivated by the current lack of material in literature treating the foregoing case. Thus, a formula of the topological derivative DJ was established for a large class of mechanical criteria, namely displacement-based functions, pointwise approximations of the von Mises and Hill-Tsai yield criteria and quadratic energy-like functionals oriented to inverse problems. The general formula of DJ relies on the concept of elastic moment tensor, the classical adjoint state and the computation of the inner and outer values (w.r.t. the inclusion) of the solution of the free-space transmission problem. The elastic moment tensor is expressed in terms of the so-called Eshelby tensor. A complete analysis of the numerical evaluation of DJ was furnished, yielding a powerful tool for potential applications on problems involving inherent anisotropy, such as bone tissue imaging, flaw identification in composites and topology optimization subject to the Hill-Tsai failure criterion.

(3) Chapter 5 addressed the optimal design of a solide oxide fuel cell as a complement of an aircraft engine. First, a simplified model of a periodical micro-tubular fuel cell and its consequent homogenization was presented, enabling a suitable tool for evaluating the physical behavior of the simplified device. Then an optimal design problem formulated as an inverse homogenization problem was established, looking for the best shape of the micro fuel tube inside the unit cell. This problem was solved via a level-set method for topology optimization, allowing the design of fuel cells which can easily be manufactured by 3D printers. The foregoing study thus suggests a promising use of these technologies in the future computer aided design of fuel cells.

Perspectives

As possible future works, we suggest the following issues:

- Incorporate other typical composite manufacturing constraints (or "best practices" rules) in the optimization process. For example the requirement that the fibers of the outer plies located on the surface of the laminate must be oriented in 90°. As a matter of fact, most of these constraints (see e.g. [36, 125]) can be managed as linear constraints, likewise those presented.

- Add more plies to the composite design problem. Thanks to the parallelizable structure of the proposed method, the main restriction in terms of numerical cost for the algorithm lies in the mixed integer programming solver needed to evaluate the constraint margin function.

- Endow the total weight of the composite structure with different multipliers (or densities) ρ_{ij} according to each fiber orientation and position within the laminate, in order to obtain

a more "uniform" distribution of the mass through the laminate. Thus, the modified total weight will read

$$\hat{V}(\Omega, \xi) = \sum_{i=1}^{N} \sum_{j=1}^{4} \rho_{ij} \xi_{ij} \int_{\Omega} \chi_i dV, \ \rho_{ij} > 0.$$

This measure tends to enforce the presence of the disadvantaged fiber orientations by assigning them lower densities. Since the objective function now depends on the stacking sequence ξ, a more general decomposition framework must be applied. See e.g. [141].

- Perform a robustness and sensitivity analysis of the topological derivative to different non-destructive control applications.

- Extend the general formula of the topological derivative to the anisotropic elastodynamic case.

- Incorporate the topological derivative in the level-set algorithm for anisotropic topology optimization [8].

- Enrich the fuel cell model by introducing electric interactions between different species [266].

Bibliography

[1] D. B. Adams, L. T. Watson, and Z. Gürdal. Blending of composite panel designs using genetic algorithms. In *Parallel and Distributed Processing Symposium., Proceedings International, IPDPS 2002, Abstracts and CD-ROM*, pages 6–pp. IEEE, 2001.

[2] D. B. Adams, L. T. Watson, Z. Gürdal, and C. M. Anderson-Cook. Genetic algorithm optimization and blending of composite laminates by locally reducing laminate thickness. *Advances in Engineering Software*, 35(1):35–43, 2004.

[3] M. Albertelli and J.-L. Vié. Algorithme mfd dédié aux level-set pour l'optimisation de formes. Technical report, Renault, École des Ponts, 2012.

[4] G. Allaire. *Shape optimization by the homogenization method*, volume 146. Springer, 2002.

[5] G. Allaire. *Conception optimale de structures*, volume 58. Springer, 2006.

[6] G. Allaire, E. Bonnetier, G. Francfort, and F. Jouve. Shape optimization by the homogenization method. *Numerische Mathematik*, 76(1):27–68, 1997.

[7] G. Allaire and C. Castro. A new approach for the optimal distribution of assemblies in a nuclear reactor. *Numerische Mathematik*, 89(1):1–29, 2001.

[8] G. Allaire, F. de Gournay, F. Jouve, and A.-M. Toader. Structural optimization using topological and shape sensitivity via a level-set method. *Control and Cybernetics*, 34:59–80, 2005.

[9] G. Allaire and A. Henrot. On some recent advances in shape optimization. *Comptes Rendus de l'Académie des Sciences-Series IIB-Mechanics*, 329(5):383–396, 2001.

[10] G. Allaire, F. Jouve, and A. Toader. A level-set method for shape optimization. *Comptes Rendus Mathematique*, 334(12):1125–1130, 2002.

[11] G. Allaire, F. Jouve, and A. Toader. Structural optimization using sensitivity analysis and a level-set method. *Journal of computational physics*, 194(1):363–393, 2004.

[12] G. Allaire, F. Jouve, and N. Van Goethem. Damage and fracture evolution in brittle materials by shape optimization methods. *Journal of Computational Physics*, 230(12):5010–5044, 2011.

[13] G. Allaire and R. Kohn. Optimal design for minimum weight and compliance in plane stress using extremal microstructures. *European journal of mechanics. A. Solids*, 12(6):839–878, 1993.

[14] G. Allaire and O. Pantz. Structural optimization with FreeFem + +. *Structural and Multidisciplinary Optimization*, 32(3):173–181, 2006.

[15] L. Ambrosio. Lecture notes on geometric evolution problems, distance function and viscosity solutions. *Calculus of variations and partial differential equations. Topics on geometrical evolution problems and degree theory*, pages 5–94, 1997.

[16] L. Ambrosio and G. Buttazzo. An optimal design problem with perimeter penalization. *Calculus of Variations and Partial Differential Equations*, 1(1):55–69, 1993.

[17] H. Ammari, E. Bretin, J. Garnier, W. Jing, H. Kang, and A. Wahab. Localization, stability, and resolution of topological derivative based imaging functionals in elasticity. *SIAM Journal on Imaging Sciences*, 6(4):2174–2212, 2013.

[18] H. Ammari, J. Garnier, V. Jugnon, and H. Kang. Stability and resolution analysis for a topological derivative based imaging functional. *SIAM Journal on Control and Optimization*, 50(1):48–76, 2012.

[19] H. Ammari and H. Kang. *Polarization and moment tensors with applications to inverse problems and effective medium theory.* Applied Mathematical Sciences, Vol. 162. Springer-Verlag, 2007.

[20] H. Ammari, H. Kang, and H. Lee. A boundary integral method for computing elastic moment tensors for ellipses and ellipsoids. *J. Comput. Math.*, 25:2–12, 2007.

[21] H. Ammari, H. Kang, H. Lee, and W.-K. Park. Asymptotic imaging of perfectly conducting cracks. *SIAM Journal on Scientific Computing*, 32(2):894–922, 2010.

[22] H. Ammari, H. Kang, G. Nakamura, and K. Tanuma. Complete asymptotic expansions of solutions of the system of elastostatics in the presence of an inclusion of small diameter and detection of an inclusion. *J. Elast.*, 67:97–129, 2002.

[23] H. Ammari, M. S. Vogelius, and D. Volkov. Asymptotic formulas for perturbations in the electromagnetic fields due to the presence of inhomogeneities of small diameter ii. the full maxwell equations. *Journal de mathématiques pures et appliquées*, 80(8):769–814, 2001.

[24] S. Amstutz. A penalty method for topology optimization subject to a pointwise state constraint. *ESAIM: Control, Optimisation and Calculus of Variations*, 16(03):523–544, 2010.

[25] S. Amstutz and H. Andrä. A new algorithm for topology optimization using a level-set method. *Journal of Computational Physics*, 216(2):573–588, 2006.

[26] S. Amstutz, I. Horchani, and M. Masmoudi. Crack detection by the topological gradient method. *Control and Cybernetics*, 34:81–101, 2005.

[27] S. Amstutz and A. A. Novotny. Topological optimization of structures subject to von mises stress constraints. *Structural and Multidisciplinary Optimization*, 41(3):407–420, 2010.

[28] S. Amstutz, A. A. Novotny, and E. A. de Souza Neto. Topological derivative-based topology optimization of structures subject to drucker-prager stress constraints. *Comp. Meth. Appl. Mech. Eng.*, 233:123–136, 2012.

[29] C. Antonio, A. T. Marques, and A. V. Soeiro. Optimization of laminated composite structures using a bilevel strategy. *Composite structures*, 33(4):193–200, 1995.

[30] J.-L. Armand, K. Lurie, and A. Cherkaev. Optimal control theory and structural design. *New directions in optimum structural design(A 85-48701 24-39). Chichester, England and New York, Wiley-Interscience, 1984,*, pages 211–229, 1984.

[31] J.-L. Auriault, C. Boutin, and C. Geindreau. *Homogenization of coupled phenomena in heterogenous media*, volume 149. John Wiley & Sons, 2010.

[32] D. Auroux, L. J. Belaid, and M. Masmoudi. Image restoration and classification by topological asymptotic expansion. *Variational formulations in mechanics: theory and applications*, pages 23–42, 2006.

[33] J. M. Ball. Convexity conditions and existence theorems in nonlinear elasticity. *Archive for rational mechanics and Analysis*, 63(4):337–403, 1976.

[34] A. Baumgartner, L. Harzheim, and C. Mattheck. Sko (soft kill option): the biological way to find an optimum structure topology. *Int. J. Fatigue*, 14:387–393, 1992.

[35] B. K. Bay, T. S. Smith, D. P. Fyhrie, and M. Saad. Digital volume correlation: three-dimensional strain mapping using x-ray tomography. *Experimental Mechanics*, 39(3):217–226, 1999.

[36] S. W. Beckwith. Designing with composites: Suggested best practices rules. *SAMPE Journal*, 45(1):17, 2009.

[37] C. Bellis and M. Bonnet. A fem-based topological sensitivity approach for fast qualitative identification of buried cavities from elastodynamic overdetermined boundary data. *Int. J. Solids Struct.*, 47:1221–1242, 2010.

[38] C. Bellis, M. Bonnet, and F. Cakoni. Acoustic inverse scattering using topological derivative of far-field measurements-based l^2 cost functionals. *Inverse Prob.*, 29:075012, 2013.

[39] C. Bellis, M. Bonnet, and B. B. Guzina. Apposition of the topological sensitivity and linear sampling approaches to inverse scattering. *Wave Motion*, 50:891–908, 2013.

[40] A. Ben Abda, M. Hassine, M. Jaoua, and M. Masmoudi. Topological sensitivity analysis for the location of small cavities in stokes flow. *SIAM J. Contr. Opt.*, 48:2871–2900, 2009.

[41] M. Bendsøe. Optimal shape design as a material distribution problem. *Structural and Multidisciplinary Optimization*, 1(4):193–202, 1989.

[42] M. Bendsøe. *Methods for optimization of structural topology, shape and material*. Springer Verlag, New York, 1995.

[43] M. Bendsøe and N. Kikuchi. Generating optimal topologies in structural design using a homogenization method. *Computer methods in applied mechanics and engineering*, 71(2):197–224, 1988.

[44] M. Bendsoe and O. Sigmund. *Topology optimization: theory, methods and applications*. Springer, 2004.

[45] M. P. Bendsøe. *Optimization of structural topology, shape, and material*. Springer, 1995.

[46] E. Beretta, E. Bonnetier, E. Francini, and A. L. Mazzucato. Small volume asymptotics for anisotropic elastic inclusions. *Inverse Prob. Imaging*, 6:1–23, 2011.

[47] M. S. Berger and P. C. Fife. On von karmans equations and the buckling of a thin elastic plate. *Bulletin of the American Mathematical Society*, 72(6):1006–1011, 1966.

[48] C. Bernardi and O. Pironneau. Sensitivity of darcy's law to discontinuities. *Chinese Annals of Mathematics*, 24(02):205–214, 2003.

[49] D. Bettebghor. *Optimisation biniveau de structures aéronautiques composites*. PhD thesis, ISAE-Sup'Aéro, Université de Toulouse, http://depozit.isae.fr/theses/2011/2011_Bettebghor_Dimitri.pdf, 2011.

[50] R. D. Bhargava and H. C. Radhakrishna. Elliptic inclusion in orthotropic medium. *J. Phys. Soc. Jpn.*, 19:396–405, 1964.

[51] F. Bloom and D. W. Coffin. *Handbook of the Thin Plate Buckling and Post Buckling*. CRC Press, 2001.

[52] D. Bojczuk and Z. Mróz. Topological sensitivity derivative and finite topology modifications: application to optimization of plates in bending. *Structural and Multidisciplinary Optimization*, 39(1):1–15, 2009.

[53] M. Bonnet. Higher-order topological sensitivity for 2-d potential problems. application to fast identification of inclusions. *Int. J. Solids Struct.*, 46:2275–2292, 2009.

[54] M. Bonnet and B. B. Guzina. Sounding of finite solid bodies by way of topological derivative. *Int. J. Num. Meth. Eng.*, 61:2344–2373, 2004.

[55] T. Borrvall and J. Petersson. Topology optimization of fluids in stokes flow. *International Journal for Numerical Methods in Fluids*, 41(1):77–107, 2003.

[56] J. Borwein and A. Lewis. *Convex analysis and nonlinear optimization: theory and examples*, volume 3. Springer, 2006.

[57] R. Bove and S. Ubertini. *Modeling solid oxide fuel cells: methods, procedures and techniques*, volume 1. Springer Science+ Business Media, 2008.

[58] D. Brackett, I. Ashcroft, and R. Hague. Topology optimization for additive manufacturing. In *22nd Annual International Solid Freeform Fabrication Symposium*, pages 348–362, 2011.

[59] C. J. Brampton and H. A. Kim. Optimization of tow steered fibre orientation using the level set method. In *10th World Congress on Structural and Multidisciplinary Optimization, Orlando FL, May*, 2013.

[60] H. Brezis. *Analyse fonctionelle*, volume 5. Masson, 1983.

[61] H. Brinkman. A calculation of the viscosity and the sedimentation constant for solutions of large chain molecules taking into account the hampered flow of the solvent through these molecules. *Physica*, 13(8):447–448, 1947.

[62] M. Bruyneel. Sfpa new parameterization based on shape functions for optimal material selection: application to conventional composite plies. *Structural and Multidisciplinary Optimization*, 43(1):17–27, 2011.

[63] M. Bruyneel, S. Grihon, and M. Sosonkina. New approach for the stacking sequence optimization based on continuous topology optimization. *8th ASMO UK/ISSMO conference on engineering optimization, London*, 2010.

[64] D. Bucur. Do optimal shapes exist? *Milan Journal of Mathematics*, 75(1):379–398, 2007.

[65] D. Bucur and G. Buttazzo. *Variational methods in shape optimization problems*. Birkhäuser Boston, 2005.

[66] M. Burger. A framework for the construction of level set methods for shape optimization and reconstruction. *Interfaces and Free boundaries*, 5(3):301–330, 2003.

[67] M. Burger, B. Hackl, and W. Ring. Incorporating topological derivatives into level set methods. *Journal of Computational Physics*, 194(1):344–362, 2004.

[68] H.-J. Butt, K. Graf, and M. Kappl. Introduction. *Physics and Chemistry of Interfaces*, pages 1–3, 2004.

[69] J. E. Cadman, S. Zhou, Y. Chen, and Q. Li. On design of multi-functional microstructural materials. *Journal of Materials Science*, 48(1):51–66, 2013.

[70] S. Campanato. *Sistemi ellittici in forma divergenza: regolarità all'interno*. Scuola normale superiore, 1980.

[71] A. Canelas, A. A. Novotny, and J. R. Roche. A new method for inverse electromagnetic casting problems based on the topological derivative. *Journal of Computational Physics*, 230(9):3570–3588, 2011.

[72] P. Cannarsa and P. Cardaliaguet. Representation of equilibrium solutions to the table problem of growing sandpiles. *Interfaces and free boundaries*, 6(4):435, 2004.

[73] A. Carpentier. *Optimisation multi-niveaux de panneaux composites*. PhD thesis, Université de Toulouse, Université Toulouse III-Paul Sabatier, http://thesesups.ups-tlse.fr/234/1/CarpentierAlban.pdf, 2008.

[74] J. Céa. Conception optimale ou identification de formes: calcul rapide de la dérivée directionnelle de la fonction coût. *Modélisation mathématique et analyse numérique*, 20(3):371–402, 1986.

[75] J. Céa, S. Garreau, P. Guillaume, and M. Masmoudi. The shape and topological optimization connection, IV WCCM, Part II (Buenos Aires, 1998). *Comp. Meth. Appl. Mech. Eng.*, 188:713–726, 2000.

[76] J. Céa, A. Gioan, and J. Michel. Quelques résultats sur l'identification de domaines. *Calcolo*, 10(3-4):207–232, 1973.

[77] J. Cea, A. Gioan, and J. Michel. Adaptation de la méthode du gradient à un problème d'identification de domaine. In *Computing Methods in Applied Sciences and Engineering Part 2*, pages 391–402. Springer, 1974.

[78] D. Cedio-Fengya, S. Moskow, and M. Vogelius. Identification of conductivity imperfections of small diameter by boundary measurements. continuous dependence and computational reconstruction. *Inverse Problems*, 14(3):553, 1998.

[79] D. J. Cedio-Fengya, S. Moskow, and M. Vogelius. Identification of conductivity imperfections of small diameter by boundary measurements. continuous dependence and computational reconstruction. *Inverse Prob.*, 14:553–595, 1998.

[80] V. J. Challis and J. K. Guest. Level set topology optimization of fluids in stokes flow. *International journal for numerical methods in engineering*, 79(10):1284–1308, 2009.

[81] A. Chambolle. A density result in two-dimensional linearized elasticity, and applications. *Archive for rational mechanics and analysis*, 167(3):211–233, 2003.

[82] I. Chavel. *Riemannian geometry: a modern introduction*. Cambridge university press, 2006.

[83] D. Chenais. On the existence of a solution in a domain identification problem. *Journal of Mathematical Analysis and Applications*, 52(2):189–219, 1975.

[84] K.-T. Cheng and N. Olhoff. An investigation concerning optimal design of solid elastic plates. *International Journal of Solids and Structures*, 17(3):305–323, 1981.

[85] A. Cherkaev. *Variational methods for structural optimization*, volume 140. Springer, 2000.

[86] P. Christensen and A. Klarbring. *An introduction to structural optimization*, volume 153. Springer, 2009.

[87] A. Christiansen, M. Nobel-Jørgensen, N. Aage, O. Sigmund, and J. Bærentzen. Topology optimization using an explicit interface representation. *Structural and Multidisciplinary Optimization*, pages 1–13, 2013.

[88] P. Ciarlet. *Theory of Plates, Mathematical Elasticity Vol II*, volume 27 of *Studies in Mathematics and its applications*. North Holland, 1997.

[89] P. G. Ciarlet. *Mathematical elasticity: Three-dimensional elasticity*, volume 1 of *Studies in Mathematics and its applications*. Elsevier, 1988.

[90] P. G. Ciarlet and P. Rabier. *Les équations de von Kármán*. Number 826 in Lecture Notes in Mathematics. Springer Verlag, 1980.

[91] F. Clarke. *Optimization and nonsmooth analysis*, volume 5. Society for Industrial Mathematics, 1987.

[92] P. Costamagna, A. Selimovic, M. Del Borghi, and G. Agnew. Electrochemical model of the integrated planar solid oxide fuel cell (ip-sofc). *Chemical Engineering Journal*, 102(1):61–69, 2004.

[93] S. C. Cowin, G. Yang, and M. Mehrabadi. Bounds on the effective anisotropic elastic constants. *J. Elast.*, 57:1–24, 1999.

[94] B. Dacorogna. *Direct methods in the calculus of variations*, volume 78 of *Applied Mathematical Sciences*. Springer, 2007.

[95] M. Dambrine and D. Kateb. On the ersatz material approximation in level-set methods. *ESAIM: Control, Optimisation and Calculus of Variations*, 16(03):618–634, 2010.

[96] V. A. Danilov and M. O. Tade. A cfd-based model of a planar sofc for anode flow field design. *International Journal of Hydrogen Energy*, 34(21):8998–9006, 2009.

[97] C. Dapogny. *Ph.D. Thesis*. PhD thesis, Université Pierre et Marie Curie, http://tel.archives-ouvertes.fr/docs/00/91/62/24/PDF/thesedapogny.pdf, 2013.

[98] C. Dapogny and P. Frey. Computation of the signed distance function to a discrete contour on adapted triangulation. *Calcolo*, 49(3):193–219, 2012.

[99] F. De Gournay. *Optimisation de formes par la méthode des courbes de niveaux*. PhD thesis, Ecole Polytechnique, http://tel.archives-ouvertes.fr/docs/00/44/60/39/PDF/these.pdf, 2005.

[100] F. de Gournay. Velocity extension for the level-set method and multiple eigenvalues in shape optimization. *SIAM journal on control and optimization*, 45(1):343–367, 2006.

[101] R. De la Torre García. *Production of Micro-Tubular Solid Oxide Fuel Cells*. PhD thesis, University of Trento, http://eprints-phd.biblio.unitn.it/541/1/PRODUCTION_OF _MICRO-TUBULAR _SOLID _OXIDE _FUEL _CELLS.pdf, 2011.

[102] D. De Leon, C. de Souza, J. Fonseca, and R. da Silva. Aeroelastic tailoring using fiber orientation and topology optimization. *Structural and Multidisciplinary Optimization*, 46(5):663–677, 2012.

[103] M. Delfour and J. Zolesio. Shape identification via metrics constructed from the oriented distance function. *Control and Cybernetics*, 34(1):137, 2005.

[104] M. C. Delfour and J.-P. Zolésio. *Shapes and geometries: metrics, analysis, differential calculus, and optimization*, volume 22. SIAM, 2011.

[105] S. Dempe. *Foundations of bilevel programming*. Springer, 2002.

[106] A. Deraemaeker, P. Ladevèze, and P. Leconte. Reduced bases for model updating in structural dynamics based on constitutive relation error. *Comp. Meth. Appl. Mech. Eng.*, 191:2427–2444, 2002.

[107] M. Doblaré, J. M. Garcıa, and M. J. Gómez. Modelling bone tissue fracture and healing: a review. *Eng. Frac. Mech.*, 71:1809–1840, 2004.

[108] C. Dobrzynski and P. Frey. Anisotropic delaunay mesh adaptation for unsteady simulations. In *Proceedings of the 17th international Meshing Roundtable*, pages 177–194. Springer, 2008.

[109] N. Dunford and J. T. Schwartz. *Linear Operators: Vol.: 2: Spectral Theory: Self Adjoint Operators in Hilbert Space*. Interscience Publishers Incorporated, 1963.

[110] M. A. Duran and I. E. Grossmann. An outer-approximation algorithm for a class of mixed-integer nonlinear programs. *Mathematical programming*, 36(3):307–339, 1986.

[111] L. Durlofsky and J. Brady. Analysis of the brinkman equation as a model for flow in porous media. *Physics of Fluids*, 30(11):3329–3341, 1987.

[112] O. Erdal and F. O. Sonmez. Optimum design of composite laminates for maximum buckling load capacity using simulated annealing. *Composite Structures*, 71(1):45–52, 2005.

[113] H. A. Eschenauer, V. V. Kobelev, and A. Schumacher. Bubble method for topology and shape optimization of structures. *Structural Optimization*, 8:42–51, 1994.

[114] J. D. Eshelby. The determination of the elastic field of an ellipsoidal inclusion and related problems. *Proc. Roy. Soc. A*, 241:376–396, 1957.

[115] L. Evans and R. Gariepy. *Measure theory and fine properties of functions*. CRC, 1991.

[116] G. R. Feijóo. A new method in inverse scattering based on the topological derivative. *Inverse Prob.*, 20:1819–1840, 2004.

[117] R. Fletcher and S. Leyffer. Solving mixed integer nonlinear programs by outer approximation. *Mathematical programming*, 66(1-3):327–349, 1994.

[118] Freefem++. http://www.freefem.org/ff++/, 2013.

[119] Freeyams. *http://www.ann.jussieu.fr/frey/software.html*, 2001.

[120] G. Friesecke, R. D. James, and S. Müller. A hierarchy of plate models derived from nonlinear elasticity by gamma-convergence. *Archive for rational mechanics and analysis*, 180(2):183–236, 2006.

[121] M. Funnell. Targeting composite wing performance–optimum location of laminate boundaries. In *Proceedings of Altair UK CAE Technology Conference 2007*, 2007.

[122] G. Gardner. Lightning strike protection for composite structures. *High Performance Composites*, 14:44, 2006.

[123] S. Garreau, P. Guillaume, and M. Masmoudi. The topological asymptotic for pde systems: the elasticity case. *SIAM J. Contr. Opt.*, 39:1756–1778, 2001.

[124] A. Gavazzi and D. Lagoudas. On the numerical evaluation of eshelby's tensor and its application to elastoplastic fibrous composites. *Comp. Mech.*, 7:13–19, 1990.

[125] D. Gay, S. V. Hoa, and S. W. Tsai. *Composite materials: design and applications*. CRC press, 2002.

[126] L. Gibiansky and A. V. Cherkaev. Design of composite plates of extremal rigidity. In *Topics in the mathematical modelling of composite materials*, pages 95–137. Springer, 1997.

[127] S. M. Giusti, A. A. Novotny, and C. Padra. Topological sensitivity analysis of inclusion in two-dimensional linear elasticity. *Eng. Anal. Bound. Elem.*, 32:926–935, 2008.

[128] J. Gomes and O. Faugeras. Reconciling distance functions and level sets. *Journal of Visual Communication and Image Representation*, 11(2):209–223, 2000.

[129] B. Gou, W. K. Na, and B. Diong. *Fuel cells: modeling, control, and applications*. CRC press, 2009.

[130] I. S. Gradshteyn and I. M. Ryzhik. *Tables of integrals, series and products (seventh edition)*. Elsevier, 2007.

[131] J. Guest, J. Prévost, and T. Belytschko. Achieving minimum length scale in topology optimization using nodal design variables and projection functions. *International Journal for Numerical Methods in Engineering*, 61(2):238–254, 2004.

[132] J. K. Guest and J. H. Prévost. Design of maximum permeability material structures. *Computer Methods in Applied Mechanics and Engineering*, 196(4):1006–1017, 2007.

[133] Z. Gürdal, R. T. Haftka, and P. Hajela. *Design and optimization of laminated composite materials*. Wiley. com, 1999.

[134] Gurobi-Optimization. Gurobi. *http://www.gurobi.com/resources/getting-started/mip-basics*.

[135] B. B. Guzina and M. Bonnet. Small-inclusion asymptotic of misfit functionals for inverse problems in acoustics. *Inverse Problems*, 22(5):1761, 2006.

[136] B. B. Guzina and I. Chikichev. From imaging to material identification: a generalized concept of topological sensitivity. *J. Mech. Phys. Solids*, 55:245–279, 2007.

[137] B. B. Guzina and H. Yuan. On the small-defect perturbation and sampling of heterogeneous solids. *Acta Mech.*, 205:51–75, 2009.

[138] J. Hadamard. *Mémoire sur le problème d'analyse relatif à l'équilibre des plaques élastiques encastrées*, volume 33. Imprimerie nationale, 1908.

[139] R. T. Haftka, Z. Gürdal, and M. Kamat. *Elements of structural optimization*, volume 11. Springer, 1992.

[140] R. T. Haftka and J. L. Walsh. Stacking-sequence optimization for buckling of laminated plates by integer programming. *AIAA journal*, 30(3):814–819, 1992.

[141] R. T. Haftka and L. T. Watson. Multidisciplinary design optimization with quasiseparable subsystems. *Optimization and Engineering*, 6(1):9–20, 2005.

[142] P. Hajela and E. Lee. Genetic algorithms in truss topological optimization. *International journal of solids and structures*, 32(22):3341–3357, 1995.

[143] J. Haslinger and J. Dvorak. Optimum composite material design. *RAIRO-M2AN Modelisation Math et Analyse Numerique-Mathem Modell Numerical Analysis*, 29(6):657–686, 1995.

[144] A. Henrot and M. Pierre. *Variation et Optimisation des formes, Une analyse géométrique*, volume 48 of *Mathématiques et Applications*. Springer, 2005.

[145] J. E. Herencia, R. T. Haftka, P. M. Weaver, and M. I. Friswell. Lay-up optimization of composite stiffened panels using linear approximations in lamination space. *AIAA journal*, 46(9):2387–2391, 2008.

[146] J. E. Herencia, P. M. Weaver, and M. I. Friswell. Optimization of long anisotropic laminated fiber composite panels with t-shaped stiffeners. *AIAA journal*, 45(10):2497–2509, 2007.

[147] F. Hettlich and W. Rundell. The determination of a discontinuity in a conductivity from a single boundary measurement. *Inverse Problems*, 14(1):67, 1998.

[148] S. Hildebrandt and A. Tromba. *The parsimonious universe: shape and form in the natural world*. Springer, 1996.

[149] M. Hintermuller. Fast level set based algorithms using shape and topological sensitivity information. *Control and Cybernetics*, 34:305–324, 2005.

[150] M. Hintermüller and A. Laurain. Electrical impedance tomography: from topology to shape. *Control & Cybernetics*, 37(4), 2008.

[151] M. Hintermüller and A. Laurain. Multiphase image segmentation and modulation recovery based on shape and topological sensitivity. *Journal of Mathematical Imaging and Vision*, 35(1):1–22, 2009.

[152] M. Hintermüller, A. Laurain, and A. A. Novotny. Second-order topological expansion for electrical impedance tomography. *Advances in Computational Mathematics*, 36(2):235–265, 2012.

[153] E. Hinton and J. Sienz. Fully stressed topological design of structures using an evolutionary procedure. *Eng. Comp.*, 12:229–244, 1995.

[154] M. F. Hordeski. *Hydrogen and Fuel Cells: Advances in Transportation and Power*. The Fairmont Press, Inc., 2009.

[155] U. Hornung. *Homogenization and porous media*, volume 6. Springer, 1997.

[156] U. Hornung and W. Jäger. Diffusion, convection, adsorption, and reaction of chemicals in porous media. *Journal of differential equations*, 92(2):199–225, 1991.

[157] B. C. Hoskin. Composite materials for aircraft structures. *B. C. Hoskin, Ed, and A. A. Baker, Ed, New York, American Institute of Aeronautics and Astronautics, Inc., 1986, 245*, 1986.

[158] S. Hosseini, K. Ahmed, and M. O. Tadé. Cfd model of a methane fuelled single cell sofc stack for analysing the combined effects of macro/micro structural parameters. *Journal of Power Sources*, 2013.

[159] X. Huang and M. Xie. *Evolutionary topology optimization of continuum structures: methods and applications.* John Wiley & Sons, 2010.

[160] T. J. Hughes. *The Finite Element Method. Linear Static and Dynamic Finite Element Analysis.* Dover Publications, Inc, New York, 1987.

[161] M. Hussain, X. Li, and I. Dincer. Mathematical modeling of planar solid oxide fuel cells. *Journal of Power Sources*, 161(2):1012–1022, 2006.

[162] C. F. Hvejsel, E. Lund, and M. Stolpe. Optimization strategies for discrete multi-material stiffness optimization. *Structural and Multidisciplinary Optimization*, 44(2):149–163, 2011.

[163] C. Hwu and T. C. T. Ting. Two-dimensional problems of the anisotropic elastic solid with an elliptic inclusion. *Quart. J. Mech. Appl. Math.*, 42:553–572, 1989.

[164] IBM-ILOG. Cplex. *http://www-01.ibm.com/software/commerce/optimization/cplex-optimizer/*.

[165] A. M. Il'in. *Matching of asymptotic expansions of solutions of boundary value problems.* American Mathematical Society, 1992.

[166] INRIA. 3d research meshes database, gamma project. *http://www-roc.inria.fr/gamma/gamma/Accueil/*, 2012.

[167] F.-X. Irisarri, D. H. Bassir, N. Carrere, and J.-F. Maire. Multiobjective stacking sequence optimization for laminated composite structures. *Composites Science and Technology*, 69(7):983–990, 2009.

[168] L. Jaafar Belaid, M. Jaoua, M. Masmoudi, and L. Siala. Application of the topological gradient to image restoration and edge detection. *Engineering Analysis with Boundary Elements*, 32(11):891–899, 2008.

[169] L. Jackowska-Strumillo, J. Sokolowski, and A. Żochowski. Topological optimization and inverse problems. *Computer Assisted Mechanics and Engineering Sciences*, 10:163–176, 2003.

[170] L. Jackowska-Strumillo, J. Sokolowski, A. Żochowski, and A. Henrot. On numerical solution of shape inverse problems. *Computational Optimization and Applications*, 23(2):231–255, 2002.

[171] R. M. Jones. *Mechanics of composite materials.* CRC Press, 1998.

[172] C. Kane and M. Schoenauer. Topological optimum design using genetic algorithms. *Control and Cybernetics*, 25:1059–1088, 1996.

[173] A. Karchevsky. Reconstruction of pressure velocities and boundaries of thin layers in thinly-stratified layers. *Journal of Inverse and Ill-Posed Problems*, 18(4):371–388, 2010.

[174] R. J. Kee, H. Zhu, R. J. Braun, and T. L. Vincent. Chapter 6 - modeling the steady-state and dynamic characteristics of solid-oxide fuel cells. In K. Sundmacher, editor, *Fuel Cell Engineering*, volume 41 of *Advances in Chemical Engineering*, pages 331 – 381. Academic Press, 2012.

[175] G. M. Kelly, J. I. Kilpatrick, M. H. Van Es, P. P. Weafer, P. J. Prendergast, and S. P. Jarvis. Bone cell elasticity and morphology changes during the cell cycle. *J. Biomech.*, 44:1484–1490, 2011.

[176] B. Kenney and K. Karan. Mathematical micro-model of a solid oxide fuel cell composite cathode. *Proceedings hydrogen and fuel cells*, pages 1–11, 2004.

[177] P. Kesavan, R. J. Allgor, E. P. Gatzke, and P. I. Barton. Outer approximation algorithms for separable nonconvex mixed-integer nonlinear programs. *Mathematical Programming*, 100(3):517–535, 2004.

[178] H. Kielhofer. *Bifurcation theory*. Springer, 2004.

[179] E. Kita and T. Toyoda. Structural design using cellular automata. *Structural and Multidisciplinary Optimization*, 19(1):64–73, 2000.

[180] V. Kobelev. bubble-and-grain method and criteria for optimal positioning inhomogeneities in topological optimization. *Structural and Multidisciplinary Optimization*, 40(1-6):117–135, 2010.

[181] R. Kohn and A. McKenney. Numerical implementation of a variational method for electrical impedance tomography. *Inverse Prob.*, 6:389–414, 1990.

[182] R. V. Kohn and G. Strang. Optimal design and relaxation of variational problems; Parts I, II, III. *Communications on Pure and Applied Mathematics*, 39(1):113–137, 1986.

[183] L. Krog, A. Tucker, and G. Rollema. Application of topology, sizing and shape optimization methods to optimal design of aircraft components. In *Proc. 3rd Altair UK HyperWorks Users Conference*, 2002.

[184] T. A. Krouskop, T. M. Wheeler, F. Kallel, B. S. Garra, and T. Hall. Elastic moduli of breast and prostate tissues under compression. *Ultrasonic imaging*, 20:260–274, 1998.

[185] A. Kumar and R. Reddy. Modeling of polymer electrolyte membrane fuel cell with metal foam in the flow-field of the bipolar/end plates. *Journal of power sources*, 114(1):54–62, 2003.

[186] V. D. Kupradze, editor. *Three-dimensional problems of the mathematical theory of elasticity and thermoelasticity*. North Holland, 1979.

[187] P. Ladevèze and D. Leguillon. Error estimate procedure in the finite element method and applications. *SIAM J. Numer. Anal.*, 20:485–509, 1983.

[188] I. Larrabide, R. Feijóo, A. Novotny, and E. Taroco. Topological derivative: a tool for image processing. *Computers & Structures*, 86(13):1386–1403, 2008.

[189] R. Le Riche and R. T. Haftka. Optimization of laminate stacking sequence for buckling load maximization by genetic algorithm. *AIAA journal*, 31(5):951–956, 1993.

[190] V. I. Lebedev and D. N. Laikov. A quadrature formula for the sphere of the 131st algebraic order of accuracy. *Doklady Mathematics*, 59(3):477–481, 1999.

[191] M. Lecumberry and S. Müller. Stability of slender bodies under compression and validity of the von kármán theory. *Archive for rational mechanics and analysis*, 193(2):255–310, 2009.

[192] R. R. B. Lehoucq, D. D. C. Sorensen, and C.-C. Yang. *Arpack User's Guide: Solution of Large-Scale Eigenvalue Problems With Implicityly Restorted Arnoldi Methods*, volume 6. Siam, 1998.

[193] G. Leugering, S. Nazarov, F. Schury, and M. Stingl. The eshelby theorem and application to the optimization of an elastic patch. *SIAM J. Appl. Math.*, 72:512–534, 2012.

[194] D. Li and X. Sun. *Nonlinear integer programming*. Springer, 2006.

[195] Y. Li and L. Nirenberg. Estimates for elliptic systems from composite material. *Communications on pure and applied mathematics*, 56(7):892–925, 2003.

[196] C.-C. Lin and Y.-J. Lee. Stacking sequence optimization of laminated composite structures using genetic algorithm with local improvement. *Composite structures*, 63(3):339–345, 2004.

[197] E. Lindgaard and E. Lund. Nonlinear buckling optimization of composite structures. *Computer methods in applied mechanics and engineering*, 199(37):2319–2330, 2010.

[198] J. L. Lions and S. K. Mitter. *Optimal control of systems governed by partial differential equations*, volume 1200. Springer Berlin, 1971.

[199] R. Lipton. Design of functionally graded composite structures in the presence of stress constraints. *International journal of solids and structures*, 39(9):2575–2586, 2002.

[200] B. Liu and R. Haftka. Single-level composite wing optimization based on flexural lamination parameters. *Structural and Multidisciplinary Optimization*, 26(1-2):111–120, 2004.

[201] B. Liu, R. T Haftka, M. A Akgün, and A. Todoroki. Permutation genetic algorithm for stacking sequence design of composite laminates. *Computer Methods in Applied Mechanics and Engineering*, 186(2):357–372, 2000.

[202] D. Liu, V. V. Toroporov, O. M. Querin, and D. C. Barton. Bilevel optimization of blended composite wing panels. *Journal of Aircraft*, 48(1):107–118, 2011.

[203] W. Liu, R. Butler, and H. A. Kim. Optimization of composite stiffened panels subject to compression and lateral pressure using a bi-level approach. *Structural and Multidisciplinary Optimization*, 36(3):235–245, 2008.

[204] W. Liu, R. Butler, A. R. Mileham, and A. J. Green. Bilevel optimization and postbuckling of highly strained composite stiffened panels. *AIAA journal*, 44(11):2562–2570, 2006.

[205] E. Lund. Buckling topology optimization of laminated multi-material composite shell structures. *Composite Structures*, 91(2):158–167, 2009.

[206] K. Lurie and A. Cherkaev. Effective characteristics of composite materials and the optimal design of structural elements. In *Topics in the mathematical modelling of composite materials*, pages 175–271. Springer, 1997.

[207] C. Mantegazza and A. Mennucci. Hamilton-jacobi equations and distance functions on riemannian manifolds. *Applied Mathematics and Optimization*, 47(1):1–26, 2003.

[208] M. Masmoudi. A synthetic presentation of shape and topological optimization. *Les problemes inverses, le contrôle et loptimisation de formes, PICOF*, 98:121–127, 1998.

[209] M. Masmoudi, J. Pommier, and B. Samet. The topological asymptotic expansion for the maxwell equations and some applications. *Inverse Prob.*, 21:547–564, 2005.

[210] MATLAB. *version 8.0 (R2012b)*. The MathWorks Inc., Natick, Massachusetts, 2012.

[211] C. Mattheck. Design and growth rules for biological structures and their application to engineering. *Fatigue & Fracture of Engineering Materials & Structures*, 13(5):535–550, 1990.

[212] V. Maz'ya, S. A. Nazarov, and B. A. Plamenevskii. *Asymptotic theory of elliptic boundary value problems under a singular perturbation of the domains (vols. 1 and 2)*. Birkhaüser, 2000.

[213] W. McLean. *Strongly elliptic systems and boundary integral equations*. Cambridge university press, 2000.

[214] Medit. *http://www.ann.jussieu.fr/frey/software.html*, 2001.

[215] M. M. Mehrabadi and S. C. Cowin. Eigentensors of linear anisotropic elastic materials. *Quart. J. Mech. Appl. Math.*, 43:14, 1990.

[216] Y. Mei and X. Wang. A level set method for structural topology optimization and its applications. *Advances in Engineering Software*, 35(7):415–441, 2004.

[217] Y. Mei and X. Wang. A level set method for structural topology optimization with multi-constraints and multi-materials. *Acta Mechanica Sinica*, 20(5):507–518, 2004.

[218] A. G. Mersha and S. Dempe. Feasible direction method for bilevel programming problem. *Optimization*, 61(5):597–616, 2012.

[219] L. Mesquita and M. P. Kamat. Optimization of stiffened laminated composite plates with frequency constraints. *Engineering Optimization*, 11(1-2):77–88, 1987.

[220] G. Michailidis. *Manufacturing Constraints and Multi-Phase Shape and Topology Optimization via a Level-Set Method*. PhD thesis, Ecole Polytechnique, http://tel.archives-ouvertes.fr/docs/00/93/73/06/PDF/thesis.pdf, 2014.

[221] A. M. Micheletti. Metrica per famiglie di domini limitati e proprieta generiche degli autovalori. *Annali della Scuola Normale Superiore di Pisa-Classe di Scienze*, 26(3):683–694, 1972.

[222] M. Miki and Y. Sugiyamat. Optimum design of laminated composite plates using lamination parameters. *AIAA journal*, 31(5):921–922, 1993.

[223] G. Milton. *The theory of composites*, volume 6. Cambridge University Press, 2002.

[224] B. Mohammadi and O. Pironneau. *Applied shape optimization for fluids*, volume 28. Oxford University Press Oxford, 2001.

[225] E. Moullet. Optimisation du design d'une pile à combustible. Technical report, École de Mines, EADS, 2013.

[226] E. Munoz. *Global optimization for structural design by generalized benders decomposition*. PhD thesis, PhD thesis, Department of Mathematics, Technical University of Denmark, http://orbit.dtu.dk/fedora/objects/orbit:82868/datastreams/file_5125176/content, 2010.

[227] T. Mura. *Micromechanics of Defects in Solids*. Martinus Nijhoff, 1987.

[228] F. Murat. Contre-exemples pour divers problemes ou le contrôle intervient dans les coefficients. *Annali di Matematica Pura ed Applicata*, 112(1):49–68, 1977.

[229] F. Murat and J. Simon. *Quelques résultats sur le contrôle par un domaine géométrique*. VI Laboratoire d'Analyse Numérique, 1974.

[230] F. Murat and J. Simon. Etude de problèmes d'optimal design. *Optimization Techniques Modeling and Optimization in the Service of Man Part 2*, pages 54–62, 1976.

[231] F. Murat and J. Simon. Sur le contrôle par un domaine géométrique, publications du laboratoire d'analyse numéerique (université paris VI). 1976.

[232] F. Murat and L. Tartar. Calcul des variations et homogénéisation, In les méthodes de l'homogénéisation: théorie et applications en physique. *Coll. Dir. Etudes et Recherches EDF*, (57):319–369, 1985.

[233] S. Nagendra, R. T. Haftka, and Z. Gürdal. Stacking sequence optimization of simply supported laminates with stability and strain constraints. *AIAA journal*, 30(8):2132–2137, 1992.

[234] S. Nagendra, D. Jestin, Z. Gürdal, R. T. Haftka, and L. T. Watson. Improved genetic algorithm for the design of stiffened composite panels. *Computers & Structures*, 58(3):543–555, 1996.

[235] S. Nagendra, S. Kodiyalam, J. E. Davis, and V. Parthasarathy. Optimization of tow fiber paths for composite design. In *Proceedings of the AIAA/ASME/ASCE/AHS/ASC 36th Structures, Structural Dynamics and Materials Conference, New Orleans, LA*, pages 1031–41, 1995.

[236] National Institute of Advanced Industrial Science and Technology. https://www.aist:go:jp/index, 2009.

[237] S. Nazarov. Elasticity polarization tensor, surface enthalpy, and eshelby theorem. *Journal of Mathematical Sciences*, 159(2):133–167, 2009.

[238] S. A. Nazarov. Elasticity polarization tensor, surface enthalpy, and eshelby theorem. *J. Math. Sci.*, 159:133–167, 2009.

[239] S. A. Nazarov, J. Sokolowski, and M. Specovius-Neugebauer. Polarization matrices in anisotropic heterogeneous elasticity. *Asympt. Anal.*, 68:189–221, 2010.

[240] P. Neittaanmäki, P. N. Aki, and D. Tiba. Existence and approximation in optimal shape design problems. *Citeseer*, 1998.

[241] B. Niu, N. Olhoff, E. Lund, and G. Cheng. Discrete material optimization of vibrating laminated composite plates for minimum sound radiation. *International Journal of Solids and Structures*, 47(16):2097–2114, 2010.

[242] J. Nocedal and S. Wright. *Numerical optimization.* Springer Science+ Business Media, 2006.

[243] A. Novotny, R. Feijóo, C. Padra, and E. Taroco. Topological derivative for linear elastic plate bending problems. *Control and Cybernetics*, 34:339–361, 2005.

[244] A. Novotny, R. Feijóo, E. Taroco, and C. Padra. Topological sensitivity analysis for three-dimensional linear elasticity problem. *Computer Methods in Applied Mechanics and Engineering*, 196(41):4354–4364, 2007.

[245] A. Novotny and J. Sokołowski. *Topological Derivatives in Shape Optimization.* Springer, 2013.

[246] A. A. Novotny, R. Feijóo, E. Taroco, and C. Padra. Topological sensitivity analysis. *Computer Methods in Applied Mechanics and Engineering*, 192(7):803–829, 2003.

[247] I. Nowak. *Relaxation and decompostion methods for mixed integer nonlinear programming*, volume 152. Birkhäuser Basel, 2005.

[248] Z. Oralbekova, K. Iskakov, and A. Karchevsky. Existence of the residual functional derivative with respect to a coordinate of gap point of medium. *Applied and Computational Mathematics*, 12(2):222–233, 2013.

[249] J. Ortega and W. Rheinboldt. On discretization and differentiation of operators with application to newton's method. *SIAM journal on numerical analysis*, 3(1):143–156, 1966.

[250] S. Osher and R. Fedkiw. *Level set methods and dynamic implicit surfaces*, volume 153. Springer Verlag, 2003.

[251] S. Osher and F. Santosa. Level set methods for optimization problems involving geometry and constraints: I. frequencies of a two-density inhomogeneous drum. *Journal of Computational Physics*, 171(1):272–288, 2001.

[252] S. Osher and J. Sethian. Fronts propagating with curvature-dependent speed: algorithms based on hamilton-jacobi formulations. *Journal of computational physics*, 79(1):12–49, 1988.

[253] J. Palsson, A. Selimovic, and L. Sjunnesson. Combined solid oxide fuel cell and gas turbine systems for efficient power and heat generation. *Journal of Power Sources*, 86(1):442–448, 2000.

[254] O. Pantz. Sensibilité de l'équation de la chaleur aux sauts de conductivité. *Comptes Rendus Mathematique*, 341(5):333–337, 2005.

[255] O. Pironneau. *Optimal shape design for elliptic systems*. Springer, 1984.

[256] S. I. Ranganathan and M. Ostoja-Starzewski. Universal elastic anisotropy index. *Phys. Rev. Lett.*, 101:055504, 2008.

[257] J. N. Reddy. *Mechanics of laminated composite plates: theory and analysis*, volume 1. CRC press Boca Raton, 1997.

[258] J. Reuther and A. Jameson. *Aerodynamic shape optimization of complex aircraft configurations via an adjoint formulation*. Research Institute for Advanced Computer Science, NASA Ames Research Center, 1996.

[259] B. Roth and R. Giffin III. Fuel cell hybrid propulsion challenges and opportunities for commercial aviation. *AIAA Paper*, 6537:2010, 2010.

[260] B. Rousselet and D. Chenais. Continuité et différentiabilité d'éléments propres: application à l'optimisation de structures. *Applied Mathematics and Optimization*, 22(1):27–59, 1990.

[261] D. Roylance. Laminated composite plates. *Massachusetts Institute of Technology Cambridge*, 2000.

[262] G. I. Rozvany. A critical review of established methods of structural topology optimization. *Structural and Multidisciplinary Optimization*, 37(3):217–237, 2009.

[263] B. Samet, S. Amstutz, and M. Masmoudi. The topological asymptotic for the Helmholtz equation. *SIAM J. Control Optim.*, 42:1523–1544, 2004.

[264] S. Samuelsen. Fuel cell/gas turbine hybrid systems. *ASME International Gas Turbine Institute*, 2004.

[265] S. Schmidt and V. Schulz. Shape derivatives for general objective functions and the incompressible navier-stokes equations. *Control and Cybernetics*, 39(3):677–713, 2010.

[266] M. Schmuck and P. Berg. Homogenization of a catalyst layer model for periodically distributed pore geometries in pem fuel cells. *Applied Mathematics Research eXpress*, 2013(1):57–78, 2013.

[267] M. Schneider and H. Andrä. The topological gradient in anisotropic elasticity with an eye towards lightweight design. *Math. Meth. in Appl. Sc.*, 2013, in press.

[268] A. Schumacher. *Topologieoptimierung von Bauteilstrukturen unter Verwendung von Lochpositionierungskriterien*. PhD thesis, Forschungszentrum für Multidisziplinäre Analysen und Angewandte Strukturoptimierung. Institut für Mechanik und Regelungstechnik, 1996.

[269] Scilab. A scientific software developed by inria and enpc, freely downloadable at http://www.scilab.org.

[270] O. Seresta, Z. Gürdal, D. B. Adams, and L. T. Watson. Optimal design of composite wing structures with blended laminates. *Composites Part B: Engineering*, 38(4):469–480, 2007.

[271] J. Sethian. *Level set methods and fast marching methods: evolving interfaces in computational geometry, fluid mechanics, computer vision, and materials science*, volume 3. Cambridge university press, 1999.

[272] J. Sethian and A. Wiegmann. Structural boundary design via level set and immersed interface methods. *Journal of computational physics*, 163(2):489–528, 2000.

[273] O. Sigmund. *Design of material structures using topology optimization*. PhD thesis, Technical University of Denmark Denmark, 1994.

[274] O. Sigmund. Materials with prescribed constitutive parameters: an inverse homogenization problem. *International Journal of Solids and Structures*, 31(17):2313–2329, 1994.

[275] O. Sigmund. Design of multiphysics actuators using topology optimization–part ii: Two-material structures. *Computer methods in applied mechanics and engineering*, 190(49):6605–6627, 2001.

[276] O. Sigmund. On the usefulness of non-gradient approaches in topology optimization. *Structural and Multidisciplinary Optimization*, 43(5):589–596, 2011.

[277] O. Sigmund and S. Torquato. Design of materials with extreme thermal expansion using a three-phase topology optimization method. *Journal of the Mechanics and Physics of Solids*, 45(6):1037–1067, 1997.

[278] M. Silva, M. Matalon, and D. A. Tortorelli. Higher order topological derivatives in elasticity. *Int. J. Solids Struct.*, 47:3053–3066, 2010.

[279] J. Simon and F. Murat. Sur le contrôle par un domaine géométrique. *Publication 76015 du Laboratoire d'Analyse Numérique de l'Université Paris VI*, (76015):222 pages, 1976.

[280] S. Singhal. Advances in solid oxide fuel cell technology. *Solid state ionics*, 135(1):305–313, 2000.

[281] A. S. Sinwel. *A New Family of Mixed Finite Elements for Elasticity*. PhD thesis, Johannes Kepler Universitat, Austria, http://www.hpfem.jku.at/publications/sinwel_thesis.pdf, 2009.

[282] J. Sobieszczanski-Sobieski and R. T. Haftka. Multidisciplinary aerospace design optimization: survey of recent developments. *Structural optimization*, 14(1):1–23, 1997.

[283] J. Sokolowski and A. Zochowski. On topological derivative in shape optimization. *INRIA*, 1997.

[284] J. Sokolowski and A. Zochowski. On the topological derivative in shape optimization. *SIAM J. Control Optim.*, 37:1251–1272, 1999.

[285] J. Sokolowski and J.-P. Zolesio. *Introduction to shape optimization.* Springer, 1992.

[286] G. Soremekun, Z. Gürdal, R. Haftka, and L. Watson. Composite laminate design optimization by genetic algorithm with generalized elitist selection. *Computers & Structures*, 79(2):131–143, 2001.

[287] G. Soremekun, Z. Gürdal, C. Kassapoglou, and D. Toni. Stacking sequence blending of multiple composite laminates using genetic algorithms. *Composite Structures*, 56(1):53–62, 2002.

[288] J. H. Starnes Jr and R. T. Haftka. Preliminary design of composite wings for buckling, strength, and displacement constraints. *Journal of Aircraft*, 16(8):564–570, 1979.

[289] C. J. Steffen Jr, J. E. Freeh, and L. M. Larosiliere. Solid oxide fuel cell/gas turbine hybrid cycle technology for auxiliary aerospace power. *Proceedings of the ASME Turbo Expo, Reno-Tahoe, United States*, 2005.

[290] J. Stegmann and E. Lund. Discrete material optimization of general composite shell structures. *International Journal for Numerical Methods in Engineering*, 62(14):2009–2027, 2005.

[291] M. Stolpe and K. Svanberg. An alternative interpolation scheme for minimum compliance topology optimization. *Structural and Multidisciplinary Optimization*, 22(2):116–124, 2001.

[292] J. Strain. Semi-lagrangian methods for level set equations. *Journal of Computational Physics*, 151(2):498–533, 1999.

[293] N. Sukumar, D. Chopp, N. Moës, and T. Belytschko. Modeling holes and inclusions by level sets in the extended finite-element method. *Computer methods in applied mechanics and engineering*, 190(46):6183–6200, 2001.

[294] S. Suresh. Nanomedicine: elastic clues in cancer detection. *Nature Nanotechnology*, 2:748–749, 2007.

[295] S. Suresh, A. Mortensen, and S. Suresh. *Fundamentals of functionally graded materials.* Institute of Materials London, 1998.

[296] M. Sussman, P. Smereka, and S. Osher. *A level set approach for computing solutions to incompressible two-phase flow.* Department of Mathematics, University of California, Los Angeles, 1994.

[297] K. Svanberg and M. Werme. Topology optimization by sequential integer linear programming. In *IUTAM Symposium on Topological Design Optimization of Structures, Machines and Materials*, pages 425–436. Springer, 2006.

[298] V. Šverak. On optimal shape design. *Journal de mathématiques pures et appliquées*, 72(6):537–551, 1993.

[299] C. Swan and I. Kosaka. Voigt-reuss topology optimization for structures with linear elastic material behaviours. *International Journal for Numerical Methods in Engineering*, 40(16):3033–3057, 1997.

[300] A. Takezawa, S. Nishiwaki, and M. Kitamura. Shape and topology optimization based on the phase field method and sensitivity analysis. *Journal of Computational Physics*, 229(7):2697–2718, 2010.

[301] L. Tartar. An introduction to the homogenization method in optimal design. *Optimal Shape Design*, pages 47–156, 2000.

[302] L. Tartar. *The general theory of homogenization: a personalized introduction*, volume 7. Springer, 2009.

[303] B. F. Tatting and Z. Gürdal. *Design and manufacture of elastically tailored tow placed plates*. National Aeronautics and Space Administration, Langley Research Center, 2002.

[304] Tetgen. *http://wias-berlin.de/software/tetgen/*, 2011.

[305] P. S. Theocaris and N. I. Ioakimidis. The inclusion problem in plane elasticity. *Quart. J. Mech. Appl. Math.*, 30:437–448, 1977.

[306] R. Tilley. *Understanding solids: the science of materials*. John Wiley & Sons, 2004.

[307] A. Todoroki and M. Sasai. Stacking sequence optimizations using ga with zoomed response surface on lamination parameters. *Advanced Composite Materials*, 11(3):299–318, 2002.

[308] R. Tokmashev, A. Tixier, and B. Guzina. Experimental validation of the topological sensitivity approach to elastic-wave imaging. *Inverse Prob.*, 29:125005, 2013.

[309] C. Truesdell. Comments on rational continuum mechanics. *Contemporary Developments in Continuum Mechanics and Partial Differential Equations (GM de Lapenha & LA Medeiros, Editors)*, pages 495–603, 1977.

[310] I. Turevsky, S. H. Gopalakrishnan, and K. Suresh. An efficient numerical method for computing the topological sensitivity of arbitrary-shaped features in plate bending. *International journal for numerical methods in engineering*, 79(13):1683–1702, 2009.

[311] J. van Campen, O. Seresta, M. M. Abdalla, and Z. Gürdal. General blending definitions for stacking sequence design of composite laminate structure. 49th AIAA/ASME/ASCE/AHS/ASC strutures, structural dynamics and material conference, Schaumburg, 2008.

[312] N. Vermaak, G. Michailidis, G. Parry, R. Estevez, Y. Brechet, and G. Allaire. Material interface effects on the topology optimization of multi-phase thermoelastic structures using a level set method. *(submitted in SMO: Structural and Multi-disciplinary Optimization)*, 2013.

[313] L. Vese and T. Chan. A multiphase level set framework for image segmentation using the mumford and shah model. *International journal of computer vision*, 50(3):271–293, 2002.

[314] M. S. Vogelius and D. Volkov. Asymptotic formulas for perturbations in the electromagnetic fields due to the presence of inhomogeneities of small diameter. *M2AN Math. Model. Num. Anal.*, 34:723–748, 2000.

[315] T. Von Karman. *Festigkeitsprobleme im maschinenbau*. 1910.

[316] M. Wang, S. Chen, X. Wang, and Y. Mei. Design of multimaterial compliant mechanisms using level-set methods. *Journal of Mechanical Design*, 127:941, 2005.

[317] M. Wang and X. Wang. Color level sets: a multi-phase method for structural topology optimization with multiple materials. *Computer Methods in Applied Mechanics and Engineering*, 193(6):469–496, 2004.

[318] M. Wang and X. Wang. A level-set based variational method for design and optimization of heterogeneous objects. *Computer-Aided Design*, 37(3):321–337, 2005.

[319] M. Wang, X. Wang, and D. Guo. A level set method for structural topology optimization. *Computer methods in applied mechanics and engineering*, 192(1):227–246, 2003.

[320] M. Y. Wang and S. Zhou. Phase field: a variational method for structural topology optimization. *Comput. Model. Eng. Sci*, 6(6):547–566, 2004.

[321] J. R. Willis. Anisotropic elastic inclusion problems. *Quart. J. Mech. Appl. Math.*, 17:157–174, 1963.

[322] T. Yamada, K. Izui, S. Nishiwaki, and A. Takezawa. A topology optimization method based on the level set method incorporating a fictitious interface energy. *Computer Methods in Applied Mechanics and Engineering*, 199(45):2876–2891, 2010.

[323] H.-S. Yang, T.-T. Guo, J.-H. Wu, and X. Ma. Inhomogeneous material property assignment and orientation definition of transverse isotropy of femur. *J. Biomed. Sc.*, 2:419–424, 2009.

[324] L. Yin and G. Ananthasuresh. Topology optimization of compliant mechanisms with multiple materials using a peak function material interpolation scheme. *Structural and Multidisciplinary Optimization*, 23(1):49–62, 2001.

[325] H. Yuan, B. B. Guzina, and R. Sinkus. Application of topological sensitivity toward tissue elasticity imaging using magnetic resonance data. *J. Eng. Mech. ASCE*, 2012.

[326] X. Yuan, S. Zhang, L. Pibouleau, and S. Domenech. Une méthode d'optimisation non linéaire en variables mixtes pour la conception de procédés. *RAIRO-Operations Research-Recherche Opérationnelle*, 22(4):331–346, 1988.

[327] M. Zhou, R. Fleury, and M. Kemp. Optimization of composite–recent advances and application. In *13th AIAA/ISSMO Multidisciplinary Analysis Optimization Conference, Fort Worth, Texas. September*, pages 13–15, 2010.

[328] S. Zhou and Q. Li. Computational design of multi-phase microstructural materials for extremal conductivity. *Computational Materials Science*, 43(3):549–564, 2008.

[329] S. Zhou and M. Wang. Multimaterial structural topology optimization with a generalized cahn–hilliard model of multiphase transition. *Structural and Multidisciplinary Optimization*, 33(2):89–111, 2007.

[330] Zuse-Institute-Berlin. Scip. *http://scip.zib.de/*.